Emerging Avenues in Band Theory: Multigap Topology and Hyperbolic Lattices

Patrick Mario Lenggenhager

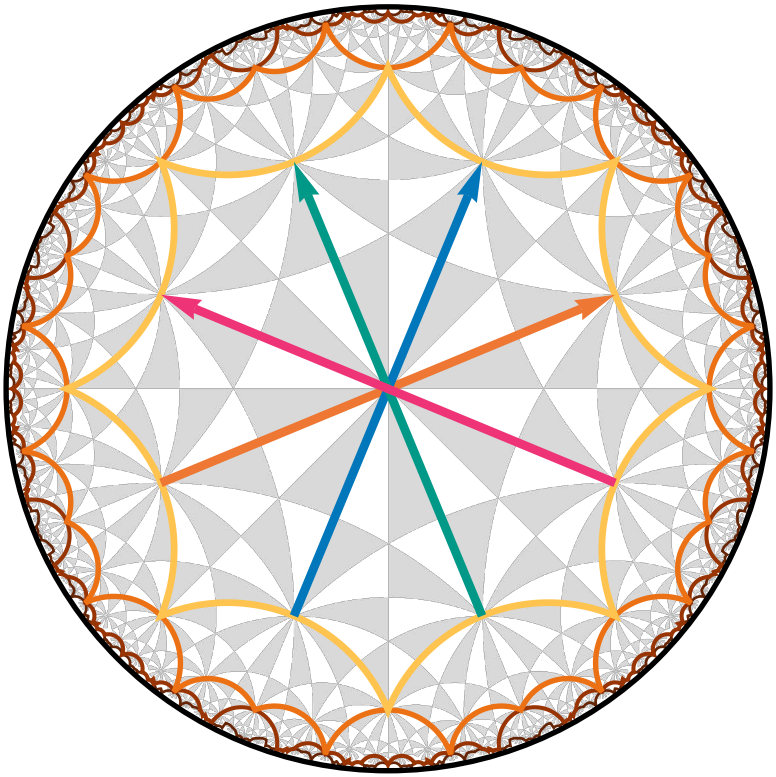

Diss. ETH No. 29553

Diss. ETH No. 29553

Emerging avenues in band theory: multigap topology and hyperbolic lattices

A thesis submitted to attain the degree of

DOCTOR OF SCIENCES
(Dr. sc. ETH Zurich)

presented by

PATRICK MARIO LENGGENHAGER
MSc ETH Physics, ETH Zurich, Switzerland

born on 10.07.1994

accepted on the recommendation of

Prof. Dr. Manfred Sigrist, thesis advisor
Prof. Dr. Tomáš Bzdušek, second advisor
Prof. Dr. Joseph Maciejko, co-examiner
Prof. Dr. Ronny Thomale, co-examiner

2023

"All models are wrong, but some are useful."
— George E. P. Box

Abstract

One of the cornerstones of condensed matter physics, the description of wave functions on periodic lattices in terms of energy bands of Bloch states, serves as the unifying thread in this thesis. This description is often referred to as *band theory*. Within its context, topological states of matter and metamaterials have taken shape as key frontiers in recent years. Related to those frontiers, this thesis delves into seemingly distinct areas: multigap topology and lattices in negatively curved space, known as *hyperbolic lattices*. While these two themes may appear disconnected at first, they are intrinsically tied together by concepts such as symmetry, topology, metamaterials, and the ubiquitous role of band theory.

The first half of the thesis explores the implications of a multigap perspective on the topology of *triple points*, an instance of triply-degenerate nodal points. With the intention to shed light on unexplored connections between different manifestations of topology and material realizations of multigap topology, we study triple points in great detail. Employing minimal models, we derive a complete symmetry classification of triple points in spinless systems, predicting the presence and absence of specific additional degeneracies manifested as nodal lines. We further elucidate the role of multigap topology in the evolution of triple points into multiband nodal links. Furthermore, our analysis extends to the characterization of pairs of triple points formed by two triplets of bands from a total of four bands, which generically result in semimetallic band structures. We prove that such *triple-point pairs* generally exhibit signatures of higher-order topology, and, in the appropriate symmetry setting, are associated with nontrivial second Stiefel-Whitney and Euler monopole charges. With a careful analysis of tight-binding models and first-principle calculations on material candidates, we provide valuable insights into how these nodal structures and their topology manifest in realistic systems.

Switching gears, the second half of the thesis ventures into the domain of hyperbolic lattices. This topic has gained traction with recent experimental realizations in several metamaterial platforms and several theoretical advancements. We start with an accessible introduction to the hyperbolic plane and regular tessellations on which hyperbolic lattices are based. Guided by this foundation, we demonstrate for the first time experimentally that hyperbolic lattices pave the way for emulating the hyperbolic plane in metamaterials, pre-

senting an in-depth analysis of the observable signatures of negative curvature. In the rest of this part, we focus on the extension of band theory to negatively curved space. We develop an algebraic framework for labeling sites in hyperbolic lattices and forming periodic boundary conditions, thus facilitating the study of discrete symmetries and tight-binding models in these structures. Our key contribution to hyperbolic band theory is the *supercell method*. It provides a previously lacking systematic access to exotic non-Abelian Bloch states that exist due to the negative curvature, thereby advancing the understanding of hyperbolic reciprocal space. This pivotal step towards a complete band-theoretic characterization of hyperbolic lattices opens new pathways to a more refined understanding of these structures and their intriguing properties.

Whether investigating topological aspects of semimetals or scrutinizing hyperbolic lattices realized in metamaterials, this thesis underscores the enduring centrality of band theory as a tool to uncover novel physical phenomena.

Zusammenfassung

Einer der Grundpfeiler der Festkörperphysik, die Beschreibung von Wellenfunktionen auf periodischen Gittern in der Form von Energiebändern von Blochzuständen, bildet das Grundmotiv dieser Dissertation. Diese Beschreibung wird oft als *Bandtheorie* bezeichnet. Als Schlüsselbereiche der aktiven Forschung im Kontext der Bandtheorie haben sich in den letzten Jahren topologische Zustände der Materie und Metamaterialien herausgebildet. Diese Arbeit befasst sich mit zwei scheinbar verschiedenen Themen in diesen Schlüsselbereichen: einerseits mit Topologie basierend auf mehreren Energielücken und andererseits mit Gittern in negativ gekrümmtem Raum, bekannt als *hyperbolische Gitter*. Obwohl diese beiden Themen auf den ersten Blick unzusammenhängend erscheinen mögen, sind sie inhärent durch Konzepte wie Symmetrie, Topologie, Metamaterialien und die allgegenwärtige Rolle der Bandtheorie miteinander verbunden.

Die erste Hälfte der Dissertation erkundet die Topologie von *Tripelpunkten*, einer Art von dreifach entarteten Knotenpunkten in der Bandstruktur, unter Einbezug mehrerer Energielücken. Wir untersuchen Tripelpunkte ausführlich aus verschiedenen Perspektiven mit der Absicht, unerforschte Zusammenhänge zwischen verschiedenen Erscheinungsformen von Topologie aufzudecken und zu untersuchen, wie Topologie mehrerer Energielücken in Materialien realisiert werden könnte. Basierend auf minimalen Modellen leiten wir eine vollständige Symmetrieklassifizierung von Tripelpunkten in spinlosen Systemen her, welche es erlaubt die Präsenz oder Absenz von spezifischen zusätzlichen Entartungen in der Form von Knotenlinien vorherzusagen. Ausserdem klären wir die Rolle der Topologie mehrerer Energielücken in der Umwandlung von Tripelpunkten zu verknüpften Mehrbandknotenlinien. Darüber hinaus erstreckt sich unsere Analyse auf die Charakterisierung von Paaren von Tripelpunkten, die durch zwei Tripletts aus insgesamt vier Bändern gebildet werden und generisch zu halbmetallischen Bandstrukturen führen. Wir beweisen, dass solche *Tripelpunktpaare* generell charakteristische Eigenschaften von Topologie höherer Ordnung aufweisen und, in der Gegenwart der notwendigen Symmetrien, mit nichttrivialen Euler- und zweiter-Stiefel-Whitney-Monopolladungen assoziiert sind. Durch eine sorgfältige Analyse von Tight-Binding-Modellen und numerischen Simulationen von Materialkandidaten bieten wir wertvolle Einblicke in die Art und Weise, wie solche Knotenstrukturen und ihre Topologie in

realistischen Systemen auftreten.

Die zweite Hälfte der Dissertation befasst sich mit hyperbolischen Gittern. Dieses Thema hat jüngst aufgrund experimenteller Realisierungen in mehreren Metamaterialplattformen und verschiedener theoretischer Fortschritte an Aufmerksamkeit gewonnen. Wir beginnen mit einer leicht zugänglichen Einführung in die hyperbolische Ebene und ihrer regelmässigen Parkettierungen, auf denen hyperbolische Gitter basieren. Auf dieser Grundlage demonstrieren wir erstmals experimentell, dass hyperbolische Gitter den Weg für die Emulation der hyperbolischen Ebene in Metamaterialien ebnen, und präsentieren eine ausführliche Analyse der messbaren Signaturen negativer Krümmung. Im Rest dieses Teils fokussieren wir uns auf die Erweiterung der Bandtheorie auf den negativ gekrümmten Raum. Wir entwickeln einen algebraischen Rahmen zur Kennzeichnung von Gitterpunkten in hyperbolischen Gittern und zur Bildung von periodischen Randbedingungen, wodurch die Erforschung diskreter Symmetrien und Tight-Binding-Modelle in diesen Strukturen erleichtert wird. Unser Hauptbeitrag zur hyperbolischen Bandtheorie ist die *Superzellenmethode*. Sie bietet einen bisher fehlenden systematischen Zugang zu exotischen, aufgrund der negativen Krümmung existierenden nicht Abelschen Blochzuständen und fördert so unser Verständnis des hyperbolischen reziproken Raums. Dieser entscheidende Schritt hin zu einer vollständigen bandtheoretischen Beschreibung von hyperbolischen Gittern öffnet neue Wege zu einem verbesserten Verständnis dieser Strukturen und ihrer faszinierenden Eigenschaften.

Ob bei der Untersuchung topologischer Aspekte von Halbmetallen oder der Erforschung hyperbolischer Gitter, die in Metamaterialien realisiert werden können, unterstreicht diese Dissertation die anhaltende Wichtigkeit der Bandtheorie als Werkzeug zur Aufdeckung neuer physikalischer Phänomene.

Acknowledgements

The four years of my PhD were an intense but enriching time, both scientifically and personally. Looking back on this journey, I owe thanks to many people who have accompanied me along the way. This includes colleagues, collaborators, and mentors, but also friends, and family. Without them, this thesis would not have been possible.

First and foremost, I would like to thank my supervisor, Tomáš Bzdušek. His patience, insight, and steadfast support were instrumental to my work. Notably, I would like to thank him for always showing his appreciation for my work. The freedom he offered allowed for the exploration of new ideas, balanced by his guidance when faced with challenges. His meticulous attention to detail, coupled with his willingness to engage in even the most technical discussions, played a pivotal role in the realization of this thesis. I enjoyed working with him tremendously and I am grateful for having had the opportunity to be his student and learn from him.

I express my gratitude to my formal supervisor, Manfred Sigrist, for his support and guidance. Although we never collaborated on research, his open door for discussions and assisting in his lectures enriched my academic journey. In his dedication for teaching, he has been a role model for me.

Given our unique arrangement, where Tomáš and I were employed at the Paul Scherrer Institute but spent a majority of our time at the University of Zurich, I am thankful to Titus Neupert for welcoming me into his group. Titus fostered a stimulating and supportive environment in his group, which I enjoyed being part of. Further, I very much appreciated the invaluable support he offered throughout my PhD and as I prepared for my next career steps.

I am deeply grateful to my colleagues both at the University of Zurich and at the Paul Scherrer Institute for discussions not only about physics but also about life, for their friendship and for the many good times we shared on hikes, conferences and in the office. In particular, I would like to thank my long-time office mates for lightening the day, providing much needed distraction and always being available for discussing physics: Martina O. Soldini, Anastasiia Skurativska, Bastien Lapierre, Ömer Mert Aksoy, and Bernhard E. Lüscher. I am grateful to Martina for her encouragement and personal support when I needed it. Discussions with M. Michael Denner and Nikita Astrakhantsev about politics, the world, and more during lunch breaks

or on group excursions were always a pleasure. I would like to specifically acknowledge those colleagues who were so kind as to read parts of this thesis and provide valuable feedback: Tarun Tummuru, Martina, Michael, Ömer, and Aleksandra Nelson. Additionally, warm acknowledgments go to Lorenzo Amato, Marta Brzezińska, Hugo Bocquet, Peter Derlet, Karim Essafi, Mark H. Fischer, Pratyay Ghosh, Manuel Grimm, Maciej Koch-Janusz, Andreas Läuchli, Xiaoxiong Liu, Markus Müller, Christopher Mudry, Aline Ramires, Artem Rakcheev, Frank Schindler, Michael Schüler, Stepan S. Tsirkin, Apoorv Tiwari, Glenn Wagner, Yun (David) Yen, and Song-Bo Zhang, for their collective contributions and shared experiences.

My gratitude extends to my coauthors, for their contributions to the work presented in this thesis. Especially, Joseph Maciejko's hospitality at the University of Alberta enabled a pleasant and fruitful research stay in Edmonton deepening the connections to my other collaborators there: Igor Boettcher, Santanu Dey, and Anffany Chen. Additionally, I greatly valued the in-depth technical discussions with Joseph during which I learned much about the programming language GAP and group theory in general. Further, he committed himself, together with Ronny Thomale, to reading my thesis by being part of the examination committee. I particularly thank Xiaoxiong and Alexander Stegmaier with whom I have worked closely on multiple projects.

Recalling earlier influences, the mentorship of my high-school physics teachers Samuel Byland and Daniel Keller in the context of the Swiss and the International Young Physicists' Tournament was foundational in my early physics journey. I am grateful to Andreas Wallraff for his support in my early research endeavors and for allowing me to do my Matura project in his group. Later, during my Master studies, Gianni Blatter ignited a passion for theoretical condensed matter physics and was influential in his support during my Masters and the transition to my PhD. Finally, it was during my time at Caltech with Gil Refael that I was first introduced to topological band theory, a subject that would become a central theme of this thesis.

On a personal note, my journey has been significantly shaped by the unwavering support of my family and friends. My father, René, has kindled my scientific curiosity from an early age and has been a constant source of advice. My mother, Herta, has been a pillar of unwavering support, going above and beyond to help me in any way she could, and my sister, Vera, has always provided a listening ear when I needed it.

Finally, I am greatly indebted to my girlfriend Kathrin Laxhuber for being there for me during the ups and downs of the past years, the many shared adventures we had exploring the world, and for her regular advice on work-related matters, which included proofreading parts of this thesis. I am deeply grateful for this combination of emotional support and intellectual exchange.

Contents

Part I.

Introduction

1. Preface

This preface provides a very broad overview over the different fundamental concepts and overarching themes of this thesis. After briefly introducing these themes, we outline the scope and structure of the thesis, emphasizing the original publications relevant for this work and highlighting their contribution to the fields. The last section summarizes the author's contributions to the publications and chapters of this thesis.

Central themes

Symmetry

Symmetry plays a crucial role across various fields of physics, spanning from particle physics, classical mechanics, to general relativity. There are continuous and discrete space-time symmetries like translations, rotations, velocity transformations (*boosts*), time-reversal, but also internal symmetries like charge conjugation and gauge symmetries. Via Noether's theorem [9], continuous symmetries of a system are related to conserved quantities, i.e., constants of motion. Further, symmetry often simplifies the mathematical description of the physical system and its behavior. In particular, a symmetry can strongly constrain possible models of a given system, allowing us to write down parametrized models with no additional input other than the observed (or postulated) symmetries. Such an approach is applied, for instance, in the quantum-field-theoretical description of high-energy physics, where a very small set of symmetries thought to be fundamental is postulated. This resulted in the highly successful *standard model* with a minimal set of parameters and a large number of falsifiable and quantitative predictions. The model explains the existence of fundamental particles, their properties, and how they interact.

Although condensed matter physics deals with significantly different energy scales—where the fundamental particles *condense* into matter by forming atoms—the role of symmetry bears a striking similarity. The aim in condensed matter physics is to understand the macroscopic properties of compounds. These properties *emerge* from an interplay of the constituents, such that the symmetries of the compound become relevant. For instance, it turns out that,

in many cases, atoms arrange in periodic structures known as *crystals*. Rather than starting from fundamental particles or even single atoms, in condensed matter theory, we often consider minimal *effective* models capturing the relevant macroscopic properties. By assuming certain symmetries, these models can be derived much in the same way as in high-energy physics. Remarkably, excitations in the compound structures often mimic new particles and are thus called *quasiparticles*, leading to another parallel to high-energy physics. The construction—guided by symmetry—and study of such effective models including their excitations, lies at the heart of much of condensed matter physics and of the work in this thesis.

Of all the symmetries, discrete translational symmetry assumes a distinct role in the realm of condensed matter physics. The ubiquitousness of systems with discrete translational symmetry, i.e., crystalline systems, together with the fact that the group structure of translations is particularly simple, elevates it to a fundamental symmetry. Bloch's theorem [10] constrains any wave function that is a solution of the Schrödinger equation [11] describing a crystalline system to a particular form known as *Bloch function*. Bloch functions are characterized by a quantum number called *crystal momentum*, or simply *momentum* in the context of crystals. Crucially, this lays the foundation for a description of the same system in *reciprocal space*, where the wave functions depend continuously on the momentum. This description, usually referred to as *band theory*, has been highly successful not only in describing single-particle effects of crystals but also in serving as a starting point for studying correlated phenomena. This thesis describes several recent developments in the context of band theory, focusing to non- or weakly interacting systems.

Symmetry strongly influences the properties of a system and as such it is not surprising that breaking some of the system's symmetries can prompt drastic changes. A simple example is the freezing of a liquid into a crystalline solid, where reducing the temperature breaks the continuous translation and rotational symmetries down to their discrete versions. This *phase transition* is accompanied by a discontinuous change of some observables (or their derivatives). This is the Landau paradigm [12, 13] of phase transitions, which states that the symmetry-breaking is indicated by an *order parameter* that distinguishes the two phases. In the case of the liquid-to-solid transition the order parameter is the difference in densities. However, there are phases that fundamentally differ from each other while having the same symmetries.

Topology

A paradigmatic example is the *integer quantum Hall effect* [14], whose experimental discovery opened a new field in condensed matter physics. In

the presence of a strong perpendicular magnetic field, a two-dimensional (2D) electron gas shows a quantized Hall resistance, i.e., the resistance to an in-plane current perpendicular to an applied voltage in the same plane. Upon increasing the magnetic field, the Hall resistance shows exceptionally flat plateaus with sharp transitions at specific values of the magnetic field. In subsequent theoretical studies [15, 16], this remarkable quantization was traced back to a topological origin. These phases, termed *topological phases of matter*, do not differ from other phases in their symmetry, but are characterized by highly nonlocal quantities, called *topological invariants*. These invariants, as their name suggests, remain constant under smooth changes of the system, explaining the robustness of quantum Hall transport signature.

Almost two decades ago, the theoretical proposal [17, 18] and experimental discovery [19, 20] of topological insulators revolutionized the field of band theory by recognizing a whole new class of topological phases that are captured by a previously marginalized geometric perspective on band theory [21–23]. The successful band-theoretic description of insulators, semiconductors and many metals relied predominantly on considerations of the dependence of energy on momentum. For instance, the quasi-classical electron velocity was often approximated by the derivative of the energy with respect to momentum. However, topological aspects are hidden in the dependence of the *wave functions* on momentum, and their inclusion leads to a plethora of new phenomena [24, 25]. For instance, topological insulators are characterized by topological invariants that can only change upon closing the bulk energy gap. This immediately implies that at the interface between two inequivalent topological insulators (one may be the vacuum), gapless modes—quasiparticles—appear; this is the so-called *bulk-boundary correspondence*. Due to the topological origin, these signatures are extremely robust, making them interesting to potential technological applications.

These ideas were subsequently extended to *semimetals* which have characteristic isolated degeneracies, known as *band nodes*, of their energy bands in momentum space. In this case, the topological invariant, referred to as a *topological charge*, manifests as an obstruction toward removing the band node. Due to their isolated nature, the low-energy excitations associated with the band nodes behave as quasiparticles, sometimes emulating particles described in high-energy theories. For instance, Weyl nodes [25–27] resemble chiral Weyl fermions [28, 29]. The resulting *Weyl semimetal* shows anomalous surface states inducing unique transport properties [30] that might even one day be used in applications such as the design of catalyst materials [31]. Besides that, Weyl semimetals have also been proposed as materials for use in photovoltaics [32]. Due to the larger variety of possible symmetries in condensed matter systems over free space, many more exotic excitations are possible [33–35], such as the

three fold degeneracies that are the subject of Part II.

Metamaterials

Metamaterials are assemblies of individual components arranged in a specific manner such that the resulting system has desired emergent properties. In that sense they are very similar to real materials which are made up of atoms—justifying the name. By choosing components smaller than the relevant wavelength at which the system is probed, the macroscopic properties and the arrangement of the components rather than the properties of the components' constituents dominate the phenomenology. Metamaterials can thus be engineered to have properties that rarely occur or are impossible to occur in real materials. Besides potential applications, they therefore provide a platform for realizing or simulating condensed matter systems in a very controlled manner. They have become very popular in studying topological properties [36–42], which often do not rely on quantum mechanics but only on wave physics, such that even classical metamaterials are sufficient to realize such phenomena.

In principle, any engineered complex network of discrete components can be seen as a metamaterial. The relevant aspect is that it allows an effective description using tools from material science and condensed matter physics. Classical metamaterials include mechanical [38, 39], phononic [40], and photonic [36] systems, as well as electric circuits [41–43]. To truly reach the quantum regime, interacting systems are required. One particularly relevant metamaterial platform is circuit quantum electrodynamics [44–48], where macroscopic superconducting objects, for instance so-called *transmon qubits*, take the role of artificial atoms. Their interactions are mediated by a network of coplanar waveguide resonators, i.e., systems hosting small numbers of photons. This is exactly the architecture used in some realizations of quantum computers. While we only implicitly touch upon metamaterials in Part II of this thesis, where they are understood as systems that can host the phenomenology described there, Part III explicitly discusses a metamaterial realization of curved space.

Hyperbolic lattices

While curved spaces are traditionally associated with gravity and cosmology, symmetries can elevate concepts from curved spaces to relevance even within the scope of basic quantum mechanics. For example, the rotational symmetry of a hydrogen atom implies that its electronic wave functions are related to the standing waves on a sphere, a positively curved space. Further, the idea of *holography* [49, 50] describes a duality between gravitational theories in

negatively curved space and strongly correlated quantum systems and thus elevates negatively curved spaces to fundamental importance in condensed matter physics [51–59]. For deep mathematical reasons, captured by Hilbert's theorem, the space of constant negative curvature, known in two dimensions (2D) as the *hyperbolic plane*, cannot be completely realized in laboratory space. This is where *hyperbolic lattices* [60] come into play, discretizations of said space, allowing its realization in metamaterials [4].

A completely different perspective on hyperbolic lattices can be gained through the consideration of symmetries [61–64]. Instead of viewing the hyperbolic lattice as approximating the continuous space, it can be considered a discrete structure in the hyperbolic plane, and, as such, exhibits translational symmetry. Geometrically, curvature can be measured by moving in a rectangle, i.e., by moving a certain distance in some direction, moving some distance in a perpendicular direction and then moving back along the first and finally along the second direction, and measuring the deviation from the starting point. The motion along the two directions and back can be interpreted as translations and their inverses, such that curvature is related to the commutator of the two independent translations. As a consequence, translations in curved spaces *do not commute*. This has immediate implications [62, 64], for instance, on the phenomenology of lattice systems in the hyperbolic plane.

Organization of the thesis

This thesis delves into two emerging topics in the field of band theory: multigap topology of triple points and hyperbolic lattices. It is structured into four parts. Part I establishes the foundation with the present preface and Chapter 2. The latter focuses on the overarching themes of symmetry and band theory. Although a comprehensive review or a pedagogical exposition of these broad, fundamental subjects would be beyond the scope of this thesis, a succinct summary of the most relevant concepts is provided. These concepts, applied in subsequent chapters, illuminate connections between the two topics. This chapter is complemented by Appendix A, which summarizes the two common Bloch conventions and highlights some of their differences. Parts II and III deal with the two main topics of this thesis and are relatively self-contained except for references to Chapter 2, such that they can be read independently. Each part concludes with a separate summary and outlook, discussing the main results, their relevance, and prospective future directions. Finally, Part IV integrates these results into the broader context of the thesis, returning to the high-level perspective taken in the preface.

Triple points and multigap topology

In Part II we present our studies of triple points, a particular class of three-fold degenerate band nodes, and their multigap topology. A traditional classification of topological insulators or semimetals partitions the energy bands into occupied and unoccupied sets, thereby identifying the gap that closes in an associated topological phase transition. However, under certain symmetry conditions, a partitioning with multiple gaps is required to capture the full topology of band nodes [65, 66]. As we demonstrated in the following series of publications, multigap topology comes naturally into play when considering degeneracies of three or more bands, establishing such band nodes as a platform for studying its consequences:

[1] **P. M. Lenggenhager**, X. Liu, S. S. Tsirkin, T. Neupert, and T. Bzdušek,
"From triple-point materials to multiband nodal links",
Physical Review B **103**, L121101 (2021)

[2] **P. M. Lenggenhager**, X. Liu, T. Neupert, and T. Bzdušek,
"Triple nodal points characterized by their nodal-line structure in all magnetic space groups",
Physical Review B **106**, 085128 (2022)

[3] **P. M. Lenggenhager**, X. Liu, T. Neupert, and T. Bzdušek,
"Universal higher-order bulk-boundary correspondence of triple nodal points",
Physical Review B **106**, 085129 (2022)

Part II commences with a brief introduction to topological band theory and multigap topology in Chapter 3, giving an overview over some of the concepts relevant to the subsequent chapters. Next, Chapter 4, which is based on Ref. 2, introduces the specific kind of triply-degenerate nodal points—the *triple points*—that this part is concerned with and includes a short literature review of other kinds. The remainder of the chapter discusses the symmetry conditions for stable triple points and the derivation of their classification in spinless systems, with some details relegated to Appendix B. The results are validated in several material examples based on first-principles calculations and with some data deferred to Appendix C.

In Chapter 5, we then turn to analyzing the multigap topology of triple points, covering Ref. 1 and parts of Refs. 2, 3. We explain how the multigap topology enforces triple points to evolve to multiband nodal links under symmetry-breaking strain and derive a relation between Berry phases and the multigap invariant (proven in Appendix D), which, in the presence of a triple point,

allows us to predict the value of the Euler monopole charge. Again, we verify our theoretical predictions with first-principle calculations on material candidates, studying one material, Li_2NaN, in detail.

Most materials hosting triple points formed by a single triplet of bands are metallic rather than semimetallic, which prevents the manifestation of boundary signatures. Chapter 6 thus examines the topology of pairs of triple points formed by four bands, i.e., two triplets that only have two bands in common, which typically result in a semimetallic state. We discuss our findings from Ref. 3, namely that triple-point pairs obey a universal higher-order bulk-boundary correspondence between the type of triple points and fractional jumps of the hinge charge. Additionally, we show that triple-point pairs can carry nontrivial second Stiefel-Whitney and Euler monopole charges and predict when that happens. Some of these derivations are relegated to Appendix E. Employing methods described in Appendix F, our findings are illustrated with minimal tight-binding models and a case study of the material Sc_3AlC, providing empirical validation.

Hyperbolic lattices

In Part III, we turn to the second principal topic of the thesis: hyperbolic lattices. First explored several decades ago [61, 67], the study of hyperbolic lattices is currently enjoying a resurgence in academic interest due to their recent experimental realization in metamaterials [68]. This has been coupled with significant theoretical progress, notably in understanding their potential to emulate continuous space [69] and in the development of a hyperbolic band theory [62–64, 70–74]. The author's contributions, as reflected in the following publications, have been towards the experimental demonstration of continuous hyperbolic space emulation by hyperbolic lattices and advances in hyperbolic band theory:

[4] **P. M. Lenggenhager**, A. Stegmaier, L. K. Upreti, T. Hofmann, T. Helbig, A. Vollhardt, M. Greiter, C. H. Lee, S. Imhof, H. Brand, T. Kießling, I. Boettcher, T. Neupert, R. Thomale, and T. Bzdušek,
"Simulating hyperbolic space on a circuit board",
Nature Communications **13**, 4373 (2022)

[5] **P. M. Lenggenhager**, J. Maciejko, and T. Bzdušek,
"Non-Abelian hyperbolic band theory from supercells",
Physical Review Letters **131**, 226401 (2023)

The author has further contributed to the exploration of hyperbolic band topology with these publications:

[6] D. M. Urwyler, **P. M. Lenggenhager**, I. Boettcher, R. Thomale, T. Neupert, and T. Bzdušek,
"Hyperbolic topological band insulators",
Physical Review Letters **129**, 246402 (2022)

[7] A. Chen, Y. Guan, **P. M. Lenggenhager**, J. Maciejko, I. Boettcher, and T. Bzdušek,
"Symmetry and topology of hyperbolic Haldane models",
Physical Review B **108**, 085114 (2023)

[8] T. Tummuru, A. Chen, **P. M. Lenggenhager**, T. Neupert, J. Maciejko, and T. Bzdušek,
"Hyperbolic non-Abelian semimetal",
preprint arXiv:2307.09876 (2023)

To acquaint the readers with the necessary background information for this part, Chapter 8 provides a concise introduction to the continuous hyperbolic plane, its representation in the Poincaré disk model, and regular tessellations. The rest of the chapter explores, based on Ref. 4, how the hyperbolic plane can be emulated experimentally using hyperbolic lattices and how such an emulation can be verified. We focus on the manifestation of the negative curvature in the Laplace-Beltrami operator which provides two characteristic signatures: a reordering of its spectrum in the hyperbolic plane compared to the Euclidean plane and wave propagation along curved geodesics. After reviewing the lattice regularization of the Laplace-Beltrami operator and developing theoretical methods for analyzing its eigendecomposition on the lattice, we finally discuss the experimental realization and present the data demonstrating signatures of negative curvature.

In Chapter 9, we consider hyperbolic lattices from the perspective of discrete symmetries. This chapter serves as a general introduction to the topic and therefore combines sections that review relevant concepts (Sections 9.1, 9.2 and 9.4) and methods with our own contributions (Sections 9.3 and 9.5). We first introduce the space groups of hyperbolic lattices, before discussing boundary conditions and the thermodynamic limit [75], thereby touching on real-space methods for computing their density of states [76]. Subsequently, we develop an algebraic framework, originally described in Ref. 5, for expressing tight-binding models, and, based on that, review the recently developed hyperbolic band theory [62, 64] before applying it to several examples. Finally, we summarize the developments in hyperbolic band topology and *review* two models [6, 8] to whose analysis the author has contributed.

The central challenge of hyperbolic band theory, the difficulty in parametrizing higher-dimensional irreducible representations of the translation group, is

addressed in Chapter 10, which introduces the *supercell method* [5] as a pivotal step towards a complete hyperbolic band theory. After motivating the concept of supercells, we describe the core ideas of our method first from a perspective in real space and then in reciprocal space. To demonstrate convergence of the method to the thermodynamic limit, we apply it to several examples, present the resulting converging density of states, and compare it to results obtained from real-space methods [75, 76].

Author's contributions

Triple points and multigap topology

Chapter 4 The author performed the complete theoretical derivations of the symmetry classification of triple points (including those given in Appendix B) under the supervision of Tomáš Bzdušek. The search for material candidates was performed together with Xiaoxiong Liu: The author combed through material databases to select the candidates on which Xiaoxiong Liu performed density-functional theory. The data was analyzed by the author together with Xiaoxiong Liu. The author wrote the original publication [2] with the help of Tomáš Bzdušek and comments by Xiaoxiong Liu and Titus Neupert.

Chapter 5 All the theoretical derivations were performed by the author under the supervision of Tomáš Bzdušek. The density-functional theory calculations and the construction of Wannier tight-binding models were performed by Xiaoxiong Liu, while the author selected the materials and analyzed the resulting tight-binding models. For the study of Li_2NaN, the author constructed the minimal effective tight-binding model based on the first-principles calculations and analysis done by Xiaoxiong Liu. Using this tight-binding model, the author subsequently studied various properties under the supervision of Tomáš Bzdušek and, in the case of the optical conductivity, under the supervision of Stepan Tsirkin. Xiaoxiong Liu additionally performed calculations of the surface spectral function based on the first-principles data. The author wrote the original publication [1] with the help of Tomáš Bzdušek and comments by Xiaoxiong Liu and Titus Neupert.

Chapter 6 The author performed all the theoretical calculations and derivations as well as the construction and analysis of the tight-binding models under the supervision of Tomáš Bzdušek. Xiaoxiong Liu performed density-functional-theory calculations on Sc_3AlC, constructed the Wannier tight-binding model, performed symmetry analysis, constructed a nanowire model of the compound,

and computed the charge distribution on it, while the author analyzed the resulting data under the supervision of Tomáš Bzdušek. The author wrote the original publication [3] with the help of Tomáš Bzdušek and comments by Xiaoxiong Liu and Titus Neupert.

Hyperbolic lattices

Chapter 8 The theoretical analysis of different tessellations, how well they approximate the continuum, and how the negative curvature manifests in the various signatures, was performed by the author under the supervision of Tomáš Bzdušek. Together with Alexander Stegmaier and Lavi K. Upreti and under the supervision of Tomáš Bzdušek, Titus Neupert, and Ronny Thomale, the author designed the circuit network, which was subsequently built by Achim Vollhardt. The experiments were performed by Stefan Imhof, Hauke Brand, and Tobias Kießling with theoretical support and loss simulations by Alexander Stegmaier with the help of Tobias Hofmann and Tobias Helbig. The author extensively analyzed the experimental data and together with everyone interpreted the results. The author wrote the original publication [4] with the help of Tomáš Bzdušek and Titus Neupert and comments by all the other authors.

Chapter 9 The author developed the algebraic framework [5] for expressing tight-binding models under the supervision of Joseph Maciejko. For Ref. 6, the author helped David Urwyler with the analysis of the edge modes and, in particular, extracted the edge dispersion of the hyperbolic Haldane model. In the context of the hyperbolic Dirac model of Ref. 8, the author performed the supercell analysis, computing the density of states with the supercell method and extracting the Bloch Hamiltonian on the 2-supercell.

Chapter 10 With the exception of Section 10.4.6, this chapter contains exclusively original work done by the author under the supervision of Tomáš Bzdušek and Joseph Maciejko, published in Ref. 5, which the author wrote with the help of Tomáš Bzdušek and Joseph Maciejko. Section 10.4.6 revisits the Dirac model from Ref. 8 and, besides the density of states that the author computed, presents some results on the nodal ring in the 2-supercell, which have been derived by Tarun Tummuru.

2. Symmetries and band theory

In this chapter, we review some of the fundamental mathematical and physical principles that underlie the description of crystalline solids, focusing on the key concept of symmetries, including translational symmetry which leads to the formulation of band theory. While numerous textbooks are available on this topic, such as the one by Bradley et al. [77], our goal is to concentrate on reviewing the concepts relevant to later chapters, while introducing the necessary terminology and notation. Hence, our intention is neither to provide an exhaustive and comprehensive summary, nor to offer a pedagogical introduction.

This chapter serves as an opportunity to emphasize the overarching themes of the thesis, particularly the role of symmetry in designing effective models and studying crystalline systems. We first delve into the fundamental concepts of *crystalline symmetries* in Section 2.1, where we introduce the notions of space groups and their representations. This lays the groundwork for understanding the symmetries present in crystalline solids and their mathematical description. Building upon this, in Section 2.2, we extend the discussion to *magnetic symmetries*, specifically discussing the classification of the Shubnikov groups and their representation theory. These groups incorporate additional antiunitary operations, such as time-reversal symmetry, which play a crucial role in later chapters.

In Section 2.3, we shift our attention to the consequences of *translational symmetry*, in particular the Bloch theorem and its implications for band theory. This perspective, based on the formulation of *reciprocal space*, forms the foundation for Part II, where we study symmetry-protected band degeneracies and their topological properties in real materials. In contrast, Part III diverges from three-dimensional (3D) crystals and explores *hyperbolic lattices* in 2D space with constant negative curvature, known as the *hyperbolic plane*. There, we discuss recent efforts, including our own contributions, to generalize band theory to this intriguing class of lattices. To establish conventions, Section 2.4 introduces the *Bloch Hamiltonian*, discussing its definition and the symmetry constraints imposed by the space group. This serves as the basis for the subsequent chapters in both parts of the thesis.

2.1. Crystalline symmetries

A crystal is a solid material whose constituents, such as atoms, are arranged in a highly ordered and repeating pattern known as a *lattice*. This lattice structure exhibits long-range translational symmetry, meaning that the arrangement of its constituents repeats indefinitely in all directions. As a result, crystals possess unique optical, electrical, and mechanical properties. To capture the translational symmetry mathematically, we introduce the concept of a *Bravais lattice*. A Bravais lattice consists of points, referred to as *sites*, that reflect the periodic arrangement of the constituents. Crucially, each site in a Bravais lattice, along with its neighborhood, is identical. In contrast, general lattices may have several inequivalent lattice sites despite the presence of translational symmetry. To account for this, we introduce the notion of a *unit cell*—a fundamental repeating unit composed of multiple sites from the full lattice. The Bravais lattice describes the arrangement of these unit cells by identifying the center of each unit cell with a Bravais-lattice site. Then, the Bravais lattice captures the translations required to replicate the entire crystal based on the unit cell.

2.1.1. Space groups

Formally, the symmetry of a 3D lattice is described by a space group. Analogous notions exist in other dimensions, but we here focus on the 3D case. A space group $\mathcal{S}$ is an infinite group of the form

$$\mathcal{S} = \bigcup_i \{R_i|\mathbf{v}_i\}\mathcal{T}, \tag{2.1}$$

where $R_i \in \mathsf{O}(3)$, $\mathbf{v}_i \in \mathbb{R}^3$ and $\mathcal{T}$ is the group of translations generated by the linearly independent *Bravais vectors* $\mathbf{a}_i$, $i = 1, 2, 3$:

$$\mathcal{T} = \left\{ \{\mathbb{1}|\mathbf{t}\} \,\middle|\, \mathbf{t} = \sum_{i=1}^{3} n_i \mathbf{a}_i, n_i \in \mathbb{Z} \right\} \cong \mathbb{Z}^3. \tag{2.2}$$

The composition law for elements of $\mathcal{S}$ is

$$\{R_2|\mathbf{v}_2\}\{R_1|\mathbf{v}_1\} = \{R_2R_1|R_2\mathbf{v}_1 + \mathbf{v}_2\}. \tag{2.3}$$

Its action on the position vector $\mathbf{r}$ is

$$\{R|\mathbf{v}\}\mathbf{r} = R\mathbf{r} + \mathbf{v} \tag{2.4}$$

and on some function $f(\mathbf{r})$ it is

$$\{R|\mathbf{v}\}f(\mathbf{r}) = f\left(\{R|\mathbf{v}\}^{-1}\mathbf{r}\right) = f\left(R^{-1}(\mathbf{r}-\mathbf{v})\right). \tag{2.5}$$

Note that $\mathcal{S}$ is a discrete subgroup of the *Euclidean group*, the group of isometries, i.e., distance-preserving transformations. It turns out that in three dimensions (3D) there are exactly 230 distinct space groups. In contrast, we call groups that do not include any elements with nontrivial translations *point groups*. In 3D there are 32 of them and we will see below how they are related to space groups.

Translations are characterized by not having any fixed points in space, i.e., there is no $\mathbf{r}$, such that $\{\mathbb{1}|\mathbf{v}\}\mathbf{r} = \mathbf{r}$ as long as $\mathbf{v} \neq 0$. Therefore, the group of translations $\mathcal{T}$ has to be *torsion-free*, i.e., it cannot contain any elements of finite order other than the identity. Additionally, $\mathcal{T}$ always is a normal subgroup of the space group, $\mathcal{T} \lhd \mathcal{S}$: for any $\{R_i|\mathbf{v}_i\} \in \mathcal{S}$ and $\{\mathbb{1}|\mathbf{t}\} \in \mathcal{T}$, it holds that

$$\{R_i|\mathbf{v}_i\}\{\mathbb{1}|\mathbf{t}\}\{R_i|\mathbf{v}_i\}^{-1} = \{\mathbb{1}|R_i\mathbf{t}\} \in \mathcal{T}. \tag{2.6}$$

Additionally, $\mathcal{T}$ is Abelian, i.e., translations commute. This becomes apparent from its definition in Eq. (2.2), where the group is written as a linear combination of its generators. As we have alluded to above, each space group is associated with a Bravais lattice.

The fact that $\mathcal{T}$ is a normal subgroup of $\mathcal{S}$ implies that the quotient $\bar{\mathcal{S}} = \mathcal{S}/\mathcal{T}$ is a group. Formally, the quotient $\bar{\mathcal{S}}$ is the set of cosets $\{R_i|\mathbf{v}_i\}\mathcal{T}$ each of which can be associated with a *coset representative* $\{R_i|\mathbf{w}_i\}$, corresponding to one particular element in $\mathcal{T}$. The set of those representatives is known as the *transversal* $T_{\mathcal{S}}(\mathcal{T})$ and is a subset of $\mathcal{S}$. Generally, it is not possible to choose the representatives such that $T_{\mathcal{S}}(\mathcal{T})$ itself forms a group: multiplication of certain elements usually results in some $\{R_i|\mathbf{v}_i\}$ with $\mathbf{v}_i \neq \mathbf{w}_i$. Only for *symmorphic* space groups, such a choice is possible. By stripping the elements of the space group of their translation part, we circumvent this issue and effectively construct the isomorphism from $\bar{\mathcal{S}}$ to the *isogonal point group*:

$$\bar{\mathcal{S}} \cong \mathcal{P} = \bigcup_{\{R|\mathbf{v}\}\in\mathcal{S}} R. \tag{2.7}$$

Note that, generally, $\mathcal{P}$ is *not* a subgroup of $\mathcal{S}$. Only if $\mathcal{S}$ is symmorphic, then $\mathcal{P} < \mathcal{S}$ and the space group is a semidirect product of the point group and translation group:

$$\mathcal{S} = \mathcal{P} \ltimes \mathcal{T}. \tag{2.8}$$

2.1.2. Representation theory of space groups

We have introduced symmetries as isometries of Euclidean space, which is reflected in their action on the position vector as described by Eq. (2.4). In quantum mechanics, a system is said to possess a symmetry if there exists an operator $\mathcal{U}$ acting on the Hilbert space that commutes with the Hamiltonian $\mathcal{H}$: $[\mathcal{U}, \mathcal{H}] = 0$. Therefore, our interest lies in understanding the action of the space group on the Hilbert space. This prompts us to explore *representations* of the space group, which describe how the group elements $g \in \mathcal{S}$ are represented as operators $\mathcal{U}_g$ on the Hilbert space. Wigner's theorem [78, 79] implies that eigenfunctions of $\mathcal{H}$ are ascribed to one of the representations of the full symmetry group, e.g., the space group. These representations can further be decomposed into *irreducible representations* and Schur's lemma then implies that the energy eigenspaces transform according to these irreducible representations. The knowledge of all irreducible representations of the space group is, therefore, imperative for symmetry analysis and will be extensively utilized in subsequent chapters. Importantly, these irreducible representations have been exhaustively tabulated and cataloged, for example in Bradley et al. [77], or, more recently, in online databases such the *Bilbao crystallographic server* [80].

While we refer the reader to established texts such as Ref. 77 for a comprehensive treatment on obtaining all irreducible representations, we briefly summarize the approach, highlighting key concepts essential for their practical application in later chapters. The process of determining all irreducible representations of a space group involves a systematic reduction to more manageable subgroups. Initially, the presence of an Abelian normal subgroup, namely the translation group, plays a crucial role. In Section 2.3, we explore how the irreducible representations of $\mathcal{T}$, labeled by the crystal momentum $\mathbf{k}$, are readily obtained, providing the foundation for constructing Bloch functions. Subsequently, our focus turns to the study of subgroups of $\mathcal{S}$ that only mix Bloch functions with the same $\mathbf{k}$. The irreducible representations of these subgroups $\mathcal{G}^{\mathbf{k}}$, known as *little groups*, induce irreducible representations of $\mathcal{S}$. In fact, all irreducible representations of $\mathcal{S}$ can be derived from those of certain little groups, such that each representation of $\mathcal{S}$ can be labeled by the corresponding crystal momentum $\mathbf{k}$ and the label of a representation of $\mathcal{G}^{\mathbf{k}}$.

However, since little groups retain translational symmetries, they remain infinite groups. To deal with this, we direct our attention to the finite *little co-group*, which emerges upon quotienting the little group by the translation group and is isomorphic to one of the 32 crystallographic point groups. In Section 2.3.3, we provide a concise summary of this aspect, shedding light on the relationship between irreducible representations of the little group and its little co-group, while refraining from an exhaustive treatment of obtaining

irreducible representations of the full space group.

We end this section with a short comment on notation. Throughout Part II we use two different sets of notation for labeling irreducible representations of space and point groups, i.e., little groups and little co-groups. For the most part we follow the notation used in Bradley et al. [77] and introduced by Mulliken [81] which uses letters A, B, E, and T with subscripts indicating symmetry properties. One-dimensional (1D) irreducible representations are denoted by A (B) if they are symmetric (antisymmetric) with respect to rotation around the principal axis, 2D irreducible representations by E, and 3D ones by T. In some cases, we use a different notation, namely the one of Koster [82], which labels representations of little groups by the name of the $\mathbf{k}$-subspace (point or line) and a subscript enumerating all irreducible representations. This notation is particularly useful when dealing with complete models such as tight-binding models which are defined in the full reciprocal space, while the notation by Mulliken [81] is more convenient for symmetry analysis at a single point or line in reciprocal space. On the Bilbao crystallographic server [80] mostly the notation by Koster [82] is used, but for the point groups, the notation by Mulliken [81] is given as well.

2.2. Magnetic symmetries

The 230 space groups can be extended by introducing an additional coordinate, which is independent from the three spatial coordinates and can take two possible values. Naturally, this implies the existence of an operation that flips that extra coordinate and we denote it by the operator $\mathcal{r}$. It satisfies $\mathcal{r}^2 = 1$ and, because it only acts on the extra coordinate leaving the spatial degrees of freedom invariant, commutes with all other symmetry operations.

Before proceeding, it is useful to establish some terminology. We briefly review the classification of space groups incorporating $\mathcal{r}$ or combinations of it with regular symmetries. The extended classification results in 1651 groups, known as the *Shubnikov space groups* or *magnetic space groups*. Similarly, including $\mathcal{r}$ into the point groups gives rise to 122 *Shubnikov point groups*, also referred to as *magnetic point groups*.

2.2.1. Shubnikov groups

Let us start by considering the Shubnikov *point* groups. We distinguish three types

I. The ordinary point groups, where $\mathcal{r}$ is not present.

II. The *gray* point groups, given by

$$\mathcal{P} + \mathcal{r}\mathcal{P}, \tag{2.9}$$

where $\mathcal{P}$ is any (ordinary) point group. They are direct product groups of the form $\mathcal{P} \otimes (1 + \mathcal{r})$. Each element of $\mathcal{P}$ thus appears once without and once composed with $\mathcal{r}$.

III. The *black and white* point groups, given by

$$\mathcal{H} + \mathcal{r}(\mathcal{P} - \mathcal{H}), \tag{2.10}$$

where $\mathcal{H} < \mathcal{P}$ is a halving subgroup of the (ordinary) point group $\mathcal{P}$. In this case, half of the elements of $\mathcal{P}$ appear without and the other half with $\mathcal{r}$.

Throughout Part II, we use Hermann-Mauguin notation [77] to label the 122 magnetic point groups.

The Shubnikov *space* groups, on the other hand, are divided into *four* types:

I. The Fedorov (ordinary) space groups, which do not contain $\mathcal{r}$.

II. The *gray* space groups, analogously to the gray point groups, given by

$$\mathcal{S} + \mathcal{r}\mathcal{S}, \tag{2.11}$$

where $\mathcal{S}$ is any (ordinary) space group.

III. The *black and white* space groups based on ordinary Bravais lattices, analogously to the black and white point groups, given by

$$\mathcal{H} + \mathcal{r}(\mathcal{S} - \mathcal{H}), \tag{2.12}$$

where $\mathcal{H}$ is a halving subgroup of the (ordinary) space group $\mathcal{S}$ and $(\mathcal{S} - \mathcal{H})$ contains no pure translations.

IV. The *black and white* space groups based on *black and white* Bravais lattices, given by

$$\mathcal{S} + \mathcal{r}\{\mathbb{1}|\mathbf{t}_0\}\mathcal{S}, \tag{2.13}$$

where $\mathcal{S}$ is any (ordinary) space group and $\mathbf{t}_0$ is the extra translation relating the black and white Bravais lattice to the appropriate ordinary Bravais lattice. Note that $\mathbf{t}_0$ is *not* a lattice vector of the *ordinary* Bravais lattice, but typically half of some combination of those.

Note that, independent of its type, any Shubnikov (point or space) group can be factorized as

$$M = G + \mathcal{r}\{S|\mathbf{v}\}G \tag{2.14}$$

with G being an ordinary group, $\mathcal{r}$ the antisymmetry and $\{S|\mathbf{v}\}$ an element of the Euclidean group satisfying $\{S|\mathbf{v}\}^2 \in G$.

If $\mathcal{r}$ is a unitary operator, determining the representations of the Shubnikov groups is straightforward. However, in a physical setting, the additional coordinate often represents the magnetic moment. In that case, $\mathcal{r}$ can be understood as the operation of time reversal, denoted by $\mathcal{T}$, which is *antiunitary*. This requires us to extend representation theory to groups containing both unitary and antiunitary operators, which we refer to as *nonunitary* groups. Therefore, we consider Shubnikov groups where $\mathcal{r}$ is antiunitary. According to Eq. (2.14), we can decompose such a group into unitary and antiunitary elements. In the next subsection, we briefly review the representation theory of nonunitary groups to provide the necessary background for our analysis in the subsequent chapters.

2.2.2. Representation theory of nonunitary groups

Given a unitary group G, we consider the inclusion of an arbitrary antiunitary symmetry element $\mathcal{a}$, e.g., time reversal or time reversal combined with another symmetry operation, to the generators, such that we obtain the *magnetic group*

$$M = G + \mathcal{a}G, \tag{2.15}$$

which mirrors the decomposition in Eq. (2.14). By construction M contains two (left) cosets: $1G$ and $\mathcal{a}G$, where 1 is the identity, such that G is a subgroup of index 2. Elements of the coset $1G$ ($\mathcal{a}G$) are unitary (antiunitary) such that M has an equal number of unitary and antiunitary elements. It follows that G is a *normal subgroup* of M and consequently the cosets form a group, the *quotient group* $M/G \cong \{1, \mathcal{a}\} \cong \mathbb{Z}_2$ that obeys $\mathcal{a}^{-1} = \mathcal{a}$ and $\mathcal{a}^2 = 1$. According to the natural group homomorphism, i.e., the canonical projection of M onto M/G, this implies that $bc \in G$ for $b, c \in \mathcal{a}G$, and that $\mathcal{a}^{-1} \in \mathcal{a}G$.

For a nonunitary group, we study *corepresentations* $\overline{\mathcal{D}}$ instead of representations $\mathcal{D}$. These satisfy the relations

$$\overline{\mathcal{D}}(g)\overline{\mathcal{D}}(h) = \overline{\mathcal{D}}(gh), \tag{2.16a}$$

$$\overline{\mathcal{D}}(g)\overline{\mathcal{D}}(b) = \overline{\mathcal{D}}(gb), \tag{2.16b}$$

$$\overline{\mathcal{D}}(b)\overline{\mathcal{D}}(g)^* = \overline{\mathcal{D}}(bg), \tag{2.16c}$$

$$\overline{\mathcal{D}}(b)\overline{\mathcal{D}}(c)^* = \overline{\mathcal{D}}(bc) \tag{2.16d}$$

for $g, h \in G$ and $b, c \in \not{a}G$. Similarly, a change of basis by some unitary matrix U acts as follows:

$$\overline{\mathscr{D}}(g) \mapsto U\overline{\mathscr{D}}(g)U^{-1}, \tag{2.17a}$$

$$\overline{\mathscr{D}}(b) \mapsto U\overline{\mathscr{D}}(b)(U^{-1})^{*}. \tag{2.17b}$$

We note that by (formally) considering the matrices $\overline{\mathscr{D}}(g)$ for $g \in G$ and $\overline{\mathscr{D}}(b)\mathcal{K}$, where $\mathcal{K}$ is complex conjugation, for $b \in \not{a}G$, they form a representation.

If the *irreducible* representations D of the unitary subgroup $G < M$ are known, the irreducible corepresentations (ICRs) $\overline{D}$ of M can be determined as follows (see Ref. 77 for more details and proofs of the statements summarized here). In general we need to distinguish three cases based on the *reality* of D: (a) real, (b) pseudoreal and (c) complex.

(a) Reality of D implies that there is a unitary matrix N such that for all $g \in G$

$$D(g) = ND^{*}(\not{a}^{-1}g\not{a})N^{-1}, \tag{2.18a}$$

$$NN^{*} = +D(\not{a}^{2}). \tag{2.18b}$$

Then, $\overline{D}$, defined by

$$\overline{D}(g) = D(g), \quad \overline{D}(b) = \pm D(b\not{a}^{-1})N \tag{2.19}$$

for all $g \in G$ and $b \in \not{a}G$, is an ICR of M. The corepresentation with the $+$ sign in Eq. (2.19) is equivalent to the one with the $-$ sign.

(b) If there is a unitary matrix N such that for all $g \in G$

$$D(g) = ND^{*}(g)N^{-1}, \tag{2.20}$$

$$NN^{*} = -D(\not{a}^{2}), \tag{2.21}$$

then D is called *pseudoreal* and $\overline{D}$ with

$$\overline{D}(g) = \begin{pmatrix} D(g) & 0 \\ 0 & D(g) \end{pmatrix}, \qquad \overline{D}(b) = \begin{pmatrix} 0 & -D(b\not{a}^{-1})N \\ D(b\not{a}^{-1})N & 0 \end{pmatrix} \tag{2.22}$$

for all $g \in G$ and $b \in \not{a}G$ is an ICR of M.

(c) Else, D is a complex representation and $\overline{D}$, defined by

$$\overline{D}(g) = \begin{pmatrix} D(g) & 0 \\ 0 & D(g) \end{pmatrix}, \qquad \overline{D}(b) = \begin{pmatrix} 0 & D(b\not{a}) \\ D(b\not{a}^{-1}) & 0 \end{pmatrix} \tag{2.23}$$

for all $g \in G$ and $b \in \not{a}G$, is an ICR of M.

The irreducible representation matrices $D(g_i)$ of a set of generators of a unitary point group G can be obtained from the Bilbao crystallographic server using the REPRESENTATIONS PG application [83]. This application also gives the reality of each irreducible representation. Applying the above procedure, we determine the relevant corepresentation matrices $\overline{D}(g_i)$. Note that recently, a new program COREPRESENTATIONS PG [84, 85] has been added to the Bilbao crystallographic server, which allows for direct extraction of the matrix corepresentations of magnetic point groups.

2.3. Bloch theorem and band theory

In this section, we explain how translational symmetry constrains the solutions to the Schrödinger equation via the *Bloch theorem*, leading to band theory and a description of those solutions in reciprocal space. We start by discussing the irreducible representations of the translation group in Section 2.3.1. This allows us to derive the Bloch theorem in Section 2.3.2, which implies a basis of the Hilbert space with sectors labeled by the irreducible representations of the translation group. Finally, in Section 2.3.3, we discuss the interplay of translations with the remaining space-group symmetries.

2.3.1. Irreducible representations of the translation group

In Section 2.1.1, we have seen that the translation group $\mathcal{T}$ is Abelian and that the translations $\{\mathbb{1}|\mathbf{t}\} \in \mathcal{T}$ are characterized by $\mathbf{n} \in \mathbb{Z}^3$. For the discussion of the irreducible representations of $\mathcal{T}$, it is convenient to constrain to a finite lattice and adopt periodic boundary conditions. Algebraically, imposing periodic boundary conditions amounts to constructing a finite-index normal subgroup $\mathcal{T}_{\text{PBC}}$ of $\mathcal{T}$ [64]. Consider a 1D chain with translation group $\mathcal{T} \cong \mathbb{Z}$, the additive group of integers. Imposing periodic boundary conditions on a finite chain with N sites $x = 1, 2, \ldots, N$ requires that the wave function ψ satisfies $\psi(x - N) = \psi(x)$, i.e., site $x = N + 1$ is identified with site $x = 1$. Then, the group of translations leaving the wave function invariant is

$$\mathcal{T}_{\text{PBC}} \cong N\mathbb{Z} = \{\ldots, -2N, -N, 0, N, 2N, \ldots\}. \tag{2.24}$$

The residual translations in the finite system, the ring with N sites, which we refer to as a length-N *cluster*, are given by the quotient

$$\mathcal{T}/\mathcal{T}_{\text{PBC}} \cong \mathbb{Z}/N\mathbb{Z} = \mathbb{Z}_N = \{0, 1, \ldots, N - 1\}, \tag{2.25}$$

which forms a group because $\mathcal{T}_{\text{PBC}} \lhd \mathcal{T}$. In contrast to both $\mathcal{T}_{\text{PBC}}$ and $\mathcal{T}$, $\mathcal{T}/\mathcal{T}_{\text{PBC}}$ is finite and its order, referred to as the *index* $|\mathcal{T} : \mathcal{T}_{\text{PBC}}|$ is N. We

recognize that $\mathcal{T}/\mathcal{T}_{\mathrm{PBC}}$ is isomorphic to the cyclic group of order N and thus has irreducible representations which are all 1D and labeled by an integer $p \in \{0, 1, \ldots, N-1\}$:

$$n \in \mathbb{Z}_N \mapsto \mathrm{e}^{-2\pi \mathrm{i} \frac{p}{N} n}. \tag{2.26}$$

The above can be easily generalized to generic 3D lattices. We assume that the lattice consists of N_i (Bravais lattice) sites, i.e., unit cells, along the direction $\mathbf{a}_i$, such that the total number of sites is $N = N_1 N_2 N_3$, and identify site $n_i = N_i + 1$ with site $n_i = 1$. Then, each translation $\mathbf{t}$ is of the form

$$\mathbf{t} = \sum_{i=1}^{3} n_i \mathbf{a}_i, \qquad n_i = 0, 1, \ldots, N_i - 1 \tag{2.27}$$

such that $\mathcal{T} \cong \mathbb{Z}^3$ and $\mathcal{T}_{\mathrm{PBC}} \cong N_1\mathbb{Z} \times N_2\mathbb{Z} \times N_3\mathbb{Z}$. The residual translation group $\mathcal{T}/\mathcal{T}_{\mathrm{PBC}}$, thus, is isomorphic to $\mathbb{Z}_{N_1} \times \mathbb{Z}_{N_2} \times \mathbb{Z}_{N_3}$, i.e., the direct product of three cyclic groups. It follows that the N irreducible representations of $\mathcal{T}$ are

$$D_{\mathbf{k}}(\{1|\mathbf{t}\}) = \mathrm{e}^{-\mathrm{i}\mathbf{k}\cdot\mathbf{t}} \tag{2.28a}$$

with

$$\mathbf{k} = \sum_{i=1}^{3} k_i \mathbf{b}_i, \qquad k_i = \frac{p_i}{N_i}, \quad p_i = 0, 1, \ldots, N_i - 1 \tag{2.28b}$$

and the *reciprocal lattice vectors* $\mathbf{b}_i$, $i = 1, 2, 3$, forming a basis of the space of irreducible representations of $\mathcal{T}$, known as *reciprocal space*. They satisfy the following defining relation:

$$\mathbf{b}_i \cdot \mathbf{a}_j = 2\pi\delta_{ij}, \tag{2.29}$$

which implies that reciprocal vectors $\mathbf{k}$ are only defined modulo reciprocal lattice vectors $\mathbf{b}_i$. This is a consequence of the discreteness of translations in real space. Thus, we can choose any set of nonequivalent $\mathbf{k}$-vectors to label the irreducible representations. Usually, we choose a connected set of such vectors, the so-called *Brillouin zone*. Taking the role of momentum (assuming units where $\hbar = 1$), $\mathbf{k}$ is known as *crystal momentum*.

To describe the thermodynamic limit, we let $N_i \to \infty$, resulting in a sequence of normal subgroups $\mathcal{T}_{\mathrm{PBC}} \lhd \mathcal{T}$ of increasing index $N = N_1 N_2 N_3$. Note that it is important that $N_i \to \infty$ for all $i = 1, 2, 3$, otherwise we obtain a quasi-1D or quasi-2D rather than a true 3D system. Thus, not *every* sequence of normal subgroups $\mathcal{T}_{\mathrm{PBC}} \lhd \mathcal{T}$ with increasing index leads to the thermodynamic limit. While here, in the Euclidean case, the requirement $\forall i = 1, 2, 3 : N_i \to \infty$ usually is sufficient, we will have to be more careful in Chapter 9, when

discussing 2D hyperbolic lattices, where the translation group is not a product of translation groups in the two spatial directions. From Eq. (2.28), we see that in the thermodynamic limit, the irreducible representations of the translation group retain their form, but the reciprocal vectors $\mathbf{k}$ uniformly cover the full Brillouin zone

$$\mathrm{BZ} = \left\{ \mathbf{k} \in \mathbb{R}^3 \,\middle|\, \mathbf{k} = \sum_{i=1}^{3} k_i \mathbf{b}_i, \quad 0 \leq k_i < 1 \right\}. \tag{2.30}$$

2.3.2. Bloch theorem

With periodic boundary conditions imposed and the irreducible representations of the translation group determined, we study the corresponding symmetric functions. Let $\Psi_{\mathbf{k}}(\mathbf{r})$ be a function that transforms according to the irreducible representation $D_{\mathbf{k}}$ of $\mathcal{T}$, i.e.,

$$\{\mathbb{1}|\mathbf{t}\}\Psi_{\mathbf{k}}(\mathbf{r}) = D_{\mathbf{k}}(\{\mathbb{1}|\mathbf{t}\})\Psi_{\mathbf{k}}(\mathbf{r}), \tag{2.31}$$

then for any $\{\mathbb{1}|\mathbf{t}\} \in \mathcal{T}$

$$\begin{aligned} \{\mathbb{1}|\mathbf{t}\}\Psi_{\mathbf{k}}(\mathbf{r}) &= \Psi_{\mathbf{k}}(\{\mathbb{1}|\mathbf{t}\}^{-1}\mathbf{r}) = \Psi_{\mathbf{k}}(\mathbf{r}-\mathbf{t}) \\ &\overset{!}{=} D_{\mathbf{k}}(\{\mathbb{1}|\mathbf{t}\})\Psi_{\mathbf{k}}(\mathbf{r}) = \mathrm{e}^{-\mathrm{i}\mathbf{k}\cdot\mathbf{t}}\Psi_{\mathbf{k}}(\mathbf{r}). \end{aligned} \tag{2.32}$$

Define $u_{\mathbf{k}}(\mathbf{r}) = \mathrm{e}^{-\mathrm{i}\mathbf{k}\cdot\mathbf{r}}\Psi_{\mathbf{k}}(\mathbf{r})$, then the above implies that for any $\{\mathbb{1}|\mathbf{t}\} \in \mathcal{T}$

$$\begin{aligned} u_{\mathbf{k}}(\mathbf{r}+\mathbf{t}) &= \mathrm{e}^{-\mathrm{i}\mathbf{k}\cdot\mathbf{r}} \underbrace{\mathrm{e}^{-\mathrm{i}\mathbf{k}\cdot\mathbf{t}}\Psi_{\mathbf{k}}(\mathbf{r}+\mathbf{t})}_{=\Psi_{\mathbf{k}}(\mathbf{r})} \\ &= \mathrm{e}^{-\mathrm{i}\mathbf{k}\cdot\mathbf{r}}\Psi_{\mathbf{k}}(\mathbf{r}) = u_{\mathbf{k}}(\mathbf{r}), \end{aligned} \tag{2.33}$$

i.e. we conclude that $\Psi_{\mathbf{k}}(\mathbf{r})$ must be of the form

$$\Psi_{\mathbf{k}}(\mathbf{r}) = \mathrm{e}^{\mathrm{i}\mathbf{k}\cdot\mathbf{r}}u_{\mathbf{k}}(\mathbf{r}), \qquad u_{\mathbf{k}}(\mathbf{r}+\mathbf{t}) = u_{\mathbf{k}}(\mathbf{r}). \tag{2.34}$$

Physically, this tells us that the solution to the Schrödinger equation for a system that has translational symmetry $\mathcal{T}$ must take the above form with $\mathbf{k}$ in the appropriate Brillouin zone. That is the statement of Bloch's theorem.

Equation (2.34) implies that the Bloch function $\Psi_{\mathbf{k}}(\mathbf{r})$ is fully described by the crystal momentum $\mathbf{k}$ and the *cell-periodic part* $u_{\mathbf{k}}(\mathbf{r})$. If $u_{\mathbf{k}}(\mathbf{r})$ is a continuous function of $\mathbf{k}$, this leads to *band theory*, the description of the Hamiltonian eigenfunctions $\Psi_{\mathbf{k}}(\mathbf{r})$ with eigenenergy E in terms of the maps $\mathbf{k} \mapsto E(\mathbf{k})$ and $\mathbf{k} \mapsto u_{\mathbf{k}}(\mathbf{r})$ defined on the reciprocal space, i.e., in the Brillouin zone.

Algebraically, the compatibility of Bloch's theorem with periodic boundary conditions imposed by $\mathcal{T}_{\mathrm{PBC}}$ can be understood as follows [64]. The periodic boundary conditions are captured by

$$\Psi_{\mathbf{k}}(g_{\mathrm{PBC}}^{-1}\mathbf{r}) = \Psi_{\mathbf{k}}(\mathbf{r}) \tag{2.35}$$

for any $g_{\mathrm{PBC}} \in \mathcal{T}_{\mathrm{PBC}}$ and Bloch's theorem states that

$$\Psi_{\mathbf{k}}(g^{-1}\mathbf{r}) = D_{\mathbf{k}}(g)\Psi_{\mathbf{k}}(\mathbf{r}) \tag{2.36}$$

for any $g \in \mathcal{T}$. Choosing $g = g_{\mathrm{PBC}}$, we obtain the requirement $D_{\mathbf{k}}(g_{\mathrm{PBC}}) = 1$. Next, we consider a translation $gg_{\mathrm{PBC}}g^{-1} \in \mathcal{T}$ with $g \in \mathcal{T}$ and $g_{\mathrm{PBC}} \in \mathcal{T}_{\mathrm{PBC}}$ and observe that by the Bloch theorem and the above requirement

$$\begin{aligned}\Psi_{\mathbf{k}}(gg_{\mathrm{PBC}}^{-1}g^{-1}\mathbf{r}) &= D_{\mathbf{k}}(gg_{\mathrm{PBC}}g^{-1})\Psi_{\mathbf{k}}(\mathbf{r}) \\ &= D_{\mathbf{k}}(g)D_{\mathbf{k}}(g_{\mathrm{PBC}})D_{\mathbf{k}}(g)^{-1}\Psi_{\mathbf{k}}(\mathbf{r}) \\ &= \Psi_{\mathbf{k}}(\mathbf{r}).\end{aligned} \tag{2.37}$$

This equality is ensured if $gg_{\mathrm{PBC}}g^{-1} \in \mathcal{T}_{\mathrm{PBC}}$, which is exactly the condition of $\mathcal{T}_{\mathrm{PBC}}$ being a normal subgroup of $\mathcal{T}$.

2.3.3. The little group and its irreducible representations

Since Bloch functions $\Psi_{\mathbf{k}}(\mathbf{r})$ form a basis of wave functions in the Hilbert space, consideration of symmetries besides the translations, requires us to understand the action of $\{R|\mathbf{v}\} \in \mathcal{S}$ on them. It follows from Eq. (2.5) that

$$\begin{aligned}\{R|\mathbf{v}\}\Psi_{\mathbf{k}}(\mathbf{r}) &= \Psi_{\mathbf{k}}(\{R|\mathbf{v}\}^{-1}\mathbf{r}) \\ &= \Psi_{\mathbf{k}}(R^{-1}(\mathbf{r}-\mathbf{v})) \\ &= \mathrm{e}^{\mathrm{i}\mathbf{k}\cdot R^{-1}(\mathbf{r}-\mathbf{v})}u_{\mathbf{k}}(R^{-1}(\mathbf{r}-\mathbf{v})) \\ &= \mathrm{e}^{\mathrm{i}(R\mathbf{k})\cdot(\mathbf{r}-\mathbf{v})}u_{\mathbf{k}}(R^{-1}(\mathbf{r}-\mathbf{v})),\end{aligned} \tag{2.38}$$

where we used that R is orthogonal and thus $R^{-1} = R^{\top}$ and by definition of the transpose $\mathbf{k}\cdot(R^{\top}\mathbf{r}) = (R\mathbf{k})\cdot\mathbf{r}$. Additionally, acting with a translation $\{\mathbb{1}|\mathbf{t}\}$ on Eq. (2.39), we obtain

$$\begin{aligned}\{\mathbb{1}|\mathbf{t}\}\{R|\mathbf{v}\}\Psi_{\mathbf{k}}(\mathbf{r}) &= \{R|\mathbf{v}+\mathbf{t}\}\Psi_{\mathbf{k}}(\mathbf{r}) \\ &= \mathrm{e}^{\mathrm{i}(R\mathbf{k})\cdot(\mathbf{r}-\mathbf{v}-\mathbf{t})}u_{\mathbf{k}}(R^{-1}(\mathbf{r}-\mathbf{v}-\mathbf{t})) \\ &= \mathrm{e}^{-\mathrm{i}(R\mathbf{k})\cdot\mathbf{t}}\mathrm{e}^{\mathrm{i}(R\mathbf{k})\cdot(\mathbf{r}-\mathbf{v})}\underbrace{u_{\mathbf{k}}(R^{-1}(\mathbf{r}-\mathbf{v})-R^{-1}\mathbf{t})}_{=u_{\mathbf{k}}(R^{-1}(\mathbf{r}-\mathbf{v}))} \\ &= D_{R\mathbf{k}}(\{\mathbb{1}|\mathbf{t}\})\{R|\mathbf{v}\}\Psi_{\mathbf{k}}(\mathbf{r}),\end{aligned} \tag{2.39}$$

because $-R^{-1}\mathbf{t} \in \mathcal{T}$ for $\mathbf{t} \in \mathcal{T}$ and $R \in \mathcal{P}$. This implies that $\{R|\mathbf{v}\}\Psi_{\mathbf{k}}(\mathbf{r})$ is a Bloch function with wave vector $R\mathbf{k}$, which can be interpreted as the action of $\{R|\mathbf{v}\}$ on $\mathbf{k}$ by $\mathbf{k} \mapsto R\mathbf{k}$, enabling us to study symmetries in reciprocal space. Recall, however, that for a given $\mathbf{k}$ there usually are multiple Bloch functions, differing in their cell-periodic part.

Consider the subgroup of $\mathcal{S}$ which, according to the action in reciprocal space defined above, leaves a given wave vector $\mathbf{k}$ invariant (up to a reciprocal lattice vector $\mathbf{b}$),

$$\mathcal{G}^{\mathbf{k}} = \{g \in \mathcal{S} | \exists \mathbf{b} \in \mathcal{T} \,:\, g\mathbf{k} = \mathbf{k} + \mathbf{b}\} < \mathcal{S}. \tag{2.40}$$

This group is called the *little group* of $\mathbf{k}$. Just as $\mathcal{S}$, it is an infinite group containing translations and therefore can be written as

$$\mathcal{G}^{\mathbf{k}} = \bigcup_i \{R_i|\mathbf{v}_i\}\mathcal{T}, \tag{2.41}$$

where i runs over a smaller index set than in Eq. (2.1). Again the cosets $\{R_i|\mathbf{v}_i\}\mathcal{T}$ (with coset representatives $\{R_i|\mathbf{w}_i\}$) form a quotient group $\overline{\mathcal{G}}^{\mathbf{k}} = \mathcal{G}^{\mathbf{k}}/\mathcal{T}$, known as the *little co-group*. It turns out to be isomorphic to the group $\mathcal{P}^{\mathbf{k}} < \mathcal{P}$ formed by the elements $R_i \in \mathcal{P}$.

It follows from Eq. (2.39) that under the action of elements of the little group $\mathcal{G}^{\mathbf{k}}$, Bloch functions with the same $\mathbf{k}$-vector are mixed. Assume the functions $\Psi_{\mathbf{k},i}(\mathbf{r})$ form a basis of the subspace of the Hilbert space associated with $\mathbf{k}$, then for $\{R|\mathbf{v}\} \in \mathcal{G}^{\mathbf{k}}$

$$\{R|\mathbf{v}\}\Psi_{\mathbf{k},i}(\mathbf{r}) = \sum_j \mathcal{D}^{\mathbf{k}}_{ij}(\{R|\mathbf{v}\})\Psi_{\mathbf{k},j}(\mathbf{r}), \tag{2.42}$$

i.e., the map $\mathcal{D}^{\mathbf{k}}$ from $\mathcal{G}^{\mathbf{k}}$ to the group of unitary matrices furnishes a unitary representation of $\mathcal{G}^{\mathbf{k}}$. If we include antiunitary symmetries, then we instead consider *corepresentations*.

If $\mathcal{G}^{\mathbf{k}}$ is symmorphic, then it has the semidirect-product structure

$$\mathcal{G}^{\mathbf{k}} = \overline{\mathcal{G}}^{\mathbf{k}} \ltimes \mathcal{T}, \tag{2.43}$$

i.e., for every $\{R|\mathbf{t}\} \in \mathcal{G}^{\mathbf{k}}$, there are unique $\{R|0\} \in \overline{\mathcal{G}}^{\mathbf{k}}$ and $\{\mathbb{1}|\mathbf{t}\} \in \mathcal{T}$, such that

$$\{R|\mathbf{t}\} = \{R|0\}\{\mathbb{1}|\mathbf{t}\}. \tag{2.44}$$

This implies that the ICRs $\overline{D}^{\mathbf{k}}(\{R|\mathbf{v}\})$ of $\mathcal{G}^{\mathbf{k}}$ are deduced from the ICRs $\overline{D}^{\mathbf{k}}(R)$ of the little co-group $\overline{\mathcal{G}}^{\mathbf{k}} < \mathcal{G}^{\mathbf{k}}$:

$$\overline{D}^{\mathbf{k}}(\{R|\mathbf{t}\}) = \overline{D}^{\mathbf{k}}(\{R|0\}\{\mathbb{1}|\mathbf{t}\}) = \overline{D}^{\mathbf{k}}(R)\mathrm{e}^{-\mathrm{i}\mathbf{k}\cdot\mathbf{t}}, \tag{2.45}$$

where we intentionally use the same symbol for corepresentations of $\overline{\mathcal{G}}^{\mathbf{k}}$ and the corresponding induced corepresentations of $\mathcal{G}^{\mathbf{k}}$. On the other hand, if the space group is nonsymmorphic, it becomes necessary to study the *projective* corepresentations of $\overline{\mathcal{G}}^{\mathbf{k}}$. Below, we briefly review how to find all ICRs of a nonsymmorphic little group and list some properties of projective corepresentations (PCRs) that will be useful throughout Part II. The review follows Ref. 77 but directly deals with magnetic groups [86, 87].

Irreducible representations of the little group

To find all ICRs of $\mathcal{G}^{\mathbf{k}}$, which generally is nonunitary, we start by factorizing $\mathcal{G}^{\mathbf{k}}$ into left cosets with respect to the translation group $\mathcal{T}$:

$$\mathcal{G}^{\mathbf{k}} = \sum_{\alpha} \{S_\alpha|\mathbf{w}_\alpha\}\mathcal{T}, \tag{2.46}$$

where S is either unitary or antiunitary. To make this explicit, we use unprimed and primed indices for unitary elements and antiunitary elements, respectively:

$$\mathcal{G}^{\mathbf{k}} = \sum_{i} \{S_i|\mathbf{w}_i\}\mathcal{T} + \sum_{i'} \{S_{i'}|\mathbf{w}_{i'}\}\mathcal{T}. \tag{2.47}$$

This decomposition is unique only up to changes of each $\mathbf{w}_\alpha$ by arbitrary lattice vectors $\mathbf{t}_\alpha \in \mathcal{T}$, where the Greek subscripts encompass both unitary and antiunitary elements.

The coset representatives $\{S_\alpha|\mathbf{w}_\alpha\}$ do not form a group, but satisfy

$$\{S_\alpha|\mathbf{w}_\alpha\}\{S_\beta|\mathbf{w}_\beta\} = \{\mathbb{1}|\mathbf{t}_{\alpha\beta}\}\{S_\gamma|\mathbf{w}_\gamma\}, \tag{2.48}$$

where $S_\gamma = S_\alpha S_\beta$ with $\mathbf{w}_\gamma$ the corresponding translation in the coset decomposition and

$$\mathbf{t}_{\alpha\beta} = \mathbf{w}_\alpha + S_\alpha \mathbf{w}_\beta - \mathbf{w}_\gamma. \tag{2.49}$$

Given a corepresentation $\overline{\mathcal{D}}^{\mathbf{k}}$ of $\mathcal{G}^{\mathbf{k}}$, then according to Eq. (2.16) and using

$$\overline{\mathcal{D}}^{\mathbf{k}}(\{\mathbb{1}|\mathbf{t}_{\alpha\beta}\}) = \mathrm{e}^{-\mathrm{i}\mathbf{k}\cdot\mathbf{t}_{\alpha\beta}} \tag{2.50}$$

it holds that

$$\overline{\mathcal{D}}^{\mathbf{k}}(\{S_i|\mathbf{w}_i\})\overline{\mathcal{D}}^{\mathbf{k}}(\{S_j|\mathbf{w}_j\}) = \mathrm{e}^{-\mathrm{i}\mathbf{k}\cdot\mathbf{t}_{ij}}\overline{\mathcal{D}}^{\mathbf{k}}(\{S_iS_j|\mathbf{w}_l\}), \tag{2.51a}$$

$$\overline{\mathcal{D}}^{\mathbf{k}}(\{S_i|\mathbf{w}_i\})\overline{\mathcal{D}}^{\mathbf{k}}(\{S_{j'}|\mathbf{w}_{j'}\}) = \mathrm{e}^{-\mathrm{i}\mathbf{k}\cdot\mathbf{t}_{ij'}}\overline{\mathcal{D}}^{\mathbf{k}}(\{S_iS_{j'}|\mathbf{w}_{l'}\}), \tag{2.51b}$$

$$\overline{\mathcal{D}}^{\mathbf{k}}(\{S_{i'}|\mathbf{w}_{i'}\})\overline{\mathcal{D}}^{\mathbf{k}}(\{S_j|\mathbf{w}_j\})^* = \mathrm{e}^{-\mathrm{i}\mathbf{k}\cdot\mathbf{t}_{i'j}}\overline{\mathcal{D}}^{\mathbf{k}}(\{S_{i'}S_j|\mathbf{w}_{l'}\}), \tag{2.51c}$$

$$\overline{\mathcal{D}}^{\mathbf{k}}(\{S_{i'}|\mathbf{w}_{i'}\})\overline{\mathcal{D}}^{\mathbf{k}}(\{S_{j'}|\mathbf{w}_{j'}\})^* = \mathrm{e}^{-\mathrm{i}\mathbf{k}\cdot\mathbf{t}_{i'j'}}\overline{\mathcal{D}}^{\mathbf{k}}(\{S_{i'}S_{j'}|\mathbf{w}_l\}). \tag{2.51d}$$

One can show that $\overline{\mathscr{D}}^{\mathbf{k}}$ only depends on the coset in the decomposition shown in Eq. (2.46) and therefore is a matrix-valued function on the quotient group $\mathscr{G}^{\mathbf{k}}/\mathscr{T}$, which is isomorphic to the little co-group $\overline{\mathscr{G}}^{\mathbf{k}}$. This implies that we can write

$$\overline{\mathscr{D}}^{\mathbf{k}}(\{S_\alpha|\mathbf{w}_\alpha\}) = \overline{\Delta}^{\mathbf{k}}(S_\alpha) \tag{2.52}$$

and $\overline{\Delta}^{\mathbf{k}}$ furnishes a *projective* corepresentation (PCR) of the little co-group $\overline{\mathscr{G}}^{\mathbf{k}}$ with factor system $\mu(S_\alpha, S_\beta) = \mathrm{e}^{-\mathrm{i}\mathbf{k}\cdot\mathbf{t}_{\alpha\beta}}$. Thus, all ICRs of $\mathscr{G}^{\mathbf{k}}$ can be found by finding the projective ICRs of $\overline{\mathscr{G}}^{\mathbf{k}}$ and only keeping those with the correct factor system

$$\mu(S_\alpha, S_\beta) = \mathrm{e}^{-\mathrm{i}\mathbf{k}\cdot(\mathbf{w}_\alpha + S_\alpha\mathbf{w}_\beta - \mathbf{w}_\gamma)}. \tag{2.53}$$

Properties of projective corepresentations

Projective corepresentations of a finite-order group G with unitary subgroup H and antiunitary complement $G - H$ generalize the notion of (ordinary) representations. A PCR $\overline{\Delta}$ is a map from G to the group of invertible matrices that satisfies

$$\overline{\Delta}(h)\overline{\Delta}(g) = \mu(h, g)\overline{\Delta}(hg), \tag{2.54a}$$

$$\overline{\Delta}(a)\overline{\Delta}(g)^* = \mu(a, g)\overline{\Delta}(ag), \tag{2.54b}$$

for any $g \in G$, $h \in H$ and $a \in G-H$. In contrast, for *ordinary* corepresentations one demands, $\mu(g, g') = 1$ for all $g, g' \in G$. The map $\mu : G \times G \mapsto \mathbb{C}$ forms a so-called *factor system* and satisfies

$$\mu(h, g)\mu(hg, g') = \mu(h, gg')\mu(g, g'), \tag{2.55a}$$

$$\mu(a, g)\mu(ag, g') = \mu(a, gg')\mu(g, g')^*, \tag{2.55b}$$

for all $g, g' \in G$, $h \in H$ and $a \in G - H$.

As for ordinary corepresentations, the similarity transformations given in Eq. (2.17) map a PCR to an equivalent PCR. If the factor system satisfies $|\mu(g, g')| = 1$ for all $g, g' \in G$, which it does in our use case, cf. Eq. (2.53), we can always find a transformation such that $\overline{\Delta}(g)$ is unitary for all $g \in G$. Additionally, given a PCR $\overline{\Delta}$

$$\overline{\Delta}'(g) = C(g)\overline{\Delta}(g) \tag{2.56}$$

for all $g \in G$ and $C : G \to \mathbb{C} \setminus \{0\}$ a function into the non-zero complex

numbers, $\overline{\Delta}'$ forms another projective representation with factor system

$$\nu(h,g) = \frac{C(h)C(g)}{C(hg)}\mu(h,g), \tag{2.57a}$$

$$\nu(a,g) = \frac{C(a)C(g)^*}{C(ag)}\mu(a,g), \tag{2.57b}$$

for all $g \in G$, $h \in H$ and $a \in G - H$. The transformation in Eq. (2.56) defines *equivalence classes of factor systems*: two factor systems μ and ν are equivalent if and only if there exists a complex-valued function C such that Eq. (2.57) is satisfied.

Thus, we are sufficiently prepared for the discussion of the Bloch Hamiltonian and constraints imposed on it by the space group.

2.4. Bloch Hamiltonian

Because Bloch functions transform in irreducible representations of a subgroup $\mathcal{T}$ of the full symmetry group $\mathcal{S}$ of the Hamiltonian, they imply that, written in the corresponding basis, the Hamiltonian is block-diagonal. This basis $\{|\mathbf{k},\alpha\rangle\}_{\mathbf{k},\alpha}$, where $\mathbf{k} \in \mathrm{BZ}$ and α denotes additional degrees of freedom inside the unit cell (orbitals, internal degrees of freedom), consists of states taking the form of Bloch functions: $\langle \mathbf{r}|\mathbf{k},\alpha\rangle = \Psi_{\mathbf{k},\alpha}(\mathbf{r})$. Expanding the Hamiltonian in that basis,

$$\mathcal{H} = \sum_{\mathbf{k},\mathbf{k}',\alpha,\beta} \langle \mathbf{k},\alpha|\mathcal{H}|\mathbf{k}',\beta\rangle \, |\mathbf{k},\alpha\rangle\langle\mathbf{k}',\beta| \,, \tag{2.58}$$

the corresponding Hamiltonian matrix is block diagonal:

$$\langle \mathbf{k},\alpha|\mathcal{H}|\mathbf{k}',\beta\rangle = H(\mathbf{k})^{\alpha\beta}\delta_{\mathbf{k},\mathbf{k}'} \tag{2.59}$$

with the blocks $H(\mathbf{k})$ forming a function of $\mathbf{k}$, known as the *Bloch Hamiltonian*. We briefly discuss two common conventions for the Bloch Hamiltonian in Section 2.4.1 with more details given in Appendix A, before turning to a summary of the constraints posed by space-group symmetries in Section 2.4.2.

2.4.1. Definition and convention

We consider a general tight-binding model on a Bravais lattice with N sites given by the second quantized Hamiltonian

$$\mathcal{H} = -\sum_{i,j,\alpha,\beta} h_{ij}^{\alpha\beta}(c_i^\alpha)^\dagger c_j^\beta, \tag{2.60}$$

with site indices i, j and orbital (or any other) degrees of freedom indexed by α, β. The amplitude for the hopping process from (j, β) to (i, α) is $h_{ij}^{\alpha\beta}$. Let $\mathbf{R}_i$ be the *position of the unit cell*, corresponding to site i of the Bravais lattice and $\boldsymbol{\delta}^\alpha$ the position of the orbital $|i, \alpha\rangle = (c_i^\alpha)^\dagger |0\rangle$ relative to the Bravais-lattice site. The actual position of the orbital (i, α) then is

$$\mathbf{r}_i^\alpha = \mathbf{R}_i + \boldsymbol{\delta}^\alpha. \tag{2.61}$$

Following Eq. (2.2), the lattice sites i are parametrized by a set of integers n_j.

To block-diagonalize $\mathcal{H}$, we change basis using a Fourier transform. Crucially, there are two conventions for this change of basis, (I) based on the position of the Bravais-lattice site $\mathbf{R}_i$ and (II) based on the actual position of the orbital $\mathbf{r}_i^\alpha$,

$$\hat{c}_{\mathrm{I};\mathbf{k}}^\alpha = \frac{1}{\sqrt{N}} \sum_{i=1}^{N} c_i^\alpha \mathrm{e}^{-\mathrm{i}\mathbf{k}\cdot\mathbf{R}_i}, \tag{2.62}$$

$$\hat{c}_{\mathrm{II};\mathbf{k}}^\alpha = \frac{1}{\sqrt{N}} \sum_{i=1}^{N} c_i^\alpha \mathrm{e}^{-\mathrm{i}\mathbf{k}\cdot\mathbf{r}_i^\alpha}. \tag{2.63}$$

Note that $\mathbf{R}_i$ depends on the choice of unit cell, while $\mathbf{r}_i^\alpha$ does not. In either case, the Hamiltonian can be rewritten as

$$\mathcal{H} = \sum_{\mathbf{k}\in\mathrm{BZ}} \sum_{\alpha,\beta} (\hat{c}_{\mathbf{k}}^\alpha)^\dagger H(\mathbf{k})^{\alpha\beta} \hat{c}_{\mathbf{k}}^\beta, \tag{2.64}$$

with the sum over the Brillouin zone and the Bloch Hamiltonians

$$H_{\mathrm{I}}(\mathbf{k})^{\alpha\beta} = -\sum_\ell h_\ell^{\alpha\beta} \mathrm{e}^{-\mathrm{i}\mathbf{k}\cdot(\mathbf{R}_\ell + \boldsymbol{\delta}^\alpha - \boldsymbol{\delta}^\beta)}, \tag{2.65}$$

$$H_{\mathrm{II}}(\mathbf{k})^{\alpha\beta} = -\sum_\ell h_\ell^{\alpha\beta} \mathrm{e}^{-\mathrm{i}\mathbf{k}\cdot\mathbf{R}_\ell}, \tag{2.66}$$

where $\ell = i - j$ emphasizes that h only depends on the difference $\mathbf{R}_\ell = \mathbf{R}_i - \mathbf{R}_j$.

While both are valid choices, it turns out that convention II is more appropriate for topology and symmetry analysis [88, 89]: certain quantities, such as the Berry curvature, can violate the point group symmetries and depend on the choice of unit cell when computing them from eigenstates of the Bloch Hamiltonian in convention I. Therefore, throughout Part II, we *exclusively* work in convention II, whose characteristic property is that the Bloch Hamiltonian is not generally periodic in $\mathbf{k}$. More precisely, for any reciprocal lattice vector

b, there is an additional phase factor depending on the relative position of the orbitals in the unit cell:

$$H_{\mathrm{II}}(\mathbf{k}+\mathbf{b})^{\alpha\beta} = H_{\mathrm{II}}(\mathbf{k})^{\alpha\beta} \mathrm{e}^{-\mathrm{i}\mathbf{b}\cdot(\boldsymbol{\delta}^{\alpha}-\boldsymbol{\delta}^{\beta})}. \tag{2.67}$$

On the other hand, convention I does not directly refer to positions and only to the lattice sites, which makes it the easier starting point to generalize the notions of band theory and Bloch Hamiltonian to hyperbolic lattices. Thus, in Part III, we use convention I.

2.4.2. Symmetry constraints

Recall that the condition for $g \in \mathcal{S}$ to be a symmetry of the Hamiltonian is

$$[\mathcal{H}, \mathcal{U}_g] = 0. \tag{2.68}$$

If we expand the Hamiltonian in an arbitrary basis $\{|i\rangle\}_i$, similar to Eq. (2.58),

$$\mathcal{H} = \sum_{i,j} \langle i|\mathcal{H}|j\rangle \, |i\rangle\langle j| \,, \tag{2.69}$$

and we know how the symmetry acts on that basis, i.e., we know the representation,

$$\mathcal{U}_g \, |i\rangle = \sum_j \mathcal{D}_{ij}(g) \, |j\rangle \,, \tag{2.70}$$

then the matrix $H_{ij} = \langle i|\mathcal{H}|j\rangle$ satisfies the constraint

$$H = \mathcal{D}(g) H \mathcal{D}(g)^{-1}. \tag{2.71}$$

Note that, due to the group structure of $\mathcal{S}$, the only independent constraints are those due to the *generators* of the symmetry group.

As we have seen above, a particularly convenient basis is provided by Bloch functions, which block-diagonalize the Hamiltonian. Adopting that basis, the Bloch Hamiltonian in the vicinity of $\mathbf{k}$ is constrained by the corresponding little group $\mathcal{G}^{\mathbf{k}}$ as follows. Let $g \in \mathcal{G}^{\mathbf{k}}$ and $\mathcal{D}^{\mathbf{k}}$ be the representation of $\mathcal{G}^{\mathbf{k}}$ in which the Hamiltonian transforms, then

$$H(\mathbf{k}) = \mathcal{D}^{\mathbf{k}}(g) H(g^{-1}\mathbf{k}) \mathcal{D}^{\mathbf{k}}(g)^{-1}. \tag{2.72}$$

If $\mathcal{G}^{\mathbf{k}}$ is nonunitary, we need to distinguish elements of the unitary subgroup $\mathcal{G}^{\mathbf{k}}_{\mathrm{u}}$ and the antiunitary complement $\mathcal{G}^{\mathbf{k}}_{\mathrm{au}}$, such that the constraints read

$$\forall g \in \mathcal{G}^{\mathbf{k}}_{\mathrm{u}} : \qquad \overline{\mathcal{D}}^{\mathbf{k}}(g) H(g^{-1}\mathbf{k}) \overline{\mathcal{D}}^{\mathbf{k}}(g)^{-1} = H(\mathbf{k}), \tag{2.73a}$$

$$\forall g \in \mathcal{G}^{\mathbf{k}}_{\mathrm{au}} : \qquad \overline{\mathcal{D}}^{\mathbf{k}}(g) H(g^{-1}\mathbf{k})^{*} \overline{\mathcal{D}}^{\mathbf{k}}(g)^{-1} = H(\mathbf{k}), \tag{2.73b}$$

where $\overline{\mathcal{D}}^{\mathbf{k}}$ is the corresponding corepresentation of $\mathcal{G}^{\mathbf{k}}$. Again, independent constraints only arise due to the *generators* of $\mathcal{G}^{\mathbf{k}}$.

Recall from Eq. (2.45) that if $\mathcal{G}^{\mathbf{k}}$ is symmorphic,

$$\overline{\mathcal{D}}^{\mathbf{k}}(\{R|\mathbf{t}\}) = \overline{\mathcal{D}}^{\mathbf{k}}(\{R|0\})\mathrm{e}^{-\mathrm{i}\mathbf{k}\cdot\mathbf{t}}. \tag{2.74}$$

Since the additional factor $\mathrm{e}^{-\mathrm{i}\mathbf{k}\cdot\mathbf{t}}$ cancels in Eq. (2.72), it is sufficient to consider the little *co*-group $\overline{\mathcal{G}}^{\mathbf{k}} \cong \mathcal{G}^{\mathbf{k}}/\mathcal{T}$ and its corepresentations instead. In contrast, the corepresentations of a nonsymmorphic $\mathcal{G}^{\mathbf{k}}$ *cannot* simply be obtained from the corepresentations of the corresponding little co-group. However, as we have explained in Section 2.3.3, they are given by *certain* PCRs of $\overline{\mathcal{G}}^{\mathbf{k}}$. Therefore, we can rewrite Eq. (2.73) in terms of elements of $\overline{\mathcal{G}}^{\mathbf{k}}$ and the PCR $\overline{\Delta}^{\mathbf{k}}$ from which $\overline{\mathcal{D}}^{\mathbf{k}}$ is deduced:

$$\overline{\Delta}^{\mathbf{k}}(S_i)H(S_i^{-1}\mathbf{k})\overline{\Delta}^{\mathbf{k}}(S_i)^{-1} = H(\mathbf{k}), \tag{2.75a}$$

$$\overline{\Delta}^{\mathbf{k}}(S_{i'})H(S_{i'}^{-1}\mathbf{k})^{*}\overline{\Delta}^{\mathbf{k}}(S_{i'})^{-1} = H(\mathbf{k}), \tag{2.75b}$$

for $S_i, S_{i'} \in \overline{\mathcal{G}}^{\mathbf{k}}$, S_i unitary and $S_{i'}$ antiunitary.

We will make extensive use of Eqs. (2.72), (2.73) and (2.75) throughout Part II to derive minimal models of varying complexity.

Part II.

Triple points and multigap topology

3. Topological band theory and multigap topology

In this chapter, we provide an overview over some of the concepts in topological band theory. A comprehensive review or historical overview is beyond the scope of this chapter, such that we focus on *illustrating* the concepts relevant to later chapters. First, in Section 3.1, we introduce some of the basic conceptual ideas of topological insulators and invariants. Then, in Section 3.2, we discuss the consequences of considering crystalline symmetries including higher-order topology, symmetry indicators and the *filling anomaly* which will play an important role in Chapter 6. In Section 3.3, we explain how these ideas can be extended to semimetals and set the basis for understanding the idea of multigap topology. Finally, in Section 3.4, we introduce the framework of homotopy as a basis for systematically defining topological invariants and present the definitions of the invariants that we use throughout this part: the Berry phase, the quanternion invariant, the Euler class, and the second Stiefel-Whitney class.

3.1. Topological invariants

The fundamental goal of topological band theory is to classify band structures of crystalline systems into equivalence classes under continuous deformation of the system. We first focus on insulating systems and generalize to semimetals in Section 3.3. Electronic insulators are characterized by an energy gap in their band structure, schematically illustrated in Fig. 3.1a, and we consider gap-preserving deformations of the corresponding Hamiltonian. Two insulators are considered to be topologically equivalent if such a deformation between them exists. Usually, some symmetries are required to be respected in this deformation process. For instance, if time-reversal symmetry is respected, then three-dimensional (3D) insulators fall into two equivalence classes: trivial and topological (nontrivial) [90–95].

From that definition of topological insulators, it is easy to understand the origin of the bulk-boundary correspondence. An interface between two topologically inequivalent insulators can be modeled as an interpolation between

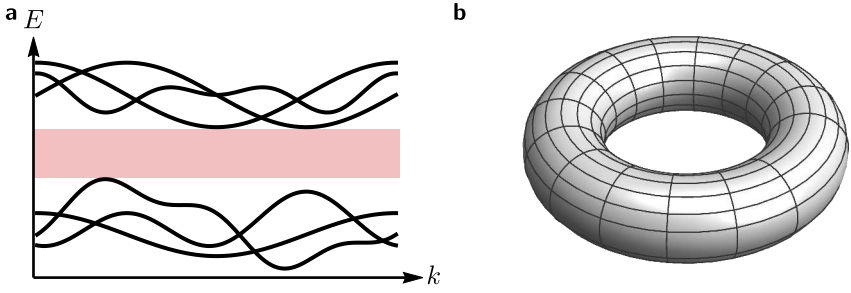

Figure 3.1.: Band structure with an energy gap. (**a**) Schematic insulating band structure (black lines) along some direction in the Brillouin zone with an energy gap (shaded in light red). (**b**) Illustration of the Brillouin-zone torus for a 2D system. The Bloch Hamiltonian $H(\mathbf{k})$ is a function defined on that torus.

the two systems, and therefore, locally, as a deformation of one into the other. By assumption, such a deformation necessarily requires the closing of the gap, implying an in-gap state localized at the interface. The vacuum of free space can be seen as an insulator as well due to the nonvanishing electron mass, which implies that the *surface* of any topological insulator hosts such in-gap states. Crucially, these conducting surface states are topologically protected since no deformation within the same equivalence class can remove them. They are often *anomalous* in that they cannot exist independently from the bulk.

Mathematically, the deformation and partitioning into equivalence classes, can be formulated as follows. The presence of translational symmetry allows us to directly work in momentum space, i.e., the fundamental object is the Bloch Hamiltonian $H(\mathbf{k})$ with $\mathbf{k}$ in the Brillouin-zone torus T^d, where d is the spatial dimension of the system, illustrated for a two-dimensional (2D) system in Fig. 3.1b. This defines a map $\mathbf{k} \mapsto H(\mathbf{k})$ from T^d (which we will refer to as the *base space*) to the space of Bloch Hamiltonians with a gapped spectrum (which we will refer to as the *target space*). The partitioning into equivalence classes is then a well-defined mathematical problem and we will elaborate on one possible way to approach it in Section 3.4. At this point, it is sufficient to note that equivalence classes are characterized by sets of *invariants*, mathematical quantities that remain invariant within the same equivalence class. The change of any of the invariants between two systems indicates that the two are topologically inequivalent.

A well-known example of a topological invariant is the *first Chern number*, which is defined in terms of the map $\mathbf{k} \mapsto H(\mathbf{k})$ or more precisely in terms of

the maps $\mathbf{k} \mapsto |u_n(\mathbf{k})\rangle$, where $|u_n(\mathbf{k})\rangle$ are eigenstates of the Bloch Hamiltonian, $H(\mathbf{k})\,|u_n(\mathbf{k})\rangle = \varepsilon_n(\mathbf{k})\,|u_n(\mathbf{k})\rangle$. To write out the expression, we define the *Berry connection*

$$\mathcal{A}^{(n)}(\mathbf{k}) = \mathrm{i}\,\langle u_n(\mathbf{k})|\boldsymbol{\nabla}_{\mathbf{k}}|u_n(\mathbf{k})\rangle \tag{3.1}$$

and the *Berry curvature*

$$\Omega_{xy}^{(n)}(\mathbf{k}) = \partial_{k_x}\mathcal{A}_y^{(n)}(\mathbf{k}) - \partial_{k_y}\mathcal{A}_x^{(n)}(\mathbf{k}), \tag{3.2}$$

where ∂_{k_x} is the partial derivative with respect to the momentum component k_x and $\boldsymbol{\nabla}_{\mathbf{k}}$ is the gradient. Then, the Chern number of the n^{th} band of a 2D system is given by

$$c_1^{(n)} = \frac{1}{2\pi}\int_{\mathrm{BZ}} \mathrm{d}^2k\,\Omega_{xy}^{(n)}(\mathbf{k}) \tag{3.3}$$

and it can be shown that it is quantized to an integer: $c_1^{(n)} \in \mathbb{Z}$.

A nontrivial Chern number, $c_1^{(n)} \neq 0$, indicates an obstruction to the existence of a smooth and periodic gauge of the eigenstates on the whole Brillouin zone. If a smooth gauge covering the whole Brillouin zone torus existed, Stoke's theorem would imply that the integral on the right hand side of (3.3) vanishes, see Appendix A.2.2. We also recognize that $c_1^{(n)}$ is a property of the eigenstates alone and does not involve the energetics. This is generally true for topological invariants, such that one often eliminates the energetics by *spectrally flattening* the Hamiltonian: while the eigenstates $|u_n(\mathbf{k})\rangle$ are kept, the dependence of ε_i on $\mathbf{k}$ is neglected and replaced by constants, while preserving the partition into bands below and above the energy gap.

The Chern number is not just an abstract mathematical tool for studying topological equivalence, but has observable consequences. It can be shown [16, 96] that the quantized Hall conductivity σ_{xy} observed in quantum Hall insulators is given by the Chern numbers of the N_{occ} occupied bands

$$\sigma_{xy} = \frac{e^2}{h}\sum_{n=1}^{N_{\mathrm{occ}}} c_1^{(n)}, \tag{3.4}$$

with the electronic charge e and Planck's constant h. The fact that $c_1^{(n)}$ is an integer then implies the quantization of the Hall conductivity. On the other hand, the conductivity can be related to the number of topological gapless edge states: each edge state provides a ballistic transport channel with conductance e^2/h, such that the difference in numbers of right and left moving modes is given by the change of the Chern number across the interface [24].

3.1.1. Parallel transport and Wilson loop operator

A more general framework for computing invariants is provided by *parallel transport* and the *Wilson loop operator* [23, 97–99]. For that, we consider the adiabatic evolution of occupied states $|u_n(\mathbf{k})\rangle$ along some path $\gamma : [0,1] \to \mathrm{BZ}$, $t \mapsto \mathbf{k} = \gamma(t)$. Adiabaticity implies that the evolved states remain in the occupied subspace along the whole path. This can be realized by parallel transport, i.e., by projecting $|u_n(\gamma(t))\rangle$ to the occupied subspace of $H(t+\delta t)$ for an infinitesimal δt. Introducing the corresponding projector

$$\mathbb{P}(\mathbf{k}) = \sum_{j=1}^{N_\mathrm{occ}} |u_j(\mathbf{k})\rangle\langle u_j(\mathbf{k})| \,, \tag{3.5}$$

the matrix of overlaps of the initial states $|u_n(\gamma(0))\rangle$ with the final states $|u_m(\gamma(1))\rangle$ is then given by

$$\mathcal{W}(\gamma)_{mn} = \lim_{\delta t \to 0} \langle u_m(\gamma(1))| \prod_{t}^{1\leftarrow 0} \mathbb{P}(\gamma(t)) |u_n(\gamma(0))\rangle \,, \tag{3.6}$$

where $\prod_t^{1\leftarrow 0}$ indicates the path-ordered product with smaller values of t to the right. The matrix $\mathcal{W}(\gamma)$ is known as the Wilson operator; it is an $(N_\mathrm{occ} \times N_\mathrm{occ})$-matrix and is generally gauge-dependent, because the initial and final states transform differently. Even if γ is a closed path, when $\mathcal{W}(\gamma)$ is referred to as a Wilson *loop* operator, final and initial state may differ if the closed path is noncontractible, as we described in Section 2.4. However, the *eigenvalues* are not affected by the gauge transformation, such that they are physical.

Noticing that the overlaps occurring in Eq. (3.6) can be considered to be expansions of the exponential

$$\begin{aligned} \langle u_m(\mathbf{k})|u_n(\mathbf{k}-\mathrm{d}\mathbf{k})\rangle &\approx \delta_{mn} - \mathrm{d}\mathbf{k}\cdot\langle u_m(\mathbf{k})|\boldsymbol{\nabla}_\mathbf{k}|u_n(\mathbf{k})\rangle \\ &\approx \exp\left(-\mathrm{d}\mathbf{k}\cdot\langle u_m(\mathbf{k})|\boldsymbol{\nabla}_\mathbf{k}|u_n(\mathbf{k})\rangle\right) \end{aligned} \tag{3.7}$$

and defining the generalization of the Berry connection to off-diagonal elements

$$\mathcal{A}^{mn} = \mathrm{i}\,\langle u_m(\mathbf{k})|\boldsymbol{\nabla}_\mathbf{k}|u_n(\mathbf{k})\rangle \,, \tag{3.8}$$

Eq. (3.6) can be written as a path-ordered exponential

$$\mathcal{W}(\gamma) = \overline{\exp}\left(\mathrm{i}\int_\gamma \mathrm{d}\mathbf{k}\cdot\mathcal{A}(\mathbf{k})\right) . \tag{3.9}$$

The spectrum of the unitary operator $\mathcal{W}(\gamma)$, whose eigenvalues take the form of phase factors $\mathrm{e}^{\mathrm{i}\vartheta_j}$, gives access to topological invariants. Let us briefly

illustrate that using two examples. Because the determinant is insensitive to the path ordering, for a closed path γ, we have

$$\det \mathcal{W}(\gamma) = \exp\left(\mathrm{i} \oint_\gamma \mathrm{d}\mathbf{k} \cdot \operatorname{Tr} \mathcal{A}(\mathbf{k})\right), \tag{3.10}$$

such that

$$\varphi(\gamma) = -\mathrm{i} \log \det \mathcal{W}(\gamma) = \oint_\gamma \mathrm{d}\mathbf{k} \cdot \operatorname{Tr} \mathcal{A}(\mathbf{k}), \tag{3.11}$$

which is known as the *Berry phase* [23] and describes the geometric phase that is picked up by adiabatic evolution in a system with nonvanishing Berry connection. If γ is noncontractible, i.e., if it winds around the Brillouin-zone torus, $\varphi(\gamma)$ is also known as the *Zak* or *Zak-Berry phase* [98, 100].

As a second example, let us consider the Chern number in a 2D system. We cover the Brillouin zone by the closed paths $\gamma_{k_y}(k_x) = \mathbf{k}$ with $k_x, k_y \in [0, 2\pi)$, then the Wilson loop operators $\mathcal{W}_x(k_y) = \mathcal{W}(\gamma_{k_y})$ have eigenvalues $\mathrm{e}^{\mathrm{i}\vartheta_j(k_y)}$ with $j = 1, 2, \ldots, N_{\mathrm{occ}}$, such that

$$\det \mathcal{W}_x(k_y) = \prod_{j=1}^{N_{\mathrm{occ}}} \mathrm{e}^{\mathrm{i}\vartheta_j(k_y)} \tag{3.12}$$

On the other hand, we find, using Eq. (3.10), that

$$\sum_{j=1}^{N_{\mathrm{occ}}} \vartheta_j(k_y) = \int_0^{2\pi} \mathrm{d}k_x \operatorname{Tr} \mathcal{A}_x(k_x, k_y). \tag{3.13}$$

We now observe that the winding number of the phases $\vartheta_j(k_y)$ is

$$\begin{aligned} w &= -\sum_{j=1}^{N_{\mathrm{occ}}} \frac{1}{2\pi} \int_0^{2\pi} \mathrm{d}k_y \, \partial_{k_y} \vartheta_j(k_y) \\ &= -\frac{1}{2\pi} \int_{\mathrm{BZ}} \mathrm{d}^2k \, \partial_{k_y} \operatorname{Tr} \mathcal{A}_x(k_x, k_y). \end{aligned} \tag{3.14}$$

While we have argued above that a nontrivial Chern number implies the nonexistence of a smooth and periodic gauge across the whole Brillouin zone, a gauge that is smooth and periodic along one direction, say k_x, does exist, as indicated by (A.35) in Appendix A.2.2. In such a gauge, $\partial_{k_x} \operatorname{Tr} \mathcal{A}_y(k_x, k_y)$ does not contribute to the integral over the Brillouin zone, such that we arrive at

$$w = \sum_{j=1}^{N_{\mathrm{occ}}} c_1^{(j)}, \tag{3.15}$$

i.e., the winding number gives the total Chern number. As we will see in Section 3.4, similar relationships hold for other invariants and we will extensively use Wilson loop operators for their computation in Chapters 5 and 6.

Let us comment on the relationship of the Wilson loop eigenvalues to the eigenvalues of the position operator and to polarization. In d dimensions, we consider a family of noncontractible loops $\gamma_{\mathbf{k}'}(k_x)$, where $\mathbf{k}'$ collects the remaining $(d-1)$ components of $\mathbf{k}$, and construct the corresponding Wilson loop operators $\mathcal{W}_x(\mathbf{k}') = \mathcal{W}(\gamma_{\mathbf{k}'})$. Then, the eigenvalues $\frac{1}{2\pi}\vartheta_j(\mathbf{k}')$ of the operator $-\frac{\mathrm{i}}{2\pi}\log\mathcal{W}_x(\mathbf{k}')$ are equivalent to the eigenvalues $\frac{1}{2\pi}\tilde{\vartheta}_{j,X}(\mathbf{k}')$ of the projected position operator

$$\mathbb{P}(\mathbf{k})\hat{x}\mathbb{P}(\mathbf{k}). \tag{3.16}$$

Note that this is not a one-to-one correspondence, since there are N_{occ} Wilson loop eigenvalues but $\mathbb{P}(\mathbf{k})\hat{x}\mathbb{P}(\mathbf{k})$ is extensive, resulting in a ladder of eigenvalues of the projected position operator:

$$\frac{\tilde{\vartheta}_{j,X}(\mathbf{k}')}{2\pi} = \frac{\vartheta_j(\mathbf{k}')}{2\pi} + X, \qquad j = 1, 2, \ldots, N_{\mathrm{occ}}, \qquad X \in \mathbb{Z}. \tag{3.17}$$

This reflects the translation invariance: eigenvalues of the position operator are repeated periodically in the lattice. This relationship also establishes the interpretation of the Wilson loop eigenvalues as components of the *Wannier centers*, the centers of localization of the electronic states, which is discussed in terms of Wannier functions further below.

Finally, the position operator is involved in the definition of *polarization* $\mathbf{P}$, which, microscopically, is defined as the product of charge and its displacement from the unit cell's center [101]. This leads to an expression of the polarization in terms of the Wilson loop operator:

$$P_x = -\frac{\mathrm{i}e}{(2\pi)^d}\int \mathrm{d}^{d-1}k' \log\det\mathcal{W}_x(\mathbf{k}'), \tag{3.18}$$

which forms the foundation of what is now called the *modern theory of polarization* [101–103]. In crystals, the polarization $\mathbf{P}$ is only defined modulo integer multiples of $e\mathbf{R}$, where $e < 0$ is the elementary electronic charge and $\mathbf{R}$ is an arbitrary Bravais lattice vector.

3.1.2. Symmetries

The classification of topological insulators, i.e., the type of topological invariant, is strongly dependent on the symmetries that are enforced to be preserved during the adiabatic deformation. Besides crystalline symmetries, on which we comment in Section 3.2, there are internal symmetries like time-reversal

symmetry that we have already met in Chapter 2. The internal symmetries differ from the crystalline symmetries in that they preserve locality, while crystalline symmetries do not. Further, recall that as a consequence of Wigner's theorem [78, 79] symmetry transformations on a Hilbert space have to be either unitary and linear or antiunitary and antilinear. In either case, the many-body operator representing the symmetry commutes with the second-quantized Hamiltonian $\mathcal{H}$.

Some of the internal symmetries are realized antiunitarily, depending on whether we consider many-body operators acting on Fock space or their single-particle representations. In fact, there are three such symmetries: *time-reversal* symmetry $\mathcal{T}$, *particle-hole* (*charge-conjugation*) symmetry $\mathcal{C}$, and *sublattice* (*chiral*) symmetry $\mathcal{S}$. On the level of many-body operators $\mathcal{T}$ and $\mathcal{C}$ are antiunitary and $\mathcal{S}$ is unitary; the corresponding single-particle representations, however, behave differently: $\mathcal{T}$ is realized as an antiunitary symmetry (it commutes with the Hamiltonian matrix), $\mathcal{C}$ as an antiunitary *antisymmetry* (it anticommutes with the Hamiltonian matrix), and $\mathcal{S}$ as a unitary antisymmetry [104]. This implies that for a Bloch Hamiltonian $H(\mathbf{k})$ transforming in the corepresentation $\overline{\mathcal{D}}$,

$$\overline{\mathcal{D}}(\mathcal{T})H(-\mathbf{k})^*\overline{\mathcal{D}}(\mathcal{T})^{-1} = H(\mathbf{k}), \tag{3.19a}$$

$$\overline{\mathcal{D}}(\mathcal{C})H(-\mathbf{k})^*\overline{\mathcal{D}}(\mathcal{C})^{-1} = -H(\mathbf{k}), \tag{3.19b}$$

$$\overline{\mathcal{D}}(\mathcal{S})H(\mathbf{k})\overline{\mathcal{D}}(\mathcal{S})^{-1} = -H(\mathbf{k}), \tag{3.19c}$$

from which we can read that, in momentum space, $\mathcal{T}$ and $\mathcal{C}$ both act as $\mathbf{k} \mapsto -\mathbf{k}$ and $\mathcal{S}$ leaves $\mathbf{k}$ invariant.

We note that, if they are present, $\mathcal{T}^2 = \pm 1$, $\mathcal{C}^2 = \pm 1$, and $\mathcal{S}^2 = 1$, where 1 is the identity operator on the Hilbert space. Furthermore, it holds that $\mathcal{S} = \mathcal{T}\mathcal{C}$, such that if both $\mathcal{T}$ and $\mathcal{C}$ are present, $\mathcal{S}$ symmetry is present as well; on the other hand, $\mathcal{S}$ can be present without the other two. This results in ten possible combinations of the three symmetries, known as the *Altland-Zirnbauer* symmetry classes [105], for which the range of values of the so-called *strong* topological invariants have been derived [106–108].

Let us further comment on the two options $\mathcal{T}^2 = \pm 1$, which will be of relevance in later chapters. A spinless particle does not have any internal structure, such that $\mathcal{T} = \mathcal{K}$. On the other hand, if the particle has a spin degree of freedom, time reversal acts on that as well. For instance, $\mathcal{T}$ acts as a π rotation $\mathrm{e}^{-\mathrm{i}\frac{\pi}{2}\sigma_y} = -\mathrm{i}\sigma_y \in \mathsf{SU}(2)$ on a spin-$\frac{1}{2}$ degree of freedom, which implies that $\mathcal{T}^2 = -1$. This is compatible with the representation-theoretic description introduced in Section 2.2. There, we have initially assumed the point group part of the symmetry group to be a subgroup of $\mathsf{O}(3)$, but later

introduced an additional binary degree of freedom that is flipped by time-reversal symmetry $\mathcal{T}$. Since this additional degree of freedom is completely independent from the spatial degrees of freedom, the corepresentations of the magnetic symmetry group are directly deduced from representation of the unitary subgroup. However, if the Hamiltonian contained terms that couple spatial (orbital) and spin degrees of freedom, i.e., a spin-orbit coupling, we would need to consider the *double groups* which are subgroups of $\mathsf{SU}(2) \times S_2$ instead [109].

In this part, we almost exclusively consider *spinless* systems, i.e., systems with $\mathcal{T}^2 = 1$. Note that while this certainly includes systems *without* spin, the *absence* of any spin degree of freedom is *not* necessary. In particular, for weak or vanishing spin-orbit coupling, the spin degree of freedom can be treated independently as described above. Another way to understand that is as follows. In the absence of spin-orbit coupling there is a full $\mathsf{SU}(2)$ symmetry on the spin part of the Hilbert space, such that any symmetry g acting on the tensor product of the spatial and spin Hilbert space can be combined with an arbitrary element of $s \in \mathsf{SU}(2)$. By choosing s to undo the action of $\mathcal{T}$ on the spin, we can ensure that $(g(1 \otimes s))^2 = 1$.

3.2. Topological crystalline insulators

In the presence of additional *crystalline* symmetries, the classification of topological phases is refined. Restricting to deformations of the Hamiltonian that preserve those symmetries throughout the process leads to a larger number of equivalence classes and the resulting phases are known as topological crystalline insulators [110–115]. While topological crystalline insulators also host protected surface states, these states can only manifest on surfaces respecting the relevant symmetries. Nevertheless, such surface states were predicted in real materials [111] and experimentally observed [114]. With the introduction of those additional equivalence classes, a sharper definition of what is *topological* became necessary, leading to the notion of *atomic limits* [116].

An atomic limit is defined as a gapped ground state with all electrons exponentially localized in position space. Intuitively, this is the ground state obtained from uncoupled atoms with bound electrons arranged in the lattice, justifying the name. Crucially, there is no unique atomic limit when crystalline symmetries have to be preserved during the deformations; several atomic limits exists that cannot be adiabatically deformed into each other [116]. These differ in *where* the electrons are exponentially localized and we consider the atomic limit where the electrons are localized at the locations of the ions as the *trivial* one. Note that the ion positions are not captured by the Bloch Hamiltonian

and must therefore be specified explicitly.

Mathematically, atomic limits are formulated in terms of *maximally localized Wannier functions*. In Section 2.3, we have discussed how eigenfunctions of the Hamiltonian take the form of Bloch functions $\Psi_{\mathbf{k}}(\mathbf{r})$. Going to real space, we define the *Wannier functions* [117, 118] centered at $\mathbf{R}$ as the Fourier transform of the Bloch functions

$$W(\mathbf{r}-\mathbf{R}) = \frac{V_{\mathrm{uc}}}{(2\pi)^d}\int_{\mathrm{BZ}} \mathrm{d}^d k\, \Psi_{\mathbf{k}}(\mathbf{r}) \mathrm{e}^{-\mathrm{i}\mathbf{k}\cdot\mathbf{R}} \tag{3.20}$$

with d the spatial dimension and V_{uc} the volume of the unit cell. The gauge freedom of the Bloch functions implies an ambiguity in the Wannier functions that manifests in different localization properties around $\mathbf{R}$, which is known as the *Wannier center*. Maximally localized Wannier functions exploit this ambiguity to maximize their localization [119–124]. If there exists a gauge with exponentially localized Wannier functions, the system is said to be an atomic limit.

Both the topology, manifested in the $\mathbf{k}$-dependence of the Bloch functions, as well as additional requirements on the Wannier functions to respect crystalline symmetries can pose constraints on that localization. Indeed, we distinguish four types of symmetry-protected topological phases: (1) *stable* topological phases which cannot be adiabatically deformed to any atomic limit and thus Wannier functions cannot be exponentially localized, (2) phases known as *obstructed atomic limits* that can be deformed to an atomic limit but not the trivial one, (3) *fragile* topological phases that can only be deformed to an atomic limit under the addition of *occupied* bands corresponding to an atomic limit, and (4) *delicate* [125, 126] topological phases that can be deformed to an atomic limit under the addition of occupied or unoccupied bands corresponding to an atomic limit.

Atomic limits can be constructed purely based on symmetry considerations. A localized electronic state, usually called an *orbital*, has to obey the local symmetries. In free space, this symmetry is $\mathsf{SO}(3)$ symmetry and the orbitals correspond to its irreducible representations, which appear as atomic orbitals of the hydrogen atoms. On a lattice, on the other hand, the full symmetry group is broken to site-symmetry groups that differ depending on the location in the lattice. These site-symmetry groups are point groups and orbitals at the corresponding position correspond to their irreducible representations. We call the positions with nontrivial site-symmetry group *Wyckoff positions*.

Representations of the site-symmetry groups *induce* so-called *elementary band representations* which are representations of the full space group [127–129]. These elementary band representations determine the transformation properties of Bloch functions of a system constructed by hybridizing symmetric orbitals

located at Wyckoff positions, i.e., of an atomic limit. In turn, elementary band representations *subduce* representations of the little groups at high-symmetry momenta. Recall from Chapter 2, that *all* irreducible representations of the space group can be obtained from irreducible representations of certain little groups. Thus, elementary band representations, constructed in real space as atomic limits, can be completely characterized by their decomposition into irreducible representations of the nontrivial little groups.

While the elementary band representations, by construction, correspond to atomic limits, in reality not all of the resulting Bloch states are actually occupied, i.e., we are *not* interested in the full band structure, but just the occupied subspace. The relevant question thus is if the occupied bands *alone*, or any subspace of bands separated by gaps from the rest, form (or are adiabatically connected to) an atomic limit, i.e., if they can be written as a direct sum of elementary band representations. In general, the result will be a *superposition* of elementary band representations. If the coefficients in that superposition are non-negative integers, the band structure corresponds to an atomic limit. The appearance of negative integer coefficients implies correspondence to an atomic limit after compensating by *adding* those elementary band representations, and thus corresponds to *fragile* topology. Finally, *stable* topology is reflected in fractional coefficients.

A systematic characterization of all elementary band representations for all space groups in terms of their decomposition into irreducible representations of little groups has been performed using spectral graph theory and forms the foundation of *topological quantum chemistry* [116, 130–132] and similar classifications [133–136]. Given a subset of bands, the decomposition into elementary band representation can be obtained, which in turn facilitates a topological classification. Since this requires the symmetry representations at high-symmetry momenta as the sole input, the resulting indicators of topology are known as *symmetry indicators*. Such symmetry-based methods are very powerful, not only in constructing effective models, as we will see throughout this part, but particularly for high-throughput calculations with the goal of finding topological materials [137–141]. Despite that, they only use partial information and therefore result in an incomplete characterization of bulk topology [142]; namely not all topological band structures can be diagnosed by these methods [133, 134].

While symmetry indicators diagnose crystalline topological phases, they were first used in the context of topological insulators, simplifying the computation of topological invariants [143, 144]. Let us illustrate this using the Chern number as an example. While the Chern number does not require any symmetry, a nontrivial value can be diagnosed more easily in the presence of inversion symmetry. Assuming a rectangular lattice with inversion symmetry, there are

four inversion-symmetric points in the Brillouin zone, conventionally denoted by Γ, X, Y, and M. Let $\#\Pi_p^{(2)}$ be the number of occupied states at $\Pi \in \{\Gamma, X, Y, M\}$ with inversion eigenvalue $e^{i\pi(p-1)}$, where $p = 1, 2$, then the Chern number of the occupied bands satisfies [142, 145]

$$c_1 = \sum_{\Pi\in\{\Gamma,X,Y,M\}} \#\Pi_2^{(2)} \mod 2. \tag{3.21}$$

Note that due to the partial information (inversion symmetry only distinguishes the parity of the full space group representations) the Chern number is only determined modulo 2. Throughout this part we will use and derive several symmetry indicator formulas, like Eq. (3.21).

The presence of crystalline symmetries extends the notion of topological phases in another direction as well. Not all topological phases in d dimensions are accompanied by $(d-1)$-dimensional protected boundary states. More generally, protected boundary states can be $(d-n)$-dimensional, for $n > 1$ leading to *higher-order topological phases*. Higher-order topology exists as all four types mentioned above: (1) stable topology, (2) obstructed atomic limits, (3) fragile topology, and (4) delicate topology. We will mostly be concerned with a manifestation of (2), the so-called *filling anomaly*.

3.2.1. Filling anomaly

Let us consider a one-dimensional (1D) example of an obstructed atomic limit, which will illustrate the concept of the filling anomaly. The model we consider is the Su-Schrieffer-Heeger (SSH) model, which was originally devised to describe polyacetylene [146]. It consists of electrons hopping on a chain with alternating hopping amplitudes t_0 and t_1 as illustrated in Fig. 3.2a. For simplicity, we deform the model in real space such that the two inequivalent sites are located at the center of the unit cell (see Fig. 3.2b); this does not change the topology. The Bloch Hamiltonian then takes the form

$$H(k) = \begin{pmatrix} 0 & t_0 + t_1 e^{ik} \\ t_0 + t_1 e^{-ik} & 0 \end{pmatrix}. \tag{3.22}$$

The model has inversion symmetry, which in the above basis is represented by $\mathcal{D}(\mathcal{P}) = \sigma_x$: $H(k) = \sigma_x H(-k)\sigma_x^{-1}$. Further, it has a sublattice (chiral) symmetry: $\mathcal{D}(\mathcal{S}) = \sigma_z$: $H(k) = -\sigma_z H(k)\sigma_z^{-1}$.

Due to the inversion symmetry, at half-filling, the Wannier center of the occupied eigenstate can only lie at inversion-symmetric positions, i.e., either in the center of the unit cell (on top of the ionic charge) or on the boundary. Diagonalizing the Hamiltonian, we find that for $t_0 > t_1$ the Wannier center

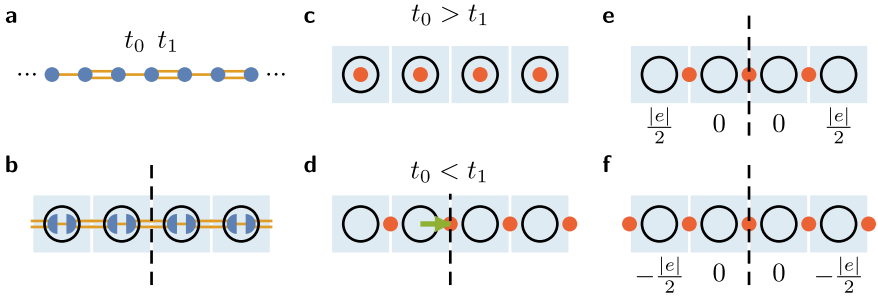

Figure 3.2.: Su-Schrieffer-Heeger model. (**a**) The model is defined as a hopping model on a chain with alternating hopping amplitudes t_0 (single orange line), t_1 (double orange line). (**b**) For $t_0 = t_1$ the unit cell (blue shaded region) contains two sites (blue half-disks), which can both be moved to the center of the unit cell. The model has inversion symmetry which is indicated by the black dashed line. We assume that the ionic charge is located at the center of the unit cell, indicated by the black circle. (**c**) For $t_0 > t_1$, the model is in the trivial phase with the Wannier centers (red disks) localized in the center of the unit cell on top of the ionic charge, such that each unit cell has vanishing total charge. (**d**) For $t_0 < t_1$, on the other hand, the model is in the topological phase with Wannier centers localized at the *boundaries* of the unit cell. Thus, in a finite piece of the chain that respects the inversion symmetry, we need to either (**e**) remove the excess electron at the boundary of the unit cell, or (**f**) add the missing one. In both cases, the two unit cells at the boundary will have nonvanishing net charge $\pm\frac{|e|}{2}$, where e is the electronic charge.

is at the center (Fig. 3.2c) and for $t_0 < t_1$ at the boundary of the unit cell (Fig. 3.2d), resulting in the trivial phase and an obstructed atomic limit, respectively. In the latter case, the displacement of electronic orbitals from ionic charge results in a dipole moment (green arrow) and thus nonvanishing polarization in the chain. If we now consider a finite piece of the chain, we find that simultaneously retaining half filling (one electronic state per unit cell) and respecting the inversion symmetry is not possible. As can be seen in Fig. 3.2d, the electron belonging to the rightmost unit cell breaks inversion symmetry. To restore inversion symmetry, we need to either remove the electron on the right (Fig. 3.2e) resulting in a system that has net charge $+|e|$ or add an electron on the left (Fig. 3.2f) resulting in a system with net charge $-|e|$, where e is the electronic charge. Due to the localization of the Wannier functions this excess of electronic or ionic charge is localized at the boundary, as indicated by the charge in each unit cell in Figs. 3.2e and 3.2f, and due to the symmetry, it is distributed symmetrically between the two boundaries.

The above example illustrates the definition of the *filling anomaly* as the impossibility to simultaneously satisfy charge neutrality and crystalline symmetries [147]. The concept does not only apply to inversion symmetry in one dimension (1D), but to any symmetry and dimension. If the symmetry results in n symmetry sectors, i.e., it is of order n, we can define the mismatch between the number of ions N_i and the number of electrons N_e required to respect the symmetry

$$\eta = N_i - N_e \mod n. \tag{3.23}$$

The filling anomaly η is defined modulo n because adding n electrons on the boundary preserves the symmetry. The excess charge is distributed symmetrically among the n symmetry sectors, such that it is given by

$$Q^{(n)} = \frac{\eta}{n}|e|\,. \tag{3.24}$$

In the example of the SSH model, this is the boundary charge and the $(2e)$-ambiguity is precisely the difference between Figs. 3.2e and 3.2f.

In d dimensions, we distinguish filling anomalies according to how they scale with the linear dimension L of the system. For example, for $d = 3$, $\eta \sim L$ gives rise to an edge charge, while $\eta \sim 1$ gives rise to a *corner charge*. While the former is related to the bulk polarization, the latter was found to be related to quadrupole moments [148]. The corner charges therefore are a manifestation of higher-order topology. Note that while in the case described above, it is the localized charges that are topologically protected rather than gapless boundary states. However, in the presence of an additional chiral symmetry, these charges are associated with such boundary states. The boundary states are pinned to zero energy and thus inside the energy gap by the chiral symmetry. If chiral-symmetry-breaking perturbations are added, the boundary states can move away from zero energy and merge into the bulk. During such a process, the charge distribution remains unchanged and protected by the filling anomaly, but the boundary states delocalize or even vanish.

In Chapter 6, we will specifically use the concept of filling anomalies in rotation-symmetric 2D insulators. Based on the methods described above, the filling anomaly for the crystals with C_n rotational symmetry can also be expressed in terms symmetry eigenvalues at high-symmetry points in the Brillouin zone [147, 149–152]. We consider the C_n-symmetric 2D crystals with $n = 2, 3, 4, 6$ depicted in Figs. 3.3a to 3.3d, respectively. Adopting the notation of Ref. 147, where the eigenvalues of the C_n-rotation operator at the C_n-symmetric high-symmetry point Π for spinless particles are denoted by

$$\Pi_p^{(n)} = \mathrm{e}^{2\pi\mathrm{i}(p-1)/n}, \quad p = 1, 2, \ldots, n \tag{3.25}$$

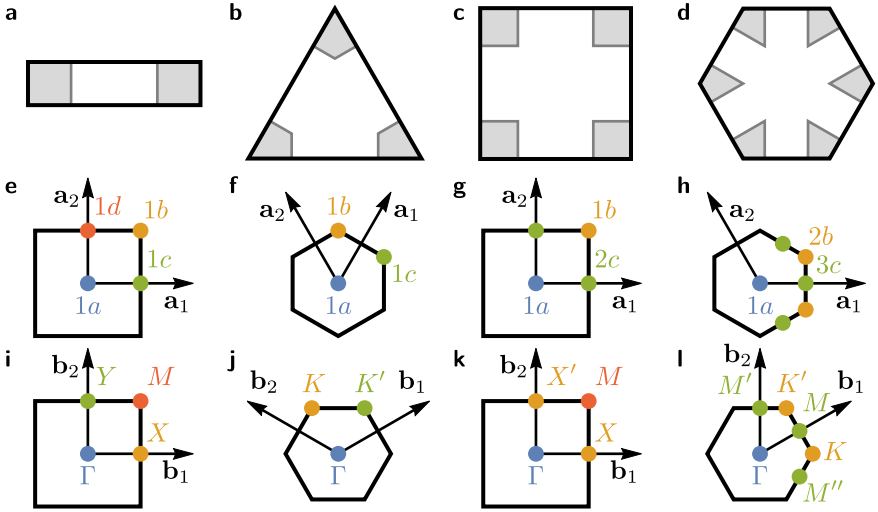

Figure 3.3.: C_n-symmetric crystals. **(a–d)** Geometry of C_n-symmetric crystals, $n = 2, 3, 4, 6$, with corners indicated as gray regions. Note the C_2 symmetry crystal which takes the form of a rectangle but the "corner charge" is computed over two adjacent corners. **(e–h)** Inequivalent Wyckoff positions labeled mX, where m is the multiplicity and $X \in \{a, b, c, d\}$ the type (indicated by the color) of the Wyckoff position; $\mathbf{a}_{1,2}$ denote the Bravais vectors. **(i–l)** High-symmetry points in the Brillouin zones of the corresponding crystals; $\mathbf{b}_{1,2}$ denote the primitive reciprocal lattice vectors. Points shown in the same color and labeled by the same letter are related by C_n symmetry. The labeling follows the conventions adopted by Ref. 151 (Ref. 147 for $n = 2$).

and define the quantities

$$\left[\Pi_p^{(n)}\right] = \#\Pi_p^{(n)} - \#\Gamma_p^{(n)}, \tag{3.26}$$

where $\#\Pi_p^{(n)}$ and $\#\Gamma_p^{(n)}$ are the number of occupied energy bands with eigenvalue $\Pi_p^{(n)}$ at high-symmetry points Π and Γ, respectively. The high-symmetry points for the four crystals are shown in Figs. 3.3i to 3.3l.

Below, we list the symmetry-indicator formulas for corner charges $Q_{\llcorner,mX}^{(n)}$ of 2D crystals with C_n symmetry. They depend on the location of the center of the sample, which is given by one of the Wyckoff positions mX, where m is the multiplicity and $X \in \{a, b, c, d\}$ the type of the Wyckoff position. The inequivalent Wyckoff positions are illustrated in Figs. 3.3e to 3.3h. In all

cases, we assume that the ionic charges are placed at the maximally-symmetric Wyckoff position $1a$.

In the absence of time-reversal symmetry (symmetry class A), Ref. 151 derives the formulas to be the following: for $n = 3$

$$Q^{(3)}_{\llcorner,1a} = \frac{e}{3}\left(\left[K_1^{(3)}\right] + \left[K_2^{(3)}\right] + \left[K_1'^{(3)}\right] + \left[K_2'^{(3)}\right]\right) \mod e, \tag{3.27a}$$

$$Q^{(3)}_{\llcorner,1b} = -\frac{e}{3}\left(\left[K_1^{(3)}\right] + \left[K_2'^{(3)}\right]\right) \mod e, \tag{3.27b}$$

$$Q^{(3)}_{\llcorner,1c} = -\frac{e}{3}\left(\left[K_2^{(3)}\right] + \left[K_1'^{(3)}\right]\right) \mod e, \tag{3.27c}$$

for $n = 4$

$$Q^{(4)}_{\llcorner,1a} = \frac{e}{4}\left(-\left[X_1^{(2)}\right] + \frac{1}{2}\left[M_1^{(4)}\right] - \frac{3}{2}\left[M_3^{(4)}\right]\right) \mod e, \tag{3.28a}$$

$$Q^{(4)}_{\llcorner,1b} = \frac{e}{4}\left(\left[X_1^{(2)}\right] - \frac{3}{2}\left[M_1^{(4)}\right] + \frac{1}{2}\left[M_3^{(4)}\right]\right) \mod e, \tag{3.28b}$$

and, for $n = 6$

$$Q^{(6)}_{\llcorner,1a} = -\frac{e}{6}\left(2\left[K_1^{(3)}\right] + \frac{3}{2}\left[M_1^{(2)}\right]\right). \tag{3.29}$$

If spinless time-reversal symmetry $\mathcal{T}$ satisfying $\mathcal{T}^2 = +1$ is present, i.e., in symmetry class AI, the formulas simplify due to constraints on the topological invariants $[\Pi_p^{(n)}]$ [151]. Throughout this part, we only need the formulas for $n = 4$,

$$Q^{(4)}_{\llcorner,1a} = \frac{e}{4}\left(-\left[X_1^{(2)}\right] + 2\left[M_1^{(4)}\right] + 3\left[M_2^{(4)}\right]\right) \mod e, \tag{3.30a}$$

$$Q^{(4)}_{\llcorner,1b} = \frac{e}{4}\left(\left[X_1^{(2)}\right] + 2\left[M_1^{(4)}\right] + 3\left[M_2^{(4)}\right]\right) \mod e, \tag{3.30b}$$

$n = 6$,

$$Q^{(6)}_{\llcorner,1a} = \frac{e}{4}\left[M_1^{(2)}\right] + \frac{e}{6}\left[K_1^{(3)}\right] \mod e, \tag{3.31}$$

and for $n = 2$ [147]:

$$Q^{(2)}_{\llcorner,1a} = \frac{e}{4}\left(-\left[X_1^{(2)}\right] - \left[Y_1^{(2)}\right] + \left[M_1^{(2)}\right]\right) \mod e. \tag{3.32}$$

3.3. Topological semimetals

So far, we have restricted our discussion to band insulators, that is band structures with a band gap at every momentum in the Brillouin zone. This

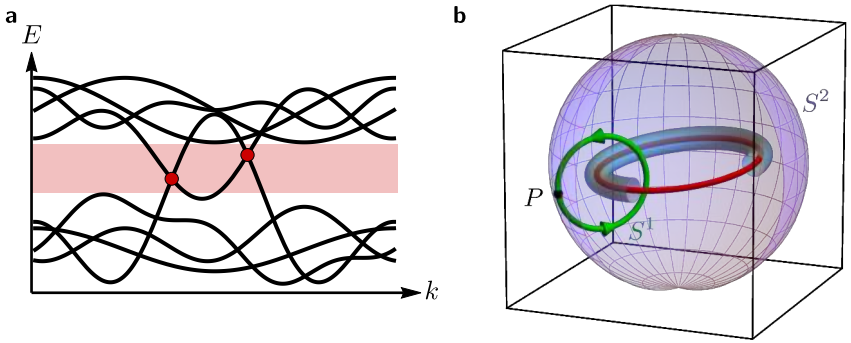

Figure 3.4.: Isolated band nodes. (**a**) Schematic semimetallic band structure (black lines) along some direction in the Brillouin zone with two isolated band nodes (red disks) in the gap (shaded in light red). (**b**) Illustration of a nodal ring (red) in momentum space with the excluded toroidal tube (blue) surrounding it. A cell decomposition results in cells that can be deformed to the indicated base point P (black), circle S^1 (green), and sphere S^2 (purple).

was crucial for the restriction of the allowed adiabatic deformations of the Hamiltonian to preserve that gap. However, the framework of topological band theory can be extended to *semimetals*, band structures with gap closures *isolated* in momentum space. Such gap closures correspond to degeneracies of two or more bands with at least one band from the set of occupied and unoccupied bands, each, as illustrated in Fig. 3.4a. The degeneracies are referred to as *band nodes*. Band nodes can be at a single point, resulting in a *nodal point*, or form a higher-dimensional manifold such as a line, resulting in a *nodal line*. Because the band nodes are isolated, we can exclude infinitesimal regions around them them from the Brillouin zone to arrive at a fully gapped—but topologically much more complicated—space. Figure 3.4b shows how this works if the band node takes the form of a ring, known as a *nodal ring*, and we exclude a small toroidal tube around it.

We then study equivalence classes of maps $\mathbf{k} \mapsto H(\mathbf{k})$ but instead of the base space being the full d-dimensional Brillouin-zone torus T^d, it will be a *perforated* torus with regions enclosing band nodes excluded. In principle, we can use the same invariants as for insulators, such as the Chern number in Eq. (3.3) or the Wilson loop spectrum in Eq. (3.12). In practice, however, the resulting space is too complicated to deal with directly. Therefore, we decompose the perforated base space into *cells* of dimensions $0 \leq d' < d$: for $d = 3$ these are points, lines, and surfaces. Most of these cells will be

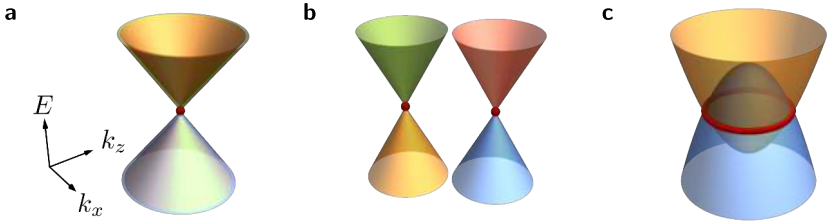

Figure 3.5.: Examples of the low-energy band structure of band nodes. (**a**) A Dirac point is a fourfold linear crossing of two twofold degenerate bands. (**b**) Weyl points are linear crossings of two bands and they appear in pairs with opposite topological charges. (**c**) Nodal lines are crossings of bands along a line instead of at a single point; here a nodal ring with linear crossing perpendicular to the ring is shown.

topologically equivalent, since their deformation in momentum space preserves their equivalence class as long as they do not cross any band nodes. Relevant inequivalent cells in the presence of a single nodal ring are shown in Fig. 3.4b and include a base point, a circle surrounding the nodal line, and a sphere enclosing the nodal ring. In three dimensions (3D), the topology of the nodal ring is then characterized, for example, by the Berry phase on the circle S^1 and the Chern number on the sphere S^2 which is also known as a *monopole charge*. In Chapters 5 and 6, we take this approach to characterize the topology of triple points and the nodal lines connected to them.

Besides the topological protection, band nodes can also be protected by symmetry, due to eigenstates transforming in appropriate irreducible corepresentations (ICRs) of the little group at their position in momentum space. Note that *protection* by symmetry does not imply that such band nodes are necessarily present. We distinguish *symmetry-enforced* band nodes, whose presence is guaranteed, from *accidental* band nodes, whose presence depends on the energetics and where the protection only implies stability to small symmetry-preserving perturbations. From the perspective of representation theory, symmetry-enforced band nodes occur when a little group has *only* ICRs of the appropriate dimension, while accidental band nodes *can* occur if an ICR of the appropriate dimension or multiple different ICRs of lower dimension exist.

Since the originally proposed Dirac and Weyl point degeneracies [25–27, 153–160] whose band structure is illustrated in Figs. 3.5a and 3.5b, various other types of band nodes have been proposed and studied: from nodal lines [161–165] forming intricate linked, knotted, and intersecting structures [166–170],

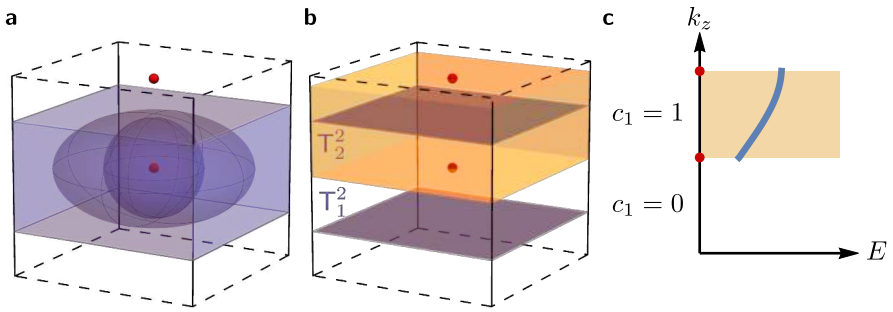

Figure 3.6.: Relation between monopole charges and two-dimensional insulators. A pair of Weyl points (red spheres) carrying chirality ± 1. The black frame represents the extent of the Brillouin zone in the two horizontal directions (k_x, k_y), but not in the vertical direction (k_z). (**a**) The chirality $c_1 = 1$ of the lower Weyl point is calculated as the Chern number on the surface enclosing it (innermost sphere), which can be continuously inflated (purple ellipsoid) until it fills the Brillouin zone in k_x- and k_y-direction (purple cuboid). (**b**) The cuboid in (a) is equivalent to two horizontal planes representing tori $\mathsf{T}^2_{1,2}$ at the appropriate positions along k_z. Assuming that $c_1[\mathsf{T}^2_1] = 0$, this leads to a region (orange) demarcated by the two Weyl points where any horizontal plane has Chern number 1. (**c**) Schematic dispersion along k_z of the topological surface state (blue) connecting the projections of the two Weyl points (red disks) onto the surface Brillouin zone.

over nodal surfaces [171–175], to nodal points with degeneracies different from two (Weyl) and four (Dirac) [176–179] in 3D. A nodal ring with linearly crossing bands, thus generalizing the Weyl point, is illustrated in Fig. 3.5c. In particular, three-fold degenerate points [180–191] (also called triply-degenerate nodal points) have been widely investigated, as they constitute a special intermediate between Weyl and Dirac points. In Chapter 4, we discuss the different kinds of triply-degenerate nodal points (depicted in Fig. 4.1), including the *triple points* which are the focus of the remainder of Chapters 4 to 6.

3D topological semimetals with Bloch Hamiltonian $H(\mathbf{k})$ can be understood as families of 2D topological insulators corresponding to cuts in momentum space, e.g., $H_{k_z}(k_x, k_y) = H(k_x, k_y, k_z)$, where for fixed k_z, $H_{k_z}(k_x, k_y)$ describes a 2D insulator. To understand how monopole charges of the 3D semimetal and the 2D insulators are related, we consider the example of a pair of Weyl points with chirality (Chern number computed on a sphere enclosing each) ± 1 separated along k_z. For simplicity, we assume that there are no other band nodes in the Brillouin zone. The sphere S^2 enclosing one of the

Weyl points with chirality $c_1[S^2]$ can be continuously deformed as long as it does not cross any band nodes; thus it can be inflated until it covers the full Brillouin zone in k_x- and k_y-direction, as illustrated in Fig. 3.6a. Due to the periodicity of the Brillouin zone, the resulting surface consists of two disconnected and oppositely oriented 2D tori $\mathsf{T}^2_{1,2}$ represented as two horizontal planes in Fig. 3.6b. This implies the following relationship between the Chern numbers

$$c_1[S^2] = c_1[\mathsf{T}^2_1] - c_1[\mathsf{T}^2_2]. \tag{3.33}$$

The horizontal planes can be moved in k_z-direction arbitrarily as long as they do not cross one of the Weyl points. Thus, we arrive at the conclusion that any plane *between* the two Weyl points carries a Chern number that differs from the Chern number of any plane *outside* of the pair precisely by $c_1[S^2]$, as indicated in Fig. 3.6b.

This relation allows us to derive the bulk-boundary correspondence for topological semimetals. A nontrivial monopole charge implies a *change* of the corresponding invariant defined on the 2D Brillouin zone of 2D systems corresponding to momentum-space cuts from one side of the node to the other. Thus, the 2D cuts on the two sides will be topologically distinct with distinct gapless edge modes. For simplicity, let us assume that cuts below the node are trivial and those above nontrivial, then the projections of the nodes onto the surface Brillouin zone will be connected by a gapless surface band, known as a *Fermi arc*, see Fig. 3.6c. If the band nodes carry higher-order topological charges, then the same mechanism results in hinge states connecting the projections of the nodes on the hinge Brillouin zone, for instance, higher-order Weyl semimetals exhibit both surface and hinge Fermi arcs [192].

3.3.1. Multigap topology

The partitioning of the energy bands into occupied and unoccupied sets is natural for insulators, where the energy gap provides a natural energy range for placing the chemical potential. In semimetals, on the other hand, the band structure is not gapped and while one can still partition the bands into two sets with isolate nodes formed between them, the choice of partitioning is somewhat arbitrary from a theoretical perspective in the context of the abstract classification problem. In principle, one could consider each band separately, leading to band nodes between any consecutive bands. In practice, one usually partitions the bands into sets such that the remaining gaps host interesting isolated band nodes, as illustrated in Fig. 3.7a. The result is a *multigap* perspective with band nodes characterized by the indices of the bands between which they are formed or equivalently by the index of the corresponding gap.

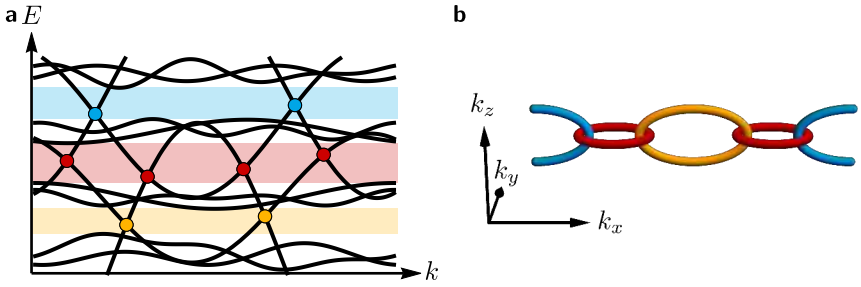

Figure 3.7.: Multigap band topology. (**a**) Schematic illustration of the partition of a band structure (black lines) into four sets of bands separated by three different energy gaps (lightly shaded in orange, red, and blue with increasing energy). Band nodes in the respective gap are indicated by appropriately colored disks. (**b**) The band structure illustrated in (a) gives rise to intricate nodal structures in momentum space, such as linked nodal rings. The band nodes are colored according to their gap.

In Fig. 3.7a and throughout this part, we assign colors (orange, red, blue, indigo) to the gaps and any nodes occurring in them according to increasing energy. The main question then is if a description of band nodes in multiple gaps goes beyond the one of the same band nodes but considered separately for each gap.

It has been shown [65, 66, 173, 193–198] that in certain symmetry settings, in particular in the presence of an antiunitary symmetry leaving momentum invariant and squaring to the identity, the topological classification is indeed *refined* by a multigap perspective. This suggests that band nodes in different energy gaps are not topologically independent, but can *interact* with each other. More concretely, Bouhon et al. [66] showed that Weyl points in adjacent gaps can be braided and pick up nontrivial relative phases when doing so, which, for instance, manifests in a pair of nodes losing the ability to annihilate after braiding one of them around a node in an adjacent gap. In 3D systems, the interaction of band nodes can manifest as linked nodal rings [199, 200], such as the ones shown in Fig. 3.7b. Their topology prevents them from being slid across each other, such that shrinking one of the rings and annihilating it becomes impossible due to the linking with a ring in an adjacent band gap. In the next section, we will introduce several multigap invariants that capture phenomena such as the ones described above. In Chapter 5, we will relate three-fold degeneracies and linked nodal rings using the perspective of multigap topology.

3.4. Homotopy classification

The topological classification of Bloch Hamiltonians introduced at the beginning of this chapter echoes the mathematical definition of *homotopy equivalence*. Two continuous maps $f_{0,1} : \mathcal{B} \to \mathcal{M}$ from a *base space* $\mathcal{B}$ to a *target space* $\mathcal{M}$ are called homotopically equivalent, denoted by $f_0 \sim f_1$, if they can be continuously deformed into each other, i.e., if there is a continuous one-parameter family of continuous maps $f_t : \mathcal{B} \to \mathcal{M}$, $t \in [0,1]$ with $f_{t=0} \equiv f_0$ and $f_{t=1} \equiv f_1$, as suggested by the notation. This results in a partitioning into equivalence classes of maps for a given pair $(\mathcal{B}, \mathcal{M})$. The homotopy classification of Bloch Hamiltonians is closely related to the theory of topological defects in ordered media, discussed in the excellent review by Mermin [201] which introduces the relevant concepts in detail.

If we choose the base space to be the Brillouin zone or a p-sphere S^p enclosing some band nodes and the target space as the space of Hamiltonian matrices with one (or more) energy gaps and respecting certain symmetries, the classification of maps coincides precisely with the classification of band topology in terms of Bloch Hamiltonians. This is illustrated in Fig. 3.8. In the band-theoretic context, the relevant target spaces are *classifying spaces* of certain Lie groups. Here, we make use of the spectral flattening mentioned earlier: the eigenstates $|u_i(\mathbf{k})\rangle$ of the Bloch Hamiltonian are partitioned into n occupied bands with energy $\varepsilon_i < 0$ and ℓ unoccupied bands with energy $\varepsilon_i > 0$:

$$H(\mathbf{k}) = \sum_{i=1}^{n+\ell} \operatorname{sign} \varepsilon_i(\mathbf{k})\, |u_i(\mathbf{k})\rangle\langle u_i(\mathbf{k})| \,. \tag{3.34}$$

Collecting the eigenstates $|u_i(\mathbf{k})\rangle$ as columns of the matrix $\mathsf{u}(\mathbf{k})$ and the eigenvalues in the diagonal matrix $\mathcal{E}$, this takes the form

$$H(\mathbf{k}) = \mathsf{u}(\mathbf{k}) \operatorname{sign}(\mathcal{E}) \mathsf{u}(\mathbf{k})^\dagger. \tag{3.35}$$

The space of such Hamiltonian matrices, i.e., the classifying space, is then given by the space of matrices u:

$$\mathcal{M} = \mathrm{Gr}_{\mathbb{C}}(n, \ell) = \mathsf{U}(n+\ell)/\mathsf{U}(n) \times \mathsf{U}(\ell), \tag{3.36}$$

known as the (complex) Grassmanian. The structure of the definition can be easily understood: $\mathsf{u}(\mathbf{k}) \in \mathsf{U}(n+\ell)$ and the partitioning into n occupied and ℓ unoccupied bands implies that there is an additional freedom where bands *within* each set can be mixed: $\mathsf{U}(n) \times \mathsf{U}(\ell)$. As indicated, the Grassmanian generally depends on the number of occupied and unoccupied bands, but we

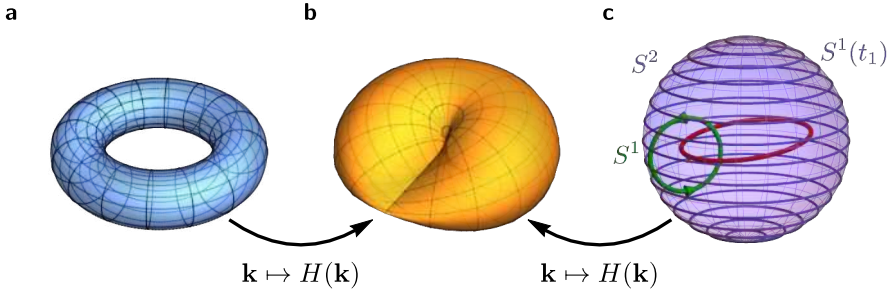

Figure 3.8.: Homotopic description of band topology. (**a**) Toroidal base space $\mathcal{B} = \mathsf{T}^d$ of a 2D system, appropriate for classifying topological insulators. (**b**) Target (classifying) space $\mathcal{M} = \mathsf{RP}^2 = \mathrm{Gr}_{\mathbb{R}}(1,1)$ of a two-band real Bloch Hamiltonian $H(\mathbf{k}) = \hat{\mathbf{h}} \cdot \boldsymbol{\sigma}$ with normalized $\hat{\mathbf{h}}$ and $\boldsymbol{\sigma}$ the vector of Pauli matrices. (**c**) Base spaces $\mathcal{B} = S^1$ (green loop) and $\mathcal{B} = S^2$ (purple sphere) used in the characterization of band nodes. The sphere S^2 can be parametrized by circles $S^1(t_1)$.

will see in an example below that the *classification* reaches a *stable limit* which does not depend on (n, ℓ) anymore.

We now focus on base spaces of the form S^p which can be obtained from a cell decomposition of the d-dimensional Brillouin zone T^d with band nodes, as illustrated in Fig. 3.4b, and characterizes a band node. The equivalence classes of maps $S^p \to \mathcal{M}$ are precisely characterized by the p^{th} *homotopy group* $\pi_p(\mathcal{M})$. More precisely, the conjugacy classes of $\pi_p(\mathcal{M})$ are in one-to-one correspondence with the equivalence classes of maps (glossing over the differences between free and based homotopy in this brief description, see, e.g., Refs. 65, 201 for more details). This allows us to define topological charges $c^{(p)}$ taking values in the conjugacy classes of $\pi_p(\mathcal{M})$. The complete topological classification is then given by *all* the homotopy groups $c^{(p)}$ with $\delta - 1 \leq p \leq d - 1$ [173], where δ is the *codimension* of the node, i.e., $d - \delta$ is the dimension of the nodal manifold. A nodal ring in $d = 3$ dimensions is a 1D manifold and as such has codimension $\delta = 2$:

$$c = c^{(1)} \oplus c^{(2)}. \tag{3.37}$$

In the presence of an antiunitary symmetry squaring to the identity, such as spinless space-time inversion $\mathcal{PT}$, there always exists a gauge in which the Bloch Hamiltonian is a real symmetry matrix [66], such that instead of the complex we need to consider the *real* Grassmanian

$$\mathrm{Gr}_{\mathbb{R}}(n, \ell) = \mathsf{O}(n + \ell)/\mathsf{O}(n) \times \mathsf{O}(\ell). \tag{3.38}$$

Here, we used that the real gauge implies that $\mathsf{u}(\mathbf{k}) \in \mathsf{O}(n+\ell)$. The first and second homotopy groups of $\mathrm{Gr}_{\mathbb{R}}(n,\ell)$ are shown in Table 3.1, where we observe that for $n,\ell \geq 3$ the stable limit is reached and the homotopy groups become independent of (n,ℓ). It becomes obvious that in order to describe multigap topology, we need to replace $\mathsf{O}(n)\times\mathsf{O}(\ell)$ by an appropriate product with more factors. Assuming a partition into N sets of bands with the i^{th} set consisting of n_i bands, the classifying space is given by the so-called *flag manifold*

$$\mathrm{Fl}_{\mathbb{R}}(n_1,\ldots,n_N) = \mathsf{O}(n_1+\cdots+n_N)/\mathsf{O}(n_1)\times\cdots\times\mathsf{O}(n_N). \tag{3.39}$$

Despite the clear mathematical correspondence between homotopy theory and the classification problem of band topology, much of the theoretical development has been achieved using two alternative techniques. In part, this is owed to the fact that handling space-group symmetries in a homotopic description is very hard. *Topological K-theory* encodes the occupied bands as a vector bundle and can handle crystalline symmetries. However, it assumes an infinite number of bands and thus does not capture fragile and delicate topology which trivialize in the stable limit. On the other hand, the symmetry indicators and topological quantum chemistry introduced above work for arbitrary number of bands and are built around symmetries. The drawback of this approach is that only partial information is used resulting again in some topological invariants being missed. With this we can identify the following fields of application of a homotopic characterization of band topology: (1) the topological stability of band degeneracies at low-symmetry positions in momentum space, (2) multigap topology, and (3) fragile or delicate topology. Throughout this part, we will touch upon all three fields, in particular we study multigap and fragile topology of band degeneracies away from high-symmetry points.

3.4.1. Relation to Wilson loop spectra

In the language of homotopy group, we can illustrate how the topological charges can be extracted from Wilson loop spectra. Let us focus on the description of a nodal ring in 3D momentum space as discussed above and illustrated in Fig. 3.4b and assume the presence of spinless $\mathcal{PT}$ symmetry. In that case, the classifying spaces are the real Grassmanians $\mathsf{Gr}_{\mathbb{R}}(n,\ell)$ whose first two homotopy groups [173] are given in Table 3.1. We first consider the topological charge $c^{(1)}$ on a circle $\mathcal{B}=S^1$ around the nodal line. Then, $c^{(1)}$ is an element of the conjugacy classes of the first homotopy group $\pi_1(\mathrm{Gr}_{\mathbb{R}}(n,\ell))$. This charge is precisely given by the Berry phase which is quantized to $\{0,\pi\}$ by the $\mathcal{PT}$ symmetry. In Eq. (3.11), we have seen that it can be expressed in

Table 3.1.: Homotopy groups of real Grassmanians. The table displays the first and second homotopy groups of the real Grassmanians $\mathsf{Gr}_{\mathbb{R}}(n,\ell)$, i.e., the classifying spaces of few-band models with n occupied and ℓ unoccupied bands in the presence of space-time inversion symmetry squaring to $+1$.

	$\pi_1(\mathsf{Gr}_{\mathbb{R}}(n,\ell))$		$\pi_2(\mathsf{Gr}_{\mathbb{R}}(n,\ell))$		
	$n=1$	$n\geq 2$	$n=1$	$n=2$	$n\geq 3$
$\ell=1$	$\mathbb{Z}$	$\mathbb{Z}_2$	$\mathbb{0}$	$2\mathbb{Z}$	$\mathbb{0}$
$\ell=2$	$\mathbb{Z}_2$	$\mathbb{Z}_2$	$2\mathbb{Z}$	$\mathbb{Z}\oplus\mathbb{Z}$	$\mathbb{Z}$
$\ell\geq 3$	$\mathbb{Z}_2$	$\mathbb{Z}_2$	$\mathbb{0}$	$\mathbb{Z}$	$\mathbb{Z}_2$

terms of the Wilson loop operator $\mathcal{W}(S^1)$:

$$c^{(1)} = -\frac{\mathrm{i}}{\pi}\log\det\mathcal{W}(S^1) \mod 2 \quad \in \mathbb{Z}_2, \tag{3.40}$$

which is consistent with the stable limit of $\pi_1(\mathsf{Gr}_{\mathbb{R}}(n,\ell))$. Note that according to Table 3.1, $n=\ell=1$ allows for a finer, delicate, $\mathbb{Z}$-valued charge, known as the *winding number*, which will play a role in Chapter 5.

Next, we consider the monopole charge $c^{(2)}$ defined on a 2-sphere enclosing the nodal ring, which can again be related to the Wilson loop operator [173], similar to what we saw for the Chern number in Eq. (3.15). We parametrize S^2 by a continuous family of closed paths $S^1(t_1)\subset S^2$ with $t_1\in[0,1]$, such that $S^1(0)$ and $S^1(1)$ are two distinct single *points*, e.g., the poles of S^2. This is illustrated in Fig. 3.8c by the purple lines of constant latitude. We then consider the induced family of Wilson loop operators $\mathcal{W}(S^1(t_1))$. The Wilson loop operator for n occupied bands is unitary and, because of the $\mathcal{PT}$ symmetry, real, such that it is an element of $\mathsf{O}(n)$. Since $\mathcal{W}(S^1(0))=\mathcal{W}(S^1(1))=\mathbb{1}$, $\mathcal{W}(S^1(t_1))$ traces a closed path in $\mathsf{SO}(n)$ and the charge $c^{(2)}_{(n,\ell)}$ is given by the homotopy equivalence classes of $\mathcal{W}^{\mathrm{occ}}(S^1(t_1))$ and $\mathcal{W}^{\mathrm{unocc}}(S^1(t_1))$. In the absence of particle-hole symmetry, those two are generally different, but their sum has to be trivial in $\pi_1(\mathsf{SO}(n+\ell))$. Recall that

$$\pi_1(\mathsf{SO}(n)) = \begin{cases} \mathbb{0}, & n=1 \\ \mathbb{Z}, & n=2 \\ \mathbb{Z}_2, & n\geq 3 \end{cases}, \tag{3.41}$$

such that we can determine the relevant group

$$c^{(2)}(n,\ell) = c^{\mathrm{occ}}\oplus c^{\mathrm{unocc}} \in \pi_1(\mathsf{SO}(n))\oplus\pi_1(\mathsf{SO}(\ell)) \tag{3.42}$$

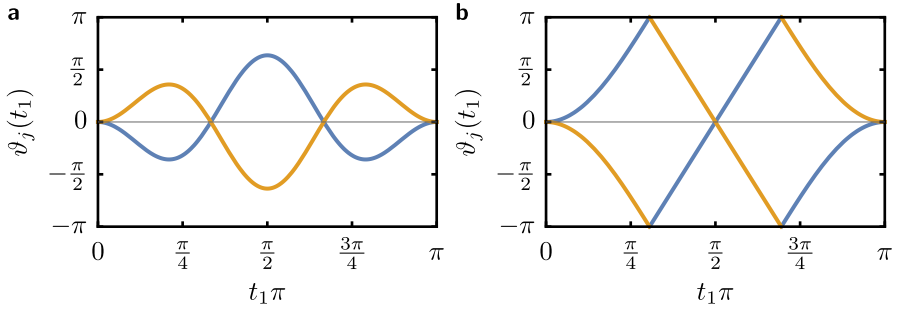

Figure 3.9.: Deducing the monopole charge from the Wilson loop spectrum. Eigenvalues $\vartheta_j(t_1)$ of the Wilson loop operator $\mathcal{W}(S^1(t_1))$ defined in Fig. 3.8c, as a function of the parameter t_1. Here, we assume a model with two occupied and one unoccupied bands resulting in two Wilson loop eigenvalues (blue/orange). According to Table 3.1 the second homotopy group is $2\mathbb{Z}$. (**a**) The eigenvalues do not wind, indicating a trivial topological charge. (**b**) Each of the two eigenvalues winds twice, resulting in a topological charge $2 \in 2\mathbb{Z}$.

under the constraint that $c^{\text{occ}} + c^{\text{unocc}}$ is trivial in $\pi_1(\mathsf{SO}(n+\ell))$ [173]. The resulting groups formed by the values of $c^{(2)}(n,\ell)$ reproduce exactly the second homotopy groups of $\mathsf{Gr}_{\mathbb{R}}(n,\ell)$ given in Table 3.1.

This identification with the homotopy group of Wilson loops allows us to determine the charge from the winding of the Wilson loop spectra for occupied and unoccupied bands [173]. We briefly illustrate how that works using $(n,\ell) = (2,1)$ as an example. According to Eq. (3.41), $c^{(2)}_{(2,1)} \in \mathbb{Z}$ such that $c^{(2)}_{(2,1)} \bmod 2 = 0$, i.e. $c^{(2)}_{(2,1)} \in 2\mathbb{Z}$. Thus, the Wilson loop spectrum of the occupied bands has an even winding and if this winding is zero (Fig. 3.9a), the monopole charge is trivial, while it is nontrivial otherwise (Fig. 3.9b). In the stable limit, on the other hand, the monopole charge is simply given by the parity of the winding which is the same for the occupied and unoccupied bands.

3.4.2. Topological invariants relevant for triple points

We briefly define and discuss the topological invariants relevant in the context of triple points which we will use throughout this part. These are the Euler charge [173, 202, 203], its stable version, the second Stiefel-Whitney charge [173, 193, 195, 196, 199, 204], and the non-Abelian multigap invariant known as

(generalized) *quaternion invariant* [65, 66, 198, 205].

Monopole charges

The topological charges described above can be more abstractly formulated as characteristic classes [206] of vector bundles. Mathematically, the Bloch Hamiltonian $H(\mathbf{k})$ defines a vector (or more generally fibre) bundle on the Brillouin-zone torus [207]. The nontriviality of the bundles is measured by a collection of invariants called *characteristic classes*. There are several kinds of characteristic classes [206]. For example complex bundles over a $2n$-dimensional base space are characterized by the Chern classes $c_n \in \mathbb{Z}$ and real bundles over an n-dimensional base space by the *Stiefel-Whitney classes* w_n with $w_n \in \mathbb{Z}_2$ for $n = 1, 2$. These are examples of *stable* classes, that is they are defined independent of the rank of the bundle. Additionally, there are fragile classes like the *Euler class* $\chi \in \mathbb{Z}$ for rank-$2n$ real bundles over a $2n$-dimensional base space. In those cases, the Stiefel-Whitney classes can be inferred from the Euler class: $w_{2n} = \chi \mod 2$.

Since we are considering systems with $\mathcal{PT}$ symmetry, the relevant characteristic classes are the Stiefel-Whitney classes in the stable limit and the Euler class for the two-band case. Indeed, the definitions of the characteristic classes and topological charges discussed above are equivalent [193, 207]. The first Stiefel-Whitney class w_1 is equal to Berry phase, the second w_2 to the $\mathbb{Z}_2$-monopole charge $c^{(2)}_{(n,\ell)}$ in the stable limit and the Euler class for a 2D base space reproduces $c^{(2)}_{(2,\ell)}$ for any ℓ, which is consistent with its relationship to the Stiefel-Whitney class.

For Chapter 5, it will be useful to write the Euler class as an integral of a curvature over the base manifold [206, 207], analogous to the Chern number in Eq. (3.3). By adopting a Hilbert-space basis for which $\mathcal{PT}$ is represented by complex conjugation [66], the eigenstates can be gauged to be purely real. For two real Bloch bands $|u_1(\mathbf{k})\rangle$ and $|u_2(\mathbf{k})\rangle$ (which possibly are degenerate with each other, but must be separated by energy gaps from all other bands) one then defines the *Euler curvature*

$$\mathbf{F}(\mathbf{k}) = \langle \boldsymbol{\nabla}_{\mathbf{k}} u_1(\mathbf{k}) | \times | \boldsymbol{\nabla}_{\mathbf{k}} u_2(\mathbf{k}) \rangle \,, \tag{3.43}$$

i.e., as the off-diagonal component of the two-band non-Abelian Berry-Wilczek-Zee connection [66, 207]. Integrating the curvature over a closed surface S^2 gives the Euler class

$$\chi = \frac{1}{2\pi} \int_{S^2} \mathrm{d}\mathbf{S} \cdot \mathbf{F}(\mathbf{k}) \in \mathbb{Z}. \tag{3.44}$$

Generalized quaternion charge

Finally, we introduce the quaternion charge as a multigap invariant. Consider an $N \times N$ real Bloch Hamiltonian in 1D for generic $N \geq 2$. By the spectral theorem, it can be written as

$$H(k) = \mathsf{u}(k)\mathcal{E}(k)\mathsf{u}(k)^T, \tag{3.45}$$

where $\mathsf{u}(k)$ is the matrix with columns being the (ordered, real, orthonormal) eigenstates $\mathbf{u}_j(k)$ and $\mathcal{E}(k)$ the diagonal matrix of (ascending) eigenenergies $\varepsilon_j(k)$ of $H(k)$. The matrix $\mathsf{u}(k)$ is an orthogonal real matrix and thus defines an N-frame, the *eigenframe*. Crucially, the frame has a remaining gauge freedom that manifests as the flipping of the sign of some of the vectors $\mathbf{u}_j$ of the frame. This is given by the N-dimensional point group $\mathsf{P}_{Nh} = \mathsf{O}(1)^N = \mathbb{Z}_2^N$ generated by N mutually perpendicular mirror symmetries. We can fix the handedness of the frame by choosing a gauge where $\mathsf{u}(k) \in \mathsf{SO}(N)$, which then reduces P_{Nh} to its special component P_N. Consequently, the space of (spectrally normalized) Hamiltonians that we should consider [65] as the classifying space is

$$\mathcal{M}(N) = \mathsf{O}(N)/\mathsf{P}_{Nh} = \mathsf{SO}(N)/\mathsf{P}_N = \mathsf{Spin}(N)/\overline{\mathsf{P}}_N, \tag{3.46}$$

where we first restricted to the special components and then lifted each group to its respective double cover. We explain further below that the first homotopy group group of $\mathcal{M}(N)$, which coincides with the discrete group $\overline{\mathsf{P}}_N$, captures the topology of nodal lines in spinless $\mathcal{PT}$-symmetric models.

We first briefly characterize the groups and lifts appearing in Eq. (3.46), more details are given in Appendix D.2. The lift of an element of $\mathsf{SO}(N)$ close to the identity of $\mathsf{Spin}(N)$ is performed by working in the corresponding Lie algebras $\mathfrak{so}(N)$ and $\mathfrak{spin}(N)$, where the lift can be simply performed on the level of the basis elements:

$$\sum_{i<j} \alpha_{ij} L_{ij} \mapsto \sum_{i<j} \alpha_{ij} t_{ij}. \tag{3.47}$$

Here, $\{L_{ij}\}_{i<j}$ and $\{t_{ij}\}_{i<j}$ are bases of $\mathfrak{so}(N)$ and $\mathfrak{spin}(N)$, respectively, and we choose

$$L_{ij} = -E_{ij} + E_{ji}, \tag{3.48a}$$

$$t_{ij} = -\frac{1}{2}\epsilon_i \epsilon_j, \tag{3.48b}$$

where $(E_{ij})_{ab} = \delta_{ai}\delta_{bj}$ is the matrix with a single non-zero element 1 at position (i, j) and ϵ_i are generators of the Clifford algebra $\mathcal{C}\ell_{0,N}$ and satisfy

$\epsilon_i\epsilon_j+\epsilon_j\epsilon_i=-2\delta_{ij}$. Furthermore, P_N is a subgroup of $\mathsf{O}(N)$, and we can obtain the generators $\{e_i\}_{i=1}^{N-1}$ of its double cover $\overline{\mathsf{P}}_N$ from the generators $\left\{\mathrm{e}^{\pi L_{1j}}\right\}_{j=2}^{N}$ of P_N:

$$e_{j-1}=\mathrm{e}^{\pi t_{1j}}=2t_{1j}=-\epsilon_1\epsilon_j \tag{3.49}$$

for $2\leq j\leq N$. From its definition we can read off that e_{j-1} encodes a π-rotation in the $(1,j)$-plane (i.e. a π-twist of the first and j^{th} band). An alternative set of generators is provided by

$$g_j=\begin{cases}e_1, & j=1\\ e_{j-1}e_j, & j\geq 2\end{cases}, \tag{3.50}$$

which corresponds to a π-rotation in the $(j,j+1)$-plane, i.e., the band inversion of the j^{th} and $(j+1)^{\text{th}}$ band. The elements of $\overline{\mathsf{P}}_N$ are then given by all possible products of elements of either set of generators together with the identity. We call this group the *generalized quaternion group* Q_N and denote its 2^N elements by

$$\pm 1,\ \pm\mathfrak{q}_1,\ \pm\mathfrak{q}_2,\ \ldots,\ \pm\mathfrak{q}_{2^{N-1}-1}, \tag{3.51}$$

where the corresponding matrix representations q_i of the elements $\mathfrak{q}_i$ are the products of generators:

$$\begin{gathered}q_1=g_1,\quad q_2=g_2,\quad \ldots,\quad q_{N-1}=g_{N-1},\\ q_N=g_1g_2,\quad q_{N+1}=g_1g_3,\quad \ldots\quad q_{2^{N-1}-1}=g_1g_2\cdots g_{N-1}.\end{gathered} \tag{3.52}$$

We now turn our attention to the topological invariants in momentum space. Closed paths γ in momentum space with non-degenerate spectrum at each point $k\in\gamma$ are characterized by the first homotopy group $\pi_1(\mathcal{M}(N))$, which is found to be [65]

$$\pi_1(\mathcal{M}(N))=\overline{\mathsf{P}}_N. \tag{3.53}$$

This implies the existence of an invariant $\mathfrak{q}(\gamma)\in\overline{\mathsf{P}}_N$, called *generalized quaternion charge* by Ref. 65. Its numerical computation is based on tracking the rotation of the eigenframe lifted to $\mathsf{Spin}(N)$ along the closed path γ. The total spin-rotation along γ can be decomposed into a linear combination of the matrices in Eq. (3.52), and if there are no band degeneracies along γ, the total rotation itself is (within numerical precision) equal to one of these matrices, i.e. it is an element of Q_N. Algorithm 1 implements these ideas and is used in Chapter 5.

Due to its non-Abelian character, the quaternion charge is only well-defined up to conjugation by elements in Q_N, such that the topology is classified by the equivalences classes of Q_N. They are [65]

Input: N-band Hamiltonian along a closed path γ:
$t \in [0,1] \mapsto H(\gamma(t))$, stepsize Δt.
Output: Generalized quaternion charge $\mathfrak{q}(\gamma) \in \mathsf{Q}_N$.
if *there is a band degeneracy along the path* **then**
  return `NULL`;
else
  initialize $V = \mathbb{1}_{2^{\lfloor N/2 \rfloor} \times 2^{\lfloor N/2 \rfloor}}$;
  diagonalize $H(\gamma(0)) \to$ frame $\mathsf{u}_0 \in \mathsf{O}(3)$;
  select special component: $\mathsf{u}_0 \operatorname{diag}(1, 1 \ldots, 1, \det(\mathsf{u}_0)) \to \mathsf{u}_0 \in \mathsf{SO}(3)$;
  for $n = 1$ **to** $\frac{1}{\Delta t}$ **do**
    diagonalize $H(\gamma(n\Delta t)) \to$ frame $\mathsf{u}_n \in \mathsf{O}(3)$;
    select special component:
     $\mathsf{u}_n \operatorname{diag}(1, 1 \ldots, 1, \det(\mathsf{u}_n)) \to \mathsf{u}_n \in \mathsf{SO}(3)$;
    compute $\mathsf{u}_{n-1}^T \mathsf{u}_n \to \Delta R_n$;
    fix gauge: $\mathsf{u}_n \operatorname{sign}(\operatorname{diag}(\Delta R_n)) \to \mathsf{u}_n \in \mathsf{SO}(3)$;
    update $\mathsf{u}_{n-1}^T \mathsf{u}_n \to \Delta R_n$;
    decompose $\log(\Delta R_n)$ into $\mathfrak{so}(N)$ basis $\to \{\alpha_{ij}\}$;
    compute lift of ΔR_n to $\mathsf{Spin}(N)$: $\mathrm{e}^{\sum_{i<j} \alpha_{ij} t_{ij}} \to \overline{\Delta R}_n$;
    update $V \overline{\Delta R}_n \to V$;
  end
  decompose V into basis of generalized quaternions
   $\frac{1}{2^{\lfloor N/2 \rfloor}} \operatorname{tr}(V) 1 + \sum_{i=1}^{2^{N-1}-1} \frac{1}{2^{\lfloor N/2 \rfloor}} \operatorname{tr}(q_i V) \mathfrak{q}_i \in \mathsf{Q}_N \to \mathfrak{q}(\gamma)$;
  return $\mathfrak{q}(\gamma)$;
end

Algorithm 1: Computation of the generalized quaternion charge $\mathfrak{q}(\gamma) \in \mathsf{Q}_N$ for an N-band Hamiltonian $H(\mathbf{k})$ along a closed path $\mathbf{k} = \gamma(t)$, based on the discussion in Ref. 65. A *frame* is defined to be the matrix with columns being the ordered real orthonormal eigenstates in order of ascending eigenenergies and $\operatorname{sign}(\operatorname{diag}(\Delta R_n))$ is the diagonal matrix consisting of the signs the diagonal entries of ΔR_n.

- $\{\pm g_1^{n_1} g_2^{n_2} \cdots g_{N-1}^{n_{N-1}}\}$, $n_i \in \{0, 1\}$ with the exceptions
- $\{+1\}$, $\{-1\}$ and
- if N is even also $\{+g_1 g_2 \cdots g_{N-1}\}$, $\{-g_1 g_2 \cdots g_{N-1}\}$,

which follow from the commutation relations between the generators. The fact that ± 1 are in distinct conjugacy classes for any N results in the paths that are classified by these charges to be stably topologically inequivalent, while

$\pm g_1 g_3 \cdots g_{N-1}$ result in an unstable topological inequivalence (since adding an additional band brings them into a single conjugacy class). The sign of the quaternion charge does become well-defined if only contours starting (and ending) at the same base-point are considered, giving rise to *based* homotopy. In that case, the invariant is given by the *group* elements of Q_N. However, usually, we want to assign the charges to the nodes enclosed by the contours, which has to be independent of the base point, giving rise to *free* homotopy. Thus, we work with the equivalence classes of Q_N.

The set of generators given in Eq. (3.50) provides a useful interpretation of the quaternion charge in terms of its factors g_j. Since g_j corresponds to a π-rotation in the $(j, j+1)$-plane, it suggests a band inversion between bands $(j, j+1)$ [65, 200] with associated π Berry phases on those two bands. Consequently, if the quaternion charge is computed on a closed loop in $\mathbf{k}$-space that does not wind around the Brillouin-zone torus, then each factor g_j indicates that a band node (in 2D) or nodal line (in 3D) between bands $(j, j+1)$ is enclosed [65]. Equivalently, we consider the Hamiltonian along the closed loop as a 1D system. Then, deforming it to a constant Hamiltonian requires a closing of the gap between bands $(j, j+1)$ for each factor g_j. We use this interpretation to explain the bulk-boundary correspondence in Li_2NaN in Section 5.3.3.

Note that the above description of the quaternion invariant and its computation assumes that the Bloch Hamiltonians at $\gamma(0)$ and $\gamma(1)$ are identical. However, we have seen in Section 2.4 that this is not usually the case when γ is noncontractible, i.e., when it winds around the Brillouin zone. In Chapter 5 and Appendix D we extend the framework to such cases and explain how to deal with it in practice.

4. Classification of triple points

This chapter is largely based on the publication "Triple nodal points characterized by their nodal-line structure in all magnetic space groups" [2]. Segments with significant text overlap with the published version may be subject to copyright by the American Physical Society.

In this chapter, we introduce the object of study of Part II, a particular instance of triply-degenerate nodal points which we call *triple points*, and derive a symmetry-classification according to the nodal-line structure in its vicinity. As discussed in Section 3.3, band nodes emerge when energy bands become degenerate in the vicinity of the Fermi energy and they can feature nontrivial topological invariants, boundary signatures, and transport properties. We have seen that besides the originally proposed Weyl and Dirac points, various other types of band nodes have been studied including triply-degenerate nodal points which constitute special intermediates between Weyl and Dirac points. Here, we focus on triple points in *spinless* systems, which we recall to be systems that are either truly spinless or electronic systems with negligible spin-orbit coupling, see Section 3.1.2. This has two reasons: First, in *spinful* systems, triple points occur only in a small number of different symmetry settings [180, 182], while we will see that spinless systems allow for more variety. Second, the spinless setting allows for interesting multigap topology, which we discuss in detail in Chapter 5.

We start the discussion in Section 4.1 by giving a brief overview over the different kinds of triply-degenerate nodal points and specifying the kind—referred to simply as *triple point*—we focus on in this and the subsequent chapters. In Section 4.2, we describe the conditions for stable triple points to occur, introduce our terminology for characterizing them and the nodal-line structure in their vicinity, and give an overview over our approach for the classification. Sections 4.3 to 4.5 contain our original work, namely the derivations of the classification for increasingly more complicated symmetry settings with the result summarized in Section 4.6. Finally, in Section 4.7 we apply the classification to electronic materials based on first-principles calculations and verify our predictions of the stability of triple points and the nodal-line structure.

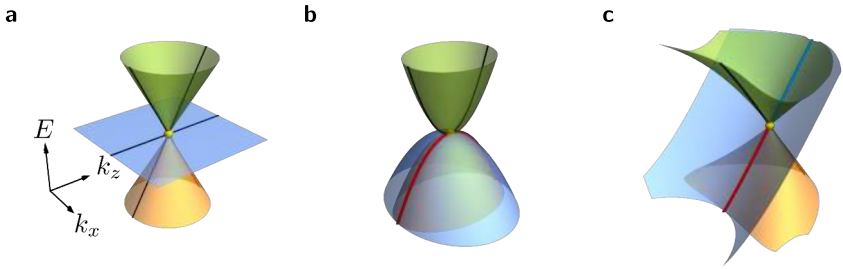

Figure 4.1.: Triply-degenerate nodal points. The band structure of three kinds of triply-degenerate nodal points is shown on the 2D cut $k_y = 0$ through momentum space with the bands for $k_x = 0$ emphasized by colored lines: non-degenerate bands are shown in black, while two-fold degeneracies in the lower (upper) gap are shown in red (blue). The triply-degenerate nodal point is shown as a yellow sphere. (**a**) Spin-1 Weyl fermion formed by an isolated three-fold degeneracy at a high-symmetry point. (**b**) Contact triply-degenerate nodal point at a high-symmetry point with red nodal line along k_z. (**c**) Triple point at a generic position on a high-symmetry line.

4.1. Triply-degenerate nodal points

Triply-degenerate nodal points are symmetry-protected three-fold degeneracies of energy bands occurring at points in momentum space. According to the discussion in Section 3.3, such three-fold band nodes occur at positions in the Brillouin zone, where the little group either hosts a 3D ICR or admits both 1D and 2D ICRs simultaneously. This allows us two distinguish three kinds of triply-degenerate nodal points [33, 176, 208–210] illustrated in Fig. 4.1: (1) isolated degeneracies at high-symmetry points formed by a 3D ICR, sometimes called *spin*-1 *(Weyl) fermions*, (2) quadratic contact points of three bands at high-symmetry points due to a 3D ICR which splits into a 2D ICR and therefore nodal line along one high-symmetry direction, and (3) crossings of a 2D ICR of the little group of a high-symmetry line (HSL) by a 1D ICR, which, for brevity we will refer to simply as *triple points*. Note that (2) only occurs in spinless systems, while (1) and (3) can be realized in both spinless and spinful systems. The focus of all of Part II is on the third kind of triply-degenerate nodal points.

Spin-1 fermions are analogues of the two-fold degenerate Weyl points as can be inferred from the dispersion shown in Fig. 4.1a. The analogy is manifested in the fact that spin-1 fermions are characterized by a nontrivial Chern monopole charge, taking a value ± 2 and giving rise to Fermi surface arcs [176], which have

been experimentally observed in real materials [211–215]. Quadratic contact points, where, as the name suggests, all bands split quadratically away from the degeneracy, on the other hand, carry trivial Chern monopole charge. While the lower two bands (orange and blue in Fig. 4.1b) can be degenerate along some directions (as indicated by the red nodal line), the third band (green) is always separated from the other away from the high-symmetry point. Thus, the Chern number is well-defined. In contrast, triply-degenerate nodal points on HSLs have received considerably less attention. From Fig. 4.1c it becomes apparent that no monopole charge enclosing the triple point can be defined due to the blue nodal line which would cross any closed surface enclosing a single triple point. In fact, we will see in this chapter that quite often even more nodal lines appear at or close to the triple points. The presence of such nodal lines presents a challenge to a topological characterization, but at the same time elevates triple points to a platform for studying the interplay of nodal lines with triply-degenerate nodal points and topology.

Initially, triple points were considered within the context of spin-orbit-coupled systems, where they were classified as type A (type B) according to the absence (presence) of attached nodal-line nodal-line arcs [180, 182]. Using photoemission spectroscopy, triple points were shown to exist in the band structure of various materials, including MoP [187], WC [191], and the ferroelectric GeTe [216]. In contrast, triple points in spinless band structures, became the subject of a systematic analysis only later [1–3, 208–210] and have been reported in several compounds [190, 217–221]. While it is difficult to find magnetic materials that are well described by spinless representations, classical metamaterials are naturally spinless and setups where time-reversal symmetry is broken are therefore expected to be described by spinless representations of magnetic groups. Recent works have systematically searched for triple points in spinless band structures of all magnetic space groups [33–35, 208–210], studied triple points at high-symmetry points in more detail [208–210], or classified triple points on HSLs according to their dispersion as linear or quadratic [209]. The missing aspects of the triple point classification according to the nodal-line structure in their vicinity, in particular whether they are type A versus type B, in spinless band structures are the subject of this chapter and were originally worked out in Refs. 1, 2. The result, summarized in Section 4.6 is a complete classification of triple points for *all* space groups, including magnetic and nonsymmorphic ones.

4.2. Stability and features of triple points

By definition, triple points are protected by symmetries that lead to at least one 1D and one 2D ICR of the little group along a *line* in the Brillouin zone. This raises the question which symmetries or combinations of symmetries are sufficient to *protect* triple points and where in the Brillouin zone they can occur. We answer those questions in Section 4.2.1, where we find that the number of distinct symmetry settings that can host stable triple points is significantly larger in the spinless compared to the spinful setting. Subsequently, in Section 4.2.2, we introduce our terminology for characterizing the nodal-line structure in the vicinity of triple points and sketch our approach for deriving a classification based on those characteristics.

4.2.1. Symmetry conditions for stable triple points

To analyze the conditions for the existence of both 1D and 2D ICRs of a little group of some line in the Brillouin zone, it is useful to distinguish the case of symmorphic and nonsymmorphic space groups. Recall from Section 2.3.3 that in symmorphic space groups, the ICRs of any little group $\mathcal{G}^{\mathbf{k}}$ are readily deduced from the ICRs of the corresponding little *co-group* $\overline{\mathcal{G}}^{\mathbf{k}}$, which is defined as the quotient group $\mathcal{G}^{\mathbf{k}}/\mathcal{T}$ and equal to one of the 122 magnetic point groups. By screening through the ICRs of magnetic point groups characterizing HSLs [77, 80, 84, 85], i.e., the ones that preserve one momentum component, we find that this condition is satisfied (1) if a rotational symmetry C_n of order $n \in \{3, 4, 6\}$ with rotation axis along the HSL is supplemented with $\mathcal{PT}$ or a *vertical* mirror symmetry m_v (i.e., one containing the rotation axis), or both; alternatively, (2) the combined symmetry $C_n\mathcal{PT}$ (which we call *antiunitary rotation*) of order $n \in \{4, 6\}$ can stabilize triple points with or without the $\mathcal{PT}$ and m_v symmetry. We summarize the 13 options in Table 4.1. In contrast, in the spinful case the *double-valued* ICRs are relevant and only *three* of the magnetic point groups listed in Table 4.1 have both 1D and 2D double-valued ICRs: $\bar{6}'$, $3m$, and $\bar{6}'m2'$.

In nonsymmorphic space groups, on the other hand, the ICRs of the little group $\mathcal{G}^{\mathbf{k}}$ are generically not related to the ordinary ICRs of the little co-group $\overline{\mathcal{G}}^{\mathbf{k}}$, but they are instead obtained from the *projective* ICRs of $\overline{\mathcal{G}}^{\mathbf{k}}$, see Section 2.3.3. However, it turns out that if $\mathcal{G}^{\mathbf{k}}$ has at least one 1D ICR $\overline{\mathcal{D}}_1$ (which in our case is satisfied by assumption), all its ICRs are deduced from projective ICRs of $\overline{\mathcal{G}}^{\mathbf{k}}$ with factor system belonging to the trivial equivalence class. This can be seen as follows. The little group $\mathcal{G}^{\mathbf{k}}$ has ICRs deduced from projective ICRs of $\overline{\mathcal{G}}^{\mathbf{k}}$ with factor system μ given by Eq. (2.53). Because $\mathcal{G}^{\mathbf{k}}$ has a 1D ICR $\overline{\mathcal{D}}_1$, there must be a corresponding 1D projective ICR $\overline{\Delta}_1$ of $\overline{\mathcal{G}}^{\mathbf{k}}$

Table 4.1.: Symmetry conditions for triple points in spinless systems. The table displays all magnetic point groups in Hermann-Mauguin notation [77] that can stabilize triple points if they occur as the little co-group of a high-symmetry line. These are exactly the magnetic point groups that (1) preserve one momentum component (such that the magnetic point group corresponds to a little co-group of some high-symmetry line), and that (2) support both 1D and 2D irreducible corepresentations. The columns and the rows indicate generators of the magnetic point group, where C_n is rotational symmetry of order n, $\mathcal{PT}$ is space-time inversion symmetry, and m_v is mirror symmetry with respect to a plane containing the rotation axis. Entries marked by ✗ violate condition (2) and can therefore not stabilize triple points.

Generators	C_3	C_4	$C_4\mathcal{PT}$	C_6	$C_6\mathcal{PT}$
$\varnothing$	✗	✗	$\bar{4}'$	✗	$\bar{6}'$
$\mathcal{PT}$	$\bar{3}'$	$4/m'$		$6/m'$	
m_v	$3m$	$4mm$	$\bar{4}'2'm$	$6mm$	$\bar{6}'m2'$
$\{\mathcal{PT}, m_v\}$	$\bar{3}'m$	$4/m'mm$		$6/m'mm$	

with the same factor system μ. Consider the equivalence transformation of factor systems induced by

$$C(g) = \overline{\Delta}_1(g)^{-1}. \tag{4.1}$$

Then, according to Eqs. (2.54) and (2.57), one easily verifies that the transformed projective corepresentations will have factor system

$$\nu(g, g') = \mu(g, g')^{-1}\mu(g, g') = 1 \tag{4.2}$$

for all $g, g' \in G$. This immediately implies that μ is a factor system in the trivial *equivalence class* (but not necessarily trivial itself).

In the setting of triple points, Eq. (4.1) therefore gives a one-to-one correspondence between the projective ICRs of $\overline{\mathcal{G}}^{\mathbf{k}}$ and the ordinary ICRs of $\overline{\mathcal{G}}^{\mathbf{k}}$. We thus find, *even for nonsymmorphic space groups*, that the little group $\mathcal{G}^{\mathrm{HSL}}$ at a HSL supports both 1D and 2D ICRs if and only if the corresponding little co-group $\overline{\mathcal{G}}^{\mathrm{HSL}}$ supports both 1D and 2D ICRs. This implies that the analysis reduces to the symmorphic case, such that even for HSLs of nonsymmorphic space groups, the conditions for stable triple points is that the little co-group of the HSL is one of the 13 magnetic point groups listed in Table 4.1. As we will see in Section 4.5, the correspondence between ICRs goes even further, ultimately allowing us to extend the full classification that we develop in Sections 4.3 and 4.4 for symmorphic space groups with *basically no changes* to nonsymmorphic space groups.

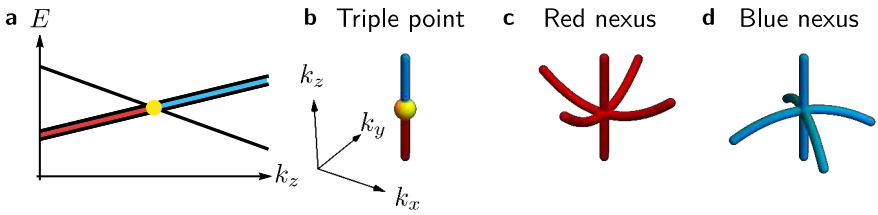

Figure 4.2.: Triple points and their characteristic nodal features. (**a**) Schematic band structure along a high-symmetry line k_z, where a non-degenerate band crosses a doubly-degenerate band. Nodal lines in the lower (upper) band gap of a three-band model are shown in red (blue), and the triple point is indicated by a yellow disk or sphere. (**b**) In the nodal-line structure, a triple point can be recognized by the change of the color of the *central nodal line* from red to blue. (**c,d**) The point where additional nodal lines (called *nodal-line arcs*) coalesce with the central nodal line is called *nexus*. All nodal lines involved in the nexus are in the same gap, i.e., a red (blue) nexus involves nodal lines in the lower (upper) gap.

In this chapter, we classify triple points based on their properties (notably according to their associated nodal-line structure which we describe in Section 4.2.2) given a concrete little group of a HSL, while we leave the systematic identification of the space groups that host triple points to other works. Given Table 4.1 and databases such as the Bilbao crystallographic server [80] this is, in principle, a straightforward task. Let us point out that, space groups that support variety of band nodes ("quasiparticles"), including triple points, were tabulated in Refs. 33–35. In the corresponding supplementary materials, the authors list for each type-II, type-III and type-IV magnetic space group, respectively, at each HSL the generators of the little co-group and the admissible nodal quasiparticles. Searching for triple points in those tables, one can find all space groups and HSLs supporting triple points as well as the relevant little co-group such that our classification can be easily applied.

4.2.2. Nodal-line structure in the vicinity of triple points

Before introducing the classification scheme in more detail, we introduce the relevant notions for describing the nodal-line structure and set some terminology. Consider a HSL with little group $\mathcal{G}^{\mathrm{HSL}}$; the little group $\mathcal{G}^{\mathbf{k}}$ of $\mathbf{k}$ is defined as the subgroup of the space group that leaves the momentum $\mathbf{k}$ invariant modulo translations by reciprocal lattice vectors. Note that $\mathcal{G}^{\mathbf{k}}$ always contains as a subgroup the (infinite) group $\mathcal{T}$ of translations by Bravais vectors. The

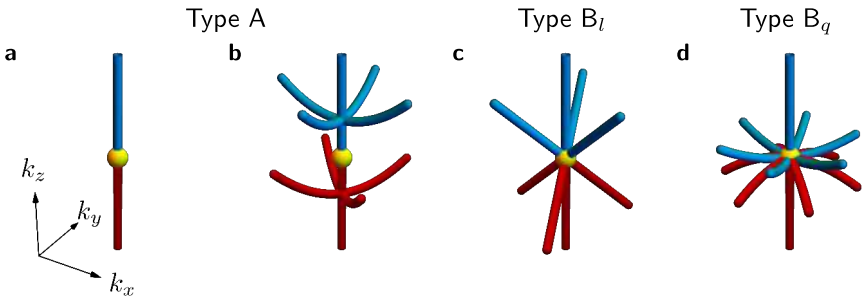

Figure 4.3.: Types and subtypes of triple points in spinless systems. Nodal lines are shown in red (blue) if they are in the lower (upper) band gap of the three-band model and the triple point is indicated in yellow. Triple points are conventionally classified as type A (type B) according to the absence (presence) of nodal-line arcs *attached to* the triple point besides the central nodal line along the high-symmetry line. Type-A triple points arise (**a**) without nexus points or (**b**) with nexus points that do generically (i.e., without fine tuning) *not* coincide with the triple point. For type-B triple points a red and blue nexus generally coincide with the triple point. We differentiate between (**c**) type B_l with three linearly attached nodal lines and (**d**) type B_q with six quadratically attached nodal lines.

existence of a triple point along the HSL means that a non-degenerate band (1D ICR of $\mathcal{G}^{\mathrm{HSL}}$) crosses a doubly degenerate band (2D ICR of $\mathcal{G}^{\mathrm{HSL}}$), such that the nodal line formed by the latter (which we call the *central* nodal line) changes the energy gap (cf. Fig. 4.2a). In such a three-band system, let us denote the two gaps (and the nodal lines in the corresponding gaps) by the colors used in the illustrations: the lower gap is red and the upper gap is blue. Then, the defining feature of a triple point is the change of the central nodal line from red to blue, see Fig. 4.2b.

Often, triple points are accompanied by additional nodal lines that coalesce with the central nodal line of the same color at some point on the HSL. We call such a point a red or blue *nexus* (point), depending on the gap in which it appears – see Figs. 4.2c and 4.2d, respectively. In some cases, the little group and the corepresentations of the bands can force nexus points to coincide with the triple point (cf. Figs. 4.3c and 4.3d), while in other cases they generically do not coincide with the triple point (cf. Fig. 4.3b) or are completely absent (cf. Fig. 4.3a). Following the terminology of Ref. 180 that introduced the classification of triple points in spinful systems, we call triple points that necessarily coincide with both a red and a blue nexus *type* B and the others

type A. Note that in contrast to nexus points coinciding with a type-B triple point, nexus points *near* a type-A triple point are not enforced by symmetry and therefore not a parameter-independent consequence of the triple point. For brevity, we term the additional nodal lines involved in the nexus points, independent of whether the nexus points coincides with the triple point or not, *nodal-line arcs*.

Going beyond the terminology of Ref. 180, we further subdivide type-B triple points into type-B_l triple points with linearly attached nodal-line arcs as shown in Fig. 4.3c and type-B_q triple points with quadratically attached nodal-line arcs as shown in Fig. 4.3d. For type-A triple points in symmetry groups that admit nexus points along the rotation axis, we additionally define the number n_a^{nexus} of nodal-line arcs attached to a nexus point and specify the codimension for colliding at least one nexus point with the triple point, i.e., quantify how many parameters need to be fine-tuned to achieve the coincidence of the triple point with the nexus of nodal-line arcs. Sometimes, because of reasons rooted in symmetry, the smallest number of nexus points that can collide with the triple point is larger than one, i.e., several nexus points necessarily collide with the triple point simultaneously. We remark that understanding these codimensions is not just an abstract academic problem, but it may become important for the analysis of real materials' band structures when the codimension is small. To illustrate this aspect, we show a particular example of a material that exhibits such a fine-tuned type-A triple point in Section 4.7.

Having determined the symmetry conditions allowing for stable triple points in Section 4.2.1, we now proceed to analyze the characteristics described above depending on the little co-group and the ICRs involved in the triple point. This involves a detailed study of $\mathbf{k}\cdot\mathbf{p}$ expansions near the triple point and such a technical analysis constitutes the bulk of Sections 4.3 to 4.5. The type, subtype, and codimension of the triple point, i.e., the absence (presence) of nexus points of nodal-line arcs at or near the triple point, is governed by the absence (presence) of nodal lines lying off the rotation axis and connecting to the rotation axis at some point. These nodal lines are protected either by vertical mirror symmetry m_v (in which case they are constrained to lie in the corresponding vertical mirror planes) or by $\mathcal{PT}$ symmetry (in which case they can curve arbitrarily inside momentum space) [162]. To reflect this dichotomy, we divide the 13 magnetic point groups shown in Table 4.1 into those *without* $\mathcal{PT}$ symmetry, discussed in Section 4.3, and those *with* $\mathcal{PT}$ symmetry, discussed in Section 4.4. For simplicity, we assume a symmorphic space group; however, in Section 4.5, we argue that this assumption can be lifted without any change to the classification results except for a relabeling of ICRs.

4.3. Classification in absence of $\mathcal{PT}$ symmetry

4.3.1. Magnetic point groups without mirror symmetry

We begin the derivation of the classification of triple points by swiftly considering those magnetic point groups in Table 4.1 that contain neither space-time-inversion symmetry $\mathcal{PT}$ nor mirror symmetry m_v. This includes the magnetic point groups $\bar{4}'$ and $\bar{6}'$ that are generated by a single element: $C_{4z}\mathcal{PT}$ and $C_{6z}\mathcal{PT}$, respectively.

These symmetries act like rotations inside the **k**-space. Therefore, the little co-group of all points lying off the rotation axis contains only the identity element, in which case the codimension for node formation is three (i.e., point nodes in 3D) [173]. It follows that nodal lines can only be stabilized along the corresponding rotation axis, preventing the existence of any stable nodal-line arcs [162]. This implies that all triple points on lines with the little co-group $\bar{4}'$ or $\bar{6}'$ are type A and that nexus points are absent (denoted by a codimension of ∞), i.e., the nodal structure is always the one shown in Fig. 4.3a.

4.3.2. Magnetic point groups with mirror symmetry

We continue with the characterization of triple points in those magnetic point groups in Table 4.1 that contain vertical mirror symmetry m_v but not $\mathcal{PT}$. This includes: $3m$, $4mm$, $\bar{4}'2'm$, $6mm$ and $\bar{6}'m2'$. The presence of vertical mirror symmetries implies that there can be stable nodal lines in the corresponding mirror planes, which may connect as nodal-line arcs either to type-B triple points or to a nexus point in the vicinity of a type-A triple point.

For each of the listed magnetic point groups we first derive a $\mathbf{k}\cdot\mathbf{p}$ expansion near the triple point within the 2D mirror planes. More precisely, we perform the expansion only in the distance from the rotation axis (k_x coordinate inside the mirror plane), whereas we keep the full dependence on the coordinate along the rotation axis (k_z). The derived $\mathbf{k}\cdot\mathbf{p}$ expansions allow us to determine the triple-point type and the number of nodal-line arcs attached to a nexus point. For the cases where the triple points are identified as type-A, we derive the codimension for colliding the triple point with a nexus point. We also determine the minimal number of nexus points that can simultaneously collide with the triple point, which requires us to relate the parameters in the $\mathbf{k}\cdot\mathbf{p}$ model within symmetry-unrelated sets of mirror planes. The discussion is subdivided into four parts. We start by deriving the $\mathbf{k}\cdot\mathbf{p}$ models for the magnetic point groups $4mm$, $\bar{4}'2'm$ and $6mm$, then deduce the nodal-line structure from the models. Next, we repeat the same steps for the magnetic point group $\bar{6}'m2'$, and finally for $3m$.

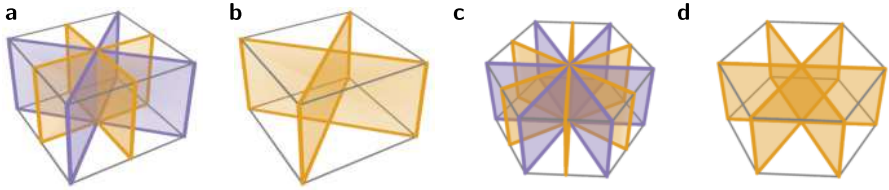

Figure 4.4.: Vertical mirror planes. Mirror planes containing the rotation axis for the magnetic point groups (**a**) $4mm$ and $4/m'mm$, (**b**) $\bar{4}'2'm$, (**c**) $6mm$ and $6/m'mm$, and (**d**) $\bar{6}'m2'$, $3m$, and $\bar{3}'m$. Mirror planes related by (rotation-)symmetry are shown in the same color, such that in (a,c) the different symmetry-unrelated sets of mirror planes can be distinguished by their color. The gray boxes are guides to the eye.

Triple-point type derivation for $4mm$, $\bar{4}'2'm$, and $6mm$

The magnetic point groups $4mm$, $\bar{4}'2'm$ and $6mm$, are all generated by two elements: a rotational symmetry C_n (or antiunitary rotational symmetry $C_n\mathcal{P}\mathcal{T}$) with $n = 4, 6$ and a vertical mirror symmetry m with mirror plane containing the rotation axis. For each of these magnetic point groups, the vertical mirror planes come in pairs that are orthogonal to each other: $4mm$ has two mirror planes along the x- and y-axes (for suitably chosen coordinates) and two diagonal mirror planes (cf. Fig. 4.4a), $\bar{4}'2'm$ has only the two diagonal mirror planes (cf. Fig. 4.4b), and $6mm$ has a total of six mirror planes at angles differing by $\frac{\pi}{6}$ (cf. Fig. 4.4c). For any vertical mirror symmetry m, we label the associated orthogonal vertical mirror symmetry by $m_\perp$. For brevity, we call the set of $\mathbf{k}$-points invariant under $m_{(\perp)}$ the $m_{(\perp)}$-plane.

The convenience of considering the pair of symmetries $(m, m_\perp)$ is that the composition of m and $m_\perp$ is simply the C_2 rotational symmetry around the HSL, and that these symmetries commute and thus can be diagonalized simultaneously. Additionally, the subgroup of the magnetic point group that maps points on the m-plane back to the m-plane is exactly the Abelian group $\{1, m, m_\perp, C_2\}$ (with 1 the identity element), which is fully generated by m and $m_\perp$. Therefore, to derive a symmetry-compatible $\mathbf{k}\cdot\mathbf{p}$ Hamiltonian inside the m-plane, it is sufficient to study the constraints from m and $m_\perp$.

To introduce concrete labels, say that a triple point is formed along the HSL by the crossing of a 1D ICR $D^{1\mathrm{D}}$ with a 2D ICR $D^{2\mathrm{D}}$. The common feature of $D^{2\mathrm{D}}$ in all the present cases is that any mirror symmetry $m \in \mathcal{G}^{\mathrm{HSL}}$ satisfies $\mathrm{tr}\big[D^{2\mathrm{D}}(m)\big] = 0$. Combined with the fact that the possible eigenvalues of m are just $+1$ and -1, the vanishing trace implies that the 2D ICR is spanned by two states with opposite eigenvalues of m. Additionally, m and $m_\perp$ commute,

Table 4.2.: Possible mirror eigenvalues in $4mm$, $\bar{4}'2'm$, and $6mm$. The two rows of D^{2D} correspond to the eigenvalues of the irreducible representations involved in the triple point and they are given in the order defined by a particular choice of basis of the 2D representation. This is well-defined, because m and $m_\perp$ commute, such that the corresponding matrix representations can be simultaneously diagonalized. Subscripts to $\pm$ indicate independent signs. In this analysis, we always rotate the basis such that $\pm_r 1 = \mp_p 1$.

	m	$m_\perp$	$C_2 = m \circ m_\perp$
D^{2D}	$\pm_p 1$	$\pm_q 1$	$(\pm_p 1)(\pm_q 1)$
	$\mp_p 1$	$\mp_q 1$	$(\pm_p 1)(\pm_q 1)$
D^{1D}	$\pm_r 1$	$\pm_t 1$	$(\pm_r 1)(\pm_t 1)$

meaning that they can be diagonalized simultaneously. Adopting a basis in which the two symmetry operators are diagonal, the possible mirror eigenvalues of the ICRs D^{2D} and D^{1D} (which appear on the operator diagonals) are shown in Table 4.2, where the only adjustable parameters are the four signs $\pm_{p,q,r,t}$.

Let $\mathcal{D}$ be the representation that captures the three bands involved in the triple point, $\mathcal{D} = D^{2D} \oplus D^{1D}$. We work in the basis in which $D^{2D}(m)$ and $D^{2D}(m_\perp)$ are diagonal, and we permute the basis of D^{2D} such that the second eigenvalue of $D^{2D}(m)$ is equal to $D^{1D}(m)$. Referring to Table 4.2, this implies

$$\pm_r 1 = \mp_p 1, \tag{4.3}$$

i.e., it fixes one of the four signs. In this basis, we then have the following matrix representations

$$\mathcal{D}(m) = \begin{pmatrix} \pm_p 1 & & \\ & \mp_p 1 & \\ & & \mp_p 1 \end{pmatrix}, \quad \mathcal{D}(m_\perp) = \begin{pmatrix} \pm_q 1 & & \\ & \mp_q 1 & \\ & & \pm_t 1 \end{pmatrix}. \tag{4.4}$$

We define orthogonal coordinates (k_x, k_z) in the m-plane such that k_z runs along the rotation axis and such that the triple point is located at $(k_x, k_z) = 0$. Then, according to Section 2.4.2, m constrains the Hamiltonian as follows:

$$H(k_x, k_z) = \mathcal{D}(m) H(k_x, k_z) \mathcal{D}(m)^{-1}, \tag{4.5}$$

and implies that

$$H(k_x, k_z) = \begin{pmatrix} \epsilon^1 & 0 & 0 \\ 0 & \epsilon^2 & f \\ 0 & f^* & \epsilon^3 \end{pmatrix} \tag{4.6}$$

with ϵ^i being real-valued functions and f a complex-valued function of k_x and k_z.

Next, we derive the low-order expansion of Eq. (4.6) in k_x, while keeping the full dependence on k_z using the additional constraint due to $m_\perp$:

$$H(k_x, k_z) = \mathcal{D}(m_\perp) H(-k_x, k_z) \mathcal{D}(m_\perp)^{-1}. \tag{4.7}$$

This implies that ϵ^i are even in k_x, and that

$$f(k_x, k_z) = (\mp_q 1)(\pm_t 1) f(-k_x, k_z), \tag{4.8}$$

i.e., f is even (odd) in k_x if the product of the signs of the C_2-characters of $D^{2\mathrm{D}}$ and $D^{1\mathrm{D}}$ is positive (negative), cf. Table 4.2. Let us denote the sign of that number by

$$s = -(\pm_q)(\pm_t). \tag{4.9}$$

Note that s is equal to the sign of the product of the C_2-characters of $D^{2\mathrm{D}}$ and $D^{1\mathrm{D}}$. Finally, the (antiunitary) rotational symmetry (C_4, $C_4\mathcal{PT}$, and C_6 for the three discussed magnetic point groups, respectively) leads to the following additional constraints: $\epsilon^1(0, k_z) = \epsilon^2(0, k_z)$ and $f(0, k_z) = 0$.

Assuming there is a triple point at $k_z = 0$ at energy $E = 0$, we have $\epsilon^i(0, 0) = 0$ for $i = 1, 2, 3$ and

$$\tilde{\epsilon}^1(k_x, k_z) = \tilde{a} k_z + \tilde{b} k_x^2, \tag{4.10a}$$

$$\tilde{\epsilon}^2(k_x, k_z) = \tilde{a} k_z + \tilde{c} k_x^2, \tag{4.10b}$$

$$\tilde{\epsilon}^3(k_x, k_z) = \tilde{d} k_z + \tilde{e} k_x^2, \tag{4.10c}$$

$$f(k_x, k_z) = A k_x^{\frac{3+s}{2}}, \tag{4.10d}$$

with $\tilde{a}, \tilde{b}, \tilde{c}, \tilde{d}, \tilde{e}$ real-valued functions and A a complex-valued function of k_z. The degeneracies of the spectrum are clearly independent of constant energy shifts (i.e., terms in the Hamiltonian that are proportional to the identity matrix), such that we can subtract $\frac{1}{2}(\tilde{\epsilon}^1 + \tilde{\epsilon}^2)\mathbb{1}$ and arrive at the following Hamiltonian

$$H(k_x, k_z) = \begin{pmatrix} a k_x^2 & 0 & 0 \\ 0 & -a k_x^2 & A k_x^{\frac{3+s}{2}} \\ 0 & A^* k_x^{\frac{3+s}{2}} & b k_z + c k_x^2 \end{pmatrix}, \tag{4.11}$$

where $a(k_z), b(k_z), c(k_z)$ are continuous real-valued functions, and $A(k_z)$ is a continuous complex-valued function. We suppress the k_z argument of the four functions in Eq. (4.11) to improve readability. The block-diagonal structure (which does *not* parallel the blocks of $D^{2\mathrm{D}} \oplus D^{1\mathrm{D}}$) arises from the two different

eigenvalues of $D(m)$ in the m-plane, and therefore persists to all orders of the expansion.

There are two possibilities for $H(k_x, k_z)$ to have degeneracies in the spectrum (corresponding to band nodes): either (1) the bottom right 2×2 block $h_{23}(k_x, k_z)$ has degenerate eigenvalues, or (2) it has an eigenvalue $a(k_z)k_x^2$. For (1), recall that spectral degeneracies of a matrix correspond to the roots of the characteristic polynomial, and that coinciding roots of a polynomial can be diagnosed by a vanishing discriminant. Therefore, we compute the discriminant of the characteristic polynomial of $h_{23}(k_x, k_z)$,

$$\left[(a+c)k_x^2 + bk_z\right]^2 + 4|A|^2 k_x^{3+s} = 0. \tag{4.12}$$

Because $s = \pm 1$, the left-hand side of the equation is a sum of two squares, and as such it has no real solutions except for $k_x = k_z = 0$, which, by construction, is the triple point.

On the other hand, condition (2) is satisfied if and only if

$$\begin{aligned} 0 &= \det\left[h_{23}(k_x, k_z) - a(k_z)k_x^2 \mathbb{1}\right] \\ &= k_x^2 \left[-2abk_z + 2a(a-c)k_x^2 - |A|^2 k_x^{1+s}\right], \end{aligned} \tag{4.13}$$

where in the second line we dropped the functional dependencies of a, b, c and A. Equation (4.13) admits two types of solutions. First, $k_x = 0$ is always a solution that defines the central nodal line along the k_z-axis. The second type of solution corresponds to zeros of the expression in the square brackets. Assuming that this solution appears close to the triple point (which is always the case for nodal-line arcs of type-B triple points), we approximate the variable functions by their values at $k_z = 0$, i.e.,

$$f(k_z) \approx f(k_z = 0) \equiv f_0 \quad \text{for } f \in \{a, b, c, A\} \tag{4.14}$$

and find the explicit root

$$k_z^{\mathrm{arc}}(k_x) = \frac{a_0 - c_0}{b_0} k_x^2 - \frac{|A_0|^2}{2a_0 b_0} k_x^{1+s} \tag{4.15}$$

that describes the nodal-line arcs.

To analyze the result in Eq. (4.15), first observe that for $s = +1$, the nodal-line arcs attach to the triple point [because $\lim_{k_x \to 0} k_z^{\mathrm{arc}}(k_x) = 0$], while they generically do *not* attach to the triple point for $s = -1$ [because $\lim_{k_x \to 0} k_z^{\mathrm{arc}}(k_x) = -|A_0|^2/2a_0b_0$]. We further read from Eq. (4.15) that the nodal-line arcs scale quadratically as a function of $k := (k_x^2 + k_y^2)^{1/2}$, i.e., $k_z^{\mathrm{arc}}(k) - k_z^{\mathrm{arc}}(0) \propto k^2$. Thus, we conclude that the triple point is type A (type

Table 4.3.: Classification of triple points in the absence of $\mathcal{PT}$ symmetry. The triple point is characterized by whether nodal-line arcs attach to it (type A) or not (type B) [180]. For all triple-point types we define n_a^{nexus} as the number of nodal-line arcs attached to a generic *nexus* point (coinciding with the triple point for type B but not for type A), the scaling of the attached nodal-line arcs $k_z \propto (k_x^2 + k_y^2)^{\mu/2}$, and the codimension giving the number of parameters that need to be tuned to collapse a nexus point to the triple point. We further distinguish type-B_q ($\mu = 2$) and type-B_l ($\mu = 1$). These properties depend on $\overline{\mathcal{G}}^{\mathbf{k}}$ and, in general, on the irreducible corepresentations (ICRs) of the bands involved in the triple point formation. We use the notation by Mulliken [81] for the ICRs with $i = 1, 2$.

$\overline{\mathcal{G}}^{\mathbf{k}}$	ICRs	Type	n_a^{nexus}	μ	Codimension
$3m$	$(E; A_i)$	B_l	6	1	0
$\bar{4}'2'm$	$({}^2B^1B; A_i)$	A	4	2	2
$\bar{6}'m2'$	$(E; A_i)$	A	6	2	1
$4mm$	$(E; A_i), (E; B_i)$	A	4	2	2
$6mm$	$(E_1; A_i), (E_2; B_i)$	A	12	2	2
	$(E_1; B_i), (E_2; A_i)$	B_q	12	2	0

B_q) if the product of C_2-characters of $D^{2\text{D}}$ and $D^{1\text{D}}$ is negative (positive). Additionally, we see from the more general Eq. (4.13) that a nexus of nodal-line arcs would coincide with a type-A triple point when $A_0 = 0$. Since $A(k_z)$ is a complex function, this is generically achieved by tuning two real parameters, i.e., the sought codimension equals 2.

To finalize the type classification for the three magnetic point groups discussed here, we determine the value of s for each combination of 2D and 1D ICRs $D^{2\text{D}} \oplus D^{1\text{D}}$. This is achieved by looking up the ICRs and C_2-characters on the Bilbao crystallographic server [222–224] using the program Corepresentations PG [84, 85]. We find that for $4mm$ and $\bar{4}'2'm$ all combinations of ICRs have $s = -1$, such that any triple points in those groups are type A. The analysis is more subtle for $6mm$: here, type-A triple points ($s = -1$) are realized for the ICR combinations $(E_1; A_i)$ and $(E_2; B_i)$, while type-B_q triple points ($s = +1$) for ICR combinations $(E_1; B_i)$ and $(E_2; A_i)$ (using the notation by Mulliken [81] for the ICRs). In the latter case we can also immediately conclude that $n_a^{\text{nexus}} = 12$ (because there are two sets of three symmetry-related mirror planes, and each mirror plane contains two nodal-line arcs starting at the triple point). These results are summarize in Table 4.3.

Nodal-line arc characterization for $4mm$, $\bar{4}'2'm$, and $6mm$

We next derive characteristics of the nodal-line arcs that appear near the type-A and at the type-B triple points just identified. Although the analysis above was performed for one particular choice of mirror-invariant m-plane, the arguments [including the results in Eqs. (4.12) to (4.15)] straightforwardly generalize.

To begin, note that the band structure respects the magnetic point group symmetry, which readily implies that

(i) nodal-line arcs described by the same Eq. (4.13) and with the same functions a, b, c, A also appear in all the symmetry-related m-planes (cf. Figs. 4.4a to 4.4c).

Additionally, note that the sign s is a characteristic of the two crossing ICRs at the HSL; especially, it does not depend on the particular choice of m. Therefore, the whole algebraic analysis can be repeated for vertical mirror planes m' that are not symmetry-related to m (colored differently in Figs. 4.4a to 4.4c). Note that for $4mm$ the mirrors m' and $m_\perp$ are different, for $6mm$ we have $m' = m_\perp$, and for $\bar{4}'2'm$ there is no m'. We therefore deduce that

(ii) nodal-line arcs in the m'-plane are defined by the same Eq. (4.13), although with a potentially different set of functions a', b', c', and A'.

In the following, we study the implications of observations (i) and (ii) for the nodal-line structure near the discussed triple points.

Let us first analyze the implications when $s = +1$, i.e., when the nodal-line arcs are attached to a type-B triple point. It follows from (i) and (ii) that the triple point must be connected to one nodal-line arc in each vertical mirror plane (such as shown in Fig. 4.3d for $6mm$). The nodal-line arcs in the two sets of mirror planes are generally in different energy gaps, which can be seen as follows. According to the derivation above, the energy of the two bands involved in the nodal line along the nodal-line arc $k_z = k_z^{\mathrm{arc}}(k_x)$ is ak_x^2. To determine in which gap the nodal line lies, we need to compare it to the energy of the third band, which can be deduced from Eqs. (4.11) and (4.13) to be[1]

$$-\left(a + \frac{|A|^2}{2a}\right) k_x^2. \tag{4.16}$$

[1] As an intermediate step, note that Eq. (4.13) with $s = +1$ and $k_x \neq 0$ implies that, near the triple point, $bk_z + ck_x^2 = ak_x^2 - (|A|^2/2a)k_x^2$, and that this is also equal to $\mathrm{tr}(H)$ after substituting for the bottom-right element of the matrix in Eq. (4.11). Since the trace is the sum of all eigenvalues, and the other two eigenvalues were determined as ak_x^2, the result in Eq. (4.16) follows.

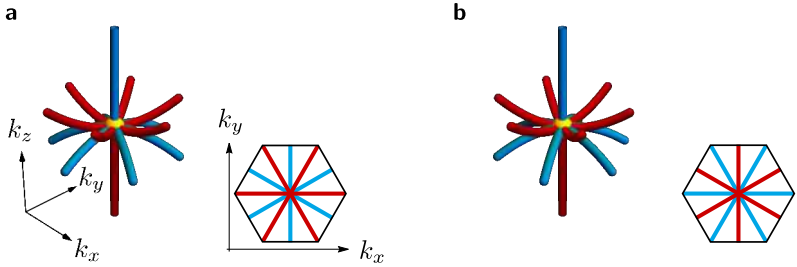

Figure 4.5.: Nodal-line structure near a type-B$_q$ triple point for little co-group $6mm$. The nodal-line arcs attached to a type-B$_q$ triple point occur in two sets of rotation-related mirror planes with nodal lines of the same color appearing in the same set. This results in the two possibilities (**a**) and (**b**) . The insets show the view on the nodal lines from the top to clarify the arrangement of the nodal-line arcs. The same nodal-line structure can be found near a type-B$_q$ triple point for little co-group $6/m'mm$.

It follows from comparing the three band energies that the nodal-line arc is in the red (blue) gap if $a_0 < 0$ ($a_0 > 0$).

Observation (ii) seems to suggest that the nodal-line arcs in symmetry-unrelated planes are independent of each other. However, as revealed in Appendix B.1, the four functions describing the expansions in m and m' obey certain constraints (explicitly derived in the supplementary data and code [225] to Ref. 2). For the magnetic point group $6mm$ and ICRs such that $s = +1$, i.e., such that the resulting triple point is type B$_q$, the derived constraints are

$$a' = -a, \quad b' = b, \quad c' = c, \quad |A'| = |A|. \tag{4.17}$$

Therefore, the nodal-line arcs in one set of planes are in the red gap, while the nodal-line arcs in the other set of planes are in the blue gap. Which set of planes contains nodal-line arcs in which gap, depends on the parameter values as illustrated in Fig. 4.5.

In the remainder of this section, we analyze the implications of (i) and (ii) for $s = -1$, i.e., when the nodal-line arcs connect to the rotation axis away from a type-A triple point. Here, note that a crossing of nodal lines in the two different gaps would automatically imply a threefold degeneracy (i.e., a triple point) at the crossing; therefore, it follows that the nexus of nodal-line arcs associated with type-A triple points are formed in the same gap (red/blue) as the central nodal line at which the arcs converge (cf. Fig. 4.3b).

First, for the magnetic point group $4mm$, the derived constraints on the

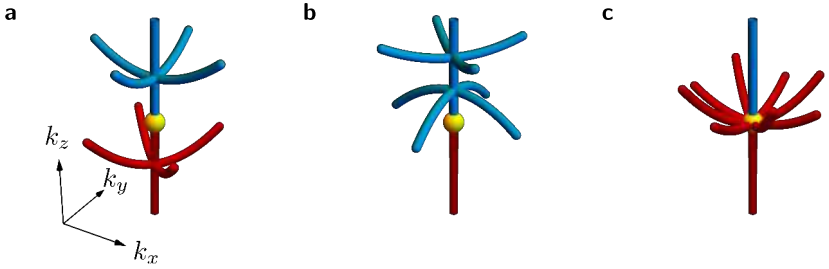

Figure 4.6.: Nodal-line structure near a type-A triple point for little co-group $4mm$. Type-A triple points can be accompanied by nearby nexus points on the central nodal line: (**a**) on opposite sides of the triple point if $\mathrm{sign}(a_0) = -\mathrm{sign}(a_0')$, or (**b**) on the same side if $\mathrm{sign}(a_0) = \mathrm{sign}(a_0')$. (**c**) If the complex parameter A_0 is fine-tuned to 0, the two nexus points (independently of their color) simultaneously collide with the triple point. An analogous discussion applies to the little co-group $4/m'mm$, with the only relevant change being the reduction of A_0 to be a real (rather than complex) parameter.

functions describing the expansion in m and m' are

$$b' = b, \quad c' = c, \quad |A'| = |A|, \tag{4.18}$$

while $a(k_z)$ and $a'(k_z)$ are unrelated. When plugged into Eq. (4.13), we find that the functions a and a' provide enough freedom to realize nexus points of nodal lines in the two sets of mirror planes that attach to the rotation axis at arbitrary and different positions. In particular, the approximate result in Eq. (4.15) derived in the lowest order in k_z suggests one nexus point for each set of symmetry-related m-planes (this can change when terms of higher order in k_z are included). The two nexus points can be on the opposite or on the same sides of the triple point, depending on the relative sign of the coefficients a_0 and a_0', see Figs. 4.6a and 4.6b. Generically, the two nexus points do not coincide, such that $n_a^{\mathrm{nexus}} = 4 = 2 \times 2$ (each nexus point arises due to nodal-line arcs in one set of two symmetry-related mirror planes, and each plane contains two nodal-line arcs attached to the central nodal line.)

Curiously, the constraint $|A| = |A'|$ implies that the two nexus points in the two pairs of planes collide with the triple point *simultaneously*. Notably, if $\mathrm{sign}(a_0) = \mathrm{sign}(a_0')$, such that the two nexus points are on the same side of the triple point for $A \neq 0$, all the nodal-line arcs converging at the fine-tuned type-A triple point for $A_0 = 0$ would be in the *same* gap, cf. Fig. 4.6c. This feature sharply contrasts to type-B triple points for which the number of attached nodal-line arcs is always distributed equally over both gaps. However, a situation

similar to a type-B triple point is also possible if $\mathrm{sign}(a_0) = -\mathrm{sign}(a_0')$ and $A_0 = 0$.

Next, we analyze type-A triple points in the magnetic point group $6mm$. In Appendix B.1, we show that the expansions in the two planes obey

$$a' = a, \quad b' = b, \quad c' = c, \quad |A'| = |A|. \tag{4.19}$$

Looking at Eq. (4.13), we find that nodal-line arcs in both sets of symmetry-related planes always attach to the *same* nexus point as illustrated in Figs. 4.7a and 4.7b, with blue and red nexus points, respectively (distinguished by the sign of a_0). Therefore, we find $n_a^{\mathrm{nexus}} = 12$, i.e., the same as for type-B triple points in the same magnetic point group. However, one should bear in mind that Eq. (4.13) was derived from a $\mathbf{k}\cdot\mathbf{p}$ expansion to finite order in k_x. It can be shown that higher-order terms discriminate between the two sets of planes, meaning that the nodal-line arcs in m-planes and m'-planes disperse differently for large enough distance k from the rotation axis. All these described features are clearly manifested by the type-A triple point of the compound AlN, see Fig. C.3 in Appendix C.1. Finally, when the complex parameter A_0 is set to zero, the 12 nodal-line arcs attached to the fine-tuned type-A triple point are all in the same gap, cf. Fig. 4.7c, such that the type-A triple point can always be distinguished from the type-B triple point.

Lastly, for $\bar{4}'2'm$ there is only one set of symmetry-related mirror planes, such that there is only a single nexus point with four nodal-line arcs: $n_a^{\mathrm{nexus}} = 4$.

Classification for $\bar{6}'m2'$

The group $\bar{6}'m2'$ is similar to the cases discussed above with one crucial difference: each of the three C_3 symmetry-related vertical mirrors m (cf. Fig. 4.4d) is paired with a *pseudo-mirror* $m_\perp\mathcal{PT}$ (here $m_\perp$ is again the mirror perpendicular to m; note that neither $m_\perp$ nor $\mathcal{PT}$ is an element of the symmetry group). We proceed analogously, but need to be careful because $m_\perp\mathcal{PT}$ is antiunitary, such that we have to deal with corepresentations rather than representations, see Sections 2.2.2 and 2.4.2. Therefore, in the mirror planes of m, the Hamiltonian takes the form given in Eq. (4.6) and is subjected to the constraint

$$H(k_x, k_z) = \overline{\mathcal{D}}(m_\perp\mathcal{PT})H(-k_x, k_z)^*\overline{\mathcal{D}}(m_\perp\mathcal{PT})^{-1}. \tag{4.20}$$

We find that in an appropriate choice of basis [84, 85]

$$\overline{\mathcal{D}}(m_\perp\mathcal{PT}) = D^{2\mathrm{D}} \oplus D^{1\mathrm{D}} = \begin{pmatrix} -\mathrm{i} & & \\ & -\mathrm{i} & \\ & & \pm 1 \end{pmatrix} \tag{4.21}$$

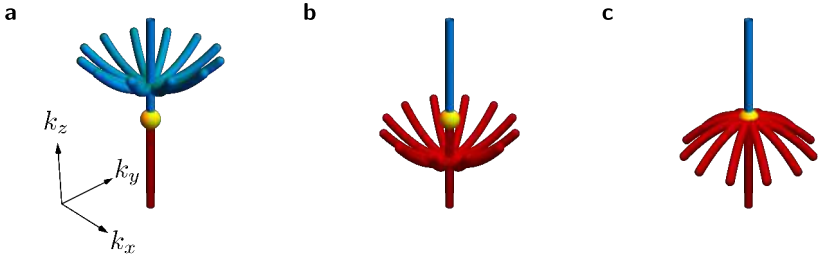

Figure 4.7.: Nodal-line structure near a type-A triple point for little co-group $6mm$. As in the case of the little co-group $4mm$ (cf. Fig. 4.6), type-A triple points in $6mm$ can be accompanied by nexus points nearby on the central nodal line. However, the points of coalescence of nodal-line arcs with the central nodal line in the inequivalent sets of mirror planes always coincide, such that we only distinguish (**a**) blue nexus points ($a_0 > 0$), (**b**) red nexus points ($a_0 < 0$), and (**c**) nexus points fine-tuned to collide with the triple point (if the complex parameter A_0 is set to zero), all with 12 nodal-line arcs attached. An analogous discussion applies to the little co-group $6/m'mm$, with the only relevant change being the reduction of A_0 to real values.

where the upper (lower) sign corresponds to choosing representation $D^{1\mathrm{D}} = A_1$ ($D^{1\mathrm{D}} = A_2$). The above constraint implies that ϵ^i are even functions of k_x, and that

$$f(k_x, k_z) = \mp \mathrm{i} f(-k_x, k_z)^*, \tag{4.22}$$

further implying that

$$f(k_x, k_z) = d(1 \mp \mathrm{i})k_x \tag{4.23}$$

for $d(k_z) \in \mathbb{R}$. By repeating the final steps performed to arrive at Eq. (4.11), we find

$$H(k_x, k_z) = \begin{pmatrix} ak_x^2 & 0 & 0 \\ 0 & -ak_x^2 & d(1 \mp \mathrm{i})k_x \\ 0 & d(1 \pm \mathrm{i})k_x & bk_z + ck_x^2 \end{pmatrix} \tag{4.24}$$

with a, b, c, d being real-valued functions of k_z.

We observe that Eq. (4.24) is identical to Eq. (4.11) with $A = d(1 \mp \mathrm{i})$ and $s = -1$, such that we can immediately obtain the implicit equation for nodal-line arcs from Eq. (4.13), namely

$$-2abk_z + 2a(a - c)k_x^2 - 2|d|^2 k_x^{1+s} = 0. \tag{4.25}$$

From here, assuming the functions a, b, c, d are approximately constant near

the triple point, we obtain the result for the nodal-line arcs

$$k_z = k_z^{\mathrm{arc}}(k_x) \equiv \frac{a_0 - c_0}{b_0} k_x^2 - \frac{d_0^2}{a_0 b_0}, \tag{4.26}$$

where $d_0 = d(k_z = 0)$. Therefore, we find that triple points in $\bar{6}'m2'$ are always type A. Since there is only one set of symmetry-related planes, only one nexus point is present in the $\mathbf{k} \cdot \mathbf{p}$ expansion, and $n_a^{\mathrm{nexus}} = 6$, because there are three mirror planes with two nodal-line arcs starting at the nexus point each. Additionally, because d is a real parameter, the codimension for colliding the nexus point with the triple point is 1, see Table 4.3.

Classification for $3m$

Finally, we discuss the remaining magnetic point group $3m$, which has three-fold rotational symmetry with three vertical mirrors that are not associated with corresponding orthogonal (pseudo-)mirror planes (cf. Fig. 4.4d). Again, we choose coordinates (k_x, k_z) in the mirror plane under consideration (the three mirror planes are equivalent due to rotational symmetry), then the Hamiltonian for all possible combinations of ICRs takes the form

$$H(k_x, k_z) = \begin{pmatrix} a k_x & 0 & 0 \\ 0 & -a k_x & A k_x \\ 0 & A^* k_x & b k_z + c k_x \end{pmatrix}, \tag{4.27}$$

where a, b, c are real-valued functions and A is a complex-valued function of k_z.

Degeneracies in the spectrum are obtained (1) if

$$[(a + c)k_x + b k_z]^2 + 4|A| k x^2 = 0, \tag{4.28}$$

with the only solution $k_x = k_z = 0$ (the triple point), and (2) if

$$0 = \det\left[h_{23}(k_x, k_z) - a k_x \mathbb{1}\right] \tag{4.29}$$

$$= k_x \left[-2ab k_z + 2a(a - c)k_x - |A|^2 k_x\right]. \tag{4.30}$$

The latter equation has two solutions. First, $k_x = 0$ (the central nodal line), and second, after approximating a, b, c, A as constants in the vicinity of the triple point,

$$k_z = \left(\frac{a_0 - c_0}{b_0} - \frac{|A_0|^2}{2 a_0 b_0}\right) k_x \tag{4.31}$$

(the nodal-line arc). Since $\lim_{k_x \to 0} k_z^{\mathrm{arc}}(k_x) = 0$, the nodal-line arc attaches to the triple point and it does so linearly as a function of $(k_x^2 + k_y^2)^{1/2}$, such that the triple point is always type B_l. We again find that $n_a^{\mathrm{nexus}} = 6$ (due to three symmetry-related mirror planes with two nodal-line arcs in each), see Table 4.3.

4.4. Classification in presence of $\mathcal{PT}$ symmetry

There are six relevant magnetic point groups with $\mathcal{PT}$ symmetry listed in Table 4.1 that can protect a triple point along a HSL: $\bar{3}'$, $\bar{3}'m$, $4/m'$, $4/m'mm$, $6/m'$ and $6/m'mm$. The discussion of these magnetic point groups is rather involved, because nodal lines can be stabilized by $\mathcal{PT}$ symmetry *anywhere* in the momentum space [173, 193], i.e., they are not constrained to symmetric planes. Although we ultimately find the resulting classification to be the same (up to a reduction of the codimension where applicable) as for the corresponding magnetic point groups *without* $\mathcal{PT}$ symmetry (specifically $3m$, $4mm$ and $6mm$ analyzed in Section 4.3.2), the minimal $\mathbf{k} \cdot \mathbf{p}$ models and their analysis are considerably more complicated, and much of the explicit algebra is carried out in a MATHEMATICA notebook [225] accompanying our original work [2].

Initially, we proceed similarly to the previous section: we construct minimal $\mathbf{k} \cdot \mathbf{p}$ models for the Hamiltonian near the triple point in the various magnetic point groups. However, due to the presence of $\mathcal{PT}$ symmetry, we cannot restrict to mirror planes and need to study the full 3D $\mathbf{k} \cdot \mathbf{p}$ models. In contrast to Section 4.3, we here find it more convenient to perform the expansion in all three momentum components of $\mathbf{k}$. Given the significantly longer expressions, we here focus on introducing the relevant methods and giving representative examples, deferring concrete calculations for all cases to the above mentioned MATHEMATICA notebook [225]. We start in Section 4.4.1 by describing how to derive those $\mathbf{k} \cdot \mathbf{p}$ models. Next, in Section 4.4.2, we introduce the techniques we developed to determine the leading-order terms of the $\mathbf{k} \cdot \mathbf{p}$ expansion. Finally, in Section 4.4.3 we discuss how to deduce the nodal-line structure near the triple point from the obtained leading-order expansions and illustrate this on a set of representative examples.

4.4.1. Minimal $\mathbf{k} \cdot \mathbf{p}$ models

The first step in deriving the classification is once more the construction of minimal $\mathbf{k} \cdot \mathbf{p}$ models describing the Hamiltonian near the triple point, similar to the discussion in Section 4.3. Because this time we are interested in expansions in all three momentum components k_x, k_y, k_z and the magnetic

point groups under consideration are larger, we use the PYTHON package KDOTP-SYMMETRY [226] instead of performing the calculations by hand. The starting point is again the set of constraints discussed in Section 2.4.2. From that, a family of $\mathbf{k}\cdot\mathbf{p}$ Hamiltonians can be determined by expanding the full Bloch Hamiltonian $H(\mathbf{q})$ around the momentum vector $\mathbf{k}$ under consideration up to some order n in $\mathbf{k}$, and restricting to terms that satisfy the constraints. The space of all $\mathbf{k}\cdot\mathbf{p}$ Hamiltonians then is the tensor product of the space of Hermitian matrices of the appropriate dimensions (given by the number of bands) and the space of polynomials in k_x, k_y, k_z up to the order n. Equation (2.73) then constrains symmetry compatible $\mathbf{k}\cdot\mathbf{p}$ Hamiltonians $H(\mathbf{k})$ to some subspace of it. The PYTHON package KDOTP-SYMMETRY implements an algorithm for finding this subspace. For a given magnetic point group and representation (composed of one 1D and one 2D ICR), this results in a *Hamiltonian family* $H_{\mathbf{a}}(\mathbf{k})$ parametrized by real parameters a_i, collected in the vector $\mathbf{a}$:

$$H_{\mathbf{a}}(\mathbf{k}) = \sum_i a_i H_i(\mathbf{k}). \tag{4.32}$$

For brevity we refer to such a parametrized family as a $\mathbf{k}\cdot\mathbf{p}$ *model*.

Because we are only interested in the occurrence of degeneracies in the spectrum of the Hamiltonian and not absolute energy values, we drop all diagonal matrices $H_i(\mathbf{k})$ that are $\mathbf{k}$-independent or proportional to the identity. Further, we are interested in the behavior near the expansion point, such that terms of leading order in $\mathbf{k}$ (leading in each momentum component separately) are sufficient. Without loss of generality (assuming the presence of a triple point), we set the energy of the 2D ICR for $\mathbf{k} = (0, 0, k_z)$ to zero and the triple-point position to the origin $\mathbf{k} = 0$. This significantly reduces the number of nonvanishing parameters a_i in Eq. (4.32). Furthermore, $(\mathcal{PT})^2 = 1$ implies that there is a basis in which $\overline{\mathcal{D}}(\mathcal{PT}) = \mathbb{1}$, i.e., $\mathcal{PT}$ is represented by complex conjugation $\mathcal{K}$ [66]. In that basis the Bloch Hamiltonian is a real symmetric matrix, such that both H_i as well as a_i are real. Usually, this condition is enforced by already starting from corepresentation matrices in the appropriate basis.

4.4.2. Condition for the occurrence of nodal-line arcs

Note that below we introduce several polynomials that are used in the analysis of spectral degeneracies. We will temporarily, i.e., restricted to Section 4.4.2, use the symbols χ, Δ, $\bar{\Delta}$, $\bar{\Delta}_0$, P, R, D, which should not be confused with their meaning throughout the rest of the thesis.

Equivalence classes of Hamiltonian families

In principle, we would have to consider all combinations of one 1D and one 2D ICR for any of the six magnetic point groups with $\mathcal{PT}$ symmetry. However, for a given magnetic point group, most combinations of ICRs lead to *equivalent* Hamiltonian families in the following sense. Let $\chi[H]$ be the characteristic polynomial of some Hamiltonian H; then we call two families $H_{\mathbf{a}}^{(1,2)}(\mathbf{k})$ equivalent if

$$\chi[H_{\tilde{\mathbf{a}}}^{(1)}(\tilde{\mathbf{k}})] = \chi[H_{\mathbf{a}}^{(2)}(\mathbf{k})] \tag{4.33}$$

for $\tilde{\mathbf{k}}$ and $\tilde{\mathbf{a}}$ related to $\mathbf{k}$ and $\mathbf{a}$ by linear transformations. In particular, this implies that the Hamiltonian spectra are also equal up to the same linear transformations of $\mathbf{k}$ and $\mathbf{a}$. Defining equivalence according to Eq. (4.33), we find [1, 225] that the $\mathbf{k}\cdot\mathbf{p}$ models for $6/m'$ and $6/m'mm$ fall into two equivalence classes, while all the other magnetic point groups only have a single equivalence class each (Table 4.4). Since nodal lines are properties of the spectrum alone, we restrict the analysis of the triple-point characteristics to one representative of each equivalence class.

Example: We illustrate this equivalence using the ICR combinations $(E_2; A_1)$ and $(E_2; A_2)$ of $6/m'mm$ as an example. We provide the $\mathbf{k}\cdot\mathbf{p}$ model for those in Ref. 225 and here directly start from the characteristic polynomials $\chi[H_{\mathbf{a}}^{(i)}(\mathbf{k})](E)$, where $i = 1, 2$ distinguishes the 1D ICRs A_i. In polar coordinates $(k_x, k_y) = k(\cos(\theta), \sin(\theta))$ and with energy E the polynomial variable, the characteristic polynomials read

$$\begin{aligned}\chi\left[H_{\mathbf{a}}^{(1)}(k,\theta,k_z)\right](E) = \frac{1}{8}\Big[&-8\left(a_3k^2+a_2k_z\right)^2\left(2a_3k^2+2a_2k_z-3E\right)\\ &-a_4^2k^4\left(a_1k^2\sin(6\theta)+2a_3k^2+2a_2k_z-2E\right)\\ &+2a_1^2k^4\left(2a_3k^2+2a_2k_z+E\right)-8E^3\Big],\end{aligned} \tag{4.34}$$

$$\begin{aligned}\chi\left[H_{\mathbf{a}}^{(2)}(k,\theta,k_z)\right](E) = \frac{1}{8}\Big[&-8\left(a_3k^2+a_2k_z\right)^2\left(2a_3k^2+2a_2k_z-3E\right)\\ &-4a_4^2k^4\left(-a_1k^2\sin(6\theta)+2a_3k^2+2a_2k_z-2E\right)\\ &+2a_1^2k^4\left(2a_3k^2+2a_2k_z+E\right)-8E^3\Big].\end{aligned} \tag{4.35}$$

We observe that

$$\chi\left[H^{(1)}_{\tilde{\mathbf{a}}}\left(k,\theta+\frac{\pi}{6},k_z\right)\right](E)=\chi\left[H^{(2)}_{\mathbf{a}}\left(k,\theta,k_z\right)\right](E) \tag{4.36}$$

with $\tilde{a}_4=2a_4$ and $\tilde{a}_i=a_i$ for $i\neq 4$.

The discriminant to leading order

Given a representative of an equivalence class, we determine the number of nodal-line arcs attached to the triple point by analyzing the discriminant $\Delta[H]$ of the characteristic polynomial $\chi[H]$, similar to the analysis in Section 4.3. However, while in the previous section the restriction to mirror planes led us to analyze the characteristic polynomial of a 2×2 Hamiltonian block depending on two variables k_x, k_z, for the presently studied magnetic point groups we are led to consider the characteristic polynomial of the full 3×3 $\mathbf{k}\cdot\mathbf{p}$ Hamiltonian depending on *three* variables k_x, k_y, k_z. Because zeroes of $\Delta[H]$ correspond to nodal lines, we need to solve the multivariate polynomial equation

$$\Delta[H_{\mathbf{a}}(\mathbf{k})]=0 \tag{4.37}$$

with parameters $\mathbf{a}$ over $\mathbf{k}\in\mathbb{R}^3$ to find the nodal lines. By construction, the line $k_x=k_y=0$ is always a solution with some multiplicity r. Determining the nodal-line arcs (if there are any) corresponds to finding additional real roots of Eq. (4.37). However, since the characteristic polynomial of the 3×3 $\mathbf{k}\cdot\mathbf{p}$ model is of high-order in the momentum components, this is a nontrivial task that requires methods beyond those described in Section 4.3.

Because we are primarily interested in nodal lines attached to the triple point at $\mathbf{k}=0$, we focus on the leading terms of $\Delta[H_{\mathbf{a}}(\mathbf{k})]$. In cylindrical coordinates (k,θ,k_z) we can consider $\theta\in[0,2\pi)$ as an additional parameter, such that the discriminant is a bivariate polynomial in k,k_z

$$\begin{aligned}\Delta_{\mathbf{a},\theta}(k,k_z)&=\Delta[H_{\mathbf{a}}(k\cos\theta,k\sin\theta,k_z)]\\&=k^r\sum_{\alpha,\beta}c_{\alpha\beta}(\theta,\mathbf{a})k^\alpha k_z^\beta\end{aligned} \tag{4.38}$$

with real coefficients $c_{\alpha\beta}(\theta,\mathbf{a})$. The particular exponents (α,β) of the bivariate monomials that appear in Eq. (4.38) depend on the choice of the magnetic point group and of its ICRs. To determine the leading-order monomials of $\Delta_{\mathbf{a},\theta}(k,k_z)$, note that nodal-line arcs attached to the triple point have an anticipated functional dependence

$$k_z^{\mathrm{arc}}(k)\propto k^\mu\quad\text{for some }\mu\in\mathbb{R}^+ \tag{4.39}$$

in the vicinity of the triple point. Such a root of $\Delta_{\mathbf{a},\theta}(k,k_z)$ is only attainable if the exponents (α',β') of the leading-order monomials $k^{\alpha'}k_z^{\beta'}$ obey $\alpha'+\mu\beta'=$ const. To determine *all* leading terms in Eq. (4.39), we need to account for arbitrary prospective scalings $0<\mu<\infty$, i.e., we need to keep all the bivariate monomials $k^\alpha k_z^\beta$ such that $k^{\alpha+\mu\beta}$ is of leading order for *at least one* value of μ.

We now describe a systematic procedure for identifying the leading terms. Let

$$M=\left\{(\alpha,\beta)\in\mathbb{R}^+\middle|\, c_{\alpha\beta}(\theta,\mathbf{a})\not\equiv 0\right\} \tag{4.40}$$

be the set of monomials that appear in $\Delta_{a,\theta}(k,k_z)$, where $f_1\not\equiv f_2$ indicates that functions f_1 and f_2 are not identical; then, for each fixed scaling $0<\mu<\infty$, the set of leading monomials is

$$L_\mu(M)=\operatorname*{argmin}_{(\alpha,\,\beta)\in M}(\alpha+\mu\beta). \tag{4.41}$$

Geometrically, $L_\mu(M)$ is the set of points in M that lie on a line of slope $-1/\mu$, such that the origin $(\alpha,\beta)=(0,0)$ is on one side and all the other points of M are on the other side of this line (cf. Fig. 4.8). Naturally, the union of such sets gives the set of all leading monomials:

$$L(M)=\bigcup_{0<\mu<\infty}L_\mu(M). \tag{4.42}$$

We note that this is equivalent to the part of the convex hull of M that faces the origin, which is useful for explicitly computing $L(M)$.

Example: We demonstrate the above method using the corepresentation $(E_1;A_1)$ of $6/m'mm$ (corresponding to equivalence class I), for which the $\mathbf{k}\cdot\mathbf{p}$ model is

$$\begin{aligned}
H_1(\mathbf{k})&=\begin{pmatrix} k_xk_y & \frac{1}{2}\left(k_y^2-k_x^2\right) & 0\\ \frac{1}{2}\left(k_y^2-k_x^2\right) & -k_xk_y & 0\\ 0 & 0 & 0\end{pmatrix},\\
H_2(\mathbf{k})&=\begin{pmatrix} k_z & 0 & 0\\ 0 & k_z & 0\\ 0 & 0 & -2k_z\end{pmatrix},\\
H_3(\mathbf{k})&=\begin{pmatrix} k_x^2+k_y^2 & 0 & 0\\ 0 & k_x^2+k_y^2 & 0\\ 0 & 0 & -2\left(k_x^2+k_y^2\right)\end{pmatrix},\\
H_4(\mathbf{k})&=\begin{pmatrix} 0 & 0 & -k_x+k_y\\ 0 & 0 & -k_x-k_y\\ -k_x+k_y & -k_x-k_y & 0\end{pmatrix}.
\end{aligned} \tag{4.43}$$

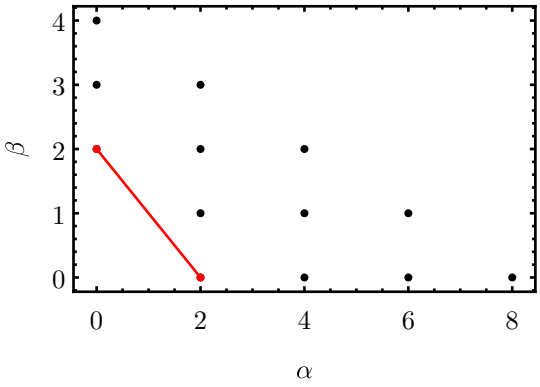

Figure 4.8.: Leading terms of the discriminant. Construction of the leading terms contributing to the discriminant of $6/m'mm$ class I given the Hamiltonian in Eq. (4.46) (red line). The black and red dots denote elements of the set M as defined in Eq. (4.40), and the red dots are elements of $L(M)$ as defined in Eq. (4.42).

The terms $H_{2,3}$ contribute directly to the three eigenenergies, while H_1 couples the two bands transforming in the same 2D ICR and H_4 couples the 2D ICR to the 1D ICR.

The corresponding characteristic polynomial in energy E is (in cylindrical coordinates; θ drops out)

$$\begin{aligned}\chi\left[H_{\mathbf{a}}(k,\theta,k_z)\right](E) = -\frac{1}{4}&\left[2\left(E-a_2k_z\right)-\left(a_1+2a_3\right)k^2\right]\\ &\times\left\{\left(2a_3k^2+2a_2k_z+E\right)\right.\\ &\times\left.\left[\left(a_1-2a_3\right)k^2+2\left(E-a_2k_z\right)\right]-4a_4^2k^2\right\}.\end{aligned} \tag{4.44}$$

Noting that the discriminant of a third-order polynomial is defined as

$$\Delta\left[\sum_{n=0}^{3}b_nx^n\right] = b_1^2b_2^2-4b_1^3b_3-4b_0b_2^3-27b_0^2b_3^2+18b_0b_1b_2b_3, \tag{4.45}$$

we find using MATHEMATICA the discriminant of the characteristic polynomial to be

$$\begin{aligned}\Delta_{\mathbf{a},\theta}(k,k_z) = \frac{1}{16}k^4&\left[a_1\left(a_1+6a_3\right)k^2+6a_1a_2k_z-4a_4^2\right]^2\\ &\times\left\{\left[\left(a_1-6a_3\right)k^2-6a_2k_z\right]^2+32a_4^2k^2\right\}.\end{aligned} \tag{4.46}$$

We next determine the leading-order terms in the discriminant following the method outlined in Eqs. (4.38) and (4.42) above. The set M (black dots) of all monomials appearing in $\Delta_{\mathbf{a},\theta}$ with nonvanishing coefficients together with the leading terms $L(M)$ (red dots) is shown in Fig. 4.8. There are only two leading terms, such that we can approximate

$$\Delta_{\mathbf{a},\theta}(k,k_z) \approx 4a_4^4k^4\left(8a_4^2k^2+9a_2^2k_z^2\right) \tag{4.47}$$

near the triple point.

4.4.3. Triple-point characterization

Knowing the general principles that determine the leading-order terms of the discriminant in Eq. (4.38), we next discuss how to derive the studied characteristics of the triple points, which are summarized in Table 4.4. The discussion is divided into several parts, corresponding to distinct collections of $\mathcal{PT}$-symmetric magnetic point groups. First, we consider the magnetic point groups where the restriction to leading-order terms reveals the absence of nontrivial roots of the discriminant, resulting in type-A triple points. In the remaining cases with and without mirror symmetry, the discriminant in Eq. (4.38) turns out to be *quasi-homogeneous*, i.e., there is a scaling factor μ for which all the monomials are of the same order. This implies that *all* the terms in the discriminant that are obtained from the leading-order $\mathbf{k}\cdot\mathbf{p}$ Hamiltonian are themselves leading. Here, we are led to develop additional arguments, which unambiguously reveal that the triple points in these magnetic point groups are always of type B. Due to the extensiveness of the underlying algebraic manipulations and the fact that they were performed using MATHEMATICA, we only present a few representative calculations and relegate the full classification to a MATHEMATICA notebook in Ref. 225 accompanying the original publication [2].

Type-A triple points

We begin with the magnetic point groups $4/m'$, $4/m'mm$, and with class-I Hamiltonians of the magnetic point groups $6/m'$ and $6/m'mm$, when the restriction to leading terms results in a significant simplification. Namely, $\Delta_{\mathbf{a},\theta}(k,k_z)/k^r$ is a quadratic polynomial in k and k_z with non-negative coefficients. We are then able to prove that for generic $\mathbf{a}$ and all θ there are no real roots other than the one at $k=0$, i.e., the central nodal line. This is exemplified by Eq. (4.47) for class I of $6/m'mm$, where it is apparent that there are no real roots apart from $k=0$. This implies that there are no nodal-line arcs attached to the triple point, such that the triple point is classified as type

Table 4.4.: Classification of triple points in the presence of $\mathcal{PT}$ symmetry. The triple point is characterized by whether nodal-line arcs attach to it (type A) or not (type B) [180]. We further distinguish type-B triple points according to the scaling of the attached nodal-line arcs $k_z \propto (k_x^2 + k_y^2)^{\mu/2}$: type-B$_q$ triple points have $\mu = 2$ and type-B$_l$ triple points have $\mu = 1$. Futhermore, we define n_a^{nexus} as the number of nodal-line arcs attached to a generic *nexus* point and the codimensions (CD) as the number of parameters that need to be tuned to collapse a nexus point to the triple point. These properties depend on $\overline{\mathcal{G}}^{\mathbf{k}}$ and, in general, on the irreducible corepresentations (ICRs) of the bands involved in the triple point formation. We use the notation by Mulliken [81] for the ICRs with $i = 1, 2$. For most little co-groups, all possible pairs of ICRs are equivalent (cf. text); only for the C_6-symmetric groups do the pairs fall into *two* equivalence classes (denoted by I and II in the second column).

$\overline{\mathcal{G}}^{\mathbf{k}}$	Class	ICRs	Type	n_a^{nexus}	μ	CD
$\bar{3}'$	–	$({}^2E^1E; A_1)$	B$_l$	6	1	0
$\bar{3}'m$	–	$(E; A_i)$	B$_l$	6	1	0
$4/m'$	–	$({}^2E^1E; A), ({}^2E^1E; B)$	A	4	2	1
$4/m'mm$	–	$(E; A_i), (E; B_i)$	A	4	2	1
$6/m'$	I	$({}^2E_2{}^1E_2; A), ({}^2E_1{}^1E_1; B)$	A	12	2	1
	II	$({}^2E_1{}^1E_1; A), ({}^2E_2{}^1E_2; B)$	B$_q$	12	2	0
$6/m'mm$	I	$(E_1; A_i), (E_2; B_i)$	A	12	2	1
	II	$(E_1; B_i), (E_2; A_i)$	B$_q$	12	2	0

A (Fig. 4.3a). The relevant point groups and corepresentations for which this situation arises are indicated in Table 4.4.

Note that while there are no nodal-line arcs *attached* to the triple point, there is a possibility (analogous to the corresponding cases without $\mathcal{PT}$ symmetry) of nexus points occurring *near* the triple point, i.e., additional nodal-line arcs coalescing at the central nodal line away from the triple point as illustrated in Fig. 4.3b. To obtain those nodal-line arcs, we depart from the same leading-order $\mathbf{k} \cdot \mathbf{p}$ Hamiltonian, but keep all terms in Eq. (4.38), i.e., M and not only $L(M)$. We find [225] that in the four-fold symmetric case there are two nexus points with four nodal-line arcs each, $n_a^{\text{nexus}} = 4$, and in the six-fold symmetric case, there is one nexus point with 12 nodal-line arcs, $n_a^{\text{nexus}} = 12$. Below we illustrate this with one example each. It is further manifest from the analytic solutions [225] that a single real-valued parameter needs to be tuned to collide the nexus point with the triple point, leading to codimension 1 (in contrast to codimension 2 in the analogous magnetic point groups without $\mathcal{PT}$ symmetry). In analogy with the magnetic point group $4mm$ (discussed in Section 4.3.2),

such fine-tuning collides the triple point simultaneously with *two* nexus points (cf. Fig. 4.6); these two nexus points could be either of the same or of opposite color. In this respect, we illustrate in Section 4.7 with Fig. 4.14 a particular example of a material (ZrO [218], the relevant HSL is $\Delta = \Gamma X$ with little co-group $4/m'mm$) for which the nexus point appears to closely coincide with a type-A triple point due to such an accidental fine-tuning of the relevant model parameter, see Section 4.7.

Example 1 ($4/m'mm$): We first consider the corepresentation $(E; A_1)$ of $4/m'mm$, which leads to the $\mathbf{k}\cdot\mathbf{p}$ model

$$
\begin{aligned}
H_1(\mathbf{k}) &= \begin{pmatrix} k_z & 0 & 0 \\ 0 & k_z & 0 \\ 0 & 0 & -2k_z \end{pmatrix}, \\
H_2(\mathbf{k}) &= \begin{pmatrix} k_x^2+k_y^2 & 0 & 0 \\ 0 & k_x^2+k_y^2 & 0 \\ 0 & 0 & -2\left(k_x^2+k_y^2\right) \end{pmatrix}, \\
H_3(\mathbf{k}) &= \begin{pmatrix} k_xk_y & 0 & 0 \\ 0 & -k_xk_y & 0 \\ 0 & 0 & 0 \end{pmatrix}, \\
H_4(\mathbf{k}) &= \begin{pmatrix} 0 & k_y^2-k_x^2 & 0 \\ k_y^2-k_x^2 & 0 & 0 \\ 0 & 0 & 0 \end{pmatrix}, \\
H_5(\mathbf{k}) &= \begin{pmatrix} 0 & 0 & k_y-k_x \\ 0 & 0 & -k_x-k_y \\ k_y-k_x & -k_x-k_y & 0 \end{pmatrix}.
\end{aligned}
\tag{4.48}
$$

We consider the discriminant of the characteristic polynomial of the corresponding Hamiltonian $H_{\mathbf{a},\theta}(k,k_z)$ *before* restricting to the leading terms, since then any additional nodal lines not attached to the triple point would be lost. Since one anticipates such nodal lines to appear in one of the mirror planes (we prove this in Ref. 225 using MATHEMATICA and discuss a similar proof below for type-B triple points), we restrict the subsequent analysis to $\theta \in \{0, \pi/4\} \bmod \pi/2$. Restricting to those values of θ, equation $\Delta_{\mathbf{a},\theta}(k,k_z) = 0$ has near the rotation axis analytic solutions

$$
\theta = \frac{\pi}{2}\mathbb{Z} \quad : \quad k_z^{\mathrm{arc}}(k) = \frac{a_5^2}{3a_1a_4} - \frac{3a_2+a_4}{3a_1}k^2, \tag{4.49a}
$$

$$
\theta = \frac{\pi}{4} + \frac{\pi}{2}\mathbb{Z} \; : \quad k_z^{\mathrm{arc}}(k) = \frac{2a_5^2}{3a_1a_3} - \frac{6a_2+a_3}{6a_1}k^2. \tag{4.49b}
$$

As long as $|a_5| \ll |a_{1,3,4}|$, i.e., as long as the coupling of the 1D to the 2D ICR is small, these nodal lines attach to the central nodal line close to the triple point, such that the $\mathbf{k}\cdot\mathbf{p}$ expansion is still reliable enough. In both sets of mirror planes ($\theta = 0$ and $\theta = \pi/4$), the position of the nexus is proportional to the same parameter $a_5 \in \mathbb{R}$, which implies codimension 1. The two sets of nodal-line arcs that lie within the two inequivalent sets of mirror planes generically lie at different distance from the triple point, implying $n_a^{\text{nexus}} = 4$. They are of the same (different) color if $\text{sign}(a_4 a_5) = +1$ (-1). Fine-tuning to $a_5 = 0$ collides both nexus points with the type-A *simultaneously* (cf. inset to Fig. 4.14c).

Example 2 ($6/m'mm$): An analogous analysis for class-I $6/m'mm$ reveals that

$$\theta = \frac{\pi}{12} + \frac{\pi}{3}\mathbb{Z} : \quad k_z^{\text{arc}}(k) = \frac{2a_4^2}{3a_1a_2} - \frac{a_1 + 6a_3}{6a_2}k^2, \tag{4.50a}$$

$$\theta = \frac{\pi}{4} + \frac{\pi}{3}\mathbb{Z} : \quad k_z^{\text{arc}}(k) = \frac{2a_4^2}{3a_1a_2} - \frac{a_1 + 6a_3}{6a_1}k^2. \tag{4.50b}$$

Note that the expressions for $k_z^{\text{arc}}(k)$ in the two sets of planes are identical, such that there is only a single nexus point with $n_a^{\text{nexus}} = 12$ nodal-line arcs in the same gap and with the same functional dependence on k for small k (including higher-order terms reveals that the nodal-line arcs generically do behave differently as a function of k in the two sets of planes). Fine-tuning to $a_4 = 0$ collides the nexus point with the type-A triple point, such that the codimension is 1.

Type-B triple points with mirror symmetries

For $\bar{3}'m$ and class-II $6/m'mm$, the discriminant $\Delta_{\mathbf{a},\theta}(k, k_z)/k^r$ of the leading-order Hamiltonian turns out to be quasi-homogeneous with $\mu = 1$ ($\mu = 2$). We find $\Delta_{a,\theta}(k, k_z)/k^r$ to be a fourth-order polynomial in k_z taking the form

$$\Delta_{\mathbf{a},\theta}(k, k_z) = \sum_{\beta=0}^{4} b_\beta(\mathbf{a}, k, \theta) k_z^\beta. \tag{4.51}$$

The nature of its real roots, i.e., the number of distinct real roots and their multiplicities, is determined [227] by the following five quantities (suppressing the dependence on $\mathbf{a}$, k and θ): the *discriminant* $\bar{\Delta}$ *of the discriminant*

$\Delta_{\mathbf{a},\theta}(k,k_z)$ *seen as a polynomial in* k_z,

$$P = 8b_2b_4 - 3b_3^2, \tag{4.52a}$$
$$R = b_3^3 - 4b_2b_4b_3 + 8b_1b_4^2, \tag{4.52b}$$
$$\bar{\Delta}_0 = b_2^2 - 3b_1b_3 + 12b_0b_4, \tag{4.52c}$$
$$D = -3b_3^4 + 16b_2b_4b_3^2 + 64b_0b_4^3 - 16\left(b_2^2 + b_1b_3\right)b_4^2. \tag{4.52d}$$

The following cases are possible:

(1) a single real root of multiplicity 2 if $\bar{\Delta} = 0 \wedge \{D > 0 \vee [P > 0 \wedge (D \neq 0 \vee R \neq 0)]\}$,

(2) a single real root of multiplicity 4 if $\bar{\Delta} = 0 \wedge D = 0 \wedge \bar{\Delta}_0 = 0$,

(3) one real root of multiplicity 3 and one of multiplicity 1 if $\bar{\Delta} = 0 \wedge \bar{\Delta}_0 = 0 \wedge D \neq 0$,

(4) two real roots of multiplicity 2 each if $\bar{\Delta} = 0 \wedge D = 0 \wedge P < 0$,

(5) two real roots of multiplicity 1 each if $\bar{\Delta} < 0$,

(6) one real root of multiplicity 2 and two of multiplicity 1 each if $\bar{\Delta} = 0 \wedge P < 0 \wedge D < 0 \wedge \bar{\Delta}_0 \neq 0$,

(7) four real roots of multiplicity 1 if $\bar{\Delta} > 0 \wedge P < 0 \wedge D < 0$, and

(8) no real roots if none of the above is satisfied.

Performing this analysis for all relevant cases [225] using MATHEMATICA, reveals that only cases (1) and (8) arise for valid choices of the parameters $\mathbf{a}$, k and θ. This implies that there is either a single real root (indicating a nodal line) or no real root (indicating the absence of nodal lines away from the rotation axis), depending on the values of the parameters $\mathbf{a}$ and θ. In particular, the requirement of a real root restricts θ to discrete values, $\frac{\pi}{4}, \frac{7\pi}{12} \pmod{\frac{2\pi}{3}}$ for $\bar{3}'m$ $[\frac{\pi}{12}, \frac{\pi}{4} \pmod{\frac{\pi}{3}}$ for class-II $6/m'mm]$, which correspond exactly to the mirror planes (cf. Figs. 4.4c and 4.4d, respectively), in which case generic values of $\mathbf{a}$ yield a root of the discriminant that continuously connects to $\mathbf{k} = \mathbf{0}$, meaning that the triple points are of type B. Additionally, the value of the scaling factor $\mu = 1$ ($\mu = 2$) fixes the attachment of the nodal-line arcs to be linear (quadratic). We therefore conclude that $\bar{3}'m$ gives type-B$_l$ triple points with $n_a^{\text{nexus}} = 6$ (Fig. 4.3c), while class-II $6/m'mm$ gives type-B$_q$ triple points with $n_a^{\text{nexus}} = 12$ (Fig. 4.3d). Although the presence, number and scaling μ of the nodal-line arcs do not depend on the parameters $\mathbf{a}$ (up to fine-tuning) of the model, the precise nodal line structure does. We illustrate three examples of the possible variations for the magnetic point group $\bar{3}'m$ in Fig. 4.9.

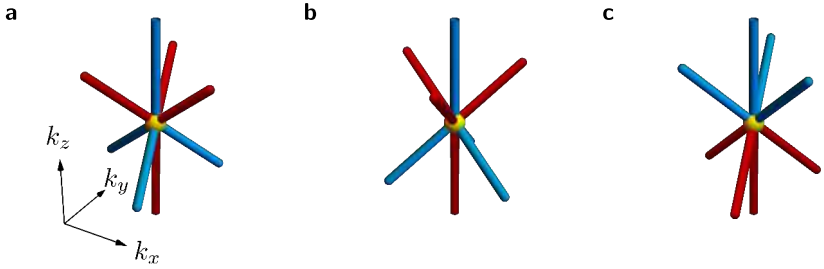

Figure 4.9.: Nodal-line structure near a type-B$_l$ triple point for little co-group $\bar{3}'m$ (or $3m$). At a type-B$_l$ triple point, the nodal-line arcs are linear in momentum space, which implies that they always changes gap (and therefore color) when passing through the triple point. Nevertheless, several different arrangements (**a–c**) are possible depending on the model parameters.

Example: Applying the above procedure to class-II $6/m'mm$, we find that for generic **a**, i.e., excluding fine-tuned models, case (1) is satisfied if

$$\theta = \frac{\pi}{12} + \frac{2\pi}{6}\mathbb{Z} \quad \vee \quad \theta = \frac{\pi}{4} + \frac{2\pi}{6}\mathbb{Z} \tag{4.53}$$

and case (8) for any other value of θ and for the fine-tuned models. Thus, we conclude that generically, there are nodal-line arcs in the two sets of six symmetry-related mirror planes and no other nodal lines near the triple point, resulting in $n_a^{\text{nexus}} = 12$. In the fine-tuned case some or all of those nodal-line arcs are not present.

Because for $6/m'mm$ the nodal-line arcs lie in the mirror planes, we can find explicit expressions $k_z^{\text{arc}}(k)$ for them by substituting the conditions on θ given in Eq. (4.53) into $\Delta_{\mathbf{a},\theta}(k, k_z) = 0$ and solving for k_z:

$$\theta = \frac{\pi}{12} + \frac{\pi}{3}\mathbb{Z} : \quad k_z^{\text{arc}}(k) = -\frac{2a_1(a_1 + 6a_3) - a_4^2}{12a_1a_2}k^2, \tag{4.54a}$$

$$\theta = \frac{\pi}{4} + \frac{\pi}{3}\mathbb{Z} : \quad k_z^{\text{arc}}(k) = \frac{2a_1(a_1 - 6a_3) - a_4^2}{12a_1a_2}k^2. \tag{4.54b}$$

We observe that $\lim_{k\to 0} k_z^{\text{arc}}(k) = 0$, such that the nodal-line arcs attach to the triple point and from Eq. (4.54) we can read off that $\mu = 2$, since $k_z(k) \propto k^2$; thus, the triple point is type B$_q$.

Type-B triple points without mirror symmetries

We finally discuss the magnetic point group $\bar{3}'$ and class-II Hamiltonians of the magnetic point group $6/m'$. In these cases, $\Delta_{\mathbf{a},\theta}(k,k_z)/k^r$ is again quasi-homogeneous with $\mu = 1$ ($\mu = 2$ for $6/m'$), and the discriminant is a fourth-order polynomial in k_z; however, in contrast to the discussion above, the presently considered magnetic point groups have no mirror symmetries, leading to an increased number of terms in the leading-order $\mathbf{k}\cdot\mathbf{p}$ Hamiltonian. While the procedure described above is in principle still applicable, we find that the conditions for real roots of $\Delta_{\mathbf{a},\theta}(k,k_z)/k^r$ become too complicated for MATHEMATICA to handle and simplify. However, we argue below that the (qualitative) nodal-line structure near the triple point is the same as in the corresponding cases with mirror symmetry, up to a rotation of the coordinates that is determined by the model parameters.

More specifically, we find that the leading-order $\mathbf{k}\cdot\mathbf{p}$ model for the magnetic point groups without mirror symmetry has two additional terms compared to the corresponding $\mathbf{k}\cdot\mathbf{p}$ models with mirror symmetry. The particular structure of these additional terms is rather fortunate: they can both be generated from terms already present in the mirror-symmetric $\mathbf{k}\cdot\mathbf{p}$ expansion via an $\mathsf{SO}(2)$ rotation of (k_x,k_y)-coordinates. In particular, one can always find a suitable rotation of the coordinates that removes one of these additional terms (the rotations needed to remove either of the two additional terms are generically *different*, making it impossible to rotate away both of these new terms simultaneously). Therefore, a suitable rotation of the momentum coordinates leaves us with only one extra term compared to the $\mathbf{k}\cdot\mathbf{p}$ models with mirror symmetry. Additionally, while the one remaining new term cannot be removed on the level of the leading-order $\mathbf{k}\cdot\mathbf{p}$ Hamiltonian, it can be removed on the level of the characteristic polynomial by another momentum-space rotation and reparametrization.

After performing both of these coordinate transformations and the reparametrization, we reduce the characteristic polynomials of $\bar{3}'$ and for class-II $6/m'$ to those of $\bar{3}'m$ and of class-II $6/m'mm$, respectively. Therefore, the triple point characterization derived above for magnetic point group with mirror symmetry translates directly to those without. Obviously, the nodal-line arcs predicted for the magnetic points groups with mirror symmetry cannot lie in (the now absent) mirror planes. In fact, they do not generally lie in planes at all. However, close to the triple point, one can always define a plane containing them, see, e.g., Fig. C.18; this is exactly the plane defined by the above described momentum-space rotations. The results are summarized in Table 4.4.

Example: We discuss the reduction of the characteristic polynomial of the $\mathbf{k}\cdot\mathbf{p}$ Hamiltonian for the magnetic point group $\bar{3}'$ to the one resulting from $\bar{3}'m$. After a reparametrization of the $\mathbf{k}\cdot\mathbf{p}$ model for the ICR combination $(E;A_1)$ of $\bar{3}'$, the Hamiltonian takes the form

$$
\begin{aligned}
H_1(\mathbf{k}) &= \begin{pmatrix} k_x+k_y & k_x-k_y & 0 \\ k_x-k_y & -k_x-k_y & 0 \\ 0 & 0 & 0 \end{pmatrix}, \\
H_2(\mathbf{k}) &= \begin{pmatrix} k_z & 0 & 0 \\ 0 & k_z & 0 \\ 0 & 0 & -2k_z \end{pmatrix}, \\
H_3(\mathbf{k}) &= \begin{pmatrix} 0 & 0 & k_x+k_y \\ 0 & 0 & -k_x+k_y \\ k_x+k_y & -k_x+k_y & 0 \end{pmatrix}, \\
H_4(\mathbf{k}) &= \begin{pmatrix} k_y-k_x & k_x+k_y & 0 \\ k_x+k_y & k_x-k_y & 0 \\ 0 & 0 & 0 \end{pmatrix}, \\
H_5(\mathbf{k}) &= \begin{pmatrix} 0 & 0 & k_y-k_x \\ 0 & 0 & -k_x-k_y \\ k_y-k_x & -k_x-k_y & 0 \end{pmatrix},
\end{aligned}
\tag{4.55}
$$

while the $\mathbf{k}\cdot\mathbf{p}$ model for the same ICR combination $(E;A_1)$ of the magnetic point group $\bar{3}'m$ is formed only by the first three terms in Eq. (4.55). In the following, we show that by appropriate rotations of $\mathbf{k}$ and reparametrizations, i.e., transformations of $\mathbf{a}$, the characteristic polynomial $\chi[H_{\mathbf{a}}^{\bar{3}'}(\mathbf{k})](E)$ can be reduced to $\chi[H_{\mathbf{a}}^{\bar{3}'m}(\mathbf{k})](E)$, implying that the nodal structures close to the respective triple points are qualitatively the same.

We first observe that the momentum-space coordinate transformation $\mathbf{k}' = R_z(-\theta_1)\mathbf{k}$, where $R_z(\theta)$ denotes a rotation around the k_z-axis about the angle θ, with

$$
\theta_1 = \arctan\left(\frac{a_5}{a_3}\right), \tag{4.56}
$$

(i) maps $a_3H_3(\mathbf{k}) + a_5H_5(\mathbf{k})$, to

$$
a_3H_3(R_z(\theta_1)\mathbf{k}') + a_5H_5(R_z(\theta_1)\mathbf{k}') = a_3'H_3(\mathbf{k}') \tag{4.57}
$$

with $a_3' = \sqrt{a_3^2+a_5^2}$, (ii) leaves $H_2(\mathbf{k})$ invariant, and (iii) transforms the linear combination $a_1H_1(\mathbf{k}) + a_4H_4(\mathbf{k})$ to

$$
a_1'H_1(\mathbf{k}') + a_4'H_4(\mathbf{k}') \tag{4.58}
$$

with $(a_1', a_4') = R(-\theta_1)(a_1, a_4)$, where $R(\theta) \in \mathsf{SO}(2)$ is the 2×2 rotation matrix about the angle θ. Therefore, we find that

$$H_{\mathbf{a}}^{\bar{3}'}(R_z(\theta_1)\mathbf{k}') = H_{\mathbf{a}'}^{\bar{3}'}(\mathbf{k}') \tag{4.59}$$

with $\mathbf{a}' = (a_1', a_2, a_3', a_4', 0)$.

Next, we compute the characteristic polynomial of $H_{\mathbf{a}'}^{\bar{3}'}(\mathbf{k}')$:

$$\begin{aligned}\chi\left[H_{\mathbf{a}'}^{\bar{3}'}(\mathbf{k}')\right](E) = {} & 2(a_3')^2(k')^3\left[(a_1'-a_4')\sin(3\theta') - (a_1'+a_4')\cos(3\theta')\right] \\ & + 2E\left[(a_1')^2 + (a_3')^2 + (a_4')^2\right](k')^2 \\ & + 2a_2'\left[2(a_1')^2 - (a_3')^2 + 2(a_4')^2\right](k')^2 k_z' \\ & + 3E(a_2')^2(k_z')^2 - 2(a_2')^3(k_z')^3 - E^3.\end{aligned} \tag{4.60}$$

Another coordinate transformation $\mathbf{k}'' = R_z(-\theta_2)\mathbf{k}'$ with

$$\theta_2 = \frac{1}{3}\arctan\left(\frac{a_1'}{a_4'}\right) \tag{4.61}$$

transforms the first term in Eq. (4.60) to

$$2(a_3')^2(k'')^3 a_1'\sqrt{1+\left(\frac{a_4'}{a_1'}\right)^2}\left[\sin(3\theta'') - \cos(3\theta'')\right], \tag{4.62}$$

while leaving all the other terms invariant. Setting $\mathbf{a}'' = (a_1'', a_2, a_3', 0, 0)$ with

$$a_1'' = \mathrm{sign}(a_1')\sqrt{(a_1')^2 + (a_4')^2} = \mathrm{sign}(a_1a_3 + a_4a_5)\sqrt{a_1^2 + a_4^2}, \tag{4.63}$$

we arrive at

$$\chi\left[H_{\mathbf{a}'}^{\bar{3}'}(R_z(\theta_2)\mathbf{k}'')\right](E) = \chi\left[H_{\mathbf{a}''}^{\bar{3}'}(\mathbf{k}'')\right](E), \tag{4.64}$$

which is the characteristic polynomial obtained from $H_{\mathbf{b}}^{\bar{3}'m}(\mathbf{k}'')$ with

$$\mathbf{b} = \left(\mathrm{sign}(a_1a_3 + a_4a_5)\sqrt{a_1^2 + a_4^2}, a_2, \sqrt{a_3^2 + a_5^2}\right). \tag{4.65}$$

We conclude that in the rotated coordinates $\mathbf{k}''$ the characteristic polynomial of the leading-order $\mathbf{k}\cdot\mathbf{p}$ model for $\bar{3}'$ is, up to reparametrization, identical to the characteristic polynomial obtained from the leading-order $\mathbf{k}\cdot\mathbf{p}$ model for $\bar{3}'m$. Any properties that only depend on the characteristic polynomial, which include nodal structures such as triple points and nodal-line arcs attached to triple points, are therefore the same. Therefore, we find that triple points on HSLs with little co-group $\bar{3}'$ are always type B_l with $n_a^{\mathrm{nexus}} = 6$ and $\mu = 1$.

4.5. Effect of nonsymmorphicity

In the previous two sections, the starting point for deriving the classification of triple points has always been the set of symmetry constraints on the Bloch Hamiltonian involving corepresentations of the little group. As discussed in Section 4.2.1, for symmorphic space groups this trivially reduces to a corresponding set of constraints involving corepresentations of the little *co-group*. On the other hand, for nonsymmorphic space groups, the set of constraints generally reduces to one involving *projective* corepresentations of the little co-group (see Section 2.4.2). Thus, we use Eq. (2.75).

By assumption, the little groups we study support stable triple points. Therefore, they must have at least one 1D ICR, such that, according to what we have shown in Section 4.2.1, the factor system of $\overline{\Delta}$ is in the trivial equivalence class. We therefore consider

$$\overline{\Delta}'(g) = \mathrm{e}^{\mathrm{i}\phi(g)}\overline{\Delta}(g), \tag{4.66}$$

where $\mathrm{e}^{\mathrm{i}\phi(g)} = \Delta_1^{-1}(g)$ plays the role of the equivalence transformation $C(g)$ by the 1D unitary projective ICR [cf. Eq. (4.1)], and $\overline{\Delta}'$ is an *ordinary* corepresentation of $\overline{\mathcal{G}}^{\mathbf{k}}$ (but not a corepresentation of $\mathcal{G}^{\mathbf{k}}$). Then,

$$\overline{\Delta}'(S_i)H(S_i^{-1}\mathbf{k})\overline{\Delta}'(S_i)^{-1} = H(\mathbf{k}), \tag{4.67a}$$

$$\overline{\Delta}'(S_{i'})H(S_{i'}^{-1}\mathbf{k})^*\overline{\Delta}'(S_{i'})^{-1} = H(\mathbf{k}), \tag{4.67b}$$

because the factors $\mathrm{e}^{\mathrm{i}\phi(S_\alpha)}$ and $\mathrm{e}^{-\mathrm{i}\phi(S_\alpha)}$ cancel. The key observation here is that the symmetry constraints on the $\mathbf{k}\cdot\mathbf{p}$ expansion are unaffected by the equivalence transformation in Eq. (4.66).

By matching the ICRs of $\mathcal{G}^{\mathbf{k}}$ to *ordinary* ICRs of $\overline{\mathcal{G}}^{\mathbf{k}}$ via Eq. (4.66), the set of constraints for any given corepresentation $\overline{\mathcal{D}}$ of $\mathcal{G}^{\mathbf{k}}$ is therefore reduced to a set of constraints for the corresponding ordinary corepresentations $\overline{\mathcal{D}}'$ of $\overline{\mathcal{G}}^{\mathbf{k}}$. The classification of triple points in nonsymmorphic space groups is therefore reduced to their classification in symmorphic space groups by properly identifying ICRs of the little group with ICRs of the little co-group. That identification of ICRs can be easily performed by looking up ICRs of both groups, matching generators of $\mathcal{G}^{\mathbf{k}}$ to those of $\overline{\mathcal{G}}^{\mathbf{k}} = \mathcal{G}^{\mathbf{k}}/\mathcal{T}$ and identifying the necessary phases $\phi(S_\alpha)$.

4.6. Summary of results

In this section, we summarize the classification of triple points according to the nodal-line structure in their vicinity, which we have developed in this chapter.

Table 4.5.: Classification of triple points in spinless systems. Triple points are classified as type A, B_q, and B_l based on the little co-group of the high-symmetry line. Additionally, we list the number n_a^{nexus} of nodal-line arcs attached to a nexus point occurring near or at the triple point (for $\bar{4}'$ and $\bar{6}'$ no nodal-line arcs are possible, which is denoted by the entry "–"), the scaling μ of those nodal-line arcs at the nexus point [$k_z \propto (k_x^2 + k_y^2)^{\mu/2}$], and the codimension for colliding at least one nexus point with the triple point (for type-B this is naturally 0 and if nexus points cannot be stabilized we denote it by ∞). For point groups with C_6 rotational symmetry, type and codimension of the triple point additionally depend on the irreducible corepresentations (ICRs) $D^{2\text{D}} \oplus D^{1\text{D}}$ of the bands involved in the formation of the triple point.

Little co-group	ICRs[a]	Type	n_a^{nexus}	μ	Codimension
$3m$, $\bar{3}'$, $\bar{3}'m$	any	B_l	6	1	0
$\bar{4}'$, $\bar{6}'$	any	A	–	–	∞
$\bar{4}'2'm$, $4mm$	any	A	4	2	2
$4/m'$, $4/m'mm$	any	A	4	2	1
$\bar{6}'m2'$	any	A	6	2	1
$6mm$	$(E_1;A)$, $(E_2;B)$	A	12	2	2
	$(E_1;B)$, $(E_2;A)$	B_q		2	0
$6/m'$, $6/m'mm$	$(E_1;A)$, $(E_2;B)$	A	12	2	1
	$(E_1;B)$, $(E_2;A)$	B_q		2	0

[a] We use the notation by Mulliken [81] for the ICRs, but drop the subscripts of the 1D ICRs if they do not affect the result. Note that for the 2D ICRs of $6/m'$ we define: ${}^2E_2\,{}^1E_2 \mapsto E_1$, and ${}^2E_1\,{}^1E_1 \mapsto E_2$ to get labels consistent with those of $6mm$ and $6/m'mm$.

We have found that the type (A or B) characterizing the absence or presence of nodal-line arcs at the triple point, the subtype (B_l or B_q) describing whether such nodal-line arcs connect linearly or quadratically, the potential presence of nexus points away from the triple points, the nexus points' codimension, as well as the number n_a^{nexus} of nodal-line arcs attached to the triple point or nexus point, depend only on the little co-group of the HSL on which the triple point occurs and the corepresentation involved. The full classification applicable to triple points appearing on HSLs in any non-magnetic or magnetic, symmorphic or nonsymmorphic space group of a spinless system is summarized in Table 4.5. The little co-groups classifying the triple points are exactly the 13 magnetic point groups given in Table 4.1.

We have found that for almost all magnetic point groups, the little co-group uniquely determines the characteristics of the triple point. The only

exception are the magnetic point groups that contain C_6 symmetry, where either type-A or type-B triple points can arise, depending on the ICRs of the bands forming the triple point. Further, the nodal-line arcs are protected either by vertical mirror symmetry m_v (in which case they are constrained to lie in the corresponding vertical mirror planes) or by $\mathcal{PT}$ symmetry (in which case they can curve arbitrarily inside momentum space) [162]. This also explains the observation that triple points in magnetic point groups $\bar{4}'$ and $\bar{6}'$ are *never* accompanied by nexus points, because the symmetry does not support nodal-line arcs away from the central line; this is denoted in Table 4.5 by a codimension of ∞.

Finally, we have observed that the subtype of type-B triple points is determined by the order of rotational symmetry. Writing $k^2 = k_x^2 + k_y^2$, we find that three-fold rotational symmetry results in three nodal-line arcs attaching linearly to the triple point $k_z \propto k$ (cf. Fig. 4.3c) in each (i.e., both red *and* blue) energy gap, while six-fold rotation gives six quadratically attaching nodal-line arcs $k_z \propto k^2$ (cf. Fig. 4.3d) in each gap. Analogously, we characterize how nodal-line arcs attach to nexus points in the vicinity of type-A triple points. We find that they always attach quadratically, $k_z \propto k^2$ (cf. Fig. 4.3b).

4.7. Material candidates

The classification of triple points derived in this chapter allows us to predict, based on symmetry properties, the possibility of stable triple points (including their type) in real materials. In Table 4.6 we list several compounds as representative triple-point materials with weak spin-orbit coupling, which are subject to our derived classification. Some of these compounds have been previously described [1, 190, 217, 218, 220, 221], while others have, to the best of our knowledge, not been reported as triple-point materials before.

For each listed material, we analyze selected triple points and verify their type against the predictions we made in the previous sections. We provide access to all the first-principles data in the supplementary data and code [225] and present relevant figures for all compounds in Appendix C.1. In Section 4.7.2, we discuss a few selected examples to illustrate our procedure and highlight some interesting aspects. The results on the triple-point types are summarized in the last three columns of Table 4.6 and agree with the classification in Table 4.5.

4.7.1. Methods

Based on the little groups that can stabilize triple points (listed in Table 4.1) and the program MKVEC on the Bilbao crystallographic server (BCS) [80, 83–85, 223, 224], one can easily scan all magnetic space groups to identify those that support triple points (i.e., both 1D and 2D ICRs) on HSLs. This search (for type-II magnetic space groups, i.e., those that exhibit no magnetic order) has been recently performed independently by Feng et al. [209] and their list of admissible little co-groups matches ours. The relevant space groups and HSLs are listed in Table II in Ref. 209. Here, we also restrict to finding representative materials in type-II magnetic space groups. Exhaustive lists of (magnetic) space groups of any type and HSLs supporting various quasiparticles, including triple points, have been published in Refs. 33–35.

For each of the type-II magnetic space groups listed in Table II in Ref. 209, we performed a search of compounds with light elements (from the first three rows of the periodic system) on the Topological Materials Database [137, 228, 229]. By looking at the irreducible representation on high-symmetry points (for the case without spin-orbit coupling) and using the program MCOMPREL [80, 84, 85] on the BCS, we inferred the ICRs and their dimension along the relevant HSL and identified crossings of 2D with 1D ICRs, i.e., triple points. This resulted in a list of several hundred candidate materials from which we selected the most promising ones [our arbitrary criteria adopted a tradeoff between triple points being close to the Fermi level (with the distance counted in number of bands rather than in energy), a small number of additional degeneracies, and well separated nodal lines] to illustrate and verify our classification.

We analyzed the selected materials as well as the materials from Refs. 1, 190, 217, 218, 220, 221 in detail by performing first-principle calculations ourselves as detailed below. For that, DFT calculations with the projected augmented wave (PAW) method are implemented in the Vienna ab initio simulation package (VASP) [230, 231] with generalized gradient approximation (GGA) using Perdew-Burke-Ernzerhof (PBE) functional pseudopotentials [232]. A $6 \times 6 \times 6$ uniform mesh for bulk k-space provided converged total energies. For the 2D planes, a 140×140 (100×100 for Si_2O and $Li_2Co_{12}P_7$) mesh is used to calculate the band gap. Using plane-wave-based wave functions and space group operators generated by VASP, we calculate the traces of matrix representations to get the irreducible representations of the energy bands at high-symmetry points in the first Brillouin zone with the help of IREP [233]. Using compatibility relations [83] we then deduce the irreducible (co-)representations of the lines of symmetry shown in the sixth row of Table 4.6.

4.7.2. Examples

Here we discuss some examples of triple point materials in order to illustrate how we used first-principle calculations to verify the predictions of our classification for the nodal-line structure near the triple points. We start with the following four materials: Na_3N hosting a type-A triple point without nexus points, CaNaP hosting a type-A triple point *with* nexus points, TiB_2 hosting a type-B_q triple point and B_2CN hosting a type-B_l triple point. The first-principles data for these four compounds are shown in Figs. 4.10 to 4.13, in the given order. In each figure, the band structure on HSLs is shown in panel (a); therein, the triple point is indicated by a yellow dot and arrow, and the bands involved in the triple point formation are labelled by their ICRs. The corresponding Brillouin zone is illustrated in panel (b).

To detect nodal lines, we perform additional DFT calculations in the appropriate planes containing the nodal lines close to the triple point. For compounds with mirror symmetries, these are the mirror planes; for the other compounds we first study slices of fixed k_z to detect any nodal lines close to the central nodal line, and if there are any, we determine the plane in which they lie in the vicinity of the central nodal line. In panel (c) we then plot the magnitude of the two gaps between the three bands involved in the triple point formation (larger color saturation implies smaller energy gap), with the lower (upper) gap data shown in red (blue) color, as usual. The triple point is located where the central nodal line changes color (and sum of the two gaps is minimal). Choosing a suitable cutoff for the gap size, we can also easily recognize the additional nodal lines and infer the number of nodal lines attached to the triple point as well as their momentum space behavior μ, which directly determines the type of the triple point.

We briefly discuss one peculiar triple point found in ZrO. According to Tables 4.5 and 4.6, ZrO supports type-A triple points on the HSL Δ (little co-group $4/m'mm$). However, in Fig. 4.14, we identify eight additional nodal lines attached to the triple point: for each of the two inequivalent mirror planes shown in Fig. 4.14c there are two nodal-line arcs and another two in the symmetry related mirror plane. Note, however, that all those nodal-line arcs are red (located in the lower gap) meaning that there are two red nexus points at the triple point. This is incompatible with type-B triple points where the triple point coincides with both a red and a blue nexus. We therefore conclude that the triple point in ZrO is type A but fine-tuned such that the two red nexus points coincide with it. Interestingly, such a configuration arises by fine-tuning a single parameter, as we discussed in Section 4.4.3 above and illustrated using the example of a triple point on a HSL with little group $4/m'mm$. The fine-tuned nodal-line structure of the minimal $\mathbf{k} \cdot \mathbf{p}$ model for a

type-A triple point on a HSL with little group $4/m'mm$ is shown in the inset in Fig. 4.14c. This supports the conclusion that there are two fine-tuned red nexus points, each with four nodal-line arcs, coinciding with the triple point, i.e., $\mathrm{sign}(a_3 a_4) = +1$ in the $\mathbf{k} \cdot \mathbf{p}$ model in Eq. (4.49) and explains the total of eight red nodal lines attached to the triple point. To verify that the nodal-line structure is indeed a consequence of fine-tuning, we include a perturbation in the form of 5% uniaxial tensile strain, which preserves the little co-group of the Δ line. This splits the two nexus points and the triple point demonstrating that the *stable* triple point is type A and that we indeed have two separate nexus points with $n_a^{\mathrm{nexus}} = 4$, cf. Fig. C.12 in the Appendix. Note that there is another triple point in this compound, illustrated in Fig. C.11, which further confirms that the attached nodal-line arcs are due to fine-tuning.

Table 4.6.: Examples of triple-point materials. For each material, the following is listed: the space group (SG), the number of its entry in the Inorganic Crystal Structure Database (ICSD), the high-symmetry line (HSL) containing the triple point, the little co-group $\overline{\mathcal{G}}^{\mathbf{k}}$ of that HSL in Hermann-Mauguin notation [77], the irreducible corepresentations (ICRs) of the bands involved, the energy of the triple point E_{TP} relative to the Fermi energy, the type, the number n_a^{nexus} of nodal-line arcs attached to a *nexus point* if there is one, the scaling of those nodal-line arcs μ ($k_z \propto (k_x^2 + k_y^2)^{\mu/2}$), and a reference to the corresponding figure.

Material	SG	ICSD no.	HSL	$\overline{\mathcal{G}}^{\mathbf{k}}$	ICRs	E_{TP}	Type	n_a^{nexus}	μ	Figure
SiO_2	82	75647	$\Lambda\,(\Gamma Z)$	$\bar{4}'$	$(BB;A)$	$-0.62\,\mathrm{eV}$	A	–	–	C.13
Li_4HN	88	409633	$\Lambda\,(\Gamma M)$	$4/m'$	$({}^2E\,{}^1E;B)$	$-0.92\,\mathrm{eV}$	A	4	2	C.14
CaNaP	107	–	$\Lambda\,(\Gamma M)$	$4mm$	$(E;A_1)$	$4.1\,\mathrm{eV}$	A	4	2	4.11
Na_2LiN	129	92309	$\Lambda\,(\Gamma Z)$	$4/m'mm$	$(E;A_1)$	$-1.0\,\mathrm{eV}$	A	–	–	C.1
B_2CN	156	183791	$\Delta\,(\Gamma A)$	$3m$	$(E;A_1)$	$9.3\,\mathrm{eV}$	B_l	6	1	4.13
MgH_2O_2	164	34401	$P\,(KH)$	$\bar{3}'$	$({}^2E\,{}^1E;A_1)$	$-1.4\,\mathrm{eV}$	B_l	6	1	C.16
P	166	53301	$\Lambda\,(\Gamma Z)$	$\bar{3}'m$	$(E;A_1)$	$1.5\,\mathrm{eV}$	B_l	6	1	C.2
$Li_2Co_{12}P_7$	174	656419	$\Delta\,(\Gamma A)$	$\bar{6}'$	$({}^2E\,{}^1E;A_1)$	$-0.17\,\mathrm{eV}$	A	–	–	C.17
C_3N_4	176	246661	$\Delta\,(\Gamma A)$	$6/m'$	$({}^2E_1\,{}^1E_1;A)$	$-9.3\,\mathrm{eV}$	B_q	12	2	C.18
					$({}^2E_2\,{}^1E_2;A)$	$-2.6\,\mathrm{eV}$	A	–	–	C.19
AlN	186	31169	$\Delta\,(\Gamma A)$	$6mm$	$(E_1;A_1)$	$-0.28\,\mathrm{eV}$	A	12	2	C.3
					$(E_2;A_1)$	$-0.85\,\mathrm{eV}$	B_q	12	2	C.4
Li_4N	187	675123	$\Delta\,(\Gamma A)$	$\bar{6}'m2'$	$(E;A_1)$	$-0.68\,\mathrm{eV}$	A	6	2	C.5
Na_2O	189	–	$\Delta\,(\Gamma A)$	$\bar{6}'m2'$	$(E;A_1)$	$-0.26\,\mathrm{eV}$	A	6	2	C.6
Li_2NaN [220]	191	92308	$\Delta\,(\Gamma A)$	$6/m'mm$	$(E_1;A_1)$	$-48\,\mathrm{meV}$	A	–	–	C.7
TiB_2 [190]	191	30330	$\Delta\,(\Gamma A)$	$6/m'mm$	$(E_1;A_1)$	$0.57\,\mathrm{eV}$	A	–	–	C.8
					$(E_2;A_1)$	$1.3\,\mathrm{eV}$	B_q	12	2	4.12
Na_3N [221]	194	–	$\Delta\,(\Gamma A)$	$6/m'mm$	$(E_2;A_1)$	$-93\,\mathrm{meV}$	B_q	12	2	C.9
					$(E_1;A_1)$	$-38\,\mathrm{meV}$	A	–	–	4.10
C_3N_4	215	83264	$\Delta\,(\Gamma X)$	$\bar{4}'2'm$	$(B_2B_1;A_1)$	$-6.5\,\mathrm{eV}$	A	–	–	C.10
ZrO [218]	225	76019	$\Delta\,(\Gamma X)$	$4/m'mm$	$(E;A_1)$	$0.12\,\mathrm{eV}$	A	4	2	C.11
					$(E;B_1)$	$2.0\,\mathrm{eV}$	A	4	2	4.14

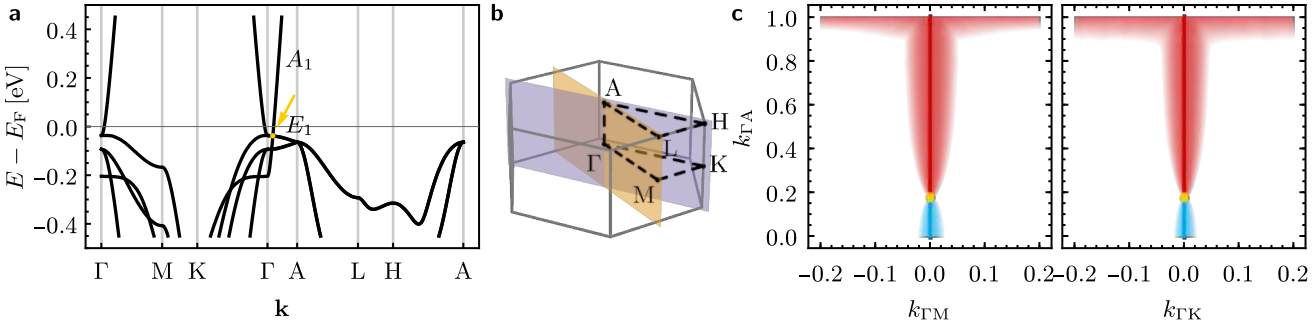

Figure 4.10.: Type-A triple point and nodal line structure of Na_3N. (**a**) Band structure along lines of symmetry with the triple point on the Δ line at $E_{TP} = -38\,\mathrm{meV}$ indicated by a yellow dot and arrow. The bands forming the triple point are labelled by irreducible corepresentations of the little co-group $6/m'mm$. (**b**) Brillouin zone (boundary in gray) with points and lines of symmetry (black dashed lines) and representatives of the two inequivalent sets of mirror planes (orange and purple planes). (**c**) Size of the lower (red) and upper (blue) gap in the two mirror planes shown in (b) encoded by the intensity of the color: higher color saturation implies smaller energy gap between the corresponding pair of bands and gaps larger than $0.01\,\mathrm{eV}$ are shown in white (gap cutoff). The triple point (yellow) and the central nodal line are emphasized by appropriately colored overlays and the data shows that the triple point is type A without any nexus points, which could in principle be stabilized.

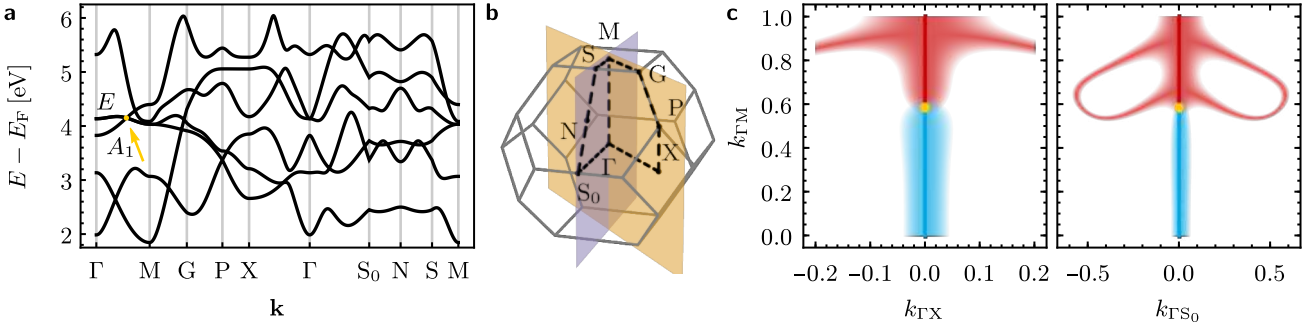

Figure 4.11.: Triple point and nodal line structure of CaNaP. Data for the triple point on the Λ line with little co-group $4mm$. The organization of the panels is in one-to-one correspondence with Fig. 4.10 with a gap cutoff $0.05\,\mathrm{eV}$. No nodal lines are attached to the triple point, such that we conclude it to be type A. Note the occurrence of a nexus of four (due to the four-fold rotational symmetry) red nodal lines near the triple point, from which we can deduce that $n_a^{\mathrm{nexus}} = 4$ and $\mu = 2$. Our theoretical analysis predicts that two parameters need to be tuned to collide the nexus point with the triple point.

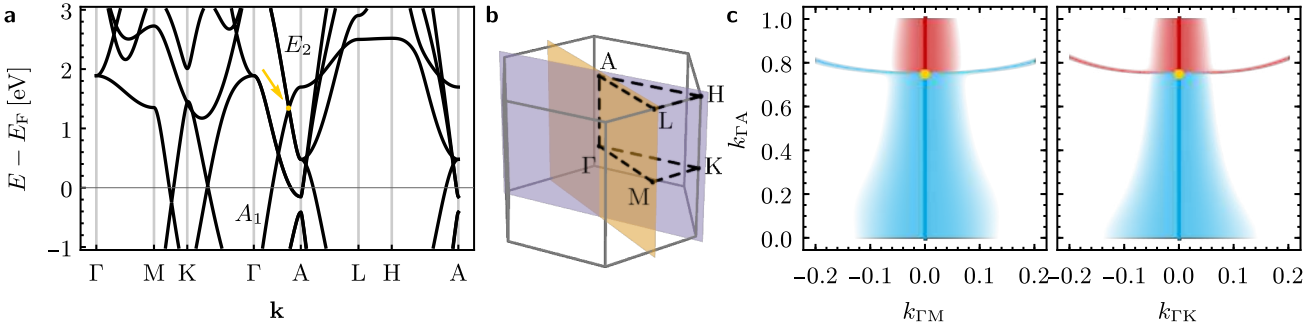

Figure 4.12.: Type-B$_q$ triple point and nodal line structure of TiB$_2$. Data for the triple point at $E_{\mathrm{TP}} = 1.3\,\mathrm{eV}$ lying on the Δ line with little co-group $6/m'mm$. The organization of the panels is in one-to-one correspondence with Fig. 4.10 with a gap cutoff $0.05\,\mathrm{eV}$. Note the nodal-line arcs attaching quadratically ($k_z \propto k_x^2 + k_y^2$) to the triple point, i.e., the two nexus points coincide with the triple point, implying that the triple point is type B$_q$. Due to the rotational symmetry, there are six nodal-line arcs in each of the two gaps (shown in red and blue, respectively), implying $n_a^{\mathrm{nexus}} = 12$.

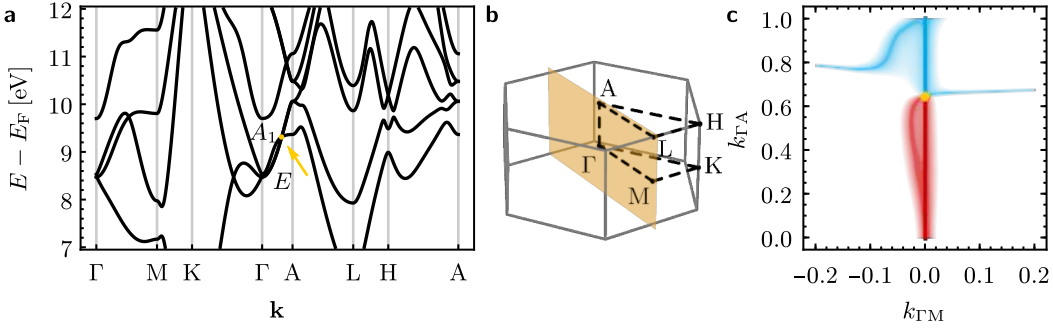

Figure 4.13.: Triple point and nodal line structure of B_2CN. Data for the triple point on the Δ line with little co-group $3m$. The organization of the panels is in one-to-one correspondence with Fig. 4.10 (except for the fact that only one inequivalent high-symmetry plane is present) and gap cutoff $0.02\,\mathrm{eV}$. Note the nodal-line arcs attaching to the triple point, i.e., the two nexus points coincide with the triple point and that the nodal lines scale linearly, $k_z \propto \sqrt{k_x^2 + k_y^2}$, implying a type-$B_l$ triple point. Due to the three-fold rotational symmetry, there are $n_a^{\mathrm{nexus}} = 6$ nodal-line arcs in total.

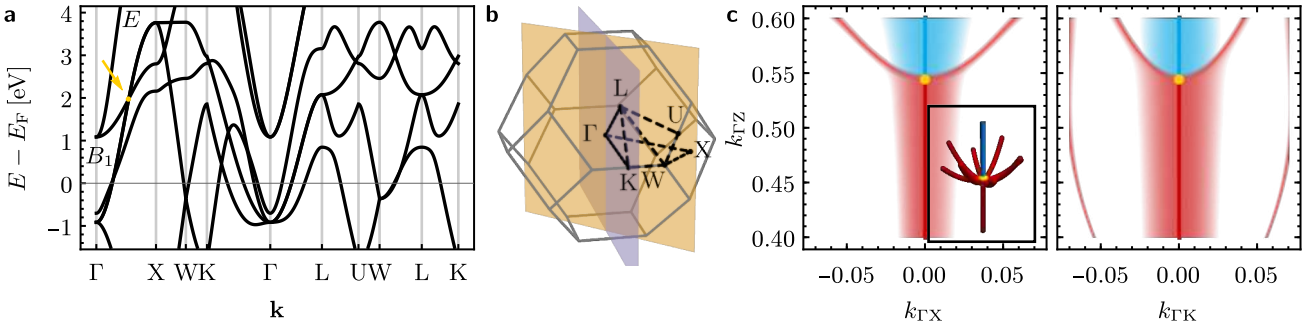

Figure 4.14.: Triple point and nodal line structure of ZrO. Data for the triple point at $E_{\mathrm{TP}} = 2.0\,\mathrm{eV}$ lying on the Δ line with little co-group $4/m'mm$. The organization of the panels is in one-to-one correspondence with Fig. 4.10 with gap cutoff $0.02\,\mathrm{eV}$. The inset of panel (c) shows the nodal-line structure of the corresponding minimal $\mathbf{k}\cdot\mathbf{p}$ model, Eq. (4.49), with parameters tuned to qualitatively reproduce the situation in ZrO. Two red nexus points coincide with the triple point, which is accidental, such that we classify the triple point despite the nodal-line arcs as type A and consider the two nexus points (separately) with $n_a^{\mathrm{nexus}} = 4$ and $\mu = 2$.

5. Multigap topology of triple points

This chapter is largely based on the publications "From triple-point materials to multiband nodal links" [1], "Triple nodal points characterized by their nodal-line structure in all magnetic space groups" [2], and "Universal higher-order bulk-boundary correspondence of triple nodal points" [3]. Segments with significant text overlap with the published version may be subject to copyright by the American Physical Society.

Recall that band nodes can be stabilized by symmetry, topology or both. The classification of triple points developed in the previous chapter has dealt with the aspect of symmetry protection. We have found that the nodal-line structure in the vicinity of triple points, in particular nodal lines attached to them, is uniquely determined by the little co-group of the HSL containing the triple point (and in some cases, the corepresentations in which the involved bands transform). As discussed in Section 3.3, this implies that triple points and their associated nodal-line structure are stable to small symmetry-preserving perturbations, i.e., as long as the nodal structures are not changed to the extent that they annihilate. In this chapter, we turn to studying the topological stability of triple points and associated nodal-line structures in spinless systems. In particular, we reveal that while the three-fold degeneracies themselves are not directly protected by a topological invariant, they imply nontrivial topology of the central nodal line with a hidden linking structure, which is only fully captured if one partitions the energy bands by multiple energy gaps.

The fact that three bands are involved in a triple point naturally requires us to adopt this multigap perspective introduced in Section 3.3.1. Multiband nodal structures in spinless systems with space-time inversion ($\mathcal{PT}$) symmetry squaring to $+1$ can be characterized by the *non-Abelian (generalized) quaternion invariant*, also known as *quaternion charge* [65, 66, 196–198], which captures topology beyond the Zak-Berry-phase quantized to 0 versus π. In Section 5.1, we compute this quaternion charge for the triple points on HSLs with $\mathcal{PT}$-symmetric little group discussed in Chapter 4 and argue that type-A triple points necessarily evolve into *multiband nodal links* under rotation-symmetry-breaking but $\mathcal{PT}$-preserving perturbations. Based on this, in Section 5.2, we

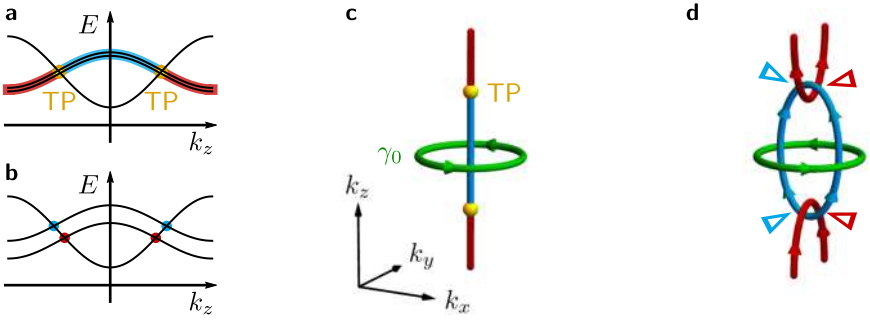

Figure 5.1.: Relation of type-A triple points to multiband nodal links. Nodal lines in the first (second) band gap are displayed in red (blue) and triple points in yellow. (**a,b**) Band structure along a high-symmetry line, and (**c,d**) the nodal-line composition near the triple point before and after applying a rotation-symmetry-breaking perturbation, respectively. The green contour γ_0 carries quaternion charge -1. The orientations of the nodal lines (with reversals indicated by triangles of the corresponding color) follow the convention of Ref. 200.

relate the triple points to a different multigap topological invariant, the Euler monopole charge. Finally, in Section 5.3, we study the triple-point metal Li_2NaN [220] using first-principle and tight-binding calculations. We show that Li_2NaN hosts an ideal triple point very close to the Fermi level which converts to a multiband nodal-link in applied strain, study the bulk-boundary correspondence for the quaternion charge, demonstrate the consequences of the nontrivial Euler monopole charge for the nodal stability and find that the strain-induced node conversion is manifested in an unusual strain-tunable optical conductivity.

5.1. Multiband nodal links from triple points

We present a simple argument revealing that type-A triple points necessarily evolve into multiband nodal links under rotation-symmetry-breaking strain. Consider a loop γ_0 (green in Fig. 5.1c) that encircles the blue nodal line extending to one side of a triple point. To study the stability of the nodal line, one would usually compute the Zak-Berry phase $\varphi(\gamma_0)$ assuming a gap between the two bands that meet at the nodal line. For a type-A triple point it must hold that $\varphi(\gamma_0) = 0$, because the loop can be moved along k_z to the other side of the triple point, where it can be shrunk to a point and

trivialized without closing the corresponding energy gap. However, from the perspective of the quaternion charge the contour γ_0 *cannot* be annihilated to a point on the other side of the triple point due to the presence of the red nodal in the adjacent energy gap. This suggests a nontrivial value $\mathfrak{q}(\gamma_0) \neq +1$ characterizing the nodal-line composition around the type-A triple point. The outlined characterization of the nodal lines is consistent with the 2D ICR being a *double* nodal line, i.e., one with a quadratic splitting of the two energy bands away from the HSL [219]. In that case, the Zak-Berry phase on γ_0 is trivial, but the quaternion charge exhibits the nontrivial value $\mathfrak{q}(\gamma_0) = -1$ [65].

Crucially, the quaternion charge remains well-defined even after the 2D ICR is split by a rotation-symmetry-breaking perturbation (Fig. 5.1b), when the triple point is lost. While the $\mathbb{Z}_2$-valued Zak-Berry phase $\varphi(\gamma_0) = 0$ cannot be directly applied to predict the fate of the nodal-line composition upon such a symmetry breaking, the value $\mathfrak{q}(\gamma_0) = -1$ implies that γ_0 *must* enclose a pair of nodal lines in some energy gap. It therefore follows that the symmetry breaking transforms the triple point into a multiband nodal link extending around the Brillouin zone (Fig. 5.1d) as long as $\mathcal{PT}$ symmetry is preserved. The topological stability of the pair of nodal lines implies that they carry parallel orientation, which is consistent with the noncommutativity of the quaternion charge [200].

While the quaternion charge $\mathfrak{q}$ can be easily computed numerically given a Bloch Hamiltonian, we make use of its relationship to the two-band winding number to compute it analytically for $\mathbf{k} \cdot \mathbf{p}$ models. In Section 5.1.1, we perform this computation for all the triple points classified in Section 4.4 and show that indeed all type-A (as well as type-B_q) triple points imply $\mathfrak{q} = -1$. This implies that all type-A triple points evolve to multiband nodal links under $\mathcal{PT}$-preserving perturbations. For type-B_q triple points, the interpretation is more subtle due to the presence of the nodal-line arcs attached to the triple point and a systematic investigation is left for future work.

5.1.1. Winding number

For two-band spinless $\mathcal{PT}$-symmetric systems, the winding number of a 2D ICR, i.e., computed on a contour around the corresponding nodal line as illustrated in Fig. 5.1c, is an integer topological invariant [173]. This integer invariant is *delicate* [125], in the sense that it ceases to be well-defined in models with three or more bands. Nevertheless, we are interested in the value of this integer invariant for the 2D ICRs involved in the triple points listed in Table 4.4, because it determines both the $\mathbb{Z}_2$-quantized Zak-Berry phase as well as the non-Abelian topological invariant carried by the central nodal line containing the triple point, which both remain well-defined in the presence of

additional bands as long as those bands are separated by gaps on the contour.

To determine the winding number of the 2D ICRs, we construct additional minimal two-band $\mathbf{k}\cdot\mathbf{p}$ models, which are simplifications of the models used in Section 4.4. Because the k_z-dependence is not directly relevant to the winding number and is not restricted by symmetry, it can be absorbed into the coefficients of the $\mathbf{k}\cdot\mathbf{p}$ expansion. This results in traceless models of the form

$$H_{\mathbf{a}}(\mathbf{k}) = \mathbf{h}_{\mathbf{a}}(k_x, k_y)\cdot\boldsymbol{\sigma} \tag{5.1}$$

with $\boldsymbol{\sigma} = (\sigma_x, \sigma_z)$ the real Pauli matrices, $\mathbf{h}_{\mathbf{a}}(k_x, k_y)$ a real two-component vector and $\mathbf{a}$ a minimal list of real parameters. By construction, $\mathbf{h}_{\mathbf{a}}(0,0) = \mathbf{0}$ for all $\mathbf{a}$, which corresponds to the central nodal line along the HSL.

The winding number $w_{2\mathrm{D}}$ of $\mathbf{h}_{\mathbf{a}}(\mathbf{k})$ along a tight contour γ_0 around that nodal line (suppressing the dependence on the parameter $\mathbf{a}$) is given by

$$w_{2\mathrm{D}} = \frac{1}{2\pi}\oint_{\gamma_0} \mathrm{d}\mathbf{k}\cdot\left(\frac{h_x(\mathbf{k})\boldsymbol{\nabla}_{\mathbf{k}}h_z(\mathbf{k}) - h_z(\mathbf{k})\boldsymbol{\nabla}_{\mathbf{k}}h_x(\mathbf{k})}{h(\mathbf{k})^2}\right). \tag{5.2}$$

For all cases except for $4/m'$, this calculation can easily be performed symbolically simply by plugging the expression for $\mathbf{h}_{\mathbf{a}}(k_x, k_y)$ into Eq. (5.2). For $4/m'$, going to polar coordinates and appropriately deforming the contour is necessary to complete the integration. The integrations are performed in a MATHEMATICA notebook published [225] alongside our original work [2]. Below, we perform an illustrative calculation for the ICR E_1 of $6/m'mm$. Interestingly, we observe that $|w_{2\mathrm{D}}|$ depends only on the magnetic point group and not on the particular choice of 2D ICR. We further observe that $|w_{2\mathrm{D}}| = \mu$, where μ is the scaling of the nodal-line arcs defined in Chapter 4 as $k_z^{\mathrm{arc}} \propto (k_x^2 + k_y^2)^{\mu/2}$. Therefore, the results can be directly read off Table 4.4 and we do not repeat them here.

Example The minimal $\mathbf{k}\cdot\mathbf{p}$ model for the 2D ICR E_1 of $6/m'mm$ reads

$$H(\mathbf{k}) = \left[a_0 + a_2\left(k_x^2 + k_y^2\right)\right]\mathbb{1} + a_1\begin{pmatrix} -2k_xk_y & k_x^2 - k_y^2 \\ k_x^2 - k_y^2 & 2k_xk_y \end{pmatrix}. \tag{5.3}$$

The resulting model can be written in terms of Pauli matrices as indicated in Eq. (5.1), while dropping the topologically unimportant term proportional to the identity; then

$$\mathbf{h}_{\mathbf{a}}(k_x, k_y) = a_1\begin{pmatrix} k_x^2 - k_y^2 \\ -2k_xk_y \end{pmatrix}. \tag{5.4}$$

The winding number defined in Eq. (5.2) then becomes

$$w_{2\mathrm{D}} = \frac{1}{2\pi}\oint_{\gamma_0}\mathrm{d}\mathbf{k}\cdot\left[\frac{1}{k_x^2 + k_y^2}\begin{pmatrix} 2k_y \\ -2k_x \end{pmatrix}\right] = -2. \tag{5.5}$$

The fact that C_3-symmetric magnetic point groups give rise to type-B_l triple points with $|w_{2\mathrm{D}}| = 1$ can be intuitively understood (at least in the presence of mirror symmetry) based on Zak-Berry phases as follows. Recall that the $\mathcal{PT}$ symmetry quantizes the Zak-Berry phase φ on any closed contour (along which a specific energy gap of the spectrum is preserved) to 0 versus π. In particular, this holds for contours around nodal lines, such that we can assign the quantized Zak-Berry phase to each nodal line (in analogy with assigning the integer winding number to nodal lines in two-band models). Nodal lines that are protected by either $\mathcal{PT}$ or mirror symmetry m_v generally carry Zak-Berry phase $\varphi = \pi$ [193]. At a type-B triple point, $\frac{1}{2}n_a^{\mathrm{nexus}}$ nodal-line arcs, each carrying Zak-Berry phase π, annihilate together with the central nodal line (here, we count nodal lines in one energy gap), therefore the Zak-Berry phase of the central nodal line must be $\varphi = \frac{1}{2}n_a^{\mathrm{nexus}}\pi \pmod{2\pi}$, which results in $\varphi = \pi$ for triple points in C_3-symmetric magnetic point groups and $\varphi = 0$ in C_6-symmetric magnetic point groups.

Finally, we consider the implications of the winding number for the quaternion charge. Note that the integer winding number is only defined for two-band blocks that are separated from the remaining bands by energy gaps; in particular, for the full three-band model exhibiting the triple point, the winding number of the central nodal line *cannot* be defined anymore. In fact, the central nodal line is transferred from one gap to another at the triple point, such that on the two sides of the triple point the integer winding number would have to be computed with respect to different energy gaps. In contrast, the non-Abelian band invariant [65, 66] is sensitive to closing *either* of the two energy gaps of the three-band model. Crucially, the quaternion charge $\mathfrak{q}$ preserves partial information contained in the integer winding number when additional (trivial) bands are added; more concretely we have the reduction [200]

$$\begin{aligned} w_{2\mathrm{D}} = 0 \mod 4 \quad &\Rightarrow \quad \mathfrak{q} = 0 \qquad \text{and} \\ w_{2\mathrm{D}} = 2 \mod 4 \quad &\Rightarrow \quad \mathfrak{q} = -1. \end{aligned} \tag{5.6}$$

We therefore conclude that triple points of type A and B_q are associated with a quaternion charge $\mathfrak{q} = -1$ computed on a contour encircling the central nodal line.

5.2. Euler monopole charge

In the previous section, we have argued that adding a small C_n-breaking but $\mathcal{PT}$-preserving perturbation transforms type-A triple points into multiband nodal links. Crucially, the linked nodal rings are in band gaps adjacent to each other, and such linking was shown to be in correspondence [199, 200] with

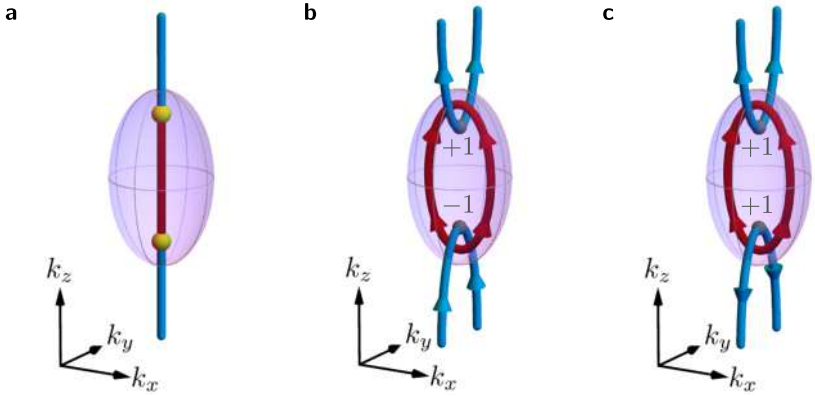

Figure 5.2.: Triple-point-induced Euler monopole charge. (**a**) Type-A triple points (yellow dots). The red (blue) line indicates nodal lines formed by the lower (upper) two bands of a three-band model. In k_z-direction, the full extent of the Brillouin zone is shown. (**b,c**) Multiband nodal link formed from (a) by breaking the rotational symmetry protecting the triple points. The flux (gray ± 1's) depends on the orientation of the two blue nodal lines at the intersection points (gray) with the disk bounded by the red nodal ring [200]. The total flux vanishes in (b) giving rise to $\chi = 0$, but is finite in (c) such that $|\chi| = 2$. In the presence of mirror $m_z : k_z \mapsto -k_z$ symmetry, the difference between the situations (b) and (c) is reflected in the mirror eigenvalues of the three bands at $k_z = 0$ versus $k_z = \pi$.

monopole charges. Thus, there *potentially* is a nontrivial monopole charge on a surface enclosing the nodal ring of interest (purple ellipsoid in Figs. 5.2b and 5.2c). By continuity, this perturbation can be switched off without closing the principal energy gap on the enclosing surface, which allows us to assign the same monopole charge also to the original nodal-line segment, i.e., on the ellipsoid in Fig. 5.2a.

In this section, we show that the nodal structure consisting of a pair of triple points formed by the same triplet of bands and a nodal-line segment connecting them can carry a nontrivial Euler charge and that its value depends on the *orientation* of the nodal lines forming the rings. This orientation in turn is determined by the sign of the quaternion charge computed on a contour around the nodal line. That sign depends on the base point and is therefore *not necessarily* periodic in the Brillouin zone. This requires us to study the relationship between the sign of the quaternion charge computed on a contour and the sign of the quaternion charge computed on the same

contour shifted by a reciprocal lattice vector. We briefly summarize our findings and their implications for the orientation of nodal lines crossing the Brillouin zone boundary in Section 5.2.1, while relegating the mathematical proofs to Appendix D. Next, in Section 5.2.2, we discuss the implications for the Euler monopole charge and show how the presence of a triple point together with a simple criterion on the Zak-Berry phase along a path winding around the Brillouin zone allows us to predict the value of the Euler monopole charge. Finally, in Section 5.2.3, we verify these predictions for several pairs of triple points in real materials based on Wannier tight-binding models obtained from first-principle calculations.

5.2.1. Quaternion charge across multiple Brillouin zones

Here, we summarize our findings on the relationship between the orientation of nodal lines and their copies in neighboring Brillouin zone, which we formally prove in Appendix D. The orientation of a nodal line can be defined using the quaternion charge introduced in Section 3.1. While the topological classification of band nodes is given by conjugacy classes of the generalized quaternion group (each conjugacy class contains either a single element or two elements that differ by a sign), the sign of the invariant becomes well-defined if the contours have a common base point P. In that case, the sign of the quaternion charge computed on a contour enclosing a single nodal line *defines* [200] the orientation of that nodal line, cf. Fig. 5.3.

The prior works [65, 200] on the non-Abelian band topology have only considered closed contours which are fully contained within a single Brillouin zone. However, to understand the orientation of nodal lines in neighboring Brillouin-zone copies, as they occur in multiband nodal links induced by triple points (Figs. 5.2b and 5.2c), one must explicitly consider paths that cross the Brillouin-zone boundary. Such paths entail additional complications, as is well known from the case of the Zak-Berry phase [98, 234]; namely, in general $H(\mathbf{k})$ and $H(\mathbf{k}+\mathbf{b})$, where $\mathbf{b}$ is any reciprocal lattice vector, are not identical, but are related by a diagonal unitary rotation, as we have described in Section 2.4. In Appendix D we explain how to compute the quaternion charge in that case and then prove a very general statement relating the values of the invariant computed on contours shifted by a reciprocal lattice vector but connected to a common base point, see e.g., the light and dark green paths γ and $\tilde{\gamma}$ in Fig. 5.3.

As a corollary of that general statement, we find that the following holds: Assuming an N-band system with $\mathcal{PT}$ symmetry squaring to $+1$ described in the orbital basis by a Hermitian Bloch Hamiltonian $H(\mathbf{k})$, let $\gamma : t \in [0,1] \mapsto \gamma(t)$ be a closed contour with no band degeneracies located inside the (first) Brillouin zone. The path starts at the *base point* $P = \gamma(0) = \gamma(1)$ and we

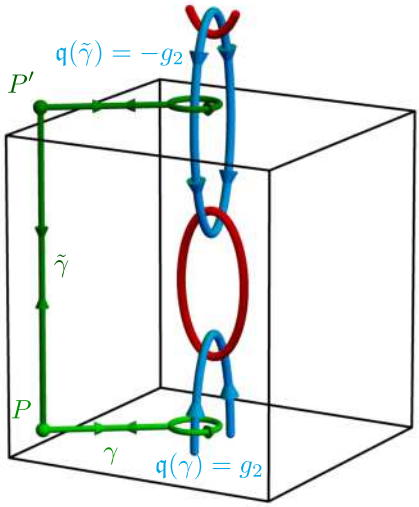

Figure 5.3.: Nodal-line orientation across multiple Brillouin zones. Definition of nodal-line orientations via the quaternion charge. The quaternion charge is computed on paths γ (light green) and $\tilde{\gamma}$ (dark green), where P' is shifted relative to P by a reciprocal lattice vector. In the three-band example shown here, $\mathfrak{q}(\gamma) = g_2$ (corresponding to a nodal line in the second gap, shown in blue) and bands 2 and 3 have different Zak-Berry phases $\varphi_2 \neq \varphi_3$. Therefore, the orientation of the upper blue nodal ring is opposite to the one of the lower ring, $\mathfrak{q}(\tilde{\gamma}) = -g_2$.

decompose (factors with smaller subscript j appearing to the right)

$$\mathfrak{q}(\gamma) = s \prod_{j \in J} g_j \tag{5.7}$$

with $s \in \{\pm 1\}$, $J \subseteq \{1, 2, \ldots, N-1\}$ a subset of the energy gaps of the N-band Hamiltonian, and g_j the generators introduced in Section 3.4.2. Then, the quaternion charge on the corresponding contour $\tilde{\gamma}$ with the same base point and enclosing the same band inversions but in the Brillouin zone shifted by the reciprocal lattice vector $\mathbf{b}$ (cf. Fig. 5.3) is

$$\mathfrak{q}(\tilde{\gamma}) = (-1)^m \mathfrak{q}(\gamma), \tag{5.8}$$

where m is the number of elements of the set

$$\{j \in J \,|\varphi_j \neq \varphi_{j+1}\} \tag{5.9}$$

with $\varphi_j \in \{0, \pi\}$ the Zak-Berry phase of the j^{th} band in the direction $\mathbf{b}$. Note that in the conditioning in Eq. (5.9) the label $j+1$ may not be in the set J.

We briefly discuss the implications for the situation depicted in Fig. 5.3. We are interested in the change of the orientation of the blue nodal ring when comparing two copies displaced by the primitive reciprocal lattice vector in k_z-direction. Recall that the orientation of nodal lines is defined via the quaternion charge of unique paths encircling those nodal lines with a fixed base point. This is exactly the situation of the above corollary with $\mathfrak{q}(\gamma) = sg_2$ (in the figure the case $s = +1$ is illustrated). The orientation changes if and only if the Zak-Berry phases of bands 2 and 3 are different, i.e., if $\varphi_2 + \varphi_3 = \pi$ mod 2π. We also remark that if $\mathfrak{q}(\gamma) = \pm 1$ (i.e., if the Zak-Berry phase of each band on γ is trivial and *no* nodal lines are enclosed by γ), we have $J = \varnothing$ and the corollary therefore immediately implies that $\mathfrak{q}(\gamma) = \mathfrak{q}(\tilde{\gamma})$. This is consistent with the fact that $\mathfrak{q} = +1$ and $\mathfrak{q} = -1$ are in *different* conjugacy classes.

5.2.2. Euler monopole charge from triple points

We now go back to the configuration of triple points and discuss the consequence of the reversal of nodal-line orientation on the Euler monopole charge introduced in Section 3.4.2. First, note that since the ordering of the ICRs along the rotation (k_z-) axis has to be the same at both $k_z = -\pi$ and $k_z = \pi$ due to the periodicity of the spectrum, it follows that the number of triple points formed by the three bands is even. In the minimal model, depicted in Fig. 5.2a, the nodal line changes the band gap twice, once from the second (blue) to the first (red) and once back to the second gap, at two triple points (yellow dots). Here we assume a single occupied and two unoccupied bands, such that the two-band subspace allows us to define the Euler monopole charge $\chi \in \mathbb{Z}$ on the purple ellipsoid in Fig. 5.2 [173].

Following Section 5.1, we consider a small perturbation leading to the multiband nodal link shown in Figs. 5.2b and 5.2c. Since each of the two nodal rings (red and blue) is linked with two rings of the other color, the purple ellipsoid *potentially* carries nontrivial Euler monopole charge χ. Note that in the minimal model with only a single pair of triple points along k_z, as shown in Fig. 5.2, the two blue half-rings that are linked with it actually belong to copies of the *same* ring shifted by the reciprocal lattice vector $\mathbf{b}$, as can be seen in Fig. 5.4. The Euler monopole charge of the red ring depends on the *orientation* of the linked blue nodal lines at the points where they cross the disk bounded by the principal (red) nodal ring [200]. This orientation at the crossing points in called flux and takes values ± 1. We can use the corollary discussed in Section 5.2.1 to distinguish the two cases $\chi = 0$ and $|\chi| = 2$ based on the Zak-Berry phases $\varphi_{2,3} \in \{0, \pi\}$ along the k_z-axis of the two bands

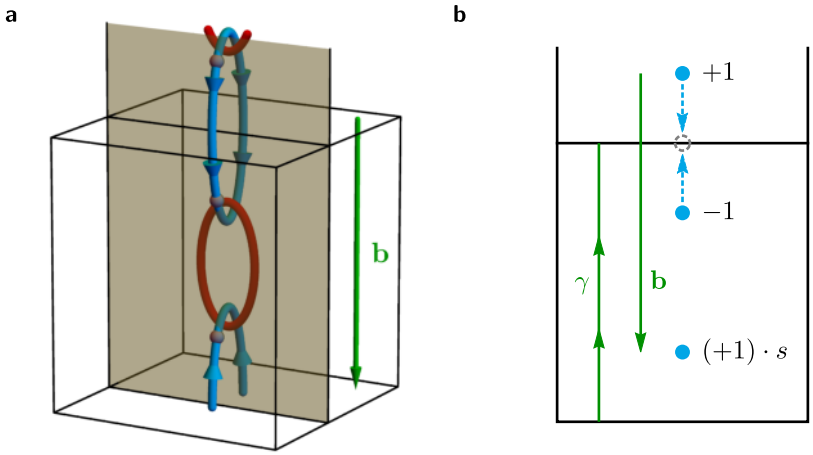

Figure 5.4.: Change of nodal-line orientation. (**a**) Nodal line configuration in the first Brillouin zone (black frame) and part of the second Brillouin zone. The two blue displayed nodal lines are displaced by a reciprocal lattice vector $\mathbf{b}$ (green arrow). The blue nodal line is intersected by a 2D plane (pale brown) at two inequivalent points (gray dots). The shown orientation of the blue nodal lines is compatible with $\varphi_2 + \varphi_3 = \pi$. (**b**) Band nodes (blue points) on the 2D plane in panel (a), with winding numbers ± 1 inherited from the orientation of the nodal lines in 3D. The two upper point nodes have opposite orientation, because they pairwise annihilate (blue arrows pointing to the gray disk) when the vertical plane is shifted away from the nodal-line composition. The point nodes displaced by $\mathbf{b}$ have winding numbers differing by a factor $s = \mathrm{e}^{\mathrm{i}(\varphi_2+\varphi_3)} = \pm 1$ [196].

involved in the formation of the blue nodal line in the adjacent energy gap. The orientation of the blue nodal line, i.e., where bands 2 and 3 are degenerate, at $\mathbf{k} + \mathbf{b}$ is *reversed* compared to the one at $\mathbf{k}$ if and only if $\varphi_2 + \varphi_3 = \pi \mod 2\pi$. Thus, two distinct scenarios can arise after breaking the rotational symmetry: Fig. 5.2b where $\varphi_2 + \varphi_3 = 0 \mod 2\pi$ implying $\chi = 0$, and Fig. 5.2c where $\varphi_2 + \varphi_3 = 0 \mod 2\pi$ implying $|\chi| = 2$.

The orientation reversal can be related to the properties of Dirac points in two dimensions (2D) derived in Ref. 196 if we consider a 2D cut (brown plane in Fig. 5.4a) through the Brillouin zone that intersects the blue nodal lines. Note that continuity implies that the two upper point nodes (i.e. upper two blue dots in Fig. 5.4b) have opposite winding number because they correspond to cuts through the *same* nodal ring, i.e., they manifestly annihilate when sliding the plane away from the nodal-link composition. According to Ref. 196 the

Table 5.1.: Materials with triple-point induced Euler monopole charge. Compounds with space-time inversion symmetry that host type-A triple points on the given high-symmetry line (HSL) and are therefore candidates for having a nontrivial Euler monopole charge. Some compounds host multiple triple points. For each material and triple point we show the space group, the HSL on which the triple point lies, the nodal line (NL) segment carrying the Euler monopole charge, i.e., the segment enclosed by the ellipsoid, the relevant Zak-Berry phases and the Euler monopole charge deduced from Wilson loop spectra. The NL segment is given in units such that 0 corresponds to Γ and 1 to the other high-symmetry point along the HSL specified in the adjacent column.

Material	SG	HSL	NL Segment	φ	χ
Na_2LiN	129	$\Gamma - Z - \Gamma$	$[-0.29, 0.29]$ $[0.29, 0.71]$	$(0, \pi)$ $(\pi, 0)$	2 2
Li_2NaN [220]	191	$\Gamma - A - \Gamma$	$[-0.08, 0.08]$ $[0.08, 0.92]$	$(0, 0)$ $(0, \pi)$	0 2
TiB_2 [190]	191	$\Gamma - A - \Gamma$	$[-0.26, 0.26]$	$(0, \pi)$	2

copy of the uppermost node with winding number +1 in an adjacent Brillouin zone (bottom-most node), i.e., shifted by the reciprocal lattice vector $\mathbf{b}$, has winding number $(+1) \cdot s$, where $s = \mathrm{e}^{\mathrm{i}(\varphi_2 + \varphi_3)}$ and φ_j is the Zak-Berry phase of band j on the contour γ winding around the 2D Brillouin zone in the direction of $\mathbf{b}$.

5.2.3. Material candidates

To verify the derived relationship between the Zak-Berry phases and the Euler monopole charge in the presence of triple points, we select some triple-point materials from Table 4.6 that each host a single pair of type-A triple points without any interfering nexus points on the corresponding HSL, namely Na_2LiN, Li_2NaN and TiB_2. For each nodal-line segment connecting the two triple points that is free of nexus points, we compute the corresponding Zak-Berry phase and Euler monopole charge and demonstrate the relationship described above. We find that all three materials host nodal-line segments with nontrivial Euler monopole charge. One of them, Li_2NaN, we study in more detail in Section 5.3.4. In particular, we additionally compute the Euler curvature and illustrate the consequences of the nontrivial Euler monopole charge on the stability of nodal-line configurations to $\mathcal{PT}$-preserving perturbations.

To compute the necessary Zak-Berry phases and Euler monopole charges, we perform first-principles calculations using density-functional theory. Then, we

construct maximally-localized Wannier functions using WANNIER90 [235] with s orbitals of alkali metal elements, d orbitals of transition metal elements and p orbitals of non-metal elements (for Li_2NaN no orbitals of Li are included). For the resulting Wannier tight-binding models we use the PYTHON package Z2PACK [236, 237] to compute the Wilson loop spectra on ellipsoids enclosing the appropriate nodal-line segments as well as the relevant Zak-Berry phases (cf. Fig. 5.4). The results are summarized in Table 5.1 and in Figs. C.20 to C.24 in Appendix C.2 we show for each triple-point material and nodal-line segment the resulting Wilson loop spectrum from which the value χ of the Euler monopole charge is deduced, as discussed in Section 3.4. By comparing the Zak-Berry phases and the values of the Euler monopole charge, we verify the condition for nontrivial Euler monopole charge discussed in Section 5.2.2. The Wannier tight-binding models as well as the Wilson loop spectra are published [238] alongside Ref. 3.

5.3. Case study: Li_2NaN

Hexagonal Li_2NaN listed in Table 4.6 was reported to be a "superior" triple-point material with negligible spin-orbit coupling [220]. As we have seen in Section 4.7, it exhibits a pair of type-A triple points at the Fermi level, which according to Section 5.1 imply nontrivial quaternion charge $\mathfrak{q} = -1$. We further find that there are no other coexisting Fermi surfaces. The material has a centrosymmetric hexagonal crystal structure with space group $P6/mmm$ (space group number 191) illustrated in Fig. 5.5a. Additionally, the corresponding 2D ICR has a nearly flat dispersion (Fig. 5.5b path ΓA), which results in a nearly hundredfold change in the density of states within a narrow energy range around the Fermi level. We therefore use Li_2NaN for a case study of the conversion of the triple points into a multiband nodal links and its consequences in a realistic setting.

This section is structured as follows. We first describe how to derive an effective tight-binding model from first-principles data obtained using density functional theory in Section 5.3.1, which we subsequently use to derive most of the results. In Section 5.3.2, we extract the nodal-line structure in the absence and presence of uniaxial tensile strain, demonstrating the conversion of triple points to multiband nodal links implied by the nontrivial quaternion invariant. Next, in Section 5.3.3, we study the bulk-boundary correspondence of the quaternion invariant and match its values to the appearance of surface states in different gaps. In Section 5.3.4, we return to discussing the Euler monopole charge induced by triple points. We verify the nontrivial Euler monopole charge with several different methods and illustrate its consequences on the stability

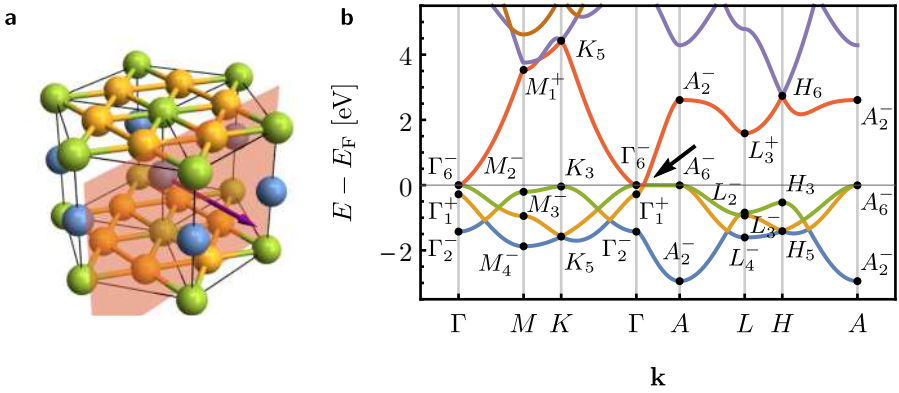

Figure 5.5.: Crystal structure and band structure of Li_2NaN. (**a**) Crystal structure with Na/Li/N (blue/yellow/green) atoms. The red plane indicates the surface termination relevant in Section 5.3.3 and the purple arrow its normal. (**b**) Band structure of Li_2NaN along the lines of symmetry in an energy window around the Fermi level, obtained from first-principles calculations. The triple point is marked by a black arrow. The irreducible representations of all bands at high-symmetry points are shown in the notation by Koster [82]. For brevity, we refer to the lowest-energy displayed band (blue) as *first*, the next (orange) as *second*, and so forth.

of nodal lines to perturbations. Finally, in Section 5.3.5, we investigate the density of states and optical conductivity of Li_2NaN as a function of strain.

5.3.1. Effective tight-binding model

To study the nodal-line structure, compute topological invariants, surface spectra and transport properties, it is most efficient to work with a minimal tight-binding model. Therefore, we first compute the band structure, irreducible representations and orbital weights using density functional theory, but then fit an effective four-band tight-binding model that reproduces the low-energy eigenstates.

First-principles calculations

We perform density-functional-theory calculations with the projected augmented wave method as implemented in the Vienna ab initio simulation package (VASP) [230, 231] with generalized gradient approximation and Perdew-Burke-Ernzerhof (PBE) approximation [232]. We use a Γ-centered $10 \times 10 \times 8$ mesh

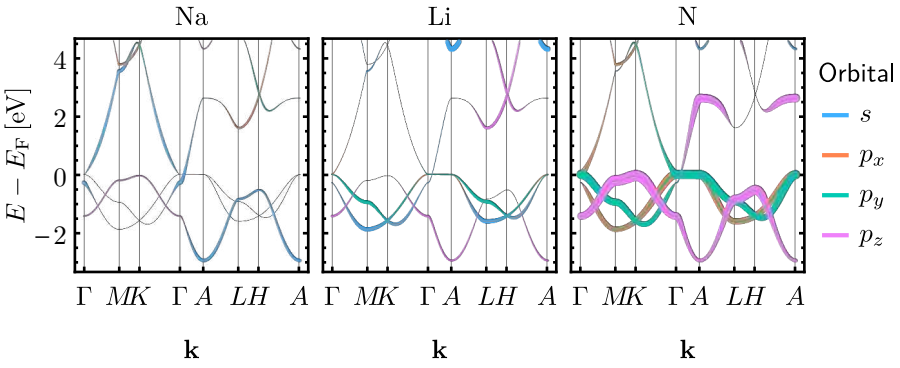

Figure 5.6.: Orbital weights in the band structure of Li_2NaN. The colored overlays show the contribution of orbitals (see legend) of the different atoms to the band structure (gray lines). The width of the overlays indicates the weight of the corresponding orbital.

in momentum space. Using plane-wave-based wave functions and space group operators generated by VASP, we calculate the traces of matrix representations to get the irreducible representations of the energy bands at high-symmetry points in the first Brillouin zone with the help of IRVSP [239]; they are shown in Fig. 5.5b. Using compatibility relations [83] we then deduce the irreducible representations of the HSLs. The contributions to energy bands from orbitals are obtained by projecting wave functions to ion-centered spherical harmonic functions with different quantum numbers and the dominant contributions are shown in Fig. 5.6. In the following we will number the bands starting from the blue band in Fig. 5.5b, which we will refer to as the *first* band, even though the first-principles results contain an additional band at even lower energy (approximately $-10\,\mathrm{eV}$).

Furthermore, we rebuild the crystal structures for compressive and tensile strain by reducing and enlarging the y-component of each lattice vector, in a way that preserves C_{2v} symmetry, such that the nodal rings will be confined to the relevant mirror planes. This is not strictly necessary but greatly simplifies the finding of nodal lines. In particular, we multiply the y-component of all lattice vectors by a factor of $1 + \varepsilon_y$ with experimentally reasonable values of ε_y in the range from -3.5% to 3.5%. The dominant effect is the splitting s of the 2D ICR along ΓA

$$2s \mathrel{\widehat{=}} E_{\mathrm{N}p_x}(\Gamma A) - E_{\mathrm{N}p_y}(\Gamma A). \tag{5.10}$$

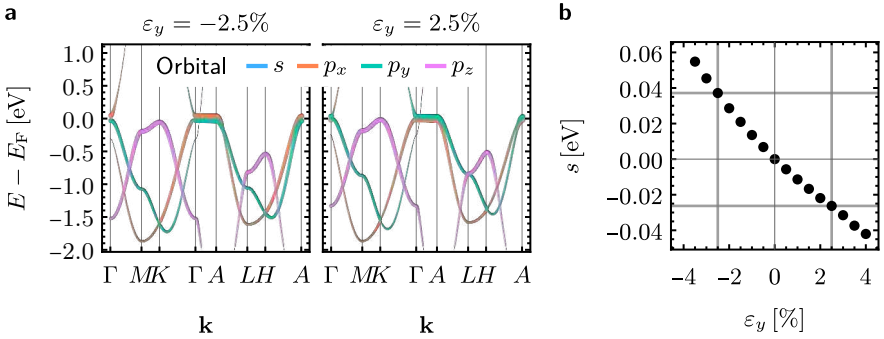

Figure 5.7.: Effect of uniaxial strain in Li_2NaN. (**a**) Band structure and contribution of the N orbitals (see colored overlays) for uniaxial strain ε_y (compression and expansion) in the y-direction obtained from first-principle calculations. The energy of the band dominated by p_x decreases for $\varepsilon_y > 0$ and increases for $\varepsilon_y < 0$. (**b**) Energy splitting s of the 2D ICR along the high-symmetry ΓA as a function of uniaxial strain ε_y extracted from data such as those shown in (a).

Extracting the value of s for different ε_y we find from Fig. 5.7a that $\varepsilon_y > 0$ corresponds to $s < 0$ and can establish the relationship $s(\varepsilon_y)$ shown Fig. 5.7b. For example, $s = -0.01\,\text{eV}$ corresponds to roughly 1% tensile strain in the y-direction.

Fitting of the tight-binding model

To construct an effective low-energy tight-binding model for Li_2NaN, we need to choose a minimal set of orbitals. From the first-principles data shown in Fig. 5.6, we deduce that the band structure close to the Fermi level is dominated by four orbitals, namely sodium (Na) s, and nitrogen (N) $p_{x,y,z}$ as shown in Table 5.2. The compound contains one of each per primitive unit cell, suggesting it is possible to construct a four-band model that reproduces the low-energy properties of Li_2NaN. Note, however, that in the first-principles data shown in Fig. 5.5b, the fourth band intersects with the fifth band multiple times, in particular leading to 2D irreducible representations at K and H. Furthermore, other orbitals become dominant at these locations, notably the lithium (Li) p_z along LH and HA (cf. Fig. 5.6). Thus, we need to artificially detach the fourth and fifth band, which prevents the resulting tight-binding model from reproducing the band structure near those crossings. Nevertheless, as these degeneracies lie at energies far from the Fermi level (3 to 4 eV), this

Table 5.2.: Orbitals contributing to the effective tight-binding model of Li_2NaN. Elements and orbitals dominating the band structure close to the Fermi level according to Fig. 5.6. The position is expressed in fractions of the primitive lattice vectors in Eq. (5.12). The last two columns give the corresponding Wyckoff position and irreducible representation (IR) of the site-symmetry group in the notation by Mulliken [81].

Element	Orbital	Position	Wyckoff position	IR
Na	s	$(0, 0, 1/2)$	b	A_{1g}
N	(p_x, p_y)	$(0, 0, 0)$	a	E_{1u}
N	p_z	$(0, 0, 0)$	a	A_{2u}

mismatch is not relevant for the low-energy properties.

We verify that such a detachment of bands is consistent with symmetries using the machinery of topological quantum chemistry [116, 133, 136]. Using the WYCKPOS and POINT applications on the Bilbao crystallographic server (BCS) [223, 224], we determine the Wyckoff positions and irreducible representations of the four orbitals in the model (cf. Table 5.2). These serve as an input for the BANDREP application [83, 116] on the BCS which calculates the elementary band representations induced from the irreducible representations of the site-symmetry group of the Wyckoff positions, which we summarize in Table 5.3. Matching them to the irreducible representations in Fig. 5.5b, we notice that not only the ones at the Dirac points at K and H need to be replaced, but also the one at L, namely

$$K_5 \to K_1, \quad H_6 \to H_3, \quad L_3^+ \to L_2^-. \tag{5.11}$$

Due to band inversions, these irreducible representations appear in the band structure at somewhat higher energies (K_1 is the eighth band at $E \approx 6.5\,\mathrm{eV}$, H_3 is the ninth band at $E \approx 8.7\,\mathrm{eV}$, and L_2^- is the fifth band at $E \approx 5.0\,\mathrm{eV}$). Finally, we need to check the compatibility relations for the modified irreducible representations of the detached fourth band to ensure that the observed band connectivity is compatible with the irreducible representations. Using the COMPATIBILITYRELATIONS application [83] on the BCS we find that both $M_1^+ \to T_1 \to K_1$ and $A_2^- \to R_3 \to L_2^- \to S_3 \to H_3 \to Q_3 \to A_2^-$ are compatible.

Having identified the relevant orbitals and the parts of the band-structure to be reproduced, we construct a symmetry-consistent tight-binding model. We use the QSYMM PYTHON package [240] to determine the symmetry-restricted family of Bloch Hamiltonians based on an input of the orbitals and the isogonal

Table 5.3.: Band representations for the effective tight-binding model of Li_2NaN. Elementary band representations at high-symmetry points (first column) induced from the irreducible representations (second row) of the site-symmetry group of the Wyckoff positions (first row) for the orbitals given in Table 5.2. The irreducible representations are given in the notation by Koster [82].

Wyckoff position Band representation	$1a$ $(6/mmm)$ $E_{1u} \uparrow G(2)$	$1a$ $(6/mmm)$ $A_{2u} \uparrow G(1)$	$1b$ $(6/mmm)$ $A_{1g} \uparrow G(1)$
Γ	$\Gamma_6^-(2)$	$\Gamma_2^-(1)$	$\Gamma_1^+(1)$
M	$M_3^-(1) \oplus M_4^-(1)$	$M_2^-(1)$	$M_1^+(1)$
K	$K_5(2)$	$K_3(1)$	$K_1(1)$
A	$A_6^-(2)$	$A_2^-(1)$	$A_2^-(1)$
L	$L_3^-(1) \oplus L_4^-(1)$	$L_2^-(1)$	$L_2^-(1)$
H	$H_5(2)$	$H_3(1)$	$H_3(1)$

point group D_{6h}. For that, we choose primitive lattice vectors

$$\mathbf{a}_1 = \begin{pmatrix} 0 \\ -a \\ 0 \end{pmatrix}, \quad \mathbf{a}_2 = \begin{pmatrix} a\sqrt{3}/2 \\ a/2 \\ 0 \end{pmatrix}, \quad \mathbf{a}_3 = \begin{pmatrix} 0 \\ 0 \\ c \end{pmatrix} \tag{5.12}$$

with a and c being the in-plane and out-of-plane lattice constants, respectively. We further fix the Hilbert-space basis $(\mathrm{N}p_x, \mathrm{N}p_y, \mathrm{N}p_z, \mathrm{Na}s)$, i.e. in terms of the irreducible representations $(E_{1u}(2), A_{2u}(1), A_{1g}(1))$.

As the input to the QSYMM package, we provide (i) the set of generators of D_{6h}, including the matrix corepresentations which are determined by the irreducible representations of the orbitals (listed in Table 5.4), and (ii) the considered hopping vectors (listed in Table 5.5) between nearby atoms. We only consider hoppings up to nearest neighbors in terms of unit cells, which results in six independent terms (all symmetry-related hopping terms are taken into account implicitly). We note that the resulting family of Bloch Hamiltonians does not consist of real matrices, which is a consequence of the corepresentation of $\mathcal{PT}$ in Table 5.4 not being $\mathbb{1}$. Because we need the Hamiltonian to be real when computing the quaternion charge, we rotate the basis such that $\overline{\mathcal{D}}(\mathcal{PT}) = \mathbb{1}$ using the unitary transformation $U = \mathrm{diag}(1, 1, 1, \mathrm{i})$.

We arrive at a 13-parameter family of Bloch Hamiltonians, which we now fit to the first-principles band structure along the lines of symmetry. We cannot expect the model to fit well everywhere, because it contains a reduced number of orbitals, and because of the symmetry-consistent replacement of irreducible representations at points K, H and L, as argued above. In order

Table 5.4.: Generators of the isogonal point group of Li_2NaN. Generators of the point group D_{6h} including their action on position and the matrix corepresentation in the Hilbert space spanned by the orbital basis $(\mathrm{N}p_x, \mathrm{N}p_y, \mathrm{N}p_z, \mathrm{Na}s)$, cf. Table 5.2.

Generator	Action on position	Corepresentation
C_6^+	$\begin{pmatrix} \frac{1}{2} & -\frac{\sqrt{3}}{2} & 0 \\ \frac{\sqrt{3}}{2} & \frac{1}{2} & 0 \\ 0 & 0 & 1 \end{pmatrix}$	$\begin{pmatrix} \frac{1}{2} & -\frac{\sqrt{3}}{2} & 0 & 0 \\ \frac{\sqrt{3}}{2} & \frac{1}{2} & 0 & 0 \\ 0 & 0 & 1 & 0 \\ 0 & 0 & 0 & 1 \end{pmatrix}$
C_{21}'	$\begin{pmatrix} 1 & 0 & 0 \\ 0 & -1 & 0 \\ 0 & 0 & -1 \end{pmatrix}$	$\begin{pmatrix} 1 & 0 & 0 & 0 \\ 0 & -1 & 0 & 0 \\ 0 & 0 & -1 & 0 \\ 0 & 0 & 0 & 1 \end{pmatrix}$
$\mathcal{T}$	$\begin{pmatrix} 1 & 0 & 0 \\ 0 & 1 & 0 \\ 0 & 0 & 1 \end{pmatrix}$	$\begin{pmatrix} 1 & 0 & 0 & 0 \\ 0 & 1 & 0 & 0 \\ 0 & 0 & 1 & 0 \\ 0 & 0 & 0 & 1 \end{pmatrix}$
$\mathcal{P}$	$\begin{pmatrix} -1 & 0 & 0 \\ 0 & -1 & 0 \\ 0 & 0 & -1 \end{pmatrix}$	$\begin{pmatrix} -1 & 0 & 0 & 0 \\ 0 & -1 & 0 & 0 \\ 0 & 0 & -1 & 0 \\ 0 & 0 & 0 & 1 \end{pmatrix}$

Table 5.5.: Hoppings included in the tight-binding model of Li_2NaN. Hopping terms between the atoms listed in Table 5.2.

Atom 1	Atom 2	Hopping vector
N	N	$\mathbf{a}_1$
N	N	$\mathbf{a}_3$
Na	Na	$\mathbf{a}_1$
Na	Na	$\mathbf{a}_3$
N	Na	$\frac{1}{2}\mathbf{a}_3$
N	Na	$\mathbf{a}_1 + \frac{1}{2}\mathbf{a}_3$

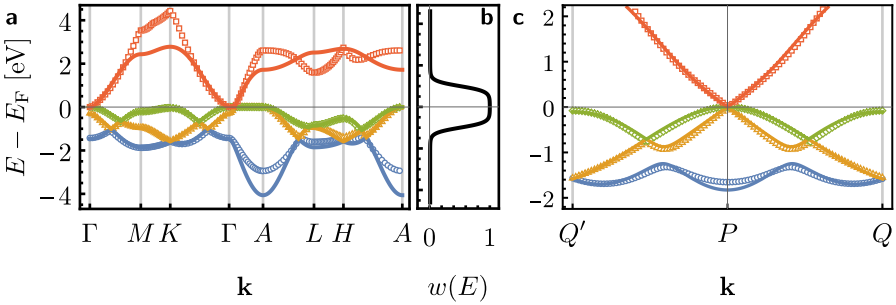

Figure 5.8.: Fitting of the effective tight-binding model for Li_2NaN. (**a**) The band structure obtained from density-functional theory calculations (only a fraction of all the points is shown for better visibility) is indicated by points and the fitted tight-binding model by solid lines. (**b**) The fitting weight function given in Eq. (5.13). (**c**) Comparison of the band structure away from high-symmetry lines around the triple point located at P. The points Q and Q' are projections of P on to the KH line.

to capture the relevant features, i.e., the energies close to the Fermi level and the band connectivity, we proceed as follows: First, we set the energy of the 2D irreducible representation along ΓA exactly to zero, which is almost exact according to the first-principles data. Then, we determine initial values for ten out of the remaining eleven parameters by diagonalizing the eleven-parameter family of Hamiltonians on lines of symmetry and using the dimension of the irreducible representations to match the resulting expressions for eigenvalues to the numerically obtained band structure. Finally, we fit the eleven parameters not fixed in the first step using a weighted least-square algorithm with the weight function

$$w(E) = \frac{w_0 + \frac{1}{2}\coth\left(\lambda\frac{\Delta E}{2}\right)\left[\tanh\left(\lambda\left(\frac{\Delta E}{2}+E\right)\right)+\tanh\left(\lambda\left(\frac{\Delta E}{2}-E\right)\right)\right]}{1+w_0}, \tag{5.13}$$

where $\lambda = 4\,\mathrm{eV}^{-1}$, $\Delta E = 2\,\mathrm{eV}$, $w_0 = 0.01$ and E is the band energy according to the first-principles calculations. The choice of weight function in Eq. (5.13), illustrated in Fig. 5.8b, ensures that the fitted model reproduces features within an approximately $\Delta E/2 = 1\,\mathrm{eV}$ wide energy window around the Fermi level more faithfully than those farther away.

The band structure of the resulting tight-binding model along the lines of symmetry is compared to the first-principles data in Fig. 5.8a. We observe that the fit is good close to the Fermi level but diminishes for energies farther

away. Except for the fourth band, the band connectivity and overall behavior of the bands is reproduced, as expected. Figure 5.8c shows the band structure along the line $Q'PQ$ with P being the position of the triple point and Q a point on the Brillouin-zone boundary directly above K at the same k_z as P. We thus expect the tight-binding model to reproduce the band structure in the energy window $[-1, 1]$ eV very well even outside the lines of symmetry and in particular near the triple point.

To convert the triple points into multiband nodal links, the C_{6v} symmetry needs to be broken. In the tight-binding model this is modelled by adding the leading C_{6v}-breaking term,

$$H_{\text{strain}}(\mathbf{k}) = s \begin{pmatrix} 1 & & & \\ & -1 & & \\ & & 0 & \\ & & & 0 \end{pmatrix}, \tag{5.14}$$

which lifts the degeneracy along the ΓA line. This term still satisfies the C_{2v} symmetry and thus corresponds to the application of uniaxial strain.

5.3.2. Nodal-line structure

To determine the nodal-line structure from the effective tight-binding model developed in the previous section, we use the ideas introduced in Chapter 4. We have developed a simple partially adaptive numerical algorithm [1] for finding nodal lines of any tight-binding model based on the fact that the discriminant of the characteristic polynomial of the Hamiltonian $H(\mathbf{k})$ vanishes if and only if there is a node at $\mathbf{k}$ (corresponding to a multiple root of the characteristic polynomial). Because the Hamiltonian is Hermitian, the roots of the characteristic polynomial are always real, which implies that the discriminant is nonnegative. Thus, the roots of the discriminant are simultaneously local minima. It is convenient to go to cylindrical coordinates

$$\mathbf{k} = \begin{pmatrix} k\cos(\theta) \\ k\sin(\theta) \\ k_z \end{pmatrix} \tag{5.15}$$

and consider $k = 0$ and $k \neq 0$ separately. The first case can be checked explicitly for roots, while we handle the second case using a grid of (θ, k_z) points. For each (θ, k_z) we sample k, detect minima and perform root finding around those. At the end, roots are selected according to a specified tolerance, duplicates are removed and the energy gap is determined by computing the eigenenergies.

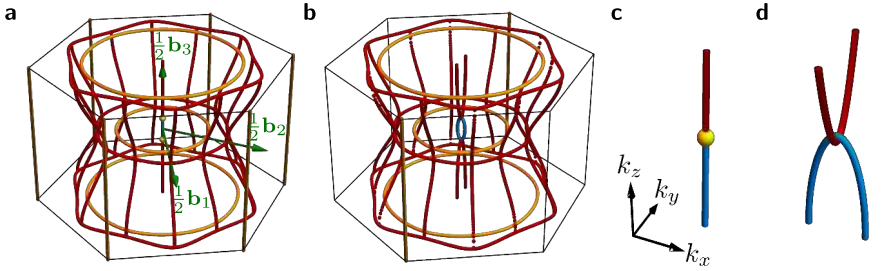

Figure 5.9.: Nodal-line structure of Li_2NaN. (**a,b**) Nodal lines inside the Brillouin zone without and with tensile strain in y-direction of approximately 1% (corresponding to $s = -0.01$), respectively. (**c,d**) Close-ups for $0 < k_z < 0.15G_3$ showing the triple point and the multiband nodal link in applied strain, respectively. The nodal lines are colored orange/red/blue for the first/second/third energy gap. Green arrows in (a) $\mathbf{b}_j$, $j = 1, 2, 3$, indicate primitive reciprocal vectors.

The algorithm has one limitation: nodal lines confined to planes with constant θ and/or k_z are not detected if the corresponding values of θ and k_z are not in the initial grid. For mirror-symmetry protected nodal lines (which are the relevant ones in our case) this can be easily alleviated by making sure that all candidate planes (according to the symmetries) are included in the (θ, k_z) grid, while other nodal lines do not generally lie inside such a plane, such that they will be detected for some values of k_z at least.

Applying the algorithm to the effective tight-binding model of Li_2NaN both without and with 1% strain, we find that the vertical nodal line at $k_x = k_y = 0$ (i.e., the 2D ICR) is well isolated from other nodal lines in the Brillouin zone, both in energy and in momentum, see Fig. 5.9a. The little group along ΓA is C_{6v} and the involved ICRs are (E_1, A_1), such that Table 4.5 predicts type-A triple points and the formation of a multiband nodal link after breaking the C_{6v} symmetry down to C_{2v}. In agreement with Figs. 5.1c and 5.1d, we observe in Figs. 5.9c and 5.9d that the central nodal line splits into linked nodal lines in adjacent band gaps with width in $k_{x/y}$-direction proportional to $\sqrt{s}$.

5.3.3. Bulk-boundary correspondence for the quaternion charge

We next examine the bulk-boundary correspondence, which has not previously been clarified for the quaternion charge. We consider a finite slab with the

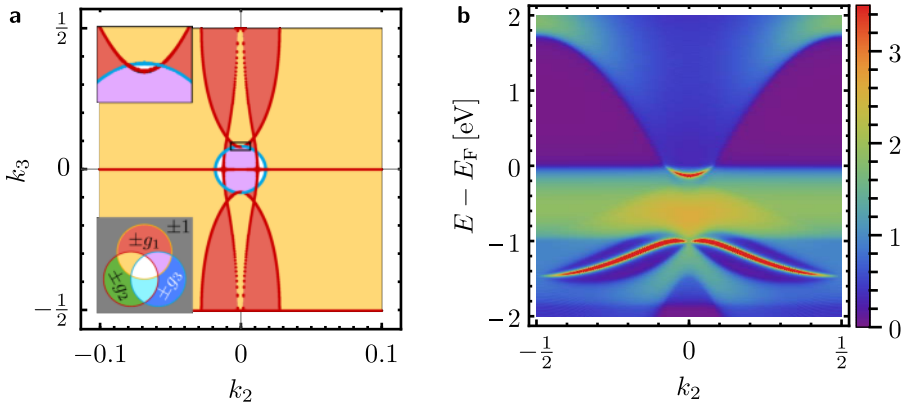

Figure 5.10.: Bulk-boundary correspondence of the quaternion charge. (**a**) Projection of the nodal lines in Fig. 5.9b onto the surface Brillouin zone, and the quaternion charge in each region. Coordinates $k_{2,3}$ and their units correspond to projections of $\mathbf{b}_{2,3}$. As indicated in the legend, we assign colors to the conjugacy classes of the quaternion charge according to the representation in terms of the generators g_1, g_2, g_3, such that e.g., the overlap of red and green (yellow) corresponds to $\pm g_1 g_2$. For illustration purposes we do not distinguish between elements of different signs even in the cases where they are in *different* conjugacy classes (± 1 and $\pm g_1 g_3$). This does not impair the presentation of results, because the gray region coincidentally is always $+1$, while the distinction of $\pm g_1 g_3$ is fragile under the addition of additional trivial bands. (**b**) Surface spectral function for $k_2 = 0$ showing direct gaps (dark blue and purple colors) and surface states (orange and red colors). The data in both panels was obtained from the fitted tight-binding model with tensile strain in y-direction of approximately 1% (corresponding to $s = -0.01$).

surface termination indicated in Fig. 5.5a. This corresponds to a projection of the Brillouin zone along the reciprocal vector $\mathbf{b}_1$ indicated in Fig. 5.9a onto the surface Brillouin zone. Each point in the surface Brillouin zone corresponds to a closed path winding around the Brillouin zone torus, carrying quaternion charge $\mathfrak{q}(k_2, k_3)$, see Fig. 5.10a. The bulk-boundary correspondence relates the value of the quaternion charge at each point to the appearance of surface states in the surface spectral function shown in Fig. 5.10b. Because the quanternion charge is a multigap invariant, it distinguishes surface states in different energy gaps. Note that the surface states are only clearly recognizable as long as the corresponding gap is sufficiently large, otherwise they can hybridize with bulk states and become weaker.

Our discussion is structured as follows. We first describe how to interpret

Fig. 5.10a and how precisely the values are related to the appearance of surface states in the various gaps. That discussion is based on the projection of the bulk and slab band structure onto the surface Brillouin zone. Only in the next step, do we introduce the surface spectral function, which we demonstrate to capture the surface states observed in the full spectrum as long as the energy gap is sufficiently large. Finally, we compare the spectral function obtained from the effective tight-binding model to the one directly obtained from first-principles calculations and find agreement.

Quaternion charge and surface states

Given a tight-binding model, the quaternion charge of the closed contour along k_1 for any (k_2, k_3) can be computed using the algorithm described in Section 3.4.2. We show the results for various values of s in Figs. 5.10a, 5.11a and 5.13. Recall that any element of Q_N is given (up to a sign) by an ordered product of some of the $(N-1)$ generators g_j, where g_j represents a band inversion of the j^{th} energy gap (cf. legend in Fig. 5.10a). As always, the transition from one value of the topological invariant to another is accompanied by a gap closing, which implies that regions of the surface Brillouin zone with different values of the quaternion charge are separated by projected nodal lines. If the change is associated with the generator g_j, the nodal line is located in the j^{th} gap, which is indicated in the legend by coloring the boundaries according to the three colors orange/red/blue corresponding to the three gaps.

To analyze the surface properties we consider a slab geometry of the tight-binding model $H(\mathbf{k})$ with termination at the surface indicated in Fig. 5.5a. In that illustration, the atoms intersected by the red layer are *included* in the slab, and the purple arrow indicates the surface normal pointing *outside* from the sample. Thus, we assume a finite-size system with open boundary conditions in the $\mathbf{a}_1$ direction and infinite size in the $\mathbf{a}_2, \mathbf{a}_3$ directions. The Bloch Hamiltonian for n layers is

$$H(k_2, k_3)_{ii'} = \int_{-1/2}^{1/2} \mathrm{d}k_1 \, H\left(\sum_{j=1}^{3} k_j \mathbf{b}_j\right) \mathrm{e}^{2\pi \mathrm{i}(i-i')k_1}, \tag{5.16}$$

where $i, i' \in \{1, 2, \ldots, n\}$ is the layer index.

We reveal surface states by computing the inverse participation ratio (IPR) of each (normalized) state vector ψ, defined as

$$\mathrm{IPR}(\psi) = \sum_{i=1}^{n} p_i(\psi)^2, \tag{5.17}$$

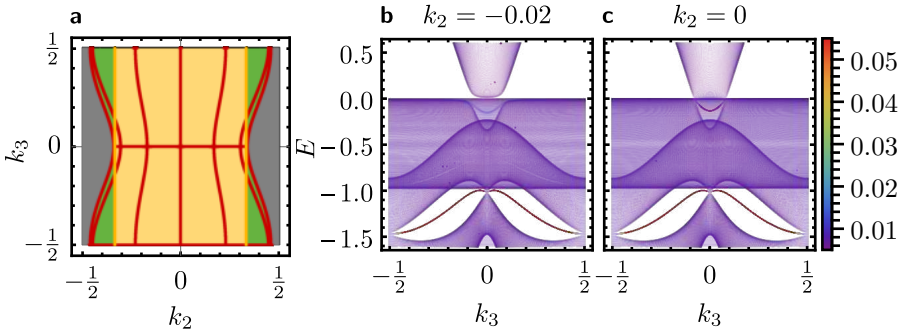

Figure 5.11.: Quaternion charge and slab band structure of Li_2NaN without strain. (**a**) Quaternion charge in the full surface Brillouin zone and the projection of bulk nodal lines. See Fig. 5.10a for the legend. (**b,c**) Band structure of the slab Hamiltonian for 200 layers and two values of k_2, corresponding to cuts through the surface Brillouin zone. The color scale indicates the inverse participation ratio according to the legend on the right. We observe two surface bands, one in gap $1-2$ and one in gap $2-3$.

where the sum is over the layer index i, and $p_i(\psi)$ is the probability of an electron in state ψ to be found in layer i (in any of the four basis orbitals). The inverse participation ratio is a measure of localization: a state ψ perfectly and uniformly localized on m layers satisfies $\mathrm{IPR}(\psi) = 1/m$, which for a completely delocalized state becomes $1/n$. In Figs. 5.11b, 5.11c, 5.12 and 5.14, we show the slab band structure projected along k_1, colored according to the inverse participation ratio, as a function of k_3 for various choices of strain s and k_2.

In general, surface states can hybridize with bulk states that project to the same point in the surface Brillouin zone and lie at the same energy. However, as long as the hybridization is not too strong, they are still localized and are thus visible via the IPR. To uncover *all* surface states, we look at the evolution of the band structure and inverse participation ratio when increasing the strain parameter s from 0 to -0.2 in Figs. 5.11b and 5.12 for $k_2 = 0$. In the presence of strain, shown in Fig. 5.12, we identify a total of four surface bands: one formed by bands $1-2$, two by $2-3$ and one by $3-4$. For large enough s, the first and last surface band are located in bulk energy gaps, while the other two clearly hybridize with bulk states. In the absence of strain, Fig. 5.11b, only two surface bands are visible, one between bands $1-2$, and one between bands $2-3$.

We next discuss the bulk-boundary correspondence between the quaternion charge in the surface Brillouin zone and the surface states. The expected

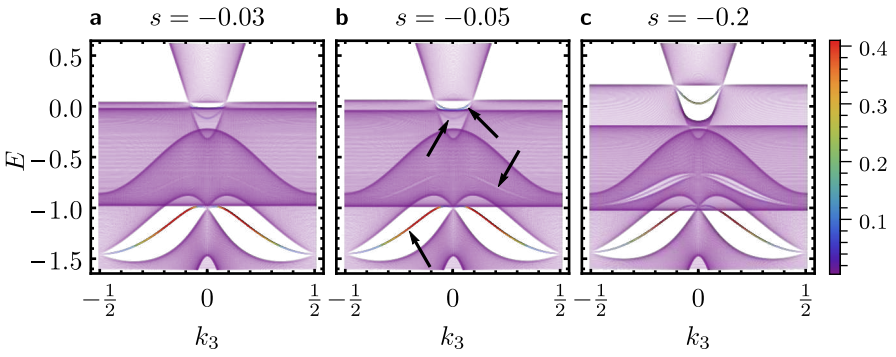

Figure 5.12.: Slab band structure of Li_2NaN for various levels of strain. Band structure of the slab Hamiltonian of Li_2NaN for 200 layers and $k_2 = 0$, plotted for increasing strain. The color scale indicates the inverse participation ratio according to the legend on the right. Generally, not all surface bands are well visible, due to hybridization with the bulk states, whose degree depends on s. However, we can deduce that there are four surface bands (indicated by black arrows), even if they are not always visible, e.g., the upper surface state in gap $2-3$ is best visible in panel (a) and the lower one in panel (c).

correspondence [65] suggests that surface states appear between bands j and $j+1$ if the quaternion charge contains the generator g_j as a factor (which corresponds to an inversion of those two bands). In Figs. 5.11a and 5.13, we show the bulk quaternion charge for the closed paths projecting onto points in the surface Brillouin zone in the absence and presence of strain, respectively. For better visibility, we show in Fig. 5.13 data for a larger strain of 5% ($s = -0.05\,\mathrm{eV}$), but the conclusions remain valid for Fig. 5.10a.

To start our comparison, we first consider the unstrained case, when the quaternion charge near $k_2 = k_3 = 0$ is $\pm g_1 g_2$ as shown in Fig. 5.11a. Note that the quaternion charge is not well-defined *at* the line $k_2 = 0$, because red nodal lines project onto the surface Brillouin zone there and the spectrum along the contour is therefore gapless. In accordance with the anticipated bulk-boundary correspondence, we find one surface band in both the first and the second energy gap, cf. Fig. 5.11c. For another comparison, we consider a large strain value $s = -0.05\,\mathrm{eV}$. The quaternion charges over the whole surface Brillouin zone are displayed in Fig. 5.13a, and we compare them to the surface states for various k_2 and k_3 displayed in Fig. 5.14. We again find a correspondence with the anticipated bulk-boundary correspondence [65], however, one has to

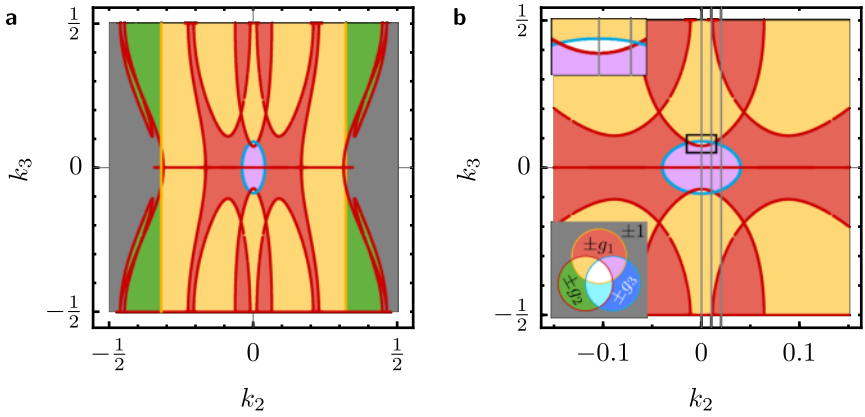

Figure 5.13.: Quaternion charge for Li_2NaN with 5% strain. Both the projection of the nodal lines in Fig. 5.9b onto the surface Brillouin zone, as well as the quaternion charge in the regions between them are shown (**a**) in the full surface Brillouin zone and (**b**) in the region $|k_2| < 0.15$, with the inset showing the details of the multiband nodal link. The three vertical gray lines in the right panel indicate the cuts for which the slab band structure and inverse participation ratio are plotted in Fig. 5.14. See the caption to Fig. 5.10 for a description of the legend.

be careful with the counting and with the inclusion of the surface bands that hybridize with the bulk states, therefore we expound a few cases in more detail.

Referring to Fig. 5.14 for surface bands and to Fig. 5.13b for the quaternion charge, we make the following observations. There are four surface states states: one between bands $1-2$, two of different extent along k_3 between bands $2-3$ and one between $3-4$. First, for all three cuts, the quaternion charge contains a factor g_1, which is consistent with the surface band in the gap $1-2$ extending over all k_3 values. Furthermore, the surface band in the gap $3-4$ corresponds to a factor g_3 which appears inside the blue nodal ring, and thus the corresponding range of k_3 shrinks for increasing k_2 until it vanishes completely at larger k_2 (not shown). Finally, for the surface bands in the $2-3$ gap, the discussion becomes a bit more involved due to the missing bulk gap, which leads to hybridization of the possible surface states with the bulk states. Nevertheless, we are able to identify two surface bands between these two bands, which are barely visible. For values of k_3 where both of these surface bands are present, we expect a trivialization ($\pm g_2^2 \sim \pm 1$) and thus correspondence to *no* factor g_2 in the quaternion charge, while g_2 should be present if there is only one of these two surface bands. Note that in Figs. 5.14a

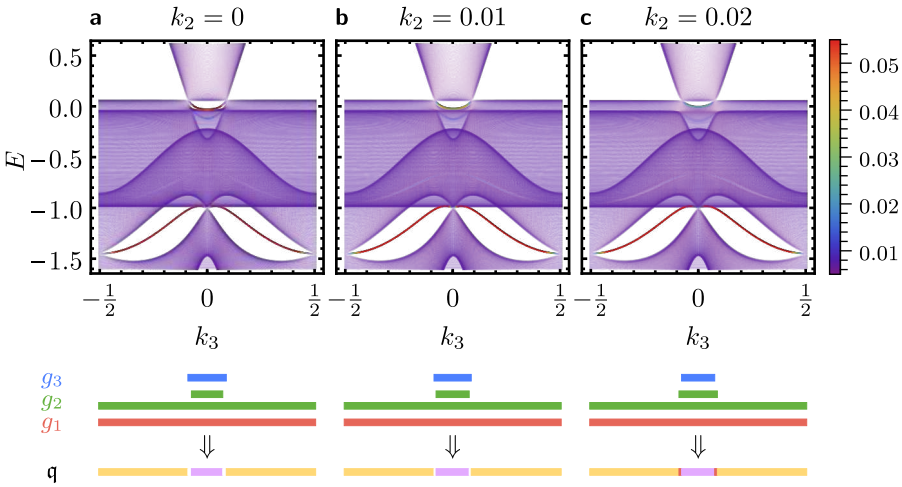

Figure 5.14.: Slab band structure of Li_2NaN with 5% strain. The band structure of the slab Hamiltonian for 200 layers is plotted for different values of k_2 corresponding to the three cuts through the surface Brillouin zone shown in Fig. 5.13b. The color scale indicates the inverse participation ratio according to the legend on the right. At the bottom, the extent of each surface band is indicated by a colored horizontal bar, where the color indicates the gap in which the surface band occurs. The color scheme follows the legend in Fig. 5.13, which is indicated by the corresponding generators g_j. Multiplying the generators g_j that are present at a given k_3 results in the quaternion charge illustrated in the bottom-most bar. The colors of this latter bar match Fig. 5.13 along the corresponding cut.

and 5.14b the $2-3$ surface band higher in energy has an extent in k_3 which is slightly smaller than the one of the $3-4$ surface band, such that a (small) region with surface bands in all three gaps results. This is consistent with the small white overlap shown in the inset of Fig. 5.13b. The white region has vanished in the third cut (Fig. 5.14c), which is reflected in the upper $2-3$ surface band now having a larger extent in k_3 than the $3-4$ surface band.

Surface spectral function

After studying the surface states through the slab band structure and inverse participation ratio, we are interested in the consequences for the surface spectrum, more precisely the surface spectral function, which we compute as follows. By diagonalizing $H(k_2, k_3)$ at each point (k_2, k_3) in the surface

Brillouin zone,

$$H(k_2, k_3)\,|i\rangle = E_i\,|i\rangle\,, \tag{5.18}$$

we obtain $4N$ eigenstates, and compute the surface spectral function

$$A_{\mathrm{S}}(E, k_2, k_3) = \sum_i \delta(E_i - E)\,\langle i|P_{\mathrm{surface}}|i\rangle\,, \tag{5.19}$$

where P_{surface} is the projector onto the outermost surface layer. For our calculations we use $n = 100$ and we replace the Dirac delta function by a Lorentzian with a half-width of 0.021 eV. The results of the calculation for the tight-binding model without and with strain are shown in Figs. 5.15a and 5.15c, respectively. Comparing to Fig. 5.12a, we observe that both the surface state in gap $1-2$ between $E = -1.5\,\mathrm{eV}$ and $-1\,\mathrm{eV}$ as well as the one in gap $2-3$ slightly below $E = 0\,\mathrm{eV}$ are visible in the surface spectrum.

Finally, we compare the surface spectral function obtained from the tight-binding model to the results obtained from the first-principles modelling, where surface states are calculated using the WannierTools package [241] which is based on the maximally localized Wannier-function tight-binding model [122] constructed by the Wannier90 package [235]. For this calculation we use the sodium s-orbital, and nitrogen p-orbitals as initial wave functions for the localization. While the minimal tight-binding model does not include the lithium atoms, thus leading to a unique surface termination along the considered direction, the explicit presence of the lithium orbitals in the first-principles calculations enables terminations at various inequivalent layers. By comparing the data, we find that the tight-binding model reproduces the first-principles calculations shown in Figs. 5.15b and 5.15d for the termination at the layer shown in Fig. 5.5a with the specifications detailed above Eq. (5.16). For this termination, the outermost layer of nitrogen atoms is enclosed in a complete hexagonal cage of lithium atoms, just like the bulk nitrogen atoms.

Figure 5.15 shows good qualitative agreement between the four-band tight-binding model and the first-principle calculations. In particular, the surface states in the relevant gaps are reproduced. The observed correspondence suggests that the basis orbitals of the constructed tight-binding model effectively correspond to a mixture of the nitrogen $p_{x,y}$ orbitals hybridized with the lithium $p_{x,y}$ orbitals of the enclosing hexagonal cage, as is indeed visible in Fig. 5.6. Since the tight-binding model implicitly assumes the same orbitals also at the boundary, the surface termination reproduced by the tight-binding model must correspond to the case when the outermost nitrogen atoms are surrounded by unbroken hexagonal cages of lithium atoms, consistent with our findings.

One obvious difference between the predictions of the tight-binding model (Figs. 5.15a and 5.15c) as compared to the first-principles data (Figs. 5.15b

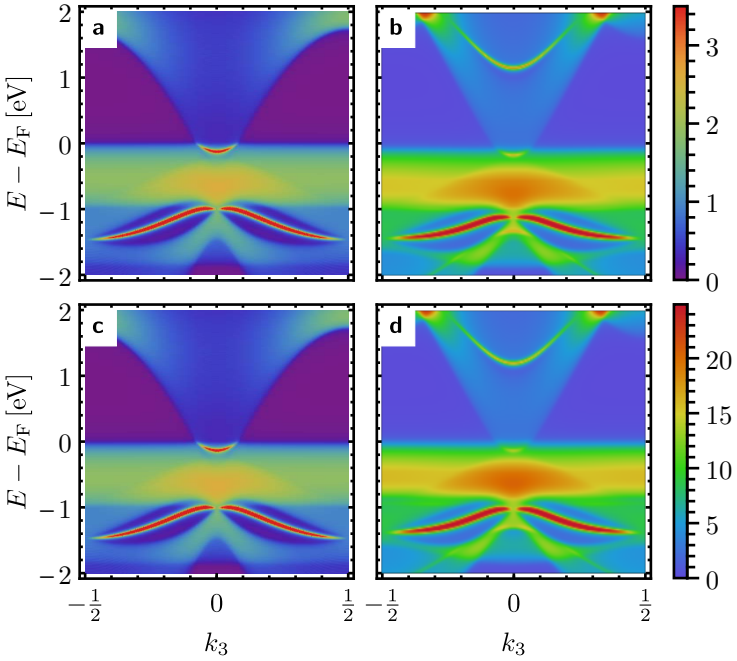

Figure 5.15.: Surface spectral function of Li_2NaN. The surface spectral function for $k_2 = 0$ as a function of E and k_3 is shown (**a,b**) in the absence of strain and (**c,d**) with 3% tensile strain (corresponding to $s \approx -0.03\,\mathrm{eV}$), which was obtained from (**a,c**) the four-band tight-binding model with 100 layers (top legend) and (**b,d**) first-principles calculations (bottom legend).

and 5.15d) is the absence of a surface band in the energy range of 1 to 2 eV, i.e., relatively far from the Fermi level. We expect this surface band to originate from a band inversion between the fourth and higher-energy bands, and that it is absent in the tight-binding modelling due to the enforced detachment of those bands, see Section 5.3.1.

5.3.4. Euler monopole charge and nodal stability

In Section 5.2.3, we have found that of the two nodal-line segments connecting the two triple points in Li_2NaN, one carries trivial and one nontrivial Euler monopole charge. We now revisit this based on the effective tight-binding model developed in Section 5.3.1. In particular, we compute the Euler monopole

charge using three different methods: (1) by using the relationship to the Zak-Berry phase discussed in Section 5.2.2, (2) by counting the winding of Wilson loop spectra, and (3) by explicitly computing the Euler curvature and integrating it to obtain the Euler monopole charge as described in Section 3.4.2. For method (1), the Zak-Berry phases of each band of the tight-binding model in k_z-direction can be easily computed using the Wilson-loop method, and we obtain $(0, 0, 0, \pi)$, with the nontrivial value carried only by the highest-energy band. We therefore predict the red nodal-line segment (connecting triple points in two adjacent Brillouin zones, cf. Fig. 5.16a) to carry Euler monopole charge $|\chi| = 2$ and the blue one (Fig. 5.16d) $\chi = 0$.

We first discuss the red nodal-line segment. The Zak-Berry phases $\varphi_{3,4}$ of the bands forming the blue nodal line (i.e., bands 3 and 4) on the green contour satisfy $\varphi_3 + \varphi_4 = \pi \mod 2\pi$. Thus, the red nodal-line segment carries Euler monopole charge $|\chi| = 2$. We arrive at the same conclusion based on the Wilson-loop spectrum computed on the purple ellipsoid shown in Fig. 5.16a: the double winding in Fig. 5.16b implies [173] $|\chi| = 2$. Using the algorithm from Ref. 66, we compute the Euler curvature on the same ellipsoid. For that, note that the Euler class defined in Eq. (3.44), is independent of the parametrization of the integration manifold S^2, such that we can parametrize the relevant ellipsoid by the spherical coordinates $(\theta, \phi) \in [0, \pi] \times [0, 2\pi)$ and define

$$F(\theta, \phi) = \left\langle \boldsymbol{\nabla}_{(\theta,\phi)} u_1(\theta, \phi) \right| \times \left| \boldsymbol{\nabla}_{(\theta,\phi)} u_2(\theta, \phi) \right\rangle . \tag{5.20}$$

The result of this computation is shown in Fig. 5.16c and we find that the integral over the full ellipsoid is $|\chi| = 2$.

The nontrivial value of χ implies a topological obstruction: the red nodal-line segment cannot be removed completely as long as $\mathcal{PT}$ symmetry is preserved. We verify this explicitly by adding a large perturbation to the tight-binding model, i.e., one that collides the two triple points and therefore goes beyond the symmetry-protection. The 1D ICR involved in the triple point has most of its weight on the nitrogen p_z orbital, such that we can move the triple points towards the A point by reducing the onsite energy of that orbital. We denote the change in energy by $\Delta\varepsilon_{\mathrm{N}p_z} = -\delta\,\mathrm{eV} < 0$. As shown in Fig. 5.17, increasing δ shrinks the red nodal-line segment until the two triple points collide at A. At that stage, the band degeneracy in the red energy gap has reduced to a single touching point at A. However, the Euler monopole charge prevents opening of the energy gap; indeed, increasing δ even further results in a conversion of the red triple-point segment into a red nodal ring in the horizontal $k_z = \pi$ plane. Crucially, the Euler monopole charge persists in $\mathcal{PT}$-symmetric systems even if the horizontal m_z symmetry was removed from the model.

We remark that the critical three-band touching obtained by colliding the

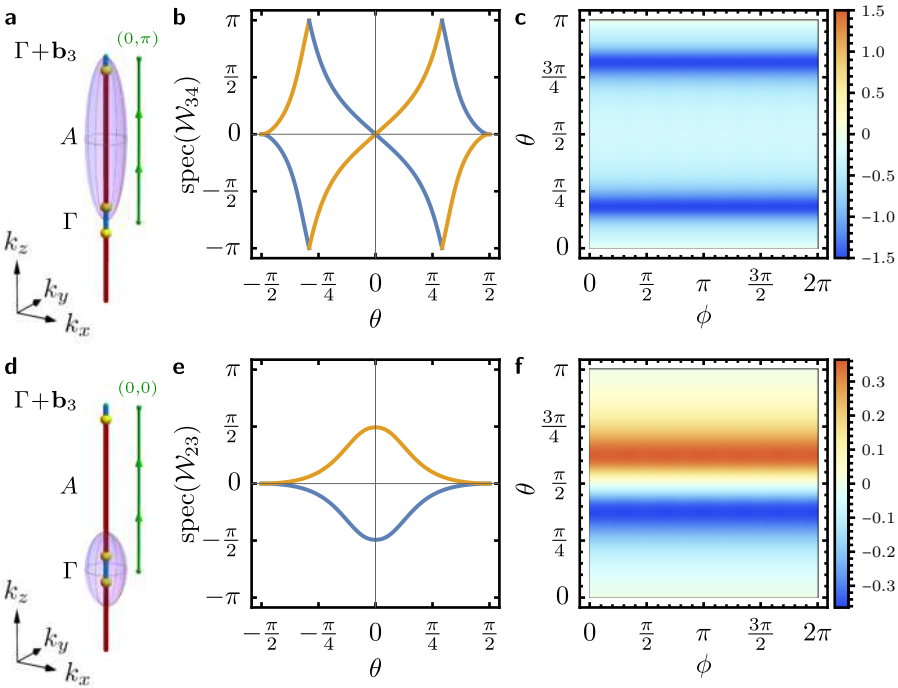

Figure 5.16.: Euler monopole charge in Li_2NaN. Verification of the Euler monopole charge $|\chi| = 2$ ($\chi = 0$) on the red (blue) nodal-line segment in Li_2NaN, based on the effective four-band tight-binding model. Panels (**a–c**) show illustrations and data for the red nodal-line segment (centered at A) and panels (**d–f**) for the blue segment (centered at Γ). (**a,d**) Nodal line and triple point configuration in the first one-and-a-half Brillouin zones $A\Gamma A\Gamma$. Nodal lines in the second and third band gap are shown in red and blue, respectively; triple points are shown in yellow. The purple ellipsoid defines the surface on which we compute the Euler class. (**b,e**) Spectrum of the Wilson loop operators $\mathcal{W}_{ij}(\theta)$ of bands i and j as indicated in the axis labels of constant latitude contours on the purple ellipsoid in panel (a,d), respectively, parametrized by the latitude angle θ. (**c,f**) Euler curvature $F(\theta, \phi)$ on the same ellipsoid. The curvature integrates to (c) $|\chi| = 2$ and (f) $\chi = 0$.

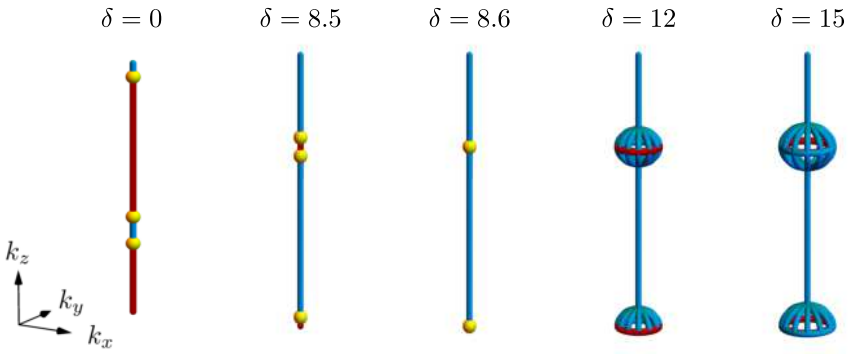

Figure 5.17.: Topological obstruction due to a nontrivial Euler monopole charge. The nodal lines of Li_2NaN near the rotation axis $A\Gamma A\Gamma$ spanning over one-and-a-half Brillouin zones are shown, with nodes in the second and third band gap shown in red and blue, respectively. The two triple points (yellow) can be forced to collide by tuning the parameter δ. The triple points collide at $\delta = -8.6$, at which point the red nodal-line segment, carrying the nontrivial Euler monopole charge, has been reduced to only a single touching point at A. Increasing δ even further, a horizontal red nodal ring forms in the ALH plane.

two triple points at the A point shares certain similarities with the Euler topology of topological acoustic triple points described by Ref. 208. The notable difference is that in our case the Euler-point degeneracy requires fine-tuning of the model parameters, whereas Ref. 208 finds this to be a *generic* feature of the acoustic phonon branches. In other words, if the collision had been enforced by symmetry, the triply-degenerate nodal point would be a quadratic touching point mentioned at the beginning of Chapter 4.

Finally, we also comment on the blue nodal-line segment. We can use the same three arguments to show that $\chi = 0$ in this case. For the argument based on the Zak-Berry phases, the relevant change is that now we need to consider bands 2 and 3, whose Zak-Berry phases along the green contour (cf. Fig. 5.16d) are both vanishing, such that $\chi = 0$. We arrive at the same conclusion by observing that the Wilson loop spectrum in Fig. 5.16e does not wind. Finally, in Fig. 5.16f, we present the Euler curvature for the purple ellipsoid shown in Fig. 5.16d. The Euler curvature turns out to be anti-symmetric with respect to reflection at $\theta = \pi/2$, such that integrating over the whole ellipsoid results in $\chi = 0$.

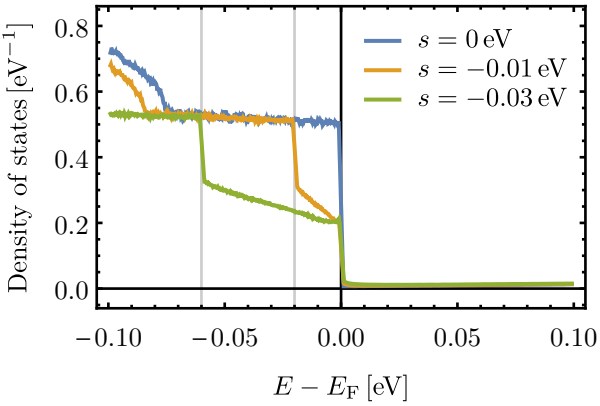

Figure 5.18.: Density of states of Li_2NaN. The density of states is shown as a function of energy E near the Fermi level E_F for various values of strain s. The data is smoothed by a moving average over ten points.

5.3.5. Density of states and optical conductivity

The nodal lines at the Fermi level and their splitting into multiband nodal links suggest a large tunability of the density of states at the Fermi level by varying the strain and nontrivial transport signatures. We first discuss the density of states and then the interband optical conductivity.

Density of states

In order to study both the density of states at the Fermi level as well as the optical conductivity, we first need to compute the Fermi energy as a function of strain. We do this by computing the *cumulative* density of states of the effective tight-binding model for various values of s using the Python package WannierBerri [242]. We use an initial momentum-space grid of 400^3 points and perform 40 iterations of adaptive refinement. By imposing charge neutrality, we can deduce the Fermi level E_F for each value of strain. With the Fermi level known, we compute the density of states near the Fermi level. Once more, we use an initial grid of 400^3 points, but then perform 2600 iterations of adaptive refinement. The results of this calculation for $s \in \{0, -0.01, -0.03\}$ eV are presented in Fig. 5.18. Note that in reality the jumps would be smeared over a region of approximately 40 meV due to the dispersion along ΓA which is assumed to be completely flat in the tight-binding model.

The single large jump from approximately $0.5\,\mathrm{eV}^{-1}$ to $7 \cdot 10^{-3}$ eV at the

Fermi level for the unstrained case is split into two consecutive jumps at approximately $-2s$ and slightly above the Fermi level for the strained case. Just as the single jump is explained by the flat dispersion of the two degenerate bands of the 2D irreducible representation along ΓA, the double jump follows from the same two bands after being split by the symmetry-breaking strain. This is consistent with the distance between the two jumps being $2s$ and thus equal to the energy splitting of the nitrogen $p_{x,y}$ orbitals.

Interband optical conductivity

Using the Kubo-Greenwood formula [243, 244] which we have implemented in the Python package WannierBerri [242], we compute the interband optical conductivity $\sigma_{ij}(\omega)$ with and without strain for the fitted tight-binding model. The *interband* contribution to the optical conductivity of a model described by a Bloch Hamiltonian with energies $\varepsilon_{n\mathbf{k}}$, where n is the band index and $\mathbf{k}$ the crystal momentum is given by

$$\sigma_{ij}(\omega) = \frac{e^2}{\hbar\Omega_\mathrm{c}} \sum_{n\neq m} (f_{m\mathbf{k}} - f_{n\mathbf{k}})\, \mathcal{A}_i^{nm}(\mathbf{k}) \mathcal{A}_j^{mn}(\mathbf{k}) \times \left(-\delta_\eta(\varepsilon_{m\mathbf{k}} - \varepsilon_{n\mathbf{k}} - \hbar\omega) + \mathrm{i}(\varepsilon_{m\mathbf{k}} - \varepsilon_{n\mathbf{k}}) \frac{\varepsilon_{m\mathbf{k}} - \varepsilon_{n\mathbf{k}} - \hbar\omega}{(\varepsilon_{m\mathbf{k}} - \varepsilon_{n\mathbf{k}} - \hbar\omega)^2 + \eta^2} \right). \tag{5.21}$$

Here, Ω_c is the unit cell volume, $f_{m\mathbf{k}} = f(\varepsilon_{m\mathbf{k}})$ the Fermi-Dirac distribution evaluated at the band energy $\varepsilon_{m\mathbf{k}}$, $\mathcal{A}^{nm}(\mathbf{k})$ the Berry connection defined in Eq. (3.8), δ_η an approximation of the delta-function with smearing parameter η. For the evaluation, we choose an initial grid of 625^3 points in momentum space with ten iterations of adaptive refinement and $\eta = 0.01\,\mathrm{eV}$. Note that in Eq. (5.21), the expression is split into a Hermitian part (first term on the second line) and an anti-Hermitian part (second term) which are evaluated separately.

Figure 5.19 shows the real and the imaginary part of all nonvanishing components of σ_{ij}. Note that in the absence of strain $\sigma_{xx} = \sigma_{yy}$ due to the symmetries. We observe that application of strain leads to a strong suppression of $\mathrm{Re}\,\sigma_{xx}$ for infrared frequencies $\hbar\omega \lesssim 2|s|$. This results from a suppression of optical transitions due to strain-induced mismatch between the chemical potential and the energy of the nodal lines [245], because at fixed filling the applied strain moves the blue (red) nodal line in Figs. 5.9c and 5.9d above (below) the chemical potential. We expect this depletion to be experimentally accessible in clean samples at low temperatures, when the Drude peak occurs at lower frequencies. Similarly, $\mathrm{Re}\,\sigma_{yy}$ is strongly suppressed for small $\hbar\omega$ when

increasing the strain parameter s. However, while the peak of $\mathrm{Re}\,\sigma_{xx}$ near $\hbar\omega \approx 0.32\,\mathrm{eV}$ is decreased when applying strain, it becomes more pronounced (and is shifted towards larger frequencies) for $\mathrm{Re}\,\sigma_{yy}$. While the imaginary part can be obtained from the real part using the Kramers-Kronig relation, it highlights the differences of σ_{xx} and σ_{yy} under strain. In both cases there is a large drop and thus a local minimum for finite but small frequencies, but in $\mathrm{Im}\,\sigma_{yy}$ this is accompanied by the formation of a sharp peak at higher frequencies. This peak is located roughly at $\hbar\omega \approx 2|s|$ and becomes very pronounced for large s.

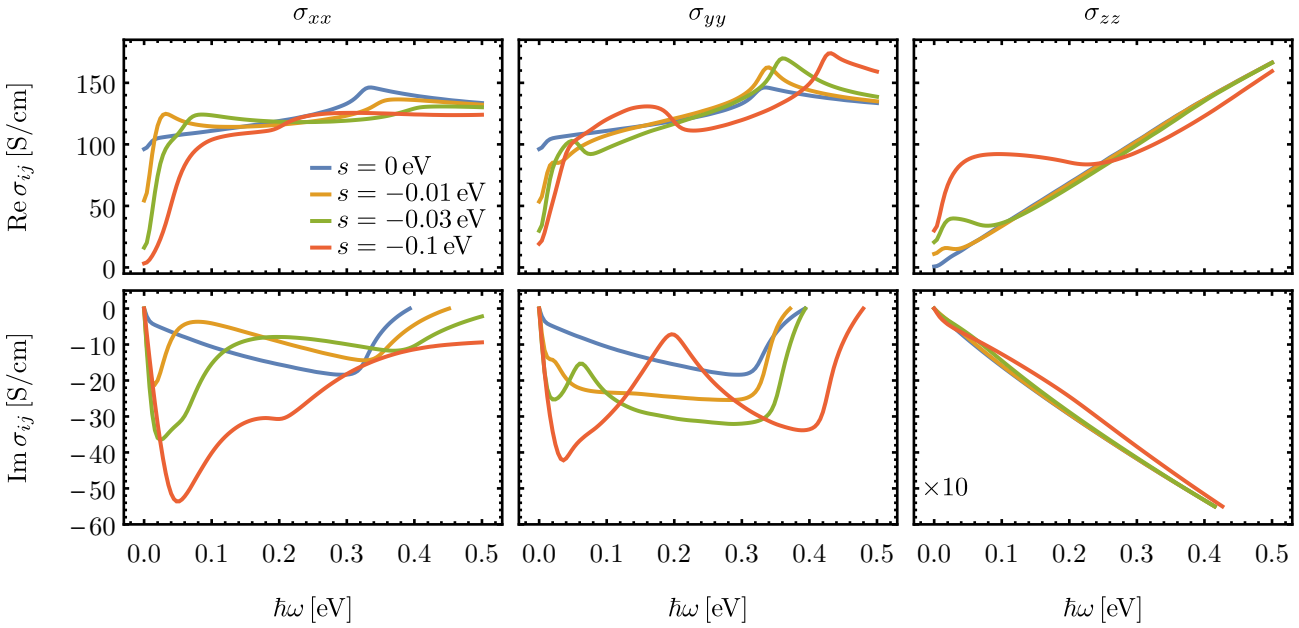

Figure 5.19.: Optical conductivity of Li_2NaN. The real and the imaginary part of the nonvanishing components σ_{xx}, σ_{yy}, and σ_{zz} of the interband optical conductivity $\sigma_{ij}(\omega)$ for different values of the strain parameter s as indicated in the inset legend in the top left. In the bottom right, the data was scaled down by a factor of 10, i.e., the actual range shown in that panel is $[-600, 0]$.

6. Multigap and higher-order topology of triple-point pairs

This chapter is largely based on the publication "Universal higher-order bulk-boundary correspondence of triple nodal points" [3]. Segments with significant text overlap with the published version may be subject to copyright by the American Physical Society.

In contrast to Weyl and Dirac points, a single triple point generically results in a *metallic* state, due to the imbalance between the degeneracy of the crossing bands as illustrated in Figs. 6.1a and 6.1b. However, *pairs* of triple points, formed when the 2D ICR consecutively crosses two 1D ICRs as shown in Fig. 6.1c, can result in a semimetal with small Fermi pockets, see Fig. 6.1d. We call such a triple-point configuration a *triple-point pair*. It involves three species of nodal lines, displayed in Figs. 6.1c and 6.1d in orange, red and blue according to increasing band index. The individual triple points correspond to locations where the 2D ICR transfers from one energy gap to another and we call the energy gap in which the nodal-line segment *between* the two triple points (here red) is formed the *principal gap* [66]. The classification derived in Chapter 4 applies to both triple points in the pair individually. However, the semimetallic nature of triple-point pairs makes them the better objects for studying associated topology.

We find that, similar to the pairs of triple points formed by the same triplet of bands that we discussed in Chapter 5, the four-band triple-point pairs considered in this chapter and the nodal-line segment connecting them can carry topological monopole charges in the presence of spinless space-time inversion symmetry. This aspect is discussed in Section 6.1, where we first argue analogously to Section 5.2 that type-(A,A) triple-point pairs always carry nontrivial second Stiefel-Whitney monopole charge (Section 6.1.1) and then compute the associated delicate invariant, the Euler monopole charge, more generally for any triple-point pair for which it is defined (Section 6.1.2).

In Section 6.2, we then derive a universal higher-order bulk-boundary correspondence for triple-point pairs. We find that each species of triple-point pairs can be assigned a unique value of a *fractional jump* of the hinge charge. As we argue in Section 6.5, the derived bulk-boundary correspondence applies

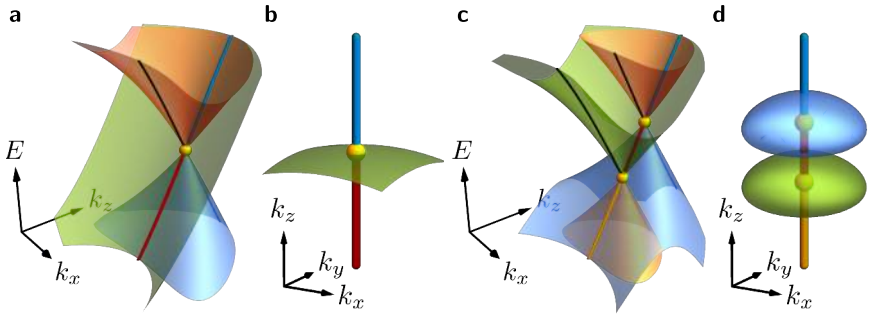

Figure 6.1.: Triple points and triple-point pairs. (**a**) Band structure of a triple point on a high-symmetry line along k_z for $k_y = 0$ with non-degenerate bands and nodal lines on the k_z-axis emphasized as black and colored lines, respectively. Triple points are indicated as yellow spheres. (**b**) Nodal-line structure of a type-A triple point and extended Fermi surface (green) for Fermi level at the triple-point energy indicating a metallic band structure. (**c**) Band structure of a triple-point pair involving four bands. (**d**) Nodal-line structure of a triple-point pair and small Fermi pockets (blue/green) for Fermi level between the two triple-points indicating a semimetallic band structure.

to *any* symmetry setting described by one of the Shubnikov space groups, including both spinful and spinless systems, non-magnetic and magnetic and symmorphic as well as nonsymmorphic space groups. In the presence of spinless $\mathcal{PT}$ symmetry, we find an additional correspondence with the values of the monopole charges and along the way also derive the bulk-boundary correspondence of rotation-symmetric 2D Stiefel-Whitney insulators (Section 6.2.1). To demonstrate our results we discuss a number of representative minimal tight-binding models in Section 6.3 and one material example, Sc_3AlC, based on first-principles calculations.

6.1. Monopole charges in presence of triple-point pairs

In this section we show that triple-point pairs in systems with spinless $\mathcal{PT}$ symmetry can be imbued with monopole charges whose values depend on the type of the triple points. For type-(A, A) triple-point pairs, this follows from an argument analogous to the one presented in Section 5.2.2. Taking the geometric interpretation of the second Stiefel-Whitney class as a linking number [199, 200], we find in Section 6.1.1 that such triple-point pairs carry

nontrivial second Stiefel-Whitney monopole charge. Then, in Section 6.1.2, we focus on triple-point pairs where the two occupied bands are separated from lower lying bands. In that case, the delicate extension of the second Stiefel-Whitney class, the Euler invariant, can be defined and we derive a symmetry-indicator formula for it.

6.1.1. Second Stiefel-Whitney monopole charge

We first consider type-(A,A) triple-point pairs and focus on the nodal-line segment between the two triple points. Recall from Chapter 4 that this nodal-line segment necessarily lies along some rotation axis of order four or six and, without loss of generality, we align k_z along that rotation axis. For simplicity, we assume that there are no additional band nodes in the principal gap for the considered range of k_z. Note that due to the periodicity in k_z, the minimal model of such a configuration involves *two* such triple-point pairs as illustrated in Fig. 6.2a. However, here it is sufficient to consider the upper half of the Brillouin zone, Fig. 6.2b, with one (red) nodal-line segment in the principal gap.

Following the argument in Section 5.1, adding a small C_n-breaking but $\mathcal{PT}$-preserving perturbation transforms triple points into multiband nodal links as illustrated in Fig. 6.2c. Crucially, the red nodal ring is linked with one nodal ring in each of the two adjacent gaps (orange and blue) and such linking was shown to be in a one-to-one correspondence with a nontrivial second Stiefel-Whitney monopole charge $w_2 = 1$ on a surface enclosing the nodal ring of interest, e.g., the purple ellipsoid in Fig. 6.2c [199]. By continuity we can switch this perturbation off without closing the principal energy gap on the enclosing surface, which allows us to assign the same monopole charge to the original nodal-line segment, i.e., on the ellipsoid in Fig. 6.2b. Similar to the consequences on the stability of the enclosed nodal-line segment we demonstrated in Section 5.3.4, $w_2 = 1$ guarantees the persistence of the red nodal line even when the rotational symmetry is broken (and the 2D ICR split) as long as the $\mathcal{PT}$ symmetry is preserved.

We next discuss implications of the monopole charge for the bulk topology, analogously to the discussion for a pair of Weyl points in Section 3.3 around Fig. 3.6. Assuming there are no additional nodal lines in the principal gap in the relevant k_z-range, the ellipsoid enclosing the red nodal-line segment can be continuously deformed as illustrated in Fig. 6.3a until it spans the whole Brillouin zone in k_x- and k_y-directions for a finite range of k_z. Due to the periodicity in the Brillouin zone, the contributions from opposite vertical faces of that surface cancel and we are left with the two horizontal planes T^2_1 and T^2_2 shown in Fig. 6.3b. Note that these are actually 2D tori which can be inter-

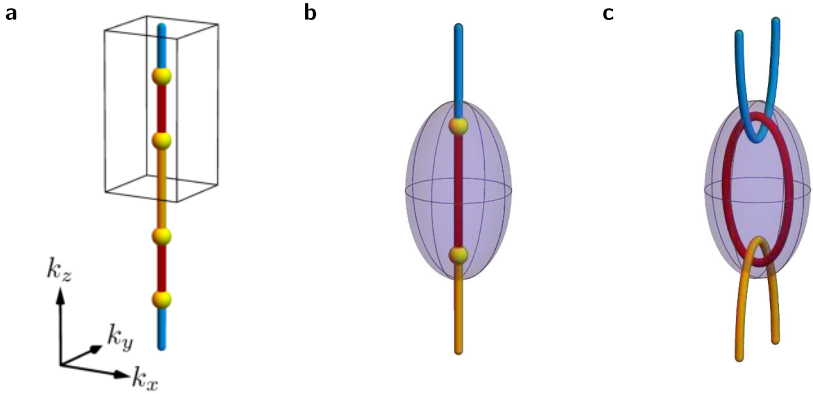

Figure 6.2.: Second Stiefel-Whitney monopole charge from triple-point pairs. (**a**) Two pairs of type-A triple points (yellow dots) formed by consecutive triplets of bands. All triple points are protected by C_4 or C_6 symmetry with respect to the z-axis. In k_z-direction the full extent of the Brillouin zone is shown. Nodal lines in the first, second and third gap of a four-band model are shown in orange, red and blue, respectively. (**b,c**) Close-up of the boxed region in (a) with the purple ellipsoid, on which the second Stiefel-Whitney class is computed with respect to the principal (red) band gap. (**c**) Multiband nodal links that form after breaking the rotational symmetry. The red nodal ring carries a nontrivial value of the second Stiefel-Whitney class. By continuity, the red nodal segment in (b) also carries a nontrivial second Stiefel-Whitney class.

preted as the Brillouin zones of a one-parameter family of effective 2D systems, namely ones with 2D Bloch Hamiltonians $H_{k_z}(k_x, k_y) := H(k_x, k_y, k_z)$.

Owing to the continuous deformation of the surface, the second Stiefel-Whitney class does not change, such that $w_2(\mathsf{T}_1^2) + w_2(\mathsf{T}_2^2) = 1 \mod 2$. Consequently, one of the two planes will be trivial, $w_2 = 0$, and the other nontrivial, $w_2 = 1$. Viewing them as 2D systems as described above, the latter is a 2D insulator with nontrivial second Stiefel-Whitney class, called *Stiefel-Whitney insulator* [199]. In the simultaneous presence of C_2 rotational and chiral symmetry, Stiefel-Whitney insulators were shown [196, 204] to have robust zero-energy corner states accompanied by half-integer corner charges. Our situation is different: we do not assume chiral symmetry, and the order of rotational symmetry necessary to protect type-A triple points is $n \in \{4, 6\}$. We derive the previously unknown (higher-order) bulk-boundary correspondence for (non-chiral) Stiefel-Whitney insulators with rotational symmetry in

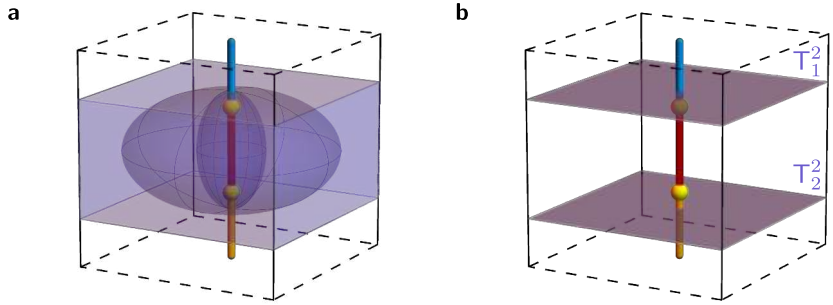

Figure 6.3.: Stiefel-Whitney insulator with rotational symmetry. Relation between a nodal-line segment carrying a nontrivial second Stiefel-Whitney monopole charge, and a pair of two-dimensional insulators characterized by the $\mathbb{Z}_2$-valued second Stiefel-Whitney class. The black frame represents the complete momentum-space extent of the Brillouin zone in the two horizontal directions (solid black lines), but not in the vertical direction (dashed black lines). (**a**) The monopole charge of the red nodal-line segment is calculated on a surface enclosing it (innermost purple ellipsoid), which can be continuously inflated (second purple ellipsoid) until it fills the whole Brillouin zone in k_x- and k_y-directions (purple cuboid). (**b**) The purple cuboid in (a) is equivalent to two horizontal planes (actually tori) T_1^2 and T_2^2 at the appropriate k_z-values.

Section 6.2.1; in particular, we show that the corner charge in the presence of trivial (nontrivial) second Stiefel-Whitney class is quantized to even (odd) multiples of $\frac{e}{n}$. We subsequently apply the result to study the bulk-hinge correspondence for triple-point pairs of both type A and type B in Section 6.2.2.

6.1.2. Euler monopole charge

If the two occupied bands involved in the triple-point-pair formation are separated from lower lying occupied bands by an energy gap, the second Stiefel-Whitney can be refined to the *Euler* monopole charge. Note that this is a different situation from the one discussed in Section 5.2: here we consider a surface enclosing a triple-point pair, i.e., two triple points formed by two triplets of bands that are shifted by one relative to each other as shown in Fig. 6.2b. As we have seen in Section 3.4.1, monopole charges such as the second Stiefel-Whitney and the Euler monopole charge can be inferred from the winding of the Wilson loop spectrum. Symmetries constrain the latter [142, 246, 247] and can therefore lead to symmetry-indicator formulas for the monopole charges. To our knowledge, no such symmetry-indicator formulas for the Euler

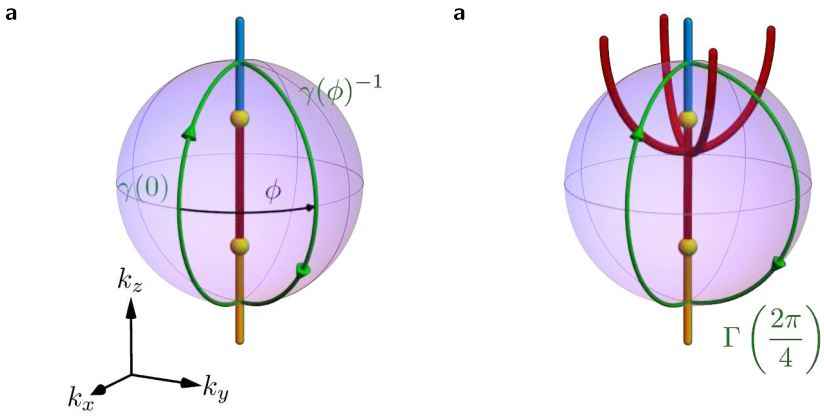

Figure 6.4.: Derivation of symmetry indicator for the Euler monopole charge. (**a**) Definition of the closed contours $\Gamma(\phi) = \gamma(\phi)^{-1} \circ \gamma(0)$ (green) on which the Wilson loop operator $\mathcal{W}(\phi)$ is computed. The spherical surface (purple) is covered by these contours as the argument is increased in the range $\phi \in [0, 2\pi)$. If the surface is not crossed by any other nodal lines than the orange and blue ones, the Euler monopole charge χ can be defined and is determined by the winding of the Wilson loop spectrum. This is the case, for example, if there are no red nexus points enclosed in the surface. (**b**) In other cases, e.g., if there is exactly one red nexus point enclosed, red nodal lines crossing the surface are *always* present. This is indicated by a π Berry phase on the path $\Gamma(2\pi/n)$, where n is the order of the rotational symmetry. The nontrivial Berry phase implies that $\Gamma(2\pi/n)$ encircles an odd number of nodal lines in the principal gap (red nodal lines).

monopole charge in the presence of rotational symmetry have been previously derived, therefore we do that here. Along the way, we identify that triple-point pairs formed by certain combinations of ICRs are necessarily associated with extended nodal lines in the principal gap, which prevents the system from exhibiting higher-order topological signatures and the monopole charge from being defined. The mathematical details of these derivations are relegated to Appendix E, while here we only outline the main steps and results.

To derive the symmetry-indicator formulas, we consider a spherical surface enclosing part of a HSL with C_n rotational symmetry in its little co-group, e.g., containing a triple-point pair, as illustrated in Fig. 6.4a. We refer to the two points where the sphere is intersected by the rotation axis as the south and north pole. Let N and N_{occ} be the total number of bands and the number of occupied bands, respectively. We assume the system to have

space-time inversion symmetry $\mathcal{PT}$ satisfying $(\mathcal{PT})^2 = +1$, such that there is a basis in which the corepresentation of $\mathcal{PT}$ is the identity matrix and the Bloch Hamiltonian a real symmetric matrix. Let further $\mathfrak{D}_0$ and $\mathfrak{D}_1$ label the symmetry representations of the occupied bands in that basis at the south and north pole of the spherical surface, respectively. In Appendix E.1 we show that the Wilson loop operator $\mathcal{W}(\phi)$ computed on the path

$$\Gamma(\phi) = \gamma(\phi)^{-1} \circ \gamma(0) \tag{6.1}$$

illustrated in green in Fig. 6.4a is constrained by C_n symmetry according to

$$\mathcal{W}\left(\phi + \frac{2\pi}{n}\right) = \mathfrak{D}_0(C_n) P(\phi)^\dagger \mathfrak{D}_1(C_n)^\dagger P(\phi) \mathcal{W}(\phi), \tag{6.2}$$

where $P(\phi) \in \mathsf{SO}(N_{\text{occ}})$ is defined by parallel transport in Eq. (E.17) in Appendix E.1. Note that in Eq. (6.1), one first traverses the path appearing to the right of the composition symbol "$\circ$".

For arbitrary N_{occ}, we consider the implication of Eq. (6.2) for the Berry phase of the occupied bands on the contours $\Gamma(\phi)$. As we discussed in Section 3.1.1, the Berry phase is given by $\varphi = \arg\det \mathcal{W}$ [234], such that

$$\varphi\left(\phi + \frac{2\pi}{n}\right) = \varphi(\phi) + \arg\det\left[\mathfrak{D}_0(C_n)\mathfrak{D}_1(C_n)^\dagger\right] \mod 2\pi. \tag{6.3}$$

Due to $\mathcal{PT}$ symmetry, $\Delta\varphi = \varphi(\phi + 2\pi/n) - \varphi(\phi)$ is quantized to 0 versus π. If $\Delta\varphi = \pi$, there is an odd number of nodal lines in the principal gap crossing the surface in each sector $[\phi, \phi + 2\pi/n]$, cf. Fig. 6.4b. This implies that the principal gap is necessarily closed somewhere on the enclosing surface, thus preventing us from assigning a monopole charge to the enclosed triple-point pair. We will see in Section 6.2.2 that this condition also prevents the corresponding triple-point pairs from exhibiting the higher-order signature at the hinges.

In the remainder of this subsection, we call a triple-point pair *admissible* whenever the principal gap on the enclosing sphere can be open. This corresponds to the case with $\Delta\varphi = 0$, which is equivalent to requiring

$$\det\left[\mathfrak{D}_0(C_n)\mathfrak{D}_1(C_n)^\dagger\right] = 1. \tag{6.4}$$

By our initial assumption, the two occupied bands involved in the triple-point pair are separated from lower lying occupied bands by an energy gap on the whole surface, such that we can ignore the lower lying bands and set $N_{\text{occ}} = 2$. Then, the absence of nodes in the principal gap implies that the Euler monopole charge on the sphere is well-defined and given by the winding number of the

Pfaffian of the logarithm of $\mathcal{W}(\phi)$ [66]. In Appendix E.3, we show that if $\mathcal{D}_0(C_n), \mathcal{D}_1(C_n) \in \mathsf{SO}(2)$, then Eq. (6.2) simplifies to

$$\mathcal{W}\left(\phi + \frac{2\pi}{n}\right) = \mathcal{D}_0(C_n)\ \mathcal{D}_1(C_n)^\dagger \mathcal{W}(\phi). \tag{6.5}$$

Since the n^{th} power of $\mathcal{D}_{0,1}(C_n)$ gives the identity, it follows that for $i \in \{0,1\}$: $\mathcal{D}_i(C_n) = \mathrm{e}^{-\frac{2\pi \mathrm{i}}{n} r_i^{(n)} s_y}$ with $r_i^{(n)} \in \mathbb{Z}$ and the Pauli matrix s_y acting on the space of the two valence bands. Then, we extract the following symmetry-indicator formula for the Euler monopole charge χ

$$\chi = r_1^{(n)} - r_0^{(n)} \mod n. \tag{6.6}$$

Note that χ is only gauge-invariant up to sign and that the relevant topological invariant therefore is $|\chi|$.

Recall that the parity of χ is the second Stiefel-Whitney class

$$w_2 = \chi \mod 2 = r_1^{(n)} - r_0^{(n)} \mod 2. \tag{6.7}$$

Thus, Eq. (6.7) is a symmetry-indicator formula for the second Stiefel-Whitney monopole charge in the presence of C_n rotational symmetry as long as n is even (otherwise the parity of χ is undetermined). Note that Eq. (6.7) only applies to systems where the two occupied bands are separated from all other bands on the ellipsoid, i.e., where there are no nodal lines in the gap below the orange one crossing the ellipsoid. In the next section, we derive a more general symmetry indicator formula for the second Stiefel-Whitney class, relaxing that condition.

6.2. Higher-order bulk-boundary correspondence

The fact that triple-point pairs can carry nontrivial monopole charges, raises the question about boundary signatures. Indeed, we find that semimetallic triple-point pairs are *generally* characterized by a higher-order bulk-boundary correspondence: each species of triple-point pair can be assigned a unique value of a *fractional jump* of the hinge charge. As we will see, this goes beyond the setting of spinless $\mathcal{PT}$ symmetry and even applies to spinful systems. However, in the presence of $\mathcal{PT}$ symmetry, multigap topology gives an additional geometric perspective in terms of monopole charges with a correspondence between the second Stiefel-Whitney monopole charge of the nodal-line segment connecting the two triple points and the value of the hinge-charge jump: a trivial second Stiefel-Whitney monopole charge implies a $\pm\frac{2e}{n}$

jump, while a nontrivial value results in a jump by $\pm\frac{e}{n}$. We remark that the hinge-charge jump associated with a triple-point pair always occurs without a change in the bulk polarization. This implies that if there is no fractional surface charge appearing on one side of the triple-point pair, then there is also no fractional surface charge on the other side of the triple-point pair, thus guaranteeing that the fractional jump in the hinge charge is observable.

The diverse range of symmetry combinations seemingly complicates the analysis. However, it turns out that all the cases of interest can be obtained by a proper perturbation of a system with $\mathcal{PT}$ symmetry. Therefore, our approach to analyze the topological invariants and the bulk-hinge correspondence of triple-point pairs is to first deal with the $\mathcal{PT}$-symmetric cases, and afterwards consider the effect of perturbations to derive the results also for the $\mathcal{PT}$-broken cases. In Section 6.5, we take two additional steps: we generalize to nonsymmorphic space groups and to the spinful setting.

This section is structured as follows. We begin in Section 6.2.1 by discussing the 2D Stiefel-Whitney insulator with C_n-rotational symmetry. There, we adapt the C_2 symmetry-indicator formula [196] for the second Stiefel-Whitney class to C_n-rotational symmetry, where $n \in \{4, 6\}$, and show that the value of the second Stiefel-Whitney class constrains the possible fractional corner charges of the C_n-symmetric 2D system with vanishing bulk polarization. According to Fig. 6.3, this can then be applied to 3D systems with triple-point pairs where the change in the second Stiefel-Whitney class is exactly equal to the corresponding monopole charge, and similarly the change in corner charge gives the hinge-charge jump. Subsequently, in Sections 6.2.2 and 6.2.3, we combine that with the classification of triple-point pairs to derive the general bulk-hinge correspondence principle for all possible triple-point-pair configurations in $\mathcal{PT}$-symmetric systems. Finally, in Section 6.2.4, we discuss the effect of breaking various symmetries. In particular, we extend the bulk-hinge correspondence principle to triple-point pairs protected by *all* magnetic point groups listed in Table 4.1.

6.2.1. Stiefel-Whitney insulator with rotational symmetry

We consider an insulating 2D system with $C_2\mathcal{T}$ and C_n symmetry, where C_2 and C_n are with respect to the same axis perpendicular to the system. Due to the $C_2\mathcal{T}$ symmetry (where C_2 acts like inversion in 2D), the insulator is characterized by the second Stiefel-Whitney class, while the C_n symmetry implies fractional corner charges [147, 150, 151] if the edge charge vanishes. For simplicity, we assume that all the positive ionic charge, which compensates for the negative charge of the filled electron bands, is located at the maximal Wyckoff position $1a$, i.e., the center of the square unit cell, see Fig. 3.3 for the

location of the Wyckoff positions. As foreshadowed by Eqs. (6.6) and (6.7), we will see in Section 6.2.2 that for $n = 3$, the second Stiefel-Whitney class is not symmetry indicated. Thus, we restrict the present discussion to $n = 4, 6$, which implies that C_2 and $\mathcal{T}$ are also symmetries of the system.

Second Stiefel-Whitney class

In the presence of C_2 symmetry, the second Stiefel-Whitney class is symmetry indicated [199] with the symmetry indicator,

$$w_2 = \sum_{\Pi \in \mathrm{TRIM}} \left\lfloor \frac{1}{2} \#\Pi_2^{(2)} \right\rfloor \mod 2, \tag{6.8}$$

given in the notation established in Section 3.2, in particular Eqs. (3.25) and (3.26). In the presence of C_4 and C_6, Eq. (6.8) simplifies due to constraints on $\#\Pi_2^{(2)}$ posed by the additional symmetries.

We first consider C_4 symmetry. The four time-reversal invariant momenta are Γ, X, X' and M, where X and X' are equivalent, see Fig. 3.3k. According to Eq. (6.8), a nontrivial second Stiefel-Whitney class is equivalent to

$$\left\lfloor \frac{1}{2} \#\Gamma_2^{(2)} \right\rfloor + 2 \left\lfloor \frac{1}{2} \#X_2^{(2)} \right\rfloor + \left\lfloor \frac{1}{2} \#M_2^{(2)} \right\rfloor = 1 \mod 2. \tag{6.9}$$

This does not constrain $\#X_2^{(2)}$ at all, but it is equivalent to either

$$\begin{aligned} & \left\lfloor \tfrac{1}{2} \#\Gamma_2^{(2)} \right\rfloor = 0 \mod 2 \quad \wedge \quad \left\lfloor \tfrac{1}{2} \#M_2^{(2)} \right\rfloor = 1 \mod 2 \\ \Leftrightarrow \quad & \#\Gamma_2^{(2)} \in \{0, 1\} \mod 4 \quad \wedge \quad \#M_2^{(2)} \in \{2, 3\} \mod 4 \\ \Rightarrow \quad & \#M_2^{(2)} - \#\Gamma_2^{(2)} = \left[M_2^{(2)} \right] \in \{1, 2, 3\} \mod 4 \end{aligned}$$

or the same with Γ and M exchanged, where the latter implies $[M_2^{(2)}] \in \{1, 2, 3\}$ mod 4 as well. Thus, $w_2 = 1$ implies $[M_2^{(2)}] \in \{1, 2, 3\}$ mod 4. On the other hand, $w_2 = 0$ implies

$$\begin{aligned} & \left\lfloor \tfrac{1}{2} \#\Gamma_2^{(2)} \right\rfloor = \left\lfloor \tfrac{1}{2} \#M_2^{(2)} \right\rfloor \mod 2 \\ \Rightarrow \quad & \left[M_2^{(2)} \right] \in \{0, 1, 3\} \mod 4. \end{aligned}$$

Furthermore, the presence of time-reversal and C_4 symmetry imply [147] that $[M_2^{(4)}] = [M_4^{(4)}]$, such that together with $[M_2^{(2)}] = [M_2^{(4)}] + [M_4^{(4)}]$, which follows from $C_4^2 = C_2$, we find

$$\left[M_2^{(2)} \right] = 2 \left[M_2^{(4)} \right]. \tag{6.10}$$

Therefore, $[M_2^{(2)}]$ has to be even. Since we already restricted $[M_2^{(2)}]$ for $w_2 = 1$ to the set $\{1, 2, 3\} \mod 4$ (and to the set $\{0, 1, 3\} \mod 4$ for $w_1 = 0$), selecting the even element of the corresponding set results in

$$w_2 = \frac{1}{2}\left[M_2^{(2)}\right] \mod 2 = \left[M_2^{(4)}\right] \mod 2. \tag{6.11}$$

Next, we consider C_6 symmetry, where the four time-reversal invariant momenta are Γ, M, M' and M'' with the latter three being equivalent, see Fig. 3.3l. Correspondingly,

$$\left\lfloor \frac{1}{2}\#\Gamma_2^{(2)} \right\rfloor + 3\left\lfloor \frac{1}{2}\#M_2^{(2)} \right\rfloor = 1 \mod 2. \tag{6.12}$$

A nontrivial value $w_2 = 1$ implies, in analogy with the analysis of the C_4-symmetric case, that

$$\left[M_2^{(2)}\right] \in \{1, 2, 3\} \mod 4, \tag{6.13}$$

while $w_2 = 0$ implies

$$\left[M_2^{(2)}\right] \in \{0, 1, 3\} \mod 4. \tag{6.14}$$

For the next step in our reasoning we need to apply the following property: if $[M_1^{(2)}] = 1 \mod 2$, then the bulk is necessarily gapless. This can be seen as follows. By assumption, the number of occupied bands with C_2-rotation eigenvalue 1 changes by an odd number between Γ and M

$$\#M_1^{(2)} - \#\Gamma_1^{(2)} = [M_1^{(2)}] = 1 \mod 2. \tag{6.15}$$

Since the C_2 symmetry acts as inversion on the 1D Brillouin-zone segment $\Gamma M \Gamma$, Eq. (6.15) implies [99] that the occupied bands carry a total Berry phase π on that segment. We further consider the triangle formed by the $\Gamma M \Gamma$ paths of the three Brillouin zones around a K point, as illustrated in Fig. 6.5. Due to the six-fold rotational symmetry the three sides of the triangle all contribute $\pi \mod 2\pi$ to the Berry phase, such that the total Berry phase along the triangular contour is $\pi \mod 2\pi$, indicating that there is an odd number of band nodes (formed *between* the occupied and the unoccupied bands) inside the triangle, i.e., the bulk is gapless. Conversely, a gapped bulk implies $[M_1^{(2)}] = 0 \mod 2$. Noting that $[M_1^{(2)}] = -[M_2^{(2)}]$, because $\sum_{p=1}^{n}[\Pi_p^{(n)}] = 0$ [147], an insulating bulk band structure equivalently requires $[M_2^{(2)}]$ to be even. Therefore,

$$w_2 = \frac{1}{2}\left[M_1^{(2)}\right] \mod 2. \tag{6.16}$$

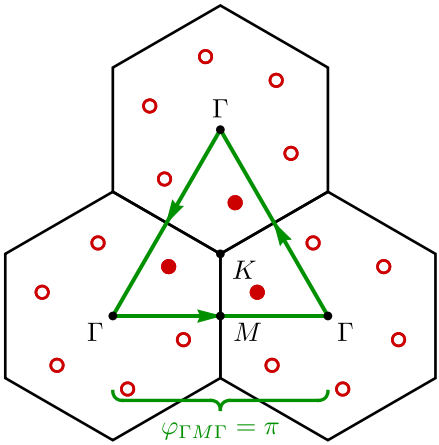

Figure 6.5.: Brillouin zones around a K point of a C_6-symmetric model. Assuming $[M_1^{(2)}] = 1 \mod 2$ the total Berry phase $\varphi_{\Gamma M\Gamma}$ of the occupied bands along the closed contour $\Gamma M\Gamma$ equals π. Therefore, the Berry phase along the triangular contour (green) is also $\varphi_{\triangle} = 3\pi = \pi \mod 2\pi$. The result implies that the triangle encloses an odd number of band nodes in the principal gap (red disks), i.e., the system is *not an insulator*.

We have therefore found that in the presence of an enlarged rotational symmetry, the second Stiefel-Whitney class is given by the symmetry-indicator formulas

$$C_4: \quad w_2 = \left[M_2^{(4)}\right] \mod 2 \tag{6.17a}$$

$$C_6: \quad w_2 = \frac{1}{2}\left[M_1^{(2)}\right] \mod 2. \tag{6.17b}$$

Corner charge

Recall from Section 3.2.1, that assuming the specific geometries of the 2D crystals shown in Fig. 6.6a, the corner charges are given by [151]

$$Q_{\llcorner}^{(4)} = \frac{e}{4}\left(\mp\left[X_1^{(2)}\right] + 2\left[M_1^{(4)}\right] + 3\left[M_2^{(4)}\right]\right) \mod e, \tag{6.18a}$$

$$Q_{\llcorner}^{(6)} = \frac{e}{4}\left[M_1^{(2)}\right] + \frac{e}{6}\left[K_1^{(3)}\right] \mod e, \tag{6.18b}$$

where $e < 0$ is the electron charge and the sign in front of $[X_1^{(2)}]$ depends on whether the center of the C_4-symmetric crystal is located at Wyckoff position

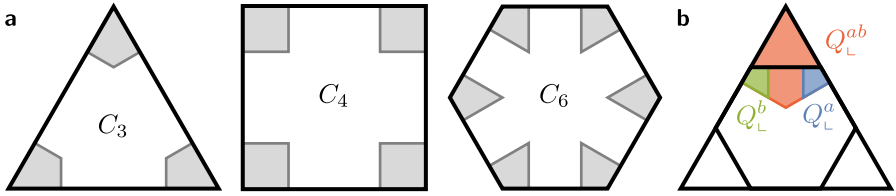

Figure 6.6.: Geometry for hinge and corner charges. (**a**) The C_n-symmetric cross-section geometries for which the hinge charges are defined, and for which the values listed in Table 6.2 apply. The corners (gray regions) in the cross sections correspond to the hinges in the 3D system. (**b**) Deformation of the C_6-symmetric sample (inner hexagon) to a C_3-symmetric sample (outer triangle). Two corners (blue and green) of the hexagon with corner charges $Q_{\llcorner}^{a}$ and $Q_{\llcorner}^{b}$ merge into a single corner (red) of the triangle with corner charge $Q_{\llcorner}^{ab} = Q_{\llcorner}^{a} + Q_{\llcorner}^{b}$.

$1a$ (upper sign) or $1b$ (lower sign), see Fig. 3.3g. Note that, consistent with the assumptions in the present discussion, Eq. (6.18) assumes the presence of time-reversal symmetry $\mathcal{T}$ with $\mathcal{T}^2 = +1$. For the corner charge to be well-defined, the bulk polarization needs to vanish. For $n = 4$ the polarization vanishes if and only if $[X_1^{(2)}] = 0 \mod 2$, while for $n = 6$ it always vanishes [147]. Therefore, vanishing polarization also implies that the center-dependent sign ambiguity in Eq. (6.18a) drops from our analysis. Combining the assumption of vanishing polarization with Eqs. (6.17) and (6.18), we now show that the nontrivial value $w_2 = 1$ constrains the corner charge.

Using Eq. (6.11) and assuming vanishing bulk polarization, we can rewrite Eq. (6.18a) as

$$Q_{\llcorner}^{(4)} = \frac{e}{4}\left(2\left[M_1^{(4)}\right] + 3w_2\right) \mod \tfrac{e}{2}, \tag{6.19}$$

where the $\frac{e}{2}$ ambiguity is a consequence of Eq. (6.11). We observe that for $w_2 = 1$ the term in the brackets is an odd integer, while it is an even integer for $w_2 = 0$. This restricts the fractional part of $Q_{\llcorner}^{(4)}$ to $\pm\frac{e}{4}$ in the first, and to 0 or $\frac{e}{2}$ in the second case. Analogously, using Eq. (6.16) we can rewrite Eq. (6.18b) for the corner charge as

$$Q_{\llcorner}^{(6)} = \frac{e}{6}\left(\left[K_1^{(3)}\right] + 3w_2\right) \mod e. \tag{6.20}$$

It follows from time-reversal symmetry that at high-symmetry points states have either real rotation eigenvalues or come in pairs with complex conjugate rotation eigenvalues. In particular, this implies that $[K_2^{(3)}] = [K_3^{(3)}]$ and

because of the same number of filled bands at points K and Γ, it follows that

$$\left[K_1^{(3)}\right] = -\left[K_2^{(3)}\right] - \left[K_3^{(3)}\right] = 0 \mod 2, \tag{6.21}$$

i.e., $[K_1^{(3)}]$ is an even integer. Thus, the term in brackets in Eq. (6.20) is an odd integer for $w_2 = 1$ and an even integer for $w_2 = 0$. This restricts $Q_{\llcorner}^{(6)}$ to $\pm\frac{e}{6}$ or $\frac{e}{2}$ in the first case, and to 0 or $\pm\frac{e}{3}$ in the second case.

In summary, we have found that $w_2 = 1$ constrains the corner charge for C_4-symmetric Stiefel-Whitney insulators to

$$Q_{\llcorner}^{(4)} \in \left\{\pm\frac{e}{4}\right\} \mod e \tag{6.22a}$$

and for C_6-symmetric Stiefel-Whitney insulators to

$$Q_{\llcorner}^{(6)} \in \left\{\pm\frac{e}{6}, \frac{e}{2}\right\} \mod e, \tag{6.22b}$$

i.e., to *odd* multiples of $\frac{e}{n}$, whereas the complementary fractional values correspond to insulators with $w_2 = 0$.

Before applying the presented formulas to study triple-point pairs in 3D, we briefly comment on some relations of the result in Eq. (6.22) to previous works. First, note that in the presence of chiral symmetry, the corner charge can only attain value 0 or $\frac{e}{2} \mod e$. This can be easily understood as follows. If the occupied states carry localized corner charge $Q \mod e$, then (by completeness of the Hilbert space) the unoccupied states carry localized corner charge $-Q \mod e$. Chiral symmetry is local in real space and maps occupied onto unoccupied states, therefore guaranteeing that $Q = -Q \mod e$. That equation has two solutions: $Q = 0, \frac{e}{2} \mod e$. On the other hand, our derivation above reveals that the value $w_2 = 1$ can result in corner charge $Q_{\llcorner}^{(6)} = \frac{e}{2} \mod e$ if and only if $[K_1^{(3)}] = 0 \mod 6$. This is compatible with the finding of Ref. 248 which showed that chiral symmetry that commutes with C_3-rotation implies $[K_1^{(3)}] = 0$. The value $\frac{e}{2} \mod e$ of the corner charge was also reported in the study of a Stiefel-Whitney insulator model with chiral and C_6 symmetry by Ref. 196. Second, the result in Eq. (6.22a) implies that the three conditions (1) C_4 symmetry, (2) $w_2 = 1$, and (3) vanishing polarization are incompatible with (4) the presence of chiral symmetry; equivalently, Stiefel-Whitney insulator with chiral and C_4 symmetry must necessarily have gapless edges. This finding is compatible with the observations of Ref. 192 made in the context of second-order nodal-line semimetals.

6.2.2. Triple-point configurations with hinge charges

In this section we apply the symmetry-indicator formulas from the previous section to study four-band triple-point-pair configurations in $\mathcal{PT}$-symmetric systems. While in Section 6.1.1 we have assumed the triple-point pairs to be demarcated by type-A triple points, we here generalize to the case of both type-A and type-B triple points. Our result provides the correspondence between triple-point pairs, their second Stiefel-Whitney monopole charge (if it is defined), and the higher-order signature in the fractional hinge charge. For simplicity, we first focus on triple points in crystals with a symmorphic space group and generalize the results to nonsymmorphic space groups in Section 6.5.1. Furthermore, we simplify the notation by omitting the bar in $\overline{D}$ ($\overline{\mathcal{D}}$) and denoting ICRs by D (corepresentations by $\mathcal{D}$), because an explicit distinction between representations and corepresentations is not necessary in this chapter.

Based on the classification derived in Chapter 4, we know that triple points can be stabilized in spinless systems on HSLs with trigonal, tetragonal or hexagonal symmetry (cf. Table 4.1). Such HSLs arise in space groups with the corresponding symmetry. For crystals with C_n symmetry, where $n \in \{2, 3, 4, 6\}$, some representative HSLs with the specified symmetry (namely ones that are realized in space groups with prismatic Brillouin zones), are listed at the top of Table 6.2 (however, the derived bulk-hinge correspondence, encoded by $\Delta Q_{\llcorner}$, χ and w_2, applies equally to *all* HSLs with the prescribed symmetry). Then, given the little co-group of any such HSL, we consider all possible combinations of ICRs leading to triple-point pairs. Recall that a triple-point pair requires a 2D ICR (D^{2D}) to be crossed consecutively by two 1D ICRs (D_a^{1D} and D_b^{1D}), as illustrated in Fig. 6.7, and can thus be characterized by the triplet $(D^{\mathrm{2D}}; D_a^{\mathrm{1D}}, D_b^{\mathrm{1D}})$ (here, the ordering of the 1D ICRs is unimportant). We first discuss which combinations of ICRs lead to admissible triple-point pairs. Then, we summarize the higher-order bulk-boundary correspondence of triple-point pairs, listed in the bottom of Table 6.2, which we subsequently derive by applying the symmetry-indicator formulas from Section 6.2.1. Finally, we show that there is no surface-charge jump, which is a necessary prerequisite for the hinge-charge jump to be well-defined.

Choosing k_z along the HSL and taking 2D cuts of the system at constant k_z, we obtain a series of 2D systems with Hamiltonian $H_{k_z}(k_x, k_y)$. We assume those 2D systems each to be at half-filling, thereby defining their chemical potential $\mu_{\mathrm{f}}(k_z)$. This fixes the principal gap to be the second one, such that principal nodes are indicated in red, cf. Fig. 6.7. Upon increasing k_z, the system goes from having D^{2D} occupied (to the left of the first triple point) to instead having $(D_a^{\mathrm{1D}}, D_b^{\mathrm{1D}})$ occupied (to the right of the second triple point).

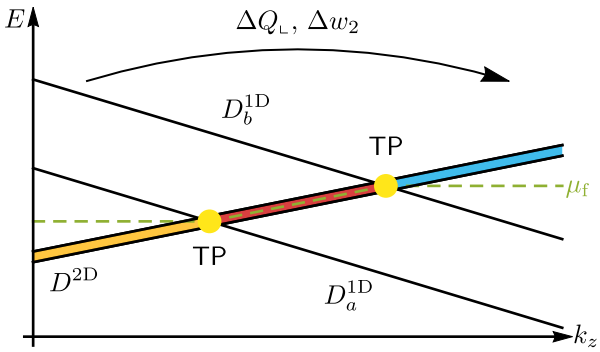

Figure 6.7.: Convention for corepresentations involved in triple-point pairs. Convention for defining the jump of the fractional hinge charge ($\Delta Q_{\llcorner}$) and of the second Stiefel-Whitney monopole (Δw_2) associated with a pair of triple points (yellow dots) in a four-band configuration. The black lines indicate the band structure along a high-symmetry line, with the 2D irreducible corepresentation (ICR) D^{2D} passing from the bottom (orange) to the central (red) to the upper (blue) energy gap with increasing momentum k_z due to crossing two 1D ICRs D_a^{1D} and D_b^{1D}. The green dashed line (μ_f) indicates half-filling at various k_z. The quantities $\Delta Q_{\llcorner}$ and Δw_2 associated with the triple-point pair are defined as the characteristics of the 2D cut in the region where D^{2D} is unoccupied (i.e., above μ_f) from which we subtract the characteristics of the 2D cut in which D^{2D} is filled (i.e., below μ_f).

Let us refer to the three ranges of k_z separated by the two triple points by the corresponding color of the central nodal line as *orange*, *red* and *blue* k_z-range. The corresponding band inversions lead to changes in the symmetry indicators $\#\Pi_p^{(n)}$, and thus potentially alter both the corner charge [cf. Eq. (6.18)] and the second Stiefel-Whitney class [cf. Eq. (6.17)] of the 2D cuts. Let us remark that, in practice, the *physical* chemical potential of the 3D system is constant and therefore locally (in k_z) deviates from the $\mu_f(k_z)$ defined above. However, generally it can be chosen such that we have half-filling with insulating bulk at least for some 2D cuts in the orange and blue k_z-ranges. Then, the jumps $\Delta Q_{\llcorner}$ and Δw_2 are still observable by comparing only k_z values corresponding to those cuts and unchanged compared to the situation with variable $\mu_f(k_z)$.

Before starting with the analysis, we briefly explain how to apply the 2D symmetry-indicator formulas to 3D systems with $\mathcal{PT}$ and arbitrary C_n symmetry. For concreteness, we assume the rotation axis to be along k_z. In this case, any 2D cut perpendicular to k_z through the 3D Brillouin zone inherits both of these symmetries. In particular, within the 2D plane $\mathcal{PT}$ acts as $(C_2\mathcal{T})_{2D}$ with $(C_2)_{2D} = C_2$ being the rotation around the k_z axis,

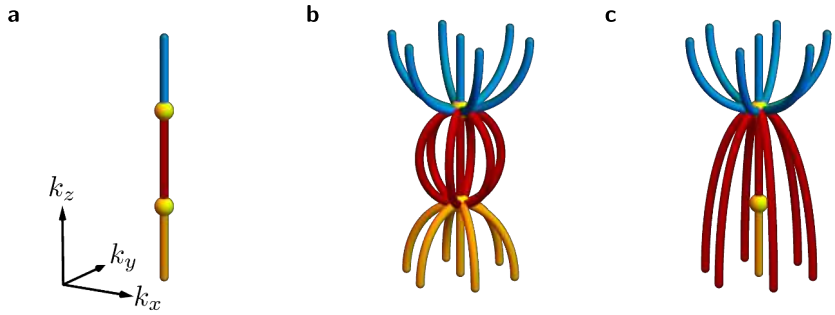

Figure 6.8.: Typical nodal-line compositions for triple-point pairs. (**a**) Two type-A triple points have no attached nodal-line arcs. (**b**) Two type-B triple points both exhibit attached nodal-line arcs in the principal gap (red), but these nodal lines *can* compactly tie the two triple points together, leaving the 2D bulk gapped in both the orange and in the blue k_z-range. (**c**) If one of the triple points is type A and the other type B, the nodal-line arcs in the principal gap *necessarily* cross into either the orange or into the blue k_z-range, making the corresponding 2D cuts gapless.

and $\mathcal{T}_{2D} = \mathcal{P}C_2\mathcal{T} = m_z\mathcal{T}$ [180] being the composition of the physical time-reversal symmetry with the horizontal mirror symmetry, $m_z : z \mapsto -z$. Note that the high-symmetry points entering the symmetry-indicator formulas need to be identified with the intersection of the corresponding HSLs in the 3D Brillouin zone with the chosen 2D plane at fixed k_z. For $\Pi^{(n)}$ we thus need to consider the C_n-invariant HSLs, while the 2D-TRIM correspond to lines invariant under $\mathcal{T}_{2D}$. The computed corner charges in the 2D cuts therefore imply the corresponding values of hinge charges in the 1D hinge Brillouin zone, while the jump of the second Stiefel-Whitney class between two 2D cuts corresponds to the second Stiefel-Whitney *monopole charge* as we explained in Section 6.1.1 and illustrated in Fig. 6.3.

Admissible triple-point pairs

The hinge charge is only well-defined for values of k_z, where the bulk of $\mathcal{H}_{k_z}$ is gapped and the surface charge vanishes [147]. Similarly, the monopole charges are only well-defined as long as there is a surface enclosing the triple-point pair that is not penetrated by nodal lines in the principal gap (red). While these conditions generally depend on the model parameters, we can formulate the following criteria for a gapped bulk, which conversely implies constraints on the admissible triple-point-pair configurations (to be precise, we call a combination

of a 2D and two 1D ICRs an *admissible triple-point-pair configuration* if it is *not* necessarily gapless in the orange or blue k_z-range).

In Section 6.1.2, we discussed a condition, summarized by Eq. (6.4), that the representations of C_n in the orange and blue k_z-ranges must necessarily fulfill in order for the triple-point pair to be admissible. We apply this condition to triple-point pairs formed by a 2D ICR D^{2D} and two 1D ICRs D_a^{1D}, D_b^{1D} as illustrated in Fig. 6.7. In that case the representation matrices of C_n in the orange and blue k_z-range appearing in Eq. (6.4) are

$$\begin{aligned} \mathscr{D}_0(C_n) &= D^{2D}(C_n), \\ \mathscr{D}_1(C_n) &= D_a^{1D}(C_n) \oplus D_b^{1D}(C_n), \end{aligned} \tag{6.23}$$

respectively. Thus, the condition for the triple-point-pair configuration to be admissible is

$$\det D^{2D}(C_n) = D_a^{1D}(C_n) D_b^{1D}(C_n). \tag{6.24}$$

Note that this is fully determined by the rotation eigenvalues, since the determinant on the left is just the product of eigenvalues, which can be extracted from the matrices in Table 6.1. We observe that all 2D ICRs have determinant 1, such that Eq. (6.24) is necessarily violated by all combinations of ICRs that involve two 1D ICRs with *different* rotation eigenvalue. For C_4 symmetries this excludes $(E; A, B)$ and for C_6 $(E_i; A, B)$ with $i = 1, 2$, where we have omitted subscripts of the 1D ICR labels, since the argument is insensitive to them. In these cases neither the jump of the hinge charge nor the Euler and second Stiefel-Whitney monopole charges are defined.

For the little co-group $C_{6(v)}$, the gaplessness can be understood from the nodal-line structure implied by the type of triple points involved, as illustrated in Fig. 6.8. A triple-point pair consisting of one type-A and one type-B triple point necessarily has nodal-line arcs in the principal gap that extend beyond the red k_z-range. In contrast, if both involved triple points are of the same type, the orange and the blue k_z-ranges can generally be gapped. On the one hand, the case of two type-A triple points is very simple since there are no additional nodal lines and the bulk is gapped in the corresponding regions of k_z. On the other hand, for two type-B triple points there must be nodal-line arcs in the principal band gap attached to both triple points. However, the nodal-line arcs can tie the two triple points together in the red k_z-range, where the gapless 2D cuts are not considered when analyzing the higher-order topology, thus leaving the orange and the blue k_z-range gapped. Note that in the applicable case, i.e., $C_{6(v)}$ which are the only point groups where both types of triple points are possible, this criterion turns out to be equivalent to Eq. (6.24).

While the above two points give necessary criteria for having a gapped bulk, they are not sufficient. Two type-A triple points do not have any nodal-line

Table 6.1.: Rotation eigenvalues of high-symmetry lines hosting triple points. Irreducible corepresentations (ICRs) of the C_n rotational symmetry in the point groups $C_{n(v)}$ with space-time inversion symmetry $\mathcal{PT}$ for $n \in \{3, 4, 6\}$. We use the notation by Mulliken [81] for the ICRs, but drop the subscripts if they do not affect the result. Note that for the 2D ICRs of the point group $C_{6(v)}$ we define: ${}^2E_2\,{}^1E_2 \mapsto E_1$, and ${}^2E_1\,{}^1E_1 \mapsto E_2$. The 2D ICRs are all SO(2) matrices and are therefore given in the form $\mathrm{e}^{-\frac{2\pi\mathrm{i}}{n} r^{(n)} s_y}$ for $r^{(n)} \in \mathbb{Z}$ and the Pauli matrix s_y.

$C_{6(v)}$	ICR	A	B	E_1	E_2
	$D(C_6)$	1	-1	$\mathrm{e}^{-\frac{2\pi\mathrm{i}}{6} s_y}$	$\mathrm{e}^{-\frac{2\pi\mathrm{i}}{6} 2 s_y}$
$C_{4(v)}$	ICR	A	B	E	
	$D(C_4)$	1	-1	$\mathrm{e}^{-\frac{2\pi\mathrm{i}}{4} s_y}$	
$C_{3(v)}$	ICR	A		E	
	$D(C_3)$	1		$\mathrm{e}^{-\frac{2\pi\mathrm{i}}{3} s_y}$	

arcs attached, but they are often accompanied by nexus points, i.e., points on the HSL away from the triple points where nodal-line arcs coalesce. If there is an even number of nexus points in the principal gap, then there are two options: (a) the nodal-line arcs connect together through the red k_z-range or (b) the nodal-line arcs extend *outside* the red k_z-range, making the orange and blue k_z-range gapless. These two cases are illustrated in Figs. 6.9a and 6.9b, respectively, for a C_4-symmetric example. Similarly, the nodal-line arcs of two type-B triple points might not connect through the red k_z-range as indicated in Fig. 6.8b but rather extend outside of it as shown in Fig. 6.9c. These cases are *not* distinguished by symmetry properties but by the model parameters. The results of our analysis, i.e., Table 6.2, apply to the cases that do have a gapped bulk in some part of both the orange and the blue k_z-range.

Let us remark that the cases disallowed by Eq. (6.24) for point group $C_{4(v)}$, which according to Table 4.1 involve a pair of type-A triple points, correspond to situations where there is one (or a larger odd number of) symmetry-imposed nexus points of nodal lines in the principal gap, i.e., with the nodal lines attaching to the red region demarcated by the two triple points. An example of such a triple-point-pair configuration is illustrated in Fig. 6.4b. Since an odd number of nexus points cannot be paired as in Fig. 6.9a, there must be extended nodal lines which render either the orange or the blue k_z-region gapless. Therefore, the corresponding triple-point pair is not admissible for the same reason as is visualized for the mixed-type triple-point pair in Fig. 6.8c.

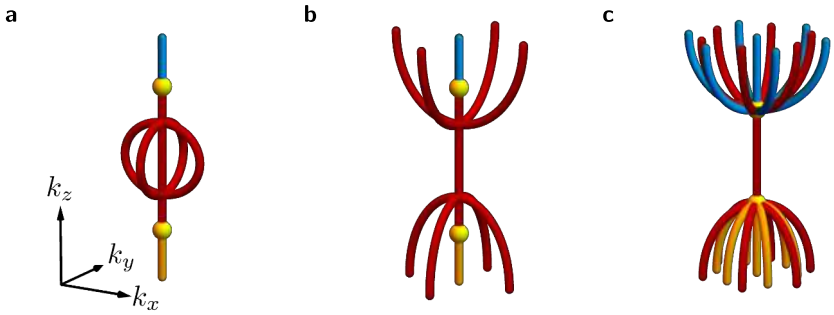

Figure 6.9.: Additional nodal-line compositions near triple-point pairs. (**a**) Type-(A, A) triple-point pair with two red nexus points whose nodal lines are tied together *inside* the red k_z-range, leaving the 2D bulk gapped in both the orange and in the blue k_z-range despite the nexus points. Here, both the monopole charges and the hinge-charge jump can be defined. (**b**) Analogous situation as in the previous panel; however, here the nodal lines extend into the orange and blue k_z-ranges, rendering the corresponding 2D cuts gapless. In this case, neither the monopole charges nor the hinge-charge jump can be defined. (**c**) Type-(B, B) triple-point pair with nodal-line arcs extending *outside* the red k_z-range, making the relevant 2D cuts gapless. The monopole charges and the hinge-charge jump are undefined. This scenario should be contrasted to Fig. 6.8b, which shows a similar situation with the nodal-line arcs tied together *inside* the red k_z-range.

Summary of results

Having clarified the necessary conditions to realize an admissible triple-point pair, let us tackle their associated hinge-charge jump. To observe the hinge charge, the system needs to be extended in the z-direction and finite in the x- and y-directions, with a geometry possessing the same C_n symmetry as the space group, see Fig. 6.6a. We need to distinguish geometries with the center of the rotational symmetry being placed at different Wyckoff positions in the unit cell. Below, we consider all possible cases for each combination of ICRs listed in Table 6.2 and compute the hinge-charge jump using the appropriate symmetry-indicator formulas [151] summarized in Section 3.2.1. Note that for this analysis the ionic charge distribution is irrelevant, because it does not depend on k_z and therefore it does not contribute to the *jump* of the hinge charge. Table 6.2 summarizes the results of this analysis. We observe that the combination of ICRs uniquely determines the jump of the hinge charge. In particular, there is a nonvanishing jump $\Delta Q_{\llcorner} \neq 0 \mod e$ quantized into multiples of $\frac{e}{n}$ for C_n symmetry for any admissible triple-point pair.

Table 6.2.: Bulk-hinge correspondence for triple-point pairs in spinless systems. We consider systems in nanowire geometry with rotational (or screw) symmetry C_n of order $n \in \{2,3,4,6\}$ [a]. The triple points occur along high-symmetry lines (HSLs; some examples are given in the second row) with little co-group $\overline{\mathcal{G}}^{\mathbf{k}}$ that have the C_n symmetry, which for even n may be generated by $C_{n/2}\mathcal{PT}$ (see third row). The fourth row lists the admissible pairs of triple-point types along the corresponding HSL and the row labelled by "ICRs" indicates the possible triplets of irreducible corepresentations of the $\overline{\mathcal{G}}^{\mathbf{k}}$ which can form a four-band triple-point pair (cf. Fig. 6.7); "any" means that all combinations of a 2D ICR with two 1D ICRs give the same result. We use the notation by Mulliken [81] for the ICRs, but drop the subscripts if they do not affect the result. Note that for the 2D ICRs of $6/m'$ we define: ${}^2E_2{}^1E_2 \mapsto E_1$, and ${}^2E_1{}^1E_1 \mapsto E_2$. Finally, we find that *each* triple-point pair is characterized by a fractional hinge-charge jump $\Delta Q_{\llcorner}$. If $\mathcal{PT}$ symmetry is present, we also assign the triple-point pairs the Euler $|\chi|$ and second Stiefel-Whitney w_2 monopole charges. The hinge charges $Q_{\llcorner}$ are computed for the geometries depicted in Fig. 6.6a.

Rotational symmetry	C_2 [a]	C_3		C_4	C_6		
Example HSLs	$\Gamma Z, MA$	$\Gamma A, KH, K'H'$		$\Gamma Z, MA$	KH [b]	ΓA	
$\overline{\mathcal{G}}^{\mathbf{k}}$ rotation generator	$C_4\mathcal{PT}$ [a]	C_3	$C_6\mathcal{PT}$ [a]	C_4	C_3	C_6	
TP types	(A, A)	(B, B)	(A, A)	(A, A)	(B, B)	(A, A)	(B, B)
ICRs	any	any		$(E;A,A)$ $(E;B,B)$	any	$(E_1;A,A)$ $(E_2;B,B)$	$(E_1;B,B)$ $(E_2;A,A)$
$\Delta Q_{\llcorner} \mod e$	$\frac{e}{2}$	$+\frac{e}{3}$		$+\frac{e}{4}$	$+\frac{e}{3}$	$+\frac{e}{6}$	$-\frac{e}{3}$
$\lvert\chi \mod n\rvert$ [d]	–	1	–	1	2	1	2
w_2	–	0 or 1 [c]	–	1	0	1	0

[a] For $C_4\mathcal{PT}$, the largest unitary rotational symmetry is C_2. Then, we consider a square geometry but the hinge charges are summed over two neighboring hinges. For $C_6\mathcal{PT}$ we consider the C_3 (triangular) geometry.
[b] Due to the double occurrence of the KH line in a C_6-symmetric system, the Brillouin zone exhibits two triple-point pairs at the same value of k_z. The values of $\Delta Q_{\llcorner}$ and w_2 represent the combined contribution of *both* of them.
[c] The second Stiefel-Whitney monopole is not symmetry indicated for $n = 3$ and both options are possible.
[d] We use the convention that $a \mod n \in (-\lfloor n/2 \rfloor, \ldots, \lfloor n/2 \rfloor]$, such that $|a \mod n| \in \{0, 1, \ldots, \lfloor n/2 \rfloor\}$.

Let us briefly comment on the jump of the *surface* charge. As already stated, the vanishing of the fractional part of the surface charge, which is related to bulk polarization [102], is a necessary condition for the hinge charge to be observable [147]. Therefore, to observe the hinge-charge *jump*, the surface charge must vanish for the k_z-ranges on *both* sides of the triple-point pair, which can only happen if the triple-point pair is not associated with a fractional jump $\Delta\mathbf{P}$ of the 2D bulk polarization. Below, we present a derivation, based on the symmetry-indicator formulas for the 2D polarization [147, 150, 151], showing that indeed $\Delta\mathbf{P} = 0 \mod e\mathbf{R}$ (where the Bravais vectors $\mathbf{R}$ constitute the usual ambiguity of bulk polarization [101]) for all tabulated triple-point pairs. Therefore, the surface charge does not present an obstacle for the definition of the hinge charges, and we expect the hinge-charge jump to be observable for an appropriate choice of the boundary termination.

To compute the jump of the second Stiefel-Whitney class, or equivalently the second Stiefel-Whitney monopole charge $w_2 = \Delta w_2$ carried by the red nodal-line segment, we proceed as follows. For systems with C_4 or C_6 symmetry the second Stiefel-Whitney class of the 2D cuts can be computed readily by applying Eq. (6.17) with the appropriate interpretation of the high-symmetry points, as described above. Consistent with the results of Section 6.1.1, we find that type-(A,A) triple-point pairs in $\mathcal{PT}$-symmetric systems universally carry $w_2 = 1$. Furthermore, we recognize the following correspondence between the bulk invariant w_2 and the hinge signature $\Delta Q_{\llcorner}$ (which is only defined modulo e): a nontrivial second Stiefel-Whitney monopole charge $w_2 = 1$ implies a fractional hinge-charge jump of the minimal nonvanishing magnitude $|\Delta Q_{\llcorner}| = \frac{e}{n}$, while $w_2 = 0$ results in a twice as large jump $|\Delta Q_{\llcorner}| = \frac{2e}{n}$.

Determining the second Stiefel-Whitney monopole charge in the case of C_3 symmetry is not as straightforward. However, we note that the second Stiefel-Whitney monopole charge is attributed to the red nodal-line segment along the HSL as illustrated in Fig. 6.2b and is therefore a feature local in k_x, k_y. Thus, it cannot depend on the specific choice of HSL in the Brillouin zone, but only on the Hamiltonian near the HSL. Noting that the little co-group of all three HSLs has the same rotational symmetry and there is only one class of combinations of ICRs, the admissible values of the second Stiefel-Whitney monopole charge w_2 are the same for all three HSLs ΓA, KH and $K'H'$. In the next paragraph we argue that, in fact, the second Stiefel-Whitney class is not symmetry indicated in the C_3-symmetric case, meaning that both $w_2 = 0$ or 1 are possible. We emphasize that this is not in contradiction to the bulk-hinge correspondence principle described above, because the fractional part of the hinge-charge jump satisfies $\pm\frac{e}{3} = \mp\frac{2e}{3} \mod e$. Thus, the hinge signatures of nontrivial and trivial second Stiefel-Whitney monopole charge become indistinguishable.

The fact that the second Stiefel-Whitney class is not symmetry indicated in

a space group with C_3 symmetry can be easily deduced from the other results in Table 6.2. In particular, note that a space group with C_6 symmetry also has C_3 symmetry. Thus, we can deform any of the possible triple-point-pair configurations on the ΓA line of a six-fold symmetric system (cf. last two columns of Table 6.2), having either $w_2 = 0$ or 1, into a triple-point-pair configuration of a C_3-symmetric system by introducing a small C_2-breaking perturbation. However, Table 6.2 shows that in the in three-fold symmetric little co-groups, only a single combination of ICRs is possible, such that any initial choice of the triple-point pair in the C_6-symmetric case results in that unique triple-point-pair type of the C_3-symmetric system (in particular, type-A triple points generally transform into type-B triple points). Since the second Stiefel-Whitney class requires only $\mathcal{PT}$ symmetry (which is preserved when breaking C_2) and the 2D cuts outside the red k_z-range remain gapped under the addition of a small perturbation, the second Stiefel-Whitney class is unaffected by the perturbation. This implies that both $w_2 = 0$ or 1 are possible for triple-point pairs in C_3-symmetric space groups, and that the second Stiefel-Whitney class is not symmetry indicated. We demonstrate this feature for two explicit models in Section 6.3.4.

Finally, we remark on the consistency of the results in Table 6.2 for a triple-point pair on the KH line of a C_6-symmetric compared to a C_3-symmetric system. Naturally, a system with six-fold rotational symmetry is also three-fold rotation symmetric, such that one expects compatibility of the results for the two cases. However, there are two caveats: (1) in a C_6-symmetric system the KH and $K'H'$ HSLs are equivalent such that there are in fact *two* symmetry-related triple-point pairs per Brillouin zone at the same value of k_z, and (2) the hinge-charge jumps in the two cases are computed for a *different geometry* of the sample, see Fig. 6.6a. Therefore, if we only consider the C_3 symmetry of a C_6-symmetric system, we have to (1) count contributions of identical triple-point pairs on the two HSLs KH and $K'H'$, and (2) deform the sample with hexagonal cross section into one with a triangular cross section by combining two corners into a single new corner as depicted in Fig. 6.6b.

With this insight, it is easily checked that the corresponding entries in Table 6.2 are fully consistent. First, for the second Stiefel-Whitney class the two monopole charge contributions are additive, $w_2^{(6)} = 2w_2^{(3)}$, which results in $w_2^{(6)} = 0 \mod 2$ for both $w_2^{(3)} = 0$ or 1. Furthermore, the corner charge of the triangular cross section $Q_{\llcorner}^{ab}$ is given by the sum of two of the corner charges of the hexagonal cross section, $Q_{\llcorner}^{ab} = Q_{\llcorner}^{a} + Q_{\llcorner}^{b}$, as illustrated in Fig. 6.6b. Note that due to the six-fold rotational symmetry $Q_{\llcorner}^{a} = Q_{\llcorner}^{b} = \frac{e}{3} \mod e$, such that for the C_6-symmetric model with a triple-point pair on KH in the *triangular geometry* we find $Q_{\llcorner}^{ab} = 2\frac{e}{3}$. On the other hand, when interpreting

the same model as being C_3-symmetric, we simply add the corner charges for a triple-point pair on KH and $K'H'$, giving $Q_{\llcorner}^{ab} = 2\frac{e}{3}$ as well.

Derivation

To derive the results in Table 6.2, we start from the classification of triple points in spinless $\mathcal{PT}$-symmetric systems presented in Chapter 4 for little co-groups $\overline{\mathcal{G}}^{\mathbf{k}} = C_{3(v)}, C_{4(v)}, C_{6(v)}$ of some HSL and we consider the situation depicted in Fig. 6.7. We compare quantities in the orange k_z-range (to the left of the first triple point, where the 2D ICR $D^{2\mathrm{D}}$ is occupied) and the blue k_z-range (to the right of the second triple point, where the two 1D ICRs $D_a^{1\mathrm{D}}$ and $D_b^{1\mathrm{D}}$ are occupied). We use the notation by Mulliken [81] for the ICRs. In particular, when defining the changes $\Delta Q_{\llcorner}$ and Δw_2, we subtract the first (orange k_z-range) from the latter (blue k_z-range). For each 2D or 1D ICR D of $\overline{\mathcal{G}}^{\mathbf{k}} \cup (\mathcal{PT})\overline{\mathcal{G}}^{\mathbf{k}}$, we look up the corresponding rotation eigenvalues on the Bilbao crystallographic server (BCS) [222–224] using the program Corepresentations PG [84, 85] and, assuming there are no other band inversions in the principal gap, compute the relevant symmetry indicators, see Tables 6.3, 6.4 and 6.6. Before proceeding with the mathematical analysis, we make two remarks. First, note that the HSL on which the triple points lie does not need to go through the center of the Brillouin zone (point Γ of the 2D cut). Namely, the little co-group $C_{3(v)}$ is also realized at the K point(s) of space groups (space groups) with three-fold or six-fold rotational symmetry, while $C_{4(v)}$ is also realized at M points of space groups with four-fold rotational symmetry.

In all cases, we assume that the space group contains $\mathcal{PT}$, acting as $(C_2\mathcal{T})_{2\mathrm{D}}$ in the 2D cuts, and C_n with order $n \in \{3, 4, 6\}$. Further, we place all ionic charge at the center of the unit cell, because ultimately, we are interested in the change of the corner charge as a function of k_z and the ionic charge distribution does not depend on k_z. If the system symmetry is C_3, then $\mathcal{T}_{2\mathrm{D}}$ ($= C_2\mathcal{PT} = m_z\mathcal{T}$) is not present, such that the corner charge is given by Eq. (3.27). For space group symmetries with rotation of order $n = 4, 6$, the C_2 combines with $\mathcal{PT}$ to give $C_2\mathcal{PT} = \mathcal{T}_{2\mathrm{D}}$, such that we can apply the simplified formulas Eqs. (3.30) and (3.31). For the second Stiefel-Whitney class, we use the results of the previous subsection, i.e., Eqs. (6.11) and (6.16). We next go in detail through all the possible cases.

Triple points along $C_{3(v)}$-symmetric lines For $C_{3(v)}$ there is only one possible configuration of two triple points, namely the one with ICRs $(E; A, A)$. The symmetry indicators (cf. Table 6.3) imply that $\Delta\#\Pi_1^{(3)} = 2$ and $\Delta\#\Pi_2^{(3)} = -1$.

Table 6.3.: Irreducible corepresentations of $3m$ and $\bar{3}'m$. Rotation eigenvalues and symmetry indicators for all irreducible corepresentations of $C_{3(v)}$ with $\mathcal{PT}$ at a high-symmetry point $\Pi = \Gamma, K, K'$ of a C_3-symmetric system or at $\Pi = K$ of a C_6-symmetric system. The list of ICRs is unchanged if $\mathcal{PT}$ symmetry is removed in the case of C_{3v}.

ICRs for		Eigenvalue of	Symmetry indicators at Π	
C_{3v}	C_3	C_3	$\#\Pi_1^{(3)}$	$\#\Pi_2^{(3)}$
A_1, A_2	A_1	1	1	0
E	${}^2E^1E$	$\mathrm{e}^{2\pi\mathrm{i}/3}, \mathrm{e}^{-2\pi\mathrm{i}/3}$	0	1

Let us first consider triple points occurring along the HSL $\Pi = \Gamma$ of a C_3-symmetric system. If the rotation center of the sample lies at Wyckoff position $1a$, then $\Delta[K_p^{(3)}] = \Delta[K_p'^{(3)}] = -\Delta\#\Gamma_p^{(3)}$. Then, according to Eq. (3.27a), the hinge-charge jump is

$$\Delta Q_{\llcorner,1a}^{(3)} = -\frac{2e}{3}\left(\Delta\#\Gamma_1^{(3)} + \Delta\#\Gamma_2^{(3)}\right) \mod e = \frac{e}{3} \mod e. \tag{6.25}$$

If the triple points instead occur along HSL $\Pi = K$ (or equivalently K') of a C_3-symmetric system (with rotation center still set to $1a$, then $\Delta\left[K_p^{(3)}\right] = \Delta\#K_p^{(3)}$ such that

$$\Delta Q_{\llcorner,1a}^{(3)} = \frac{e}{3}\left(\Delta\#K_1^{(3)} + \Delta\#K_2^{(3)}\right) \mod e = \frac{e}{3} \mod e. \tag{6.26}$$

It is easily verified by using Eqs. (3.27b) and (3.27c) that the derived results for $\Delta Q_{\llcorner}$ remain unchanged if the rotation center of the finite system is instead located at Wyckoff position $1b$ or $1c$.

If $\Pi = K$ of a C_6-symmetric system, then we need to use Eq. (3.31) instead, resulting in the same

$$\Delta Q_{\llcorner}^{(6)} = \frac{e}{6}\Delta\#K_1^{(3)} \mod e = \frac{e}{3} \mod e. \tag{6.27}$$

This concludes the derivation of $\Delta Q_{\llcorner}^{(n)} = \frac{e}{3} \mod e$ for triple-point pairs along $C_{3(v)}$-symmetric lines.

We briefly analyze the jump Δw_2 of the second Stiefel-Whitney class. We have argued above that the second Stiefel-Whitney class is not symmetry indicated for C_3-symmetric systems. For C_6, on the other hand, we use Eq. (6.16) to find

$$\Delta w_2 = \frac{1}{2}\Delta\left[M_1^{(2)}\right] = 0, \tag{6.28}$$

because, by assumption, there is neither a band inversion at Γ nor at M.

Table 6.4.: Irreducible corepresentations of $4mm$ and $4/m'mm$. Rotation eigenvalues and symmetry indicators for all irreducible corepresentations of $C_{4(v)}$ with $\mathcal{PT}$ at a high-symmetry point $\Pi = \Gamma, M$ of a C_4-symmetric system. The list of ICRs is unchanged if $\mathcal{PT}$ symmetry is removed in the case of C_{4v}.

ICRs for		Eigenvalues of		Symmetry indicators at Π		
C_{4v}	C_4	C_2	C_4	$\#\Pi_1^{(2)}$	$\#\Pi_1^{(4)}$	$\#\Pi_2^{(4)}$
A_1, A_2	A	1	1	1	1	0
B_1, B_2	B	1	-1	1	0	0
E	E	$-1, -1$	$\mathrm{i}, -\mathrm{i}$	0	0	1

Triple points along $C_{4(v)}$-symmetric lines Next, we consider lines with $C_{4(v)}$ symmetry; ICRs and symmetry indicators are given in Table 6.4. Here, we need to distinguish three triple-point configurations, namely $(E; A, A)$, $(E; B, B)$ and $(E; A, B)$, and two HSLs (namely $\Pi = \Gamma$ and $\Pi = M$). The differences $\Delta\#\Pi_1^{(2)}$, $\Delta\#\Pi_1^{(4)}$ and $\Delta\#\Pi_2^{(4)}$ for the various triple-point configurations are listed in Table 6.5. By recalling Eq. (6.11), we find that for all cases

$$\Delta w_2 = \Delta\left[M_2^{(4)}\right] \mod 2 = 1 \mod 2, \tag{6.29}$$

in agreement with the fact that the triple points are type A (cf. Section 6.1.1).

To identify the jump in the hinge charge, we have to analyze the two HSLs separately. First, for $\Pi = \Gamma$ we have $\Delta[\mathrm{P}_p^{(n)}] = -\Delta\#\Gamma_p^{(n)}$ for both $\mathrm{P} \in \{X, M\}$, and the change in corner charge is given by

$$\Delta Q_{\llcorner}^{(4)} = -\frac{e}{4}\left(\mp\Delta\#\Gamma_1^{(2)} + 2\Delta\#\Gamma_1^{(4)} + 3\Delta\#\Gamma_2^{(4)}\right) \mod e, \tag{6.30}$$

where the negative (positive) sign of $\Delta\#\Gamma_1^{(2)}$ corresponds to setting the center of the system to Wyckoff position $1a$ ($1b$). Observe in Table 6.4 that $\Delta\#\Pi_1^{(2)}$ is *even* for all triple-point pairs, which means that the '$\mp$' sign ambiguity is unimportant, and both Wyckoff positions lead to the same value of the hinge-charge jump.

In contrast, for $\Pi = M$ we obtain contributions from $\Delta[M_p^{(4)}] = \Delta\#M_p^{(4)}$, leading to

$$\Delta Q_{\llcorner}^{(4)} = \frac{e}{4}\left(2\Delta\#M_1^{(4)} + 3\Delta\#M_2^{(4)}\right) \mod e. \tag{6.31}$$

Careful evaluation of Eqs. (6.30) and (6.31) for all combinations of ICRs gives the following results: For triple-point pairs along either Γ or M, $\Delta Q_{\llcorner}^{(4)} = \frac{e}{4}$ for both $(E; A, A)$ and $(E; B, B)$. The results are summarized in Table 6.5.

Table 6.5.: Jumps for triple-point pairs protected by C_4. Changes in symmetry indicators ($\Delta\#\Pi_p^{(n)}$), hinge charge ($\Delta Q_{\llcorner}^{(4)}$) and second Stiefel-Whitney class (Δw_2) associated with the different configurations of triple-point pairs. Each triple-point pair is specified by the irreducible corepresentations (ICRs) $(D^{2D}; D_a^{1D}, D_b^{1D})$ on a four-fold rotation axis, corresponding to the high-symmetry point $\Pi = \Gamma, M$ in a 2D cut perpendicular to the rotation axis. The changes are defined by subtracting the characteristics of the systems with D^{2D} occupied from those of the system with $D_{a,b}^{1D}$ occupied. The hinge-charge jump is computed using Eq. (6.30) for $\Pi = \Gamma$ and Eq. (6.31) for $\Pi = M$, while Δw_2 is computed from Eq. (6.11)).

ICRs	$(E; A, A)$	$(E; B, B)$
$\Delta\#\Pi_1^{(2)}$	2	2
$\Delta\#\Pi_1^{(4)}$	2	0
$\Delta\#\Pi_2^{(4)}$	-1	-1
$\Delta Q_{\llcorner}^{(4)} \mod e$	$+\frac{e}{4}$	$+\frac{e}{4}$
$\Delta w_2 \mod 2$	1	1

Although our analysis in the presence of C_4-rotational symmetry explicitly assumed a primitive tetragonal Bravais lattice, the result in Table 6.2 generalizes *with no alterations* to the body-center tetragonal case. To understand this, note that the derivation of the hinge-charge jump here is based on considering a 2D system with C_4 symmetry. It is found that (1) the ICRs at the Γ and at the M point of the 2D square lattice are *identical*, and that (2) the corner-charge jump associated with a band inversion of a 2D ICR with two 1D ICRs is *also identical* for both the Γ and at the M point. The 3D models with tetragonal (either primitive or body-centered) symmetry are obtained from the 2D systems by interpreting the band-inversion-tuning parameter as a third momentum component, k_z. The difference between the two Bravais lattices merely corresponds to the way the periodically changing Hamiltonians $H_{k_z}(\mathbf{k}_{2D}) = H_{k_z+2\pi}(\mathbf{k}_{2D})$ are glued together: for the body-centered case, $H_{k_z}(\mathbf{k}_{2D}) = H_{k_z+\pi}(\mathbf{k}_{2D} + \Gamma - M)$, whereas such a constraint is absent for the primitive case. It is clear that the mathematical analysis of the hinge-charge jump applies irrespective of this additional constraint.

Triple points along $C_{6(v)}$-symmetric lines There is only one HSL with little co-group $C_{6(v)}$ (namely Γ in C_6-symmetric systems), and considering the possible crossings of ICRs (listed in Table 6.6) results in six distinct triple-point-pair configurations. We first focus on the cases where the two triple points are of the same type, which gives the four triple-point pairs listed in Table 6.7. By

Table 6.6.: Irreducible corepresentations of $6mm$ and $6/m'mm$. Rotation eigenvalues and symmetry indicators for all irreducible corepresentations of $C_{6(v)}$ with $\mathcal{PT}$ at the high-symmetry point Γ of a C_6-symmetric system. The list of ICRs is unchanged if $\mathcal{PT}$ symmetry is removed in the case of C_{6v}.

ICRs for		Eigenvalues of		Symmetry indicators at Γ	
C_{6v}	C_6	C_2	C_3	$\#\Gamma_1^{(2)}$	$\#\Gamma_1^{(3)}$
A_1, A_2	A	1	1	1	1
B_1, B_2	B	-1	1	0	1
E_1	${}^2E_2^1E_2$	$-1,-1$	$\mathrm{e}^{2\pi\mathrm{i}/3}, \mathrm{e}^{-2\pi\mathrm{i}/3}$	0	0
E_2	${}^2E_1^1E_1$	$1,1$	$\mathrm{e}^{2\pi\mathrm{i}/3}, \mathrm{e}^{-2\pi\mathrm{i}/3}$	2	0

combining $\Delta[\Pi_p^{(n)}] = -\Delta\#\Gamma_p^{(n)}$ (for $\Pi \in \{M, K\}$) with Eqs. (3.31) and (6.16), we calculate the jumps

$$\Delta Q_{\llcorner}^{(6)} = -\frac{e}{4}\Delta\#\Gamma_1^{(2)} - \frac{e}{6}\Delta\#\Gamma_1^{(3)} \mod e, \tag{6.32}$$

$$\Delta w_2 = -\frac{1}{2}\Delta\#\Gamma_1^{(2)} \mod 2. \tag{6.33}$$

The computed values of $\Delta Q_{\llcorner}^{(6)}$ and of Δw_2 for all the triple-point pairs where both triple points are of the same type are listed in Table 6.7. We find that a nontrivial change of the second Stiefel-Whitney class, which occurs for two type-A triple points, is associated with a hinge-charge jump $\Delta Q_{\llcorner}^{(6)} = +\frac{e}{6}$. In contrast, pairs of type-B triple points are characterized by trivial $\Delta w_2 = 0$ and are associated with a hinge-charge jump of $\Delta Q_{\llcorner}^{(6)} = -\frac{e}{3}$.

Finally, there is the possibility to have two triple points of *different types*, i.e., one type A and one type B, by choosing one of the following ICR combinations: $(E_1; A_i, B_j)$, $(E_2; A_i, B_j)$. In these two cases, we find that $\Delta[M_1^{(2)}] = -\Delta\#\Gamma_1^{(2)} = 1 \mod 2$ (i.e., it is an *odd number*. This implies that the value of $[M_1^{(2)}]$ must be odd on one side of the triple-point pair. However, recall from Section 6.2.1 that a gapped bulk requires $[M_1^{(2)}] = 0 \mod 2$. It therefore follows that the bulk is necessarily gapless on one side of the triple-point pair, such that the hinge-charge jump cannot be defined in this case. This finding is consistent with the intuitive explanation given in the main text, where the different type of the two triple points forces the attached nodal-line arcs to cross the orange or blue k_z-range. In Fig. 6.8c a 2D cut in the orange k_z-range would correspond to the situation shown in Fig. 6.5 with the red disks corresponding to places where the red attached nodal-line arcs cross the 2D cut.

Table 6.7.: Jumps for triple-point pairs protected by C_6. Changes in symmetry indicators ($\Delta\#\Gamma_1^{(n)}$), hinge charge ($\Delta Q_{\llcorner}^{(6)}$) and second Stiefel-Whitney class (Δw_2) associated with the different configurations of triple-point pairs along the Γ line of C_6-symmetric systems. Each triple-point pair is specified by the irreducible corepresentations (ICRs) $(D^{2D}; D_a^{1D}, D_b^{1D})$ along the Γ line. For simplicity we use the labels of ICRs for C_{6v}, the corresponding notation for C_6 can be extracted from Table 6.6. The changes are defined by subtracting the characteristics of the systems with D^{2D} occupied from those of the system with $D_{a,b}^{1D}$ occupied. The values of $\Delta Q_{\llcorner}^{(6)}$ and Δw_2 are computed from Eqs. (6.32) and (6.33), respectively.

TP types	(A, A)		(B, B)	
ICRs	$(E_1; A_i, A_j)$	$(E_2; B_i, B_j)$	$(E_1; B_i, B_j)$	$(E_2; A_i, A_j)$
$\Delta\#\Gamma_1^{(2)}$	2	-2	0	0
$\Delta\#\Gamma_1^{(3)}$	2	2	2	2
$\Delta Q_{\llcorner}^{(6)} \mod e$	$+\frac{e}{6}$	$+\frac{e}{6}$	$-\frac{e}{3}$	$-\frac{e}{3}$
$\Delta w_2 \mod 2$	1	1	0	0

No jump of the surface charge

For the hinge-charge jump to be observable, it is important that the surface charge (more precisely, the surface charge *density*; this corresponds to the edge charge density of the 2D cuts at fixed k_z) is vanishing [147] for the k_z-ranges on both sides of the triple-point pair. This can only be true if the *jump* of the surface charge associated with the triple-point pair is zero. Here we show that this is indeed true for all the triple-point pairs shown in Table 6.2.

Before deriving the desired fact mathematically from the corresponding symmetry-indicator formulas, let us present a simple argument based on the quantization of Berry phase. Namely, recall that for a boundary of a high-symmetry orientation with respect to the crystalline axes, the surface charge is in a one-to-one correspondence [101] with the Berry phase along a closed momentum-space ($\mathbf{k}$) path along the direction perpendicular to the considered surface. Here, first recall that stable triple points require the presence of either $\mathcal{PT}$ symmetry (in which case the Berry phase is quantized to 0 versus π on *any* closed $\mathbf{k}$-path due to the reality condition [173]) or of m_v mirror symmetry (in which case the mirror symmetry acts like inversion on the straight $\mathbf{k}$-paths perpendicular to the boundaries considered in Fig. 6.6a, thus quantizing the Berry phase of interest to 0 versus π [100]).

The quantization of the Berry phase implies that the surface charge can only change if the $\mathbf{k}$-paths of the required orientation encounter a bulk nodal line (carrying the π-quantum of Berry phase). However, a look at Fig. 6.8 reveals

that for both type-(A,A) and type-(B,B) triple-point pairs it is possible to continuously shift a horizontal $\mathbf{k}$-path from the orange k_z-range to the blue k_z-range without encountering any (red) nodal line in the principal gap. We therefore anticipate the surface charge to be identical in both k_z-ranges (and therefore the hinge-charge jump to be observable) at least when the boundaries are oriented symmetrically with respect to the crystal axes.

More formally, we now derive the same conclusion for an *arbitrarily* oriented C_n-symmetric system. In such a case the surface charge density of a gapped 2D crystal is given [102] by $\sigma_{\text{surf}} = \mathbf{P}\cdot\hat{\mathbf{n}}$, where $\mathbf{P}$ is the bulk polarization and $\hat{\mathbf{n}}$ the surface normal. To prove that $\Delta\sigma_{\text{surf}} = 0$ across the triple-point pair for arbitrary boundary termination, it needs to be true that $\Delta\mathbf{P}\cdot\hat{\mathbf{n}} = 0$ when moving across the triple-point pair. Similar to the corner charge, the bulk polarization $\mathbf{P}^{(n)}$ of a 2D crystal with C_n rotational symmetry can be expressed [147, 150, 151] using symmetry indicators. For C_3-symmetric crystals, we use the result of Refs. 150, 151 which does not assume time-reversal symmetry to be present,

$$\mathbf{P}^{(3)} = \frac{e}{3}\left(2\left[K_1^{(3)}\right] + \left[K_1'^{(3)}\right] + \left[K_2^{(3)}\right] + 2\left[K_2'^{(3)}\right]\right)(\mathbf{a}_1+\mathbf{a}_2) \mod e\mathbf{R}, \tag{6.34}$$

while for C_n with $n = 4, 6$, we can use the simplified expressions from Ref. 147:

$$\mathbf{P}^{(4)} = \frac{e}{2}\left[X_1^{(2)}\right](\mathbf{a}_1+\mathbf{a}_2) \mod e\mathbf{R}, \tag{6.35}$$

$$\mathbf{P}^{(6)} = 0 \mod e\mathbf{R}. \tag{6.36}$$

Here $\mathbf{a}_1$ and $\mathbf{a}_2$ are lattice basis vectors and $\mathbf{R} = m_1\mathbf{a}_1 + m_2\mathbf{a}_2$ with $m_1, m_2 \in \mathbb{Z}$ is a general Bravais lattice vector.

We now briefly apply the symmetry-indicator formulas in Section 6.2.2 and Eq. (6.36) to show that the polarization jump $\Delta\mathbf{P}^{(n)}$ associated with the triple-point pairs in C_n-symmetric systems is always vanishing. First, for a triple-point pair along the Γ line of a C_3-symmetric system [cf. Eq. (6.25)], we obtain from Section 6.2.2 the jump of the bulk polarization

$$\begin{aligned}\Delta\mathbf{P}^{(3)} &= -e\left(\Delta\#\Gamma_1^{(3)} + \Delta\#\Gamma_2^{(3)}\right)(\mathbf{a}_1+\mathbf{a}_2) \mod e\mathbf{R}\\ &= 0 \mod e\mathbf{R}.\end{aligned} \tag{6.37}$$

Similarly, for a triple-point pair along the K line [cf. Eq. (6.26)]

$$\begin{aligned}\Delta\mathbf{P}^{(3)} &= \frac{e}{3}\left(2\Delta\#K_1^{(3)} + \Delta\#K_2^{(3)}\right)(\mathbf{a}_1+\mathbf{a}_2) \mod e\mathbf{R}\\ &= 0 \mod e\mathbf{R},\end{aligned} \tag{6.38}$$

where we have read from Table 6.3 that $\Delta\#K_1^{(3)} = 2$ and $\Delta\#K_2^{(3)} = -1$ for a triple-point pair formed by ICRs $(E; A_i, A_j)$.

Furthermore, note that per Section 6.2.2 the polarization always vanishes in C_6-symmetric systems. Therefore $\Delta\mathbf{P}^{(6)} = 0 \mod e\mathbf{R}$ for triple-point pairs along both the K line [cf. Eq. (6.27)] and the Γ line [cf. Eq. (6.32)] of C_6-symmetric systems. Next, for triple-point pairs along the Γ line of C_4-symmetric systems [cf. Eq. (6.30)] we find from Eq. (6.35) that the change in bulk polarization is

$$\begin{aligned}\Delta\mathbf{P}^{(4)} &= -\frac{e}{2}\Delta\#\Gamma_1^{(2)}\,(\mathbf{a}_1 + \mathbf{a}_2) \mod e\mathbf{R} \\ &= 0 \mod e\mathbf{R}.\end{aligned} \tag{6.39}$$

where we have read from Table 6.5 that $\Delta\#\Gamma_1^{(2)}$ is even for all possible triple-point pairs. Finally, note that triple-point pairs along the M line [cf. Eq. (6.31)] do not have an effect on the symmetry indicator $\left[X_1^{(2)}\right]$ in Eq. (6.35), therefore again $\Delta\mathbf{P}^{(4)} = 0 \mod e\mathbf{R}$. We conclude that all triple-point pairs listed in Table 6.2 are associated with no jump in surface charge, thus making the hinge-charge jump observable for an appropriate choice of the boundary termination.

6.2.3. Euler monopole charge

After having calculated the second Stiefel-Whitney monopole charge and hinge-charge jump associated with triple-point pairs, we come back to the Euler monopole charge whose values for the same configurations was already shown in Table 6.2. The symmetry-indicator formula for the Euler class, Eq. (6.6), is, in contrast to the other formulas, already formulated in 3D. It involves the corepresentations of C_n in the orange and blue k_z-ranges, see Eq. (6.23). By going through all allowed combinations of ICRs, we verify the assumption that $D^{2\mathrm{D}}(C_n)$ and $D_a^{1\mathrm{D}}(C_n) \oplus D_b^{1\mathrm{D}}(C_n)$ are $\mathsf{SO}(2)$ matrices and then extract $r_0^{(n)} = r_{2\mathrm{D}}^{(n)}$, $r_1^{(n)} = r_{1\mathrm{D}+1\mathrm{D}}^{(n)}$ to compute χ. The results are summarized in Table 6.8 and we observe that in *all* cases where it is defined, the Euler monopole charge is nontrivial and consistent with the independently calculated w_2, via the relation $w_2 = \chi \mod 2$. Note that for $n = 3$, χ is determined only modulo 3 and thus has undetermined parity, which is consistent with the second Stiefel-Whitney class not being symmetry indicated in that case.

Note that only the absolute value of the Euler class is well-defined, since the sign is gauge-dependent, and the symmetry-indicator formula determines the Euler monopole charge modulo n, where n is the order of the rotational symmetry. Due to these these ambiguities, $\{0, 1, \ldots, \lfloor n/2 \rfloor\}$ is the largest set

Table 6.8.: Monopole charges associated with triple-point pairs. Euler class χ and second Stiefel-Whitney class w_2 computed on a surface enclosing a triple-point pair for all possible combinations of irreducible corepresentations (ICRs) in systems with space-time inversion symmetry $\mathcal{PT}$ squaring to the identity and assuming that on that surface the two-band subspace of occupied bands is separated from the remaining bands by energy gaps. Combinations of ICRs leading necessarily to a gapless bulk below or above the triple-point pair are excluded. The first column gives the order n of rotational symmetry protecting the triple points. In the second column we list possible combinations of one 2D and two 1D ICRs, using the notation by Mulliken [81]. Note that we drop the subscript of the ICRs if the choice of the subscript does not affect the result. Furthermore, for the 2D ICRs of the point group $C_{6(v)}$ we define: ${}^2E_2\,{}^1E_2 \mapsto E_1$, and ${}^2E_1\,{}^1E_1 \mapsto E_2$. For convenience we list the triple-point types in the third column.

n	ICRs	Type	$\lvert\chi \mod n\rvert$ [a]	w_2
6	$(E_1; A, A)$	(A, A)	1	1
	$(E_1; B, B)$	(B, B)	2	0
	$(E_2; A, A)$	(B, B)	2	0
	$(E_2; B, B)$	(A, A)	1	1
4	$(E; A, A)$	(A, A)	1	1
	$(E; B, B)$	(A, A)	1	1
3	$(E; A, A)$	(B, B)	1 or 2 [b]	1 or 0 [b]

[a] Here we use the convention that $\chi \mod n \in (-\lfloor n/2 \rfloor, \ldots, \lfloor n/2 \rfloor]$, such that $\lvert\chi \mod n\rvert \in \{0, 1, \ldots, \lfloor n/2 \rfloor\}$, see text.
[b] Explicitly, we find $\chi = -1$, which cannot be distinguished from 2. However, because χ is only well-defined up to a sign, χ could also take the value 1. This implies that the parity of χ is not uniquely determined by the symmetry indicator and thus w_2 is not constrained by C_3 symmetry.

of unique values of the Euler monopole charge that can be distinguished based on the ICRs of the two valence bands. More precisely, all values of χ such that $\chi = mn \pm p$ (with n the order of the rotational symmetry, p an element of the just specified set, and $m \in \mathbb{Z}$) are not distinguishable from $\chi = p$. With the convention that $\chi \mod n \in (-\lfloor n/2 \rfloor, \ldots, \lfloor n/2 \rfloor]$, we write $\lvert\chi \mod n\rvert$ to indicate the representative of the corresponding equivalence class of all such indistinguishable values of χ. In particular, for $n = 6$, values $\lvert\chi\rvert = 4$ and $\lvert\chi\rvert = 5$ are indistinguishable from $\lvert\chi\rvert = 2$ and $\lvert\chi\rvert = 1$, respectively; while for $n = 4$, the value $\lvert\chi\rvert = 3$ is indistinguishable from $\lvert\chi\rvert = 1$. For these two cases the parity of χ is well defined, such that the second Stiefel-Whitney monopole charge, given by $w_2 = \chi \mod 2 \in \mathbb{Z}_2$, is uniquely determined. In contrast, for $n = 3$, the symmetry-indicator formula for χ can only distinguish values

$|\chi| = 0$ and $|\chi| = 1$, with $|\chi| = 2$ being indistinguishable from $|\chi| = 1$. This implies that the parity is not fixed by the symmetry indicators and therefore the second Stiefel-Whitney monopole charge in C_3-symmetric models is not determined from the symmetry eigenvalues.

6.2.4. Effect of symmetry breaking

The discussion so far has focused on spinless systems with $\mathcal{PT}$ symmetry, corresponding to the magnetic point groups in rows two and four of Table 4.1. This has allowed us to characterize the triple-point pairs with the Stiefel-Whitney monopole charge. However, as we have seen in Chapter 4, stable triple-point pairs can exist even when the $\mathcal{PT}$ symmetry is removed; in this case, the monopole charges cease to exist, but the bulk-hinge correspondence of the triple-point pairs persists. In this subsection, we discuss the effect of symmetry breaking on the derived bulk-hinge correspondence of triple-point pairs, summarized in Table 6.9. First, we argue that the hinge-charge jumps derived for the cases with m_v and $\mathcal{PT}$ symmetry still apply when the $\mathcal{PT}$ symmetry is broken while m_v remains present. We continue with a discussion of how the derived results generalize to the cases where the triple-point pairs are protected by the antiunitary $C_n\mathcal{PT}$ rotational symmetry. Finally, we briefly analyze the effect of breaking other combinations of symmetries, which generally leads to the loss of triple-point pairs and to the formation of other species of band nodes.

Triple points protected by C_n and mirror symmetry

We first discuss the effect of breaking $\mathcal{PT}$ symmetry while keeping the rotational symmetry C_n. According to Table 4.1, mirror symmetry m_v is then required to protect triple points. The crucial observation is that if both $\mathcal{PT}$ and mirror m_v symmetry are present in the little co-group, then the ICRs are not modified by the removal of $\mathcal{PT}$ [84, 85], i.e., the ICRs of the unitary symmetries of the full group are exactly given by the ICRs of the unitary subgroup. As a consequence, the classification of triple-point pairs in systems with m_v symmetry based on ICRs is *identical* both with and without $\mathcal{PT}$ symmetry; in fact, our analysis in Section 4.5 revealed that the *type* (A versus B) produced by the crossing of specified ICRs is also unaffected by the removal of $\mathcal{PT}$. An analogous statement also applies to the result that the ICR combination $(E; A, B)$ is necessarily gapless, see Appendix E.4.

To derive the hinge-charge jumps $\Delta Q_{\llcorner}$ associated with triple-point pairs protected by m_v symmetry without $\mathcal{PT}$, we should, in principle, repeat the above-described analysis with the symmetry-indicator formulas that do not

Table 6.9.: Effect of symmetry breaking on triple-point pairs. We initially consider triple-point pairs (TPPs) in the combined presence of $\mathcal{PT}$ (space-time inversion), C_n (rotation of order $n \in \{3, 4, 6\}$) and m_v (vertical mirror) symmetries, corresponding to the first row of the table. They are characterized by the second Stiefel-Whitney monopole charge w_2, by symmetry indicators ($\#\Pi_p^{(n)}$), and by the fractional hinge-charge jump (integer multiples of e/n). We then consider the breaking of the various symmetries and find that triple-point pairs can evolve into higher-order Weyl points (HO-Weyl), into nodal lines (NLs), or into Weyl points or nodal lines without higher-order topology (indicated as "various").

$\mathcal{PT}$	C_n	$C_n\mathcal{PT}$	m_v	Nodes	Bulk invariant	Hinge charge
✓	✓	✓	(✓)	TPPs	w_2, $\#\Pi_p^{(n)}$	$e/n\,\mathbb{Z}$
✗	✓	✗	✓	TPPs	$\#\Pi_p^{(n)}$	$e/n\,\mathbb{Z}$
✗	$C_{n/2}$[a]	✓	(✓)	TPPs	$\#\Pi_p^{(n)}$	$2e/n\,\mathbb{Z}$
✓	✗	✗	(✓)	NLs	w_2	not quantized
✗	✓	✗	✗	HO-Weyl	$\#\Pi_p^{(n)}$	$e/n\,\mathbb{Z}$
✗	✗	✗	(✓)	various	-	not quantized

[a] The requirement of the presence of $C_{n/2}$ restricts n to $4, 6$.

assume time-reversal symmetry, i.e., Eqs. (3.27) to (3.29), and the ICRs of the point groups without $\mathcal{PT}$ symmetry. However, as described in the previous paragraph, the ICRs (and therefore the rotation eigenvalues) are identical to the ICRs of the corresponding point groups *with* $\mathcal{PT}$ symmetry, such that Eqs. (3.28) and (3.29), for the cases we are considering, still simplify to Eqs. (3.30) and (3.31). This implies that the jumps in the symmetry indicators are not changed when breaking $\mathcal{PT}$ symmetry while keeping the rotational symmetry C_n, and the hinge-charge jumps $\Delta Q_{\llcorner}$ remain unaltered as well. On the other hand, the monopole charges are not defined in the absence of $\mathcal{PT}$ symmetry. Therefore, all results in Table 6.2 except for the last two rows apply to systems with mirror m_v symmetry but no $\mathcal{PT}$ symmetry.

Triple points protected by the antiunitary $C_n\mathcal{PT}$ symmetry

Since triple points can also be protected by the antiunitary rotational symmetry $C_n\mathcal{PT}$ (cf. Table 4.1), $\mathcal{PT}$ symmetry can alternatively be broken while keeping $C_n\mathcal{PT}$. In such a case, the C_n rotational symmetry is broken, while $C_{n/2} = (C_n\mathcal{PT})^2$ is a symmetry of the system. We have to distinguish two scenarios: the triple points are either protected by $C_6\mathcal{PT}$ or by $C_4\mathcal{PT}$. Note that, as we discuss in Appendix E.4, Eq. (6.24) still applies in these magnetic point

groups, yet a careful analysis reveals that this constraint does not imply the inadmissibility of any triple-point-pair configurations.

We begin with analyzing the case of $C_6\mathcal{PT}$, where the largest remaining rotational symmetry is C_3; therefore, a triangular geometry needs to be considered and the relevant rotational symmetry quantizing the hinge charges is C_3. Furthermore, we find [84, 85] that the corresponding magnetic point groups with and without m_v symmetry ($\bar{6}'m2'$ and $\bar{6}'$, respectively) have the same unitary subgroup as the $\mathcal{PT}$-symmetric magnetic point groups $\bar{3}'m$ and $\bar{3}'$, respectively, with matching ICRs. As a consequence, the hinge-charge jump is the same as for the other little co-groups with C_3 rotational symmetry, i.e., no change in the bulk-boundary correspondence. This has motivated us to group C_3 and $C_6\mathcal{PT}$ within a single column of Table 6.2. We remark, however, that although the ICRs of the subgroup and the higher-order bulk-boundary correspondence are equivalent to the C_3 case, this is not true for the corresponding triple-point types, which depend on the ICRs of the full point group. Recall from Chapter 4 that irrespective of the presence (magnetic point group $\bar{6}'m2'$) versus absence (magnetic point group $\bar{6}'$) of m_v symmetry, the triple points protected by $C_6\mathcal{PT}$ are *always* type A.

Similarly, C_4 and $\mathcal{PT}$ can be broken while keeping $C_4\mathcal{PT}$. However, in that case the largest remaining rotational symmetry is C_2, such that in a square geometry only the *sum* over two adjacent hinges gives a quantized charge [147]. The resulting little co-groups are the magnetic point groups $\bar{4}'2'm$ (with m_v mirrors) and $\bar{4}'$ (without m_v mirrors), which are subgroups of the $\mathcal{PT}$-symmetric magnetic point groups $4/m'mm$ and $4/m'$, respectively. It is easily verified [84, 85] that all four listed magnetic point groups have equivalent C_2-rotation eigenvalues for the 1D and 2D ICRs: all 1D ICRs are *even* while all 2D ICRs are *odd* under C_2. Since in the presence of $C_4\mathcal{PT}$ the hinge-charge jump is completely determined by C_2-rotation eigenvalues, the hinge-charge jump of triple-point pairs protected by $C_4\mathcal{PT}$ is, in principle, the same as in the C_4 case. However, since only the sum of charges on two adjacent hinges is quantized, the resulting jump is doubled to $\Delta Q_{\llcorner} = 2 \times \frac{e}{4} \mod e = \frac{e}{2} \mod e$. The triple points protected by $C_4\mathcal{PT}$ are always type A, i.e., of the same type as before the $\mathcal{PT}$ breaking. With this analysis, we explained the "C_2" column in Table 6.2, and established the higher-order bulk-boundary correspondence for all triple-point pairs listed in Table 4.1.

Breaking the symmetry protection of triple points

Besides breaking the symmetry in ways that keep the triple points robust, we briefly discuss the effect of breaking symmetries that protect the triple points. We find that this generically results in the conversion of the triple points to

other species of band nodes [249]. The case of broken C_n symmetry (with or without m_v) in the presence of $\mathcal{PT}$ symmetry has already been discussed implicitly in Section 6.1.1 for type-(A,A) triple-point pairs, where we revealed their conversion into multiband nodal links carrying a nontrivial second Stiefel-Whitney monopole. Using the results in Table 6.2, we can now extend this discussion to generic triple-point pairs. If the triple-point pair carries $w_2 = 1$, then the second Stiefel-Whitney monopole implies stable multiband nodal links upon breaking the rotational symmetry. On the other hand, note that $w_2 = 0$ only arises for type-(B,B) triple-point pairs. Since these are characterized by the attached nodal-line arcs carrying a π-flux of Berry phase [161], and this quantization is unaffected by the broken rotational symmetry, a small C_n-breaking perturbation leaves behind a nodal-line composition with a trivial second Stiefel-Whitney monopole. In both cases, $w_2 \in \{0,1\}$, the absence of rotational symmetry implies the *absence* of the hinge-charge quantization for all geometries depicted in Fig. 6.6.

We next analyze the situation where C_n is kept but both m_v and $\mathcal{PT}$ are broken. In such cases, the rotational symmetry ensures that the hinge-charge jump associated with the triple-point pair is maintained. At the same time, it is impossible to protect nodal lines (including the 2D ICR along the HSL) without $\mathcal{PT}$ and m_v [162] using C_n alone, and instead Weyl points [27] become the generic band degeneracy. Therefore, the breaking of both m_v and $\mathcal{PT}$ symmetry results in a *higher-order Weyl semimetal* with Weyl points along the rotation axis [250–252], characterized by quantized hinge-charge jumps.

We remark that in spinless systems higher-order *Dirac* points [253–256] cannot be obtained by perturbing a triple-point pair; and vice versa, a triple-point pair cannot be created by perturbing a higher-order Dirac point. Nonetheless, the results in Table 6.2 readily generalize to include the higher-order Dirac points that are realized in C_6-symmetric models by crossing two different 2D ICRs [256]. Indicating such a crossing as $(E_1;E_2)$, we formally write $(E_1;E_2) \sim (E_1;D_a^{1\mathrm{D}},D_b^{1\mathrm{D}}) - (E_2;D_a^{1\mathrm{D}},D_b^{1\mathrm{D}})$. This equation represents the fact that the two pairs of triple-point pairs can be evolved into the higher-order Dirac point: to see this, assume that along k_z the two 1D ICRs (for simplicity dispersionless) are first crossed by a 2D ICR E_1 with increasing energy and subsequently by 2D ICR E_2 with decreasing energy. By shifting the energy of the dispersionless 1D ICRs to higher values, the nodal feature at half-filling indeed evolves from two triple-point pairs into a single Dirac point. However, this continuous change preserves the total topological characterization of the band nodes, therefore (cf. Table 6.2) we deduce that the higher-order Dirac point is characterized by hinge-charge jump $\Delta Q_{\llcorner}^{(6)} = \frac{e}{6} - \left(-\frac{e}{3}\right) = \frac{e}{2} \mod e$ and by a nontrivial Stiefel-Whitney monopole $w_2 = 1 - 0 = 1 \mod 2$.

Finally, if C_n and $\mathcal{PT}$ are broken and only m_v is kept, then both the second Stiefel-Whitney class as well as the rotational symmetry indicators become invalid. As a consequence, no higher-order topology remains. Depending on the details of the perturbation, the m_v symmetry could leave behind mirror-protected nodal lines or the system opens an energy gap. If m_v is also broken, then depending on the details of the perturbation the system either becomes a Weyl semimetal or opens an energy gap.

6.3. Minimal models

In the previous section, we have shown that triple-point-pair configurations demarcate a nodal-line segment that can be characterized by an Euler and second Stiefel-Whitney monopole charge (if $\mathcal{PT}$ is present) and by a fractional hinge-charge jump (for all cases). Here we verify these theoretical predictions by analyzing several concrete tight-binding models: First, in Section 6.3.1, we introduce a C_4-symmetric model with two type-(A,A) triple-point pairs. Then, in Sections 6.3.2 and 6.3.3, we present two C_6-symmetric models, one involving type-(A,A) and the other involving type-(B,B) triple-point pairs. Finally, in Section 6.3.4, we discuss two C_3-symmetric models, one with trivial and one with nontrivial second Stiefel-Whitney monopole charge. In all models, we confirm that the hinge-charge jump as well as the monopole charges follow the predictions of Table 6.2.

For simplicity, all the discussed models retain both the $\mathcal{PT}$ symmetry and the mirror m_v symmetry. It follows from Table 4.1 and from the subgroup relations discussed therein, that models for all other species of triple-point pairs can, in principle, be obtained by applying an appropriate perturbation to one of the C_4 or C_6 models discussed in the following subsections. We utilize this feature in Section 6.3.4, where we break the C_2 symmetry in each of the two C_6-symmetric models. This construction allows us to explicitly show that the second Stiefel-Whitney class is not symmetry-indicated in C_3 symmetric systems, as previously stated (but not proved) in Sections 6.1.2 and 6.2.

To construct these tight-binding models, we proceed as follows. We first choose a point group (D_{4h} and D_{6h} for our models) containing the little co-group $\overline{\mathcal{G}}^{\mathbf{k}}$, which we want to protect the triple-points, as a subgroup. The choice of orbitals determines the irreducible representations of the point group. Using the 3D GenPos application on the Bilbao crystallographic server, we determine a set of possible generators of that point group, and then find their matrix representations using the Representations PG application [83]. To find the ICRs corresponding to the irreducible representations of the chosen orbitals after inclusion of $\mathcal{PT}$ symmetry with $(\mathcal{PT})^2 = +1$, we follow Ref. 77.

Given the set of generators, their ICRs and a generating set of hopping vectors, we use the PYTHON package QSYMM [240] to construct a family of symmetry-allowed Bloch Hamiltonians. Finally, we tune the parameters in that family of Hamiltonians such that we obtain a four-band triple-point pair, accompanied by the minimal number of additional nodal lines. This is achieved by first introducing a double band inversion at Γ by setting selected intra-orbital hopping parameters to be nonvanishing, and then by adding inter-orbital terms until we gap out all band nodes that are not required by symmetry or topology. Note that the type of the triple points can be predicted using the classification developed in Chapter 4. Using topological quantum chemistry and the BANDREP application on the Bilbao crystallographic server [83, 116, 131], we deduce the ICRs at the high-symmetry points, and using the COMPATIBILITY RELATIONS [83] infer the ones along the relevant rotation axis.

6.3.1. C_4-symmetric model

We start with the model that has the simplest geometry in real space. It is a hopping model of spinless particles on a tetragonal lattice (with lattice constants set to $a = c = 1$ for simplicity) and has the (symmorphic) space group $P4/mmm$ (No. 123) with isogonal point group D_{4h}. As illustrated in Fig. 6.10a, we place (p_x, p_y) orbitals transforming in the ICR E_u at Wyckoff position $1a$, and the orbitals d_{xy} and $d_{x^2-y^2}$, transforming in $B_{1\mathrm{g}}$ and $B_{2\mathrm{g}}$, respectively, at Wyckoff position $1c$. The site-symmetry group of both considered Wyckoff positions corresponds to the complete D_{4h} point group.

In the basis $(\mathrm{i}p_x, \mathrm{i}p_y, d_{xy}, d_{x^2-y^2})$, the model has Bloch Hamiltonian

$$\begin{aligned} H^{(4)}_{\mathsf{AA}}(\mathbf{k}) = &- \left[t_1 + 2t_2\left(\cos k_x + \cos k_y + \cos k_z\right)\right]\gamma_3 + t_3\left(\gamma_{14} - \gamma_{25}\right) \\ &- t_4\left(\cos k_x - \cos k_y\right)\left(\gamma_{14} + \gamma_{25}\right) + 2t_5 \sin k_x \sin k_y \left(\gamma_{15} - \gamma_{24}\right) \\ &+ 2\sqrt{2}t_6\left(\cos\tfrac{k_x}{2}\sin\tfrac{k_y}{2}\,\gamma_1 - \cos\tfrac{k_y}{2}\sin\tfrac{k_x}{2}\,\gamma_2\right), \end{aligned} \tag{6.40}$$

where $\gamma_1 = \sigma_x \otimes \tau_x$, $\gamma_2 = \sigma_x \otimes \tau_z$, $\gamma_3 = \sigma_z \otimes \mathbb{1}_\tau$, $\gamma_4 = \sigma_x \otimes \tau_y$ and $\gamma_5 = \sigma_y \otimes \mathbb{1}_\tau$ are Gamma matrices obeying $\{\gamma_a, \gamma_b\} = 2\delta_{ab}$, and $\gamma_{ab} = \frac{\mathrm{i}}{2}[\gamma_a, \gamma_b]$; Pauli matrices σ_i act on the Wyckoff position degree of freedom, and Pauli matrices τ_i act on the orbital degree of freedom at fixed Wyckoff position. The point group is generated by a $\frac{\pi}{2}$-rotation around the z-axis $C_{4z} = -\operatorname{diag}(\mathrm{i}\tau_y, \mathbb{1}_\tau)$, a π-rotation around the y-axis $C_{2y} = -\sigma_z \otimes \tau_z$, and inversion $\mathcal{P} = -\sigma_z \otimes \mathbb{1}_\tau$. Additionally, the Hamiltonian possesses time-reversal symmetry $\mathcal{T}$. Note that we have intentionally chosen the basis of p-orbitals to be *imaginary*, which results in $\mathcal{PT}$ is represented by complex conjugation $\mathcal{K}$, such that the Bloch

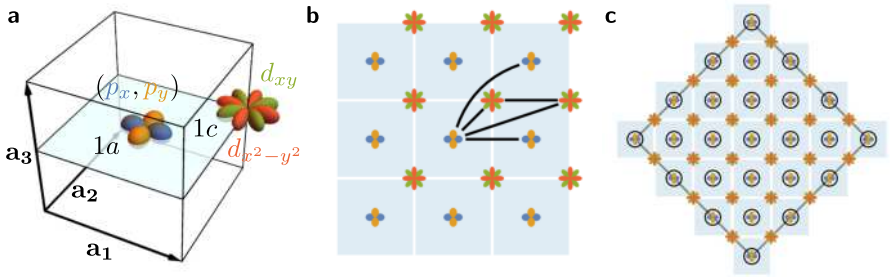

Figure 6.10.: Definition of the C_4-symmetric model. (**a**) Real-space unit cell spanned by the lattice vectors $\mathbf{a}_{1,2,3}$ with the four orbitals: (p_x, p_y) at Wyckoff position $1a$ and d_{xy}, $d_{x^2-y^2}$ at $1c$. (**b**) Single layer (for fixed z) of the 3D lattice. The blue shaded regions indicate the projection of the unit cells with the orbitals indicated in the same colors as in (a). Black lines (where further symmetry-related lines are dropped to maintain clarity) indicate the in-plane hopping processes included in the model. (**c**) In-plane termination for the nanowire geometry. The blue shadowed regions denote unit cells with ionic charge $2|e|$ placed at the center (black circle). To establish terminology, we say that the depicted geometry consists of 3.5×3.5 unit cells.

Hamiltonian is a real matrix [66]. In real space, Eq. (6.40) corresponds to the tight-binding model with in-plane hopping indicated by black lines in Fig. 6.10b, whereas the nonvanishing out-of-plane hopping processes (not illustrated) are strictly vertical and intra-orbital. We choose the model parameters such that the p orbitals have lower energy at all high-symmetry points with the exception of a double band inversion at Γ: $t_1 = 4$, $t_2 = t_6 = -1$, $t_3 = t_4 = \frac{1}{4}$ and $t_5 = -\frac{1}{4}$. The resulting band structure is shown in Fig. 6.11a.

The HSL ΓZ has little co-group C_{4v} combined with $\mathcal{PT}$, corresponding to the magnetic point group $4/m'mm$ of Table 4.1. The eigenstates of the model in Eq. (6.40) along ΓZ transform according to one 2D ICR E (p-like) and two 1D ICRs B_1 and B_2 (d-like). The degeneracy of p-orbitals along ΓZ can be interpreted as a nodal line, which due to the double band inversion at Γ is crossed by the two remaining d-like bands at four places, $k_z = \pm\kappa_1, \pm\kappa_2$, resulting in two triple-point pairs at (κ_1, κ_2) and $(-\kappa_2, -\kappa_1)$, respectively, visible in Fig. 6.11b. We observe that the triple points are not attached to additional nodal lines lying off the rotation axis, consistent with the classification from Chapter 4 that predicts all triple points on C_{4v}-symmetric HSLs to be type A. The only other band degeneracy exhibited by the model is the 2D ICR along the vertical hinge MA of the Brillouin zone, corresponding to a vertical nodal line formed by the two unoccupied p-like bands; however,

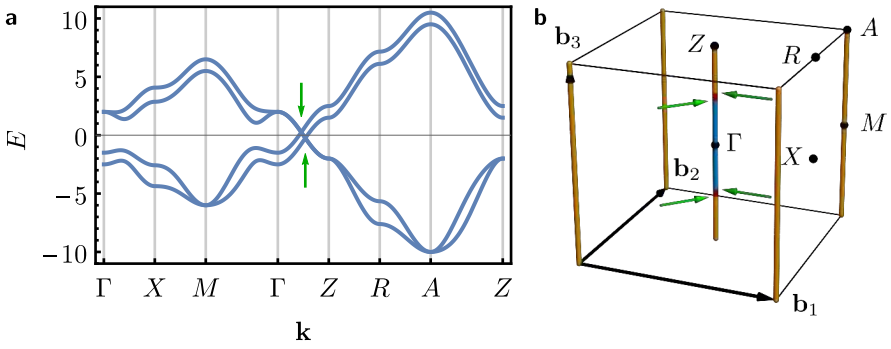

Figure 6.11.: Band structure and nodal lines of the C_4-symmetric model. (**a**) Band structure along the high-symmetry lines. (**b**) Brillouin zone spanned by the reciprocal lattice vectors $\mathbf{b}_{1,2,3}$ with high-symmetry points $\{\Gamma, Z, X, R, M, A\}$ shown. Nodal lines in the first, second and third band gap are displayed in orange, red, and blue color, respectively. The four triple points of the model are indicated by green arrows.

this nodal line does not have any effect on the discussed phenomenology.

As we argued in Section 6.1.1 and proved using symmetry indicators in Section 6.2, each four-band triple-point pair along a C_4-rotation axis (which are automatically type A) demarcates a nodal-line segment in the principal gap (red in Fig. 6.12a) which carries second Stiefel-Whitney monopole charge $w_2 = 1$. This can be diagnosed by computing the Wilson-loop spectrum of the lower two bands on an ellipsoid (purple in Fig. 6.12a) containing one such nodal-line segment. Figure 6.12a shows that there is a single winding, confirming that indeed $|\chi| = 1$ and $w_2 = 1$. As discussed in Section 6.1.1, w_2 can alternatively be obtained by comparing the second Stiefel-Whitney class on insulating 2D cuts below and above the triple-point pair. Figure 6.13a shows the Wilson-loop spectrum of the occupied bands for $k_z = 0, \pi$. For $k_z = 0$, the eigenvalues wind once around the 2D Brillouin-zone torus, and for $k_z = \pi$, they do not wind, such that $\Delta w_2 = 1$, consistent with the monopole charge. Note that the $\mathcal{PT}$ symmetry of the model allows us to compute the second Stiefel-Whitney class for a cut at *each* value of k_z where the central energy gap is open, plotted as a yellow dashed line in Fig. 6.13b.

To uncover the quantized fractional hinge-charge jump predicted by Table 6.2, we next consider a nanowire geometry, i.e., a system which is finite in x- and y- but infinite in z-direction, at half-filling. Thus, only the momentum $k_z \in [-\pi, \pi]$ that runs along the fourfold rotation axis remains a good quantum number and the Brillouin zone is reduced to a *hinge Brillouin zone*. To

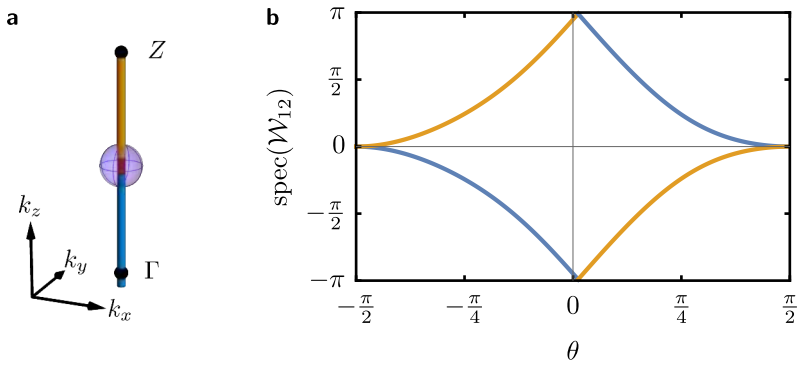

Figure 6.12.: Second Stiefel-Whitney monopole charge of the C_4-symmetric model. (**a**) Nodal configuration near the high-symmetry line ΓZ and the ellipsoid (purple) on which the monopole charge is computed. (**b**) Spectrum of the Wilson-loop operator $\mathcal{W}_{12}(\theta)$ of the lower two bands computed on that ellipsoid, parametrized by the latitude $\theta \in [-\pi/2, \pi/2]$. The spectrum shows a single winding (odd parity) and thus implies $|\chi| = 1$ and $w_2 = 1$.

observe the quantized hinge charges and the predicted hinge-charge jump, the termination of the nanowire has to preserve the C_4 symmetry; here, we opt to study the model in the rotated square geometry shown in Fig. 6.10c. To fully specify the model, we also need to choose where to place the ionic charges, namely $2|e|$ per unit cell to compensate for the half filling of the electron bands. Here, $e < 0$ is the elementary electron charge. The placement is not fixed by the tight-binding model itself and in a real material would depend on the chemical composition. While the ionic charge distribution affects the value of the hinge charge and can even lead to fractional hinge or corner charges for systems that are electronically completely trivial [257], it does not affect the hinge-charge *jump*, because of its independence of k_z. For concreteness, we assume the ionic charge to be concentrated at the center of the 2D projection of the unit cell (Wyckoff position $1a$), as indicated with black circles in Fig. 6.10c. However, other distributions of the ionic charge are possible; in particular, moving charge $n|e|$ from $1a$ to $1b$ changes the corner charge of a 2D system by $-\frac{n|e|}{4}$, as is easily verified from Eqs. (17-19) in Ref. 151.

At fixed k_z in the hinge Brillouin zone, we can view the bulk Hamiltonian as being described by an effective 2D model, $H_{k_z}(k_x, k_y)$ on the 2D lattice with 20.5×20.5 unit cells (compare Fig. 6.10c for 3.5×3.5 unit cells). We use exact diagonalization to study the corresponding family of Hamiltonians $\mathcal{H}_{k_z}$ in real

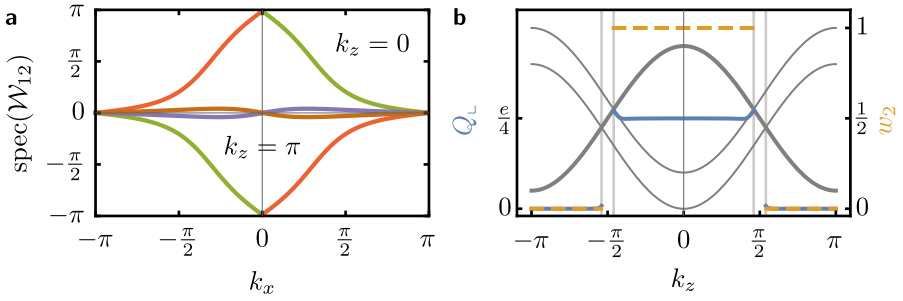

Figure 6.13.: Second Stiefel-Whitney class and hinge-charge in the C_4-symmetric model. (**a**) Wilson-loop spectrum of the two occupied bands in the 2D Brillouin zone for fixed $k_z = 0$ and $k_z = \pi$, respectively. For $k_z = 0$, we observe a winding with odd parity, indicating $w_2 = 1$, while for $k_z = \pi$, the absence of a winding implies $w_2 = 0$. (**b**) Quantized hinge charges (blue solid line) in a nanowire geometry identified using exact diagonalization, and second Stiefel-Whitney class (yellow dashed line) obtained from the Wilson-loop winding; both plotted as a function of k_z in the wire geometry. Cuts at fixed k_z can each be interpreted as 2D flakes as shown in Fig. 6.14 that are characterized by a corner charge $Q_\mathrm{L}(k_z)$. The edge charge of the model vanishes. For reference, the bulk band structure along k_z for $k_x = k_y = 0$ is displayed in gray with the 1D (2D) degenerate bands plotted by a thin (thick) lines.

space and compute the charge distribution of all occupied states for various k_z. Results for $k_z = 0$ and $k_z = \pi$ are shown in Figs. 6.14a and 6.14b, respectively. On length scales smaller than a unit cell, we observe strong oscillations, which make it impossible to directly integrate the charge on a corner or even detect any possible localization. This is a typical problem for the case of ionic crystals and is usually tackled by coarse-graining the charge distribution [150, 151, 258]. We perform a discrete version of such a coarse-graining by following a scheme explained in Appendix F.1. Considering each orbital position, i.e., the two per unit cell, as a separate site of a square lattice, we compute the charge on the *dual square lattice* (cf. Fig. F.1b) by distributing charge on each site of the original lattice with equal weights to the nearest sites of the dual lattice. This coarse-grains the charge distribution to the length scale of one unit cell and significantly reduces the oscillations, as shown in Figs. 6.14c and 6.14d.

After coarse-graining, we can integrate over various regions to find the bulk, edge and corner charges. First, we observe that the bulk and edge charge vanish for both $k_z = 0, \pi$ as can be seen in Figs. 6.14c and 6.14d. Due to the double band-inversion at Γ, the model has vanishing Berry phases along the path $M\Gamma M$ (perpendicular to the edge), which implies [102] that the bulk

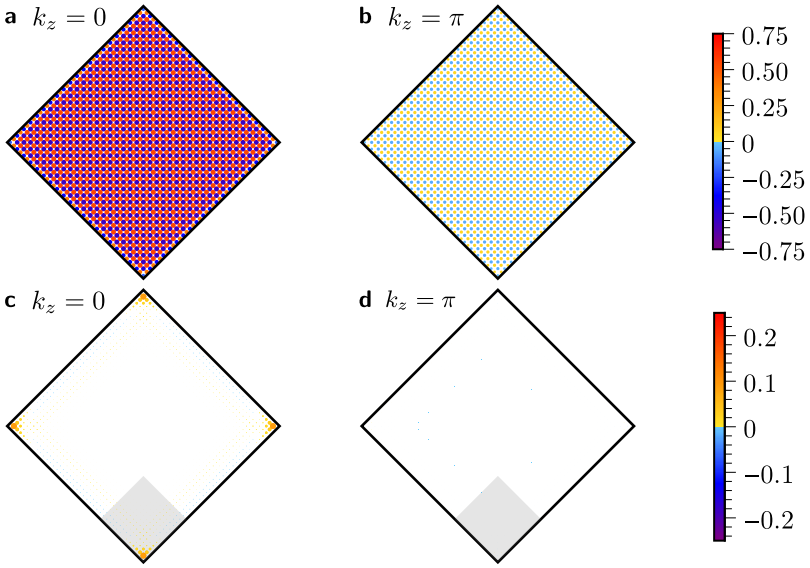

Figure 6.14.: Charge distribution of the C_4-symmetric model. Assuming the compensating ionic charge to be located at Wyckoff position $1a$, we plot the total charge distribution at $k_z = 0$ (**a,c**) and at $k_z = \pi$ (**b,d**) . The termination is illustrated for fewer unit cells in Fig. 6.10c. The total charge at each lattice site is indicated by a disk with its value encoded both in the area of the disk and the color scale (see legend on the right of each row). Note that the disks are scaled separately for each panel: compared to panel (a) the disks are enlarged by factors of (b) 2, (c) 3 and (d) 6 to increase visibility. To remove sub-unit-cell oscillations of the charge distribution observable in (a,b), we perform coarse-graining of the data, resulting in panels (c) and (d), respectively.

polarization [101] and therefore the edge charge vanish. On the other hand, the corner charge only vanishes for $k_z = \pi$. The nonvanishing corner-charge at $k_z = 0$ is a consequence of the corner-induced filling anomaly [147] which we introduced in Section 3.2.1. This excess charge is strongly localized near the four corners. Integrating over the gray area indicated in the figure, and taking care that the integration region forms 90° angles with the edges [150], we find $Q_\llcorner = 0.2498e$ for $k_z = 0$ and $Q_\llcorner = 8 \cdot 10^{-9} e$ for $k_z = \pi$. The deviations from the expected values $\frac{e}{4}$ and 0 are due to finite-size effects, and can be further reduced by increasing the total system size and the coarse-graining scale while keeping the relative size of the integration region fixed. The finite-size effects become more prominent the smaller the gap is, which can be observed in

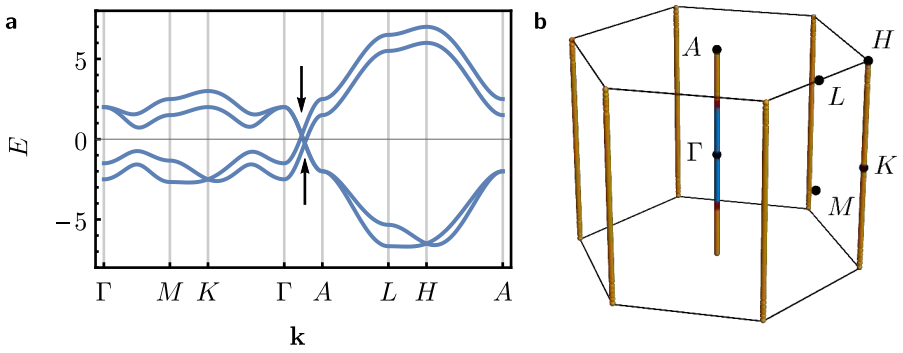

Figure 6.15.: Band structure and nodal lines of the C_6-symmetric model with two type-A triple points. (**a**) Band structure with the two triple points indicated by black arrows. (**b**) Nodal-line structure in the full Brillouin zone with the high-symmetry points indicated. Nodal lines in the first, second and third band gap of the four-band model are shown in orange, red and blue, respectively.

Fig. 6.13b in terms of the deviations from the quantized values for k_z near to the closing of the principal gap (i.e., in the vicinity of each triple point), where the localization length of the corner charge is expected to grow.

Based on the results for all k_z shown in Fig. 6.13b, we observe that the model has vanishing edge charge (related to vanishing Berry phase of the occupied bands), and a k_z-dependent corner charge (which is interpreted as a hinge charge of the 3D system) $Q_{\llcorner}(k_z)$ plotted as a blue line. Three regions can be identified: (1) $Q_{\llcorner} = \frac{e}{4}$ for $|k_z| < \kappa_1$, (2) $Q_{\llcorner} = 0$ for $|k_z| > \kappa_2$, and (3) the region $\kappa_1 \leq |k_z| \leq \kappa_2$ where the bulk is gapless and the corner charge therefore undefined. These regions reflect exactly the regions defined by which gap the central nodal line is located in, cf. Fig. 6.11b. In particular, we observe a jump of the hinge charge from region (2) to region (1) by $\Delta Q_{\llcorner} = +\frac{e}{4}$. As we have seen above, this is accompanied by a jump of the second Stiefel-Whitney class by +1 and both agree with the prediction of Table 6.2, since the ICRs of the bands involved in the two triple points on the HSL ΓZ are $(E; B_1, B_2)$.

6.3.2. C_6-symmetric model with type-A triple points

To realize a type-(A, A) triple-point pair along a C_6-rotational symmetry, we consider the ΓA line of the hexagonal space group $P6/mmm$ (No. 191) with lattice constants $a = c = 1$. More specifically, we consider a model with $(d_{xy}, d_{x^2-y^2})$ orbitals transforming in the 2D ICR E_{2g} and orbitals $f_{x(x^2-3y^2)}$

and $f_{y(3x^2-y^2)}$ transforming in 1D ICRs B_{1u} and B_{2u}, respectively, all placed at the Wyckoff position $1a$ with site-symmetry group D_{6h}. We adopt the basis $(d_{xy}, d_{x^2-y^2}, \mathrm{i}f_{x(x^2-3y^2)}, \mathrm{i}f_{y(3x^2-y^2)})$, such that $\mathcal{PT}$ is represented simply by complex conjugation. In the above basis, the Bloch Hamiltonian with only nearest neighbor in-plane as well as the nearest vertical hopping terms is

$$\begin{aligned} H^{(6)}_{\mathsf{AA}}(\mathbf{k}) = &- \left[t_1 + 2t_2\left(\cos k_x + 2\cos\tfrac{k_x}{2}\cos\tfrac{\sqrt{3}k_y}{2}\right) + t_3\cos k_z\right]\gamma_3 \\ &- t_4\left(\gamma_{14} - \gamma_{25}\right) - t_5\left[\left(\cos k_x - \cos\tfrac{k_x}{2}\cos\tfrac{\sqrt{3}k_y}{2}\right)\left(\gamma_{14} + \gamma_{25}\right)\right. \\ &\qquad \left. - \sqrt{3}\sin\tfrac{k_x}{2}\sin\tfrac{\sqrt{3}k_y}{2}(\gamma_{15} - \gamma_{24})\right] \\ &- 2t_6\left[\sin\tfrac{k_x}{2}\left(2\cos\tfrac{k_x}{2} + \cos\tfrac{\sqrt{3}k_y}{2}\right)\gamma_1 - \sqrt{3}\cos\tfrac{k_x}{2}\sin\tfrac{\sqrt{3}k_y}{2}\gamma_2\right], \end{aligned} \tag{6.41}$$

with the Gamma matrices defined as after Eq. (6.40) and Pauli matrices σ_i acting on the angular-momentum degree of freedom (coupling d - to f-orbitals), and Pauli matrices τ_i acting on the orbital degree of freedom at fixed angular-momentum. The generators of D_{6h} have matrix representations $C_{6z} = \mathrm{diag}(R(-2\pi/3), -\mathbb{1}_\tau)$, where $R(\theta)$ is the 2D rotation matrix, $m_v = \sigma_z \otimes \tau_z$, and $\mathcal{P} = \sigma_z \otimes \mathbb{1}_\tau$.

We tune the parameters such that the d-orbitals have lower energy than the f-orbitals at all high-symmetry points with the exception of a double-band-inversion at Γ: $t_1 = 3$, $t_2 = -\frac{1}{2}$, $t_3 = -2$, $t_4 = \frac{1}{4}$, $t_5 = \frac{1}{6}$ and $t_6 = -\frac{1}{3}$. Consequently, on ΓA two 1D ICRs (B_1, B_2) consecutively cross the 2D ICR (E_2) resulting in two type-A triple points. The band structure and the nodal-line configuration of the model are displayed in Figs. 6.15a and 6.15b, respectively. We remark that apart from the two-fold degeneracy along the ΓA line, the model also exhibits two-fold degeneracies along the KH lines; however, these lie within the occupied band subspace and therefore have no effect on the discussed features. The model exhibits no additional nodal lines. For the computation of the hinge charges, we set the compensating ionic charge to also reside at site $1a$.

According to Table 6.2, we expect a jump of $+\frac{e}{6}$ in the hinge charge and $+1$ both in the Euler and second Stiefel-Whitney class when going from the orange k_z-range to the blue k_z-range. More precisely, based on a symmetry eigenvalue analysis and Eqs. (6.8) and (6.18), we expect that the second Stiefel-Whitney class is 1 in the blue k_z-range and 0 in the orange k_z-range, while the hinge charge should be $\frac{e}{6}$ and 0, respectively. The results for the second Stiefel-Whitney class are verified by computing the Wilson-loop spectra of the lower two bands on horizontal cuts through the Brillouin zone as a function of k_z.

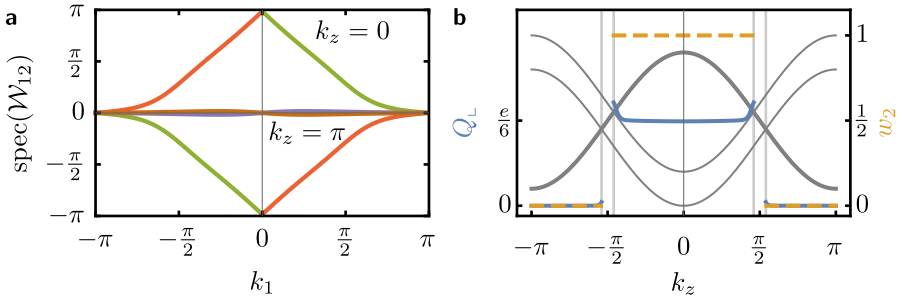

Figure 6.16.: Second Stiefel-Whitney class and hinge-charge in the C_6-symmetric model with two type-A triple points. (**a**) Spectrum of the Wilson-loop operator $\mathcal{W}_{12}$ of the lower two bands on horizontal cuts through the Brillouin zone (parameterized by the projection k_1 of the momentum onto the first reciprocal lattice vector). Green/red lines show the spectrum for $k_z = 0$ (single winding) and purple/brown lines for $k_z = \pi$ (no winding). (**b**) Hinge Brillouin zone with hinge charge $Q_\llcorner$ (blue solid line, left axis), second Stiefel-Whitney class w_2 (orange dashed line, right axis) and the projection of the bulk dispersion along $k_x = k_y = 0$ (gray). The doubly-degenerate band is displayed with a thicker line.

The second Stiefel-Whitney class is then given by the parity of the winding of the spectrum. Two examples, for $k_z = 0$ and $k_z = \pi$, are shown in Fig. 6.16a, and demonstrate that indeed $|\chi| = 1$ and $w_2 = 1$ for $k_z = 0$. Figure 6.16b shows w_2 as a function of k_z with the visible jumps at the position of the two triple points along the ΓA line.

To verify the results for the hinge charge, we construct a system finite in x- and y-directions with 16 hexagonal shells in the cross section (the cross section illustrated in Fig. 6.17a has three shells). Using exact diagonalization we find the charge distribution at half-filling for 2D cuts of the Brillouin zone that lie outside of the red k_z-range. Figure 6.17b shows the results of such analysis for $k_z = 0$. The charge is strongly localized at the corners of the 2D cross section while it vanishes both in the bulk as well as along the edges. Note that while the charge vanishes on the edges (integrating over the gray edge area in Fig. 6.17b we obtain $8 \cdot 10^{-4}|e|$), we also observe small oscillations of the charge in the direction perpendicular to the edges which visually obscure the localization of the corner charge. To reduce these oscillations, we perform coarse-graining similar to the one described in the previous subsection. The major technical difference is that here we coarse-grain over a hexagonal supercell with two shells, i.e., seven unit cells, in one iteration, see Fig. F.1c. After two iterations

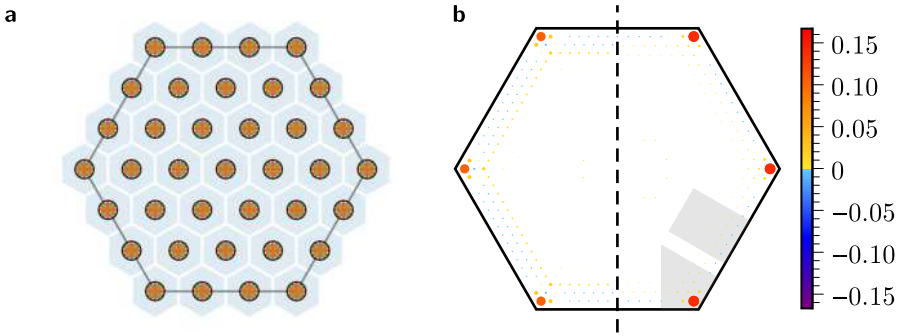

Figure 6.17.: Charge distribution in the C_6-symmetric model with two type-A triple points. (**a**) Cross-section through a hexagonal nanowire three shells wide; light blue hexagons indicate the model's unit cells. The orbitals are represented in color and all placed on top of each other in the center of the unit cell. The ionic charge is concentrated at the same position, indicated by the black circles. (**b**) Charge distribution for a cut through a 16-shell wide nanowire at $k_z = 0$. The charge at each site is indicated by a disk with its value encoded both in the area of the disk and the color scale (see legend on the right). The left half shows the charge distribution on the original lattice, and the right half shows the charge after two iterations of coarse-graining. A hinge charge of $Q_{\llcorner} = \frac{e}{6}$ with a strong localization is observed.

we end up with a coarse grained lattice that is smaller by two shells. Integrating over the gray corner area in Fig. 6.17b we obtain $0.1652e$, where the deviation from $\frac{e}{6}$ can be traced back to finite-size effects. As can be seen in Fig. 6.16b those finite-size effects grow stronger with decreasing energy gap.

6.3.3. C_6-symmetric model with type-B triple points

We next consider a C_6-symmetric model with type-(B, B) triple-point pair realized in the same space group ($P6/mmm$, No. 191) and on the same hexagonal lattice with lattice constants $a = c = 1$. The following four orbitals are placed at Wyckoff position $1a$: $f_{x(x^2-3y^2)}$ and $f_{y(3x^2-y^2)}$ transforming, respectively, in 1D ICRs B_{1u} and B_{2u}, together with (p_x, p_y) transforming in the ICR E_{1u}. Once more we adopt a basis such that $\mathcal{PT}$ is represented by $\mathcal{K}$: $(\mathrm{i}p_x, \mathrm{i}p_y, \mathrm{i}f_{x(x^2-3y^2)}, \mathrm{i}f_{y(3x^2-y^2)})$. Then, the Bloch Hamiltonian with only the

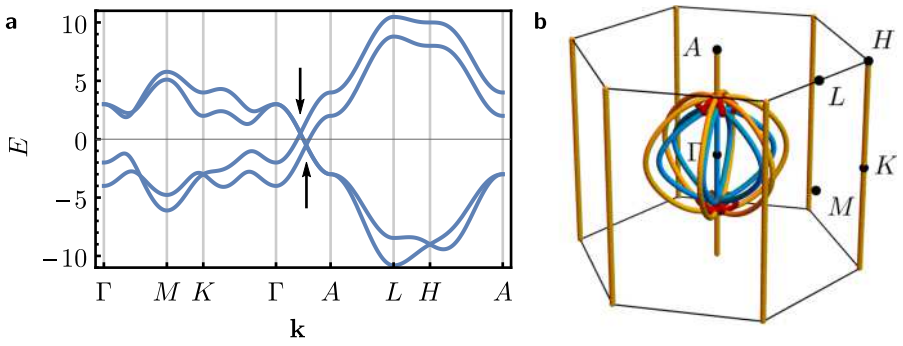

Figure 6.18.: Band structure and nodal lines of the C_6-symmetric model with two type-B triple points. (**a**) Band structure with the two triple points indicated by black arrows. (**b**) Nodal-line structure in the full Brillouin zone with the high-symmetry points indicated. Nodal lines in the first, second and third band gap of the four-band model are shown in orange, red and blue, respectively. Due to the triple points being type B, there are nodal-line arcs attached to them, visible in the nodal-line structure.

nearest neighbor in-plane and the nearest vertical hopping terms is

$$\begin{aligned} H^{(6)}_{\mathrm{BB}}(\mathbf{k}) = &- \left[t_1 + 2t_2\left(\cos k_x + 2\cos\tfrac{k_x}{2}\cos\tfrac{\sqrt{3}k_y}{2}\right) + t_3\cos k_z\right]\gamma_3 \\ &- t_4\left(\gamma_{14} - \gamma_{25}\right) - t_5\left[\left(\cos k_x - \cos\tfrac{k_x}{2}\cos\tfrac{\sqrt{3}k_y}{2}\right)\left(\gamma_{15} - \gamma_{24}\right)\right. \\ &\qquad \left. + \sqrt{3}\sin\tfrac{k_x}{2}\sin\tfrac{\sqrt{3}k_y}{2}\left(\gamma_{14} + \gamma_{25}\right)\right] \\ &- \sqrt{2}t_6\left[\left(\cos k_x - \cos\tfrac{k_x}{2}\cos\tfrac{\sqrt{3}k_y}{2}\right)\left(\gamma_1 - \gamma_2\right)\right. \\ &\qquad \left. - \sqrt{3}\sin\tfrac{k_x}{2}\sin\tfrac{\sqrt{3}k_y}{2}\left(\gamma_1 + \gamma_2\right)\right], \end{aligned} \tag{6.42}$$

with the Gamma matrices defined as after Eq. (6.40) and Pauli matrices σ_i acting on the angular-momentum degree of freedom (coupling p - to f-orbitals), and Pauli matrices τ_i acting on the orbital degree of freedom at fixed angular-momentum. The generators of D_{6h} have matrix representations $C_{6z} = \mathrm{diag}(R(2\pi/6), -\mathbb{1}_\tau)$, $m_v = \mathrm{diag}(\tau_x, -\tau_z)$, and $\mathcal{P} = -\mathbb{1}_\sigma \otimes \mathbb{1}_\tau$.

As in the previously discussed tight-binding models, we set the parameters to produce a double-band-inversion at Γ: $t_1 = 4$, $t_2 = -\frac{2}{3}$, $t_3 = -3$, $t_4 = -\frac{1}{2}$, $t_5 = -\frac{1}{3}$ and $t_6 = \frac{6}{5}$. As a consequence, the p-orbitals have lower energy than the f-orbitals at all high-symmetry points except Γ. Then, two 1D ICRs (B_1,

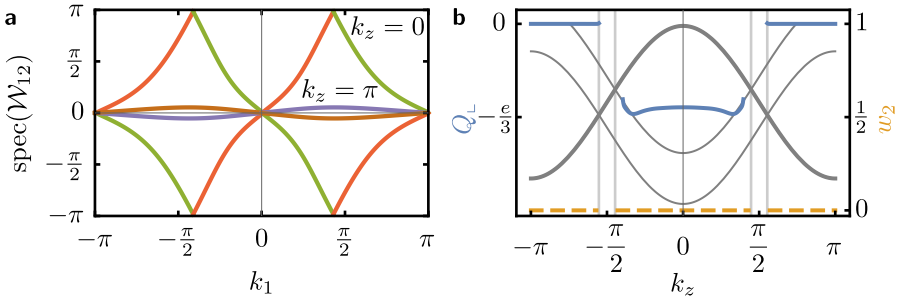

Figure 6.19.: Second Stiefel-Whitney class and hinge-charge in the C_6-symmetric model with two type-B triple points. (**a**) Spectrum of the Wilson-loop operator $\mathcal{W}_{12}$ of the lower two bands on horizontal cuts through the Brillouin zone (parameterized by the projection k_1 of the momentum onto the first reciprocal lattice vector). Green/red lines show the spectrum for $k_z = 0$ (double winding) and purple/brown lines for $k_z = \pi$ (no winding). (**b**) Hinge Brillouin zone with hinge charge $Q_\llcorner$ (blue solid line, left axis), second Stiefel-Whitney class w_2 (orange dashed line, right axis) and the projection of the bulk dispersion along $k_x = k_y = 0$ (gray). The doubly-degenerate band is displayed with a thicker line.

B_2) consecutively cross the 2D ICR (E_2) resulting in two type-B triple points. The band structure and the nodal-line configuration are shown in Figs. 6.18a and 6.18b, respectively. We observe the characteristic nodal-line arcs attached to the type-B triple points; as desired, the nodal-line arcs in the principal gap (shown in red) are tied together in the red k_z-range (cf. Fig. 6.8b). There are no further degeneracies in the principal band gap of the model. According to Table 6.2, we expect a jump of $-\frac{e}{3}$ in the hinge charge and no jump of the second Stiefel-Whitney class when the 2D ICR along ΓA moves from the occupied to the unoccupied band subspace but an Euler monopole charge $|\chi| = 2$. More precisely, based on a symmetry eigenvalue analysis and Eqs. (6.8) and (6.18), we anticipate that the second Stiefel-Whitney class vanishes in *both* regions, while the hinge charge is expected to be 0 and $-\frac{e}{3}$ in the orange and blue k_z-range, respectively, assuming that the compensating ionic charge is placed at position $1a$.

We verify these predictions numerically. First, in Fig. 6.19a, we plot the Wilson-loop spectra of the lower two bands on horizontal cuts at both $k_z = 0$ and $k_z = \pi$. Since they both exhibit even winding number, we confirm that $w_2 = 0$ on both sides of the triple-point pairs. We observe that the Wilson-loop spectrum for the 2D cut at $k_z = 0$ has winding number ± 2, meaning that the

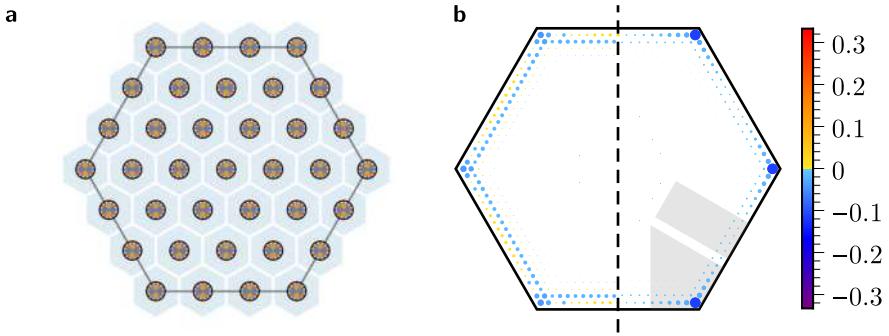

Figure 6.20.: Charge distribution in the C_6-symmetric model with two type-B triple points. (**a**) Cross-section through a hexagonal nanowire three shells wide; light blue hexagons indicate the model's unit cells. The orbitals are represented in color and all placed on top of each other in the center of the unit cell. The ionic charge is concentrated at the same position, indicated by the black circles. (**b**) Charge distribution for a cut through a 16-shell wide nanowire at $k_z = 0$. The charge at each site is indicated by a disk with its value encoded both in the area of the disk and the color scale (see legend on the right). The left half shows the charge distribution on the original lattice, and the right half shows the charge after two iterations of coarse-graining. The hinge charge is approximately $Q_{\llcorner} = -\frac{e}{3}$, but the localization length is larger than in Fig. 6.17b, such that finite-size effects produce a visible deviation from the ideal quantized value of the corner charge in Fig. 6.19b.

corresponding 2D model is an Euler insulator [202]. The double winding also implies that each triple-point pair with its attached (red) nodal-line arcs (the *nodal-line nexus*) carries an Euler class $|\chi| = 2$ on both the occupied and the unoccupied band subspace, as predicted. Therefore, as long as $\mathcal{PT}$ symmetry is present, the only way to gap out the red nodal-line nexus is to annihilate it with the other nodal-line nexus [173]. We remark that this topological obstruction is trivialized in the presence of additional occupied and unoccupied bands [200].

To calculate the hinge charge, we construct a system finite in x- and y-directions with 20 hexagonal shells in the cross section (in Fig. 6.20a we illustrate a system with three hexagonal shells). By exact diagonalization, we find the charge distribution at half-filling for values of k_z where the spectrum is gapped. In Fig. 6.20b, the charge distribution for $k_z = 0$ is shown. The charge is still localized at the corners of the 2D cross section and vanishes both in the bulk as well as along the edges. However, due to trivial in-gap

states and therefore a reduced energy gap, we observe an oscillation of the charge distribution in the direction perpendicular to the edge, as well as a significantly larger localization length for the corner charge than what we found in the previous hexagonal model. In fact, the chosen system is too small to achieve convergence, but it is sufficient to support the theoretical predictions in Table 6.2. Integrating the coarse-grained charge distribution over the gray edge area in Fig. 6.20b we obtain $4 \cdot 10^{-2}|e|$; while over the gray corner area we find $-0.2983e$, which is close to the ideal result $-\frac{e}{3}$ in the absence of finite-size effects. We repeat the same analysis for 2D cuts for multiple values of k_z, and plot the dependence of the second Stiefel-Whitney class and of the hinge charge as a function k_z (where the gap is open) in Fig. 6.19b.

6.3.4. C_3-symmetric models

In this section, we explicitly show that, in the presence of $\mathcal{PT}$ symmetry, there exist C_3-symmetric models where the triple-point pairs carry either $w_2 = 0$ or $w_2 = 1$. We therefore confirm that the second Stiefel-Whitney monopole charge in C_3-symmetric space groups is not symmetry indicated, thus justifying the ambiguous entry in Table 6.2. This freedom is present despite the fact that, according to Table 4.1, C_3-symmetric HSLs only support a single species of triple points, namely type B_l with three attached nodal line arcs and with the central nodal line carrying Berry phase π.

We can obtain such C_3-symmetric models by reducing the C_6 symmetry of the models discussed in Sections 6.3.2 and 6.3.3 down to C_3 (while keeping $\mathcal{PT}$). Perturbations achieving that are given by

$$\begin{aligned}\Delta H^{(3)}_{\mathsf{AA}}(\mathbf{k}) = \delta_{C_3} \begin{pmatrix} 1 & 0 \\ 0 & 0 \end{pmatrix} \otimes \\ \left[\begin{pmatrix} -173 \sin k_x & 0 \\ 0 & 2 \sin \frac{k_x}{2} \left(58 \cos \frac{k_x}{2} + 115 \cos \frac{\sqrt{3} k_y}{2} \right) \end{pmatrix} \right. \\ \left. + \; 200 \cos \tfrac{k_x}{2} \, \sin \tfrac{\sqrt{3} k_y}{2} \, \tau_x \right] \sin k_z ,\end{aligned} \tag{6.43a}$$

and

$$\Delta H^{(3)}_{\mathsf{BB}}(\mathbf{k}) = U_{\mathrm{BB}} \Delta H^{(3)}_{\mathrm{AA}}(\mathbf{k}) U^{\dagger}_{\mathrm{BB}}, \tag{6.43b}$$

where

$$U_{\mathsf{BB}} = \frac{1}{\sqrt{2}} \begin{pmatrix} 1 & -1 \\ 1 & 1 \end{pmatrix} \otimes \begin{pmatrix} 1 & 0 \\ 0 & 0 \end{pmatrix} + \mathbb{1} \otimes \begin{pmatrix} 0 & 0 \\ 0 & 1 \end{pmatrix}, \tag{6.43c}$$

respectively, resulting in the Hamiltonians $H^{(3)}_{\mathsf{AA}}(\mathbf{k})$ and $H^{(3)}_{\mathsf{BB}}(\mathbf{k})$. In contrast to the C_6-symmetric models, the subscript of the Hamiltonian does *not* denote

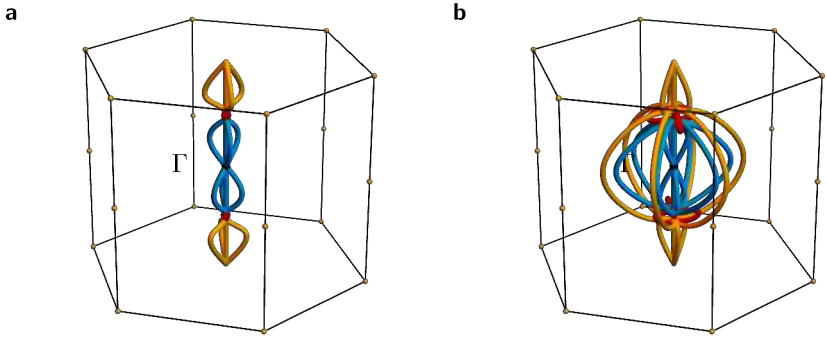

Figure 6.21.: Nodal lines of the C_3-symmetric models. (**a**) Model obtained from breaking the C_6 symmetry of the model discussed in Section 6.3.2 by adding the trigonal perturbation given in Eq. (6.43) with $\delta_{C_3} = 8 \cdot 10^{-4}$. (**b**) Model obtained from breaking the C_6 symmetry of the model discussed in Section 6.3.3 by adding the same perturbation. In both cases, the triple points evolve into type-B$_l$ triple points; however, the connectivity of the nodal-line arcs is different.

the types of triple points, because a C_3-symmetric little co-group only allows for type-B triple points, as we have seen in Chapter 4. Instead, the subscript indicates from which C_6-symmetric model the corresponding C_3-symmetric model is derived.

The resulting nodal-line structure when perturbing the (A, A)- and (B, B)-model is shown in Figs. 6.21a and 6.21b, respectively. Note that the second Stiefel-Whitney monopole charges of the triple-point pairs in the parent hexagonal models are not changed by the trigonal perturbation: as long as the enclosing ellipsoid (purple in Figs. 6.22a and 6.22c) is chosen to be sufficiently large to contain the lobes of red nodal lines, the principal gap does not close on that ellipsoid, keeping the Wilson-loop winding invariant. We confirm this by explicitly computing the Wilson-loop spectra on the enclosing ellipsoids of the perturbed models, plotted in Figs. 6.22b and 6.22d.

We briefly comment on the change of the nodal-line configurations from Fig. 6.15b and Fig. 6.18b to Figs. 6.22a and 6.22c, respectively. In both cases, the central nodal line stretched along ΓA initially carries quaternion charge -1 (corresponding to Berry phase 2π [65], i.e., it is a quadratic nodal line) before switching on the trigonal perturbation. Let us first consider the case of type-A triple points ($w_2 = 1$, Figs. 6.21a and 6.22a). Here, as soon as the perturbation is switched on, all three segments of the central nodal line, i.e., in the orange, red, as well as blue k_z-range, split into four nodal lines with Berry phase π

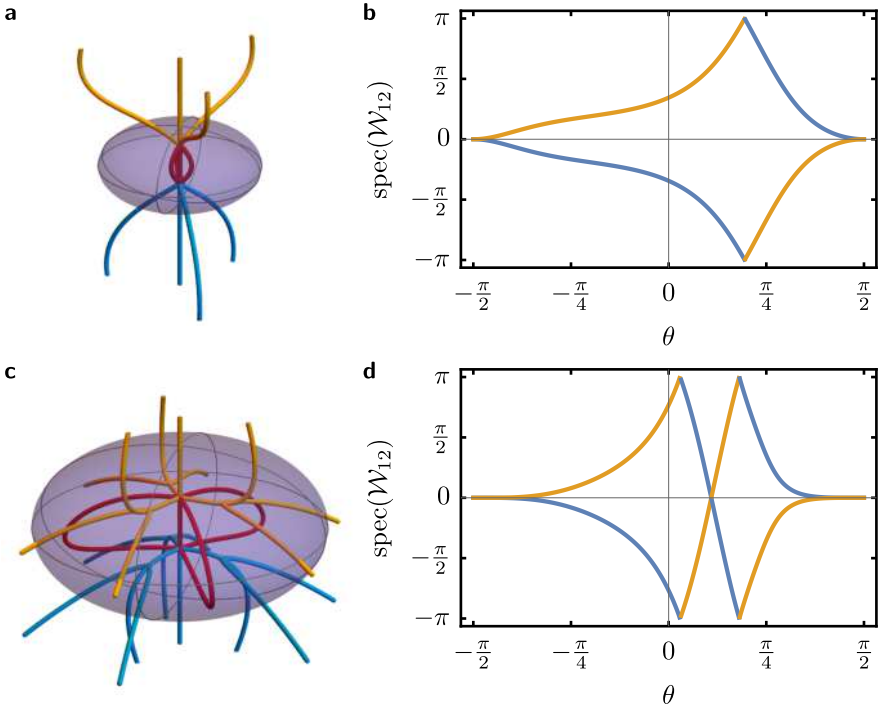

Figure 6.22.: Wilson loop spectra of the C_3-symmetric models. (**a,c**) Close-ups of the red nodal-line segment. In both cases the triple points are clearly type B_l with three attached nodal-line arcs per energy gap. (**b,d**) Wilson-loop spectra on the purple ellipsoids shown in (a,c), respectively. The single winding in (c) implies $|\chi| = 1$ and $w_2 = 1$ and the double winding in (f) implies $|\chi| = 2$ and $w_2 = 0$.

each. One nodal line of the quadruplet is still pinned to the ΓA line, while the other three nodal lines are related by the C_3 symmetry and remain attached to the triple points. As a result, the hexagonal type-A triple points with no attached nodal-line arcs have transformed into trigonal type-B_l triple points with three attached nodal-line arcs in each gap, as detailed in Fig. 6.22a.

For the hexagonal model with type-B triple points ($w_2 = 0$, Figs. 6.21b and 6.22c), the process is similar; in particular, one observes the same splitting of the central quadratic nodal line into four linear nodal lines around the HSL. However, in this case the hexagonal nodal-line configuration starts out with six attached nodal lines per gap, because the hexagonal triple points have been type B_q. Here the three new nodal-line arcs either annihilate with three of the original nodal-line arcs (in the principal gap, red) or combine with the original nodal-line arcs to form intersecting nodal chains (other two gaps, orange and blue) [166]. As a result, we find that the hexagonal type-B_q triple points have been transformed into trigonal type-B_l triple points with three attached nodal lines per gap, as predicted by Table 4.5. The intersection of the orange and of the blue nodal lines visible in Fig. 6.22c is stabilized by the non-Abelian band topology in the presence of m_v and $\mathcal{PT}$ symmetry, as discussed in Ref. 65.

6

6.4. Case study: strained Sc_3AlC

In this section, we discuss Sc_3AlC [259] as a concrete material example that illustrates the introduced phenomenology. When subjected to large uniaxial strain, Sc_3AlC exhibits a triple-point pair with type-A triple points on the $Z\Gamma Z$ line and no interfering nodal lines. Based on first-principles calculations and an ab-initio Wannier tight-binding model, we compute the second Stiefel-Whitney monopole charge and the hinge-charge jump. We find that the second Stiefel-Whitney monopole charge takes value $w_2 = 1$ and that a fractional hinge-charge jump $\Delta Q_{\llcorner} = \frac{e}{4}$ is present, in agreement with the values predicted by Table 6.2. This demonstrates the higher-order bulk-boundary correspondence introduced in Section 6.2. While this example demonstrates that the higher-order topology of triple points can arise in crystalline solids and is not an artefact of simple models, the large values of strain required to realize the presented band structures imply that this particular material is most probably not amenable to experimental studies, and that further research is needed to find realistic material candidates.

The compound Sc_3AlC has a cubic crystal structure with space group $Pm\bar{3}m$ (No. 221) and exhibits a three-fold degenerate touching point at Γ and triple points on the ΓX, ΓY and ΓZ lines (which are all equivalent), see Fig. 6.23a. Furthermore, the spin-orbit coupling is expected to be small due to the elements

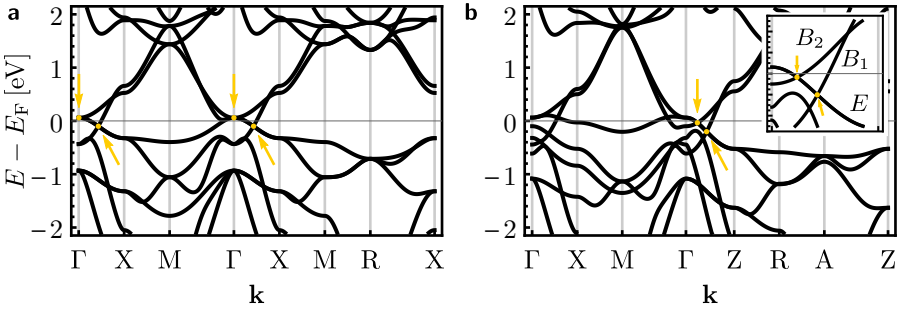

Figure 6.23.: Band structure of Sc_3AlC without and with strain. (**a**) Without strain two triple points formed by the same triplet of bands are forced to coincide at the Γ point and a second triple point (formed by an adjacent triple of bands) arises on the ΓX line. (**b**) Under 6.6% uniaxial compressive strain in z-direction, the two coinciding triple points at Γ are separated which generates a triple-point pair on the ΓZ line (which becomes distinct from the ΓX line due to the symmetry breaking). The inset shows a close-up of the band structure near the triple-point pair with the relevant bands labelled by their irreducible corepresentations. Triple points are indicated by yellow arrows.

involved being light, therefore, we can neglect it and treat the electrons as spinless. Then, the system possesses $\mathcal{PT}$ symmetry squaring to +1. Applying uniaxial compressive strain along one of the equivalent crystal axes (which we choose to be the z-direction) removes the triple points on the ΓX and ΓY lines leaving only those on the ΓZ line, and splits the touching point at Γ into two additional triple points on the ΓZ line, see Fig. 6.23b for approximately 6.6% strain. The result is a configuration of two inversion-symmetry-related triple-point pairs on the ΓZ line with one triple-point pair shown in the inset in Fig. 6.23b. The strained material has a simple tetragonal crystal structure with space group $P4/mmm$ (No. 123).

We study the material by first obtaining the band structure and wave functions from density-functional-theory (DFT) calculations with the projected augmented wave (PAW) method implemented in the Vienna ab initio simulation package (VASP) [230, 231] with generalized gradient approximation (GGA) and Perdew-Burke-Ernzerhof (PBE) approximation [232]. We use a Γ-centered $8 \times 8 \times 8$ k-mesh. Uniaxial compressive strain in z-direction is modelled by reducing the lattice constant in that direction by the appropriate amount. The lattice structure of Sc_3AlC is obtained from the Materials Project database [260] (material identifier mp-4079 [259]) with lattice vectors $a = 4.512\,\text{Å}$ ($a = 4.512\,\text{Å}$ and $c = 4.212\,\text{Å}$ after strain). We construct Wannier functions using

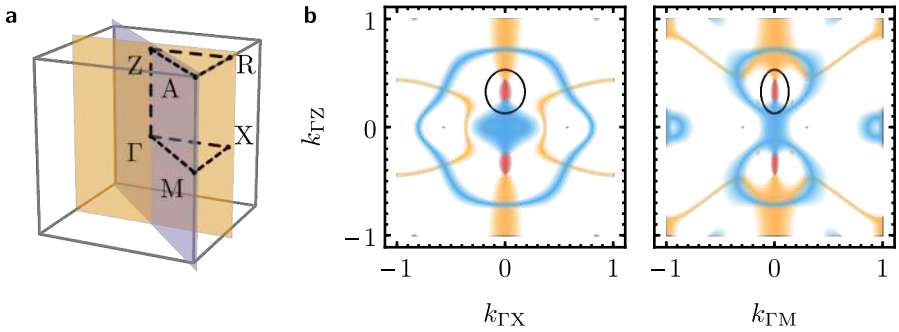

Figure 6.24.: Nodal-line structure of Sc_3AlC with strain. (**a**) The Brillouin zone of the tetragonal lattice of strained Sc_3AlC. The high-symmetry points and mirror planes are indicated. (**b**) Nodal lines in the relevant three gaps (orange, blue, red according to increasing energy) determined from the Wannier-tight-binding model for the mirror planes shown in (a). The triple point is clearly type A. The cross sections of the ellipsoid on which we compute the second Stiefel-Whitney monopole charge with the mirror planes are indicated by black ellipses.

WANNIER90 [235] resulting in a Wannier tight-binding model with s, p, d orbitals of Sc and s, p orbitals of Al and C. We process disentanglement with a frozen window from $-20\,\mathrm{eV}$ to $4\,\mathrm{eV}$ relative to E_F but do not perform maximum localization [123]. The hoppings of the Wannier model are symmetrized [261, 262] in real space.

To check for conflicting nodal lines in the Brillouin zone, we perform additional DFT calculations on the two inequivalent mirror planes $X\Gamma Z$ and $M\Gamma Z$. The results are shown in Fig. 6.24b and we observe that the only nodal lines in the principal gap are the two nodal-line segments (red) spanning between the triple points of each triple-point pair. In particular, there are no additional nodal lines attached to the triple points off the HSL, confirming that the triple points are type A, in agreement with Table 4.1. This allows us to define an ellipsoid (whose intersections with the two mirror planes are indicated by the black ellipses in Fig. 6.24b) enclosing the triple-point pair on which the relevant second Stiefel-Whitney monopole charge is defined. Using the Wannier tight-binding model and the PYTHON package Z2PACK [236, 237] we compute the Wilson-loop spectrum on the ellipsoid, cf. Fig. 6.25, and find that it winds once, therefore indicating $w_2 = 1$.

We further proceed to study the hinge-charge jump in strained Sc_3AlC. First, we calculate the traces of matrix representations obtained from VASP to

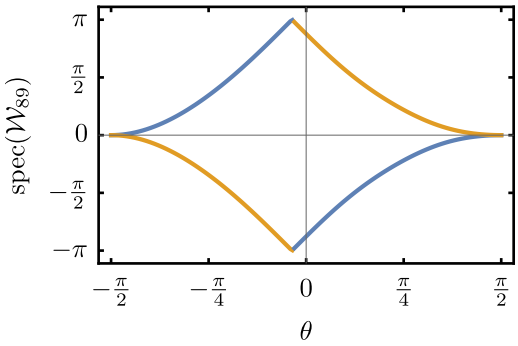

Figure 6.25.: Second Stiefel-Whitney monopole charge in Sc_3AlC. The Wilson-loop spectrum of the relevant bands computed on the ellipsoid indicated in Fig. 6.24b shows a single winding, which implies $w_2 = 1$.

get the ICRs of the energy bands at high-symmetry points in the first Brillouin zone with the help of Irvsp [239]. The corepresentations at HSLs are then inferred using compatibility relations obtained from the Bilbao crystallographic server (BCS) [83, 222–224]. The ICRs of the bands forming the triple-point pair are found to be $(E; B_1, B_2)$, see the inset in Fig. 6.23b. Based on Table 6.2, the knowledge of the rotational symmetry C_4, the HSL ΓZ and the ICRs of the little co-group of that line allows us to predict the fractional part of the hinge-charge jump $\Delta Q_{\llcorner}$ to be $+\frac{e}{4}$.

To compute the hinge-charge jump explicitly and to verify the above prediction, we use the Python package PythTB to construct a nanowire with a C_4-symmetric cross section of 9.5×9.5 unit cells from the bulk Wannier tight-binding model, see Fig. 6.26a. Recall that the placement of the ionic charge in the unit cell does not influence the hinge charge *jump*. Therefore, we choose it such that it simplifies our calculations: we assume all ionic charge of a unit cell to be concentrated at Wyckoff position $1b$ (at the corner of the 2D projection of the unit cell), which is also the location of the center of the cross-section, cf. Fig. 6.26a. The band structure of the nanowire is shown in Fig. 6.26b as a function of the remaining momentum k_z. Each state ψ is colored according to the inverse participation ratio $\sum_i p_i(\psi)^2$ where $p_i(\psi)$ is the probability of finding an electron in state ψ at site i in the 2D cross section. Together with the gray overlay of the bulk states, we can easily identify the in-gap surface (green) and hinge (red) states.

We now select two k_z-values at which the principal gap is open in the spectrum of the nanowire, indicated in Fig. 6.26b by a yellow diamond and a

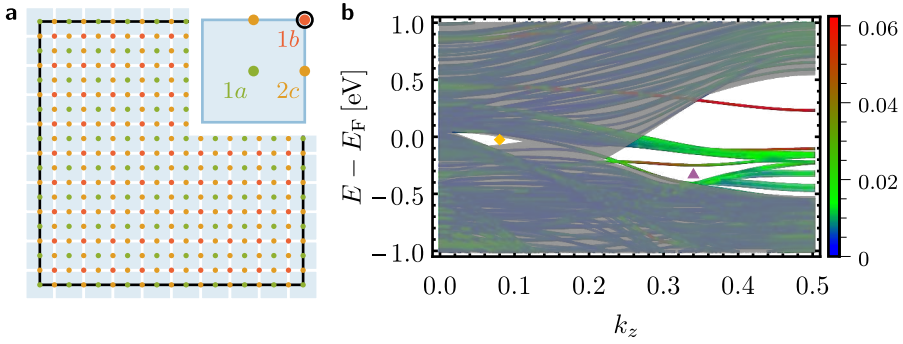

Figure 6.26.: Nanowire of strained Sc_3AlC. (**a**) Cross section at fixed z with 9.5×9.5 unit cells (blue shaded squares). Two-dimensional Wyckoff positions in the unit cell are shown as green, red and orange points with their labels in the inset. The scandium atoms project onto Wyckoff positions $1b$ and $2c$, the aluminum atoms onto $1a$ and the carbon atoms onto $1b$. Note the C_4 symmetry of the cross section with the center at Wyckoff position $1b$. The black circle in the inset denotes the location of the ionic charge of $8|e|$ per unit cell. (**b**) Band structure of the nanowire (colored lines) as a function of momentum k_z in the hinge Brillouin zone. The projected bulk bands (transparent gray) are overlaid on the nanowire spectrum. The coloring of the bands (see legend on the right) encodes the inverse participation ratio, with a larger value indicating localization on fewer sites. Consequently hinge-localized states are colored red, surface-localized states green, and bulk states blue. The two energy gaps to the left and to the right of the studied triple-point pair are marked by a yellow square ($k_z = 0.08$) and by a purple triangle ($k_z = 0.34$), respectively.

purple triangle. Assuming that all states below the indicated gap are occupied, we compute the total charge distribution in the nanowire. The results for $k_z = 0.08$ and $k_z = 0.34$, after coarse-graining over a unit cell as discussed in Appendix F.1, are shown in Figs. 6.27a and 6.27b, respectively. Integrating over successively larger square regions at one of the corners (gray squares in Figs. 6.27a and 6.27b), we observe that the corner charge (corresponding to the hinge charge of the 3D model at the selected value of k_z) converges to $\frac{e}{4}$ and 0 for $k_z = 0.08$ and $k_z = 0.34$, respectively. This verifies that the jump is $\Delta Q_{\llcorner} = \frac{e}{4}$, as predicted.

The localization of the charge at the corners is already visible in Figs. 6.27a and 6.27b and the edge charge (corresponding to the surface charge of the 3D model) is clearly vanishing; however, there are strong oscillations of the charge on the edges. These oscillations are due to trivial surface states, which

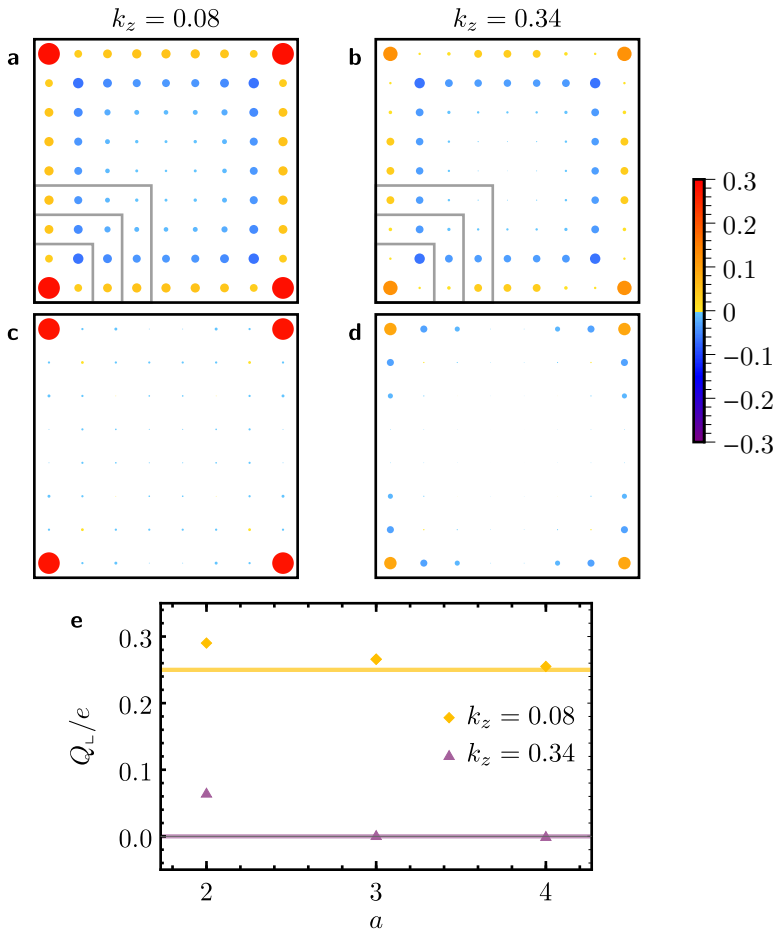

Figure 6.27.: Charge distribution and hinge-charge jump in strained Sc_3AlC. (**a,b**) Charge distribution coarse-grained over one unit cell for $k_z = 0.08$ and 0.34, respectively. The magnitude of the charge (in units of e) is shown by both the area of the circles as well as the color (see legend on the right). (**c,d**) Charge distribution for the same values of k_z after removing the contributions from the edge based on slab calculations. In (c) the localization of a non-zero charge on the corners is clearly visible. (**e**) Integrated corner charge (corresponding to the hinge at the selected values of k_z) for the two k_z-cuts with filling as indicated in Fig. 6.26b as a function of the side length a of the square integration region shown as gray squares in panels (a,b). The corner charge for $k_z = 0.08$ converges to $\frac{e}{4}$ and for $k_z = 0.34$ to 0 (yellow versus purple solid lines).

can be revealed by computing the charge distribution on a slab. Following Appendix F.2, we use the information about the charge distribution on the slab to remove this edge signal. This reveals the strong localization of the net charge on the corners shown in Figs. 6.27c and 6.27d. Note that this *removal* of the charge oscillations is performed in a charge neutral way, i.e., by changing neither the corner nor the edge charge.

6.5. More general symmetry settings

In this section, we argue that the results derived in this chapter apply to more general symmetry settings than we have assume so far. In Section 6.5.1, we show that the higher-order bulk-boundary correspondence presented in Table 6.2 is valid for HSLs in nonsymmorphic space groups as well by mapping ICRs of the little group to ICRs of the little co-group as described in Section 4.5. Next, in Section 6.5.2, we argue that even the assumption of spinless particles can be relaxed and we sketch the derivation of the hinge-charge jump for the two magnetic point groups that protect triple points in the spinful setting, finding results consistent with the spinless case.

6.5.1. Nonsymmorphic space groups

Up to now, we have simplified the presented analysis by excluding nonsymmorphic space groups, i.e., space groups containing symmetries like screw rotations and glide planes. In this section, we discuss these excluded cases, arguing that the inclusion of nonsymmorphic elements in the space group does not change the bulk-hinge correspondence. In particular, we reveal that Table 6.2 applies to triple-point pairs in nonsymmorphic space groups as well, with the only differences being that (i) the first row of the table "C_n" should be interpreted as only the point-group part of the possibly present nonsymmorphic screw symmetry (i.e., without the translation), and (ii) the mapping of ICRs of the little group to the ICRs of the little *co-group* should be performed as described in Section 4.5.

Recall from Section 4.5 that nonsymmorphic symmetries do not alter the classification of triple points. More precisely, as long as the HSL supports triple points (i.e., both 1D and 2D ICRs of the little group exist – due to nonsymmorphicity this property may be lost for certain HSLs on the Brillouin-zone boundary), the symmetry constraints on the Bloch Hamiltonian $H(\mathbf{k})$ due to some corepresentation of the little group $\mathcal{G}^{\mathbf{k}}$ of the HSL supporting triple points, are *equivalent* to the constraints due to a corresponding corepresentation of the little co-group $\overline{\mathcal{G}}^{\mathbf{k}}$ (which consists of the corresponding point-group

symmetries, i.e., without the translation). However, although nonsymmorphic symmetries have trivial implications for the triple-point classification, they may nontrivially affect the rotation eigenvalues that enter the symmetry-indicator formulas for the fractional corner/hinge charges (in particular if the rotational symmetry is replaced by a screw rotation).

Here, we argue in two steps that even in the case of a screw rotation, there is no change to the bulk-hinge correspondence derived in Section 6.2. First, we discuss how to apply the symmetry-indicator formulas for corner charges in C_n-symmetric 2D systems [147, 151] to compute momentum-resolved hinge-charges in a wire-geometry of 3D crystals with a screw rotation (instead of pure rotation) symmetry. Along the way, we derive that the symmetry-indicator formulas for corner charges (without assuming time-reversal symmetry) are symmetric under cyclic permutation of the rotation eigenvalues. Next, we consider the mapping of ICRs between the little group and the little co-group of the HSL on which the triple points lie. We show that this mapping is compatible with the application of the symmetry-indicator formulas for the hinge charge, allowing us to establish the generalization of the bulk-hinge correspondence to triple-point pairs protected by a screw symmetry.

Fractional hinge charges due to screw rotational symmetry

Consider any space group with a nonsymmorphic rotational symmetry around the z-axis, $\{C_n|\mathbf{w}\}$, where $n = 2, 3, 4, 6$ and $\mathbf{w}$ is the nonsymmorphic translation. Note that the x, y components of $\mathbf{w}$, i.e., the ones perpendicular to the rotation axis, can be removed by shifting the rotation axis (this may potentially result in a change of the fractional translations associated with other symmetry elements in the space group, but this is not relevant for our argument). We end up with the screw symmetry $S_n = \{C_n|\frac{m}{n}\mathbf{e}_z\}$ with $m \in \mathbb{Z}$ that together with the translations $\mathbf{t} \in \mathcal{T}$ by lattice vectors generate a subgroup G of the full space group (i.e., we drop the potentially present time-reversal symmetry as well as all point-group operations that are not generated by C_n).

Let $\mathcal{D}$ be the representation of G in which the eigenfunctions of the Hamiltonian transform and $\mathcal{D}^{\mathbf{k}}$ its restriction to the $\mathbf{k}$-sector, i.e., a representation of the little group $G^{\mathbf{k}}$. Then, for any $\{R|\mathbf{v}\} \in G$,

$$\mathcal{D}^{\mathbf{k}}(\{R|\mathbf{v}\})H(R^{-1}\mathbf{k})\mathcal{D}^{\mathbf{k}}(\{R|\mathbf{v}\})^{-1} = H(\mathbf{k}). \tag{6.44}$$

In analogy to Section 6.2, we take a 2D cut at fixed k_z and define the 2D Hamiltonian $H_{k_z}(k_x, k_y) = H(\mathbf{k})$, which still satisfies Eq. (6.44) at any $\mathbf{k}_{\text{2D}} = (k_x, k_y)$ and for any $\{R|\mathbf{v}\} \in G$. In particular, for any 2D high-symmetry point Π invariant under S_n^ℓ for some power ℓ of the screw symmetry, where

$0 < \ell < n$ is a divisor of n, H_{k_z} commutes with the operator $\mathscr{D}^{\mathbf{k}}(S_n^\ell)$ which admits eigenvalues

$$s_p^{(n/\ell)} = \mathrm{e}^{\mathrm{i}\frac{\ell}{n}[-mk_z+2\pi(p-1)]}, \quad p = 1, 2, \ldots, \frac{n}{\ell}. \tag{6.45}$$

The above follows because $\mathscr{D}^{\mathbf{k}}(S_n^\ell)$ is a representation and $(S_n^\ell)^{n/\ell} = S_n^n = \{1|m\mathbf{e}_z\}$, where $m\mathbf{e}_z \in \mathcal{T}$ is a lattice translation and therefore $\mathscr{D}^{\mathbf{k}}(\{1|m\mathbf{e}_z\}) = \mathrm{e}^{-\mathrm{i}mk_z}\mathbb{1}$, which has eigenvalues $\mathrm{e}^{-\mathrm{i}mk_z}$; thus, eigenvalues of $\mathscr{D}^{\mathbf{k}}(S_n^\ell)$ are $(n/\ell)^{\text{th}}$ roots of $\mathrm{e}^{-\mathrm{i}mk_z}$.

Next, we define the operator

$$\mathscr{D}'^{\mathbf{k}_{2D}}(C_n) = \mathrm{e}^{\mathrm{i}\frac{1}{n}(mk_z+2\pi p')}\mathscr{D}^{\mathbf{k}}(S_n), \tag{6.46}$$

which is a symmetry of the 2D Hamiltonian for any $p' \in \mathbb{Z}$:

$$\mathscr{D}'^{\mathbf{k}_{2D}}(C_n)H_{k_z}(C_n^{-1}\mathbf{k}_{2D})\mathscr{D}'^{\mathbf{k}_{2D}}(C_n)^{-1} = H_{k_z}(\mathbf{k}_{2D}). \tag{6.47}$$

We observe that $\mathscr{D}'^{\mathbf{k}_{2D}}(C_n)$, together with $\mathscr{D}'^{\mathbf{k}_{2D}}(\{1|\mathbf{t}_{2D}\}) = \mathscr{D}^{\mathbf{k}}(\{1|\mathbf{t}_{2D}\})$, furnishes a representation of the 2D space group pn, i.e., the 2D symmetry group generated by C_n rotation with respect to a point and by translations. This implies that the Hamiltonian H_{k_z} describes a 2D system with C_n symmetry, and that the rotation eigenvalues of its energy bands at a $C_{n/\ell}$-invariant high-symmetry point Π are

$$r_{p,p'}^{(n/\ell)} = \mathrm{e}^{2\pi\mathrm{i}\frac{p+p'-1}{n/\ell}} \tag{6.48}$$

where we recognize $\mathrm{e}^{2\pi\mathrm{i}\frac{p+p'-1}{n/\ell}} = \Pi_{p+p'}^{(n/\ell)}$ as defined in Eq. (3.25). With these eigenvalues, the symmetry-indicator formulas for the corner charge in 2D systems with rotational symmetry C_2, C_3, C_4, and C_6 [147, 151], e.g., Eqs. (3.27) to (3.29), can be directly applied to compute the fractional hinge charges even for nonsymmorphic 3D space groups.

Note that a nontrivial symmetry of the formulas for the corner charges can now be easily deduced. Namely, the non-uniqueness of Eq. (6.46) due to the freedom of choosing $p' \in \mathbb{Z}$ implies that the symmetry-indicator formulas for the corner charges must be symmetric under *cyclic permutations of the rotation eigenvalues* (which correspond to the replacement $p' \mapsto p' + 1$). In particular, this applies irrespective of the nonsymmorphicity, as can be seen by setting $m = 0$ in the symmetry S_n above. We are not aware whether this symmetry has been previously pointed out, but it is easily verified explicitly for the symmetry class A (i.e., without time-reversal symmetry), which we checked using the

generating Wannier configurations discussed in Appendix A of Ref. 151. Time-reversal symmetry implies that the number of bands with rotation eigenvalues $\Pi_p^{(n/\ell)}$ and $(\Pi_p^{(n/\ell)})^*$ must match; however, this matching will generically be lost after performing a cyclic permutation of rotation eigenvalues. For this reason, the symmetry-indicator formulas derived under the assumption that time-reversal symmetry is present, i.e., Eqs. (3.30) and (3.31), do not manifest the symmetry under cyclic permutations of the rotation eigenvalues. If n is even, a reduced symmetry of the symmetry-indicator formulas under $p' \mapsto p' + \frac{n}{2}$ remains.

In summary, we have shown that the fractional hinge charges of crystals with screw symmetry $\{C_n|\frac{m}{n}\mathbf{e}_z\}$ are characterized by the same symmetry-indicator formulas that apply for corner charges in 2D systems with rotational symmetry C_n, after the k_z-dependence of the screw eigenvalues is removed. It remains to be shown that this removal is compatible with the identification of ICRs of the little group with those of the little co-group described in Section 4.5.

Bulk-hinge correspondence of triple-point pairs

The characterization of triple points in Table 4.1 is phrased in terms of ICRs of the little *co-group* $\overline{\mathcal{G}}^{\mathbf{k}}$ of the HSL on which the triple points lie, even though the symmetry constraints on the nodal-line structure near the triple points involve the ICRs of the little *group* $\mathcal{G}^{\mathbf{k}}$. For symmorphic space groups, this is explained by the fact that the ICRs of $\mathcal{G}^{\mathbf{k}}$ restricted to elements $\{R|0\} \in \mathcal{G}^{\mathbf{k}}$ (forming a group isomorphic to $\overline{\mathcal{G}}^{\mathbf{k}}$) are identical to the ones of $\overline{\mathcal{G}}^{\mathbf{k}}$: the ICR ς of $\mathcal{G}^{\mathbf{k}}$ is injectively mapped to the ICR D of $\overline{\mathcal{G}}^{\mathbf{k}}$ by

$$\forall \{R|0\} \in \mathcal{G}^{\mathbf{k}} : D(R) = \varsigma(\{R|0\}). \tag{6.49}$$

For nonsymmorphic space groups, on the other hand, this is not the case. Nevertheless, we have shown in Section 4.5 that for little groups that support triple points a different mapping between ICRs ς of $\mathcal{G}^{\mathbf{k}}$ restricted to $\overline{\mathcal{G}}^{\mathbf{k}}$ and ICRs D of $\overline{\mathcal{G}}^{\mathbf{k}}$ exists: Let $\varsigma^{1\mathrm{D}}$ be any 1D ICR of $\mathcal{G}^{\mathbf{k}}$ (e.g., the one that facilitates the formation of the discussed triple point), then the ICR ς of $\mathcal{G}^{\mathbf{k}}$ is injectively mapped to the ICR D of $\overline{\mathcal{G}}^{\mathbf{k}}$ by

$$\forall \{R|\mathbf{v}\} \in \mathcal{G}^{\mathbf{k}} : D(R) = \varsigma^{1\mathrm{D}}(\{R|\mathbf{v}\})^{-1}\varsigma(\{R|\mathbf{v}\}). \tag{6.50}$$

Note that, in contrast to the symmorphic case, the restriction of ς to $\overline{\mathcal{G}}^{\mathbf{k}}$ is *not* a representation of $\overline{\mathcal{G}}^{\mathbf{k}}$ but a *projective* representation.

Here, we are interested in the rotation eigenvalues at HSLs, i.e., the eigenvalues of $D(C_{n/\ell})$ at momenta invariant under $C_{n/\ell}$ symmetry. It follows from

Eq. (6.50) that the eigenvalues $s^{(n/\ell)}$ of $\varsigma(S_{n/\ell})$ and $r^{(n/\ell)}$ of $D(C_{n/\ell})$ are related as

$$r^{(n/\ell)} = D^{1\mathrm{D}}(S_{n/\ell})^{-1} s^{(n/\ell)}. \tag{6.51}$$

However, as a 1D ICR, $D^{1\mathrm{D}}(S_{n/\ell})$ must be one of the eigenvalues defined in Eq. (6.45), i.e., $s^{(n/\ell)}_{\tilde{p}}$ for some $\tilde{p} \in \mathbb{Z}$. Then,

$$r^{(n/\ell)} = \mathrm{e}^{\mathrm{i}\frac{1}{n}(mk_z - 2\pi(\tilde{p}-1))} s^{(n/\ell)}, \tag{6.52}$$

which is fully compatible with Eq. (6.46) for $p' = 1 - \tilde{p}$ in the sense that if $s^{(n/\ell)}$ is one of the eigenvalues of $\mathscr{D}^{\mathbf{k}}(S_n)$, then $r^{(n/\ell)}$ is the corresponding eigenvalue of $\mathscr{D}'^{\mathbf{k}_{2\mathrm{D}}}(C_n)$. In particular, we observe that the k_z-dependence on the right-hand side of Eq. (6.52) cancels, and $r^{(n/\ell)}$ does not depend on k_z.

Given a triple-point pair formed by four bands transforming according to certain ICRs of the little group, the relevant rotation eigenvalues used to compute the hinge-charge jump should be obtained by applying the construction described above. However, the preceding paragraph implies that the same results are obtained if we first map the ICRs of the little group to ICRs of the little co-group [cf. Eq. (6.50)] and then apply the symmetry-indicator formulas in Eqs. (3.27) to (3.29) to the rotation eigenvalues obtained from the ICRs of the little co-group. In fact, the non-uniqueness of $D^{1\mathrm{D}}$ in Eq. (6.50) (if 1D ICRs of $\mathscr{G}^{\mathbf{k}}$ exist) amounts precisely to the non-uniqueness of p' in Eq. (6.46), further evincing how the two presented descriptions are two facets of the same argument. We therefore conclude, that both the triple-point types and the hinge-charge jumps can be determined from the ICRs of the little co-group, which implies that the bulk-hinge correspondence summarized in Table 6.2 directly applies to nonsymmorphic space groups as well.

6.5.2. Spinful systems

The presented analysis of the higher-order bulk-boundary correspondence of triple-point pairs is easy to generalize to the spinful case. According to the classification of triple points by Ref. 180, in spinful systems without magnetic order, triple points can be protected on the HSLs ΓA, KH and $K'H'$ of space groups with three-fold rotational symmetry. Only two magnetic point groups (as little co-groups of HSLs) can protect triple points: C_{3v} $(3m)$ resulting in type-B_l triple points, and C_{3v} supplemented with $m_z\mathcal{T}$ $(\bar{6}'m2')$ resulting in type-A triple points. The spinful ICRs of the two magnetic point groups are equivalent, such that we do not need to consider them separately for the discussion of the hinge-charge jump and of the bulk-polarization jump (which only depend on the rotation eigenvalues). The main difference between the

two cases is that the additional antiunitary symmetry $m_z\mathcal{T}$ in $\bar{6}'m2'$ forces the nodal-line arcs (characteristic of type-B triple points) to coalesce on the rotation axis, resulting in the type-A triple points. For both magnetic point groups there are two spinful 1D ICRs $D_1^{1\mathrm{D}}$, $D_2^{1\mathrm{D}}$ and only a single spinful 2D ICR $D^{2\mathrm{D}}$, giving rise to three different triple-point pairs $(D^{2\mathrm{D}}; D_a^{1\mathrm{D}}, D_b^{1\mathrm{D}})$ with $a, b \in \{1, 2\}$. However, $D_1^{1\mathrm{D}}$ and $D_2^{1\mathrm{D}}$ have identical rotation eigenvalues; therefore, they are not distinguished in the corresponding symmetry indicators, and they all result in the *same* value of jumps $\Delta Q_{\llcorner}$ and $\Delta\mathbf{P}$.

For simplicity, we restrict the explicit analysis to the case when the C_3 rotation center of the sample resides at the $1a$ Wyckoff position (a straightforward analysis using the symmetry-indicator formulas from Ref. 151 reveals that our results remain true if the rotation center resides at Wyckoff position $1b$ or $1c$). Similar to Section 6.2, we set all ionic charge to Wyckoff position $1a$. Then, the corner charge on a 2D cut is given by (cf. class A in Ref. 151)

$$Q_{\llcorner}^{(3)} = \frac{e}{3}\left(\left[K_1^{(3)}\right] + \left[K_2^{(3)}\right] + \left[K_1'^{(3)}\right] + \left[K_2'^{(3)}\right]\right) \mod e. \tag{6.53}$$

The square bracket is defined in the exact same way as in the spinless case, $[\Pi_p^{(n)}] = \#\Pi_p^{(n)} - \#\Gamma_p^{(n)}$; however the labelling of rotation eigenvalues in Eq. (3.25) is replaced by

$$\Pi_p^{(n)} = \mathrm{e}^{2\pi\mathrm{i}(p-1)/n}\mathrm{e}^{\pi\mathrm{i}/n}, \quad p = 1, 2, \ldots, n. \tag{6.54}$$

The bulk polarization can similarly be expressed in terms of the symmetry indicators as [150, 151]

$$\mathbf{P}^{(3)} = \frac{e}{3}\left(2\left[K_1^{(3)}\right] + \left[K_2^{(3)}\right] + \left[K_1'^{(3)}\right] + 2\left[K_2'^{(3)}\right]\right)(\mathbf{a}_1 + \mathbf{a}_2) \mod e\mathbf{R}. \tag{6.55}$$

By performing an analysis (not appended) similar to the one detailed in Section 6.2.2 for the spinless case, we derive the bulk-hinge correspondence for spinful triple-point pairs in triangular geometry. Independent of the HSL on which the triple-point pair lies and regardless of the Wyckoff position of the rotation center, the hinge-charge jump is universally found to be

$$\Delta Q_{\llcorner} = \frac{e}{3} \mod e \tag{6.56}$$

and the jump of the bulk-polarization

$$\Delta\mathbf{P} = 0 \mod e\mathbf{R}. \tag{6.57}$$

We observe that even in spinful systems, all triple-point pairs carry fractional hinge-charge jump.

The derived results directly apply to triple-point pairs reported in WC-type crystalline materials reported by Ref. 180. In particular, TaN exhibits a type-(A,A) triple-point pair characterized by a hinge-charge jump $\frac{e}{3}$ along the ΓA line. Furthermore, this material is very close to the ideal semimetallic triple-point-pair case, with only small additional Fermi pockets around the K-point and A-point of the Brillouin zone. We have considered extracting the predicted hinge-charge jump for TaN from first-principles calculations (as we have done for Sc_3AlC under strain), however the absence of a surface gap has prevented us from doing so. In the future, a systematic check of the materials that host triple-point pairs for open surface gaps could lead to a better material candidate.

7. Conclusions and outlook

We have conducted an in-depth investigation into a specific species of accidental band degeneracies called triple points, which occur at various positions along high-symmetry lines. Notably, triple points are always accompanied by two *central* nodal lines, each residing in a different energy gap and extending in opposite directions along the high-symmetry line. In Chapter 4, we have developed a comprehensive symmetry-based classification for triple points in spinless systems. This classification applies to all space groups, including both magnetic and nonsymmorphic ones, thereby providing a crucial piece of information for the growing collection of symmetry-protected and symmetry-enforced band nodes [33, 263–266] which helps understanding band structures of real materials. Unlike other classification schemes that differentiate triply-degenerate nodal points in spinless systems based on the linear or quadratic momentum-space dispersion of the departing bands [208–210], our classification focuses on the *nodal-line structure* in the vicinity of the triple point. This approach draws inspiration from a similar classification scheme applied to triple points in *spinful* systems [180].

In our investigation, we have found that the nodal-line structure at the triple point is uniquely (up to fine-tuning) determined by symmetry. More precisely, the little co-group of the high-symmetry line and in some cases, specifically in the presence of sixfold rotational symmetry, the choice of irreducible corepresentations of the bands involved in the triple point, can enforce a complicated nodal-line structure attached to the triple point. We differentiate between triple points without additional nodal-line arcs attached (besides the central nodal line), referred to as type-A, and those *with* linearly (type B_l) or quadratically (type B_q) attached nodal-line arcs. Even type-A triple points can exhibit nodal-line arcs branching out from *nexus points* on the central nodal line, but not from the triple point itself. However, they are usually not enforced by symmetry and their presence thus depends on system-specific details beyond symmetry. Remarkably, in contrast to spinful systems, triple points in spinless systems display a wide range of nodal-line compositions.

An intriguing aspect that sets triple points apart from completely isolated point nodes is their interaction with other band degeneracies. By definition, triple points mark the transfer of a nodal line from one energy gap to an adjacent energy gap. In Chapter 5, we have demonstrated that this necessitates

a multigap description, and, in the presence of spinless space-time inversion symmetry, gives rise to nontrivial multigap topology. Specifically, a nontrivial value of the quaternion charge facilitates the conversion of triple points into multiband nodal links under symmetry-breaking perturbations. A similar mechanism has previously been exemplified by the predicted conversion of Weyl points to nodal rings in ZrTe [66, 249]. Subsequently, the conversion of various types of band nodes has been explored [267–269] leveraging the non-Abelian topology described by the quaternion charge. In particular, it has been recognized that triple points play an important role in the transfer of non-Abelian charges [267, 268], serving as sources and sinks of the charges' flow [269]. Recently, a Morse-theory perspective on the evolution of nodal lines has been proposed [270]. While this proposal is based on a single-gap picture, it would be intriguing to explore its generalization to the multigap, complementing the description provided by non-Abelian charges.

The topological characterization of triple points exhibits greater intricacy compared to isolated point nodes. For instance, spin-1 fermions—isolated triply-degenerate nodal points—are characterized by a Chern monopole charge ± 2 and display both surface Fermi arcs as well as chiral Landau bands [209]. In contrast, directly characterizing triple points with monopole charges is not feasible due to the presence of the central nodal line, which renders any enclosing surface gapless. To overcome this challenge, we have focused on studying *pairs of triple points*, where the two triple points are either formed by the same or by an adjacent triplet of energy bands, sharing two of the three bands. This approach has led us to conclude that, in the presence of spinless space-time inversion symmetry, such pairs of triple points can be characterized by the fragile Euler monopole charge and its stable counterpart, the second Stiefel-Whitney monopole charge. We have explored the three-band case in Chapter 5 and demonstrated the implications of the nontrivial Euler charge on the conversion of band nodes. Additionally, in Chapter 6, we have investigated the four-band case and derived predictions for the values of both the Euler and second Stiefel-Whitney classes based on our classification of triple points. Importantly, this reflects the relationship of the monopole charges to nodal-links and the quaternion charge.

While the full understanding of the signatures associated with the Euler class remains a topic of ongoing research, several aspects have been explored. For instance, it has been discovered that Euler-obstructed Cooper pairing in 3D systems gives rise to higher-order nodal superconductivity with Majorana zero hinge-modes [271]. The normal-state platform is provided by spinless monopole charged nodal semimetals, including configurations like the triple-point pairs discussed in Chapter 6. A related subject, briefly touched upon in Chapter 6, is the bulk-boundary correspondence of 2D Stiefel-Whitney and Euler insulators.

Formulating a first-order bulk-boundary correspondence poses a challenge due to the fact that often the edge spectra of insulators with nontrivial Euler or second Stiefel-Whitney class are gapped. While our focus has been on higher-order topology, a recent approach based on the entanglement spectrum has revealed a correspondence with edge-localized entanglement eigenstates [272].

This brings us to the question of boundary signatures associated with triple-point pairs, which we have addressed in Chapter 6. The key finding of our analysis is that nodal-line segments demarcated by a pair of type-A or by a pair of type-B triple points are generally characterized by a *fractional jump of the hinge charge*, serving as a signature of higher-order topology. These results extend to nonsymmorphic space groups and even beyond the spinless case. Consequently, our findings overcome the previously unsuccessful attempts to establish a general bulk-boundary characterization of triple points in surface states [180, 181, 186, 273] In the future, it will be intriguing to speculate whether a similar universal higher-order bulk-boundary correspondence can be found for other previously reported 1D nodal structures. For example, besides the nodal-line segment spanned by a triple-point pair, nodal-line chains [65, 166, 274], gyroscopes [164, 275, 276], and starfruits [277] were proposed. They all require crossing of bands with particular choices of symmetry eigenvalues which is associated with a change of the symmetry indicators, potentially implying similar phenomenology of higher-order topological hinge-charge jumps. Given the abundance of material candidates exhibiting various nodal-line compositions, exploring such generalizations would be of both theoretical and experimental interest in the future.

For completeness, let us mention a complementary characterization of triple points that has been developed in Refs. 183, 278. The surface enclosing a triple point is unavoidably intersected by nodal lines and the authors propose to study invariants on the resulting punctured closed surfaces. By removing infinitesimal regions at these crossings, a fully gapped surface is obtained, albeit punctured. Through their analysis, a $\mathbb{Z} \times \mathbb{Z}$ classification has been established, leading to intriguing predictions such as half-integer conductance. The exploration of diverse strategies for understanding the topology of triple points illuminates their multifaceted nature and sets the stage for further investigations into the properties of these band degeneracies.

To demonstrate the validity of our classification, we have compiled a table of materials with presumably negligible spin-orbit coupling that host triple points of different symmetry and types Utilizing first-principles calculations, we have determined the nodal-line structure near these triple points and found agreement between our the theoretical characterization and the observed realizations. Additionally, we have conducted more detailed investigations

of selected materials, such as Li_2NaN and Sc_3AlC, to unveil their multigap topology, including the Euler and second Stiefel-Whitney monopole charges, as well as the universal bulk-hinge correspondence. It is important to emphasize that our results extend beyond the realm of electronic materials with negligible spin-orbit coupling. Photonic [269, 279–281], phononic [208, 267, 268, 282, 283] and magnonic bands are natural systems where our considerations apply as well, opening up avenues for experimental exploration.

While our analysis has primarily focused on electronic materials that are well-described by spinless representations of type-II Shubnikov space groups (with $\mathcal{PT}$ squaring to $+1$), recent works have indicated that type-III and IV magnetic space groups might not be ideally suited to capture band structure features of certain magnetic materials with negligible spin-orbit coupling, dubbed *altermagnets* by Refs. 284, 285. On the other hand, classical metamaterials, including discrete spring systems, elastic structures, acoustic and phononic systems, as well as classical electric circuits, offer potential avenues for realizing spinless representations of magnetic space groups. For example, it is easily revealed that the displacement vector of coupled 2D pendula transforms according to a 2D spinless representation. Time-reversal symmetry can be broken by applying a magnetic field perpendicular to the plane of motion and charging the pendula electrically or by placing a gyroscope with certain angular momentum in each pendulum [38, 286, 287]. The symmetry of the resulting system is then captured by a magnetic space group. This correspondence highlights the broader applicability of spinless representations of magnetic space groups beyond electronic systems.

However, the failure of spinless representation theory in describing the altermagnets introduces a captivating research direction for the future. For the altermagnets, *spin symmetry groups* [288, 289] (where "spin" describes a magnetic pattern, and should not be confused with the double cover of orthogonal groups) were proposed as the proper substitute of magnetic space groups. The characterization of band degeneracies in spin symmetry groups was systematically studied only recently [290], and it is likely that many of them support high-symmetry lines with both 1D and 2D irreducible corepresentations, leading potentially to a further variety of triple points beyond the ones classified in Chapter 4. More generally, Ref. 290 foreshadows that such altermagnets may admit novel types of band structure nodes and topologies that are impossible with magnetic space groups alone. We anticipate exciting discoveries in this direction, which will further expand our understanding of band degeneracies and their realization in diverse materials.

Part III.

Hyperbolic lattices

8. Regular tessellations of the hyperbolic plane

Curved spaces, traditionally studied in high-energy physics and cosmology, have gained significant interest in condensed matter physics for two reasons. First, the discovery of holographic principles [49, 50] revealed a fundamental hidden structure underlying certain interacting quantum many-body systems that allows to compute their properties from a theory in *hyperbolic space* of constant negative curvature. Remarkably, this understanding has been applied successfully to analyze strongly correlated electronic systems and to gain insights into the nature of quantum entanglement in condensed matter systems [51–59]. This calls for tabletop simulations of hyperbolic space and discretization of the negatively curved space has recently been identified [69] as a promising route, leading to experimental realizations in metamaterials such as coupled waveguide resonators [68] and electric-circuit networks [4].

Second, it has been recognized that the *hyperbolic lattices* resulting from discretizing the hyperbolic plane are interesting in their own right, opening up a new research direction, namely, the study of *hyperbolic matter*. The negative curvature implies exotic crystalline symmetries, such as noncommuting translations and higher-order rotational symmetries, and an increased relevance of boundary effects due to the boundary making up a macroscopic part of the system. This has important consequences, for instance, in band theory and topology, and has sparked a resurgence of interest of the condensed-matter and metamaterials communities in hyperbolic lattices. In Chapters 9 and 10, we will discuss how to extend band theory to hyperbolic lattices and study models showing band topology. Crucially, the experimental realizations of hyperbolic lattices, which we discuss in this chapter, demonstrate that hyperbolic lattices can be viewed as a particular class of complex networks, elevating their effective description in curved space to a tool for engineering metamaterials with potential applications such as topological lasing.

In this chapter, we introduce some of the basic notions before focusing on how hyperbolic lattices can be used to approximate the hyperbolic plane. We start in Section 8.1 with a short review of the geometry of the hyperbolic plane and the representation we will be using throughout this and the subsequent chapters. Then, in Section 8.2, we review regular tessellations in two-dimensional (2D)

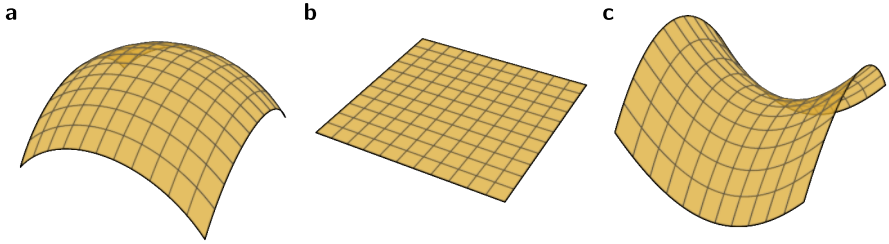

Figure 8.1.: Illustration of curved two-dimensional spaces. The Gaussian curvature K can be written as the inverse product of the principal radii R_i of curvature, $K = \frac{1}{R_1 R_2}$, and we can read off their sign from the mesh shown in the figure, i.e., whether the mesh lines curve up- or downwards. (**a**) Positively curved space with $\mathrm{sign}(R_1) = \mathrm{sign}(R_2)$, such as a patch of the sphere. (**b**) The flat, Euclidean, plane with $R_1 = R_2 = \infty$. (**c**) Negatively curved space with $\mathrm{sign}(R_1) = -\mathrm{sign}(R_2)$, e.g., the neighborhood of a saddle point.

spaces with positive, vanishing and negative curvature, and describe how this allows us to construct hyperbolic lattices encoding the negative curvature of the hyperbolic plane. In Section 8.3, we discuss how the discrete lattice approximates the continuum, focusing on the Laplace operator. In that context, we present some of our results [4] on competing criteria for choosing a tessellation for that purpose. Finally, in Section 8.4, we turn to our original work [4], of realizing a hyperbolic lattice in an electric-circuit network and, crucially, observing the effective negative curvature.

8.1. Introduction to the hyperbolic plane

The *hyperbolic plane* is the 2D space with constant negative Gaussian curvature and can thus be considered to be analogous to the sphere, the 2D space with constant *positive* curvature. Figure 8.1 shows patches of 2D spaces with positive, vanishing and negative curvature. Note that while the sphere can be easily immersed in three-dimensional (3D) Euclidean space, the hyperbolic plane *cannot*. The mathematical reason for this is encompassed in Hilbert's theorem, which states that that there exists no complete regular surface of constant negative Gaussian curvature immersed in $\mathbb{R}^3$. While this does not prevent the embedding of so-called *pseudospheres* in $\mathbb{R}^3$ under the standard Euclidean metric, the *entire* hyperbolic plane cannot be embedded in this way. For this reason, we instead work with the *Poincaré disk model* of the

hyperbolic plane, which we introduce below.

There are four models of hyperbolic geometry that are commonly used: the hyperboloid model, the Poincaré disk model, the Klein model, and the Poincaré half-plane model. In Section 8.1.1, we briefly introduce the hyperboloid model, whose stereographic projection defines the Poincaré disk model as we show in Section 8.1.2. Throughout this part of the thesis, we will be using the Poincaré disk model for visualizing the hyperbolic plane, its tessellations, and models defined on it.

8.1.1. Hyperboloid model

The hyperboloid model employs a single sheet ($t > 0$) of the 2D two-sheeted hyperboloid of revolution in $(2+1)$-dimensional (t, x, y) Minkowski space with metric

$$g_{\mathbb{R}^{1,2}} = -\,\mathrm{d}t^2 + \mathrm{d}x^2 + \mathrm{d}y^2\,. \tag{8.1}$$

The surface, depicted in Fig. 8.2a, is exactly the 2D surface with fixed timelike distance κ from the origin, i.e., $t^2 - x^2 - y^2 = \kappa^2$ and can be parametrized by

$$\begin{aligned} t &= \kappa \cosh(\alpha), \\ x &= \kappa \sinh(\alpha)\cos(\beta), \\ y &= \kappa \sinh(\alpha)\sin(\beta). \end{aligned} \tag{8.2}$$

The induced metric on the hyperboloid sheet then is

$$g_{\mathbb{H}} = \kappa^2\,\mathrm{d}\alpha^2 + \kappa^2 \sinh^2(\alpha)\,\mathrm{d}\beta^2\,. \tag{8.3}$$

This provides an orthogonal parametrization, i.e., a metric of the form $g = a(\alpha,\beta)\,\mathrm{d}\alpha^2 + b(\alpha,\beta)\,\mathrm{d}\beta^2$, such that the Gaussian curvature K is simply given by [291]

$$\begin{aligned} K &= -\frac{1}{2\sqrt{ab}}\left(\partial_\alpha \frac{\partial_\alpha b}{\sqrt{ab}} + \partial_\beta \frac{\partial_\beta a}{\sqrt{ab}}\right) && (8.4) \\ &= -\frac{1}{2\kappa^2 \sinh(\alpha)}\partial_\alpha \frac{\partial_\alpha \sinh^2(\alpha)}{\sinh(\alpha)} \\ &= -\frac{1}{\kappa^2} < 0, && (8.5) \end{aligned}$$

where ∂_α denotes the partial derivative with respect to α. This shows that the hyperboloid in Minkowski space indeed has constant negative curvature and therefore realizes the hyperbolic plane $\mathbb{H}$.

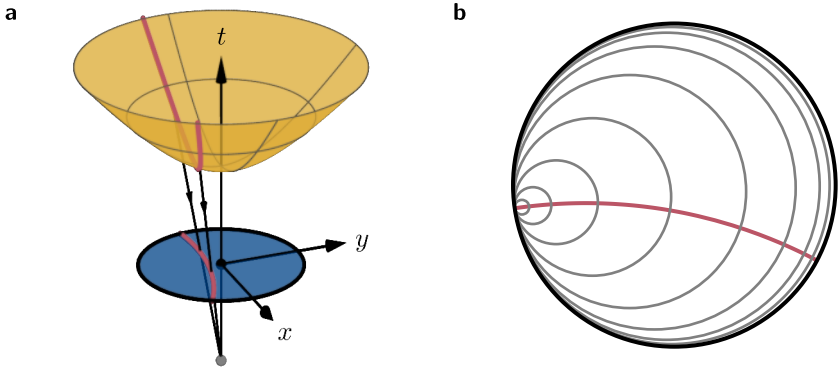

Figure 8.2.: Hyperboloid and Poincaré disk model of the hyperbolic plane. (**a**) The hyperboloid (orange) defined by $t^2 - x^2 - y^2 = \kappa^2 = 1$ in (2+1)-dimensional (t, x, y) Minkowski space is mapped (black rays) by the stereographic projection through the point $(-1, 0, 0)$ (gray dot) to the unit disk (blue) at $t = 0$. The geodesics (red) are given by intersections of the hyperboloid with planes passing through the origin $(0, 0, 0)$ (black dot), and are mapped by the projection to circular arcs perpendicular to the boundary of the Poincaré disk. (**b**) Poincaré disk with the same geodesic (red) that is shown in (a). Additionally, several circles (gray) with center at one end of the geodesic and linearly increasing radius are shown to illustrate distance along the geodesic.

8.1.2. Poincaré disk model

Naturally, Minkowski space is neither amenable to experimental realizations nor to graphical visualizations. Therefore, we rely on the Poincaré disk model [292, 293], which can be derived as the stereographic projection of the hyperboloid model to the unit disk in $\mathbb{R}^2$ and allows us to suitably visualize the hyperbolic plane. As illustrated in Fig. 8.2a by black rays, the hyperboloid is stereographically projected onto the plane at $t = 0$ through the point $(-\kappa, 0, 0)$, i.e., the tip of the lower sheet. A point (t, x, y) on the hyperboloid sheet is then projected to the point

$$\frac{\kappa}{\kappa + t}\,(x, y) \tag{8.6}$$

in the plane $t = 0$. We observe that this point lies in the disk with radius κ. Thus, we rescale the x and y coordinates by $\frac{1}{\kappa}$ and after adopting complex coordinates $z := x + \mathrm{i}y \in \mathbb{C}$ and substituting Eq. (8.2), the hyperbolic plane in

the *Poincaré disk* $\mathbb{D} = \{z \in \mathbb{C} : |z| < 1\}$ is parametrized by

$$z = \frac{\sinh(\alpha)}{1 + \cosh(\alpha)} \mathrm{e}^{\mathrm{i}\beta}. \tag{8.7}$$

Performing the change of coordinates given in Eq. (8.7), the metric of the hyperbolic plane becomes

$$g_{\mathbb{H}} = (2\kappa)^2 \frac{\mathrm{d}x^2 + \mathrm{d}y^2}{\left(1 - x^2 - y^2\right)^2} = (2\kappa)^2 \frac{\mathrm{d}z\, \mathrm{d}z^*}{(1 - |z|^2)^2}, \tag{8.8}$$

where $z^* = x - \mathrm{i}y$ is the complex conjugate coordinate. The Gauss curvature is a scalar and therefore independent of the coordinates: $K = -\kappa^{-2}$. For convenience, we fix $\kappa = \frac{1}{2}$ (leading to curvature $K = -4$), such that the metric takes a simple form. Then, the hyperbolic (geodesic) distance between two points $z, z' \in \mathbb{D}$ is given by

$$d(z, z') = \frac{1}{2} \operatorname{arcosh}\left(1 + \frac{2|z - z'|^2}{(1 - |z|^2)(1 - |z'|^2)}\right). \tag{8.9}$$

The geodesics of the Poincaré disk are circular arcs that intersect the boundary $|z| = 1$ orthogonally as illustrated in Fig. 8.2b; straight lines through the origin are geodesics as well. Note that angles in the Poincaré Disk are given by the usual Euclidean angles.

For later reference, we briefly discuss the isometries of $\mathbb{D}$, i.e., the analogue of the Euclidean group mentioned in Chapter 2. Isometries of $\mathbb{D}$ are maps that preserve the hyperbolic distance given in Eq. (8.9) and they can be grouped into orientation-preserving and orientation-reversing maps. The orientation-preserving maps are given by Möbius transformations

$$z \mapsto \frac{az + b}{b^* z + a^*} \tag{8.10}$$

with complex numbers a, b satisfying $|a|^2 - |b|^2 = 1$. These maps form the projective unitary group $\mathsf{PSU}(1,1) = \mathsf{SU}(1,1)/\{\pm\mathbb{1}\}$. All orientation-reversing maps can be obtained by composing an orientation-preserving map with complex conjugation $z \mapsto z^*$, such that the full group is the semidirect product $\mathsf{PSU}(1,1) \ltimes \mathbb{Z}_2$.

While it has been suggested [294] that a nontrivial metric can be implemented in metamaterials via spatial variations of the electromagnetic permittivity of continuous media, the difficulty to induce these variations in a controlled manner limits the applicability of such approaches. Here, we follow a different

approach: by discretizing continuous space, the effective metric is encoded in properties of the resulting *graph*. The advantage of working with the Poincaré disk model and the corresponding metric in Eq. (8.8) is that the Poincaré disk is embedded in $\mathbb{R}^2$, i.e., 2D laboratory space. In the next section we introduce regular tessellations as a systematic way to discretize a surface with constant curvature.

8.2. Introduction to regular tessellations

The covering of a surface using one or more geometric shapes, known as *tiles*, such that the tiles neither overlap nor leave gaps, is called a *tessellation* or *tiling*. Here, we are interested in tessellations of 2D surfaces with constant curvature. A tessellation is called (a) *spherical* for positive, (b) *Euclidean* for vanishing, and (c) *hyperbolic* for negative curvature. Further, we restrict ourselves to periodic tessellations and polygonal tiles. As we will see in the subsequent chapters, these two constraints result in symmetries that can be exploited in the analysis of condensed-matter models defined on the discretized space. In particular, the periodicity implies a translational symmetry and the polygonal tiles induce mirror and rotational symmetries. Within the periodic polygonal tessellations, we further distinguish *regular* tessellations, where all polygons are identical, from *semiregular*, also known as *Archimedean*, tessellations, where more than one type of polygon appears but they are still arranged such that each *corner* is identical. Note that all periodic Euclidean tessellations are classified into 17 wallpaper groups (the 2D analogues of the space groups) and we will touch upon a symmetry classification for general regular tessellations in Chapter 9.

Throughout Part III, we will mostly deal with regular tessellations. Thus, we introduce them in detail in Section 8.2.1, only briefly commenting on semiregular tessellations. In preparation for Section 8.3, we then discuss in Section 8.2.2, how tessellations can be interpreted as graphs and how properties such as distance and curvature manifest.

8.2.1. Regular tessellations

Regular polygonal tessellations are obtained by tiling the surface with q identical copies of regular geodesic p-sided polygons (p-gons) meeting at each corner and are conventionally denoted by the Schläfli symbol $\{p, q\}$. A polygon is called *regular* if its internal angles are equal and its side lengths are equal and it is called geodesic if its sides are geodesics. As we will see in more detail in Section 8.2.2, the curvature of the surface determines p and q with

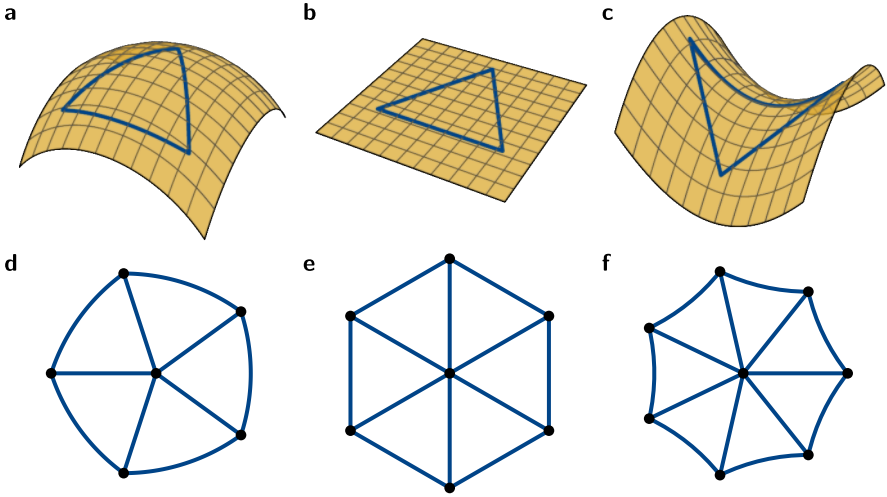

Figure 8.3.: Regular tessellations of curved surfaces. Geodesic triangle on a (**a**) positively curved spherical, (**b**) flat Euclidean, and (**c**) negatively curved saddle-shaped surface. Tessellation by regular triangles: (**d**) spherical $\{3, 5\}$ tessellation with larger internal angles of the triangles, (**e**) Euclidean $\{3, 6\}$ tessellation, and (**f**) hyperbolic $\{3, 7\}$ tessellation with smaller internal angles.

(a) positive curvature resulting in $(p-2)(q-2) < 4$, (b) vanishing curvature in $(p-2)(q-2) = 4$, and (c) negative curvature in $(p-2)(q-2) > 4$. The internal angles of a p-gon in the Euclidean plane sum to $(p-2)\pi$, while positive curvature implies a value larger than that and negative curvature a smaller value.

This can be intuitively understood by considering triangular tessellations, i.e., $\{3, q\}$ tessellations. As illustrated in Figs. 8.3a to 8.3c, the curvature of the surface influences the internal angles of triangles on that surface: (a) the internal angles of spherical triangles sum to a value larger than π, (b) for Euclidean triangles it is exactly equal to π, while in hyperbolic triangles it is smaller than π. The result is that spherical $\{3, q\}$ tessellations have $q < 6$, Euclidean $q = 6$ and hyperbolic $q > 6$, with the limiting cases shown in Figs. 8.3d to 8.3f, respectively. Figures 8.4a and 8.4b show two examples of hyperbolic tessellations: the $\{3, 7\}$ and $\{3, 9\}$ tessellation, respectively. Note that the polygons appearing in the same regular tessellation are all identical and the different sizes of the polygons that can be observed in the figures are due to the metric, which distorts distances close to the boundary, as illustrated

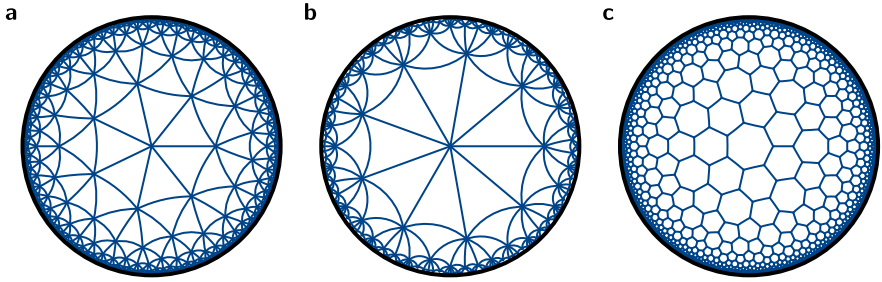

Figure 8.4.: Regular versus semiregular tessellations. Tessellations (blue) (**a**) $\{3,7\}$, (**b**) $\{3,9\}$, and (**c**) $6^2.7$ of the hyperbolic plane in Poincaré disk representation (the unit circle is shown in black). In all three tessellations, the corners are identical, but (a,b) are regular tessellations with all tiles identical, while (c) is semiregular and has both hexagons and heptagons as tiles.

in Fig. 8.2b.

We observe that the triangles in Fig. 8.4b are larger than the ones in Fig. 8.4a. As we will see in Section 8.2.2, the internal angles are not determined by the local curvature, but rather by the total curvature *enclosed*. Since for constant local curvature smaller polygons enclose less total curvature, the sum of their internal angles will be closer to $(p-2)\pi$ than the one for larger polygons. Consequently, if the curvature $K \neq 0$ of the surface is fixed, the side length of the polygons of a $\{p,q\}$ tessellation is uniquely determined. In contrast, for $K = 0$, the polygons can be arbitrarily scaled. As we have mentioned above, we fix the curvature of the hyperbolic plane to $K = -4$ and therefore the integers p and q completely characterize the tessellation.

Let us briefly summarize some geometric properties of the polygons [63]. In the Poincaré disk, the vertices of a single polygon centred at the origin are given by $z_j = r\mathrm{e}^{\mathrm{i}(2\pi j/p+\delta)}$, for an arbitrary phase δ and $j = 1, 2, \ldots, p$. Here, the circumradius r_c is given by

$$r_c = \sqrt{\frac{\cos\left(\frac{\pi}{p}+\frac{\pi}{q}\right)}{\cos\left(\frac{\pi}{p}-\frac{\pi}{q}\right)}} \tag{8.11}$$

and the corresponding *hyperbolic* distance of each vertex from the origin is

artanh(r). The hyperbolic side length d_0 is then given by

$$\sinh(d_0) = \sin\left(\frac{\pi}{p}\right) \sinh\left(2\,\mathrm{artanh}\left(r_c\right)\right). \tag{8.12}$$

We briefly comment on semiregular tessellations, which consist of q polygonal tiles joining identically at each corner. If the i^{th} polygon has n_i sides, $i = 1, 2, \ldots, q$, the tessellation is specified by $n_1.n_2.\cdots.n_q$, where repeated values of n_i are sometimes contracted and denoted by powers, e.g., the 6.6.7 tessellation illustrated in Fig. 8.4c is abbreviated as $6^2.7$.

8.2.2. Tessellations as graphs

The polygonal tessellations discussed above, can be interpreted as graphs with the vertices given by the corners of the polygons, the edges by their sides and the faces by the polygons themselves. The graph exists independent of its embedding and we can define quantities directly on the graph. Thus, the hyperbolic metric, Eq. (8.8), is automatically realized by the graph distance, because the sides of the polygons, i.e., the edges of the graph, all have the same (hyperbolic) length in the continuous hyperbolic space. This implies that the connectivity of the graph directly encodes the (negative) curvature.

The Euler characteristic χ of a graph with $\mathcal{V}$ vertices, $\mathcal{E}$ edges and F faces is defined as

$$\chi = \mathcal{V} - \mathcal{E} + \mathcal{F}. \tag{8.13}$$

The graph induced by the semiregular tessellation $n_1.n_2.\cdots.n_q$ therefore has Euler characteristic per vertex

$$\frac{\chi}{\mathcal{V}} = 1 - \frac{q}{2} + \sum_{i=1}^{q} \frac{1}{n_i} = \frac{1}{2}\left(2 - \sum_{i=1}^{q} \frac{n_i - 2}{n_i}\right). \tag{8.14}$$

For the regular $\{p, q\}$ tessellation, this simplifies to

$$\frac{\chi}{\mathcal{V}} = -\frac{pq - 2(p+q)}{2p} \tag{8.15}$$

and we find that for the tessellations shown in Fig. 8.3, the Euler characteristic per vertex is (d) $\frac{\chi}{\mathcal{V}} = \frac{1}{6}$, (e) 0, and (f) $-\frac{1}{6}$.

The Gauss-Bonnet theorem relates the Euler characteristic to the Gaussian curvature. Let Σ be a compact 2D Riemannian manifold with geodesic boundary, then

$$\int_{\Sigma} \mathrm{d}A\, K = 2\pi\chi. \tag{8.16}$$

Recall that the *dual graph* is the graph that has a vertex for each face of the original graph (and vice versa). If we now choose Σ to be a single face of the dual graph, then

$$A_0 K = 2\pi \frac{\chi}{\mathcal{V}}, \tag{8.17}$$

where A_0 is the face's area. We recognize that the Euler characteristic per vertex is proportional to the Gaussian curvature and that the sign of the Euler characteristic determines the sign of the Gaussian curvature. Equations (8.15) and (8.17) directly imply the conditions on p, q for spherical, Euclidean, and hyperbolic tessellations mentioned in the first paragraph of Section 8.2.1. Additionally, for fixed Gaussian curvature, $K = -4$, Eq. (8.17) allows us to compute the area per vertex A_0:

$$A_0 = \frac{\pi}{4}\left(\sum_{i=1}^{q} \frac{n_i - 2}{n_i} - 2\right) = \pi \frac{pq - 2(p+q)}{4p}. \tag{8.18}$$

The polygons making up the tessellations shown in Fig. 8.4 have area (a) $\frac{\pi}{12}$, (b) $\frac{\pi}{4}$, and (c) $\frac{\pi}{84}$.

8.3. Approximating the continuum

This section is largely based on the publication "Simulating hyperbolic space on a circuit board" [4].

Having introduced regular tessellations, we turn to one of the original motivations for studying them: the realization of the hyperbolic plane. Before discussing the relevant experimental aspects, we first need a tool to quantify how well the *graph* approximates the *continuous space*. We base our analysis on the Laplace operator which encodes the behavior of physical systems at vastly different scales, describing heat flow, fluids, as well as electric, gravitational, and quantum fields. A key input for the *Laplace-Beltrami operator*, as the Laplace operator in curved space is called, is the curvature of that space. We briefly review some of the operator's properties in Section 8.3.1 before discussing its lattice regularization obtained from an arbitrary $\{p, q\}$ tessellation in Section 8.3.2. Subsequently, in Section 8.3.3, we compare three different tessellations to illustrate the aspects relevant to how well the continuum can be approximated in the experiment.

8.3.1. Laplace-Beltrami operator

The general Laplace-Beltrami operator for a given metric tensor g_{ij} is

$$\triangle = \frac{1}{\sqrt{\det(g)}} \sum_{i,j} \partial_i \left(\sqrt{\det(g)} g^{ij} \partial_j \right), \tag{8.19}$$

where g^{ij} is the matrix inverse of g_{ij}. In Euclidean space, we have $(g_{\mathbb{R}^2})_{ij} = \delta_{ij}$, such that $\triangle_{\mathbb{R}^2} = \partial_x^2 + \partial_y^2$ is the usual Laplace operator. With the hyperbolic metric on the Poincaré disk, Eq. (8.8), the hyperbolic Laplace-Beltrami operator is

$$\triangle_{\mathbb{H}} = \left(1 - \left(x^2 + y^2\right)\right)^2 \left(\partial_x^2 + \partial_y^2\right). \tag{8.20}$$

In polar coordinates $x = r\cos(\theta)$, $y = r\sin(\theta)$, the two operators read

$$\triangle_{\mathbb{R}^2} = \partial_r^2 + \frac{1}{r}\partial_r + \frac{1}{r^2}\partial_\theta^2, \tag{8.21}$$

$$\triangle_{\mathbb{H}} = \left(1 - r^2\right)^2 \left(\partial_r^2 + \frac{1}{r}\partial_r + \frac{1}{r^2}\partial_\theta^2\right). \tag{8.22}$$

For given boundary conditions, the differential operator $\triangle$ is characterized by its spectrum and the eigenmodes. Here, we consider Dirichlet boundary conditions for the disk of radius $0 < r_0 < 1$, labeled by $\mathbb{D}_{r_0}$. We are then interested in the solutions to the *Dirichlet problem*

$$(\triangle + \lambda)\, u(x,y) = 0, \qquad u(x,y)|_{(x,y)\in\partial\mathbb{D}_{r_0}} = 0, \tag{8.23}$$

i.e., the eigenmodes u of $-\triangle$ with vanishing amplitude at $r = r_0$. Note that these solutions correspond to the eigenmodes of a drum of radius r_0 in the corresponding geometry. Below, we show that both in Euclidean and hyperbolic space, the solutions can be expressed in terms of special functions and their zeroes. Given that the Poincaré disk is embedded in $\mathbb{R}^2$, by considering such a disk, we can directly compare the Euclidean and hyperbolic solutions, as shown Fig. 8.5.

Euclidean space

We first discuss the solutions to Eq. (8.23) in the Euclidean case. The differential equation is separable, such that we can make the ansatz $u(x,y) = R(r)\Theta(\theta)$ and find

$$-\frac{\Theta''(\theta)}{\Theta(\theta)} = \frac{r^2 R''(r) + r R'(r) + r^2 \lambda R(r)}{R(r)}. \tag{8.24}$$

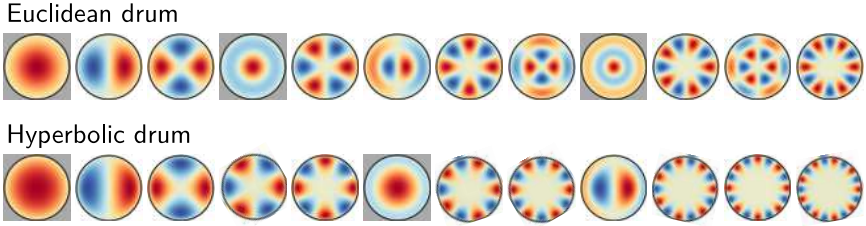

Figure 8.5.: Eigenmodes of a Euclidean and hyperbolic drum. Comparison of the first few eigenmodes of the (**a**) Euclidean and (**b**) hyperbolic drum of radius $r_0 = 0.94$ according to increasing eigenvalues $\lambda^{n\ell}$. Their spatial profile $u^{n\ell}$ is shown with red (yellow, blue) denoting maxima (zeros, minima). The number of radial zeros inside the disk, n, and the angular momentum (number of angular zeroes), ℓ, can easily be inferred from the plots. Modes with $\ell = 0$ are indicated with a gray background.

Since, we are on the disk, $\Theta(\theta + 2\pi) = \Theta(\theta)$, such that $\Theta(\theta) = \mathrm{e}^{\mathrm{i}\ell\theta}$ for $\ell \in \mathbb{Z}$ and

$$r^2 R''(r) + rR'(r) + (k^2 r^2 - \ell^2)R(r) = 0, \tag{8.25}$$

where we substituted $\lambda = k^2$. With the further substitution $\varrho = kr$, we obtain

$$\varrho^2 R''(\varrho) + \varrho R'(\varrho) + (\varrho^2 - \ell^2)R(\varrho) = 0, \tag{8.26}$$

which is the Bessel equation with solutions given by the Bessel functions of the first kind $\mathcal{J}_\ell(z)$

$$u_{\mathrm{E}}^{n\ell}(r, \theta) = \mathcal{J}_\ell(k_{n\ell} r)\mathrm{e}^{\mathrm{i}\ell\theta}, \tag{8.27}$$

where $k_{n\ell}$ is the $(n+1)^{\text{th}}$ zero of $k \mapsto \mathcal{J}_\ell(kr_0)$.

From the angular part of the solution it follows that ℓ can be interpreted as the angular momentum. Furthermore, $k_{n\ell} = \frac{z_{\ell,n+1}}{r_0}$, where $z_{\ell,n}$ is the n^{th} zero of $\mathcal{J}_\ell(z)$. The radial zeroes r_m of $u_{\mathrm{E}}^{n\ell}(r, \theta)$ are then given by

$$r_m = \frac{z_{\ell,m}}{k_{n\ell}} = r_0 \frac{z_{\ell,m}}{z_{\ell,n+1}}, \tag{8.28}$$

such that $m = 1, 2, \ldots, n$ for the nontrivial zeroes $r_m < r_0$. Thus, $u_{\mathrm{E}}^{n\ell}$ has exactly n nontrivial radial zeroes.

Hyperbolic space

We proceed analogously in the hyperbolic case, where the same ansatz results in the equation

$$(1 - r^2)^2 r^2 R''(r) + (1 - r^2)^2 rR'(r) + (\lambda r^2 - \ell^2(1 - r^2)^2)R(r) = 0. \tag{8.29}$$

Introducing $s := (1+r^2)/(1-r^2)$, this can be rewritten as

$$2sR'(s) - 4r^2(1-s^2)R''(s) + (\lambda r^2 - \ell^2(1-r^2)^2)R(s) = 0 \tag{8.30}$$

Dividing by $-4r^2$ and setting $\lambda = -4q(q+1) = 1+k^2$, we find

$$\left((1-s^2)\partial_s^2 - 2s\partial_s + \left(q(q+1) - \ell^2\frac{1}{1-s^2}\right)\right) R(s) = 0, \tag{8.31}$$

whose solutions are the associated Legendre functions $P_q^\ell(s)$, such that we obtain

$$u_{\mathrm{H}}^{n\ell}(r,\theta) = P^\ell_{\frac{1}{2}(-1+\mathrm{i}k_{n\ell})}\left(\frac{1+r^2}{1-r^2}\right)\mathrm{e}^{\mathrm{i}\ell\theta} \tag{8.32}$$

with $k_{n\ell}$ being the $(n+1)^{\text{th}}$ zero of

$$k \mapsto P^\ell_{\frac{1}{2}(-1+\mathrm{i}k)}\left(\frac{1+r_0^2}{1-r_0^2}\right). \tag{8.33}$$

Again we can interpret $\ell \in \mathbb{Z}$ as the angular momentum and n as the number of radial zeroes of $u_{\mathrm{H}}^{n\ell}$.

Spectra and eigenmodes

We plot in Figs. 8.5a and 8.5b the first few solutions to Eq. (8.23) on the Euclidean and Poincaré disk with $r_0 = 0.94$, respectively. We observe a significant reordering of the eigenmodes characterized by (n,ℓ): while in the Euclidean case the first eigenmode with $n=1$ is the fourth (not counting degenerate eigenmodes separately), in the hyperbolic case, it is only the sixth mode. This reordering becomes even more apparent when considering the angular momentum dispersion $\ell \mapsto \lambda^{n\ell}$ displayed in Fig. 8.6. In both the Euclidean and the hyperbolic case, several branches (corresponding to different values of n, indicated by numbers to the right of each branch) are discernible. The spectral reordering manifests as a reduced slope of the branches (relative to their spacing) compared to their behavior for the Euclidean drum. Consequently, eigenmodes with large ℓ and small n appear much earlier in the spectrum in hyperbolic compared to Euclidean space. The spectral reordering is stronger for larger radii r_0. This is intuitively understood from the fact that the circumference of a hyperbolic drum grows superlinearly with its radius, such that oscillations in the angular direction stretch over larger distances. This makes them energetically favorable over oscillations in the radial direction, resulting in the observed reordering.

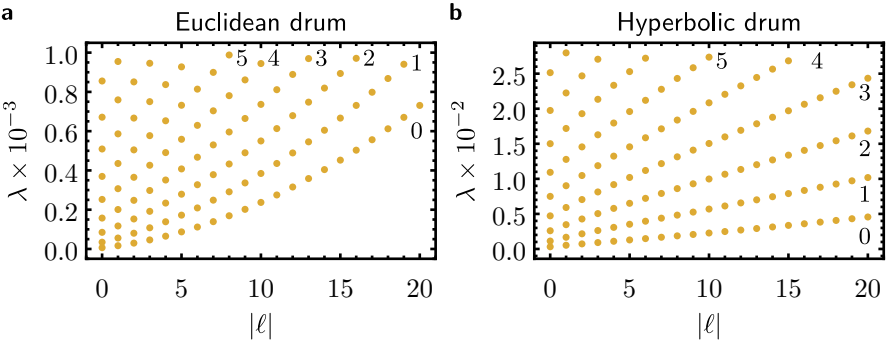

Figure 8.6.: Angular momentum dispersion of eigenmodes. Eigenfrequency $\lambda^{n\ell}$ versus angular momentum ℓ for eigenmodes $u^{n\ell}$ of the continuum Laplace-Beltrami operator, i.e., solutions to Eq. (8.23) with $r_0 = 0.94$, for (**a**) the Euclidean and (**b**) the hyperbolic geometry. For the first six branches, the value of n is indicated by black numbers.

8.3.2. Lattice regularization

We now return to the interpretation of the tessellations as graphs discussed in Section 8.2.2. Recall that the metric of the underlying continuous space manifests in the connectivity without reference to the positions of the vertices. The embedding only comes into play when relating graph distance to a metric in continuous space. The graph naturally induces a lattice regularization of the Laplace-Beltrami operator in terms of the Laplacian matrix of the graph. Following [69], we show that to leading order in the characteristic length d_0 of the tessellation, the Laplacian matrix is given by the continuum operator.

The graph Laplacian of a simple (i.e., undirected) graph is given by

$$\mathcal{L} = \mathcal{A} - \mathcal{D}, \tag{8.34}$$

where $\mathcal{D}$ is the degree matrix (the diagonal matrix containing the number of adjacent sites for each site as entries) and $\mathcal{A}$ the adjacency matrix ($\mathcal{A}_{ab} = 1$ if sites a and b are adjacent and zero otherwise). Assuming the graph represents a lattice regularization of a continuum obtained from a semiregular tessellation $n_1.n_2.\cdots.n_q$, any function $u(z)$ induces a function on the lattice with sites labeled by $a = 1, 2, \ldots$, via $a \mapsto u(z_a) =: u_a$. The action of the Laplacian

matrix is then given by

$$\mathcal{L}_{ab}u_b = \mathcal{A}_{ab}u_b - \mathcal{D}_{ab}u_b = \sum_{i=1}^{q} u(z_{a+e_k}) - qu(z_a), \tag{8.35}$$

where $a + e_i$ labels the sites adjacent to site a.

If only a finite segment of the (hyperbolic) plane is tiled, the tessellation has a boundary, which corresponds to vertices of the graph that are attached to fewer edges than the bulk vertices. Naturally, this is reflected both in the adjacency matrix $\mathcal{A}$ as well as in the degree matrix $\mathcal{D}$. However, if we impose Dirichlet boundary conditions for $u(z)$ as we do in Eq. (8.23), then u vanishes on the boundary sites, which allows us to drop them from the matrix description. Consequently, we are left only with the bulk part of $\mathcal{L}$, simplifying the analysis.

Following Appendix B of Ref. 69, we show that the action of $\mathcal{L}$ on u_a can be expressed in terms of the Laplace-Beltrami operator, thereby establishing a precise relationship between the continuum operator and its lattice regularization. After deriving that relationship both for Euclidean and hyperbolic tessellations, we illustrate it by studying a lattice approximating the continuous Euclidean and hyperbolic drum with $r_0 = 0.94$, each, whose eigenmodes and spectra were shown in Figs. 8.5 and 8.6. For that purpose we choose the $\{3, 6\}$ and $\{3, 7\}$ lattice shown in Figs. 8.7a and 8.7b to approximate the Euclidean and hyperbolic drum, respectively. We then study the eigenvectors and spectra of the Laplacian matrix and compare them to the eigenmodes and spectra of the Laplace-Beltrami operator in the continuum.

Euclidean space

We first discuss a Euclidean tessellation with coordination q, i.e., where each site has q adjacent sites. Let h be the Euclidean distance between two adjacent sites, then

$$z_{a+e_i} = z_a + h\mathrm{e}^{\mathrm{i}\phi_a}\mathrm{e}^{\mathrm{i}\frac{2\pi}{q}(i-1)} =: z_a + hw_{ai}, \tag{8.36}$$

where ϕ_a is a site-dependent phase factor, and we can expand $u(z_{a+e_i})$ in powers of h:

$$\begin{aligned} u(z_{a+e_i}) &= u(z_a) + \frac{\mathrm{d}}{\mathrm{d}h}u(z_{a+e_i})\bigg|_{h=0} h + \frac{1}{2}\frac{\mathrm{d}^2}{\mathrm{d}h^2}u(z_{a+e_i})\bigg|_{h=0} h^2 + \mathcal{O}\big(h^3\big) \\ &= u(z_a) + \left(w_{ai}\partial_z + w_{ai}^*\partial_z^*\right)u(z)\big|_{z=z_a} h \\ &\quad + \frac{1}{2}\left(w_{ai}\partial_z + w_{ai}^*\partial_z^*\right)^2 u(z)\bigg|_{z=z_a} h^2 + \mathcal{O}\big(h^3\big) \end{aligned} \tag{8.37}$$

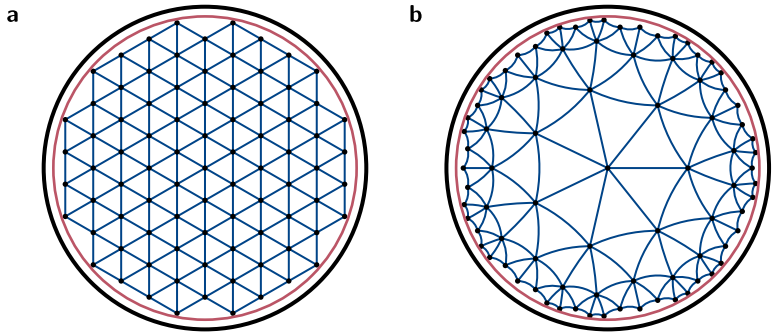

Figure 8.7.: Euclidean $\{3,6\}$ and hyperbolic $\{3,7\}$ lattice. Lattices obtained from (**a**) the $\{3,6\}$ tessellation of the Euclidean plane and (**b**) the $\{3,7\}$ tessellation of the hyperbolic plane. Both lattices have 85 sites and (b) is exactly the one realized in our experiment and discussed in Section 8.4.

with $\partial_z = \partial/\partial_z$, $\partial_z^* = \partial/\partial_{z^*}$. Note that for any $m \in \mathbb{Z}$,

$$\sum_{i=1}^{q} w_{ai}^m = \mathrm{e}^{\mathrm{i}\phi_a} \sum_{i=1}^{q} \mathrm{e}^{\mathrm{i}\frac{2\pi m}{q}(i-1)} = 0, \tag{8.38}$$

and $|w_{ai}| = 1$, such that ϕ_a drops from the subsequent calculations:

$$\sum_{i=1}^{q} u(z_{a+e_a}) = qu(z_a) + qh^2\, \partial_z \partial_z^* u(z)|_{z=z_a} + \mathcal{O}\big(d^3\big). \tag{8.39}$$

Since $\triangle_{\mathbb{R}^2} = 4\partial_z\partial_z^*$, we finally find

$$\mathcal{L}_{ab} u_b = \frac{q}{4} h^2 \triangle_{\mathbb{R}^2} u(z_a) + \mathcal{O}\big(h^3\big). \tag{8.40}$$

With $q = 6$ for a $\{3,6\}$ tessellation this results in

$$\sum_b \mathcal{L}_{ab} u_b = \frac{3}{2} h^2 \triangle_{\mathbb{R}^2} u_a + \mathcal{O}\big(h^3\big). \tag{8.41}$$

Hyperbolic space

We proceed analogously for hyperbolic tessellations with coordination q and hyperbolic distance d_0 between adjacent sites. It is helpful to first transform the Poincaré disk by the automorphism

$$z \mapsto v(z) = \frac{z_a - z}{1 - z z_a^*}. \tag{8.42}$$

This transformation corresponds to a π-rotation that exchanges z_a and the origin. In particular, note that it squares to identity, implying that $z \mapsto v(z)$ and its inverse $z \mapsto v^{-1}(z)$ are equivalent. Recall further that the hyperbolic distance between the origin and an arbitrary point z in the unit disk takes the form $d = \operatorname{artanh}(|z|)$. In the transformed coordinates, z_{a+e_i} takes the simple form

$$v_{a+e_i} = v(z_{a+e_i}) = h\mathrm{e}^{\mathrm{i}\phi_a}\mathrm{e}^{\mathrm{i}\frac{2\pi}{q}(i-1)} = hw_{ai} \tag{8.43}$$

with $h = \tanh(d_0)$, $u(z_{a+e_i}) = u(z(v_{a+e_i}))$, and ϕ_a again a site-dependent phase factor that subsequently drops out from the calculations. Expanding in powers of h, we obtain

$$\begin{aligned} u(z_{a+e_i}) &= u(z_a) + \frac{\mathrm{d}}{\mathrm{d}h}u(z(v_{a+e_i}))\bigg|_{h=0} h + \frac{1}{2}\frac{\mathrm{d}^2}{\mathrm{d}h^2}u(z(v_{a+e_i}))\bigg|_{h=0} h^2 + \mathcal{O}\big(h^3\big) \\ &= u(z_a) - (1-|z_a|^2)\left(w_{ai}\partial_z + w_{ai}^*\partial_z^*\right)u(z)|_{z=z_a}\, h \\ &\quad + \frac{1}{2}(1-|z_a|^2)^2\left(w_{ai}\partial_z + w_{ai}^*\partial_z^*\right)^2 u(z)\Big|_{z=z_a} h^2 + \mathcal{O}\big(h^3\big) \end{aligned} \tag{8.44}$$

Since w_{ai} are still the same as in the Euclidean case, Eq. (8.35) becomes

$$\mathcal{L}_{ab}u_b = \frac{q}{4}h^2\,(1-|z|^2)^2\,\triangle_{\mathbb{R}^2}u(z)\Big|_{z=z_a} + \mathcal{O}\big(h^3\big) \tag{8.45}$$

and recalling that $(1-|z|^2)^2\,\triangle_{\mathbb{R}^2} = \triangle_{\mathbb{H}}$, we finally arrive at

$$\mathcal{L}_{ab}u_b = \frac{q}{4}h^2\,\triangle_{\mathbb{H}}u(z_a) + \mathcal{O}\big(h^3\big). \tag{8.46}$$

With $q = 7$ for a $\{3,7\}$ tessellation this results in

$$\sum_b \mathcal{L}_{ab}u_b = \frac{7}{4}h^2\,\triangle_{\mathbb{H}}u_a + \mathcal{O}\big(h^3\big), \tag{8.47}$$

where $h = \tanh(d_0) = 0.496\,970$, and $d_0 = 0.545\,275$.

Spectra and eigenvectors

Since the leading contribution to the Laplacian matrix $\mathcal{L}$ is the Laplace-Beltrami operator, in the long-wavelength limit, eigenvectors $\mathbf{u}$ of $\mathcal{L}$ can be associated with eigenmodes $u^{n\ell}(z)$ of the Laplace-Beltrami operator and eigenvalues with $\lambda^{n\ell}$:

$$-\mathcal{L}\mathbf{u} = \tilde{\lambda}\mathbf{u} = \frac{q}{4}h^2\lambda\mathbf{u}, \tag{8.48}$$

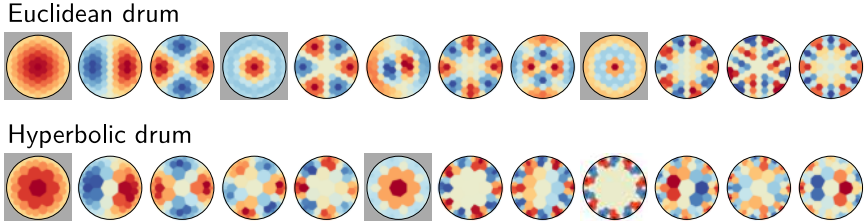

Figure 8.8.: Eigenvectors of the graph Laplacian. Comparison of the first few eigenvectors of the graph Laplacian obtained from (**a**) the Euclidean $\{3, 6\}$ and (**b**) the hyperbolic $\{3, 7\}$ tessellation, sorted according to increasing eigenvalue. Their spatial profile is shown with red (yellow, blue) denoting maxima (zeros, minima). The number of radial zeros inside the disk, n, and the angular momentum (number of angular zeroes), ℓ, can easily be inferred from the plots for the first few modes, but it gets successively harder with increasing n and ℓ. Modes with $\ell = 0$ are indicated with a gray background.

where $\tilde{\lambda}$ is the eigenvalue of $-\mathcal{L}$ and $\lambda = \frac{4}{qh^2}\tilde{\lambda}$ the rescaled quantity corresponding to the eigenvalue of the Laplace-Beltrami operator. Figures 8.8a and 8.8b show these eigenvectors for the Euclidean $\{3, 6\}$ and hyperbolic $\{3, 7\}$ tessellations shown in Figs. 8.7a and 8.7b, respectively. Comparing to Fig. 8.5, we find very good agreement for the long-wavelength modes and increasingly larger deviations for the later modes, as expected. We observe that the ordering of the first twelve (not counting degeneracies) Euclidean and the first eight hyperbolic modes is reproduced by the eigenvectors on the lattice. Crucially, the *reordering* on the hyperbolic compared to the Euclidean drum is reproduced.

For a quantitative comparison of the Laplacian matrix and the Laplace-Beltrami operator, we need to match the eigenvectors of the former to the eigenmodes of the latter. Due to lattice effects, we cannot simply order them according to their eigenvalues. Instead, we compute the overlap, i.e., the inner product, of the eigenvectors $\mathbf{u}^\beta$ of the graph Laplacian with the discretized eigenmodes $u^\alpha(z)$ of the Laplace-Beltrami operator:

$$\left\langle u^\alpha(z) \middle| \mathbf{u}^\beta \right\rangle = \sum_a \left(u^\alpha(z_a)\right)^* u_a^\beta, \tag{8.49}$$

with z_a the positions of the lattice sites in the Poincaré disk and α the numbered index corresponding to (n, ℓ). We show this overlap for several examples of eigenvectors in Fig. 8.9a. The quantum numbers (n, ℓ) of the continuous eigenmode with maximal overlap with a given eigenvector then determine the

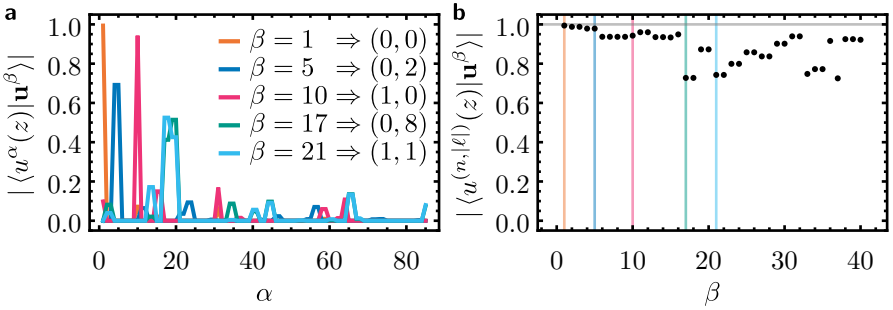

Figure 8.9.: Overlap of eigenvectors with continuous eigenmodes. (**a**) Absolute value of the overlap of the indicated eigenvectors $\mathbf{u}^{\beta}$ of the graph Laplacian with each of the first 85 eigenmodes $u^{(n,+|\ell|)}(z)$ and $u^{(n,-|\ell|)}(z)$ of the Laplace-Beltrami operator as defined in Eq. (8.49). For each, the maximum overlap is identified and, from the corresponding eigenmode, n and ℓ are extracted (see inset legend). (**b**) Total overlap of the first 40 eigenvectors $\mathbf{u}^{\beta}$ with the eigenmodes $u^{(n,\pm|\ell|)}$ that have maximal overlap according to Eq. (8.50). The eigenvectors shown in (a) are emphasized by appropriately colored vertical lines.

quantum numbers of that eigenvector. Note that modes with nonvanishing angular momentum generally have nonvanishing overlap with both degenerate eigenmodes $u^{(n,\pm\ell)}(z)$. This is reflected in the data in Fig. 8.9a: the maximal overlap of $\beta = 1$ and $\beta = 10$ is larger than for the other eigenvectors which in turn have equal overlap with two neighboring eigenmodes (corresponding to $\pm\ell$).

We therefore asses how close eigenvector $\mathbf{u}^{\beta}$ and matching eigenmode are by computing the *total overlap* of $\mathbf{u}^{\beta}$ with the eigenmodes $u^{(n,\pm\ell)}$:

$$\left|\left\langle u^{(n,|\ell|)}(z)\middle|\mathbf{u}^{\beta}\right\rangle\right| = \sqrt{\sum_{\ell'=\pm\ell} \left|\left\langle u^{(n,\ell')}(z)\middle|\mathbf{u}^{\beta}\right\rangle\right|^2}, \tag{8.50}$$

see Fig. 8.9b. As expected, the total overlap decreases with increasing quantum numbers due to the departure from the long-wavelength limit. Nevertheless, we observe that the total overlap is very close to 1 up to (and excluding) $\beta = 17$, which corresponds to the first eigenvector whose position in the ordered spectrum does not agree with the continuum case anymore: $\alpha = 17$ is the one with $(n, |\ell|) = (1, 1)$, while $\beta = 17$ has maximal overlap with $(0, 8)$. For the mode reordering to be observable, the overlap has to be close to 1 for all the modes up to (and including) the $(1, 0)$ mode, which in our case is mode

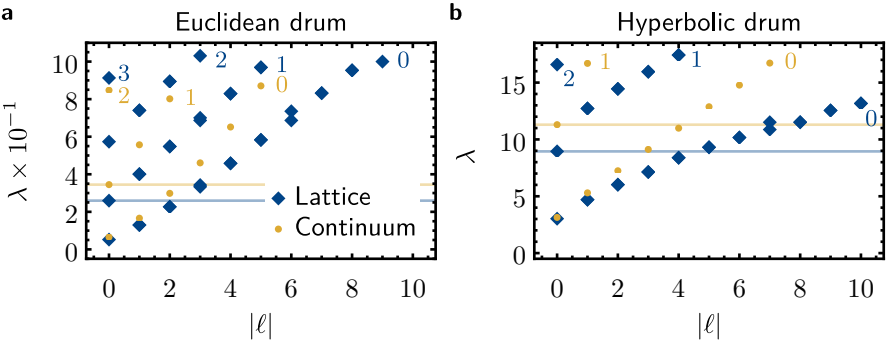

Figure 8.10.: Angular momentum dispersion on the lattice. Rescaled eigenvalue λ versus angular momentum ℓ for the continuous Laplacian eigenmodes (yellow) and the eigenvectors of the Laplacian matrix (blue) of the graph obtained from (**a**) the Euclidean $\{3, 6\}$ and (**b**) hyperbolic $\{3, 7\}$ tessellation. The value of n is indicated by appropriately colored numbers, such that the quantum number of each eigenvector can be read off and the eigenvalue λ for $(n, \ell) = (1, 0)$ is indicated by a horizontal line to emphasize the reordering.

10.

With the angular momentum ℓ known for each eigenvector, we can once more consider the angular momentum dispersion and corroborate the reordering in the hyperbolic compared to the Euclidean case on the lattice. The results are shown in Fig. 8.10 and compared to the corresponding dispersion obtained in the continuum. Indeed, as in the continuum, a strong spectral reordering is observed and it is emphasized by horizontal lines at the eigenvalue of the $(1, 0)$ modes. As we demonstrate in Section 8.3.3, this reordering is a universal feature of the spatial curvature and does, therefore, not rely on the details of the tessellation, as long as it adequately approximates the continuum. Note that due to the small number of sites of the lattices considered here, the quantitative agreement of the eigenvalues is not great, but it is improved significantly when increasing the number of sites as we will see in Section 8.3.3. However, the overlap of the eigenmodes shown in Fig. 8.9b is more than sufficient to guarantee the reordering.

While the above considerations allow us to quantify how well the spectrum and eigenvectors of the graph Laplacian reproduce the corresponding quantities in the continuum, this relies on the characteristic length of the tessellation h to be small, i.e., the tessellation to be dense. However, for practical purposes

this is only one relevant criterion for choosing the appropriate tessellation. In the next section, we discuss these criteria and compare three exemplary tessellations with respect to them.

8.3.3. Comparison of tessellations

For our experiments, three different aspects of the modeled lattice are important:

(1) the lattice should provide a good approximation of the continuum,

(2) a large fraction of the Poincaré disk should be covered to obtain strong signatures of the negative curvature, and

(3) $\ell = 0$ modes should be easy to excite and distinguish from $\ell \neq 0$ modes.

While aspects (1) and (2) can both be satisfied by having a sufficiently large number of vertices, in practice, there will be a trade off between the two aspects: for a fixed number of vertices, tessellations with larger area per vertex cover a larger fraction r_0 of the Poincaré disk, while for fixed coverage r_0 a good approximation of the continuum is naturally achieved by tessellations that feature small area per vertex (i.e., which tile the hyperbolic plane densely), as we have seen in Section 8.3.2. Finally, (3) depends on the symmetry properties of the lattice: a vertex at the origin of the disk allows for easy excitation and identification of $\ell = 0$ modes and a high order of rotational symmetry prevents $\ell \neq 0$ modes from having nonvanishing weight at the origin of the disk, which would impede the identification of $\ell = 0$ modes.

Below, we analyze and compare three different tessellations with respect to these three aspects: (a) $\{3, 7\}$, (b) $\{7, 3\}$, and (c) $6^2.7$, illustrated in Figs. 8.11a to 8.11c. The area per vertex for those is, according to Eq. (8.18), (a) $\pi/12$, (b) $\pi/28$, and (c) $\pi/84$. We compare these three tessellations with respect to three properties: First, we consider the accuracy of approximating the continuum. This is determined by the density of the tessellation, which in turn depends on the vertex configuration (or equivalently on A_0). Subsequently, we examine the total (integrated) curvature that can be obtained in a finite lattice with a fixed number of vertices. Finally, we discuss the effect of rotational symmetry with respect to a central vertex on the spectrum and the profile of the eigenmodes. Overall, these considerations favour the $\{3, 7\}$ tessellation.

Approximating the continuum

Here, we analyze how well the three tessellations shown in Fig. 8.11 approximate the continuum by comparing the spectra of the graph Laplacian on the lattice

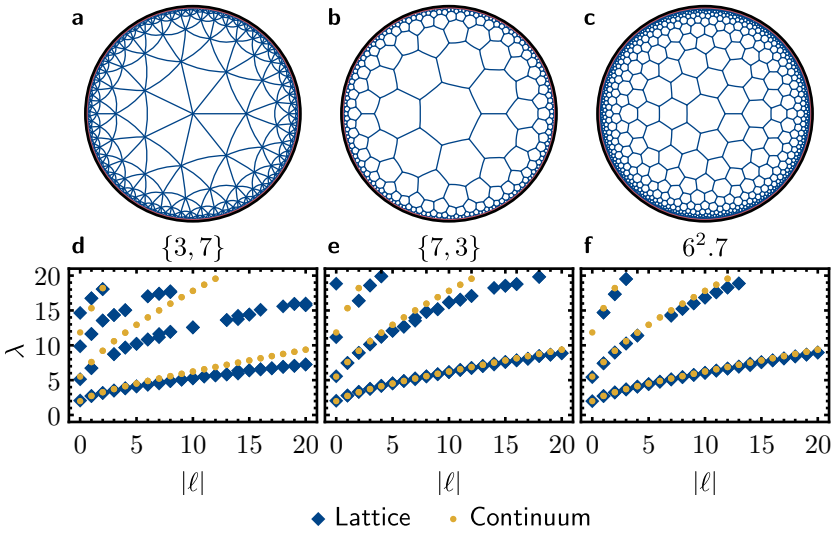

Figure 8.11.: Comparison of tessellations for fixed disk radius. (**a,b,c**) Tessellations $\{3,7\}$, $\{7,3\}$, and $6^2.7$ of the hyperbolic plane in Poincaré disk representation, respectively, covering a disk of radius $r_0 = 0.99$ (red circle). This results in 589, 1197, and 3857 vertices, respectively. (**d,e,f**) Angular momentum dispersion of the eigenvectors of the graph Laplacian (blue diamonds) and of the eigenmodes of the Laplace-Beltrami operator on the hyperbolic drum with the same radius r_0 (yellow dots).

to the ones of the Laplace-Beltrami operator on a corresponding disk. All three tessellations cover approximately the same disk of radius $r_0 < 1$; however, due to them having different area per vertex A_0, the number of vertices significantly varies between the three cases. More specifically, for each of the three tessellations we compare the spectrum of the graph Laplacian $\mathcal{L}$ to the spectrum of the Laplace-Beltrami operator with Dirichlet boundary conditions for a disk of the same radius r_0.

We have already discussed this problem analytically in Section 8.3.2 and have found that the graph Laplacian $\mathcal{L}$ is approximated by the Laplace-Beltrami operator up to corrections of order h^3, where $h = 0.496\,970$ for $\{3,7\}$, $h = 0.275\,798$ for $\{7,3\}$, and $h = 0.165\,657$ for $6^2.7$. We therefore anticipate these corrections to be smallest for the $6^2.7$ tessellation, in agreement with the area per vertex being smallest for this tessellation. To verify this explicitly for the three tessellations on disks of radius $r_0 = 0.99$, we numerically compute

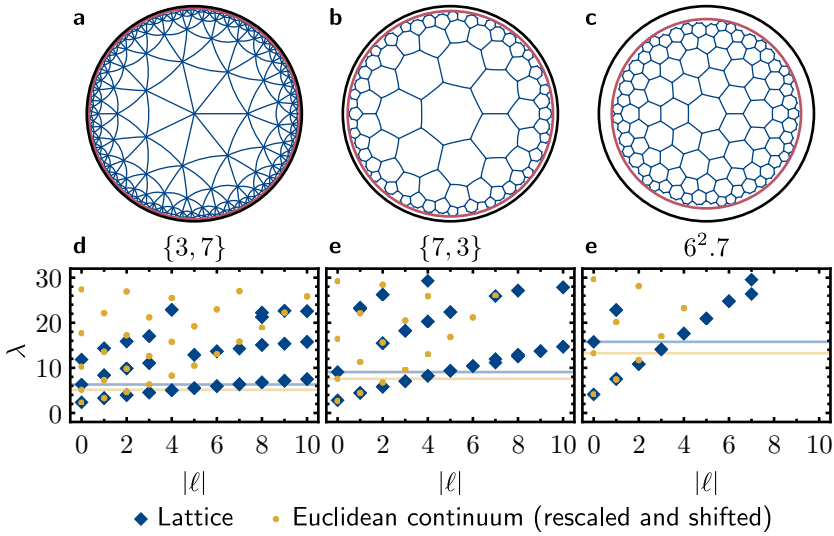

Figure 8.12.: Comparison of tessellations for fixed number of vertices. (**a,b,c**) Tessellations $\{3,7\}$, $\{7,3\}$, and $6^2.7$, with 274, 273, and 280 vertices and bounding circle with radius $r_0 = 0.98$, 0.955, and 0.88, respectively. (**d,e,f**) Angular momentum dispersion of the eigenvectors of the graph Laplacian (blue diamonds) and of the eigenmodes of the *Euclidean* Laplace operator with the same radius r_0 (yellow dots). Horizontal lines of the corresponding color indicate the eigenvalue of the $(n,\ell) = (1,0)$ mode in each geometry. The difference in the number of modes below the line quantifies the spectral reordering between the hyperbolic and the Euclidean disk. Note that the eigenvalues λ_{E} of the Euclidean drum are rescaled and shifted to allow for a better qualitative comparison to the hyperbolic dispersion, i.e., to emphasize the reordering of eigenstates.

the spectrum (eigenvalue as a function of angular momentum) and compare the dispersion to the one obtained from the continuum, as we did in Fig. 8.10. Note that because of finite-size effects, it can be difficult to correctly identify the angular momentum of certain highly excited states. The results are shown in Fig. 8.11 and we observe that the difference between lattice (blue diamonds) and continuum (yellow disks) dispersion is smaller for tessellations with small area per site, i.e., when the total number of sites is larger.

Signatures of negative curvature

Above, we have answered the question which of the three tessellations gives the best approximation of the continuum for a disk with fixed radius r_0. Experimentally, however, we are interested in a different question: For a given number of vertices, which tessellation gives the strongest signatures of negative curvature? Naturally, we expect tessellations that cover a larger area of the Poincaré disk to exhibit stronger signatures of the negative curvature. Therefore, a large area per vertex is desirable and the $\{3, 7\}$ tessellation is the one with the largest area per vertex out of the three under consideration.

We fix the (approximate) number of sites to 275 and construct the tessellations such that they consist of full shells, i.e., such that they are rotationally symmetric. The resulting lattices are shown in Fig. 8.12. We then compare the angular momentum dispersion to the dispersion obtained from the eigenmodes of the continuum Laplace-Beltrami operator on the *Euclidean* drum of the same radius r_0, each. The reordering of the eigenstates compared to the Euclidean case, is with a difference of four states strongest for the $\{3, 7\}$ tessellation and reduced to only a single state for $6^2.7$. Therefore, to reveal the spectral reordering in an experimental realization with a limited number of sites, it is desirable to opt for the $\{3, 7\}$ tessellation.

Role of rotational symmetry

Finally, we discuss the role of rotational symmetry. The tessellations shown in Figs. 8.11b and 8.11c can be shifted such that they have a vertex at the center of the disk. This is advantageous in order to to excite and detect $\ell = 0$ modes which have a maximum amplitude at the center of the disk. However, in the case of the $\{7, 3\}$ tessellation, the original seven-fold rotational symmetry is broken down to a three-fold rotational symmetry, while in the case of the $6^2.7$ tessellation no rotational symmetry is remaining at all. These shifted tessellations are displayed in Figs. 8.13b and 8.13c.

In Figs. 8.13d to 8.13f we show for each of the first 20 eigenvectors of the graph Laplacian of each considered tessellation their angular momentum ℓ and their weight at the central vertex. From the continuum we expect that only $\ell = 0$ modes have nonvanishing weight at that vertex. This, indeed, holds on the $\{3, 7\}$ lattice for all $|\ell| \leq 6$. However, we observe that eigenvalues of the two $|\ell| = 7$ modes (and similarly for integer multiples of 7) are split (Fig. 8.13d), in stark contrast with the continuum case where such modes are degenerate. We also observe that one of these two modes acquires a non-zero weight at the central vertex. An analogous feature is observed for the $\{7, 3\}$ tessellation, where the modes with $|\ell|$ being integer multiples of 3 are similarly

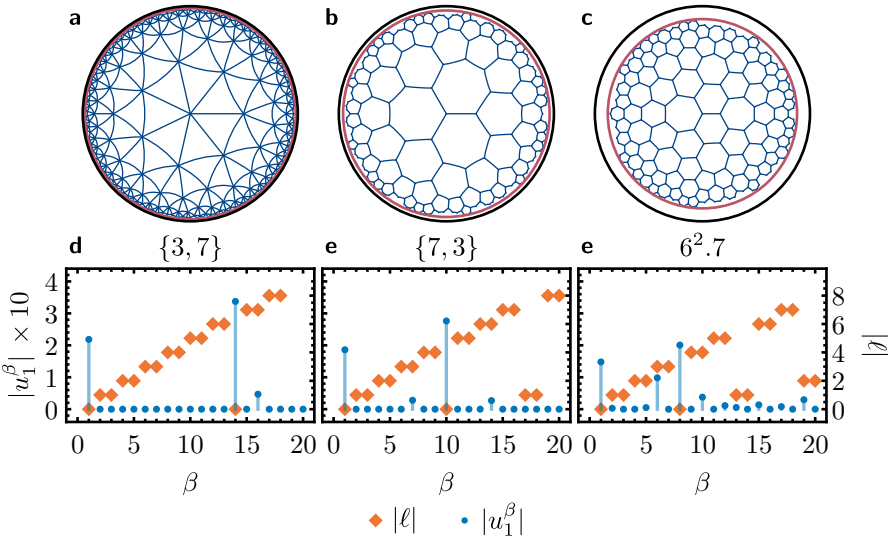

Figure 8.13.: Comparison of tessellations with different order of rotational symmetry. (**a,b,c**) Centred tessellations $\{3,7\}$, $\{7,3\}$, and $6^2.7$ with 274, 271, and 271 vertices and a bounding circle of each tessellation with radius $r_0 = 0.98$, 0.96, and 0.88, respectively. (**d,e,f**) For the first 20 eigenvectors (counting degenerate modes), the absolute value of their weight at the central vertex $|u_1^\beta|$ (orange diamonds, left vertical axis) and absolute value of their angular momentum $|\ell|$ (blue dots, right vertical axis) are shown.

contaminated. Finally, the situation for the $6^2.7$ tessellation is even less ideal as here most of the modes acquire a nonvanishing weight at the central vertex.

Therefore, we conclude that a small order of rotational symmetry leads to a larger number of $\ell \neq 0$ eigenmodes with nonvanishing weight at the central vertex. This in turn prevents us from easily detecting (and exciting) $\ell = 0$ modes via the central vertex.

8.4. Electric-circuit realization

This section is largely based on the publication "Simulating hyperbolic space on a circuit board" [4].

In the previous section, we have argued that, in the long-wavelength limit, a hyperbolic lattice approximates the continuous hyperbolic plane. This allows us to realize the negatively curved space experimentally by implementing the

corresponding graph. While it has been suggested [294] that a nontrivial metric can be implemented in metamaterials via spatial variations of the electromagnetic permittivity of continuous media, it is very challenging to induce these variations in a controlled manner, which limits the applicability of such approaches. An approach relying on discretization of space overcomes these experimental limitations and therefore is much more promising. Crucially, in any network, the physical distances between its nodes are fundamentally decoupled from the effective metric that enters the long-wavelength description of its degrees of freedom. Thus, any network where links can be engineered in a controlled manner is amenable to implementation of the graph approximating the hyperbolic plane. This opens the door to realizations in many of the metamaterials that have become popular in recent years. Indeed, the first experimental realization of a hyperbolic lattice utilized a network of coplanar waveguide resonators [68].

In our work [4], which we describe in this section, we instead turn to electric-circuit networks [41–43, 295–299] and go beyond previous works by measuring static and dynamic signatures of the negative curvature: we observe the reordering of Laplacian eigenmodes discussed in Section 8.3 and propagation of wave packets along hyperbolic geodesics. Compared to other experimental platforms, electric circuits significantly excel in their flexibility of design, ease of fabrication, and high accessibility to measurements. Our results showcase both a versatile platform to emulate hyperbolic lattices in tabletop experiments, and a set of methods to verify the effective hyperbolic metric in this and other platforms. We start in Section 8.4.1 by briefly reviewing the description of electric circuit networks and how the graph Laplacian enters in that description. Next, in Section 8.4.1, we describe the experimental realization of a hyperbolic drum and give details on the circuit elements, before presenting and discussing the results of our static and dynamic measurements in Sections 8.4.3 and 8.4.4, respectively.

8.4.1. Electric-circuit networks

We briefly review the theoretical description of electric-circuit networks [41–43]. We consider a linear electric-circuit network, that consists of capacitors (C), inductors (L) and (Ohmic) resistors (R). The voltage of each of those elements is known:

$$V^{\mathrm{R}} = RI, \tag{8.51a}$$

$$V^{\mathrm{C}} = \frac{Q}{C}, \tag{8.51b}$$

$$V^{\mathrm{L}} = -L\dot{I}, \tag{8.51c}$$

where $V^{\mathrm{R,C,L}}$ is the voltage across the corresponding circuit element, Q the charge accumulated on it, $I = \dot{Q}$, its time derivative, is the current flowing through it, R the resistance, C the capacitance, and L the inductance. Placing all three elements in parallel, according to Kirchhoff's law, the currents add and all the voltages are equal such that we obtain for the current I flowing from point a to b

$$\dot{I} = C\ddot{V} + \frac{1}{R}\dot{V} - \frac{1}{L}V, \tag{8.52}$$

with $V = V_b - V_a$.

The relationship in Eq. (8.52) can be generalized to a circuit network consisting of nodes labelled by $a = 1, 2, \ldots$, where any two nodes a and b are potentially connected by a resistor, capacitor and inductor in parallel. Let V_a and I_a be the voltage and external input current on node a, and

$$J^{\mathrm{C}}_{ab} = C, \tag{8.53a}$$

$$J^{\mathrm{R}}_{ab} = \frac{1}{R}, \tag{8.53b}$$

$$J^{\mathrm{L}}_{ab} = -\frac{1}{L}. \tag{8.53c}$$

the matrix elements of the *reduced Laplacian matrices* of capacitances, conductances and inverse inductances, which encode the capacitance, resistance, and inductance between nodes a anb b, respectively. Further, we include the contribution $J^{\mathrm{R,C,L}}_{a0}$ from circuit elements between node a and the ground (voltage drop $-V_a$) in the diagonal elements

$$J^{\mathrm{R,C,L}}_{aa} = -J^{\mathrm{R,C,L}}_{a0} - \sum_{b\neq a} J^{\mathrm{R,C,L}}_{ab}. \tag{8.54}$$

Then, Kirchhoff's law applied to the full network results in

$$\begin{aligned}\dot{I}_a &= \sum_{b\neq a} \left(J^{\mathrm{C}}_{ab}\left(\ddot{V}_b - \ddot{V}_a\right) + J^{\mathrm{R}}_{ab}\left(\dot{V}_b - \dot{V}_a\right) + J^{\mathrm{L}}_{ab}\left(V_b - V_a\right)\right) \\ &\quad + J^{\mathrm{C}}_{a0}\left(-\ddot{V}_a\right) + J^{\mathrm{R}}_{a0}\left(-\dot{V}_a\right) + J^{\mathrm{L}}_{a0}\left(-V_a\right) \\ &= \sum_b \left(J^{\mathrm{C}}_{ab}\ddot{V}_b + J^{\mathrm{R}}_{ab}\dot{V}_b + J^{\mathrm{L}}_{ab}V_b\right).\end{aligned} \tag{8.55}$$

Fourier transforming Eq. (8.55) $t \mapsto \omega$, we obtain

$$I_a = \sum_b J_{ab}(\omega)V_b, \tag{8.56}$$

with I_a and V_a the input current and voltage amplitude (for angular frequency ω) at node a, respectively, and the generally frequency-dependent *(grounded) circuit Laplacian* [41]

$$J_{ab}(\omega) = -\mathrm{i}\omega J^{\mathrm{C}}_{ab} + J^{\mathrm{R}}_{ab} + \frac{1}{\mathrm{i}\omega} J^{\mathrm{L}}_{ab}. \tag{8.57}$$

To motivate the name, we briefly consider the continuum limit of a homogeneous circuit network. The input current I at some position is related to the divergence of the current density $\mathbf{j}$ via $I = \boldsymbol{\nabla} \cdot \mathbf{j}$, with $\mathbf{j} = \sigma \mathbf{E} = -\sigma \boldsymbol{\nabla} V$, σ the conductivity, $\mathbf{E}$ the electric field due to an applied voltage V, and $\boldsymbol{\nabla}$ the del operator. Hence,

$$I = -\boldsymbol{\nabla} \cdot (\sigma \boldsymbol{\nabla} V) = -\sigma \triangle V, \tag{8.58}$$

establishing the interpretation of J as the restriction of the continuum Laplace operator $\triangle$ to the grounded circuit.

Let us now consider an ideal circuit network that implements a given graph i.e., we neglect resistances and other parasitic effects. Each vertex of the graph is realized as a node coupled to ground via an inductance L and to nodes corresponding to adjacent vertices in the graph with capacitance C. Assume further that nodes on the boundary are each additionally capacitively coupled to ground to make up for the missing adjacent vertices. These couplings to ground can be thought of as additional grounded nodes, such that this effectively implements Dirichlet boundary conditions. Applying the above assumptions to Eq. (8.57), we obtain

$$J(\omega) = -\mathrm{i}\omega C(\mathcal{A} - \mathcal{D}) + \frac{1}{\mathrm{i}\omega L} \mathbb{1}, \tag{8.59}$$

where the degree matrix $\mathcal{D}$ enters through the second term in Eq. (8.54). We recognize that the grounded circuit Laplacian is given by the graph Laplacian $\mathcal{L} = \mathcal{A} - \mathcal{D}$ and a contribution from the inductive grounding proportional to the identity matrix:

$$J(\omega) = -\mathrm{i}\omega C \mathcal{L} + \frac{1}{\mathrm{i}\omega L} \mathbb{1}. \tag{8.60}$$

Eigenmodes

The simple form of Eq. (8.60) implies that the eigenvectors of $J(\omega)$ are simply given by the eigenvectors $\mathbf{u}^\beta$ of the Laplacian matrix $\mathcal{L}$, which has eigendecomposition

$$-\mathcal{L}\mathbf{u}^\beta = \frac{q}{4} h^2 \lambda^\beta \mathbf{u}^\beta. \tag{8.61}$$

Assuming J to be Hermitian and the circuit to be grounded (which both are true in our case), implies the following spectral representation of the circuit Laplacian

$$J(\omega) = \sum_{\beta} j^{\beta}(\omega)\mathbf{u}^{\beta}(\mathbf{u}^{\beta})^{\dagger} \tag{8.62}$$

with eigenvalues

$$j^{\beta}(\omega) = \frac{1 - \frac{q}{4}h^2\lambda^{\beta}\omega^2 LC}{\mathrm{i}\omega L}. \tag{8.63}$$

The eigenvector index β can be decomposed into principal and orbital index $\beta = (n, \ell)$ to match the eigenmodes of the Dirichlet problem in the continuum and we have used the rescaled eigenvalues λ^{β} which approximates the corresponding eigenvalues in the continuum.

The inverse of J is called the *circuit Green function* and can be obtained from the spectral decomposition of J:

$$\mathcal{G}(\omega) = \sum_{\beta} \frac{1}{j^{\beta}(\omega)}\mathbf{u}^{\beta}(\mathbf{u}^{\beta})^{\dagger}. \tag{8.64}$$

Assuming current fed into node a, i.e., $I_a = \sum_c I\delta_{ca}$, the impedance of that node to ground $Z_a(\omega) = V_a/I_a$ can be written in terms of the eigenmodes of $J(\omega)$

$$Z_a(\omega) = G_{aa}(\omega) = \sum_{\beta} \frac{1}{j^{\beta}(\omega)}\left|u_a^{\beta}\right|^2, \tag{8.65}$$

and the stationary voltage response, i.e., after equilibration, at some other node b is given by

$$V_b = G_{ba}(\omega)I_a = \sum_{\beta} \frac{1}{j^{\beta}(\omega)}u_b^{\beta}(u_a^{\beta})^*. \tag{8.66}$$

We observe that in both cases the result is a superposition of eigenmodes of J with the weight proportional to $1/j^{\beta}(\omega)$, which has a resonance at

$$\omega^{\beta} = \frac{2}{h\sqrt{LCq\lambda^{\beta}}}. \tag{8.67}$$

In turn, it follows that a resonance of Z_a at frequency $f^{\beta} = \omega^{\beta}/(2\pi)$ corresponds to an eigenmode of the hyperbolic drum with eigenvalue

$$\lambda^{\beta} = \frac{1}{7\pi^2 h^2 LC}\frac{1}{(f^{\beta})^2}. \tag{8.68}$$

Note the spectral reversal where the lowest-frequency (small λ) eigenmodes of the Laplace-Beltrami operator correspond to the highest-frequency (large f) oscillations of the electric circuit. If the circuit is probed at one of the resonance frequencies ω^β, then the dominant contribution to V_b is

$$V_b \approx \frac{1}{j^\beta(\omega^\beta)} u_b^\beta (u_a^\beta)^* = \frac{u_b^\beta}{u_a^\beta} V_a, \tag{8.69}$$

where j^β does not diverge in practice due to the presence of small resistive terms (see Section 8.4.5 for a discussion of the impact of parasitic resistances). This implies that the voltage profile $\mathbf{V}$ encodes the corresponding eigenvector $\mathbf{u}^\beta$.

Signal propagation

Having related the resonance frequencies and eigenmodes of the circuit network to the eigenvalues and eigenmodes of the Laplace-Beltrami operator of the effective space approximated by the implemented graph, we discuss how a similar correspondence appears in a dynamic setting. The propagation of waves in a continuous medium is generally given by the following differential equation involving the Laplace-Beltrami operator for the appropriate metric:

$$\frac{1}{c^2}\frac{\partial^2}{\partial t^2} u(t,z) - \triangle u(t,z) = 0 \tag{8.70}$$

with the wave speed c determined by the medium. In the Euclidean case, for example, the wave-equation leads to the dispersion $\omega(k) = c|\mathbf{k}|$ with the 2D momentum vector $\mathbf{k}$; thus, phase and group velocity are equal: $v_p = v_g = c$. If we add an additional inhomogenous source term $S(t,z)\sin(\omega t)$, where S is localized both in space (where the excitation happens) and in time (pulse-like), i.e.,

$$\frac{1}{c^2}\frac{\partial^2}{\partial t^2} u(t,z) - \triangle u(t,z) = S(t,z)\sin(\omega t). \tag{8.71}$$

The source term leads to an excitation of eigenmodes of $-\triangle$, according to its frequency spectrum and the pulse propagates with speed c.

For an electric-circuit network implementing a tessellation, there are some important differences to the dynamics, even though the situation is conceptually the same. According to Kirchhoff's law, the differential equation governing the circuit network is, according to Eq. (8.52),

$$\frac{\partial}{\partial t} I_a = C\mathcal{L}_{ab}\frac{\partial^2}{\partial t^2} V_b - \frac{1}{L} V_a, \tag{8.72}$$

where $I_a(t)$ and $V_a(t)$ are the input current and voltage at node a. The continuum limit therefore is

$$C\frac{\partial^2}{\partial t^2}\triangle V(t,z) - \frac{1}{L}V(t,z) = \frac{\partial}{\partial t}I(t,z) \tag{8.73}$$

where the voltage field $V(t,z)$ takes the role of $u(t,z)$ and the time-derivative of the input current $\frac{\partial}{\partial t}I(t,z)$ the role of the source.

The modified wave-equation

$$LC\frac{\partial^2}{\partial t^2}\triangle u(t,x,y) - u(t,x,y) = 0 \tag{8.74}$$

results in the group velocity v_g having the opposite sign compared to the phase velocity v_p. In the Euclidean case, for example, the dispersion is

$$\omega(k) = \frac{1}{\sqrt{LC}}\frac{1}{k}, \tag{8.75}$$

which implies

$$v_g = \frac{\mathrm{d}\omega}{\mathrm{d}k} = -\frac{1}{\sqrt{LC}}\frac{1}{k^2} = -v_p. \tag{8.76}$$

Nevertheless, the effective propagation is governed by the Laplace-Beltrami operator, thereby encoding the metric. Metamaterials with this property of a negative refractive index are referred to as *negative-index* or *left-handed* metamaterials.

8.4.2. Hyperbolic drum

In Section 8.3, we have established that the 85-site $\{3,7\}$ lattice shown in Fig. 8.7b is suitable for realizing the hyperbolic plane and detecting effects of negative curvature. As described in Section 8.4.1, the graph can be implemented in an electric-circuit network by coupling nodes corresponding to adjacent vertices with a capacitance C and grounding each node with an inductance L. The ideal circuit diagram for a single pair of adjacent nodes is shown in Fig. 8.14c. The Dirichlet boundary conditions are easily implemented by additionally grounding the boundary nodes with capacitances C such that the lack of adjacent nodes is compensated, i.e, in the resulting network each node is connected to seven capacitors. We have built such a circuit network using ceramic capacitors with $C = 1\,\mathrm{nF}$ and 1% tolerance and power inductors with inductance $L = 10\,\mu\mathrm{H}$, 5% tolerance and a minimal quality factor of 40 at 1 MHz. Finally, each node is made accessible for in- and output via SMB

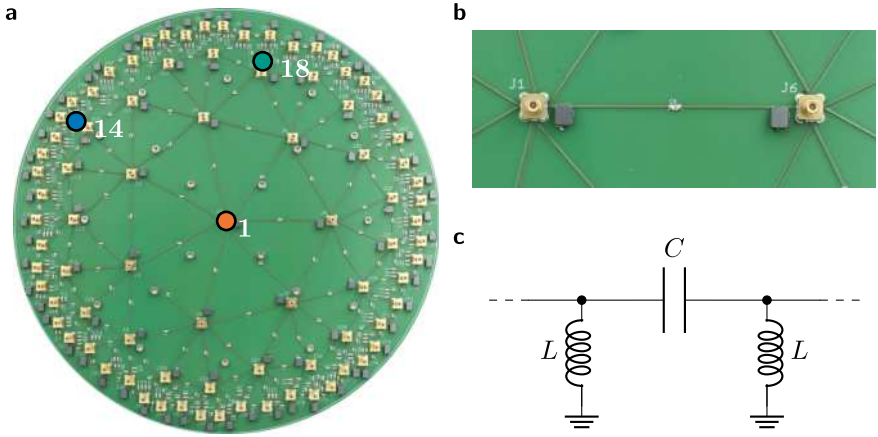

Figure 8.14.: Circuit board implementation of the hyperbolic lattice. (**a**) Photograph of the circuit board containing the circuit network realizing the hyperbolic $\{3, 7\}$ lattice with 85 sites (corresponding to $r_0 = 0.94$) shown in Fig. 8.7b. Nodes 1, 14, and 18 are indicated by colored disks and the corresponding node number. (**b**) Close-up of the circuit components: a golden SMB connector at each node, capacitors (small silver components) in the middle of the wires connecting two nodes and an inductor (dark gray component) beside each node. (**c**) Ideal circuit diagram of a pair of adjacent nodes coupled by a capacitor C and each grounded via an inductor L.

connectors. The resulting circuit board is shown in Fig. 8.14a with a close-up of the components in Fig. 8.14b.

We perform three experiments to characterize the effective negative curvature realized by the network in the long-wavelength limit. First, we measure impedance peaks at different nodes to identify Laplacian eigenmodes. Second, these eigenmodes are resonantly excited and their voltage profile is subsequently measured. Each of these static experiments, discussed in Section 8.4.3, allows us to observe the reordering of the eigenmodes compared to the Euclidean case and therefore signifies the negative curvature. In the final experiment, discussed in Section 8.4.4, the circuit is stimulated by a current pulse at a node close to the boundary and the voltage across the circuit is measured as a function of time. We observe wave propagation along hyperbolic geodesics which further corroborates the realization of negative curvature. At the end, we briefly comment on the effect of parasitic resistances in Section 8.4.5.

8.4.3. Eigenmodes of the Laplacian

In Section 8.4.1, we have found that the circuit network shows impedance resonances at frequencies directly related to the eigenvalues of the graph Laplacian [Eq. (8.67)] and that the eigenmodes of the circuit correspond to the eigenvectors of the graph Laplacian [Eq. (8.69)]. This makes the eigenvectors directly accessible to experiments allowing us to verify the spectral reordering and check how well they reproduce the continuous eigenmodes. To measure the circuit's eigenmodes, we proceed in two steps: first, we determine the resonance frequencies and second, we excite and measure the eigenmodes directly.

An impedance analyzer was used to measure the impedance to ground Z_a as a function of frequency $f = \omega/2\pi$ for each node a. These measurements were performed in a two-terminal measurement configuration using a Zurich Instruments MFIA 5 MHz impedance analyzer. A short/open compensation routine was used to remove the residual impedance and stray capacitance of the test fixture. The impedance of all 85 circuit nodes has been recorded for frequencies in the range from 250 kHz to 1.75 MHz. To exclude transmission line effects in the measurement, the maximum cable length was restricted to be below 1.8 m. The data for three input nodes are shown in Fig. 8.15a and we clearly recognize several resonance peaks.

We observe that the resonances at high frequencies are well-separated but become harder to tell apart at lower frequencies. This is a consequence both of the higher density of eigenvectors with large λ and the scaling $f \propto \frac{1}{\sqrt{\lambda}}$ given in Eq. (8.67). Because $\ell \neq 0$ modes ideally have vanishing weight at the central node, we expect mostly $\ell = 0$ modes to contribute to resonances of Z_1, and the other nodes to show additional resonances. Comparing the impedance of input node 1 (orange curve) to nodes 14 and 18 (blue and green curves), we indeed observe four additional peaks at input node 14 and 18 located between the two highest-frequency peaks at input node 1. This implies that the second $\ell = 0$ mode, i.e., the first mode with $n > 0$, is the sixth eigenmode, which reproduces the expected spectral reordering.

The second set of experiments allows us to explicitly verify the above interpretation of modes depending on the node. From data as the one shown in Fig. 8.15a, we extracted all resonance frequencies and for each identified the node with highest impedance. Based on this information, we specifically targeted and excited the corresponding eigenmodes by feeding a resonant input current into the appropriate node. The current signal was obtained by applying a sinusoidal reference voltage signal with fixed peak-to-peak voltage of 1 V produced by one of the three Zurich Instrument MFIA 5 MHz impedance analyzers (used as lock-in amplifiers) across a shunt resistor of 12 Ω. To measure the resulting voltage profile with phase sensitive detection, the

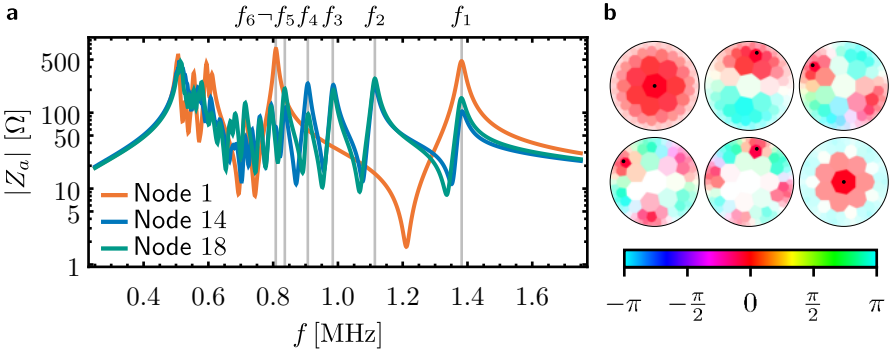

Figure 8.15.: Impedance resonances and eigenmodes. (**a**) Measurement of impedance to ground Z_a of the circuit at node a as a function of input frequency f for different nodes (see Fig. 8.14a for an identification of the nodes). Each impedance peak indicates an eigenmode at that frequency, which can be excited at the corresponding input node. The highest six frequencies are indicated by vertical gray lines and the corresponding eigenmodes are shown in (b). (**b**) Measurement of the voltage profile of the first six eigenmodes (only one mode is shown for each pair of degenerate modes). The saturation encodes the magnitude as a fraction of the voltage (white denotes 0 and full saturation 1) at the input node (black dots), and the color encodes the phase relative to the reference voltage (see legend).

remaining two lock-in amplifiers, synchronized in frequency and phase with the first, were used. All voltage signals demodulated with the reference signal were filtered with a digital low-pass filter of eighth order and a cutoff frequency of $f_{-3\,\mathrm{dB}} = 0.7829\,\mathrm{Hz}$. The readout of the real and imaginary part of the voltage took place after at least 16 filter time constants which corresponds to at least 99 % settling of the low-pass filters in a step response. For the modes at the highest six frequencies, indicated in Fig. 8.15a, both magnitude (relative to the voltage at the input node) and phase (relative to the reference signal) are shown in Fig. 8.15b.

Using the method discussed around Eq. (8.49), the explicit values of ℓ and n for each mode can be deduced from the measured voltage profiles $\mathbf{V}^\beta$ by computing their overlap with the eigenmodes $u^{(n,\ell)}(z)$ of the Laplace-Beltrami operator in the continuum. We show this overlap for some exemplary modes in Fig. 8.16 and observe that the first few eigenmodes only significantly overlap with one (for $\ell = 0$) or two (for $\ell \neq 0$ due to the degeneracy of $\pm\ell$ modes) continuous eigenmodes. To those eigenmodes, we can easily assign values of n

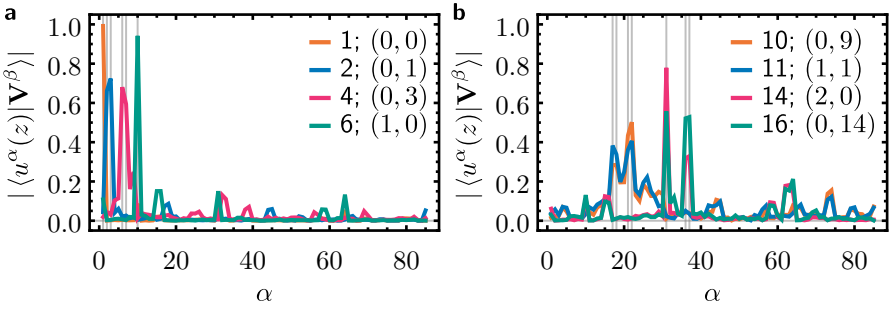

Figure 8.16.: Overlap of measured with continuous eigenmodes. Absolute value of the overlap of some exemplary measured modes $\mathbf{V}^\beta$ with the eigenmodes $u^\alpha(z)$ of the Laplace-Beltrami operator. The vertical gray lines indicate the eigenmodes $u^\alpha(z)$ with maximal overlap allowing us to assign quantum numbers $(n, |\ell|)$ to each mode (see legends). (**a**) The low-energy modes (small λ) only show significant overlap with a single mode with $\ell = 0$ (modes 1 and 6) or a pair of modes with $\pm\ell$ (modes 2 and 4) and can therefore be easily matched to continuous eigenmodes. (**b**) For some specific modes, however, this is not the case: Modes 10 and 11 both have significant overlap with both $(n, |\ell|) = (0, 9)$ and $(1, 1)$, which can be understood from the fact that these two modes are close to being accidentally degenerate, as can be seen in Fig. 8.17a. On the other hand, the breaking of the continuous rotational symmetry by the lattice lifts the degeneracy of the $(1, -14)$ and $(1, +14)$ mode such that one of them ends up close in eigenvalue to the $(2, 0)$ mode, leading to their hybridization.

and ℓ. In particular, this allows us to extract the dispersion of the rescaled measured eigenfrequencies λ with the angular momentum $|\ell|$. In Fig. 8.17a, we show the result of this analysis as red squares for all 16 eigenmodes that we were able to excite, measure, and identify successfully. We observe an almost perfect match with the theoretically predicted values (blue diamonds) for most of the measured modes. However, higher modes are increasingly difficult to excite and detect, due to the finite resolution in frequency and space.

To quantify the deviation of the measured eigenmodes from the theoretical prediction in terms of eigenvectors of the graph Laplacian, we use (1) the point-wise difference and (2) the overlap of the modes. The former is plotted in Fig. 8.18 and analyzed in Fig. 8.17b, which shows the mean and standard deviation of the point-wise difference between experiment and theory (blue squares). Figure 8.17b also shows the overlap of the experimentally measured eigenmodes with the theoretical predictions (orange triangles). Furthermore, we compare the measured and predicted eigenvalues in Fig. 8.17a, i.e., the

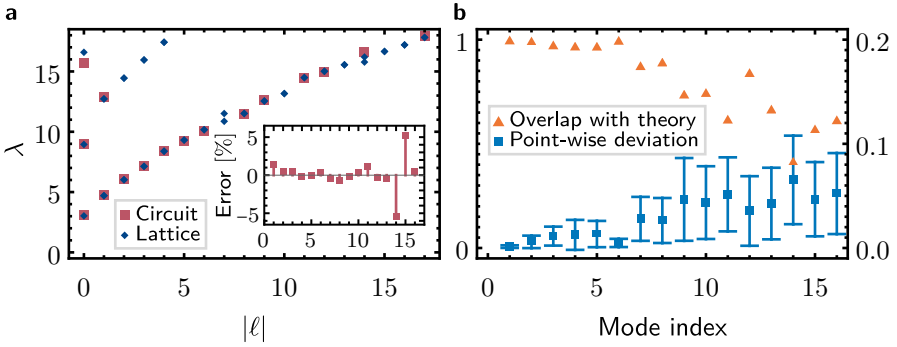

Figure 8.17.: Comparison of measured eigenmodes and eigenvalues to theory. (**a**) Angular momentum dispersion of the experimental eigenmodes (red squares) and the one on the lattice (blue diamonds). The inset shows the relative error in the experimental data compared to the theoretical prediction (horizontal axis: mode index according to increasing λ in the experimental data); there are only two outliers (modes 14 and 15) with a relative error significantly larger than 1%. (**b**) Comparison of the experimental eigenmodes to the ones on the lattice. The orange triangles show the absolute overlap of the experimentally and theoretically obtained eigenvectors and the blue squares the mean of the absolute value of the point-wise deviation (interval marks indicate the standard deviation computed over all the nodes in the circuit). Mode 14 (but not 15) can again be identified as an outlier.

eigenvalue as a function of $|\ell|$ for both the experimental as well as theoretical (lattice) data with relative errors shown in the inset.

We observe that the relative error for almost all of the 16 eigenmodes is below 2% (cf. Fig. 8.17a); the two outliers, modes 14 and 15, are discussed below. In contrast, Fig. 8.17b shows that the measured eigenmodes agree very well with theory for modes 1 to 6 after which the deviations start to increase. This is reflected both in the overlap of the measured modes with the theoretically expected ones, as well as in the point-wise deviations at the individual circuit nodes (plotted also in Fig. 8.18). Note that additionally, due to parasitic effects, the experimental data shows increasing deviations in the phase compared to the theory where only $0, \pi$ phases occur (cf. Fig. 8.18).

The deviations in λ, i.e., in the eigenfrequencies of the circuit, are weakly dependent on the index of the excited modes (except for the outliers mentioned above). This indicates that these deviations most likely can be attributed to parasitic effects and to disorder in the circuit components, as these are both expected to exhibit such a weak dependence on the index of the excited

modes. The eigenfrequencies are extracted from impedance measurements such as the ones shown in Fig. 8.15a; as long as the peaks are well separated, they can be accurately measured. Note that problems can arise when two modes are close to each other in eigenvalue compared to the width of the corresponding resonance peaks (see Section 8.4.5), which is the case for modes 10 and 11. Figure 8.16b shows that both modes have significant overlap with the $(n, |\ell|) = (0, 9)$ and $(1, 1)$ eigenmodes of the continuum Laplace-Beltrami operator. This makes it more challenging to excite and assign quantum numbers to those modes. On the other hand, the mode profiles are much more sensitive to other error sources. First, in the experiment, it is impossible to excite exactly a single mode, generally a superposition of several modes is excited. When the eigenmodes are well separated in frequency or if the input node lies in a nodal plane of many other eigenmodes, the additional eigenmodes have a small weight in the superposition. However, with increasing mode number the frequency separation is reduced, such that the deviations from theory increase gradually.

Finally, we comment on the missing data for the $|\ell| = 7$ mode as well as the large difference of the experimentally extracted and theoretically predicted eigenvalues for the $(n, |\ell|) = (2, 0)$ and $(1, 14)$ modes (modes 14 and 15 have a relative error that is significantly larger than the typical error, cf. Fig. 8.17a). As discussed in Section 8.3.3, for rotational symmetry of finite order some modes with $\ell \neq 0$ attain a nonvanishing amplitude at the origin and the degeneracy with the second mode with identical $n, |\ell|$ is lifted (only one of the two modes has a significant amplitude at the origin). We have not managed to cleanly excite the $(1, 7)$ modes, but the described phenomenon is visible in the data for the $(1, 14)$ mode (cf. Fig. 8.18). This also allows us to understand the large deviation of the eigenvalues of the $(2, 0)$ and $(1, 14)$ modes: both have significant weight at the origin (cf. Fig. 8.18) and eigenvalues that are expected to be very close to each other (cf. Fig. 8.17a). Therefore, it is difficult to excite only one of them, such that the experimentally excited modes are very likely superpositions of the two. This is reflected in the overlap of the measured modes with the eigenmodes of the continuum Laplace-Beltrami operator in Fig. 8.16b. While, based on the voltage profile the lower mode, is identified as the $\ell = 0$ mode, the eigenvalues would suggest the opposite (cf. Fig. 8.17a). Choosing different input nodes could resolve this issue.

In conclusion, we find that getting accurate data on the eigenvalues is not a problem as long as the modes can be cleanly excited, while the error in the eigenmode profiles increases gradually with increasing mode number. Nevertheless, correctly identifying the modes remains possible even with reduced accuracy of the mode profiles. To recognize the reordering of the eigenmode compared to flat space, the accuracy of our experimental setup is more than

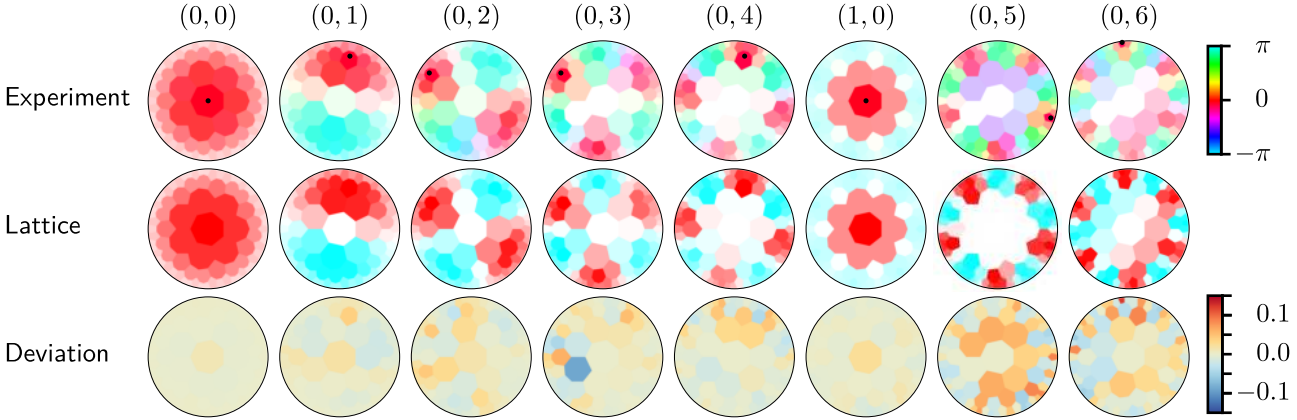

Figure 8.18.: Comparison of measured eigenmodes to eigenvectors of the graph Laplacian. The three rows show the following data. **Experiment**: voltage profile of the measured eigenmodes with saturation encoding the magnitude as a fraction of the voltage (white denotes 0 and full saturation 1) at the input node (black dots) and color encoding the phase relative to the reference voltage (see legend on the right). **Lattice**: eigenvectors obtained from diagonalizing the Laplacian matrix defined by hyperbolic lattice (saturation and color as for the experiment). **Deviation**: difference between the normalized experimental data and the data on the lattice (see legend on the right). For each mode the quantum numbers n and $|\ell|$ are extracted by determining the continuous eigenmode with maximal overlap and given at the top in the format $(n, |\ell|)$. The modes from experiment and theory are matched according to those numbers.

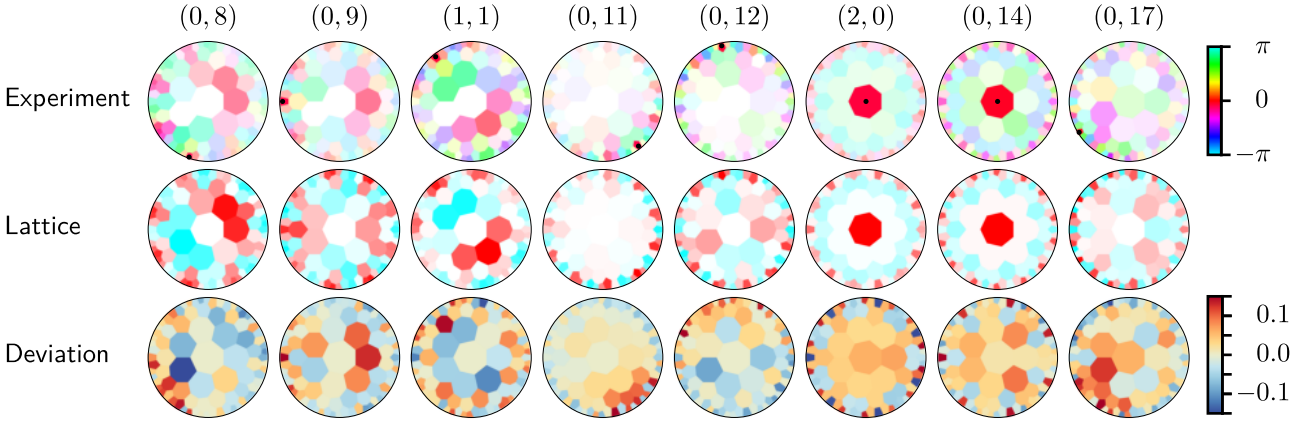

Figure 8.18. (continued): The remaining eight eigenmodes and their deviation from theory.

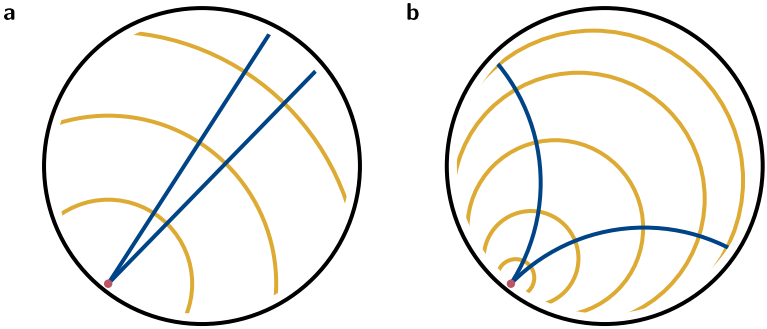

Figure 8.19.: Wave propagation on a continuous drum. Schematic illustration of the wave propagation after exciting (**a**) a Euclidean and (**b**) a hyperbolic drum with a short and spatially localized pulse at location of the red disk. The waves travel along geodesics (blue lines) originating from the source and wave fronts at different times are given by concentric circles (yellow) perpendicular to the geodesics. Several equidistant circles with radii $0.5, 1, 1.5, \ldots$ (in the appropriate metric) are shown for both cases, illustrating distances $d_{\mathbb{H}}$ and $d_{\mathbb{R}^2}$ to the source.

sufficient: only the first six modes are required, for which the overlap with theory exceeds 95%. We have thus demonstrated that, already without any additional optimization, it is possible to find good agreement with theory for higher modes as well.

8.4.4. Signal propagation along geodesics

The final experiment probes a dynamical signature of curved space: signal propagation along geodesics. In curved space, signals propagate not along Euclidean straight lines but along geodesics. For wave propagation, this implies that the wave fronts are always perpendicular to those geodesics and thus influenced by curvature. Figure 8.19 schematically compares wave propagation on a Euclidean and hyperbolic drum: the drum is excited on a point close to the boundary and waves are emitted radially from that point. The wave fronts (yellow) are circles of constant distance from the point of emission and thus perpendicular to the geodesics (blue) originating from there. The negative curvature of the hyperbolic plane makes the geodesics curve outwards, thereby distorting the wave fronts (Fig. 8.19b) which can be clearly distinguished from the Euclidean case (Fig. 8.19a).

Such an experiment can be easily performed in our circuit network by feeding a current pulse into the circuit at a node close to the boundary. To

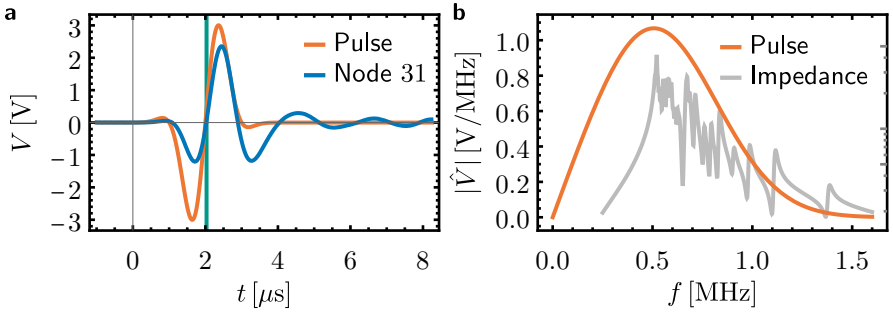

Figure 8.20.: Broadband excitation pulse. (**a**) Excitation pulse (orange) fed as a current pulse into node 31 at the boundary, and the voltage response measured at the same node (blue). The time corresponding to the instantaneous phases in Fig. 8.21 is marked by a green vertical line. (**b**) Frequency spectrum (orange) of the excitation pulse shown in (a), demonstrating the wide range of frequencies contained in the pulse by comparison to the impedance to ground $|Z_{31}|$ (gray; shown on a logarithmic scale on the right axis from 20 to 500 Ω).

approximate the continuum response, a large number of eigenmodes should be excited, which we achieved by stimulating the circuit in the frequency range with the highest density of resonances which can be inferred from Fig. 8.15a. The measurements were carried out by seven Picoscope 4824, which are eight channel USB oscilloscopes with 20 MHz bandwidth and 12 bit resolution. The circuit was stimulated at node 31 by the broadband pulse

$$V(t) = V_0 \sin(2\pi f t) \mathrm{e}^{-\frac{1}{2}(4(ft-1))^2} \tag{8.77}$$

with $V_0 = 4.3\,\mathrm{V}$ and $f = 500\,\mathrm{kHz}$ shown in Fig. 8.20a. As shown by its frequency spectrum in Fig. 8.20b, the pulse indeed excites a large number of the circuits' eigenmodes. The pulse was generated by a 50 Ω function generator and the output current fed directly into the input node. Since the oscilloscopes do not provide a separate trigger channel, one channel of each instrument was fed with a rectangular pulse synchronized with the excitation pulse to trigger the instruments. An edge trigger at 1 V in rapid trigger mode was used and sampling was set to 40 MS/s, i.e., every 25 ns.

After exciting the circuit, the voltage was measured as a function of time at each node. Assuming equal behavior of the circuit under repeated stimulation, which was verified during the measurement process by repeating the process described below ten times, the measurement was performed in two steps. First, the seven oscilloscopes were used to measure the voltage at nodes 1 through

49 (including the input node 31), then, in the second run, the input node and nodes 38 through 85 were measured. Finally, the measured real-valued voltage signals $V(t)$ were transformed into complex-valued ones using the Hilbert transform, giving access to the instantaneous phase as the argument of the complex-valued signal

$$v(t) = V(t) + \frac{\mathrm{i}}{\pi} \int_{-\infty}^{\infty} d\tau \frac{V(\tau)}{t - \tau}. \tag{8.78}$$

We observe the pulse to propagate in the Poincaré disk, in particular the wave fronts seem to *fall into* node 31 [300], a consequence of the circuit network having a negative index of refraction as discussed in Section 8.4.1. A snapshot of the instantaneous phase profile is shown in Fig. 8.21a, where the phase fronts can be easily identified by the positions of equal instantaneous phase.

Since the connectivity of the nodes implements the metric of the Poincaré disk, these phase fronts form concentric hyperbolic circles, highlighted by black circles in Fig. 8.21a, up to corrections due to boundary reflections. In Fig. 8.21, we have chosen an early time during the excitation such that contributions from such reflections do not have a significant impact on the measured phases. Finally, when plotting the phase as a function of hyperbolic $d_{\mathbb{H}}$ and Euclidean $d_{\mathbb{R}^2}$ distance in Figs. 8.21b and 8.21c, respectively, we observe that the correlation of the phase with $d_{\mathbb{H}}$ is stronger than with $d_{\mathbb{R}^2}$. This manifests that the propagation of the signal indeed follows hyperbolic rather than Euclidean geodesics, thereby verifying that the system effectively realizes the hyperbolic metric.

8

8.4.5. Parasitic resistance

So far we have neglected any parasitic effects in the circuit and employed an ideal description of the circuit in terms of perfect capacitors and inductors. Such an ideal circuit would have infinite resonance peaks, which is, unsurprisingly not observed in Fig. 8.15a. Parasitic resistances of circuit elements are captured by the quality factor Q, which is defined through the impedance as

$$\mathsf{Q}(\omega) = \frac{|Z(\omega)|}{\mathrm{Re}(Z(\omega))}. \tag{8.79}$$

In particular, the quality factor modifies Eq. (8.69) and broadens the resonance peak. Thus, resolving individual peaks in the resonance spectrum requires a sufficiently high quality factor for all circuit elements. With increasing parasitic resistances, the resonance peaks of individual modes widen and flatten, making them harder to identify in an impedance spectrum. Here, we demonstrate that

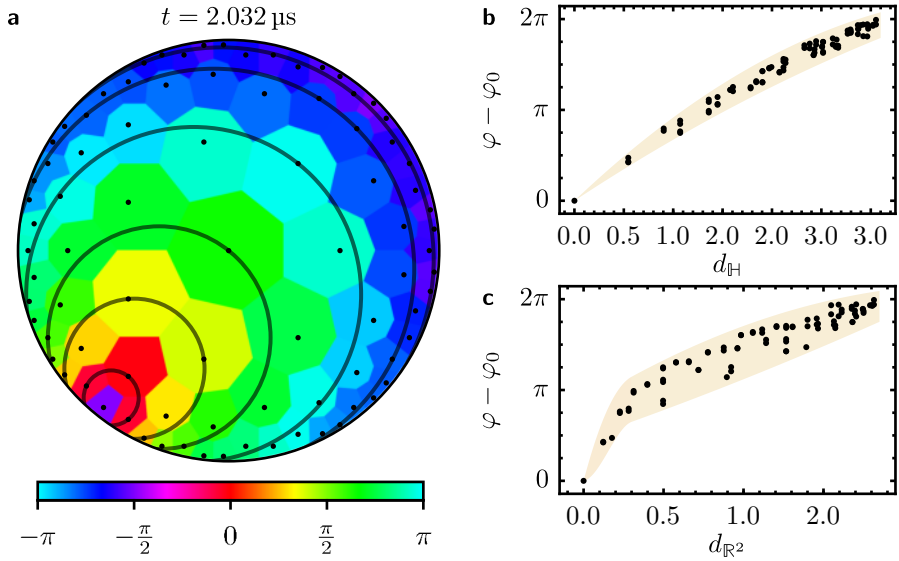

Figure 8.21.: Measured signal propagation. (**a**) Instantaneous phases of the pulse propagating on the hyperbolic drum (see legend) at time $t = 2.032\,\mu s$. The nodes are indicated by black dots, and concentric hyperbolic circles with center at node 31 are shown in black to illustrate the hyperbolic metric. (**b**) Difference of the instantaneous phase φ at each node to the one at the source of the signal (node 31) φ_0 as a function of hyperbolic distance $d_{\mathbb{H}}$ to the source. (**c**) Difference of the instantaneous phase φ at each node to the one at the source of the signal (node 31) φ_0 as a function of Euclidean distance $d_{\mathbb{R}^2}$ to the source. The shaded region in (b,c) indicates the approximate spread of the instantaneous phase as a function of $d_{\mathbb{H}}$ and $d_{\mathbb{R}^2}$, respectively.

most of the deviations of the real circuit from the ideal network can be captured by a finite quality factor Q of the inductors and that the effective quality factor of the circuit network must be above 50. For $\mathsf{Q} \gg 1$, we approximate

$$|Z_L| \approx |\mathrm{i}\omega L| \qquad \Rightarrow \qquad Z_L = \omega \left(\mathrm{i} + \frac{1}{\mathsf{Q}}\right) L. \tag{8.80}$$

Figure 8.22 compares simulated impedance spectra of node 18 for several constant quality factors of the inductors to the measured values. For $\mathsf{Q} = 50$ and 20, all relevant impedance peaks can be easily identified, while at $\mathsf{Q} = 10$, the peak at 0.906 MHz is no longer recognizable. We observe that the measured data is consistent with $\mathsf{Q} > 50$ in the relevant frequency interval. For a given

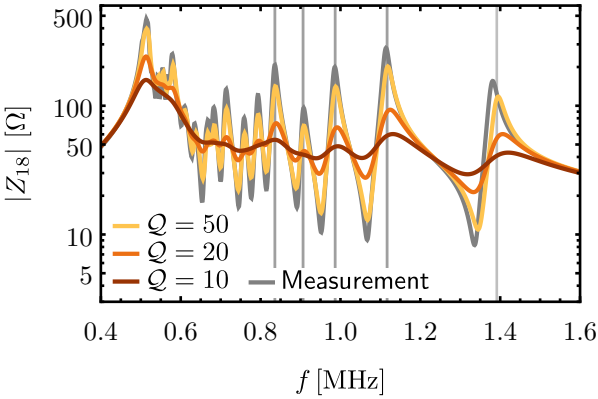

Figure 8.22.: Effect of parasitic resistance. Comparison of the simulated impedance spectrum (yellow to red lines; see legend) at node 18 for different quality factors Q of the inductors to the measured data (gray line).

eigenvector u of the graph Laplacian $\mathcal{L}$ with corresponding eigenvalue $\tilde{\lambda}$, the Laplacian equation

$$\left(\mathrm{i}\omega CQ + \frac{1}{\omega(\mathrm{i} + 1/\mathsf{Q})L}\mathbb{1}\right) u = 0 \tag{8.81}$$

reduces to the scalar equation

$$i\omega C\tilde{\lambda} + \frac{1}{\omega(\mathrm{i} + 1/\mathsf{Q})L} = 0, \tag{8.82}$$

which is equivalent to that of a simple serial RLC oscillator. Since real and imaginary part of a serial oscillator's eigenfrequency are related by

$$\frac{\mathrm{Re}(\omega_0)}{\mathrm{Im}(\omega_0)} \approx 2\mathsf{Q}, \tag{8.83}$$

we expect decay times of free oscillations in the circuit network to exceed 100 oscillation periods.

9. Hyperbolic crystals

So far we have considered regular hyperbolic tessellations predominantly as a platform for implementing tabletop realizations of continuous hyperbolic space. However, as we have described at the beginning of Chapter 8, they can naturally be interpreted as *hyperbolic crystals*, making them interesting in their own right from a condensed-matter perspective. In Chapter 2, we have defined crystals as structures with (1) its constituents arranged in a repeating pattern, (2) leading to translational symmetry. Clearly, the regular tessellations such as the one shown in Fig. 8.4a satisfy the first criterion. In this chapter we will see that the second criterion is satisfied as well: regular hyperbolic tessellations do possess translational symmetry, justifying the term *hyperbolic lattices* or *hyperbolic crystals*. However, as a consequence of the negative curvature, these translations *do not commute*, leading to far-reaching changes to how we describe models defined on the lattices. Throughout this chapter we will discuss several consequences of the negative curvature and contrast them to the case of Euclidean lattices.

We start in Section 9.1 by introducing the space groups of hyperbolic lattices derived from regular tessellations, the so-called *triangle groups*, and discussing the translation subgroup. Next, in Section 9.2, we discuss some of the difficulties surrounding (periodic) boundary conditions and the thermodynamic limit of hyperbolic lattices. In Section 9.3, we introduce the algebraic scheme for compactly and efficiently defining hyperbolic tight-binding models described in our original work [5]. Subsequently, in Section 9.4, we review the initial efforts in developing a *hyperbolic band theory*, laying the foundations for our own contributions [5] discussed in Chapter 10. Finally, in Section 9.5, we summarize the current understanding of hyperbolic topological insulators, reviewing several recent works including some of our own [6, 7].

9.1. Symmetries of hyperbolic lattices

In this section, we elucidate the symmetries of $\{p, q\}$ lattices, i.e., lattices obtained from regular $\{p, q\}$ tessellations. We start from the full space group in Section 9.1.1, then describe how to identify the translation group in Section 9.1.2, before commenting on the point group in Section 9.1.3. Throughout

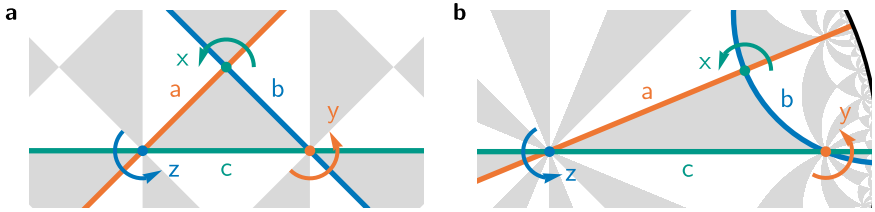

Figure 9.1.: Generators of the triangle group. Fundamental Schwarz triangle (gray) with reflections a, b, and c across its sides and rotations x = ab, y = bc, and z = ca around its corners for (**a**) the Euclidean $\{4,4\}$, i.e., square, lattice, and (**b**) the hyperbolic $\{8,8\}$ lattice. Schwarz triangles with equal orientation as the fundamental one are shown in gray and those with opposite orientation (obtained by an odd number of reflections) in white.

this section, we illustrate the algebraic objects using the $\{4,4\}$ (Euclidean square) and the hyperbolic $\{8,8\}$ lattice as examples. The description of hyperbolic lattices in terms of these symmetry groups will be the foundation for most of the subsequent sections and in particular of the next chapter.

9.1.1. Space group

The full space group of a $\{p,q\}$ lattice is given [63] by the *triangle group* which has *presentation*

$$\Delta(r,q,p) = \left\langle \mathsf{a},\mathsf{b},\mathsf{c} \middle|\, \mathsf{a}^2, \mathsf{b}^2, \mathsf{c}^2, (\mathsf{ab})^r, (\mathsf{bc})^q, (\mathsf{ca})^p \right\rangle, \tag{9.1}$$

with $r = 2$. The group is therefore generated by a, b, and c, subject to the so-called *relators* appearing to the right of the vertical line, which are set to the identity. The geometric meaning of the generators is illustrated in Fig. 9.1: a, b, and c are reflections across the sides of a triangle, called *fundamental Schwarz triangle*, with internal angles $\frac{2\pi}{r}$, $\frac{2\pi}{q}$, and $\frac{2\pi}{p}$. The order of p, q, r is immaterial, since it only permutes the generators.

Reflecting the fundamental Schwarz triangle across each of its sides and repeating the same with all the resulting triangles results in a tessellation of the whole (Euclidean or hyperbolic) plane by *Schwarz triangles*. This is illustrated in Figs. 9.2a and 9.2b for the $\{4,4\}$ and $\{8,8\}$ lattice, respectively, where triangles with the same orientation are colored in gray and those with opposite in white. Note that these are not *regular* tessellations, because there are three inequivalent classes of vertices, corresponding to the three vertices

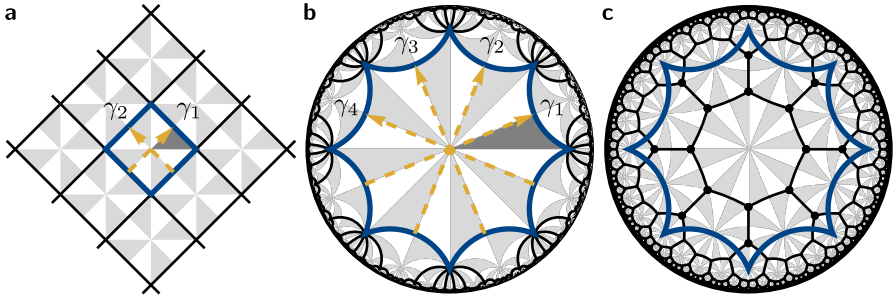

Figure 9.2.: Tessellation by triangle groups. Triangle group of (**a**) the $\{4,4\}$, (**b**) the $\{8,8\}$, and (**c**) the $\{8,3\}$ lattice. The lattices are shown by black lines, Schwarz triangles with equal orientation as the fundamental one are in light gray and those with opposite orientation in white. In each lattice, the boundary of a symmetric minimal unit cell is indicated by a blue polygon. Additionally, in (a,b) the generators γ_i of the translation group are shown as arrows and the fundamental Schwarz triangle is emphasized as a filled dark gray triangle. The Bravais lattice of the $\{8,3\}$ lattice is the $\{8,8\}$, such that the former has multiple sites (black disks) per unit cell.

of the fundamental Schwarz triangle. Due to the group property, the above implies that each Schwarz triangle is related to the fundamental one by an element of the space group Δ. Formally, we define the right group action of Δ on the abstract set S of all Schwarz triangles. Then, S is the orbit of the fundamental Schwarz triangle $s_f \in S$ under right action of Δ:

$$S = s_f \cdot \Delta, \tag{9.2}$$

which provides an algebraic way of describing the tessellation.

Sometimes it is more convenient to work with the proper subgroup of Δ, i.e., the group of orientation-preserving elements. This group has presentation

$$\Delta^+(r,q,p) = \langle \mathsf{x},\mathsf{y},\mathsf{z} | \, \mathsf{xyz}, \mathsf{x}^r, \mathsf{y}^q, \mathsf{z}^p \rangle \tag{9.3}$$

with the generators $\mathsf{x} = \mathsf{ab}$, $\mathsf{y} = \mathsf{bc}$, and $\mathsf{z} = \mathsf{ca}$ being pairs of reflections on two sides of the fundamental Schwarz triangle. As can be deduced from Fig. 9.1, the geometric meaning of these generators is that of rotations around the corners of the triangle. For p, q such that $\{p,q\}$ is hyperbolic, Δ^+ is a discrete subgroup of $\mathsf{PSU}(1,1)$, the group of isometries of the hyperbolic plane. Such groups are known as *Fuchsian groups*. The full triangle group is the semidirect product of the proper triangle group with the group of reflections $\mathbb{Z}_2$:

$$\Delta(r,q,p) = \Delta^+(r,q,p) \ltimes \mathbb{Z}_2. \tag{9.4}$$

This simple structure allows us to easily transition between descriptions in terms of Δ and those in terms of Δ^+. Graphically, the decomposition in Eq. (9.4) is expressed by the coloring of the triangles, e.g., in Fig. 9.2: $s_f \cdot \Delta^+$ reproduces the gray triangles and $s_f \cdot \mathsf{a}\Delta^+$ the white ones.

9.1.2. Translation subgroup and Bravais lattice

A translation γ is an orientation-preserving symmetry operation without a fixed-point. A group whose elements have this property, i.e., a group with no elements of finite order, is called *torsion-free*. Analogous to the Euclidean case described in Section 2.1, the group of translations must be a normal subgroup of the space groups, denoted by the symbol "$\triangleleft$", such that conjugation of a translation by any other space-group element is again a translation. Thus, we define [7, 63] the (hyperbolic) *translation group*, conventionally denoted by Γ, as the largest torsion-free normal subgroup of orientation-preserving elements of Δ. As a subgroup of Δ^+, Γ is a Fuchsian group and is finitely generated with $2\mathfrak{g}$ independent generators $\gamma_1, \gamma_2, \ldots, \gamma_{2\mathfrak{g}}$.

Let us consider the two examples $\{4,4\}$ and $\{8,8\}$. In the square lattice, the (Euclidean) translation group is the Abelian group $\mathbb{Z}^2$ generated by translations in x- and y-direction. In terms of the generators of Δ^+, they can be written as $\mathsf{z}\mathsf{y}^{-1}$ and $\mathsf{y}^{-1}\mathsf{z}$, respectively, as can be deduced from Fig. 9.2a. With the relators in Eq. (9.3) it indeed becomes clear that $\mathsf{z}\mathsf{y}^{-1}$ and $\mathsf{y}^{-1}\mathsf{z}$ commute, making the translation group Abelian. On the other hand, the translation group of the $\{8,8\}$ lattice has *four* independent generators [62, 64], despite the two spatial dimensions:

$$\Gamma_{\{8,8\}} = \left\langle \gamma_1, \gamma_2, \gamma_3, \gamma_4 \middle| \gamma_1\gamma_2^{-1}\gamma_3\gamma_4^{-1}\gamma_1^{-1}\gamma_2\gamma_3^{-1}\gamma_4 \right\rangle . \tag{9.5}$$

They are shown in Fig. 9.2b as arrows and in terms of the generators of Δ are given by $\gamma_i = \mathsf{z}^{5-i}\mathsf{x}\mathsf{z}^{i-1}$. Crucially, the group Γ is *non-Abelian*, i.e., its elements do not commute.

The translation group defines a decomposition of the infinite lattice into copies of a unit cell via the coset decomposition of Δ into (disjoint) right cosets of Γ (which are equal to the left cosets, because $\Gamma \triangleleft \Delta$)

$$\Delta = \bigcup_{g_j \in T_\Delta(\Gamma)} \Gamma g_j = \bigcup_{g_j \in T_\Delta(\Gamma)} g_j \Gamma, \tag{9.6}$$

where the set $T_\Delta(\Gamma)$, known as the *transversal*, is a specific choice for the set of representatives of Δ/Γ. The number of elements in $T_\Delta(\Gamma)$ is equal to the number of cosets in Δ/Γ and is called the *index* $|\Delta : \Gamma|$ of Γ in Δ:

$$|\Delta : \Gamma| = |\Delta/\Gamma|. \tag{9.7}$$

We can rewrite Eq. (9.6) by taking the union over elements of Γ:

$$\Delta = \bigcup_{\gamma\in\Gamma} T_\Delta(\Gamma)\gamma. \tag{9.8}$$

This implies that the set S of all Schwarz triangles is decomposed as

$$S = s_f \cdot \Delta = \bigcup_{\gamma\in\Gamma} s_f \cdot (T_\Delta(\Gamma)\gamma) = \bigcup_{\gamma\in\Gamma} (s_f \cdot T_\Delta(\Gamma)) \cdot \gamma, \tag{9.9}$$

i.e., S is divided into copies of the unit cell

$$C = s_f \cdot T_\Delta(\Gamma), \tag{9.10a}$$

under action of the translation group

$$S = \bigcup_{\gamma\in\Gamma} C \cdot \gamma = C \cdot \Gamma, \tag{9.10b}$$

The Schwarz triangles then tile the unit cell, which in turn tessellates the full plane, see Fig. 9.2. Above, we have emphasized the fact that $T_\Delta(\Gamma)$ is a set of chosen representatives of the cosets in Δ/Γ by labeling elements by g_j with the index j enumerating the representatives of different cosets. The choice of $T_\Delta(\Gamma)$ determines the unit cell in real space (relative to the fundamental Schwarz triangle), e.g., whether it is a connected region and whether it is symmetric under point-group operations. Naturally, the centers of the translated copies of the unit cell form a Bravais lattice.

In practice, the translation group, and thus the unit cell C and Bravais lattice, can be obtained by searching for the largest normal subgroup $\Gamma \lhd \Delta^+$, which corresponds to the normal subgroup with smallest index $|\Delta^+ : \Gamma|$. This search can be performed using low-index-normal-subgroup algorithms from computational group theory, which, for instance, are implemented in the programming language GAP. However, many normal subgroups of proper triangle groups have been tabulated. For example, Ref. 301 lists the presentations of the quotient groups Δ^+/Γ in terms of the generators of Δ^+. We illustrate how to obtain Γ using the $\{8,3\}$ lattice as an example. According to Ref. 301, the smallest quotient group of the proper triangle group $\Delta^+(2,3,8)$ with one of its normal subgroups is

$$\Delta^+(2,3,8)/\Gamma = \left\langle \mathsf{x},\mathsf{y},\mathsf{z} \middle| \mathsf{x},\mathsf{y},\mathsf{z},\mathsf{x}^2,\mathsf{y}^3,\mathsf{z}^8,\mathsf{zyxz}(\mathsf{zy})^{-1}\mathsf{xz} \right\rangle. \tag{9.11}$$

This directly gives the natural homomorphism of the quotient group $\Delta^+/\Gamma \to \Delta^+$, whose kernel is isomorphic to Γ. We determine this kernel using GAP

and find that it is isomorphic to the following finitely presented group

$$\begin{aligned}\Gamma_{\{8,3\}} &= \left\langle \gamma_1,\gamma_2,\gamma_3,\gamma_4 \middle|\, \gamma_4\gamma_1\gamma_2^{-1}\gamma_3\gamma_4^{-1}\gamma_1^{-1}\gamma_2\gamma_3^{-1} \right\rangle \\ &= \left\langle \gamma_1,\gamma_2,\gamma_3,\gamma_4 \middle|\, \gamma_1\gamma_2^{-1}\gamma_3\gamma_4^{-1}\gamma_1^{-1}\gamma_2\gamma_3^{-1}\gamma_4 \right\rangle, \end{aligned} \tag{9.12}$$

where in the last step, we have simplified the relator and thus obtained the same translation group as for the $\{8,8\}$ lattice. This implies that the Bravais lattice of the $\{8,8\}$ and the $\{8,3\}$ lattice are the *same*. However, the $\{8,3\}$ has a nontrivial unit cell with several sites, while the $\{8,8\}$ lattice has only a single site per unit cell. The two lattices and their unit cells are shown in Figs. 9.2b and 9.2c.

9.1.3. Point group

Since Γ is a normal subgroup of Δ, $\Gamma \lhd \Delta$, the quotient Δ/Γ is isomorphic to the *point group* G of the hyperbolic lattice. Using this isomorphism, we can define the induced right action from G on C, such that

$$C = s_f \cdot G, \tag{9.13}$$

which immediately implies that G is the symmetry group that leaves the unit cell invariant. The order of the point group $|G|$ is equal to the index $|\Delta : \Gamma|$ and gives the number of Schwarz triangles in the unit cell.

Since Δ has a trivial $\mathbb{Z}_2$ factor, the same holds for G:

$$G = G^+ \ltimes \mathbb{Z}_2, \tag{9.14a}$$

where G^+ is the *proper point group*. In particular, the semidirect-product structure and the fact that $\Gamma \lhd \Delta^+$ implies that

$$G^+ \cong \Delta^+/\Gamma. \tag{9.14b}$$

Equation (9.14) allows us to construct G from Δ^+ without referring to the full group Δ.

Examples

According to Eqs. (9.5) and (9.12), the $\{8,8\}$ and $\{8,3\}$ lattice have the same translation group

$$\Gamma = \left\langle \gamma_1,\gamma_2,\gamma_3,\gamma_4 \middle|\, \gamma_1\gamma_2^{-1}\gamma_3\gamma_4^{-1}\gamma_1^{-1}\gamma_2\gamma_3^{-1}\gamma_4 \right\rangle, \tag{9.15}$$

which manifests in the same unit cell on the Poincaré disk in Figs. 9.2b and 9.2c. However, their point groups $G^+ \cong \Delta^+/\Gamma$ differ and have the

following presentations in terms of generators of the corresponding (proper) groups $\Delta^+(2,8,8)$ and $\Delta^+(2,3,8)$:

$$G^+_{\{8,8\}} = \left\langle \mathsf{x},\mathsf{y},\mathsf{z} \middle| \mathsf{x}^2, \mathsf{y}^8, \mathsf{z}^8, \mathsf{xyz}, \mathsf{xzy}, \mathsf{y}^3\mathsf{z}^{-1} \right\rangle, \tag{9.16}$$

$$G^+_{\{8,3\}} = \left\langle \mathsf{x},\mathsf{y},\mathsf{z} \middle| \mathsf{x}^2, \mathsf{y}^3, \mathsf{z}^8, \mathsf{xyz}, \left(\mathsf{xz}^4\right)^2 \right\rangle, \tag{9.17}$$

with $|G^+_{\{8,8\}}| = 8$ and $|G^+_{\{8,3\}}| = 48$. The order of the (proper) point group is reflected in the number of (gray) triangles inside the unit cell in Figs. 9.2b and 9.2c.

We can simplify the presentation of $G^+_{\{8,8\}}$ by eliminating some of the generators. Looking at the relators, we observe that $\mathsf{y}^3\mathsf{z}^{-1} = \mathsf{y}^8 = 1$ imply

$$\mathsf{z}^3 = \left(\mathsf{y}^3\right)^3 = \mathsf{y}^9 = \mathsf{y}, \tag{9.18}$$

giving us $\mathsf{y} = \mathsf{z}^3$ and together with $\mathsf{xyz} = \mathsf{x}^2 = 1$, $\mathsf{x} = \mathsf{z}^4$, such that

$$G^+_{\{8,8\}} \cong \left\langle \mathsf{z} \middle| \mathsf{z}^8 \right\rangle. \tag{9.19}$$

The relations $\mathsf{x} = \mathsf{z}^4$ and $\mathsf{y} = \mathsf{z}^3$ can be easily read from Fig. 9.2b, where rotating the fundamental Schwarz triangle (dark gray) around its top most vertex, i.e., acting with x results in the triangle $s_f \cdot \mathsf{z}^4$ shifted by γ_1 and similarly for y, we have $s_f \cdot \mathsf{y} = s_f \cdot \mathsf{z}^3\gamma_4^{-1}$.

9.2. Boundary conditions and the thermodynamic limit

The usual starting point for studying lattices in Euclidean space is Bloch's theorem, which labels Hamiltonian eigenstates by irreducible representations of the translation group. It allows a description of the thermodynamic limit based on a finite unit cell together with reciprocal space. While Bloch's theorem has been generalized [62–64, 70–74] to hyperbolic lattices, this comes with fundamental difficulties. First, Bloch's theorem requires periodic boundary conditions (PBC), but forming finite PBC *clusters* that approximate the thermodynamic limit is highly nontrivial [64, 75, 302]. Second, Euclidean translation groups are Abelian, such that only one-dimensional (1D) irreducible representations exist. In contrast, hyperbolic translation groups admit higher-dimensional irreducible representations; therefore, hyperbolic band theory requires *non-Abelian* Bloch states besides the usual Abelian ones [64]. In this section, we focus on the first difficulty, postponing the discussion of the

second to Section 9.4 and our proposal for its resolution to Chapter 10. We first comment on open boundary conditions in Section 9.2.1, before turning to periodic boundary conditions in Section 9.2.2.

9.2.1. Finite flakes with open boundary conditions

One way to circumvent these difficulties is to study finite *flakes* with open boundary conditions instead. Defining tight-binding models on such lattices is straightforward once the underlying graph is known: the Hamiltonian is simply given by the adjacency matrix with each edge between vertices i and j weighted by the corresponding hopping amplitude h_{ij}:

$$\mathcal{H} = -\sum_{i,j} \mathsf{h}_{ij} c_i^\dagger c_j. \tag{9.20}$$

This is exactly the procedure that we have applied in Chapter 8, where we have studied a particularly simple tight-binding model, namely the one with constant hopping to nearest neighbors: $\mathsf{h}_{ij} = 1$ if i, j are nearest neighbors and zero otherwise. Finite $\{p, q\}$ flakes can be conveniently constructed using the vertex-inflation procedure [303], which we have applied in Ref. 7. Starting from a central p-sided polygonal tile, additional tiles are added iteratively in shells, such that in each iteration vertices that formerly were on the boundary are equipped with q tiles in total.

Based on the total (hyperbolic) area of a disk of Euclidean radius $r_0 < 1$

$$A(r_0) = \int_0^{2\pi} \mathrm{d}\phi \int_0^{r_0} \mathrm{d}r \, \frac{r}{(1-r^2)^2} = \frac{\pi r_0^2}{1-r_0^2}, \tag{9.21}$$

and estimating the radius of the N^{th} shell to be Nd_0, where d_0 is the hyperbolic lattice constant, we can get a rough estimate of the scaling of the number of vertices $\mathcal{V}$ with the number N of shells:

$$\lim_{N\to\infty} \mathcal{V}(N) \sim A(\tanh(Nd_0)) \sim \left(\mathrm{e}^{2d_0}\right)^N, \tag{9.22}$$

i.e., the total number of sites increases exponentially with the linear extent of the lattice with the rate e^{2d_0} increasing with increasing magnitude of curvature per tile. Working with finite flakes thus is a suitable approach mostly if we are interested in small systems. Even more, hyperbolic lattices exhibit a macroscopic fraction of boundary sites, which is advantageous when interested in boundary effects [6, 304–306], but challenging when studying bulk properties.

Nevertheless, some bulk properties, such as the bulk density of states, can be estimated, albeit inefficiently, by projecting to the bulk part of the system [6,

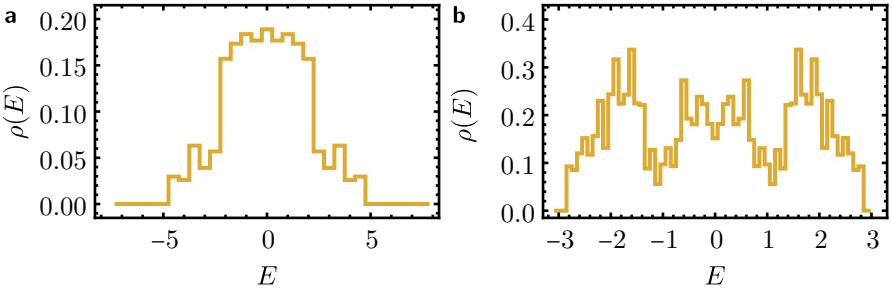

Figure 9.3.: Bulk density of states obtained from flakes. The local density of states on a single unit cell of a finite (**a**) $\{8,8\}$ flake with 3 shells (9800 sites) and (**b**) $\{8,3\}$ flake with 5 shells (2888 sites) with open boundary conditions as an estimate for the bulk density of states on the infinite lattice. Lattices and unit cells are shown in Figs. 9.2b and 9.2c, respectively.

307]. As we have seen, this requires discarding a successively larger fraction of the system, the larger the whole system is. We demonstrate this here for simple tight-binding models with constant nearest neighbor hopping on the $\{8,8\}$ and $\{8,3\}$ lattice. The Hamiltonian is given by

$$\mathcal{H} = -\sum_{\langle i,j\rangle} c_i^\dagger c_j \tag{9.23}$$

where $\langle i,j\rangle$ denotes all ordered nearest-neighbor pairs on the given lattice. The spectrum and eigenstates are thus given by the eigenvalues and eigenvectors of the adjacency matrix. To extract the bulk density of states, we consider the local density of states on the sites in the innermost unit cell [6, 307], i.e., each state is weighted by its weight on those sites. The resulting histograms for the density of states are shown in Fig. 9.3.

Continued-fraction method

If we are interested in the density of states, the problem of diagonalizing large systems and discarding most of the resulting states can be alleviated by using the *continued-fraction method* [76, 308–310]. The method relies on expanding the diagonal matrix elements, for a state $|i\rangle$, of the Green function $\mathcal{G}(E) = (E-\mathcal{H})^{-1}$, without applying periodic boundary conditions:

$$\mathcal{G}_{ii}(E) = \cfrac{1}{E - a_1 - \cfrac{b_1}{E-a_2-\cfrac{b_2}{E-a_3-\cfrac{b_3}{\ddots}}}}, \tag{9.24a}$$

where (a_n, b_n) are rational numbers depending on $|i\rangle$. On the lattice, we can choose a basis of the Hilbert space such that the state $|i\rangle$ is localized on site i. Crucially, in infinite lattices, all sites are equivalent and thus the density of states $\rho(E)$ is equal to the *local* density of states $\rho_i(E)$ of any site i, which can be expressed in terms of the Green function as

$$\rho_i(E) = -\frac{1}{\pi} \lim_{\varepsilon \to 0^+} \operatorname{Im}\left(\mathcal{G}_{ii}(E + \mathrm{i}\varepsilon)\right). \tag{9.24b}$$

Since the method does not rely on translational symmetry, it can be applied to hyperbolic lattices without any modifications [76].

Equation (9.24) reduces the computation of the density of states to the problem of finding the coefficients (a_n, b_n), a task that can be done recursively [308–310], as we briefly review now. Effectively, the recursion method constructs a non-normalized orthogonal basis $|n\}$ of the Hilbert space in which the Hamiltonian is a tridiagonal matrix

$$\{m|\mathcal{H}|n\} = a_n \delta_{m,n} + \sqrt{b_{n-1}}\delta_{m,n-1} + \sqrt{b_n}\delta_{m,n+1}, \tag{9.25}$$

starting from an initial state $|1\} = |i\rangle$ fully localized on site i. That basis is given by the recursion relation [308]

$$|2\} = \mathcal{H}|1\} - a_1|1\}, \tag{9.26a}$$

where the coefficient a_1 is determined by the orthogonality condition $\{2|1\} = 0$, and

$$|n+1\} = \mathcal{H}|n\} - a_n|n\} - b_{n-1}|n-1\}, \tag{9.26b}$$

where the coefficients a_n and b_{n-1} are determined by orthogonality to $|m\}$ with $m \leq n$. Crucially, $\{m|n+1\} = 0$ for $m < n-1$ is already guaranteed, such that only two conditions are nontrivial and we find

$$a_n = \frac{\{n|\mathcal{H}|n\}}{\{n|n\}}, \tag{9.27a}$$

$$b_{n-1} = \frac{\{n|n\}}{\{n-1|n-1\}}. \tag{9.27b}$$

Expanding the diagonal matrix element of the Green function $\mathcal{G}_{ii} = \langle i|\mathcal{G}|i\rangle$, one arrives at Eq. (9.24a) with the coefficients (a_n, b_n) given by Eq. (9.27).

If the coefficients converge to asymptotic values (a_∞, b_∞), it is possible to terminate the continued fraction and replace all (a_n, b_n) for $n > N$ by their

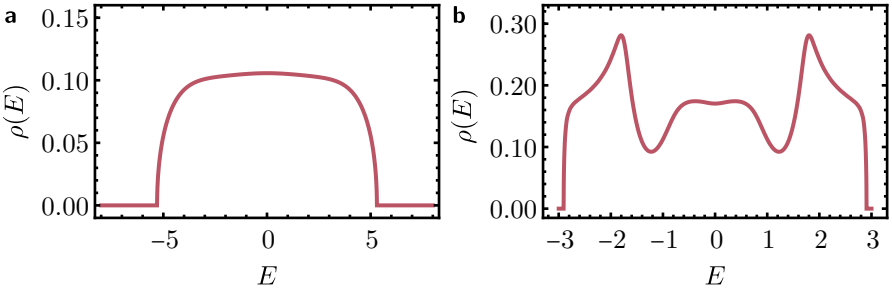

Figure 9.4.: Density of states obtain using the continued-fraction method.. Density of states of the nearest-neighbor hopping model with constant hoppings on (**a**) the $\{8, 8\}$ and (**b**) the $\{8, 3\}$ lattice obtained using the continued-fraction method from flakes with graph radius $N = 10$ and 35 with number of sites on the order of 10^8 and 10^9, respectively. Data reproduced from Ref. 76 with permission from the authors.

asymptotic values (a_∞, b_∞). This allowing us to analytically evaluate the remainder of the fraction [308, 310]

$$t_\infty(E) = \cfrac{1}{E - a_{N+1} - \cfrac{b_{N+1}}{E - a_{N+2} - \cfrac{b_{N+2}}{\cdots}}} = \frac{1}{E - a_{N+1} - b_{N+1} t_\infty(E)}, \tag{9.28}$$

giving

$$t_\infty(E) = \frac{E - a_\infty}{2b_\infty} \left(1 - \sqrt{1 - \frac{4b}{(E - a_\infty)^2}}\right). \tag{9.29}$$

The termination can be interpreted as embedding the finite flake with size determined by N (as we discuss in the next paragraph) in an effective medium to suppress boundary effects which are particularly relevant in hyperbolic lattices. A unique limit for the coefficients is only guaranteed if the spectrum of $\mathcal{H}$ is gapless [76]. Otherwise, the termination procedure has to be adapted to account for multiple limits, e.g., distinguishing odd and even n or similar.N Nevertheless, this allows extrapolation to the thermodynamic limit.

The coefficients (a_n, b_n) are directly related to the moments M_n of the density of states $\rho(E)$, which are defined as

$$M_n = \int_{-\infty}^{\infty} \mathrm{d}E\, \rho(E) E^n = \sum_i \langle i | \mathcal{H}^n | i \rangle \,. \tag{9.30}$$

One can show [308] that the first N pairs of coefficients determine the first $2N$ moments exactly and that this requires access to a graph with linear extent

(measured in the graph distance) of N [76]. Recall that the total number of sites of the corresponding hyperbolic flake increases exponentially with N.

To illustrate this method and for later use as a benchmark to compare the result of reciprocal-space methods to, we apply it to nearest-neighbor hopping models with constant hopping on the $\{8,8\}$ and $\{8,3\}$ lattice discussed above, see Figs. 9.2b and 9.2c, respectively. Figures 9.4a and 9.4b reproduce the resulting density of states from Ref. 76 obtained from flakes with graph radius $N = 10$ and 35 with number of sites on the order of 10^8 and 10^9, respectively.

9.2.2. Periodic-boundary-condition clusters

Alternatively, bulk properties can be directly probed in finite systems using periodic boundary conditions which are intimately related to translational symmetry. Indeed, the idea of periodic boundary conditions is to work on a single unit cell and identify all translated copies with that one unit cell. However, in contrast to Euclidean lattices, formulating periodic boundary conditions on hyperbolic lattices is nontrivial due to the non-commutativity of the translation group. In both cases, it requires to define the lattice on a closed manifold rather than in the infinite plane. We first take a geometric perspective and review the concept of *patterns*, which are finite hyperbolic graphs embedded into closed Riemann surfaces, following the exposition in Ref. 63. Then, we take an algebraic perspective and discuss how *clusters* of unit cells with periodic boundary conditions, known as *PBC clusters*, manifest as normal subgroups of the translation group Γ [64, 311]. Finally, we comment on the thermodynamic limit; in particular, we briefly discuss a recent work [75, 302] that argued that by choosing particular sequences of translation groups, convergence to the thermodynamic limit can be achieved.

Geometric perspective: patterns

We consider a 2D connected Riemann surface. By the *uniformization theorem* [312] every such surface is conformally equivalent to a surface $\Sigma_\mathfrak{g}$ with constant curvature $+1$, 0, or -1, i.e., spherical, Euclidean or hyperbolic, additionally characterized by its *genus* $\mathfrak{g}$, i.e., the number of holes. If $\mathfrak{g} = 0$, i.e., $\Sigma_\mathfrak{g}$ is simply-connected, it is equivalent to either the sphere, the complex plane, or the Poincaré disk, depending on the curvature (positive, zero, or negative, respectively). In Section 8.2, we have discussed tessellations of such surfaces. Holes are only possible for zero or negative curvature. If $\mathfrak{g} > 0$, zero curvature implies $\mathfrak{g} = 1$ and $\Sigma_\mathfrak{g}$ is equivalent to the torus (Fig. 9.5a), while negative curvatures leads to a hyperbolic surface with $\mathfrak{g} \geq 2$, for instance the genus-2 surface shown in Fig. 9.5e.

The concept of regular tessellations can be extended to surfaces with holes and if the surface is closed, the graph will be regular and have no boundary. Due to the absence of a boundary, a $\{p, q\}$ pattern on a closed surface satisfies

$$pF = 2E = q\mathcal{V}, \tag{9.31}$$

where F, $\mathcal{E}$, and $\mathcal{V}$, are the number of faces, edges, and vertices, respectively. Similarly to Section 8.2.2, we consider the Euler characteristic of the pattern,

$$\chi = \mathcal{V} - \mathcal{E} + \mathcal{F}, \tag{9.32}$$

where the restriction to the Euler characteristic per vertex is not necessary anymore due to the graph being finite. For orientable surfaces $\Sigma_{\mathfrak{g}}$, χ is even and related to the genus by

$$\chi = 2(1 - \mathfrak{g}). \tag{9.33}$$

Given a $\{p, q\}$ lattice, we call solutions to Eq. (9.31) *compactifications* of the lattice on a surface of genus $\mathfrak{g}$. We illustrate a $\{4, 4\}$ pattern on a genus-1 surface (torus) and a $\{8, 8\}$ pattern on a genus-2 surface in Figs. 9.5a and 9.5e, respectively.

We observe from Eqs. (9.31) to (9.33) that for hyperbolic $\{p, q\}$ patterns, larger graphs are compactified on surfaces with larger genus: scaling $(\mathcal{F}, \mathcal{E}, \mathcal{V})$ by an integer, scales χ by the same integer and thus increases $\mathfrak{g}$:

$$\mathfrak{g} - 1 = \frac{pq - 2(p + q)}{4p}\mathcal{V}. \tag{9.34}$$

This is not the case for Euclidean patterns which have $\mathfrak{g} = 1$: due to $\chi = 0$, scaling $(\mathcal{F}, \mathcal{E}, \mathcal{V})$ does not change the genus, such that on the same torus shown in Fig. 9.5a, a $\{4, 4\}$ pattern with 48 square tiles instead of the single one can be drawn, see Fig. 9.5b. This can be understood geometrically by considering the total area of $\Sigma_{\mathfrak{g}}$ and the area of each face of the pattern. As we have described in Section 8.2.1, the size of the polygons is arbitrary for Euclidean, but fixed by p, q (for fixed curvature K) for hyperbolic tessellations. On the other hand, the area of a hyperbolic surface $\Sigma_{\mathfrak{g}}$ is similarly fixed by the Gauss-Bonnet theorem, Eq. (8.16)

$$KA = 4\pi(1 - \mathfrak{g}), \tag{9.35}$$

such that a larger number of polygons can only be accommodated by increasing $\mathfrak{g}$. For $K = 0$, Gauss-Bonnet does not constrain the area, since both sides of the equation vanish in that case.

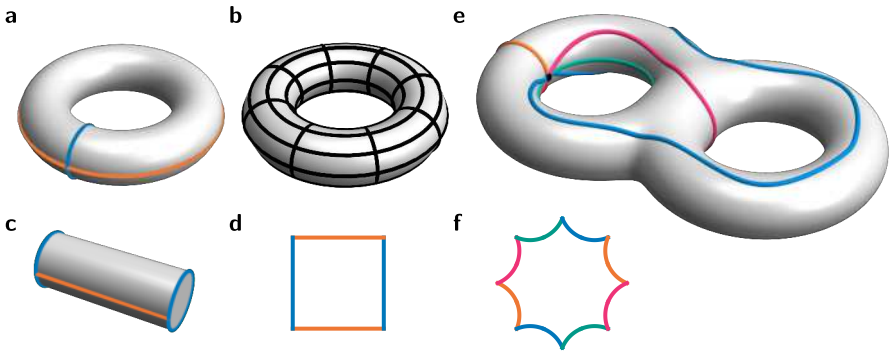

Figure 9.5.: Euclidean and hyperbolic patterns. (**a**) Euclidean $\{4,4\}$ pattern on the torus ($\mathfrak{g}=1$) with a single square tile. Of the four sides two each coincide and the resulting lines are shown in orange and blue. (**b**) $\{4,4\}$ pattern with 48 tiles. By cutting the torus in (a) along the blue circle, we obtain (**c**) a cylinder, and cutting again along the orange line, we arrive at (**d**) the square tile. (**e**) Hyperbolic $\{8,8\}$ pattern with a single octagonal tile on a genus-2 surface. Again, pairs of sides coincide resulting in four colored loops on the surface. (**f**) The cut and unfolded octagonal tile from (e).

Algebraic perspective: clusters and supercells

In analogy to the Euclidean case that we discussed in Section 2.3.1, imposing periodic boundary conditions on hyperbolic lattices amounts to constructing a normal subgroup Γ_{PBC} of the translation group Γ defined in Section 9.1.2 [64, 311]. Periodic boundary conditions then imply that we identify translations $\gamma_{\mathrm{PBC}} \in \Gamma_{\mathrm{PBC}}$ with the identity, such that the resulting finite system, the PBC cluster, has the residual translation group $\Gamma/\Gamma_{\mathrm{PBC}}$ of order $N = |\Gamma : \Gamma_{\mathrm{PBC}}|$. The PBC cluster thus consists of N unit cells and in the language of Section 9.1 we can express the Schwarz triangles making up the PBC cluster C_{PBC} in terms of the transversal $T_\Gamma(\Gamma_{\mathrm{PBC}})$:

$$C_{\mathrm{PBC}} = \bigcup_{\eta_i \in T_\Gamma(\Gamma_{\mathrm{PBC}})} C \cdot \eta_i. \tag{9.36}$$

As in the case of unit cells, the choice of transversal influences whether C_{PBC} forms a *connected* cluster; we usually restrict ourselves to such connected clusters. Defining periodic boundary conditions for a single unit cell then amounts to choosing $\Gamma_{\mathrm{PBC}} = \Gamma$. The result is a minimal compactification of the lattice on a smooth compact Riemann surface $\Sigma_{\mathfrak{g}}$ of genus $\mathfrak{g} \geq 2$ as discussed above, i.e., a pattern.

The advantage of working with PBC clusters over the infinite lattice is that they are *finite* which manifests as the finite order of the residual translation group $\Gamma/\Gamma_{\mathrm{PBC}}$. In practice, normal subgroups of a given index N of a finitely-presented group Γ can be systematically enumerated using methods in computational group theory [313]. For instance, low-index normal subgroups can be found using the Firth-Holt algorithm [314, 315] implemented [316] in GAP. However, for large N, both the number of normal subgroups as well as the computation time increase, such that a complete search becomes impractical. Instead, larger-index normal subgroups can be constructed from intersections of small-index normal subgroups [8].

Often, periodic boundary conditions are used not only to eliminate boundary effects in finite systems, but to approximate the infinite lattice more efficiently than with open boundary conditions. However, this latter application requires a great deal of care in the case of hyperbolic lattices. For 2D Euclidean lattices, we have seen that the full translation group is isomorphic to the Abelian group $\mathbb{Z}^2$, all normal subgroups defining periodic boundary conditions are isomorphic to $N_1\mathbb{Z}\times N_2\mathbb{Z}$ for integers N_1, N_2, resulting in the group of residual translations

$$\begin{aligned}\mathbb{Z}^2/(N_1\mathbb{Z}\times N_2\mathbb{Z}) &\cong (\mathbb{Z}/N_1\mathbb{Z})\times(\mathbb{Z}/N_2\mathbb{Z})\\ &\cong \mathbb{Z}_{N_1}\times\mathbb{Z}_{N_2}.\end{aligned} \tag{9.37}$$

For hyperbolic lattices, neither Γ nor Γ_{PBC} generally take such simple forms and for fixed Γ, the group structure of $\Gamma_{\mathrm{PBC}} \lhd \Gamma$ can vary greatly. In particular, while $\Gamma/\Gamma_{\mathrm{PBC}}$, like Γ, generally is non-Abelian, for certain normal subgroups Γ_{PBC} of Γ, $\Gamma/\Gamma_{\mathrm{PBC}}$ is Abelian. We refer to the corresponding PBC clusters as *non-Abelian* and *Abelian* clusters, respectively. Maciejko et al. [64] found that for low index N a large fraction of connected clusters is Abelian. Clearly, one cannot expect that these Abelian clusters generally provide a faithful approximation of the infinite lattice with its non-Abelian translation group.

To develop criteria for selecting appropriate normal subgroups, we consider the coset decomposition of Γ

$$\Gamma = \bigcup_{\eta_i\in T_\Gamma(\Gamma_{\mathrm{PBC}})} \eta_i\Gamma_{\mathrm{PBC}}. \tag{9.38}$$

which allows us recover the full lattice from a finite PBC cluster C_{PBC}:

$$S = C\cdot\Gamma = C_{\mathrm{PBC}}\cdot\Gamma_{\mathrm{PBC}}. \tag{9.39}$$

While Eqs. (9.10b) and (9.39) look formally identical, generally Γ_{PBC} is *not* a translation group as we defined it in Section 9.1.2: while it is a normal subgroup of Γ and thus a subgroup of Δ, it is not generally a *normal* subgroup

of Δ. By instead restricting to $\tilde{\Gamma}$ that are normal subgroups of both Δ and Γ, we ensure that $\tilde{\Gamma}$ has all the necessary properties of a translation group such that $\tilde{C} = s_f \cdot \tilde{\Gamma}$ forms a (non-primitive) unit cell, which we refer to as a *supercell* [5].

Thermodynamic limit

It turns out that restricting to supercells rather than generic PBC clusters is an important step towards achieving a faithful approximation of the infinite lattice, i.e., one that converges to the thermodynamic limit upon increasing the system size [5, 75, 302]. Lux et al. [75, 302] have shown that a sequence of PBC clusters satisfying the following two conditions, results in a converging finite approximation of the infinite lattice:

$$\Delta^+ = \Gamma^{(0)} \rhd \Gamma^{(1)} \rhd \Gamma^{(2)} \rhd \cdots , \tag{9.40a}$$

$$\bigcap_{n\geq 0} \Gamma^{(n)} = \{1\}. \tag{9.40b}$$

In particular, they argue [302] that bulk properties converge to the *physical* thermodynamic limit. Their results [75] for the moments of the density of states of the $\{8, 8\}$ agree well with those obtained using the continued-fraction method [76]. Based on a sequence with six clusters of up to 131 072 sites, they were able to extract the first six moments exactly.

However, going to larger clusters becomes computationally expensive. This suboptimal scaling of real-space methods based on periodic boundary conditions is due to the increasing number of noncontractible loops $2\mathfrak{g}$ with increasing system size [76], which we saw in Eq. (9.34). Thus, after a detour into the formalism for describing tight-binding models on the infinite lattice and on supercells in Section 9.3, we will, in Section 9.4 and Chapter 10, turn to a reciprocal-space description, which appears to mitigate this problem.

9.3. Description of tight-binding models

This section is largely based on the supplement to the publication "Non-Abelian hyperbolic band theory from supercells" [5]. Segments with significant text overlap with the published version may be subject to copyright by the American Physical Society.

Generically, a tight-binding model is defined in real space by orbitals at certain positions with nontrivial on-site symmetry group, so-called *Wyckoff positions*, and couplings between them. Thus, the first step in describing

hyperbolic tight-binding models is to find and enumerate these Wyckoff positions: in Section 9.3.1 we describe how to label the Wyckoff positions based on the triangle group, first in the infinite lattice, then on the lattice subdivided into unit cells. Then, in Section 9.3.2, we discuss generic forms of hopping Hamiltonians defined in infinite lattices and on PBC clusters.

9.3.1. Algebraic labeling of Wyckoff positions and unit cells

To systematically define generic tight-binding models in real space, we developed an algebraic framework for labeling the potential positions of orbitals, i.e., the lattice sites [5]. These sites are typically located at high-symmetry positions, i.e., points with nontrivial on-site symmetry group, and depend on the underlying space group (the triangle group). Here, we limit our attention to the maximally symmetric positions, i.e., those whose site-symmetry groups are not a proper subgroup of any other site-symmetry group [317] (which for the regular $\{p, q\}$ tessellations correspond to centers of rotational symmetries). These are enumerated in Eq. (9.43).

Next, we discuss how to subdivide the infinite lattice into unit cells and identify a set of representatives of all high-symmetry positions contained within the unit cell; these are known as (maximally symmetric) Wyckoff positions and enumerated in Eq. (9.44). Based on this, we relabel all sites in the infinite lattice in terms of the unit cell they are contained in and the corresponding Wyckoff position, resulting in Eq. (9.52). Finally, we comment on how these labels can easily be adapted when restricting to a finite PBC cluster.

Tiling by Schwarz triangles

Recall from Section 9.1 that the infinite lattice can be seen as an infinite set S of Schwarz triangles tiling the plane. The vertices of those triangles form a hyperbolic triangular lattice where each site has a nontrivial on-site symmetry group generated by the reflection symmetries with mirror lines passing through the vertex, see Fig. 9.1. Because each edge in the tessellation is shared by two Schwarz triangles with opposite orientations, it is sufficient to work directly with the proper triangle group Δ^+ which gives only Schwarz triangles of one orientation. The proper subgroup of the above-mentioned on-site symmetry group of a given vertex is then generated by the rotation around that vertex, see again Fig. 9.1. The set V^{lat} of all vertices can be divided into three subsets $V_{\mathsf{z}}^{\mathrm{lat}}$, $V_{\mathsf{y}}^{\mathrm{lat}}$, $V_{\mathsf{x}}^{\mathrm{lat}}$ according to which vertex of the fundamental Schwarz triangle they originate from under action of Δ^+. Thus, we have $V^{\mathrm{lat}} = V_{\mathsf{z}}^{\mathrm{lat}} \cup V_{\mathsf{y}}^{\mathrm{lat}} \cup V_{\mathsf{x}}^{\mathrm{lat}}$. Below we discuss $V_{\mathsf{z}}^{\mathrm{lat}}$, but the discussion for the other two sets is equivalent.

The on-site symmetry group of a vertex in $V_{\mathsf{z}}^{\text{lat}}$ is

$$\Delta_{\mathsf{z}}^{+} = \langle \mathsf{z} |\, \mathsf{z}^{p} \rangle \tag{9.41}$$

and is exactly the stabilizer of that vertex if we define a right action of Δ^+ on the abstract set $V_{\mathsf{z}}^{\text{lat}}$. By the orbit-stabilizer theorem, there exists a bijection between the orbit $V_{\mathsf{z}}^{\text{lat}} \cdot \Delta^+$ of some $V_{\mathsf{z}}^{\text{lat}} \in V_{\mathsf{z}}^{\text{lat}}$ (assumed to be a vertex of the fundamental Schwarz triangle) and the quotient $\Delta^+/\Delta_{\mathsf{z}}^+$, or, equivalently, between $V_{\mathsf{z}}^{\text{lat}}$ and the right transversal

$$V_{\mathsf{z}}^{\text{lat}} \cong T_{\Delta^+}(\Delta_{\mathsf{z}}^+). \tag{9.42}$$

Thus, the vertices are labelled by $(\mathsf{w}, [t]_{\mathsf{w}})$ for $\mathsf{w} \in \{\mathsf{x}, \mathsf{y}, \mathsf{z}\}$ and $[t]_{\mathsf{w}} \in \Delta^+/\Delta_{\mathsf{w}}^+$ where a set of distinct cosets $[t]$ is given by a choice of representatives, i.e., the right transversal $T_{\Delta^+}(\Delta_{\mathsf{w}}^+)$ mentioned above:

$$V^{\text{lat}} \cong \left\{ (\mathsf{w}, [t]_{\mathsf{w}}) \,:\, \mathsf{w} \in \{\mathsf{x}, \mathsf{y}, \mathsf{z}\}, t \in T_{\Delta^+}(\Delta_{\mathsf{w}}^+) \right\}. \tag{9.43}$$

Note that for the orbit-stabilizer theorem it is important to pair right action with right cosets (and right transversal). Alternatively, we can work with the full groups Δ and Δ_{z} to arrive at the same conclusion: Eq. (9.4) then implies $V_{\mathsf{z}}^{\text{lat}} \cong T_{\Delta}(\Delta_{\mathsf{z}})$ and analogously for x, y.

Bravais lattice and unit cells

The lattice formed by the vertices of the Schwarz triangles does not generally form a Bravais lattice. To obtain the Bravais lattice corresponding to a triangle group $\Delta(r, q, p)$, a translation group $\Gamma \lhd \Delta^+$ needs to be identified as discussed in Section 9.1.2. The translation group then defines the subdivision of the infinite lattice S into copies of the unit cell C via the quotient group $G \cong \Delta/\Gamma$ according to Eqs. (9.10b) and (9.13): $S = C \cdot \Gamma$ and $C = s_f \cdot G$. To label vertices, it is again sufficient to work with the proper subgroups, which, according to Eq. (9.14b), satisfy $G^+ \cong \Delta^+/\Gamma$. Further, for any $\mathsf{w} \in \{\mathsf{x}, \mathsf{y}, \mathsf{z}\}$, Δ_{w}^+, by definition in terms of a single rotation generator, does not have any torsion-free elements, such that the stabilizer G_{w}^+ of $V_{\mathsf{w}}^{\text{lat}}$ (modulo translations in Γ) under the right action of G^+ is isomorphic to the full stabilizer: $G_{\mathsf{w}}^+ \cong \Delta_{\mathsf{w}}^+$. This now allows us to label the vertices in the unit cell, i.e., the Wyckoff positions: $V^{\text{cell}} = V_{\mathsf{z}}^{\text{cell}} \cup V_{\mathsf{y}}^{\text{cell}} \cup V_{\mathsf{x}}^{\text{cell}}$ with $V_{\mathsf{w}}^{\text{cell}} \cong T_{G^+}(G_{\mathsf{w}}^+)$, i.e.,

$$V^{\text{cell}} \cong \left\{ (\mathsf{w}, [\delta]_{\mathsf{w}}) \,:\, \mathsf{w} \in \{\mathsf{x}, \mathsf{y}, \mathsf{z}\}, \delta \in T_{G^+}(G_{\mathsf{w}}^+) \right\}, \tag{9.44}$$

where $[\delta]_{\mathsf{w}} \in G^+/G_{\mathsf{w}}^+$. Note that the subscript again indicates the quotient group in which the coset lies. We now want to write the infinite set V^{lat}

describing *all* vertices in terms of translated Wyckoff positions, i.e., in terms of the finite set V^{cell} and translations in Γ.

By the coset decomposition

$$\Delta^+ = \bigcup_{g_j \in T_{\Delta^+}(\Gamma)} g_j \Gamma, \tag{9.45}$$

any $t \in \Delta^+$ can be written as

$$t = g_j \gamma', \tag{9.46}$$

for unique $g_j \in T_{\Delta^+}(\Gamma)$ and $\gamma' \in \Gamma$. Using the quotient group isomorphism $i : \Delta^+/\Gamma \to G^+$, the image $i([g_j])$ of the unique coset $[g_j] \in \Delta^+/\Gamma$ associated with $g_j \in T_{\Delta^+}(\Gamma)$ can be rewritten using the right coset decomposition (for any choice of $\mathsf{w} \in \{\mathsf{x}, \mathsf{y}, \mathsf{z}\}$):

$$G^+ = \bigcup_{\delta_k \in T_{G^+}(G^+_{\mathsf{w}})} G^+_{\mathsf{w}} \delta_k, \tag{9.47}$$

i.e.,

$$i([g_j]) = i([\mathsf{w}^n])\delta_k \tag{9.48}$$

with unique $n \in \{0, 1, \ldots, |G^+_{\mathsf{w}}| - 1\}$ and $\delta_k \in T_{G^+}(G^+_{\mathsf{w}})$. Note that $n = n(j)$ and $k = k(j)$, i.e., they implicitly depend on the specific choice of j, but we suppress this dependence for better readability. Applying the inverse of i and recognizing that $i^{-1}(\delta_k) = [g]$ for a unique $g \in T_{\Delta^+}(\Gamma)$, which we denote by $g_{u_{\mathsf{w}}}$ to emphasize that $i([g_{u_{\mathsf{w}}}]) \in T_{G^+}(G^+_{\mathsf{w}})$, results in

$$[g_j] = [\mathsf{w}^n][g_{u_{\mathsf{w}}}], \tag{9.49}$$

which in turn implies (due to $\Gamma \lhd \Delta^+$)

$$g_j = \mathsf{w}^n g_{u_{\mathsf{w}}} \gamma'', \tag{9.50}$$

for a unique $\gamma'' \in \Gamma$. Thus, we have shown that for any choice $\mathsf{w} \in \{\mathsf{x}, \mathsf{y}, \mathsf{z}\}$, an arbitrary $t \in \Delta^+$ can be written as

$$t = \mathsf{w}^n g_{u_{\mathsf{w}}} \gamma \tag{9.51}$$

for a unique $n \in \{0, 1, \ldots, |G^+_{\mathsf{w}}| - 1\}$, $g_{u_{\mathsf{w}}} \in T_{\Delta^+}(\Gamma)$ with $i([g_{u_{\mathsf{w}}}]) \in T_{G^+}(G^+_{\mathsf{w}})$, and $\gamma \in \Gamma$. Note that the order of the elements in Eq. (9.51) is important (and is influenced by the fact that we use right action). The rotation w^n is to the very left, as required by the orbit-stabilizer theorem; when generating the set V^{lat} by right action from the three vertices $V^{\text{lat}}_{\mathsf{w}}$, $\mathsf{w} \in \{\mathsf{x}, \mathsf{y}, \mathsf{z}\}$, w^n leaves $V^{\text{lat}}_{\mathsf{w}}$ invariant due to being in its stabilizer Δ^+_{w}. The order of $g_{u_{\mathsf{w}}}$ and γ, on

the other hand, is physically motivated (mathematically, the opposite order would be equally valid, since $\Gamma \lhd \Delta^+$ implies that $g_{u_\mathsf{w}}\gamma$ could be written with *different* translation to the left of g_{u_w} instead): g_{u_w} specifies the position of the vertex in each unit cell and then the *whole* unit cell containing all vertices is translated by γ.

This allows us to label all Wyckoff positions in the unit cell by $u = (\mathsf{w}, [g_{u_\mathsf{w}}]_\mathsf{w})$ where $[g_{u_\mathsf{w}}]_\mathsf{w} \in T_{G^+}(G^+_\mathsf{w})$. Correspondingly, Wyckoff positions in the infinite lattice can be labelled by (u, γ), where $\gamma \in \Gamma$ labels the unit cell, i.e.,

$$V^{\text{lat}} \cong \bigcup_{\gamma\in\Gamma} \{(u,\gamma) \,:\, u = (\mathsf{w}, [g_{u_\mathsf{w}}]_\mathsf{w}), \mathsf{w} \in \{\mathsf{x},\mathsf{y},\mathsf{z}\}, \\ g_{u_\mathsf{w}} \in T_{\Delta^+}(\Gamma), i([g_{u_\mathsf{w}}]) \in T_{G^+}(G^+_\mathsf{w})\} \,. \tag{9.52}$$

More practically, determining the set V^{lat} of distinct vertices requires first choosing $T_{\Delta^+}(\Gamma) \subset \Delta^+$ and then finding the subset of elements g_{u_w} satisfying $i([g_{u_\mathsf{w}}]) \in T_{G^+}(G^+_\mathsf{w})$.

The software package [318] accompanying our original work [5] includes algorithms that, given G^+ as input, construct (1) a list of Wyckoff positions in the unit cell labelled by $u = (\mathsf{w}, u_\mathsf{w})$, (2) the compactified nearest-neighbor graph formed by them, including corresponding translations γ for edges crossing the unit cell boundary, and (3) a minimal list of translation generators chosen from those to ensure that they are translations to adjacent unit cells. Figure 9.6 illustrates the output of these algorithms for two examples, $\Delta^+(2,8,8)$ and $\Delta^+(2,3,8)$. The Wyckoff positions (green triangles, orange disks, and blue squares) are explicitly shown, while the minimal translation generators and compactifications are indicated by the unit cell (dark blue polygon) and its boundary identifications (black numbers).

9

Derived lattices

The vertices and nearest-neighbor edges of the triangular tessellation defined by $\Delta(r,q,p)$ take the role of a prototype for various classes of hyperbolic lattices. These include the $\{p,q\}$ lattices that we have so far focused on, generalized *kagome* lattices, and *dice* lattices. Here, we briefly discuss those lattices and how they can be obtained from the nearest-neighbor graph defined by the triangular tessellation due to $\Delta(r,q,p)$. This amounts to defining which Wyckoff positions make up the lattice and how the edges of the new lattice graph are obtained from the ones of the triangular tessellation.

The $\{p,q\}$ lattices are obtained from $\Delta(2,q,p)$, by interpreting the q-fold symmetric Wyckoff positions $V^{\text{lat}}_\mathsf{y}$ as sites of the $\{p,q\}$ lattice, the p-fold ones, $V^{\text{lat}}_\mathsf{z}$, as plaquettes (tiles), and the two-fold ones, $V^{\text{lat}}_\mathsf{x}$, as edges. This defines a

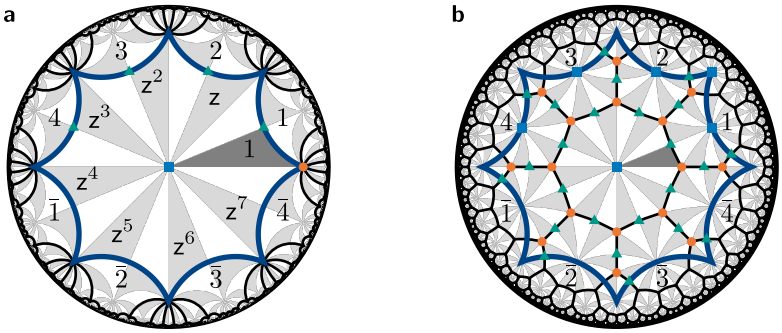

Figure 9.6.: Wyckoff positions from triangle group. Tiling of the Poincaré disk by Schwarz triangles (gray/white triangles) of (**a**) $\Delta(2,8,8)$ and (**b**) $\Delta(2,3,8)$ with Wyckoff positions $V_{\mathsf{x}}^{\mathrm{cell}}$, $V_{\mathsf{y}}^{\mathrm{cell}}$, and $V_{\mathsf{z}}^{\mathrm{cell}}$, indicated by green triangles, orange disks, and blue squares, respectively. The $\{p,q\}$ lattice (black lines) corresponding to the triangle group $\Delta(2,q,p)$ is obtained by interpreting the oranges disks as vertices, the green triangles as edges and the blue squares as faces. The fundamental Schwarz triangle is shown in dark gray, the boundary of the unit cell C is shown as a dark blue polygon and its edge identifications are indicated by black numbers: the edge $\bar{1}$ is related to 1 by the translation generator $\gamma_1 \in \Gamma$. In (a) additionally, the gray triangles in C are labeled by elements $T_{\Delta^+}(\Gamma)$, which determine the labels of the Wyckoff positions.

simple algorithm to obtain the lattice from the triangular tessellation graph. The line graph of a $\{p,3\}$ lattice defines the so-called p-gon kagome lattice; the line graph is obtained by replacing each edge with a vertex and considering the new vertices to be adjacent (connected by and edge) if the original edges shared a vertex. In terms of Wyckoff positions, this is easily realized: the sites of the p-gon kagome lattice are the 2-fold Wyckoff positions $V_{\mathsf{x}}^{\mathrm{lat}}$, edges are obtained wherever the same 3-fold Wyckoff position in $V_{\mathsf{y}}^{\mathrm{lat}}$ is adjacent to the sites in $V_{\mathsf{x}}^{\mathrm{lat}}$ under consideration. As a consequence, elements of both $V_{\mathsf{y}}^{\mathrm{lat}}$ and $V_{\mathsf{z}}^{\mathrm{lat}}$ become plaquettes, the former become the triangular and the latter the p-gonal ones. Finally, we mention the p-gon dice lattice, which is obtained from $\Delta(2,3,p)$ simply by eliminating the sites in $V_{\mathsf{x}}^{\mathrm{lat}}$.

PBC clusters

If instead of working on the infinite lattice, we constrain to a finite PBC cluster defined by $\Gamma_{\mathrm{PBC}} \lhd \Gamma$, then the translation γ in Eq. (9.51) can be further

decomposed using the coset-decomposition in Eq. (9.38):

$$\gamma = \eta_i \gamma_{\mathrm{PBC}}, \tag{9.53}$$

with unique $\eta_i \in T_\Gamma(\Gamma_{\mathrm{PBC}})$ and $\gamma_{\mathrm{PBC}} \in \Gamma_{\mathrm{PBC}}$. Now, η_i labels the Bravais lattice sites. Restricting to the finite cluster implies that sites related by γ_{PBC} are identified. Formally, this is implemented by specifying the Bravais-lattice site not by elements of Γ, but by cosets $[\eta]_{\mathrm{PBC}} \in \Gamma/\Gamma_{\mathrm{PBC}}$. Consequently, the Wyckoff positions are labeled by elements $[t]_{\mathrm{PBC}}$ of $\Delta^+/\Gamma_{\mathrm{PBC}}$:

$$[t]_{\mathrm{PBC}} = \mathsf{w}^n g_{u_\mathsf{w}} [\eta]_{\mathrm{PBC}}. \tag{9.54}$$

Examples

Let us apply these concepts to the usual two examples: the triangle groups $\Delta^+(2,8,8)$ and $\Delta^+(2,3,8)$ and the corresponding $\{8,8\}$ and $\{8,3\}$ lattices.

Starting with $\Delta^+(2,8,8)$, we recall that the proper point group of the unit cell is

$$G^+ = \langle \mathsf{z} \,|\, \mathsf{z}^8 \rangle = \{1, \mathsf{z}, \mathsf{z}^2, \ldots, \mathsf{z}^7\} = T_{\Delta^+}(\Gamma) \tag{9.55}$$

with homomorphism $\Delta^+ \to G^+$ defined on the generators of Δ^+ by $\mathsf{x} \mapsto \mathsf{z}^4$, $\mathsf{y} \mapsto \mathsf{z}^3$, and $\mathsf{z} \mapsto \mathsf{z}$. Note that, because the homomorphism acts trivially on z, we use z both for the generator of Δ^+ as well as for the one of G^+ even though G^+ is not a subgroup of Δ^+. The stabilizer groups of the three vertices of the fundamental Schwarz triangle are $G^+_\mathsf{x} = \{1, \mathsf{z}^4\}$, and $G^+_\mathsf{y} = G^+_\mathsf{z} = G^+$, such that

$$T_{G^+}(G^+_\mathsf{x}) = \{1, \mathsf{z}, \mathsf{z}^2, \mathsf{z}^3\}, \tag{9.56a}$$

$$T_{G^+}(G^+_\mathsf{y}) = \{1\}, \tag{9.56b}$$

$$T_{G^+}(G^+_\mathsf{z}) = \{1\}. \tag{9.56c}$$

With the transversals appropriately chosen, Eq. (9.52) gives the following Wyckoff positions in the unit cell:

- $V^{\mathrm{cell}}_\mathsf{x}$, the two-fold rotation symmetric vertices of the fundamental Schwarz triangle and the triangles rotated by $\frac{\pi}{8}$, $\frac{2\pi}{8}$, and $\frac{3\pi}{8}$ around the origin of the unit cell, and
- $V^{\mathrm{cell}}_\mathsf{y}$ and $V^{\mathrm{cell}}_\mathsf{z}$, the two eight-fold rotation symmetric vertices of the fundamental Schwarz triangle, respectively.

They are shown in Fig. 9.6a together with the $\{8,8\}$ lattice obtained by interpreting $V^{\mathrm{lat}}_\mathsf{y}$ as vertices, $V^{\mathrm{lat}}_\mathsf{x}$ as edges, and $V^{\mathrm{lat}}_\mathsf{z}$ as plaquettes, and the unit cell.

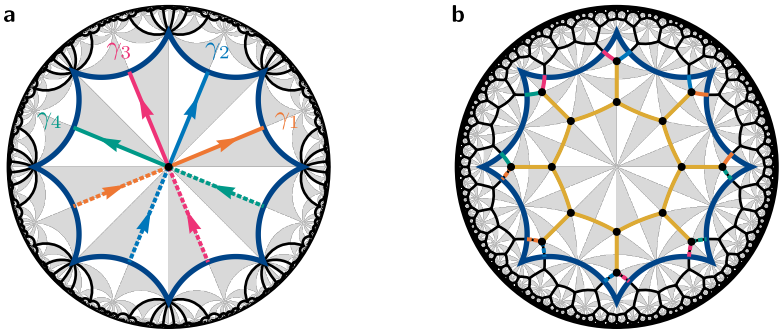

Figure 9.7.: Graph representation of hopping Hamiltonian. The graph representation of the nearest-neighbor hopping Hamiltonian on (**a**) the $\{8,8\}$ and (**b**) the $\{8,3\}$ lattice. Lattice sites (orbitals) are shown as black disks, the unit cell as a dark blue polygon and the edges representing hopping processes $h^{uv}(\gamma)$ are colored according to their corresponding translation γ with $\gamma = 1$ shown in yellow, γ_1, γ_2, γ_3, and γ_4 in orange, blue, magenta, and green, respectively. Edges crossing the unit cell are continued as dashed lines on the translation-related side of the unit cell.

We next turn to $\Delta^+(2,3,8)$, for which we use our GAP software package [318] and do not give explicit expressions. With $|G^+| = 48$, $|G^+_{\mathsf{x}}| = 2$, $|G^+_{\mathsf{y}}| = 3$, and $|G^+_{\mathsf{z}}| = 8$, we find that

$$|V^{\text{cell}}_{\mathsf{x}}| = 24, \qquad |V^{\text{cell}}_{\mathsf{y}}| = 16, \qquad |V^{\text{cell}}_{\mathsf{z}}| = 6, \tag{9.57}$$

such that the $\{8,3\}$ lattice has 16 sites and six plaquettes per unit cell. Figure 9.6b shows all 48 Wyckoff positions including the derived $\{8,3\}$ lattice with its 16 sites (orange disks) and six plaquettes.

9.3.2. Hopping Hamiltonian

We now develop the formalism for defining hopping Hamiltonians on hyperbolic lattices, based on the algebraic description of the lattice introduced above. To do so, we assume a generic model with orbitals $u = (\mathsf{w}, [g_{u_{\mathsf{w}}}]_{\mathsf{w}})$ at certain Wyckoff positions in the unit cell C with translation group Γ and hopping amplitude $h^{uv}(\gamma)$ for hopping from orbital v in the unit cell to orbital u in the unit cell translated by γ. Using the decomposition given in Eqs. (9.51) and (9.52), the corresponding Hamiltonian can be written as

$$\mathcal{H} = \sum_{\check{\gamma},\gamma' \in \Gamma} \sum_{u,v} h^{uv}\left(\check{\gamma}\gamma'^{-1}\right) c^{u\dagger}_{\check{\gamma}} c^{v}_{\gamma'}, \tag{9.58}$$

where $c_\gamma^{u\dagger}$ is the creation operator for the orbital u in the unit cell γ. Note that the more generic amplitude $h^{uv}(\breve{\gamma}, \gamma')$ simplifies to $h^{uv}(\breve{\gamma}\gamma'^{-1})$ due to translation invariance. Alternatively, we can rewrite the sum over $\breve{\gamma}, \gamma'$ as a sum over γ' and $\gamma = \breve{\gamma}\gamma'^{-1}$:

$$\mathcal{H} = \sum_{\gamma,\gamma'\in\Gamma} \sum_{u,v} h^{uv}(\gamma)\, c^u_{\gamma\gamma'}{}^\dagger c^v_{\gamma'}, \tag{9.59}$$

where γ now indicates the relative translation of the unit cell containing orbital u to the one containing orbital v. This Hamiltonian can be interpreted as a compact graph, with the orbitals in the unit cell as vertices and edges with weights $(h^{uv}(\gamma), \gamma)$, where γ determines the range of the hopping. Such graphs are illustrated in Figs. 9.7a and 9.7b for the nearest-neighbor hopping model on the $\{8,8\}$ and $\{8,3\}$ lattice, respectively.

To restrict to the finite PBC cluster characterized by Γ_{PBC}, where Bravais lattice sites, i.e., unit cells, are labeled by cosets in $\Gamma/\Gamma_{\text{PBC}}$ instead of elements of Γ, we replace the creation and annihilation operators $c_\gamma^{u(\dagger)}$ by $c^u_{[\gamma]_{\text{PBC}}}{}^{(\dagger)}$, such that Eq. (9.59) becomes

$$\mathcal{H}_{\text{PBC}} = \sum_{[\gamma']_{\text{PBC}}\in\Gamma/\Gamma_{\text{PBC}}} \sum_{\gamma\in\Gamma} \sum_{u,v} h^{uv}(\gamma)\, c^u_{[\gamma\gamma']_{\text{PBC}}}{}^\dagger\; c^v_{[\gamma']_{\text{PBC}}}. \tag{9.60}$$

Note that the argument of h^{uv} is *not* replaced by a coset; this accounts for long-range hopping processes exceeding the extent of the PBC cluster. To make this more concrete, we can choose a transversal $T_\Gamma(\Gamma_{\text{PBC}})$ of the quotient group and sum over its $N = |\Gamma : \Gamma_{\text{PBC}}|$ elements $\eta_i \in T_\Gamma(\Gamma_{\text{PBC}})$:

$$\mathcal{H}_{\text{PBC}} = \sum_{i=1}^{N} \sum_{\gamma\in\Gamma} \sum_{u,v} h^{uv}(\gamma)\, c^u_{[\gamma\eta_i]_{\text{PBC}}}{}^\dagger\; c^v_{[\eta_i]_{\text{PBC}}}. \tag{9.61}$$

9.4. Hyperbolic band theory

In Section 2.3.2, we have seen that in Euclidean space, translational symmetry leads to the Bloch theorem, constraining the form of Hamiltonian eigenstates and leading to a reciprocal-space description. Despite the non-Abelian nature of hyperbolic translation groups, it turns out that a generalized *automorphic Bloch theorem* [64] involving one- and higher-dimensional irreducible representations of the translation group can be proven. We first review the automorphic Bloch theorem and the mathematical structure of hyperbolic reciprocal space in Section 9.4.1, then discuss how it implies a description in terms of a Bloch

Hamiltonian defined in hyperbolic reciprocal space in Section 9.4.2. In Section 9.4.3 we discuss how to explicitly construct 1D irreducible representations and the resulting approximation, termed *Abelian hyperbolic band theory*. We apply it to the two simple examples of constant-hopping nearest-neighbor models on the $\{8,8\}$ and $\{8,3\}$ lattice and compare the resulting density of states to the one obtained on finite flakes with open boundary conditions.

9.4.1. Automorphic Bloch theorem

As in the Euclidean case, eigenstates of a translation-invariant Hamiltonian must transform according to representations of the corresponding translation group Γ. Let $\gamma \in \Gamma$, $\mathscr{D}$ the unitary representation of Γ acting on the Hilbert space according to which the eigenstate vector $\psi_{\mathscr{D}}$ transforms, and $\gamma(z)$ the action of γ on coordinates z in the Poincaré disk, then

$$\psi_{\mathscr{D}}(\gamma^{-1}(z)) = \mathscr{D}(\gamma)\psi_{\mathscr{D}}(z). \tag{9.62}$$

This is the automorphic Bloch theorem [64]. By repeating the calculation in Eq. (2.37), we can see that Eq. (9.62) is compatible with the choice of periodic boundary conditions described in Section 9.2.2. The periodic boundary condition due to a normal subgroup $\Gamma_{\text{PBC}} \lhd \Gamma$ is the constraint $\psi_{\mathscr{D}}(\gamma_{\text{PBC}}^{-1}(z)) = \psi_{\mathscr{D}}(z)$, i.e., $\mathscr{D}(\gamma_{\text{PBC}}) = \mathbb{1}$ for all $\gamma_{\text{PBC}} \in \Gamma_{\text{PBC}}$. With that, Eq. (9.62) implies that for any $\gamma \in \Gamma$ and $\gamma_{\text{PBC}} \in \Gamma_{\text{PBC}}$ the following holds:

$$\begin{aligned}\psi_{\mathscr{D}}(\gamma\gamma_{\text{PBC}}^{-1}\gamma^{-1}(z)) &= \mathscr{D}(\gamma\gamma_{\text{PBC}}\gamma^{-1})\psi_{\mathscr{D}}(z)\\ &= \mathscr{D}(\gamma)\mathscr{D}(\gamma_{\text{PBC}})\mathscr{D}(\gamma)^{-1}\psi_{\mathscr{D}}(z)\\ &= \mathscr{D}(\gamma)\mathscr{D}(\gamma)^{-1}\psi_{\mathscr{D}}(z)\\ &= \psi_{\mathscr{D}}(z),\end{aligned} \tag{9.63}$$

which holds if $\gamma\gamma_{\text{PBC}}^{-1}\gamma^{-1} \in \Gamma_{\text{PBC}}$, i.e., if $\Gamma_{\text{PBC}} \lhd \Gamma$.

The crucial difference to the Euclidean case is that, here, $\mathscr{D}$ generally decomposes into unitary irreducible representations D with dimension $d \geq 1$, $D : \Gamma \mapsto \mathsf{U}(d)$, such that eigenstates of the Hamiltonian belong to d-fold degenerate multiplets that mix under translations. We can then define hyperbolic reciprocal space as the space of irreducible representations of Γ, which contains a tower of Brillouin zones $\text{BZ}^{(1,d)}$, each encompassing d-dimensional irreducible representations. Here, the first number in the superscript denotes the translation group under consideration and 1 indicates the full translation group Γ; the relevance of this part of the notation will become clear in the next chapter. The structure of $\text{BZ}^{(1,d)}$ for $d > 1$ differs vastly from the one of $\text{BZ}^{(1,1)}$. The latter, being the space of 1D irreducible representations, forms a $2\mathfrak{g}$-dimensional torus

$\mathsf{T}^{2\mathfrak{g}}$, known as the Jacobian variety of the Riemann surface $\Sigma_\mathfrak{g}$ on which the lattice is compactified. The space $\mathsf{T}^{2\mathfrak{g}}$ can be parametrized by generalized Bloch phase factors similar to the Euclidean case.More generally, $\mathrm{BZ}^{(1,d)}$ is a so-called *moduli space* $\mathcal{M}(\Sigma_\mathfrak{g}, \mathsf{U}(d))$, a well-known object in algebraic geometry. For $d > 1$, the moduli space does not admit the simple toroidal structure of $\mathcal{M}(\Sigma_\mathfrak{g}, \mathsf{U}(1))$. While the abstract mathematical structure of $\mathcal{M}(\Sigma_\mathfrak{g}, \mathsf{U}(d))$ is well-understood, there exist no explicit parametrizations for $d > 1$.

9.4.2. Bloch Hamiltonian

This subsection is largely based on the supplement to the publication "Non-Abelian hyperbolic band theory from supercells" [5]. Segments with significant text overlap with the published version may be subject to copyright by the American Physical Society.

The automorphic Bloch theorem implies a basis that block-diagonalizes the Hamiltonian into blocks defined by irreducible representations of the translation groups. These blocks, which we derive in this subsection, are generalizations of the Euclidean Bloch Hamiltonian. Note that the Bloch Hamiltonian depends on the choice of unit cell C, i.e., translation group Γ. To avoid dealing with an infinite-dimensional Hilbert space, we first restrict to a finite but large supercell (PBC cluster) made up of N copies of unit cells and only at the end take the limit $N \to \infty$ to recover the infinite lattice. As discussed in Section 9.2.2, in order to achieve convergence to the thermodynamic limit, this requires us to consider a sequence of normal subgroups $\Gamma^{(n)} \lhd \Delta^+$ satisfying Eq. (9.40), resulting in a sequence of supercells $C^{(n)}$. For each supercell $C^{(n)}$, this reduces the full translation group $\Gamma = \Gamma^{(1)}$ to the quotient group $\Gamma/\Gamma^{(n)}$, such that we avoid dealing with the former infinite group. The result is a discretization of reciprocal space in terms of irreducible representations of $\Gamma/\Gamma^{(n)}$, which, according to Refs. 75, 302, approximates the space of the irreducible representations of Γ, i.e., the full reciprocal space, and converges to the latter for $n \to \infty$.

Starting from Eq. (9.61) with $\Gamma_{\mathrm{PBC}} = \Gamma^{(n)}$, we now derive the corresponding Bloch Hamiltonian implementing the translational symmetry due to the finite translation group $\Gamma/\Gamma^{(n)}$. With $\eta_j \in T_\Gamma(\Gamma^{(n)})$, $[\eta_j] \in \Gamma/\Gamma^{(n)}$, and $N = \left|\Gamma : \Gamma^{(n)}\right|$, the Hamiltonian reads

$$\mathcal{H}_{n\text{-PBC}} = \sum_{j=1}^{N} \sum_{\gamma\in\Gamma} \sum_{u,v} h^{uv}(\gamma)\, c^{u}_{[\gamma\eta_j]}{}^{\dagger}\, c^{v}_{[\eta_j]}. \tag{9.64}$$

Due to the (disjoint) coset decomposition

$$\Gamma = \bigcup_{i=1}^{N} \eta_i \Gamma^{(n)}, \tag{9.65}$$

translating the Bravais site j by $\gamma \in \Gamma$ maps to a site i with

$$\gamma \eta_j \Gamma^{(n)} = \eta_i \Gamma^{(n)}, \tag{9.66}$$

which defines an action of Γ on the cosets in $\Gamma/\Gamma^{(n)}$: $[\gamma\eta_j] = [\eta_i]$. Thus, the creation (annihilation) operator at translated sites can be expanded as follows [64] (note that in contrast to Ref. 64, we are using right cosets):

$$c^{u\ \dagger}_{[\gamma\eta_j]} = \sum_i c^{u\ \dagger}_{[\eta_i]}\, \mathcal{U}_{ij}\left([\gamma]\right), \tag{9.67}$$

where the matrices

$$\mathcal{U}_{ij}\left([\gamma]\right) = \delta_{[\eta_i],[\gamma\eta_j]} \tag{9.68}$$

form the so-called *regular representation* of $\Gamma/\Gamma^{(n)}$. The regular representation can be decomposed into a direct sum of all irreducible representations $D^{(\lambda)}$, each appearing with multiplicity equal to their dimension d_λ [64], i.e., there exists a unitary transformation $\mathcal{P}$ such that

$$\mathcal{P}\mathcal{U}\left([\gamma]\right)\mathcal{P}^{-1} = \bigoplus_{\lambda=1}^{\mathcal{N}} d_\lambda D^{(\lambda)}\left([\gamma]\right), \tag{9.69}$$

where $\mathcal{N} < N^{(n)}$ is the number of conjugacy classes of $\Gamma/\Gamma^{(n)}$ and $\sum_{\lambda=1}^{\mathcal{N}} d_\lambda^2 = N^{(n)}$.

The above implies that $\mathcal{H}_{n\text{-PBC}}$ can be written in terms of those blocks:

$$\begin{aligned}
\mathcal{H}_{n\text{-PBC}} &= \sum_{i,j=1}^{N} \sum_{\gamma\in\Gamma} \sum_{u,v} h^{uv}(\gamma)\, c^{u\ \dagger}_{[\eta_i]}\, \mathcal{U}_{ij}\left([\gamma]\right) c^{v}_{[\eta_j]} \\
&= \sum_{k,l} \sum_{u,v} \left(\sum_i \mathcal{P}_{ki} c^{u}_{[\eta_i]} \right)^{\dagger} \sum_{\gamma\in\Gamma} h^{uv}(\gamma) \left(\bigoplus_{\lambda=1}^{\mathcal{N}} d_\lambda D^{(\lambda)}\left([\gamma]\right) \right)_{kl} \sum_j \mathcal{P}_{lj} c^{v}_{[\eta_j]} \\
&= \sum_{k,l} \sum_{u,v} \hat{c}^{u\dagger}_{k} \left(\bigoplus_{\lambda=1}^{\mathcal{N}} d_\lambda \sum_{\gamma\in\Gamma} h(\gamma) \otimes D^{(\lambda)}\left([\gamma]\right) \right)^{uv}_{kl} \hat{c}^{v}_{l},
\end{aligned} \tag{9.70}$$

with

$$\hat{c}^{u}_{k} = \sum_i \mathcal{P}_{ki} c^{u}_{[\eta_i]}. \tag{9.71a}$$

We recognize the Bloch Hamiltonian

$$H(D) = \sum_{\gamma\in\Gamma} h(\gamma) \otimes D\left([\gamma]\right) \tag{9.71b}$$

with the hopping matrix $h(\gamma)$ on the unit cell C having components $h^{uv}(\gamma)$, such that

$$\mathcal{H}_{n\text{-PBC}} = \sum_{k,l}\sum_{u,v} \hat{c}_k^{u\dagger} \left(\bigoplus_{\lambda=1}^{\mathcal{N}} d_\lambda H(D)\right)_{kl}^{uv} \hat{c}_l^v. \tag{9.71c}$$

Finally, we take the limit $n \to \infty$, i.e., we let the supercell $C^{(n)}$ encompass the whole infinite lattice. Formally, this implies the replacement of $\Gamma/\Gamma^{(n)}$ by Γ, such that Eq. (9.59) is block-diagonalized as

$$\mathcal{H} = \sum_{k,l}\sum_{u,v} \hat{c}_k^{u\dagger} \left(\bigoplus_{\lambda} d_\lambda H\left(D^{(\lambda)}\right)\right)_{kl}^{uv} \hat{c}_l^v \tag{9.72a}$$

with Bloch Hamiltonian

$$H(D) = \sum_{\gamma\in\Gamma} h(\gamma) \otimes D(\gamma), \tag{9.72b}$$

where D is now an irreducible representation of Γ, and

$$\hat{c}_k^u = \sum_i \mathcal{P}_{ki} c_{\eta_i}^u. \tag{9.72c}$$

Let us remark that in Eq. (9.72a), we have kept the symbol "$\oplus$", even though in reality the direct sum now goes over a *continuous* space of infinitely many irreducible representations and a suitable measure over the representation space needs to be introduced [73].

In principal, diagonalizing $H(D)$ for all irreducible representations of Γ gives a full reciprocal-space description of the tight-binding model on the *infinite* lattice. However, in practice, as mentioned above, this is challenging due to the complicated structure of the spaces of irreducible representations of Γ. Thus, we next discuss the straightforward approximation of restricting to 1D irreducible representations.

9.4.3. Abelian hyperbolic band theory

The space of 1D irreducible representations, $\mathrm{BZ}^{(1,1)} = \mathcal{M}(\Sigma_\mathfrak{g}, \mathsf{U}(1))$, forms a $2\mathfrak{g}$-dimensional torus $\mathsf{T}^{2\mathfrak{g}}$ and can be interpreted physically as the set of

independent magnetic fluxes threading the $2\mathfrak{g}$ noncontractible cycles on $\Sigma_\mathfrak{g}$, analogous to the two noncontractible cycles of the compactified 2D Euclidean unit cell which forms a torus (distinct from the Brillouin zone torus) Σ_1. Thus, the *Abelian Brillouin zone* can be defined on the generators γ_i of Γ:

$$\mathrm{BZ}^{(1,1)} = \left\{\gamma_i \mapsto D_\mathbf{k}(\gamma_i) = \mathrm{e}^{\mathrm{i}k_i} \,:\, \mathbf{k} \in [0, 2\pi)^{2\mathfrak{g}} \cong \mathsf{T}^{2\mathfrak{g}}\right\}. \tag{9.73}$$

Restricting to a finite PBC cluster defined by $\Gamma^{(n)}$, only irreducible representations $D_\mathbf{k}$ satisfying $D_\mathbf{k}(\gamma^{(n)})$ for all $\gamma^{(n)} \in \Gamma^{(n)}$ are retained. This results in a discretization of $\mathrm{BZ}^{(1,1)}$ with momentum components k_i being rational multiples of 2π. The precise set of points $\mathbf{k}$ in the discretized Abelian Brillouin zone, however, depends on the details of the cluster and can be obtained by simultaneously diagonalizing the translation operators $\mathcal{U}([\gamma])$ defined in Eq. (9.68) [64].

With Eq. (9.73), we obtain the *Abelian Bloch Hamiltonian* from Eq. (9.72b):

$$H(\mathbf{k}) = \sum_{\gamma\in\Gamma} h(\gamma)\, \mathrm{e}^{\mathrm{i}\sum_{i=1}^{2\mathfrak{g}} K_i(\gamma)k_i}, \tag{9.74}$$

where $K_i(\gamma)$ is the number of times the generator γ_i appears in γ minus the number of times its inverse appears. Diagonalizing $H(\mathbf{k})$ for all $\mathbf{k} \in [0, 2\pi]^{2\mathfrak{g}}$ results in the Abelian band structure $\mathbf{k} \mapsto E_\alpha(\mathbf{k})$ with the band index α.

Note that, a priori, restricting to 1D irreducible representations is a rather crude approximation of the full reciprocal space and thus of the full band structure. Nevertheless, good agreement of Abelian hyperbolic band theory with bulk-projected spectra on flakes has been found in some models [6, 7, 319], while crucial features are missed in others [8]. Below we demonstrate how to obtain density of states for the constant-hopping nearest-neighbor models on the $\{8, 8\}$ and $\{8, 3\}$ using Abelian hyperbolic band theory.

Examples

To set up the Abelian Bloch Hamiltonian of the constant-hopping nearest-neighbor model on the $\{8, 8\}$ lattice, we need to construct the corresponding compactified graph of nearest neighbors on the unit cell. The unit cell has a single site, which, in contrast to Fig. 9.6a, we can place at the center of the octagonal unit cell. Then, the hopping matrix is a single number with $h(\gamma_i) = h(\gamma_i^{-1}) = -1$ for $i = 1, 2, 3, 4$ and otherwise zero and results in the Abelian Bloch Hamiltonian [64]

$$H(\mathbf{k}) = -\sum_{i=1}^{4} \mathrm{e}^{\mathrm{i}k_i} + \text{c.c.} = -2\sum_{i=1}^{4} \cos(k_i) = E(\mathbf{k}). \tag{9.75}$$

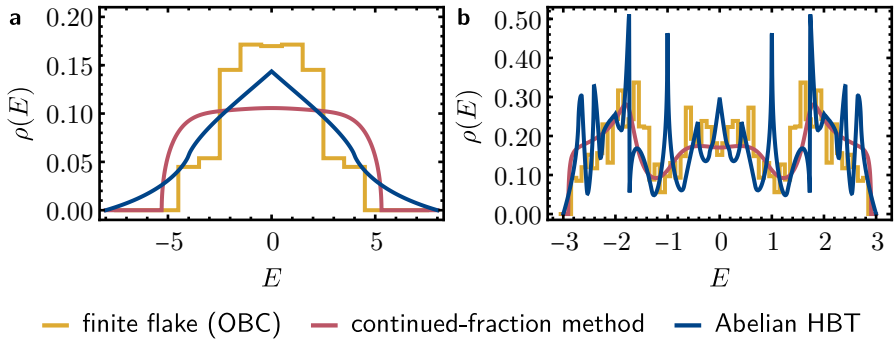

Figure 9.8.: Density of states from Abelian hyperbolic band theory. Density of states of the constant-hopping nearest-neighbor model on (**a**) the $\{8,8\}$ and (**b**) the $\{8,3\}$ lattice obtained from diagonalizing finite flakes with open boundary conditions (OBC) in yellow, from the continued-fraction method in red, and from Abelian hyperbolic band theory in blue.

The Abelian Bloch Hamiltonian can be obtained from the graph representation shown in Fig. 9.7a simply by multiplying each hopping amplitude $h^{uv}(\gamma_i)$ by $\mathrm{e}^{\mathrm{i}k_i}$. From that, we get the density of states [64, 76]

$$\rho(E) = \int_0^{2\pi} \frac{\mathrm{d}^4k}{(2\pi)^4} \delta(E(\mathbf{k}) - E) \tag{9.76}$$

$$= \frac{1}{\pi} \int_0^{\infty} \mathrm{d}\epsilon \, \mathcal{J}_0(2\epsilon)^4 \cos(\epsilon E), \tag{9.77}$$

where $\mathcal{J}_0$ is the Bessel function of the first kind. The result is shown in Fig. 9.8a and compared to the data obtained from diagonalizing finite flakes with open boundary conditions (previously shown in Fig. 9.3a) and via the continued-fraction method (previously shown in Fig. 9.4a).

Analogously, we construct the Abelian Bloch Hamiltonian for the constant-hopping nearest-neighbor model on the $\{8,3\}$ lattice, whose graph representation is shown in Fig. 9.7b; the resulting density of states is presented in Fig. 9.4b. The translation group is the same as the one of the $\{8,8\}$ lattice, such that the Abelian Brillouin zone is again 4D with momenta k_1, k_2, k_3, k_4. For both lattices, we observe that while the broad features of the density of states obtained from the three methods agree, there are significant deviations. On the one hand, the data obtained from Abelian hyperbolic band theory (blue) shows spurious peaks and dips, on the other hand there is clearly nonvanishing

density of states outside the range predicted by the continued-fraction method (red). Interestingly, the finite-size effects present in the data obtained from finite flakes (yellow) does mimic some of the spurious features seen in the results obtained from Abelian hyperbolic band theory. While this is difficult to disentangle from bin-size related effects, we speculate that it might be related to the fact that the higher-dimensional irreducible representations that dominate [5, 76] the spectrum in the thermodynamic limit are less prominent because the finite flakes cannot support them [320]. This is consistent with the findings of Ref. 64 that the spectra of small PBC clusters usually have a high fraction of Abelian states.

9.5. Hyperbolic band topology

So far we have only discussed simple constant-hopping nearest neighbor models on hyperbolic lattices. However, with the formalism introduced in Section 9.3.2, it is straightforward to define more complicated tight-binding models. If we restrict to finite-range hopping processes, we simply need to fix the matrices $h(\gamma)$ for a finite number of $\gamma \in \Gamma$, which allows us to introduce, for instance, next-nearest-neighbor hoppings and hopping amplitudes with phases, as long as the translational symmetry Γ is preserved. This allows us to study *hyperbolic matter*, i.e., tight-binding models realizing interesting physics on hyperbolic lattices. Note that such complicated hoppings can still be realized in metamaterials and this has been done in electric-circuit networks [321–324].

Of particular interest are models showing nontrivial band topology; the reason for that interest is two-fold. On the one hand, the intricate structure of hyperbolic reciprocal space rooted in the nonvanishing curvature has consequences for the set of topological invariants. For instance, focusing on the Abelian Brillouin zone, a 2D hyperbolic lattice has 4D momentum space permitting topological invariants that only occur in higher dimensions of Euclidean space. On the other hand, the bulk-boundary correspondence, a characteristic feature of band topology, is severely impacted by the fact that the boundary of a hyperbolic lattice can make up a macroscopic part of the system. If similar bulk-boundary correspondences exist for hyperbolic lattices, and we will see that they do, this can potentially be useful for applications making use of topological boundary states, such as topological lasing, because a large boundary-to-bulk ratio is desirable for large efficiency.

Several models with band topology have been proposed, studied and even realized experimentally. First and foremost, the paradigmatic Haldane model of a Chern insulator [96], originally defined on the honeycomb lattice, has been generalized to hyperbolic lattices [6, 7, 306, 307, 321, 323] demonstrating the

existence of hyperbolic topological insulators and robust chiral edge states protected by the Chern number. Additionally, the hyperbolic Haldane model has been realized in an electric circuit network [321], making use of the platform we introduced in Ref. 4 and discussed in Section 8.4.1. Doubling the hyperbolic Haldane model results in the *hyperbolic Kane-Mele model* [6, 307] realizing a time-reversal-symmetric topological insulator with robust helical edge states protected by time-reversal symmetry. Further, Hofstadter butterflies on hyperbolic lattices have been studied [325] and it has been found that while the universality persists, there is no fractal structure.

Besides first-order topological insulators, higher-order topology has been investigated. Adding a time-reversal-breaking mass term on the boundary of a first-order topological insulator gaps out the gapless boundary state. A sign change of the mass term introduces a domain wall that binds a topological zero-energy state according to the Jackiw-Rebbi mechanism [326]. This was demonstrated in hyperbolic lattices [306] starting from a generalization of the Bernevig-Hughes-Zhang model [327]. Following the same procedure, Ref. 305 related the appearance of those zero-energy states to the quadrupole moment and to exotic rotational symmetry of order higher than six.

Finally, the fact that Abelian momentum space has dimension larger or equal to four implies the existence of *second Chern numbers* which usually appear in the four-dimensional generalization of the quantum Hall effect and are defined on 4D manifolds in momentum space. A model exhibiting a nontrivial second Chern number can be obtained by reinterpreting the Dirac tight-binding model of a 4D quantum Hall insulator on a 2D hyperbolic $\{8, 8\}$ lattice [8, 322]. Such a model has been experimentally realized in electric circuit networks [322] and proposed as a topological insulator. However, studies of the non-Abelian Bloch states show that this model is instead a hyperbolic *non-Abelian* semimetal [8], as we will show in Section 10.4.6.

Below, we discuss two of the models mentioned above in more detail: the Haldane model of a Chern insulator on the $\{8, 3\}$ lattice from Ref. 6 in Section 9.5.1, and the Dirac model on the $\{8, 8\}$ lattice with nontrivial second Chern number from Ref. 8 in Section 9.5.2. For each, we define the model on the unit cell and briefly summarize the results. Here, we focus on Abelian hyperbolic band theory, supported by results obtained in real space. Since Abelian hyperbolic band theory is not complete, we will revisit both models in the next chapter and study the missing non-Abelian Bloch states. We will show that the topological gaps found in the Haldane model are indeed stable to the addition of non-Abelian Bloch states, while the gap in the Dirac model is not, leading to a hyperbolic semimetal protected by the second Chern number.

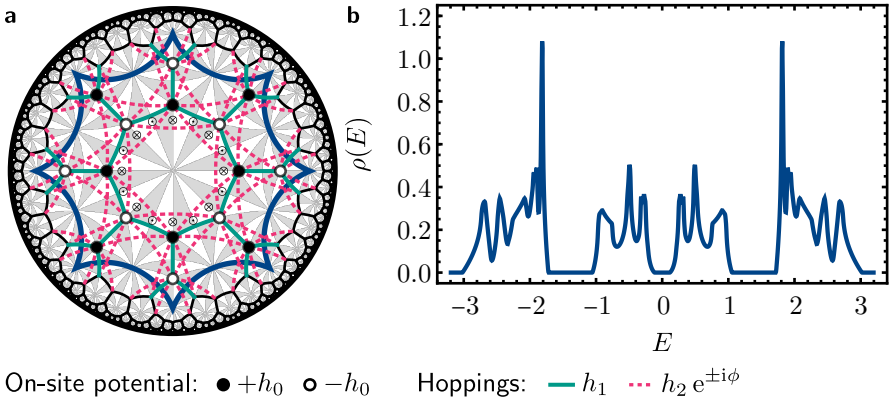

Figure 9.9.: Haldane model on the $\{8,3\}$ lattice. (**a**) Definition of the Haldane model with staggered sublattice potential $\pm h_0$ (filled/empty disks), nearest-neighbor hoppings h_1 (solid green lines), and next-nearest neighbor hoppings $h_2\mathrm{e}^{\pm\mathrm{i}\Phi}$ (dashed magenta lines; see legend at the bottom). The sign of the phase of the latter is positive for anticlockwise hopping on each octagonal plaquette, resulting in the alternating pattern of fluxes $\pm\Phi$ indicated in the central octagon with the symbols $\odot$ and $\otimes$. (**b**) Density of states obtained from Abelian hyperbolic band theory by randomly sampling the Abelian Brillouin zone with 10^8 points and an energy resolution of 0.005. The data has been smoothed with a moving average with window 0.01.

9.5.1. Haldane model on the $\{8,3\}$ lattice

To generalize the Haldane model originally defined on the honeycomb lattice [96], we simply replace the hexagons, for instance, by octagons, but keep the rest of the construction: nearest-neighbor hoppings h_1 along the sides of the polygon, next-nearest neighbor hoppings with magnitude h_2 and phases $\mathrm{e}^{\pm\mathrm{i}\Phi}$ when going counterclockwise around each polygon, resulting in the typical alternating pattern of fluxes $\pm\Phi$ and vanishing total flux per plaquette. While this construction can more generally be applied to a wide range of hyperbolic lattices [7], we here focus on the $\{8,3\}$ lattice, on which the hyperbolic Haldane model was originally studied [6, 307, 321]. The Hamiltonian takes the form [7]

$$\mathcal{H} = h_1 \sum_{\langle i,j\rangle} \left(c_i^\dagger c_j + \mathrm{h.c.}\right) + h_2 \sum_{\overleftarrow{ij}} \left(\mathrm{e}^{\mathrm{i}\Phi} c_i^\dagger c_j + \mathrm{h.c.}\right) + h_0 \left(\sum_{i\in A} c_i^\dagger c_i - \sum_{i\in B} c_i^\dagger c_i\right) \tag{9.78}$$

where $\overleftarrow{ij}$ denotes hopping from site j to i in mathematically positive direction (counterclockwise) for a given octagon and Φ is the flux parameter. Additionally, there is a staggered sublattice potential, also known as *sublattice mass* $\pm h_0$ on the two sublattices A and B (filled and empty sites in the figure). According to Eq. (9.59), this defines the hopping matrix $h(\gamma)$ on the unit cell, which is nonvanishing only for $\gamma = 1$ and for $\gamma = \gamma_i^{(-1)}$, $i = 1, 2, 3, 4$.

The dependence on the flux Φ has been analyzed in Refs. 6, 7; here, we focus on the choice of parameters eventually made by Ref. 6: $h_1 = 1$, $h_2 = 1/6$, $\Phi = \pi/2$, and $h_0 = 1/3$. With that choice, the bulk spectrum has three gaps, as can be seen in the density of states obtained using Abelian hyperbolic band theory shown in Fig. 9.9b. Recall from Section 9.4.3 that the Abelian Brillouin zone of the $\{8, 3\}$ lattice is four dimensional, such that the Abelian Bloch Hamiltonian defined in Eq. (9.74) takes the form

$$H(\mathbf{k}) = h(1) + \sum_{j=1}^{4} h(\gamma_j)\, \mathrm{e}^{\mathrm{i}k_j} + \text{h.c.}, \tag{9.79}$$

with $\mathbf{k} = (k_1, k_2, k_3, k_4)$. In the 4D Abelian Brillouin zone, first Chern numbers can be defined in the six planes spanned by pairs (k_i, k_j), which are all related by symmetry (differing in their sign) [7]. Crucially, using Wilson loop calculations, these first Chern numbers are found to be *nontrivial* when the chemical potential is placed in one of the outer gaps, but they vanish for the gap at $E = 0$. Further, computing the real-space Chern number [328], which does not rely on translational symmetry, consistent results are obtained: the real-space Chern number is -1 for the outer two gaps but 0 for the gap at $E = 0$.

To probe the bulk-boundary correspondence [6], one can adopt open boundary conditions. This reveals a finite (boundary) density of states in the outer two gaps but a vanishing one in the gap at $E = 0$. In Section 10.4.4, we verify that none of those presumed boundary states arises due to non-Abelian Bloch states, i.e., that these are true boundary states. We have performed three checks to corroborate their topological origin. First, unitary time evolution of a wave packet localized in a region on the boundary and spectrally localized in the appropriate gap results in chiral propagation around the boundary. Snapshots of such a time evolution are shown in Fig. 9.10a. Second, by computing overlaps of the boundary states with the Laplace-Beltrami operator, each state can be ascribed an angular momentum, as described in Section 8.3.2 around Eq. (8.49). The angular-momentum dispersion thus extracted is shown in Fig. 9.10b and clearly shows a chiral in-gap state connecting valence to conductance band. Its slope matches the propagation speed of the wave packet. Third, introducing random on-site disorder does neither change the localization

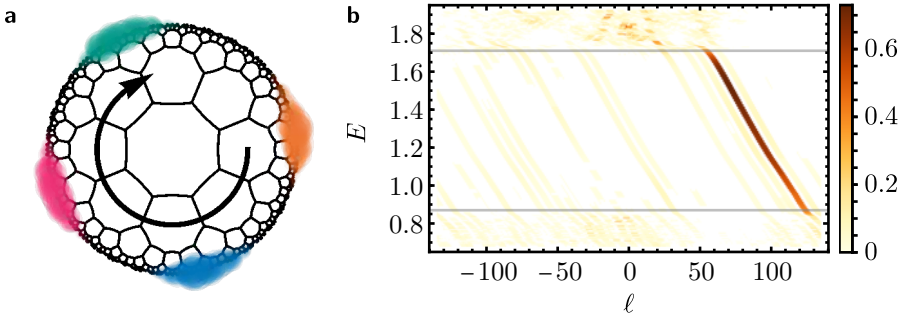

Figure 9.10.: Topological boundary states of the $\{8,3\}$ Haldane model. (**a**) Snapshots of the time evolution of a Gaussian wave packet initialized as a superposition of the (boundary) states within an energy window of width 0.025 around 1.3 on a flake with 1864 sites. The wave packet is shown in orange, blue, magenta, green for 0, 250, 500, 750 time steps (in units of inverse energy). (**b**) The overlap (encoded by the color) of eigenstates at energy E with eigenfunctions of the Laplace-Beltrami operator with angular momentum ℓ on a flake with 896 sites reveals the linear boundary-state dispersion (red line). The gray horizontal lines indicate the energy gap; the data is artificially coarse-grained by a factor of 2 for better visibility. Data reproduced from Ref. [6].

property of the boundary states under consideration and nor perturb the chiral propagation of the wave packet. These observations strongly indicate that the boundary states are topological, thereby establishing a bulk-boundary correspondence between the first Chern number and chiral boundary states in hyperbolic lattices.

9.5.2. Dirac model on the $\{8,8\}$ lattice

The hyperbolic Dirac model is inspired by the tight-binding model for a 4D Euclidean quantum Hall insulator [329, 330] with Hamiltonian

$$\mathcal{H} = \sum_i \sum_{j=1}^{4} \left(\frac{\mathbb{\Gamma}_5 + \mathrm{i}\mathbb{\Gamma}_j}{2} c^\dagger_{i+e_j} c_i + \mathrm{h.c.} \right) + m \sum_i \mathbb{\Gamma}_5 c^\dagger_i c_i, \tag{9.80}$$

with $\mathbb{\Gamma}_j$, $j = 1, \ldots, 5$, the five Gamma matrices satisfying the $\mathsf{SO}(5)$ Clifford algebra $\{\mathbb{\Gamma}_i, \mathbb{\Gamma}_j\} = 2\delta_{ij}\mathbb{1}$ and $i + e_j$ denoting the nearest-neighbor of site i in one of the four orthogonal directions $j = 1, 2, 3, 4$. We use the following

representation in terms of Pauli matrices σ_i

$$\mathbb{\Gamma}_1 = \sigma_1\sigma_0, \tag{9.81a}$$
$$\mathbb{\Gamma}_2 = \sigma_2\sigma_0, \tag{9.81b}$$
$$\mathbb{\Gamma}_3 = \sigma_3\sigma_1, \tag{9.81c}$$
$$\mathbb{\Gamma}_4 = \sigma_3\sigma_2, \tag{9.81d}$$
$$\mathbb{\Gamma}_5 = \sigma_3\sigma_3, \tag{9.81e}$$

which ensures that $\mathbb{\Gamma}_j$ is real (imaginary) for j odd (even). The $\mathbb{\Gamma}_j$ act on the four components of the c_i which correspond to internal/orbital degrees of freedom at site $i \in \mathbb{Z}^4$. Viewing the four directions as hyperbolic translations, i.e., $i + e_i \mapsto \gamma_j(z_i)$, Eq. (9.80) can be easily reinterpreted [8] as a tight-binding model on the $\{8,8\}$ lattice, whose translation group has four generators γ_i:

$$\mathcal{H} = \sum_{\gamma\in\Gamma}\sum_{j=1}^{4}\left(\frac{\mathbb{\Gamma}_5 + \mathrm{i}\mathbb{\Gamma}_j}{2}c^\dagger_{\gamma_j\gamma}c_\gamma + \text{h.c.}\right) + m\sum_{\gamma\in\Gamma}\mathbb{\Gamma}_5 c^\dagger_\gamma c_\gamma. \tag{9.82}$$

Figure 9.11a illustrates the relevant hopping processes.

The Abelian Bloch Hamiltonian takes the form

$$H(\mathbf{k}) = \sum_{j=1}^{4}\sin(k_j)\mathbb{\Gamma}_j + \left(m + \sum_{j=1}^{4}\cos(k_j)\right)\mathbb{\Gamma}_5, \tag{9.83}$$

which evidently is equivalent to the (full) Bloch Hamiltonian of the original 4D Euclidean model. In particular, this immediately implies that, as in the Euclidean case, at half-filling the model undergoes topological phase transitions at $|m| = 0, 2, 4$ and otherwise has an energy gap at $E = 0$ with a nontrivial second Chern number. The density of Abelian Bloch states for $m = 3$ is shown in Fig. 9.11b, where we recognize the clear energy gap. However, in Section 10.4.6, we will show that this energy gap is filled with non-Abelian Bloch states and that the model is not insulating but rather a topological semimetal.

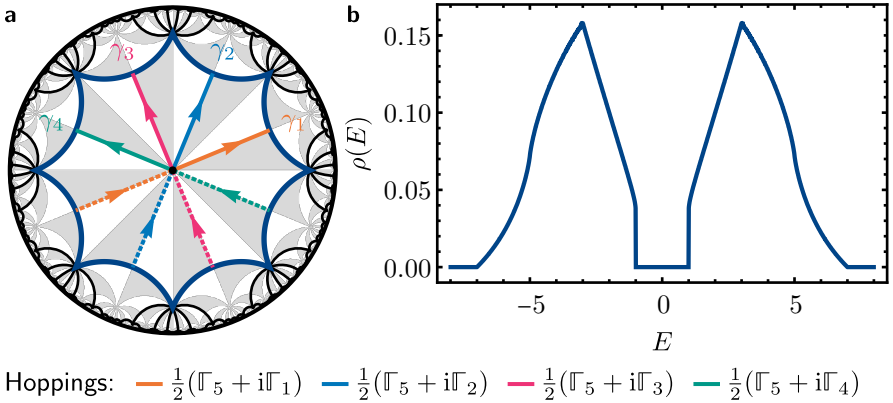

Figure 9.11.: Dirac model on the $\{8,8\}$ lattice. (**a**) Definition of the Dirac model with four orbitals at the single central site of the $\{8,8\}$ lattice (black disk) coupled by hopping matrices $h(\gamma_j) = \frac{1}{2}(\mathbb{\Gamma}_5 + \mathrm{i}\mathbb{\Gamma}_j)$ (see legend) and an on-site mass term $h(1) = m\mathbb{\Gamma}_5$. The hoppings (colored arrows) are shown in a single unit cell (blue polygon): if they leave the unit cell, the part entering from the translation-related side is shown as a dashed line. (**b**) Density of states obtained from Abelian hyperbolic band theory for $m = 3$ by randomly sampling the Abelian Brillouin zone with 10^9 points and an energy resolution of 0.005. The data has been smoothed with a moving average with window 0.01.

10. Supercell method

This chapter is largely based on the publication "Non-Abelian hyperbolic band theory from supercells" [5]. Segments with significant text overlap with the published version may be subject to copyright by the American Physical Society.

In the previous chapter, we have seen that applying the automorphic Bloch theorem introduced in Section 9.4.1 to hyperbolic lattices is not as straightforward as in the Euclidean case. The presence of non-Abelian Bloch states due to higher-dimensional irreducible representations of the translation group and the lack of explicit parametrizations of those states poses a challenge to a complete reciprocal-space description. Restricting to the Abelian Bloch states, which are easily parametrized by generalized Bloch phase factors, is possible but clearly not sufficient, as we have seen in Section 9.4.3. Indeed, Ref. 76 argues, based on results obtained in real space using the continued fraction method reviewed in Section 9.2.1, that 1D irreducible representations have vanishing weight in the total density of states in the thermodynamic limit. While strictly speaking the relevant irreducible representations in the infinite lattice are infinite-dimensional, this does not preclude approximations based on finite-dimensional irreducible representations.

In this chapter, based on our original work [5], we introduce the *supercell method* to gain systematic access to non-Abelian Bloch states through the application of Abelian hyperbolic band theory combined to particular sequences of unit cells. We describe how such sequences can be constructed for various hyperbolic $\{p, q\}$ lattices using results from geometric group theory [301] and tools from computational group theory. Crucially, and in contrast to previous methods [75, 76, 302], as a reciprocal-space approach, the supercell method results in a description in terms of bulk states of the infinite lattice labeled by translation quantum numbers, i.e., momenta. Further, our method is computationally more efficient than real-space methods and we demonstrate convergence of the density of states to the thermodynamic limit.

We start by motivating the use of supercells in Section 10.1, before describing their systematic construction and how to extend models defined on a single primitive cell to supercells in Section 10.2. Next, in Section 10.3, we turn to the interpretation of applying Abelian hyperbolic band theory to sequences of supercells in the reciprocal space of the infinite hyperbolic lattice and

argue that Abelian Bloch states in supercells can be viewed as non-Abelian Bloch states in the unit cell. To demonstrate the method, we apply it to the computation of the density of states of several different models in Section 10.4. These models range from basic constant-hopping nearest-neighbor models on the $\{8,8\}$, $\{8,3\}$, and octagon-kagome lattice to topological models including the Haldane model on the $\{8,3\}$ lattice, a generalization of the Benalcazar-Bernevig-Hughes (BBH) model [148] of a quadrupole insulator to the $\{6,4\}$ lattice, and the Dirac model of a hyperbolic non-Abelian semimetal on the $\{8,8\}$ lattice. Finally, in Section 10.5, we discuss various aspects of convergence of the supercell method.

10.1. Supercells

As we have seen in Sections 2.1 and 9.1.2, a lattice consists of copies of some chosen unit cell, generated by discrete translations forming the translation group Γ. While one commonly chooses a smallest *primitive cell*, implying a maximal translation group Γ, one can instead consider a *supercell*, or collection of multiple primitive cells. Accordingly, only a subgroup Γ' of translations Γ is required to generate the lattice. An example pair of primitive cell and supercell of the Euclidean $\{4,4\}$ square lattice and the hyperbolic $\{8,8\}$ lattice is illustrated in Figs. 10.1a and 10.1d, respectively. In both examples, the supercell consists of two copies of the primitive cell with the second copy arranged symmetrically around the first; we refer to the supercell as 2-*supercell* making the number of primitive cells explicit.

Dividing the lattice into copies of a chosen cell facilitates periodic boundary conditions, where the lattice is compactified on a closed manifold by identifying sides related by certain translations. We have seen in Section 9.2.2, that, due to the negative curvature, hyperbolic PBC clusters are compactified on manifolds of genus $\mathfrak{g} \geq 2$. According to the Riemann-Hurwitz formula [331], the genus $\mathfrak{g}_{\text{sc}}$ of a compactified supercell grows linearly with the number N of primitive cells it is made up of:

$$\mathfrak{g}_{\text{sc}} - 1 = N(\mathfrak{g}_{\text{pc}} - 1), \tag{10.1}$$

where $\mathfrak{g}_{\text{pc}}$ is the genus of the compactified primitive cell. For $\{p,q\}$ lattices this follows directly from Eq. (9.34), which states that with p, q fixed, $\mathfrak{g} - 1$ is proportional to the number of vertices. For example, in the $\{8,8\}$ lattice, the primitive cell is compactified on a genus-2 surface, and the 2-supercell on a genus-3 surface, as illustrated in Fig. 10.1e. In contrast, Fig. 10.1b demonstrates how Euclidean cells are always compactified on surfaces with $\mathfrak{g} = 1$, independent of their size.

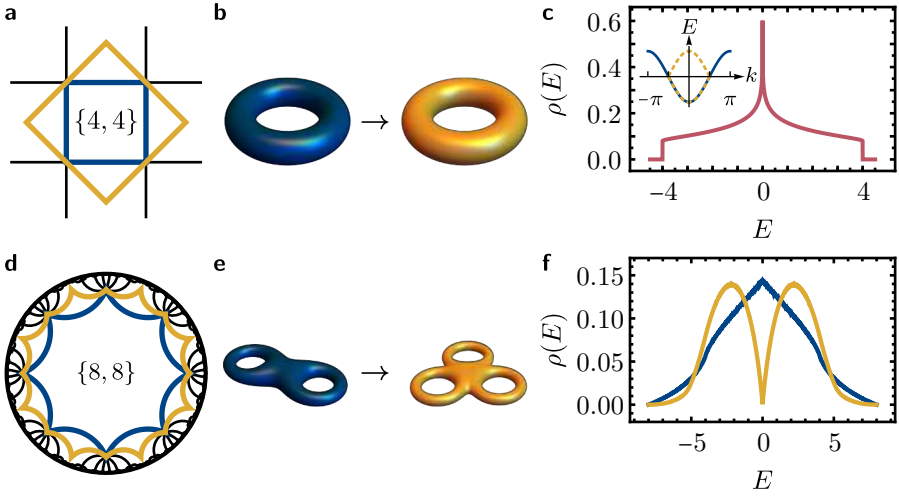

Figure 10.1.: Supercells and their compactification. Supercell construction for (**a–c**) the Euclidean $\{4, 4\}$ and (**d–f**) hyperbolic $\{8, 8\}$ lattice. (**a,d**) Primitive cell (blue polygon) and symmetrized 2-supercell (yellow polygon). (**b,e**) Compactified primitive cells (blue) and supercells (yellow) in real space. (**c**) Density of states ρ of the nearest-neighbor hopping model on the $\{4, 4\}$ lattice as a function of energy E showing the characteristic van Hove singularity. The inset shows the momentum-space dispersion for the primitive cell (solid blue line) and for the supercell (yellow dashed line). (**f**) Density of Abelian Bloch states of the nearest-neighbor hopping model on the $\{8, 8\}$ lattice for the primitive cell (blue), for the 2-supercell (yellow).

Translational symmetry further enables a reciprocal-space description of the infinite lattice, considering not just a single PBC cluster but all its translation-related copies. In the following we refer to a unit whose translation-related copies cover the infinite lattice as a *cell*, either primitive or supercell, depending on its size. On the other hand, we continue to call finite pieces of the lattice endowed with periodic boundary conditions *PBC clusters*. We emphasize that any cell gives rise to a corresponding PBC cluster by considering only a single copy of said cell and imposing periodic boundary conditions. The latter is possible because, by definition, a supercell is characterized by a subgroup Γ' of Γ as described in Section 9.2.2. The converse is not true, however: the condition on PBC clusters, $\Gamma_{\mathrm{PBC}} < \Gamma$, is weaker than the one on supercells, $\Gamma' \lhd \Delta$, i.e., because Γ_{PBC} is a subgroup of the translation group but itself *not* a valid translation group. Thus, PBC clusters generically do not form a

subdivision of the lattice into supercells.

The choice of cell affects the reciprocal-space description. To illustrate this, consider the constant-hopping nearest-neighbor hopping models on the $\{4,4\}$ and $\{8,8\}$ lattices with Hamiltonians $\mathcal{H} = -\sum_{\langle i,j\rangle} c_i^\dagger c_j$. For Euclidean lattices, the Brillouin zone is reduced due to the enlargement of the cell, leading to band folding as shown in the inset in Fig. 10.1c; however, the states and thus the computed DOS are independent of the cell size. By contrast, Fig. 10.1f indicates that, in the hyperbolic case, the density of Abelian Bloch states changes significantly when going from a primitive cell to a 2-supercell, which implies a significant dependence of the set of captured states on the choice of supercell.

Since the number of bands provided by Abelian hyperbolic band theory scales linearly with the size of the unit cell, the above observation motivates us to study Abelian Bloch states on increasingly larger supercells in the hope that we can capture some of the elusive non-Abelian Bloch states. In Section 10.3, we argue that this is indeed the case: applying Abelian hyperbolic band theory to a supercell gives *additional* Bloch states which can be interpreted as non-Abelian Bloch states of the primitive cell. Further, we find that by iterating this procedure, convergence to the thermodynamic limit is achieved.

10.2. Real-space perspective

The *supercell method* provides a natural and systematic way to form sequences of PBC clusters suited to a reciprocal-space interpretation. We construct increasingly larger supercells $C^{(m)}$ by recursively accreting smaller (super)cells in a symmetric fashion, starting with a single primitive cell $C = C^{(1)}$. Forcing the supercells to be symmetric ensures that the normal subgroup $\Gamma^{(m)}$ defining the PBC cluster associated with the supercell $C^{(m)}$ is a normal subgroup of the triangle group Δ and thus a valid translation group compatible with the space group:

$$\forall m \geq 1 \,:\, \Gamma^{(m)} \lhd \Delta. \tag{10.2a}$$

The recursive construction further leads to a nested sequence of finite-index normal subgroups,

$$\Gamma^{(1)} \rhd \Gamma^{(2)} \rhd \cdots \rhd \Gamma^{(m)} \rhd \cdots, \tag{10.2b}$$

where Eq. (10.2a) implies that the subgroup relationships in Eq. (10.2b) are normal. Note that Eq. (10.2) is identical to Eq. (9.40a) and based on our numerical results, we conjecture that the supercell sequences can be extended in a way that satisfies the additional constraint Eq. (9.40b) put forward by

Lux et al. [75, 302] as a condition for sequences that lead to a well-defined thermodynamic limit [332]. While the supercell method allows for different sequences satisfying the conditions, we anticipate that of them converge to the same limit, consistent with our observations in Section 10.5.

The size of the supercell used in the subdivision of the infinite lattice cannot influence any observable. However, as we in Fig. 10.1f, it can influence the description of the system in reciprocal space. In particular, it affects the division of Bloch states into Abelian and non-Abelian ones. Before turning to those effects manifesting in reciprocal space, we briefly summarize how to *obtain* such supercell sequences and then revisit the framework for labeling Wyckoff positions and defining tight-binding models introduced in Section 9.3. We extend the framework to deal with a division of the infinite lattice not into primitive cells but into supercells that themselves consist of multiple primitive cells.

10.2.1. Obtaining supercell sequences

Supercell sequences with the property given in Eq. (10.2) can naively be obtained by first enumerating all low-index normal subgroups Γ' of a given triangle group $\Delta(r, q, p)$ up to a certain index and subsequently checking their subgroup relations to identify appropriate sequences. The same algorithms used for finding PBC clusters, described in Section 9.2.2, can be applied here with the difference that we are interested in normal subgroups of Δ instead of Γ. This process is computationally expensive, in particular, because most of the normal subgroups found by the algorithm are discarded. However, by relying on existing tables of such normal subgroups or equivalently of the quotient groups Δ/Γ', this becomes very efficient for short sequences. For instance, Ref. 301 provides such a list of quotient groups of all hyperbolic triangle groups up to a certain genus, labeling the n^{th} quotient group of genus $\mathfrak{g}$ by $\mathrm{T}\mathfrak{g}.n$. We adopt the same notation to refer to quotients taking from that list.

To obtain longer sequences, a search as the one described above can be complemented by forming intersections of normal subgroups, similar to the algorithm for finding large PBC clusters described in Ref. 8. Given a *set* of normal subgroups $\Gamma'_n \lhd \Delta = \Gamma^{(0)}$, generally not forming a single sequence, the groups defined by

$$\Gamma^{(n+1)} = \Gamma^{(n)} \cap \Gamma'_{n+1}, \qquad n = 0, 1, \ldots, \tag{10.3a}$$

form the normal sequence

$$\Delta = \Gamma^{(0)} \rhd \Gamma^{(1)} \rhd \Gamma^{(2)} \rhd \cdots . \tag{10.3b}$$

This follows from the fact that the intersection of two normal subgroups $\Gamma^{(n)}, \Gamma'_{n+1} \lhd \Delta$ is (1) again a normal subgroup of Δ [8], and (2) additionally a normal subgroup of both original normal subgroups: $\Gamma^{(n+1)} \lhd \Gamma^{(n)}$, $\Gamma^{(n+1)} \lhd \Gamma'_{n+1}$. This allows us to significantly extend the normal sequence beyond the length of sequences that can be found by an exhaustive search of low-index normal subgroups. Such computations can be easily performed using GAP [333].

10.2.2. Labeling primitive cells in a supercell

In Section 9.3.1, we have discussed how to label maximally symmetric Wyckoff positions and unit cells in an infinite lattice and in finite PBC clusters. We now add two additional levels of subdivision. Instead of covering the lattice directly with copies of a primitive cell, we subdivide the lattice into large *super-supercells* composed of supercells, which themselves are composed of primitive cells. The motivation for doing this is that we may wish to consider the subdivision of large but finite PBC clusters into supercells instead of the infinite hyperbolic lattice. Such a finite PBC cluster can be realized as a single instance of a super-supercell. In general, the primitive cells covering the infinite lattice can thus be labeled by the following hierarchy: the position of the super-supercell, the position of the supercell within this super-supercell, and the position of the primitive cell within the supercell. Similarly, primitive cells in the large PBC cluster can be labeled by the position of the supercell within the cluster and the position of the primitive cell within the supercell.

We assume a normal sequence of translation groups satisfying Eq. (10.2). Let $n > m > 1$, such that the subdivision described above is realized by the primitive cell $C^{(1)}$, the supercell $C^{(m)}$, and the super-supercell $C^{(n)}$. Recall that, without subdivision, the primitive cells $C^{(1)}$ within the infinite lattice are labeled by $\gamma^{(1)} \in \Gamma^{(1)}$. Analogously, $C^{(m)}$ and $C^{(n)}$ in the infinite lattice are labeled by $\gamma^{(m)} \in \Gamma^{(m)}$ and $\gamma^{(n)} \in \Gamma^{(n)}$, respectively.

Ignoring the super-supercells in a first step, we utilize the fact that $\Gamma^{(m)}$ is a normal subgroup of $\Gamma^{(1)}$. The resulting coset decomposition,

$$\Gamma^{(1)} = \bigcup_{\eta_i^{(1)} \in T_{\Gamma^{(1)}}(\Gamma^{(m)})} \eta_i^{(1)} \Gamma^{(m)}, \tag{10.4}$$

implies that any $\gamma^{(1)} \in \Gamma^{(1)}$ can be decomposed into unique $\eta_i^{(1)} \in T_{\Gamma^{(1)}}(\Gamma^{(m)})$ and $\gamma^{(m)} \in \Gamma^{(m)}$:

$$\gamma^{(1)} = \eta_i^{(1)} \gamma^{(m)}, \tag{10.5}$$

where $\eta_i^{(1)} \in T_{\Gamma^{(1)}}(\Gamma^{(m)})$ labels the primitive cells $C^{(1)}$ within the supercell $C^{(m)}$, such that we can introduce new labels for the Wyckoff positions $\mu =$

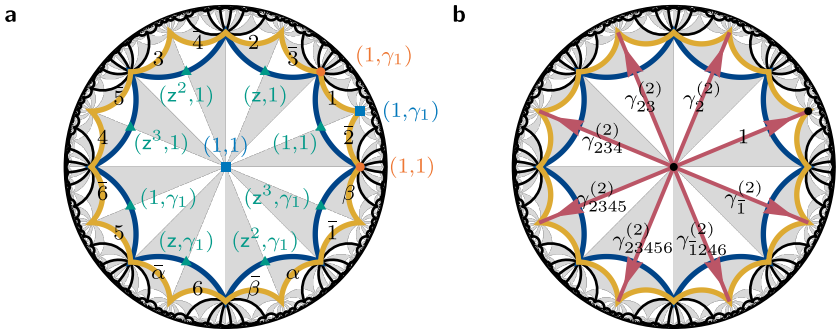

Figure 10.2.: Wyckoff positions and nearest neighbors in supercell. (**a**) Wyckoff positions of the 2-supercell (bounded by the yellow polygon) T3.11 of $\Delta(2,8,8)$ shown as green triangles, orange disks, and blue squares for $\mathsf{w} = \mathsf{x},\mathsf{y},\mathsf{z}$, respectively. They are labeled according to their decomposition into Wyckoff positions of the primitive cell (bounded by the blue polygon) as $(g_{u_\mathsf{w}}, \eta_i^{(1)})$ giving the position in the supercell as $g_{u_\mathsf{w}}\eta_i^{(1)}$. The edge identifications of the supercell are indicated by black numbers as follows: $\bar{1}$ is related to 1 by the translation generator $\gamma_1^{(2)} \in \Gamma^{(2)}$ and edges related by composite translations are labeled by $\alpha = \gamma_{\bar{3}\bar{1}}^{(2)}$ and $\beta = \gamma_{\bar{4}2}^{(2)}$, where we introduced the shorthand $\gamma_{\bar{3}\bar{1}}^{(2)} = {\gamma_3^{(2)}}^{-1}{\gamma_1^{(2)}}^{-1}$ (**b**) Extension of the constant-hopping nearest-neighbor model on the primitive cell of the $\{8,8\}$ lattice illustrated in Fig. 9.7a to the 2-supercell. The two sites $\mu \cong (g_{u_\mathsf{z}}, \eta_i^{(1)})$ in the supercell are shown as black dots and hoppings $\mathsf{h}^{\mu\nu}(\gamma^{(2)})$ between them by red arrows with γ given in black.

$(u, \eta_i^{(1)})$ in the supercell in terms of their labels u in the primitive cell appearing in Eq. (9.52). This is illustrated in Fig. 10.2a for a 2-supercell of $\Delta(2,8,8)$ based on Eq. (9.56) and $T_{\Gamma^{(1)}}(\Gamma^{(m)}) = \{1, \gamma_1\}$.

Note that we have chosen notation such that the superscript always indicates the translation group in the sequence, e.g., $\eta_i^{(1)} \in \Gamma^{(1)}$. Let us comment on the order of group elements. The same argument as for the position of γ in Eq. (9.51) applies here: $\eta_i^{(1)}$, which describes the internal structure of the supercell, appears to the left of the translation $\gamma^{(m)}$ connecting different copies of the supercell. With that order, if two primitive cells in some supercell are related by a translation generator $\eta_i^{(1)}$, the corresponding copies of the primitive cells in the translated supercell are still related by $\eta_i^{(1)}$.

We next consider the larger super-supercell $C^{(n)}$, which consists of copies of the smaller supercell $C^{(m)}$. Using the fact that for $\gamma^{(m)} \in \Gamma^{(m)}$ there exist unique $\eta_{i'}^{(m)} \in T_{\Gamma^{(m)}}(\Gamma^{(n)})$ and $\gamma^{(n)} \in \Gamma^{(n)}$ such that $\gamma^{(m)} = \eta_{i'}^{(m)}\gamma^{(n)}$, we

find that any $\gamma^{(1)} \in \Gamma^{(1)}$ can be decomposed into unique $\eta_i^{(1)} \in T_{\Gamma^{(1)}}(\Gamma^{(m)})$, $\eta_{i'}^{(m)} \in T_{\Gamma^{(m)}}(\Gamma^{(n)})$ and $\gamma^{(n)} \in \Gamma^{(n)}$:

$$\gamma^{(1)} = \eta_i^{(1)} \eta_{i'}^{(m)} \gamma^{(n)}. \tag{10.6}$$

Note that $\Gamma^{(n)} \subset \Gamma^{(m)} \subset \Gamma^{(1)}$, such that all group elements appearing in Eq. (10.6) are elements of $\Gamma^{(1)}$.

10.2.3. Tight-binding model on a supercell

Starting from the generic form of a tight-binding model on a hyperbolic lattice with translation group $\Gamma = \Gamma^{(1)}$, given in Eq. (9.58),

$$\mathcal{H} = \sum_{\gamma,\gamma' \in \Gamma^{(1)}} \sum_{u,v} h^{uv}(\gamma)\, c^u_{\gamma\gamma'}{}^{\dagger} c^v_{\gamma'}, \tag{10.7}$$

we implement the subdivision of the infinite lattice into supercells $C^{(m)}$ as described above. Applying the unique decomposition given in Eq. (10.5) to γ and $\gamma\gamma'$, the Hamiltonian becomes

$$\mathcal{H} = \sum_{\substack{\gamma''^{(m)},\gamma'^{(m)} \in \Gamma^{(m)} \\ \eta_i^{(1)},\eta_j^{(1)} \in T_{\Gamma^{(1)}}(\Gamma^{(m)})}} \sum_{u,v} h^{uv} \left(\eta_i^{(1)} \gamma''^{(m)} \gamma'^{(m)-1} \eta_j^{(1)-1} \right) c^u_{\eta_i^{(1)}\gamma''^{(m)}}{}^{\dagger}\; c^v_{\eta_j^{(1)}\gamma'^{(m)}}. \tag{10.8}$$

This can be written more compactly by recognizing that $T_{\Gamma^{(1)}}(\Gamma^{(m)})$ is a finite set with $N^{(1,m)} = |\Gamma^{(1)} : \Gamma^{(m)}|$ elements:

$$\mathcal{H} = \sum_{\gamma^{(m)},\gamma'^{(m)} \in \Gamma^{(m)}} \sum_{i,j=1}^{N^{(1,m)}} \sum_{u,v} \mathsf{h}^{uv}_{ij}\left(\gamma^{(m)}\right) c^u_{\eta_i^{(1)}\gamma^{(m)}\gamma'^{(m)}}{}^{\dagger}\; c^v_{\eta_j^{(1)}\gamma'^{(m)}}, \tag{10.9a}$$

where

$$\mathsf{h}^{uv}_{ij}\left(\gamma^{(m)}\right) = h^{uv}\left(\eta_i^{(1)} \gamma^{(m)} \eta_j^{(1)-1}\right) \tag{10.9b}$$

is the hopping matrix within the supercell. Using the labels $\mu = (u, \eta_i^{(1)})$, $\nu = (v, \eta_j^{(1)})$ for Wyckoff positions in the supercell and by defining

$$c^{\mu}_{\gamma^{(m)}} = c^u_{\eta_i^{(1)}\gamma^{(m)}\gamma'^{(m)}}, \qquad \mathsf{h}^{\mu\nu}(\gamma^{(m)}) = \mathsf{h}^{uv}_{ij}(\gamma^{(m)}), \tag{10.10a}$$

this becomes

$$\mathcal{H} = \sum_{\gamma^{(m)},\gamma'^{(m)} \in \Gamma^{(m)}} \sum_{\mu,\nu} \mathsf{h}^{\mu\nu}\left(\gamma^{(m)}\right) c^{\mu}_{\gamma^{(m)}\gamma'^{(m)}}{}^{\dagger}\; c^{\nu}_{\gamma'^{(m)}}, \tag{10.10b}$$

which has the identical form as Eq. (10.7). The graph representation of $\mathsf{h}^{\mu\nu}(\gamma^{(m)})$ for the nearest-neighbor hopping model on the $\{8,8\}$ lattice and $m=2$ is shown in Fig. 10.2b.

Following the procedure in Section 9.3.2, we restrict to a single copy of the supercell by specifying the primitive cell not by elements of $\Gamma^{(1)}$, but by cosets $[\eta_i^{(1)}]_{(1,m)} \in \Gamma^{(1)}/\Gamma^{(m)}$, where $\eta_i^{(1)} \in T_{\Gamma^{(1)}}(\Gamma^{(m)})$. Here, we have introduced the subscript $(1,m)$ to indicate the quotient in which the coset lies. This results in the following form of the Hamiltonian on a finite PBC cluster:

$$\mathcal{H}_{m\text{-PBC}} = \sum_{\gamma^{(m)}\in\Gamma^{(m)}} \sum_{i,j=1}^{N^{(1,m)}} \sum_{u,v} h^{uv}\left(\eta_i^{(1)}\gamma^{(m)}{\eta_j^{(1)}}^{-1}\right) {c^u_{\left[\eta_i^{(1)}\right]_{(1,m)}}}^{\dagger} c^v_{\left[\eta_j^{(1)}\right]_{(1,m)}}, \tag{10.11}$$

which is equivalent to Eq. (9.60) up to relabeling.

We proceed to the next level of subdivision: the larger super-supercell $C^{(n)}$. Using the unique decomposition given in Eq. (10.6) and simplifying, Eq. (10.7) becomes

$$\sum_{\gamma''^{(n)},\gamma'^{(n)}\in\Gamma^{(n)}} \sum_{i',j'}^{N^{(m,n)}} \sum_{\mu,\nu} \mathsf{h}^{\mu\nu}\left(\eta_{i'}^{(m)}\gamma^{(n)}{\eta_{j'}^{(m)}}^{-1}\right) {c^{\mu}_{\eta_{i'}^{(m)}\gamma^{(n)}\gamma'^{(n)}}}^{\dagger} c^{\nu}_{\eta_{j'}^{(m)}\gamma^{(n)}}. \tag{10.12}$$

This can once more be restricted to a PBC cluster, in this case to the one corresponding to a single instance of $C^{(n)}$, resulting in

$$\begin{aligned}\mathcal{H}_{n\text{-PBC}} = \sum_{\gamma^{(n)}\in\Gamma^{(n)}} \sum_{i',j'}^{N^{(m,n)}} \sum_{i,j}^{N^{(1,m)}} \sum_{u,v} h^{uv}\left(\eta_i^{(1)}\eta_{i'}^{(m)}\gamma^{(n)}{\eta_{j'}^{(m)}}^{-1}{\eta_j^{(1)}}^{-1}\right) \\ \times {c^u_{\left[\eta_i^{(1)}\eta_{i'}^{(m)}\right]_{(1,n)}}}^{\dagger} c^v_{\left[\eta_j^{(1)}\eta_{j'}^{(m)}\right]_{(1,n)}},\end{aligned} \tag{10.13}$$

where primitive cells are now labeled by cosets $[\eta_j^{(1)}\eta_{j'}^{(m)}]_{(1,n)} \in \Gamma^{(1)}/\Gamma^{(n)}$.

Suppressing once more the internal structure of $C^{(m)}$ in terms of copies of $C^{(1)}$, by introducing the annihilation operators

$$c^{\mu}_{\left[\eta_{i'}^{(m)}\right]_{(m,n)}} = c^u_{\left[\eta_i^{(1)}\eta_{i'}^{(m)}\right]_{(1,n)}}, \tag{10.14}$$

where $[\eta_{i'}^{(m)}]_{(m,n)} \in \Gamma^{(m)}/\Gamma^{(n)}$ now labels the copies of $C^{(m)}$, rather than copies of $C^{(1)}$ as did $[\eta_i^{(1)}\eta_{i'}^{(m)}]_{(1,n)}$, and μ takes care of copies of $C^{(1)}$ within $C^{(m)}$, such that still all copies of $C^{(1)}$ are captured. See Fig. 10.2a for an illustration

of the 2-supercell of the $\{8,8\}$ lattice. Then, with $N^{(m,n)} = |\Gamma^{(m)} : \Gamma^{(n)}|$,

$$\mathcal{H}_{n\text{-PBC}} = \sum_{i',j'=1}^{N^{(m,n)}} \sum_{\mu,\nu} \sum_{\gamma^{(n)}\in\Gamma^{(n)}} \mathsf{h}^{\mu\nu}\left(\eta_{i'}^{(m)}\gamma^{(n)}\eta_{j'}^{(m)^{-1}}\right) {c^{\mu}_{\left[\eta_{i'}^{(m)}\right]_{(m,n)}}}^{\dagger} c^{\nu}_{\left[\eta_{j'}^{(m)}\right]_{(m,n)}}. \tag{10.15}$$

Crucially, for fixed m, Eq. (10.15) provides an approximation of Eq. (10.9a), i.e., formally we can write

$$\lim_{n\to\infty} \mathcal{H}_{n\text{-PBC}} = \mathcal{H} \tag{10.16}$$

if the supercell sequence satisfies Eq. (9.40). In Section 10.3, this will allow us to approximate the subdivision of the infinite lattice into m-supercells on a finite PBC cluster.

10.3. Reciprocal-space perspective

We have seen in Section 9.4 that the Bloch theorem and band theory can be extended to hyperbolic lattices, resulting in a block-diagonalization of the Hamiltonian in terms of blocks of Bloch Hamiltonians given by Eq. (9.72a). Naturally, this applies independent of the chosen translation group and unit cell, in particular it also applies to models defined on a supercell $\Gamma^{(m)}$, such as Eq. (10.9a), with the Hamiltonian being block-diagonalized with blocks

$$H(D) = \sum_{\gamma^{(m)}\in\Gamma^{(m)}} \mathsf{h}\left(\gamma^{(m)}\right) \otimes D(\gamma^{(m)}). \tag{10.17}$$

Recall that the Abelian Brillouin zone of 1D irreducible representations is the $2\mathfrak{g}$-dimensional torus $\mathsf{T}^{2\mathfrak{g}}$ parametrized by momenta $\{0 \le k_i < 2\pi\}_{i=1}^{2\mathfrak{g}}$ and the irreducible representations are defined on the $2\mathfrak{g}$ generators γ_i of Γ by $D_{\mathbf{k}}(\gamma_i) = \mathrm{e}^{\mathrm{i}k_i}$. On the other hand, the Brillouin zones of higher-dimensional irreducible representations lack an explicit parametrization. Remarkably, as we explain below, Abelian hyperbolic band theory applied to a sequence of supercells provides systematic access to those non-Abelian Bloch states.

Considering the sequence (10.2) of translation groups, each $\Gamma^{(m)}$ has a tower of d-dimensional irreducible representations with $d \ge 1$, which we denote by $\mathrm{BZ}^{(m,d)}$. These towers of Brillouin zones are illustrated schematically in Fig. 10.3. However, due to the subgroup relationships, the irreducible representations of different $\Gamma^{(m)}$ are *not* independent. First, the restriction of a d-dimensional irreducible representation of $\Gamma^{(m)}$ to its subgroup $\Gamma^{(m+1)}$ is a d-dimensional (possibly reducible) *subduced* representation of

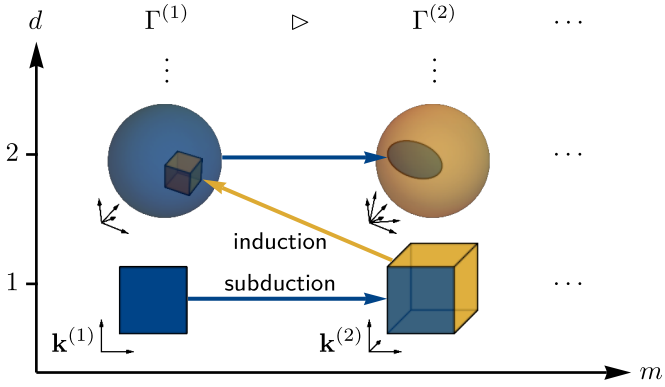

Figure 10.3.: Brillouin-zone towers of normal sequence of translation groups. Illustration of the spaces of d-dimensional irreducible representations $\mathrm{BZ}^{(m,d)}$ of a sequence of translation subgroups $\Gamma^{(m)}$ corresponding to supercells with $N^{(1,m)} = |\Gamma^{(1)} : \Gamma^{(m)}|$ primitive cells. The spaces $\mathrm{BZ}^{(m,1)}$ of 1D irreducible representations are hypertori (illustrated as square and cube) with dimension growing linearly with $N^{(1,m)}$, while the spaces of higher-dimensional irreducible representations are more complicated (illustrated as balls). The irreducible representations of $\Gamma^{(m)}$ of dimension d subduce (blue arrow) representations of $\Gamma^{(m+1)}$ of the same dimension and induce (yellow arrow) representations of $\Gamma^{(m-1)}$ of higher dimension.

$\Gamma^{(m+1)}$. Second, any d-dimensional irreducible representation of $\Gamma^{(m)}$ implies a $(d|\Gamma^{(m-1)}/\Gamma^{(m)}|)$-dimensional (possibly reducible) *induced* representation of $\Gamma^{(m-1)}$ [334]. Thus, 1D irreducible representations of $\Gamma^{(m)}$ subduce 1D irreducible representations of $\Gamma^{(m+1)}$, but because $\mathrm{BZ}^{(m+1,1)}$ has larger dimension than $\mathrm{BZ}^{(m,1)}$, there must be 1D irreducible representations of $\Gamma^{(m+1)}$ that induce higher-dimensional irreducible representations of $\Gamma^{(m)}$. Therefore, by studying the well-understood 1D irreducible representations of supercells in the sequence, we gain access to a successively larger portion of higher-dimensional irreducible representations of $\Gamma^{(1)}$. While this scheme does not reproduce *all* irreducible representations, we conjecture that it gives a representative subspace and converges to the thermodynamic limit [302] for $m \to \infty$.

10.3.1. Bloch Hamiltonian on a large PBC cluster

Above, we have discussed the Bloch Hamiltonian and the irreducible representations in the context of an infinite hyperbolic lattice. To deal with the infinite spaces in a controlled manner, we now make use of the subdivision into super-supercells $C^{(n)}$ introduced in Section 10.2. Equation (10.15) can be brought

to a form analogous to Eq. (9.64) by defining $\gamma^{(m)} = \eta_{i'}^{(m)} \gamma^{(n)} \eta_{j'}^{(m)\,-1}$ and recognizing that $\eta_{i'}^{(m)} = \gamma^{(m)} \eta_{j'}^{(m)} \gamma^{(n)\,-1}$ and $[\eta_{i'}^{(m)}]_{(m,n)} = [\gamma^{(m)} \eta_{j'}^{(m)}]_{(m,n)}$:

$$\mathcal{H}_{n\text{-PBC}} = \sum_{j'=1}^{N^{(m,n)}} \sum_{\gamma^{(m)} \in \Gamma^{(m)}} \sum_{\mu,\nu} \mathsf{h}^{\mu\nu}\left(\gamma^{(m)}\right) c^{\mu}_{\left[\gamma^{(m)} \eta_{j'}^{(m)}\right]_{(m,n)}}{}^{\dagger} c^{\nu}_{\left[\eta_{j'}^{(m)}\right]_{(m,n)}} . \tag{10.18}$$

Repeating the derivation from Section 9.4.2 working with the regular representation of $\Gamma^{(m)}/\Gamma^{(n)}$ results in the Bloch decomposition analogous to Eq. (9.71):

$$\mathcal{H}_{n\text{-PBC}} = \sum_{k,l} \sum_{\mu,\nu} \hat{c}_k^{\mu\dagger} \left(\bigoplus_{\lambda=1}^{\mathcal{N}} d_\lambda H(D) \right)^{\mu\nu}_{kl} \hat{c}_l^{\nu} \tag{10.19a}$$

with

$$\hat{c}_k^{\mu} = \sum_{i'} \mathcal{P}_{ki'} c^{\mu}_{\left[\eta_{i'}^{(m)}\right]_{(m,n)}} , \tag{10.19b}$$

$$H(D) = \sum_{\gamma^{(m)} \in \Gamma^{(m)}} \mathsf{h}\left(\gamma^{(m)}\right) \otimes D\left(\left[\gamma^{(m)}\right]_{(m,n)}\right), \tag{10.19c}$$

and D an irreducible representation of $\Gamma^{(m)}/\Gamma^{(n)}$.

By the third isomorphism theorem [335], the sequence of normal subgroups $\Gamma^{(m+1)} \lhd \Gamma^{(m)}$ implies that, for fixed n, the quotients $\Gamma^{(m)}/\Gamma^{(n)}$ also form a sequence of normal subgroups:

$$\Gamma^{(m+1)}/\Gamma^{(n)} \lhd \Gamma^{(m)}/\Gamma^{(n)}. \tag{10.20}$$

Therefore, the subduction and induction of representations apply to that space as well. This implies that irreducible representations of $\Gamma^{(1)}/\Gamma^{(n)}$, describing the spectrum of the finite PBC cluster given by the super-supercell $C^{(n)}$, can be sampled by considering the induced representations of 1D irreducible representations of $\Gamma^{(m)}/\Gamma^{(n)}$, just as we argued that 1D irreducible representations of $\Gamma^{(m)}$ induce representations of $\Gamma^{(1)}$. Since the $\Gamma^{(n)}$ form a normal sequence, the space of irreducible representations of $\Gamma^{(1)}/\Gamma^{(n)}$ provides an approximation of the thermodynamic limit [75] and converges to the full reciprocal space for $n \to \infty$. We thus anticipate that the supercell method applied to a normal sequence forms an approximation of the thermodynamic limit as well, albeit one that requires working with significantly smaller supercells $C^{(m)}$ rather than the full PBC clusters corresponding to $C^{(n)}$, which here only takes care of implementing a controlled limit.

10.4. Examples

We illustrate the supercell method by computing the density of states for selected hopping models on hyperbolic lattices. In Sections 10.4.1 and 10.4.2, we apply the supercell method to the constant-hopping nearest-neighbor models on the $\{8,8\}$ and $\{8,3\}$ lattice that we have already used for illustrations before. Next, in Section 10.4.3, we turn to a model that is closely related to the latter: the previously studied octagon-kagome model [319] hosting a flat band. Finally, we discuss three topological models: in Section 10.4.4, the $\{8,3\}$-Haldane [6, 7] model which we already introduced in Section 9.5.1, in Section 10.4.5, a generalization of the Benalcazar-Bernevig-Hughes (BBH) model [148] to the $\{6,4\}$ lattice, and, in Section 10.4.6, the Dirac model on the $\{8,8\}$ lattice introduced in Section 9.5.2. Each model is defined on a symmetric primitive cell and the density of states is computed by randomly sampling $\mathrm{BZ}^{(m,1)}$ in a sequence satisfying Eq. (10.2b). We observe rapid convergence with system size: Figs. 10.4b, 10.5b, 10.6b, 10.7b, 10.9 and 10.10b show data for systems with only up to 64 (64), 32 (512), 32 (768), 32 (512), 64 (1536), and 32 (128) primitive cells (sites), respectively. As we will show in Section 10.5, even for the largest of those systems, the density of states obtained from the corresponding PBC cluster (without applying Abelian hyperbolic band theory) is extremely far from converged, demonstrating the computational power of our reciprocal-space approach.

10.4.1. Nearest-neighbor model on $\{8,8\}$ lattice

We have already extensively discussed the $\{8,8\}$ lattice throughout Chapters 9 and 10. Let us briefly summarize the most important information here. The space group of the $\{8,8\}$ lattice is $\Delta(2,8,8)$ and the primitive cell is given by the smallest quotient T2.6 of Δ by one of its normal subgroups $\Gamma^{(1)}$ [301]:

$$G^{(1)} = \left\langle \mathsf{a},\mathsf{b},\mathsf{c} \middle|\, \mathsf{a}^2,\mathsf{b}^2,\mathsf{c}^2,(\mathsf{ab})^2,(\mathsf{bc})^8,(\mathsf{ca})^8,(\mathsf{abc})^2,(\mathsf{bc})^3(\mathsf{ca})^{-1} \right\rangle, \tag{10.21}$$

with the generators a, b, c of the triangle group $\Delta(2,8,8)$. With $G^{(1)}$ isomorphic to the quotient group $\Delta/\Gamma^{(1)}$, $\Gamma^{(1)}$ is given by the kernel of that isomorphism, which can be extracted using GAP. With our algorithm for constructing symmetric unit cells [318], we obtain the well-known translation group of the Bolza cell:

$$\Gamma^{(1)} = \left\langle \gamma_1,\gamma_2,\gamma_3,\gamma_4 \middle|\, \gamma_1\gamma_2^{-1}\gamma_3\gamma_4^{-1}\gamma_1^{-1}\gamma_2\gamma_3^{-1}\gamma_4 \right\rangle \tag{10.22}$$

with the embedding homomorphism $\Gamma \to \Delta^+(2,8,8)$, $\gamma_i \mapsto \mathsf{z}^{5-i}\mathsf{x}\mathsf{z}^{i-1}$. The $\{8,8\}$ lattice only retains sites $V_{\mathsf{z}}^{\mathrm{lat}} \cong T_{G^+}(G_{\mathsf{z}}^+) = \{1\}$, such that there is a single site per primitive cell, as illustrated in Fig. 9.6a. The nearest-neighbor

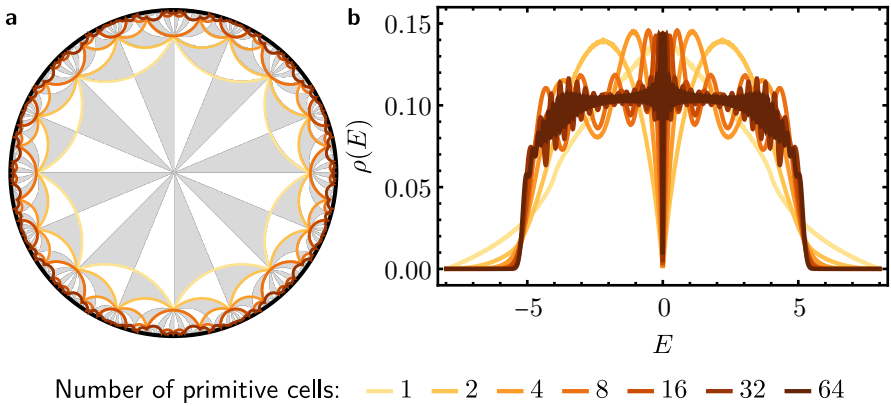

Figure 10.4.: Nearest-neighbor model on the $\{8,8\}$ lattice. (**a**) Supercells obtained from the sequence of quotient groups T2.6, T3.11, T5.13, T9.20, T17.29, T33.44, T65.78 with 1, 2, 4, 8, 16, 32, 64 primitive cells per supercell (see legend). (**b**) Density of states obtained using the supercell method applied to the sequence of supercells shown in (a). The data was obtained by randomly sampling 10^9 Abelian momenta, analyzing the spectrum with an energy resolution of 0.005 and smoothing the resulting density of states $\rho(E)$ using a moving average with window 0.01.

hopping amplitude is $h(\gamma_i) = -1$ for $i = 1, 2, 3, 4$ (and zero otherwise) as shown in Fig. 9.7a.

Using GAP, we have found a normal sequence of translation subgroups $\Gamma^{(m)} \lhd \Delta(2,8,8)$ via the appropriate quotient groups $G^{(m)} \cong \Delta/\Gamma^{(m)}$ given in Ref. 301

$$\text{T2.6}, \text{T3.11}, \text{T5.13}, \text{T9.20}, \text{T17.29}, \text{T33.44}, \text{T65.78}. \tag{10.23}$$

With the help of our GAP software package HyperCells [318], we perform the following two steps for each translation group $\Gamma^{(m)}$ in the sequence. First, the corresponding symmetric and connected cell $C^{(m)}$ is determined by making an appropriate choice of transversal $T_{\Delta^+(2,8,8)}(\Gamma^{(m)})$; the resulting supercell boundaries are illustrated in Fig. 10.4a. Second, the model defined on the unit cell by hopping amplitudes $h^{uv}(\gamma)$ is reinterpreted on the supercell using Eq. (10.9), giving a new weighted graph encoding the hopping matrix $\mathsf{h}(\gamma^{(m)})$ on the supercell. Finally, using our accompanying Mathematica package HyperBloch [336], we construct the corresponding Abelian Bloch Hamiltonian $H^{(m)}\left(\mathbf{k}^{(m)}\right)$ based on Eqs. (9.74) and (10.17) and diagonalize it for 10^9 randomly sampled points in $\mathsf{T}^{2\mathfrak{g}^{(m)}}$, corresponding to the Abelian Brillouin

zone given in Eq. (9.73). From the eigenenergies thus obtained, we compute the density of states $\rho^{(m)}(E)$ for an energy resolution of $\mathrm{d}E = 0.005$, which is then smoothed using a moving average with window $2\,\mathrm{d}E = 0.01$. The results are shown in Fig. 10.4b demonstrating convergence with increasing m. Note that due to the very low number of sites used in this example, namely 64, the density of states is not fully converged. We will examine the convergence in more detail in Section 10.5 and see in the next few examples, which involve larger numbers of sites, that convergence is easily achieved.

Let us point out one prominent and important feature in the data: the density of states near the band edges is strongly suppressed with increasing supercell size. This suppression is consistent with the expected behavior. Assuming a generic quadratic scaling of the energy dispersion with the (Abelian) momentum near the band edge, $E \propto \mathbf{k}^2$, we obtain the density of states by integrating over the $2\mathfrak{g}$-dimensional Abelian Brillouin zone:

$$\rho(E) \sim \int \mathrm{d}^{2\mathfrak{g}}k\, \delta(E - v\mathbf{k}^2) \propto E^{\mathfrak{g}-1}. \tag{10.24}$$

According to Eq. (10.1), $\mathfrak{g}$ grows linearly with the number N of primitive cells contained in the supercell, which explains the suppression near band edges for all the examples considered here. This suppression is an important feature of the supercell method, since Abelian hyperbolic band theory includes states that lie outside the energy range with finite density in the thermodynamic limit [76]. Equation (10.24) implies that these states are suppressed *exponentially* in the size of the supercell.

10.4.2. Nearest-neighbor model on $\{8,3\}$ lattice

We next turn to the $\{8,3\}$ lattice, whose space group is $\Delta(2,3,8)$ and the smallest quotient of Δ by one of its normal subgroups $\Gamma^{(1)}$, defining the primitive cell, is T2.1 [301]:

$$G^{(1)} = \left\langle \mathsf{a},\mathsf{b},\mathsf{c} \middle|\, \mathsf{a}^2, \mathsf{b}^2, \mathsf{c}^2, (\mathsf{ab})^2, (\mathsf{bc})^3, (\mathsf{ca})^8, \mathsf{c}(\mathsf{abc})^2\mathsf{a}(\mathsf{abc})^{-1}\mathsf{c}^{-1}\mathsf{abca} \right\rangle, \tag{10.25}$$

resulting once more in the translation group of the Bolza cell, as we have shown in Section 9.1.2. Given that the $\{8,3\}$ lattice is defined by the hyperbolic tessellation where three octagons meet at each vertex, it only retains sites $V_{\mathsf{y}}^{\mathrm{lat}} \cong T_{G^+}(G_{\mathsf{y}}^+)$, which results in the 16 sites per primitive cell shown in Fig. 9.6b. The hopping amplitudes between those sites in the primitive cell define a 16×16 matrix $h^{uv}(\gamma)$ which is equal to -1 if $\gamma = 1$ and u and v are nearest neighbors in the primitive cell or if $\gamma = \gamma_i$ with $i = 1,2,3,4$ and v is

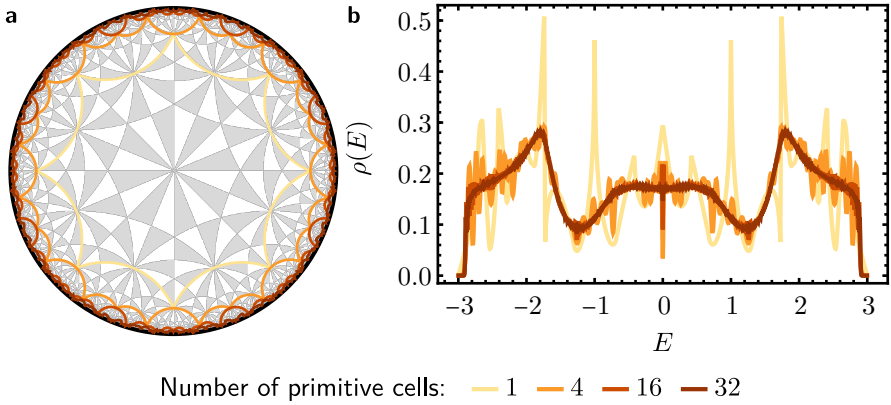

Figure 10.5.: Nearest-neighbor model on the $\{8,3\}$ lattice. (**a**) Supercells obtained from the sequence of quotient groups T2.1, T5.1, T17.2, T33.1 with 1, 4, 16, 32 primitive cells per supercell (see legend). (**b**) Density of states obtained using the supercell method applied to the sequence of supercells shown in (a). The data was obtained by randomly sampling 10^8 Abelian momenta, analyzing the spectrum with an energy resolution of 0.005 and smoothing the resulting density of states $\rho(E)$ using a moving average with window 0.01.

a nearest neighbor of the copy of u in the primitive cell translated by γ, and zero otherwise, as illustrated in Fig. 9.7a.

Again, we choose a normal sequence of translation subgroups $\Gamma^{(m)} \lhd \Delta$, $\Delta = \Delta(2,3,8)$, in terms of quotient groups $G^{(m)} \cong \Delta/\Gamma^{(m)}$ given in Ref. 301,

$$\mathrm{T2.1}, \mathrm{T5.1}, \mathrm{T17.2}, \mathrm{T33.1}, \tag{10.26}$$

and construct the corresponding symmetric and connected cells $C^{(m)}$, see Fig. 10.5a. The density of states $\rho^{(m)}(E)$ obtained from random sampling of 10^8 points in $\mathsf{T}^{2\mathfrak{g}^{(m)}}$ is shown in Fig. 10.5b. In contrast to Fig. 10.4b, the density of states is well-converged for the largest supercell, which has 512 sites.

10

10.4.3. Nearest-neighbor model on octagon-kagome lattice

The octagon-kagome lattice is the line graph of the $\{8,3\}$ lattice, i.e., with sites on the edges of the $\{8,3\}$ lattice, such that it has the same space group $\Delta(2,3,8)$. The sites of the octagon kagome lattice are given by $V_{\mathsf{x}}^{\mathrm{lat}} \cong T_{\Delta^+}(\Delta_{\mathsf{x}}^+)$ and the corresponding nearest-neighbor adjacency graph on the primitive cell is

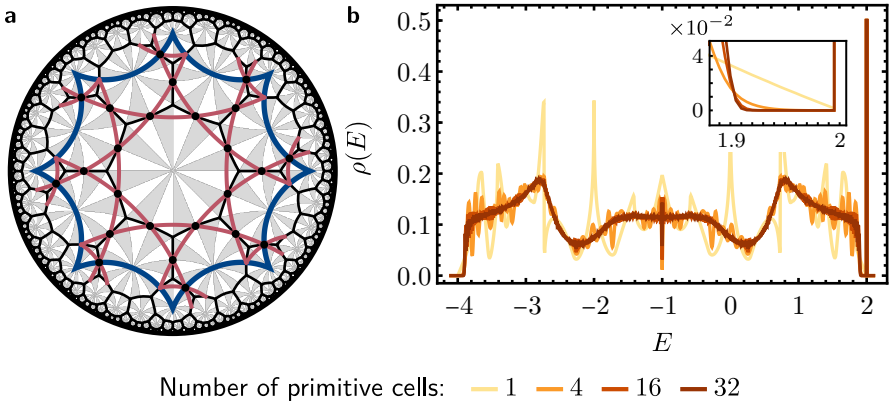

Figure 10.6.: Nearest-neighbor model on the octagon-kagome lattice. (**a**) Definition of the constant-hopping nearest-neighbor model on the octagon-kagome lattice which is the line graph of the $\{8, 3\}$ lattice, such that the same sequences of supercells are used. (**b**) Density of states obtained using the supercell method applied to the sequence of supercells obtained from the sequence of quotient groups T2.1, T5.1, T17.2, T33.1 with 1, 4, 16, 32 primitive cells per supercell (see legend). The data was obtained by randomly sampling 10^8 Abelian momenta, analyzing the spectrum with an energy resolution of 0.005. The inset shows a close-up of the region between the dispersive part of the spectrum and the flat band.

illustrated in Fig. 10.6a. Given that the space group is the same, the primitive cell and supercells are the same as for the $\{8, 3\}$ lattice and we use the same sequence given in Eq. (10.26) and illustrated in Fig. 10.5a.

Hyperbolic kagome lattices are of particular interest because they host extensive flat bands [68, 319], i.e., energy bands with constant energy across an extended region of reciprocal space. Flat-band systems have gained significant attention because they are fertile grounds for engineering strongly correlated states [337]. This is due to the fact that the ratio of interaction potential energy to the kinetic energy diverges for a flat band, such that interactions dominate the physics. Bzdušek et al. [319] have studied several hyperbolic flat-band systems, including the octagon-kagome lattice. They found that a fixed fraction, $\frac{1}{3}$ for the octagon-kagome lattice, of all states (Abelian or non-Abelian) participate in the flat band and that this fraction remains unchanged when restricting to Abelian states. Additionally, using real-space arguments, the authors describe a band touching between the flat band and the dispersive bands. This raises the question if these features survive in the thermodynamic

limit.

Figure 10.6b shows the density of states $\rho^{(m)}(E)$ obtained from randomly sampling 10^8 points in $\mathsf{T}^{2\mathfrak{g}^{(m)}}$ for an energy resolution of $\mathrm{d}E = 0.005$ for the sequence in Eq. (10.26). No smoothing is applied in this case, given that the flat band is expected to be at a precise value of energy. We observe that the density of states is almost identical to the one of the $\{8, 3\}$ lattice, Fig. 10.5b, up to a shift in energy by -1 and the expected flat band at $E = 2$ (and an associated rescaling due to the normalization); this is consistent with what is expected from graph theory [338]. As predicted by Ref. 319, the fraction of states in the flat band is precisely one third: $\rho(2)\,\mathrm{d}E = \frac{1}{3}$, independent of the supercell. However, the density of states *between* the flat band and the dispersive bands is suppressed *exponentially* with increasing m, such that in the thermodynamic limit the flat band is *detached*. This suggests that the previously observed gaplessness is a finite-size effect.

10.4.4. Haldane model on $\{8, 3\}$ lattice

In Section 9.5.1, we have introduced the Haldane model as a prototypical model for hyperbolic topological insulators. While we have found that the Haldane model on the $\{8, 3\}$ lattice hosts topologically nontrivial band gaps separating bands with nontrivial Chern number, it is not clear from those considerations if the band gaps are true gaps or finite-size gaps. This is easily checked using the supercell method, which we do here.

Given that the model is defined on the $\{8, 3\}$ lattice, the supercells are once more the ones given in Eq. (10.26). In particular, we use the same primitive cell as in Section 9.5.1, such that the density of states $\rho^{(1)}(E)$ matches exactly the results from Abelian hyperbolic band theory presented there and in Refs. 6, 307. With random sampling of 10^8 points in $\mathsf{T}^{2\mathfrak{g}^{(m)}}$, we compute the density of states with an energy resolution of $\mathrm{d}E = 0.005$ and smooth it using a moving average with window $2\,\mathrm{d}E = 0.01$. The resulting data is shown in Fig. 10.7b. Crucially, the characteristic density of states suppression near the edges of all three gaps (see inset) indicates that the gaps obtained from Abelian hyperbolic band theory are stable to the inclusion of non-Abelian Bloch states and are not caused by finite-size effects. Together with the real space calculations reviewed in Section 9.5.1, this suggests persistence of the bulk topology in the thermodynamic limit.

10.4.5. Benalcazar-Bernevig-Hughes model on $\{6, 4\}$ lattice

Motivated by the higher-order topological phenomena on hyperbolic flakes [305, 306] described in Section 9.5, we introduce a generalization of the Benalcazar-

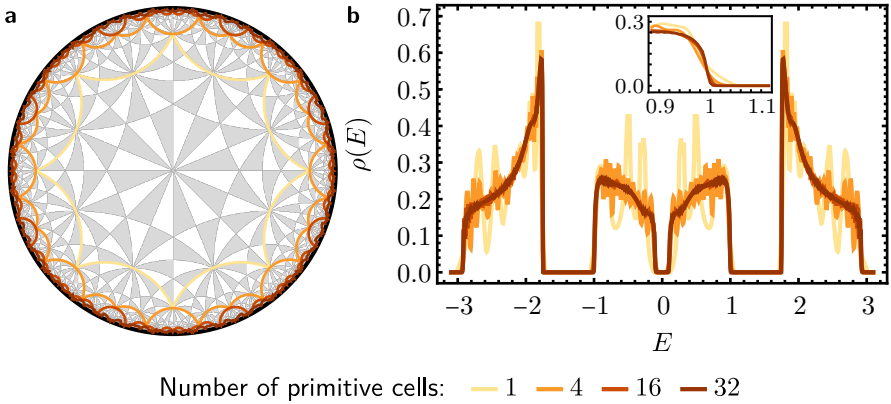

Figure 10.7.: Haldane model on the $\{8,3\}$ lattice. (**a**) Supercells obtained from the sequence of quotient groups T2.1, T5.1, T17.2, T33.1 with 1, 4, 16, 32 primitive cells per supercell (see legend). (**b**) Density of states obtained using the supercell method applied to the sequence of supercells shown in (a). The data was obtained by randomly sampling 10^8 Abelian momenta, analyzing the spectrum with an energy resolution of 0.005 and smoothing the resulting density of states $\rho(E)$ using a moving average with window 0.01. The inset shows the lower band edge of one of the topological gaps, demonstrating the suppression of the density of states *inside* the gap.

Bernevig-Hughes model of a quadrupole insulator to the $\{6,4\}$ lattice. The corresponding space group is the triangle group $\Delta(2,4,6)$ and the primitive cell (blue polygon in Fig. 10.8a) is given by the smallest quotient T2.2 of Δ with one of its normal subgroups $\Gamma^{(1)}$ [301]:

$$G^{(1)} = \left\langle \mathsf{a},\mathsf{b},\mathsf{c} \middle|\, \mathsf{a}^2,\mathsf{b}^2,\mathsf{c}^2,(\mathsf{ab})^2,(\mathsf{bc})^4,(\mathsf{ca})^6,(\mathsf{bca}^{-1}\mathsf{c}^{-1})^2 \right\rangle, \tag{10.27}$$

giving

$$\begin{aligned}\Gamma^{(1)} &= \left\langle \gamma_1,\gamma_2,\gamma_3,\gamma_4 \middle|\, \gamma_4\gamma_1\gamma_3\gamma_4^{-1}\gamma_3^{-1}\gamma_2^{-1}\gamma_1^{-1}\gamma_2 \right\rangle \\ &= \left\langle \gamma_1,\gamma_2,\gamma_3,\gamma_4 \middle|\, \gamma_1\gamma_2\gamma_3\gamma_4\gamma_3^{-1}\gamma_1^{-1}\gamma_4^{-1}\gamma_2^{-1} \right\rangle. \end{aligned} \tag{10.28}$$

Here, we consider the following supercell sequence [301]:

$$\mathrm{T2.2}, \mathrm{T5.4}, \mathrm{T9.3}, \mathrm{T33.11}, \mathrm{T65.9}, \tag{10.29}$$

which is illustrated in Fig. 10.8b.

Similar to its original version on the square lattice [148], the model is defined on a lattice with fourfold coordination and has four orbitals per site shown

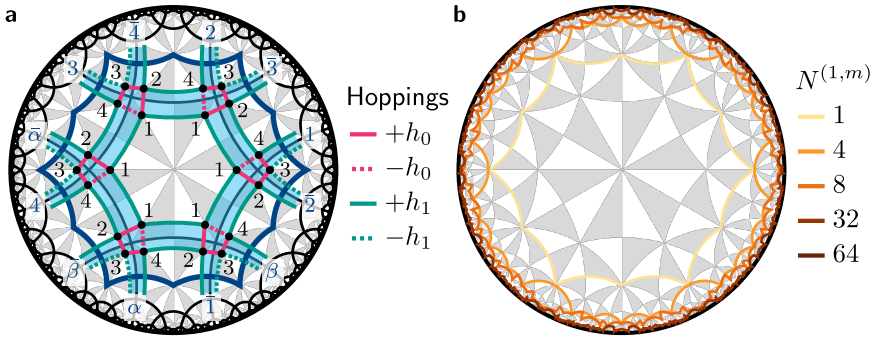

Figure 10.8.: Benalcazar-Bernevig-Hughes model on the $\{6, 4\}$ lattice. (**a**) Definition of the model. There are four orbitals (black dots labeled by black numbers) at each site, coupled by inter-site hoppings $\pm h_0$ (magenta) and intra-site hoppings $\pm h_1$ (green). Light blue shading of plaquettes bounded by magenta/green lines indicates π-fluxes and dashed lines indicate negative hopping amplitudes for the chosen gauge. The primitive cell (blue polygon) and its edge identifications are shown: the edge $\bar{1}$ is related to 1 by the translation generator γ_1 ($\tilde{\gamma}_1$ for the supercell). Edges related by composite translations are labeled by $\alpha = \gamma_3^{-1}\gamma_1^{-1}$, $\bar{\alpha}$, $\beta = \gamma_4^{-1}\gamma_2^{-1}$, and $\bar{\beta}$. (**b**) Supercells obtained from the sequence of quotient groups T2.2, T5.4, T9.3, T33.11, T65.9 with 1, 4, 8, 32 primitive cells per supercell (see legend on the right).

as black dots in Fig. 10.8a. The four orbitals, labeled by numbers 1 to 4 are coupled cyclically by an on-site term with amplitude h_0 (magenta lines) and assigning each orbital to one of the four hexagons meeting at the lattice site, the orbitals on different sites assigned to the same hexagon are again coupled cyclically by a hopping with amplitude h_1 (green lines). Additionally, the model exhibits π-fluxes through the quadrilateral plaquettes, as illustrated in Fig. 10.8a. To encode these fluxes, a single magenta hopping per square plaquette carries a minus sign (dashed magenta line) and the other three a plus sign (solid magenta line) and the green bonds forming a hexagon centered at the corner of the primitive cell all carry a minus sign (dashed green line). Note that while the chosen gauge does not respect all the symmetries, the physical flux pattern does.

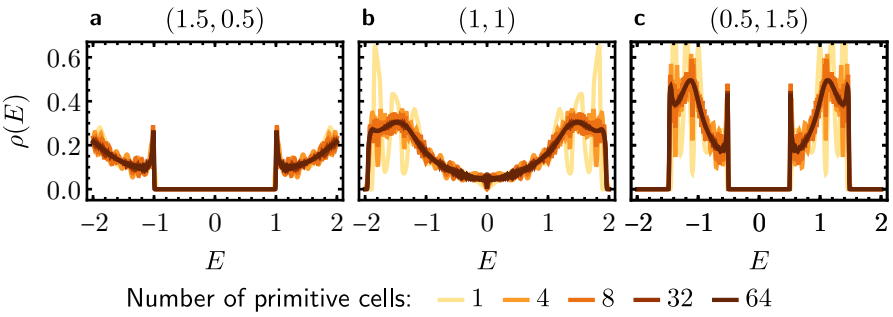

Figure 10.9.: Density of states of the $\{6, 4\}$ Benalcazar-Bernevig-Hughes model. Density of states obtained using the supercell method applied to the sequence of supercells shown in Fig. 10.8b. The data was obtained by randomly sampling 10^8 (10^6 for the supercells with 32 and 64 primitive cells) Abelian momenta, analyzing the spectrum with an energy resolution of 0.005 and smoothing the resulting density of states $\rho(E)$ using a moving average with window 0.01. The top labels give the hopping parameters (h_0, h_1) distinguishing the (**a**) trivial, (**b**) critical, and (**c**) nontrivial phase.

This results in the following Hamiltonian

$$\mathcal{H} = h_1 \left[\sum_{\langle i,j\rangle_\mathrm{c}} \vec{c}_i^\dagger \begin{pmatrix} 1 & 0 & 0 & 0 \\ 0 & 0 & 0 & 1 \\ 0 & 0 & 0 & 0 \\ 0 & 0 & 0 & 0 \end{pmatrix} \vec{c}_j + \sum_{\langle i,j\rangle_\mathrm{b}} \vec{c}_i^\dagger \begin{pmatrix} 0 & 0 & 0 & 0 \\ 0 & 0 & 0 & 1 \\ 0 & 0 & -1 & 0 \\ 0 & 0 & 0 & 0 \end{pmatrix} \vec{c}_j + \mathrm{h.c.} \right] + h_0 \sum_i \vec{c}_i^\dagger \begin{pmatrix} 0 & 1 & 0 & -1 \\ 1 & 0 & 1 & 0 \\ 0 & 1 & 0 & 1 \\ -1 & 0 & 1 & 0 \end{pmatrix} \vec{c}_i, \tag{10.30}$$

where $\langle i, j\rangle_\mathrm{c}$ denotes nearest neighbors within the primitive cell, $\langle i, j\rangle_\mathrm{b}$ denotes nearest neighbors crossing the boundary of the primitive cell and the matrices are given in the basis of orbitals 1, 2, 3, 4 (in that order). The corresponding boundary identifications are shown in Fig. 10.8a by blue symbols.

The intra-site hopping amplitude h_0 may differ from the inter-site hopping h_1. As in the Euclidean case, this arrangement leads to a *trivial* phase for $|h_0| \gg |h_1|$ with effectively independent rings centered at lattice sites, and a *nontrivial* phase for $|h_0| \ll |h_1|$ with effectively independent rings centered on the plaquettes. Figure 10.9 shows the density of states for the two phases

and the transition computed by random sampling of 10^8 (10^6 for T33.11 T65.9) points in $\mathsf{T}^{2\mathfrak{g}^{(m)}}$ and the usual energy resolution and smoothing (see caption). The trivial and the nontrivial phase both exhibit an energy gap that remains stable when going to larger supercells. The gap closes at $h_0/h_1 \approx 0.77$, indicating a phase transition. Interestingly, for small supercells the transition appears semimetallic with vanishing density of states at $E = 0$. However, this is a finite-size effect and the density of states ultimately converges to a finite value, implying a *metallic* transition.

10.4.6. Dirac model on $\{8, 8\}$ lattice

As a final example, we revisit the Dirac model introduced in Section 9.5.2 and show that it is a topological semimetal [8]. Being defined on the $\{8, 8\}$ lattice, we use the sequence of supercells given in Eq. (10.23) and depicted in Fig. 10.4a. With random sampling of Abelian momenta in supercells containing up to 64 primitive cells, we obtain the converging density of states shown in Fig. 10.10b. We observe that there clearly are in-gap states but that the density of states vanishes at zero energy. These observations are validated using two additional independent methods: finite PBC clusters and random sampling of higher-dimensional irreducible representations. Together with a codimension and scaling analysis of the density of states, this suggests a semimetallic band structure with band nodes at zero energy [8].

Since the density of states near zero energy is well approximated by the one obtained from Abelian hyperbolic band theory on the 2-supercell shown in Fig. 10.2, much insight can be gained already from such an approximation. The spectrum of the Abelian Bloch Hamiltonian $H^{(2)}(\mathbf{k}^{(2)})$, $\mathbf{k}^{(2)} \in [0, 2\pi)^6$, on that supercell forms a *nodal ring* whose projection onto three of the six momentum components is shown in Fig. 10.10a. Even more, one can perform a low-energy expansion and obtain a $\mathbf{k} \cdot \mathbf{p}$ model [8] that allows us to study the nodal ring analytically. This reveals that the spectral gap vanishes when

$$\left(\tilde{k}_1^{(2)}\right)^2 + \left(\tilde{k}_2^{(2)}\right)^2 = 6\,(4 - |m|) \tag{10.31}$$

where $\tilde{k}_j^{(2)}$ are components in transformed coordinates. Thus, the nodal manifold is indeed a ring with radius that shrinks to zero for $|m| \to 4$ inducing a topological phase transition, analogous to the collision and annihilation of a pair of Weyl nodes. The "inside" of the nodal ring can be associated with 4D subspaces orthogonal to the plane of the ring hosting a nontrivial second Chern number, see Fig. 10.10a.

Indeed the Abelian Brillouin zone $\mathrm{BZ}^{(1,1)}$ of the primitive cell is simply one of those 4D subspaces. Due to $\Gamma^{(2)} < \Gamma^{(1)}$, $\mathrm{BZ}^{(1,1)}$ is completely embedded

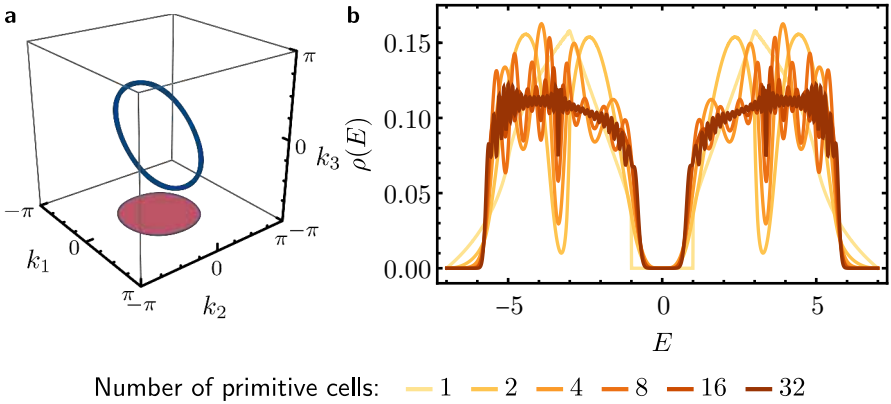

Figure 10.10.: Dirac model of a hyperbolic non-Abelian semimetal. (**a**) Projection of the nodal ring (blue) to the first three momentum components of the 6D Brillouin zone. In the (k_1, k_2)-plane, the projection of the nodal ring bounds a region (red) consisting of points that correspond to projections of 4D subspaces orthogonal to the (k_1, k_2)-plane with nontrivial second Chern number. (**b**) Density of states obtained using the supercell method applied to the sequence of supercells T2.6, T3.11, T5.13, T9.20, T17.29, T33.44 (see legend) shown in Fig. 10.4a. The data was obtained by randomly sampling 10^9 Abelian momenta, analyzing the spectrum with an energy resolution of 0.005 and smoothing the resulting density of states $\rho(E)$ using a moving average with window 0.01.

in the Abelian Brillouin zone of the 2-supercell: $\mathrm{BZ}^{(1,1)} \subset \mathrm{BZ}^{(2,1)}$. We can express the generators $\gamma_j^{(2)}$, $j = 1, 2, \ldots, 6$ of $\Gamma^{(2)}$ in terms of the generators γ_j, $j = 1, 2, 3, 4$ of $\Gamma^{(1)}$, which implies the following relationships between the momenta

$$\begin{aligned} k_1^{(2)} &= k_4^{(1)} + k_1^{(1)}, \quad k_2^{(2)} = k_2^{(1)} - k_1^{(1)}, \quad k_3^{(2)} = k_3^{(1)} - k_2^{(1)}, \\ k_4^{(2)} &= k_4^{(1)} - k_3^{(1)}, \quad k_5^{(2)} = -k_1^{(1)} - k_4^{(1)}, \quad k_6^{(2)} = k_1^{(1)} - k_2^{(1)}. \end{aligned} \tag{10.32}$$

This example demonstrates the power of a reciprocal-space perspective in understanding spectra and band topology.

10.5. Convergence to the thermodynamic limit

In this section, we discuss various aspects of convergence of the supercell method, illustrating them using the constant-hopping nearest-neighbor models

on the $\{8,8\}$ and $\{8,3\}$ lattice. First, in Section 10.5.1, we show the convergence of the density of states obtained from a fixed supercell with increasing density of random sampling of the Abelian Brillouin zone. We here also observe that for the typical size of the largest supercell considered, the density of states obtained from the spectrum at $\mathbf{k} = 0$—the spectrum of the corresponding PBC cluster—does generally not reproduce the characteristic features of the density of states in the thermodynamic limit; in contrast, the density of states converges rapidly upon the introduction of nontrivial momenta, i.e., under random sampling of the Abelian Brillouin zone. Then, in Section 10.5.2, we compare the convergence of different normal sequences of supercells, and observe that the density of states converges to the same limit, thereby consolidating our expectation. Finally, in Section 10.5.3, we compare the results for the largest supercells to the data obtained using the continued-fraction method introduced in Section 9.2.1. This shows that the supercell method does indeed converge to the thermodynamic limit and that several moments of the density of states can be extracted exactly, despite the very small unit cells compared to the flakes used in real-space methods such as the continued-fraction method.

10.5.1. Convergence with sampling of the Abelian Brillouin zone

Besides allowing a meaningful labeling of eigenstates and therefore simplifying a symmetry analysis [7], one of the main powers of the reciprocal-space description is that it allows us to work with small systems but nevertheless obtain good approximations of the spectra of larger systems. Formally, Bloch states facilitate approximations of models on large PBC clusters, i.e., Eq. (10.15) or even its limit for $n \to \infty$, by diagonalizing only matrices defined on smaller supercells, i.e., Eqs. (9.74) and (10.9b). To demonstrate this power, we compare

(1) the density of states obtained from treating a given supercell as a PBC cluster in the form of Eq. (10.11) with matrix $\mathsf{h}_{ij}^{uv}\left(\gamma^{(m)}\right) = h^{uv}\left(\eta_i \gamma \eta_j^{-1}\right)$, which corresponds to evaluating the Bloch Hamiltonian in Eq. (10.17) at the trivial representation, to

(2) the density of states obtained from treating the same supercell as a unit cell of a larger PBC cluster, where the same matrix $\mathsf{h}_{ij}^{uv}\left(\gamma^{(m)}\right)$ appears in Eq. (10.17), and randomly sampling the Abelian Brillouin zone given in Eq. (9.73) with increasing number of sampled points.

Note that (1) is, in essence, the approach of Ref. 302, where the authors diagonalize h_{ij}^{uv} on extremely large PBC clusters whose associated translation

groups also form sequences of normal subgroups, albeit different ones from the ones studied here.

In Figs. 10.11a and 10.11b, we show the data described above for the constant-hopping nearest-neighbor model on the supercell T65.78 of the $\{8,8\}$ lattice. The density of states obtained from simply diagonalizing the 64-site PBC cluster is shown in Fig. 10.11a and is very far from the converged density of states. On the other hand, Fig. 10.11b shows that upon introducing Abelian momenta, the density of states rapidly converges, with 10^4 (dark red line) randomly sampled points already reproducing most of the features, and 10^7 (black line) being basically indistinguishable from the converged curve shown in Fig. 10.4b. Note that here we are considering convergence for a *fixed* supercell in the number of sampled momenta, and not in the sequence of supercells; in the latter case T65.78 would be considered not fully converged.

We repeat the same analysis for the constant-hopping nearest-neighbor model on the smaller supercell T33.1 of the $\{8,3\}$ lattice, which contains $32 \times 16 = 512$ sites. As for the previous model, the density of states obtained from simply diagonalizing the 512-site PBC cluster is shown in Fig. 10.11c and is very far from the converged density of states. On the other hand, Fig. 10.11d shows again that upon introducing Abelian momenta, the density of states rapidly converges with 100 (light orange line) randomly sampled points already reproducing most of the features and 10^4 (dark red line) being basically indistinguishable from the converged curve shown in Fig. 10.5b. A similar convergence can be observed for the Haldane model on the same supercell.

10.5.2. Comparison of different supercell sequences

Since the supercell method does not produce unique normal sequences but allows for many different sequences for the same lattice and choice of primitive cell, it remains to be demonstrated that different sequences converge to the same limit. For the $\{8,8\}$ lattice, two alternative normal sequences to the one given in Eq. (10.23) are [301]

$$\mathrm{T2.6}, \mathrm{T3.11}, \mathrm{T5.13}, \mathrm{T9.22}, \mathrm{T17.35}, \mathrm{T33.58}, \mathrm{T65.81}; \tag{10.33}$$

$$\mathrm{T2.6}, \mathrm{T10.22}, \mathrm{T37.37}, \mathrm{T73.71}, \tag{10.34}$$

and the corresponding density of states data for 10^7 randomly sampled points in $\mathsf{T}^{2\mathfrak{g}^{(m)}}$ is shown in Figs. 10.12a and 10.12b, respectively. Comparing those two figures to Fig. 10.4b, we observe that they converge to the same limit.

The same observation can be made for the $\{8,3\}$ lattice. Two alternative

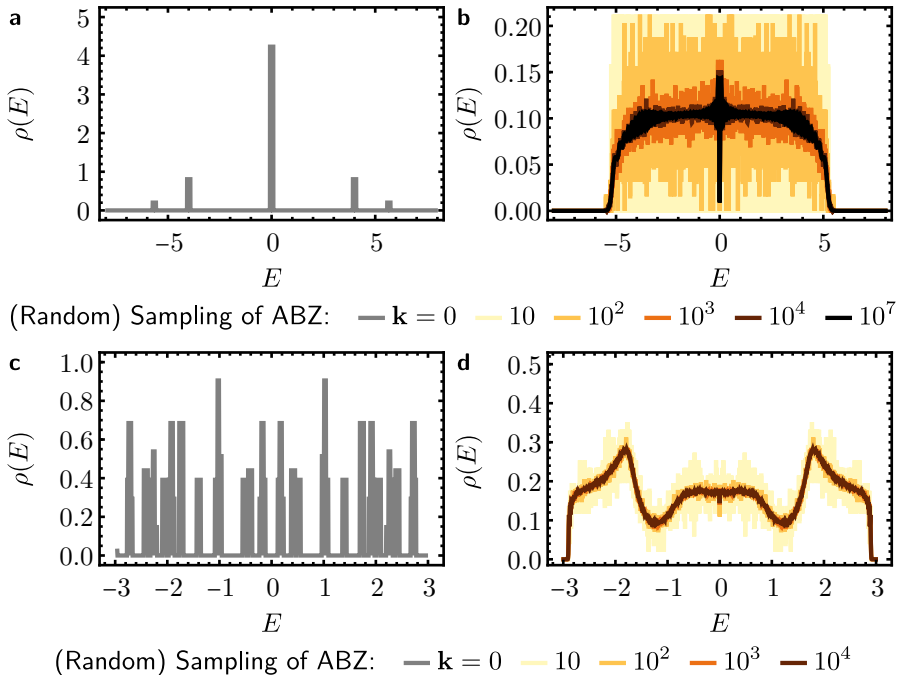

Figure 10.11.: Convergence with sampling of Abelian Brillouin zone. Convergence of density of states of the constant-hopping nearest-neighbor model defined on (**a,b**) the 64-supercell T65.78 of the $\{8, 8\}$ lattice and (**c,d**) the 32-supercell T33.1 of the $\{8, 3\}$ lattice. (**a,c**) Density of states obtained from treating the cell as a PBC cluster with 64, 512 sites and a bin width of 0.16, 0.08, respectively. (**b,d**) Density of states obtained from treating the cell as the unit cell of the infinite lattice and randomly sampling Abelian momenta; the energy resolution is $\mathrm{d}E = 0.005$ and smoothing window 0.01.

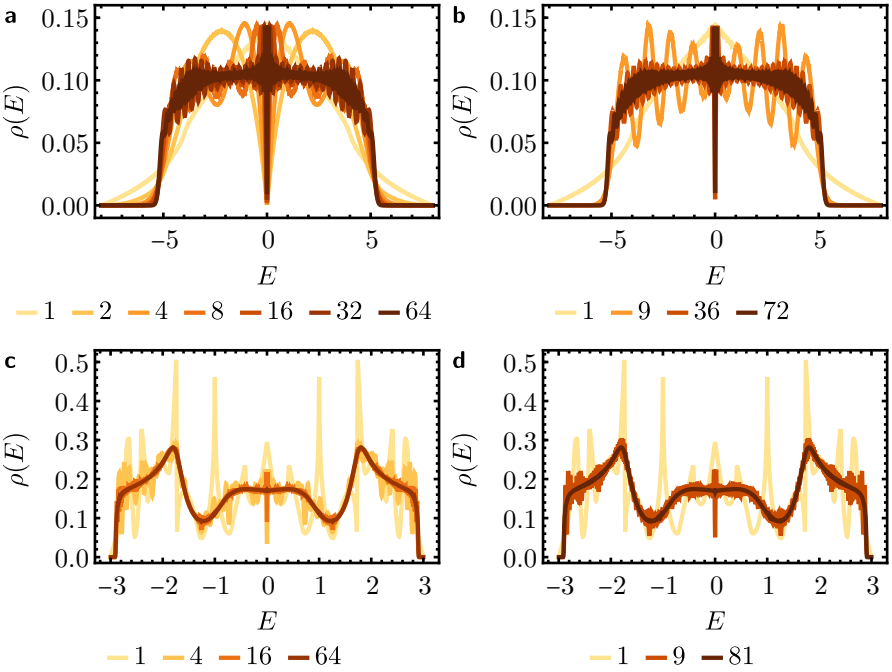

Figure 10.12.: Convergence of different supercell sequences. Density of states of the constant-hopping nearest-neighbor model on (**a,b**) the $\{8,8\}$ lattice (cf. Fig. 10.4b) and (**c,d**) the $\{8,3\}$ (cf. Fig. 10.5b) for the following sequences: (**a**) T2.6, T3.11, T5.13, T9.22, T17.35, T33.58, T65.81, (**b**) T2.6, T10.22, T37.37, T73.71, (**c**) T2.1, T5.1, T17.2, T65.1, and (**d**) T2.1, T10.1, T28.1, T82.1. In all cases, the energy resolution is 0.005 with a moving average with window 0.01.

normal sequences to the one given in Eq. (10.26) are [301]

$$\mathrm{T}2.1, \mathrm{T}5.1, \mathrm{T}17.2, \mathrm{T}65.1; \tag{10.35}$$
$$\mathrm{T}2.1, \mathrm{T}10.1, \mathrm{T}28.1, \mathrm{T}82.1, \tag{10.36}$$

and the corresponding density of states data for 10^7 randomly sampled points in $\mathsf{T}^{2\mathfrak{g}^{(m)}}$ is shown in Figs. 10.12c and 10.12d, respectively, and should be compared to Fig. 10.5b.

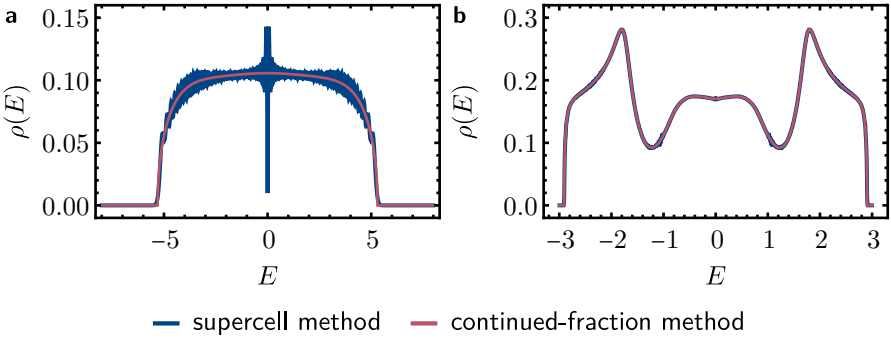

Figure 10.13.: Comparison to continued-fraction method. Density of states of the nearest-neighbor hopping model on (**a**) the $\{8,8\}$ lattice and (**b**) the $\{8,3\}$ lattice obtained using the supercell method (blue) and the continued-fraction method (red; data from Ref. 76 reproduced with permission). In (a) the supercell T73.71 with 72 sites and in (b) T82.1 with 1296 sites was used and in both cases, the energy resolution is 0.005 with a moving average with window 0.01.

10.5.3. Comparison to continued-fraction method

Finally, to establish that the supercell method does indeed converge to the thermodynamic limit, we compare our results to the density of states obtained using the real-space continued-fraction method introduced in Section 9.2.1. Results obtained using that method were in turn shown [76] to be consistent with those obtained from large PBC clusters in Refs. [75, 302], thereby establishing a well-defined thermodynamic limit. In particular, we compare our results obtained for supercells of the $\{8,8\}$ and $\{8,3\}$ lattice that contain 72 and 1296 sites, respectively, to the results of Ref. 76 obtained on flakes with number of sites on the order of 10^8 and 10^9. Figure 10.13 compares the density of states obtained from the two methods and we observe that in both cases the data obtained from the supercell method clearly converges to those obtained using the continued-fraction method. In particular for the $\{8,3\}$ lattice (Fig. 10.13b), almost no difference is discernible. Even our results for the $\{8,8\}$ lattice, despite not being fully converged, reproduce but the core features.

For a more quantitative comparison of the data, we compute the moments of the density of states, defined in Eq. (9.30). Due to the symmetry of the spectra for both the $\{8,8\}$ as well as $\{8,3\}$ lattice, all odd moments vanish. In Fig. 10.14, we show the deviations of the moments of the density of states

obtained from the supercell method to those obtained analytically in Ref. 76. For $\{8, 8\}$, we observe that although the density of states obtained from the 72-site supercell T73.71 is not yet converged, the relative error of the even moments remains below 10^{-4} up to the 16^{th} moment, see Fig. 10.14b, and the first three even moments are reproduced exactly when rounding to the nearest integer. The accuracy of the odd moments, which should all vanish identically, is similar: the first five odd moments are below 10^{-10} and up to the 15^{th} moment, all of them are below 10^{-4}, as can be seen in Fig. 10.14a. For $\{8, 3\}$, we have achieved a significantly better level of convergence and accordingly find that the first seven even moments, i.e., up to the 14^{th} moment, are obtained exactly, while the relative error remains below 10^{-4} for the first 18 even moments, see Fig. 10.14d. Fig. 10.14c shows further that the first seven odd moments are below 10^{-10} and up to the 27^{th} moment, all of them are below 10^{-4}. All numerical computations for the supercell method were performed with machine precision.

Overall, the comparison with the exact moments gives further evidence to the convergence of the supercell method to the thermodynamic limit and affirms our expectation that other quantities besides the density of states, where our reciprocal-space perspective can fully manifest its efficacy, will experience similar convergence.

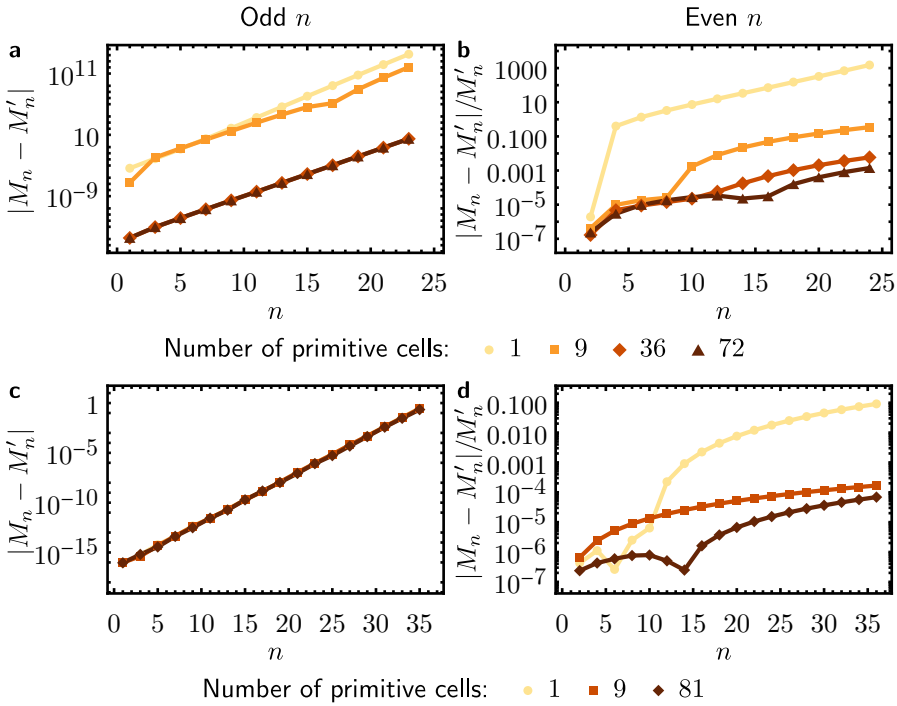

Figure 10.14.: Errors of moments of density of states. Deviation of the moments defined in Eq. (9.30) as obtained through the supercell method (M_n) compared to the exact results from Ref. 76 obtained using the continued-fraction method (M'_n) on PBC clusters of 10^8 and 10^9 of (**a,b**) the $\{8,8\}$ and (**c,d**) the $\{8,3\}$ lattice. (**a,c**) The exact odd moments all vanish identically; thus we show the absolute deviation $|M_n|$. (**b,d**) For the even moments, the relative error $|M_n - M'_n|/M'_n$ is displayed instead. In each case, data for the whole supercell sequence is shown (see legend at the bottom of each row).

11. Conclusions and outlook

Let us remind the reader of the two motivations for studying hyperbolic lattices that we described in the preface. On the one hand, they provide a regularization of the continuous hyperbolic plane, enabling flexible experimental table-top emulators of physics in negatively curved space. On the other hand, nontrivial tight-binding models can be easily defined on hyperbolic lattices leading to *hyperbolic matter* in which condensed-matter consequences of curved space manifest. For both motivations, experimental realizations in metamaterials are crucial, elevating hyperbolic lattices from objects of academic interest to building blocks for engineering metamaterials.

In Chapter 8, we demonstrated the potential of hyperbolic lattices to successfully enable experimental emulation of the negatively curved hyperbolic plane as suggested theoretically [69]. This emulation builds on the concept of *metamaterials*. In real materials, crystalline symmetries naturally arise as subgroups of the symmetries of free space through symmetry breaking instigated by the arrangement of atoms. In metamaterials, on the other hand, both the constituents and their arrangement can be artificially engineered. In discrete metamaterials, the symmetries are encoded in the graph describing the constituents and their interactions, through its connectivity and weights. Therefore, systems possessing symmetries that are not subgroups of the symmetries of laboratory space, such as those derived from curved space, can be realized.

Further, we have established the experimental viability of two methods for verifying the hyperbolic nature, i.e., the negative curvature, of the effective model realized in a metamaterial. This is an important step towards realizing more complicated models. Those two methods rely on approximating the Laplace-Beltrami operator using a simple nearest-neighbor tight-binding model and then observing (1) a reordering of eigenmodes compared to flat space, or (2) the propagation of a pulse along hyperbolic geodesics. The methods are, at least in principle, transferable to most other metamaterials platforms. While it may generally be more challenging to experimentally access the necessary (spatially or time-resolved) information in other platforms, the first method can be applied in a minimal fashion requiring access to significantly less experimental data. It is sufficient to measure the response at two vertices, one at the origin and one away from it, in order to distinguish $\ell = 0$ from $\ell \neq 0$

modes and observe the predicted mode reordering.

We have chosen electric-circuit networks as the metamaterial platform for our experiments. With an implementation encompassing only 85 lattice sites, we have readily observed an excellent approximation of the hyperbolic plane; at the same time, no technical constraint hinders significantly enlarging the number of sites in future applications. In particular, using existing chip manufacturing technology and commercially available components, electric circuits representing lattices with approximately 10^4 sites should be within reach. In combination with the presented results, the efficient fabricability and high scalability of electric circuits elevates them to a versatile platform for emulating classical hyperbolic models, with several advantages over the previously considered methods [68, 294]. First, electric circuits provide easy means for embedding hyperbolic lattices on a flat physical geometry, while allowing for unconnected wire crossings. Such flexibility was utilized to include coupling beyond nearest neighbors and to implement several of the topological models introduced in Section 9.5, including the Haldane model on the $\{6, 4\}$ lattice [321], the Dirac model on the $\{8, 8\}$ lattice [322], and a Haldane model with defects [323]. The development of a new circuit element called *phase element* even allows implementations of twisted boundary conditions [324]. In the future, this could be used to study the impact of non-Abelian Bloch states experimentally [320].

While electric-circuit networks are a powerful platform, they are limited to classical physics. This does not influence single-particle physics and band topology, which only requires wave-phenomena that are present in electric circuits. However, probing correlated quantum states requires a quantum realization. One promising avenue is circuit quantum electrodynamics, where superconducting qubits are coupled to coplanar waveguide resonators. While the first experimental implementation of a hyperbolic lattice was indeed done in a network of coplanar waveguide resonators [68], no qubits were coupled to it, such that the implementation did not go beyond classical physics. Nevertheless, with circuit quantum electrodynamics being an established platform for quantum computation, it can be expected to be feasible to couple qubits to networks of coplanar waveguide resonators arranged as hyperbolic lattices in the near future. This would provide a realization of spin models on hyperbolic lattices with the possibility to probe the holographic principles touched upon in Chapter 8.

The most famous holographic principle is the so-called AdS/CFT correspondence [49, 50], which conjectures a duality between the bulk theory in a negatively curved Anti-de-Sitter (AdS) space and a strongly-interacting conformal field theory (CFT) on its boundary. Hyperbolic lattices provide a natural realization of the spatial part of the metric of AdS space and they

have recently been used to study the duality theoretically [339–342] and experimentally in classical electric circuits [343]. This demonstrates the potential for hyperbolic lattices to be used in theoretical and experimental studies of holography, gravity, and duality.

In Chapters 9 and 10, we have turned to the study of crystalline hyperbolic matter, i.e., models with hyperbolic translational symmetry. The resulting hyperbolic band theory comes with multiple fundamental challenges related to periodic boundary conditions, the thermodynamic limit, and the presence of higher-dimensional irreducible representations of the translation group. With the *supercell method* introduced in Chapter 10, we have tackled all three challenges simultaneously. On the one hand, the method provides an algebraic framework for defining tight-binding models and constructing symmetric unit cells with periodic periodic boundary conditions. On the other hand it enables a systematic study of non-Abelian Bloch states in hyperbolic lattices by applying Abelian hyperbolic band theory to sequences of supercells, in analogy to zone folding in solid-state physics. This provides a substantial step toward a complete reciprocal-space description, which we believe to be consistent with recent work [75, 302] on the thermodynamic limit in real space. While real-space methods scale suboptimally due to the increasing number of noncontractible loops [76], the combination of real-space supercells with reciprocal-space momenta in our approach appears to mitigate this problem and additionally provides true bulk states instead of finite-size approximations. Our density of states results on gapless elementary nearest-neighbor models are in agreement with previous results obtained using a different method [76], but we additionally studied topological models exhibiting energy gaps. Our method has three substantial advantages over Ref. 76: first, it gives direct access to bulk eigenstates, second, it allows for parallel computation through separating the Hilbert space into momentum-sectors, and third, there is no extra computational cost for longer-range hoppings.

We anticipate our reciprocal-space supercell method to facilitate advances in hyperbolic band theory such as symmetry analysis [7], low-energy expansions [8], and topological band theory, including the recently studied 2D hyperbolic model [322] with nontrivial second Chern number [8]. While we have mostly relied on tabulated mathematical results [301] to provide sequences of normal subgroups $\Gamma^{(m)}$, we have outlined an algorithm for extending the sequences in Section 10.2.1. We anticipate that further developments in understanding hyperbolic reciprocal space will accelerate studies of hyperbolic quantum matter.

As we have described in Section 9.5, many of the ideas and models of band topology can be translated to hyperbolic lattices [6, 305–307, 322, 325, 344, 345]. This includes the existence of a bulk-boundary correspondence with

robust boundary states on the macroscopic boundary of a finite flake, which makes hyperbolic lattices particularly interesting in the context of topological lasers [346, 347]. Topological lasers utilize the robustness of topological boundary modes. In Euclidean lattices, only a small fraction of the sites are participating in the boundary modes, and going to hyperbolic lattices with their macroscopic boundary could increase the laser's efficiency significantly. Going beyond the phenomenology present in Euclidean lattices, requires to focus on the characteristic feature of hyperbolic lattices—the noncommutativity of translations or equivalently the presence of non-Abelian Bloch states. With the discovery of a hyperbolic non-Abelian semimetal [8] briefly discussed in Section 10.4.6, whose experimental signatures are still unclear, we have made a first step in that direction.

Studying correlated and topologically ordered systems made up of interacting fermionic or spins is an interesting future direction with important implications once quantum realizations of hyperbolic lattices become available. Topologically ordered phases, such as the ground state of the Kitaev model on a trivalent lattice [328], have a ground state degeneracy that grows exponentially with the genus of the base manifold. The fact that compactified hyperbolic lattices naturally lead to large-genus surfaces suggests a massive ground state degeneracy. The Kitaev model provides a particularly appealing opportunity as it permits a mapping to Majorana particles and potentially a solution in reciprocal space.

Part IV.

Conclusion

12. Conclusion

In this thesis, we have described work related to two emerging aspects of band theory: multigap topology in semimetals and lattices in spaces with constant negative curvature. Band theory, which describes crystals in terms of Bloch states, assumes a homogeneous system and the absence of interactions, yielding a single-particle picture. Despite this, it provides the foundation for the study of systems beyond those assumptions. Perturbative approaches can be employed for low disorder strength and weak interactions. Moreover, translational symmetry can maintain its significance even for larger deviations from these assumptions. Despite being an established field, the relatively late discovery of the relevance of topology in band theory demonstrates that new understanding can still be gained. Part II provides one such avenue taking the relatively new *multigap* perspective, which allowed us to relate several concepts to each other and further our understanding of the topology of certain band-node configurations. Part III on the other hand discussed how to extend these very successful notions to the setting of hyperbolic space with the purpose of establishing hyperbolic band theory as a fundamental tool and starting point for studying the physics of *hyperbolic lattices*.

Let us briefly summarize the main results. In Part II, we have classified [2, 180] and extensively discussed a specific instance of band nodes formed by three energy bands, the *triple points* [180, 182, 187, 191, 216]. Due to the involvement of three bands, such band nodes form a prototypical platform for multigap topology [65, 66, 196, 199, 205] and we have illuminated several consequences and relationships involving crystalline symmetries, triple points, multigap topology and higher-order topology [1, 3]. Further, we have demonstrated our findings not only with minimal models derived from symmetry considerations but verified that they are relevant to real materials by studying many examples based on first-principle calculations.

Part III dealt with fundamental questions arising in the study of lattices in hyperbolic space, i.e., the space with constant negative curvature. In contrast to its analogue with positive curvature—the sphere—the hyperbolic plane does not occur naturally. Thus, the first question we addressed was whether hyperbolic lattices can be used to realize the hyperbolic plane in experiments [68, 69]. We have demonstrated experimentally that a hyperbolic lattice, implemented in an electric-circuit network, indeed emulates the continuous hyperbolic plane [4].

The second question we considered was whether a band-theoretic description of hyperbolic lattices can exist despite the noncommutativity of translations originating form the nonvanishing curvature. We have described the foundations and recent progress in the development of a *hyperbolic band theory* [62, 64], including our own contributions [5–8]. In particular, we have proposed the *supercell method* as a solution to one of the challenges that arise in negatively curved space: the presence of higher-dimensional irreducible representations of the translation group which are hard to parametrize. Our method transcends a rudimentary approximation involving only a small subspace of the *complete* reciprocal space.

Part V.

Appendices

A. Bloch conventions

Different conventions for Bloch Hamiltonians on non-Bravais lattices can lead to different band geometries; in particular different Berry curvatures. Physical quantities on the other hand have to be independent of this choice, which can require different definitions for the different conventions [88, 89, 234]. In particular, we expect that the definition of topological invariants is independent of the convention as long as the invariant does not require a nonlocal symmetry. In that case the invariant should be insensitive to adiabatic displacement of the orbitals within the unit cell. In this appendix, we discuss the two conventions for the Bloch Hamiltonian introduced in Section 2.4.1 and their differences.

A.1. Bloch Hamiltonian

As in Section 2.4.1, we consider a general tight-binding model on a Bravais lattice with N sites given by the second quantized Hamiltonian

$$\mathcal{H} = -\sum_{i,j,\alpha,\beta} h_{ij}^{\alpha\beta} (c_i^\alpha)^\dagger c_j^\beta, \tag{A.1}$$

with site indices i, j and orbital (or any other) degrees of freedom indexed by α, β. The amplitude for the hopping process from (j, β) to (i, α) is $h_{ij}^{\alpha\beta}$. Let $\mathbf{R}_i$ be the *position of the unit cell*, corresponding to site i of the Bravais lattice and δ^α the position of the orbital $|i, \alpha\rangle = (c_i^\alpha)^\dagger |0\rangle$ relative to the Bravais-lattice site. The actual position of the orbital (i, α) then is

$$\mathbf{r}_i^\alpha = \mathbf{R}_i + \delta^\alpha. \tag{A.2}$$

Following Eq. (2.2), the lattice sites i are parametrized by a set of integers n_j.

To block-diagonalize $\mathcal{H}$, we change basis using a Fourier transform. Crucially, there are two conventions for this change of basis, (I) based on the position of the Bravais-lattice site $\mathbf{R}_i$ and (II) based on the actual position of the orbital

$\mathbf{r}_i^\alpha$,

$$\hat{c}^\alpha_{\mathrm{I};\mathbf{k}} = \frac{1}{\sqrt{N}} \sum_{i=1}^{N} c_i^\alpha \mathrm{e}^{-\mathrm{i}\mathbf{k}\cdot\mathbf{R}_i}, \tag{A.3}$$

$$\hat{c}^\alpha_{\mathrm{II};\mathbf{k}} = \frac{1}{\sqrt{N}} \sum_{i=1}^{N} c_i^\alpha \mathrm{e}^{-\mathrm{i}\mathbf{k}\cdot\mathbf{r}_i^\alpha}. \tag{A.4}$$

Note that $\mathbf{R}_i$ depends on the choice of unit cell, while $\mathbf{r}_i^\alpha$ does not. The momentum $\mathbf{k}$ lies in the Brillouin zone defined by the unitarity of the Fourier transform (the conditions are the same for (I) and (II) because $\mathbf{r}_i^\alpha - \mathbf{r}_j^\alpha = \mathbf{R}_i - \mathbf{R}_j$ and δ^α can be factored out of the sum over i):

$$\frac{1}{N} \sum_{\mathbf{k}} \mathrm{e}^{\mathrm{i}\mathbf{k}\cdot(\mathbf{R}_i - \mathbf{R}_j)} = \delta_{i,j}, \tag{A.5}$$

$$\frac{1}{N} \sum_{i} \mathrm{e}^{\mathrm{i}(\mathbf{k}-\mathbf{k}')\cdot\mathbf{R}_i} = \delta_{\mathbf{k},\mathbf{k}'}. \tag{A.6}$$

The momentum can be written in terms of reciprocal lattice vectors $\{\mathbf{b}_j\}_{j=1}^d$

$$\mathbf{k} = \sum_{j=1}^{d} q_j \mathbf{b}_j, \qquad \mathbf{a}_i \cdot \mathbf{b}_j = 2\pi\delta_{ij}, \tag{A.7}$$

then two conditions become

$$\sum_{q_j \in \mathrm{BZ}_j} \mathrm{e}^{2\pi\mathrm{i} q_j \Delta n_j} = 1, \qquad \sum_{p_i=0}^{N_i-1} \mathrm{e}^{2\pi\mathrm{i}\Delta q_i n_i} = 1 \tag{A.8}$$

for $j = 1, \ldots, d$. They are fulfilled if BZ_j contains numbers of the form m_j/N_j with m_j being N_j consecutive integers. Thus,

$$\mathrm{BZ} = \left\{ \sum_{i=1}^{d} \frac{m_i}{N_i u} \mathbf{b}_i \,\middle|\, \forall i = 1, \ldots, d \,:\, m_i + \mathbb{Z} = 0, 1, \ldots, N_i - 1 \right\}. \tag{A.9}$$

In either case, the Hamiltonian can be rewritten as

$$\mathcal{H} = \sum_{\mathbf{k}\in\mathrm{BZ}} \sum_{\alpha,\beta} (\hat{c}^\alpha_{\mathbf{k}})^\dagger H(\mathbf{k})^{\alpha\beta} \hat{c}^\beta_{\mathbf{k}}, \tag{A.10}$$

with the Bloch Hamiltonians

$$\begin{aligned} H_{\mathrm{I}}(\mathbf{k})^{\alpha\beta}\delta_{\mathbf{k},\mathbf{k}'} &= -\frac{1}{N}\sum_{i,j} h_{ij}^{\alpha\beta}\mathrm{e}^{-\mathrm{i}\left(\mathbf{k}\cdot\mathbf{R}_i-\mathbf{k}'\cdot\mathbf{R}_j\right)} \\ &= -\frac{1}{N}\sum_{i,j} h_{ij}^{\alpha\beta}\mathrm{e}^{-\mathrm{i}\left(\mathbf{k}\cdot\mathbf{R}_i-\mathbf{k}'\cdot\mathbf{R}_j\right)} \\ &= -\sum_{\ell} h_{\ell}^{\alpha\beta}\mathrm{e}^{-\mathrm{i}\mathbf{k}\cdot\mathbf{R}_\ell}\underbrace{\frac{1}{N}\sum_{j}\mathrm{e}^{-\mathrm{i}(\mathbf{k}-\mathbf{k}')\cdot\mathbf{R}_j}}_{=\delta_{\mathbf{k},\mathbf{k}'}} \\ &= -\sum_{\ell} h_{\ell}^{\alpha\beta}\mathrm{e}^{-\mathrm{i}\mathbf{k}\cdot\mathbf{R}_\ell}\delta_{\mathbf{k},\mathbf{k}'}, \end{aligned} \tag{A.11}$$

$$\begin{aligned} H_{\mathrm{II}}(\mathbf{k})^{\alpha\beta}\delta_{\mathbf{k},\mathbf{k}'} &= -\frac{1}{N}\sum_{i,j} h_{ij}^{\alpha\beta}\mathrm{e}^{-\mathrm{i}\left(\mathbf{k}\cdot\mathbf{r}_i^{\alpha}-\mathbf{k}'\cdot\mathbf{r}_j^{\beta}\right)} \\ &= -\sum_{\ell} h_{\ell}^{\alpha\beta}\mathrm{e}^{-\mathrm{i}\mathbf{k}\cdot(\mathbf{R}_\ell+\delta^{\alpha}-\delta^{\beta})}\delta_{\mathbf{k},\mathbf{k}'}, \end{aligned} \tag{A.12}$$

where we used translation invariance, i.e. that $h_{ij}^{\alpha\beta} = h_{i-j}^{\alpha\beta}$ and set $\ell = i - j$ and $\mathbf{R}_\ell = \mathbf{R}_i - \mathbf{R}_j$. We observe that

$$H_{\mathrm{I}}(\mathbf{k}+\mathbf{b})^{\alpha\beta} = H_{\mathrm{I}}(\mathbf{k})^{\alpha\beta}, \tag{A.13}$$

$$H_{\mathrm{II}}(\mathbf{k}+\mathbf{b})^{\alpha\beta} = H_{\mathrm{II}}(\mathbf{k})^{\alpha\beta}\mathrm{e}^{-\mathrm{i}\mathbf{b}\cdot(\delta^{\alpha}-\delta^{\beta})}; \tag{A.14}$$

while H_{I} is periodic in momentum, H_{II} is not.

Note that the two different conventions for the Fourier transforms are related to each other via the transformation

$$\hat{c}_{\mathrm{I};\mathbf{k}}^{\alpha} = \frac{1}{\sqrt{N}}\sum_{i} c_i^{\alpha}\mathrm{e}^{-\mathrm{i}\mathbf{k}\cdot\mathbf{r}_i^{\alpha}}\mathrm{e}^{\mathrm{i}\mathbf{k}\cdot\delta^{\alpha}} = \hat{c}_{\mathrm{II};\mathbf{k}}^{\alpha}\mathrm{e}^{\mathrm{i}\mathbf{k}\cdot\delta^{\alpha}} \tag{A.15}$$

and the Hamiltonians via

$$H_{\mathrm{I}}(\mathbf{k})^{\alpha\beta} = H_{\mathrm{II}}(\mathbf{k})^{\alpha\beta}\mathrm{e}^{\mathrm{i}\mathbf{k}\cdot(\delta^{\alpha}-\delta^{\beta})} \tag{A.16}$$

or in matrix notation

$$H_{\mathrm{I}}(\mathbf{k}) = U(\mathbf{k})H_{\mathrm{II}}(\mathbf{k})U(\mathbf{k})^{\dagger}, \qquad U(\mathbf{k})^{\alpha\beta} = \mathrm{e}^{\mathrm{i}\mathbf{k}\cdot\delta^{\alpha}}\delta_{\alpha,\beta}. \tag{A.17}$$

It turns out that convention (II) leads to a Bloch Hamiltonian and Berry curvature which respect the symmetries of the underlying lattice, while convention (I) does not; even more, convention (I) is not unique and in particular dependent on the choice of the unit cell [88, 89].

Change of Origin and Unit Cell

Consider a change of origin $\mathbf{r}_i^\alpha \mapsto \mathbf{r}_i^\alpha + \mathbf{r}_0$. Then, in both conventions, we have

$$\hat{c}_{\mathbf{k}}^\alpha \mapsto \mathrm{e}^{-\mathrm{i}\mathbf{k}\cdot\mathbf{r}_0}\hat{c}_{\mathbf{k}}^\alpha, \qquad H'(\mathbf{k}) = H(\mathbf{k}), \tag{A.18}$$

which is just a gauge transformation.

A change of unit cell in convention (II) leaves the Bloch Hamiltonian invariant. In convention (I), on the other hand, has a significant effect: $\mathbf{R}_i \mapsto \mathbf{R}_i + \sum_\mu e_\mu^\alpha \mathbf{a}_\mu$ with $e_\mu^\alpha \in \{0, 1\}$. In particular this is dependent on the orbital:

$$\hat{c}_{\mathrm{I};\mathbf{k}}^\alpha \mapsto \mathrm{e}^{-\mathrm{i}\sum_\mu e_\mu^\alpha \mathbf{k}\cdot\mathbf{a}_\mu}\hat{c}_{\mathrm{I};\mathbf{k}}^\alpha, \qquad H'_{\mathrm{I}}(\mathbf{k})^{\alpha\beta} = H_{\mathrm{I}}(\mathbf{k})^{\alpha\beta}\mathrm{e}^{-\mathrm{i}\sum_\mu (e_\mu^\alpha - e_\mu^\beta)\mathbf{k}\cdot\mathbf{a}_\mu}. \tag{A.19}$$

A.2. Topology

We illustrate the effect on the geometry and topology using some examples. Let $|u_n(\mathbf{k})\rangle$ be the eigenstate of the Bloch Hamiltonian $H(\mathbf{k})$ corresponding to the n-th band:

$$H(\mathbf{k})\,|u_n(\mathbf{k})\rangle = \varepsilon_n(\mathbf{k})\,|u_n(\mathbf{k})\rangle \tag{A.20}$$

with the components

$$u_n(\mathbf{k})^\alpha = \langle 0|c_{\mathbf{k}}^\alpha|u_n(\mathbf{k})\rangle\,. \tag{A.21}$$

Obviously, the eigenstates of the two conventions are related by

$$|u_{\mathrm{I};n}(\mathbf{k})\rangle = U(\mathbf{k})\,|u_{\mathrm{II};n}(\mathbf{k})\rangle\,. \tag{A.22}$$

A.2.1. Berry Connection and Curvature

The Berry connection of band n is defined as

$$\mathcal{A}^{(n)}(\mathbf{k}) = \mathrm{i}\,\langle u_n(\mathbf{k})|\boldsymbol{\nabla}_{\mathbf{k}}|u_n(\mathbf{k})\rangle\,. \tag{A.23}$$

Under a $U(1)$ gauge transformation on the n-th band $|u_n(\mathbf{k})\rangle \mapsto \mathrm{e}^{\mathrm{i}\vartheta(\mathbf{k})}\,|u_n(\mathbf{k})\rangle$ this transforms as

$$\mathcal{A}^{(n)}(\mathbf{k}) \mapsto \mathcal{A}^{(n)}(\mathbf{k}) - \boldsymbol{\nabla}_{\mathbf{k}}\vartheta(\mathbf{k}) \tag{A.24}$$

independent of the convention.

The Berry curvature is given by

$$\Omega_{\mu\nu}^{(n)}(\mathbf{k}) = \partial_{k_\mu}\mathcal{A}_\nu^{(n)}(\mathbf{k}) - \partial_{k_\nu}\mathcal{A}_\mu^{(n)}(\mathbf{k}), \tag{A.25}$$

and is invariant under a $U(1)$ gauge transformation as given above:

$$\Omega_{\mu\nu}^{(n)}(\mathbf{k}) \mapsto \Omega_{\mu\nu}^{(n)}(\mathbf{k}) - \partial_{k_\mu}\partial_{k_\nu}\vartheta(\mathbf{k}) + \partial_{k_\nu}\partial_{k_\mu}\vartheta(\mathbf{k}) = \Omega_{\mu\nu}^{(n)}(\mathbf{k}). \tag{A.26}$$

We analyze the relation between those quantities for the two different Bloch conventions:

$$\begin{aligned}\mathcal{A}_I^{(n)}(\mathbf{k}) &= \mathrm{i}\,\langle u_{II;n}(\mathbf{k})|U(\mathbf{k})^\dagger \boldsymbol{\nabla}_\mathbf{k} U(\mathbf{k})|u_{II;n}(\mathbf{k})\rangle \\ &= \mathcal{A}_{II}^{(n)}(\mathbf{k}) + \mathrm{i}\,\langle u_{II;n}(\mathbf{k})|U(\mathbf{k})^\dagger\,(\boldsymbol{\nabla}_\mathbf{k} U(\mathbf{k}))|u_{II;n}(\mathbf{k})\rangle \\ &= \mathcal{A}_{II}^{(n)}(\mathbf{k}) - \langle u_{II;n}(\mathbf{k})|\mathbf{D}|u_{II;n}(\mathbf{k})\rangle \end{aligned} \tag{A.27}$$

$$\begin{aligned}\Omega_{I;\mu\nu}^{(n)}(\mathbf{k}) &= \Omega_{II;\mu\nu}^{(n)}(\mathbf{k}) \\ &\quad - \langle \partial_{k_\mu} u_{II;n}(\mathbf{k})|D_\nu|u_{II;n}(\mathbf{k})\rangle - \langle u_{II;n}(\mathbf{k})|D_\nu|\partial_{k_\mu} u_{II;n}(\mathbf{k})\rangle \\ &\quad + \langle \partial_{k_\nu} u_{II;n}(\mathbf{k})|D_\mu|u_{II;n}(\mathbf{k})\rangle + \langle u_{II;n}(\mathbf{k})|D_\mu|\partial_{k_\nu} u_{II;n}(\mathbf{k})\rangle \end{aligned} \tag{A.28}$$

with the diagonal (vector valued) matrix $\mathbf{D}^{\alpha\beta} = \delta^\alpha \delta^{\alpha,\beta}$. Clearly, the Berry curvature is different for the different conventions. For convention (I) it even depends on the choice of unit cell.

A.2.2. Chern Number

The Chern number for a two-dimensional (2D) system is given in terms of the Berry curvature as

$$c_1^{(n)} = \frac{1}{2\pi}\int_{\mathrm{BZ}} \mathrm{d}k_x\,\mathrm{d}k_y\,\Omega_{xy}^{(n)}(\mathbf{k}). \tag{A.29}$$

Because the Berry curvature is gauge invariant, so is the Chern number. According to the Chern theorem the Chern number is always an integer. Alternatively, the Chern number can be expressed as a line integral of the Berry connection. To see that, we first rewrite the integral over a simply connected manifold, which is obtained by cutting the torus twice. This gives a (normalized) square S, parametrized by $\kappa = (\kappa_x, \kappa_y) \in [0,1]^2$, with boundary conditions such that the physical states are periodic:

$$c_1^{(n)} = \frac{1}{2\pi}\int_S \mathrm{d}\kappa_x\,\mathrm{d}\kappa_y\,\Omega_{xy}^{(n)}(\kappa) \tag{A.30}$$

The boundary condition implies that the states $|u_n(\kappa)\rangle$ can only differ by a $U(1)$ gauge transformation along the cuts. For the two cuts along κ_x (at $\kappa_y = 0, 1$) and along κ_y (at $\kappa_x = 0, 1$) the phase difference is then given by functions $\vartheta_x(\kappa_x)$ and $\vartheta_y(\kappa_y)$, such that

$$|u_n(\kappa_x, 1)\rangle = \mathrm{e}^{\mathrm{i}\vartheta_x(\kappa_x)}\,|u_n(\kappa_x, 0)\rangle\,, \qquad |u_n(1, \kappa_y)\rangle = \mathrm{e}^{\mathrm{i}\vartheta_y(\kappa_y)}\,|u_n(0, \kappa_y)\rangle\,. \tag{A.31}$$

By applying Stoke's theorem, the surface integral can be rewritten as a line integral of the Berry connection along the boundary of S:

$$c_1^{(n)} = \frac{1}{2\pi} \int_{\partial S} \mathrm{d}\kappa \cdot \mathcal{A}^{(n)}(\kappa). \tag{A.32}$$

Single-valuedness requires that the gauge transformation relating $(1,1)$ to $(0,0)$ is unique up to integer multiples of 2π independent of whether one passes around the boundary clockwise or counterclockwise:

$$|u_n(1,1)\rangle = \mathrm{e}^{\mathrm{i}(\vartheta_x(1)+\vartheta_y(0))} |u_n(0,0)\rangle = \mathrm{e}^{\mathrm{i}(\vartheta_x(0)+\vartheta_y(1))} |u_n(0,0)\rangle\,, \tag{A.33}$$

which implies

$$\vartheta_x(1) - \vartheta_x(0) - \vartheta_y(1) + \vartheta_y(0) \in 2\pi\mathbb{Z}. \tag{A.34}$$

Substituting the above relationships between the eigenstates into Eq. (A.32) and noting that $\mathcal{A}_x^{(n)}(\kappa_x, 0) - \mathcal{A}_x^{(n)}(\kappa_x, 1) = \partial_{\kappa_x}\vartheta_x(\kappa_x)$ and analogously for the y-component, we arrive at

$$c_1^{(n)} = \frac{1}{2\pi} \left(\vartheta_x(1) - \vartheta_x(0) - \vartheta_y(1) + \vartheta_y(0)\right) \in \mathbb{Z}, \tag{A.35}$$

proving that the Chern number is indeed an integer.

Finally, we show that the Chern number is independent of the choice of Bloch convention:

$$\begin{aligned} c_{1;I}^{(n)} - c_{1;II}^{(n)} &= \frac{1}{2\pi} \int_{\partial S} \mathrm{d}\kappa \cdot \left(\mathcal{A}_I^{(n)}(\kappa) - \mathcal{A}_{II}^{(n)}(\kappa)\right) \\ &= -\frac{1}{2\pi} \int_{\partial S} \mathrm{d}\kappa \cdot \langle u_{II;n}(\mathbf{k}) | \mathbf{D} | u_{II;n}(\mathbf{k}) \rangle \\ &= 0. \end{aligned} \tag{A.36}$$

Note that the integrand $\langle u_{II;n}(\mathbf{k}) | \mathbf{D} | u_{II;n}(\mathbf{k}) \rangle$ is gauge invariant and thus the terms from equivalent sides of ∂S cancel, because they differ only in their sign (due to opposite orientation). We have shown that

$$c_{1;I}^{(n)} = c_{1;II}^{(n)}. \tag{A.37}$$

B. Details on the classification of triple points

This chapter is largely based on Appendix C.2 to the publication "Triple nodal points characterized by their nodal-line structure in all magnetic space groups" [2]. Segments with significant text overlap with the published version may be subject to copyright by the American Physical Society.

In this appendix, we prove that the parameters of the $\mathbf{k}\cdot\mathbf{p}$ models in symmetry-unrelated mirror planes, used in Section 4.3, obey certain relationships. We used this to derive the classification of triple points in the absence of space-time inversion $\mathcal{PT}$ symmetry.

B.1. Relationship between independent sets of mirror planes

The functional form of the $\mathbf{k}\cdot\mathbf{p}$ models in Eq. (4.11) has been derived with rather general assumptions, such that it applies to *arbitrary* mirror planes containing the rotation axis. In this respect, note that point groups $4mm$ and $6mm$ each have two sets of symmetry-related mirror planes (cf. differently colored planes in Fig. 4.4). Within each set, the mirror planes are related to each other by rotational symmetry, such that the parameters a, b, c and A are identical. In contrast, momenta in the two sets are *not* related by symmetry; therefore, the functions a, b, c, A and a', b', c', A' that encode the Hamiltonian in the two planes, respectively, are *a priori* not related to each other.

Nevertheless, a relationship between the two sets of functions can be established. This is achieved by considering the full three-dimensional (3D) $\mathbf{k}\cdot\mathbf{p}$ model, i.e., one not restricted to mirror planes, but which reduces to the functional form in Eq. (4.11) (with suitable choice of functions a, b, c, A) for both sets of mirror planes. In this section, we clarify how to relate the parameters of the $\mathbf{k}\cdot\mathbf{p}$ model in the independent sets of mirror planes of point groups $4mm$ and $6mm$ without determining the full 3D $\mathbf{k}\cdot\mathbf{p}$ model.

We consider a point group G with two generators: an n-fold rotation C_n (for simplicity, n is assumed even; in our application $n = 4, 6$) and a vertical

mirror m_0 (such that the mirror plane contains the axis of rotation). The elements of the group correspond to powers of the n-fold rotation, C_n^l for $l \in \{0, 1, \ldots, n-1\}$, and two types of mirror symmetries

$$m_l = C_n^l m_0 C_n^{-l}, \tag{B.1a}$$
$$m_l' = C_n^l m_0' C_n^{-l} \tag{B.1b}$$

where $m_0' = C_n m_0$ and $l \in \{0, 1, \ldots, n/2-1\}$. Note that, additionally, all mirrors m satisfy

$$m = C_n^l m C_n^l \tag{B.2}$$

for any l. The partitioning in Eq. (B.1) corresponds to two conjugacy classes of mirrors:

$$\mathsf{c}(m_0) = \left\{m_0, m_1, \ldots, m_{n/2-1}\right\}, \tag{B.3a}$$
$$\mathsf{c}(m_0') = \left\{m_0', m_1', \ldots, m_{n/2-1}'\right\}. \tag{B.3b}$$

In contrast, rotations with $l \notin \{0, n/2\}$ appear in two-element conjugacy classes

$$\left\{C_n^l, C_n^{-l}\right\} \tag{B.4}$$

(with $mC_n^l m^{-1} = C_n^{-l}$) whereas rotations with $l \in \{0, n/2\}$ constitute single-element conjugacy classes. Furthermore, each mirror m, is accompanied by a perpendicular mirror $m_\perp$ (for $4mm$ both are in the same conjugacy class, while for $6mm$ they are in different conjugacy classes).

The Hamiltonian satisfies the constraint in Eq. (2.72) for both generators of the point group, i.e.,

$$H(\mathbf{k}) = \mathscr{D}(C_n) H\left(C_n^{-1}\mathbf{k}\right) \mathscr{D}(C_n)^{-1}, \tag{B.5a}$$
$$H(\mathbf{k}) = \mathscr{D}(m) H\left(m^{-1}\mathbf{k}\right) \mathscr{D}(m)^{-1}. \tag{B.5b}$$

Restricting to the plane M in momentum space, which we define[1] as the set of $\mathbf{k}$ points invariant under m, Eq. (B.5) leads to the two constraints

$$H(\mathbf{k}) = \mathscr{D}(m) H(\mathbf{k}) \mathscr{D}(m)^{-1}, \tag{B.6a}$$
$$H(\mathbf{k}) = \mathscr{D}(m_\perp) H\left(m_\perp^{-1}\mathbf{k}\right) \mathscr{D}(m_\perp)^{-1}, \tag{B.6b}$$

for $\mathbf{k} \in M$. We recognize Eq. (B.6) as an incarnation of Eqs. (4.5) and (4.7), which we employed in the derivation of the $\mathbf{k}\cdot\mathbf{p}$ Hamiltonians in M (cf. Section 4.3.2).

[1] Note that the set M is called m-plane in the main text; however, the mathematically involved discussion that follows requires a more compact notation (only adopted in the present appendix).

We now formally perform the $\mathbf{k}\cdot\mathbf{p}$ analysis based on Eq. (B.6). To do that, we decompose in-plane momentum vectors into orthogonal coordinates $\mathbf{k} = (k_M, k_z)$ (with k_z, as usual, along the rotation axis), and sometimes utilize the unit vectors $\mathbf{e}_M$ and $\mathbf{e}_z$ in the two directions, respectively. Next, note that any $\mathbf{k}\cdot\mathbf{p}$ Hamiltonian is encoded by a collection of parameters a_i (which in our case are taken to be functions of k_z, since the k_z-dependence is not constrained by elements of G; for brevity we call them *coefficients*) that multiply matrix-valued polynomial functions $h_i(k_M)$ subject to Eq. (B.6) (for brevity we call $h_i(k_M)$ *terms in the* $\mathbf{k}\cdot\mathbf{p}$ *model*). Finally, we truncate the expansion such that the polynomials have order of at most N in k_M. Then, for $\mathbf{k} \in M$, and collecting the parameters a_i in the vector $\mathbf{a}$, we write

$$H_M^{(N)}[\mathbf{a}](\mathbf{k}) = \sum_i a_i(k_z) h_i\left(k_M\right). \tag{B.7}$$

To summarize, the multiple decorations of the Hamiltonian appearing on the left-hand side of Eq. (B.7) remind us that $H_M^{(N)}[\mathbf{a}]$ is a parameterized (parameters $\mathbf{a}$) and truncated (order N) expansion of the Hamiltonian $H(\mathbf{k})$ restricted to the plane M. Note that Eq. (B.7) is incarnated, for example, in Eq. (4.11), when setting $\mathbf{a} = (a, b, c, A)$.

It is important to keep in mind that an equation with the same functional form as Eq. (B.7) applies to *any* of the n mirror planes [because for each such a plane one can choose a pair of orthogonal mirror symmetries characterized by constraints analogous to Eq. (B.6)]; in particular, the functional form of h_i can be considered to be independent of M (while both its argument k_M as well as the basis in which the resulting $H_M^{(N)}$ is given depend on the mirror plane under consideration). To simplify our subsequent analysis of the symmetry constraints, we find it convenient to further adopt the notation

$$h_M^i(\mathbf{k}) := h_i\left(k_M\right) = h_i\left(\mathbf{k}\cdot\mathbf{e}_M\right) \tag{B.8}$$

(one should keep in mind here that h_M^i depends nontrivially only on the k_M-component of $\mathbf{k}$). Generically, the parameters $\mathbf{a}$ are different in different mirror planes. However, due to rotational symmetry, they are constrained to be identical in all mirror planes in the same conjugacy class. We are therefore left with two sets of parameters $\mathbf{a}$ and $\mathbf{a}'$ for the mirror planes M_0 and M_0', respectively. The goal of this appendix is to relate $\mathbf{a}$ and $\mathbf{a}'$.

To motivate the subsequent technical analysis, let us summarize here the steps that have to be taken to arrive at the sought relation (working out these steps fills the remainder of this Appendix).

1. Given any term $h_M^i(\mathbf{k})$ that appears in the $\mathbf{k}\cdot\mathbf{p}$ expansion of the Hamiltonian restricted to a mirror plane, i.e., satisfies Eq. (B.6), we show in

Eqs. (B.9) and (B.11) to (B.14) that by symmetrizing $h^i_M(\mathbf{k})$ we obtain a term $\hat{h}^i_{\mathsf{c}(m)}(\mathbf{k})$ that appears in the $\mathbf{k}\cdot\mathbf{p}$ expansion of the full Hamiltonian, i.e., satisfies Eq. (B.5).

As indicated by the notation, the terms in the full Hamiltonian produced by such a symmetrization, only cover one conjugacy class of mirror planes; some terms that would appear in a $\mathbf{k}\cdot\mathbf{p}$ expansion of the full Hamiltonian and are relevant in its restriction to mirror planes from the other conjugacy class are missing.

2. We next turn to relating the two conjugacy classes. We *observe* that the point groups and representations under consideration satisfy a useful property that relates the representations of symmetry-unrelated mirror symmetries to each other, cf. Eq. (B.15a), giving us the previously unknown transformation U between the bases in which $h^i_{M_0}(\mathbf{k})$ and $h^i_{M'_0}(\mathbf{k})$ are expressed in terms of the same functions h_i, cf. Eq. (B.17).

3. Based on the symmetrized terms $\hat{h}^i_{\mathsf{c}(m_0)}(\mathbf{k})$ and $\hat{h}^i_{\mathsf{c}(m'_0)}(\mathbf{k})$, we next define the *reconstructed* $\mathbf{k}\cdot\mathbf{p}$ *model* $\hat{H}^{(N)}[\mathbf{B}](\mathbf{k})$ as the $\mathbf{k}\cdot\mathbf{p}$ model obtained from all those symmetrized terms, i.e., from both $\mathsf{c}(m_0)$ and $\mathsf{c}(m'_0)$, cf. Eq. (B.19). The basis transformation U then allows us to write all those terms using the matrix-valued polynomial functions h_i, cf. Eq. (B.20).

4. Finally, we evaluate $\hat{H}^{(N)}[\mathbf{B}](\mathbf{k})$ in the planes M_0 and M'_0 and compare the result to $H^{(N)}_{M_0}[\mathbf{a}](\mathbf{k})$ and $H^{(N)}_{M'_0}[\mathbf{a}'](\mathbf{k})$, respectively. This allows use to express $\mathbf{a}$ and $\mathbf{a}'$ in terms of $\mathbf{B}$ and therefore determine if and how $\mathbf{a}$ and $\mathbf{a}'$ are related.

To start the analysis of step 1 in the above list, note that each term $h^i_M(\mathbf{k})$ in $H^{(N)}_M[\mathbf{a}](\mathbf{k})$ satisfies Eq. (B.6) and originates from a term in the full $\mathbf{k}\cdot\mathbf{p}$ Hamiltonian $H^{(N)}(\mathbf{k})$ that satisfies Eq. (B.5). Let further $\mathbf{n}_M = C_n^{n/2}\mathbf{e}_M$ be the normal of the mirror plane M corresponding to the mirror symmetry m (here m is chosen to be one of the representatives of the conjugacy classes, i.e., either m_0 or m'_0). In order to find symmetry-compatible terms appearing in the 3D expansion $H^{(N)}(\mathbf{k})$, we define for any $\mathbf{k}\in\mathbb{R}^3$ a *symmetrized* matrix-valued polynomial function

$$\hat{h}^i_{\mathsf{c}(m)}(\mathbf{k}) = \sum_{l=0}^{n-1} \mathscr{D}(C_n)^l h^i_M\left(C_n^{-l}\left(\mathbf{k}|_{M_l}\right)\right)\mathscr{D}(C_n)^{-l}, \tag{B.9}$$

where $M_l = C_n^l M$ and

$$\mathbf{k}|_M = \mathbf{k} - (\mathbf{n}_M\cdot\mathbf{k})\,\mathbf{n}_M. \tag{B.10}$$

Note that

$$\begin{aligned} C_n^{-l}\left(\mathbf{k}|_{M_l}\right) &= C_n^{-l}\left[\mathbf{k} - (\mathbf{n}_{M_l}\cdot\mathbf{k})\,\mathbf{n}_{M_l}\right] \\ &= C_n^{-l}\mathbf{k} - \left[\left(C_n^{-l}\mathbf{n}_{M_l}\right)\cdot\left(C_n^{-l}\mathbf{k}\right)\right]\left(C_n^{-l}\mathbf{n}_{M_l}\right) \\ &= C_n^{-l}\mathbf{k} - \left[\mathbf{n}_M\cdot\left(C_n^{-l}\mathbf{k}\right)\right]\mathbf{n}_M \\ &= \left(C_n^{-l}\mathbf{k}\right)\big|_M\,, \end{aligned} \tag{B.11}$$

where we utilized that $\mathbf{n}\cdot\mathbf{k} = (S\mathbf{n})\cdot(S\mathbf{k})$ for any orthogonal symmetry S. The final line of Eq. (B.11) reveals that the argument of h^i_M in Eq. (B.9) lies in M as it is supposed to.

We proceed to show that $\hat{h}^i_{\mathsf{c}(m)}(\mathbf{k})$ defined by Eq. (B.9) satisfies Eq. (B.5). First, by substituting $l = p+1$ and using $C_n^0 = C_n^n$ (both corresponding to the identity element), we easily find that

$$\begin{aligned} \hat{h}^i_{\mathsf{c}(m)}(\mathbf{k}) &= \sum_{l=1}^{n} \mathfrak{D}(C_n)^l h^i_M\left(\left(C_n^{-l}\mathbf{k}\right)\big|_M\right)\mathfrak{D}(C_n)^{-l} \\ &= \sum_{p=0}^{n-1} \mathfrak{D}(C_n)^{p+1} h^i_M\left(\left(C_n^{-(p+1)}\mathbf{k}\right)\Big|_M\right)\mathfrak{D}(C_n)^{-(p+1)} \\ &= \mathfrak{D}(C_n)\hat{h}^i_{\mathsf{c}(m)}(C_n^{-1}\mathbf{k})\mathfrak{D}(C_n)^{-1}, \end{aligned} \tag{B.12}$$

which reveals that $\hat{h}^i_{\mathsf{c}(m)}(\mathbf{k})$ obeys Eq. (B.5a). Furthermore, for any mirror symmetry $\tilde{m}$, it holds that

$$\begin{aligned} \tilde{m}^{-1}\left(\mathbf{k}|_M\right) &= \tilde{m}^{-1}\left[\mathbf{k} - (\mathbf{n}_M\cdot\mathbf{k})\,\mathbf{n}_M\right] \\ &= \tilde{m}^{-1}\mathbf{k} - \left[(\tilde{m}^{-1}\mathbf{n}_M)\cdot\left(\tilde{m}^{-1}\mathbf{k}\right)\right]\left(\tilde{m}^{-1}\mathbf{n}_M\right) \\ &= \left(\tilde{m}^{-1}\mathbf{k}\right)\big|_{\tilde{m}M}\,, \end{aligned} \tag{B.13}$$

where we again used that $\mathbf{n}\cdot\mathbf{k} = (S\mathbf{n})\cdot(S\mathbf{k})$, and additionally that mirrors are their own inverses, $\tilde{m} = \tilde{m}^{-1}$. Using Eqs. (B.2), (B.6a), (B.9) and (B.11)

and $C_n^{-l} = C_n^{n-l}$, we find

$$\begin{aligned}
\hat{h}^i_{\mathsf{c}(m)}(\mathbf{k}) &\overset{(B.11)}{=} \sum_{l=0}^{n-1} \mathscr{D}(C_n)^l h^i_M\left(\left(C_n^{-l}\mathbf{k}\right)\big|_M\right) \mathscr{D}(C_n)^{-l} \\
&\overset{(B.6a)}{=} \sum_{l=1}^{n} \mathscr{D}\left(C_n^l m\right) h^i_M\left(m^{-1}\left(C_n^{-l}\mathbf{k}\right)\big|_M\right) \mathscr{D}\left(m^{-1}C_n^{-l}\right) \\
&\overset{(B.2)}{=} \sum_{l=1}^{n} \mathscr{D}\left(mC_n^{-l}\right) h^i_M\left(\left(C_n^l m^{-1}\mathbf{k}\right)\big|_M\right) \mathscr{D}\left(C_n^l m^{-1}\right) \\
&= \sum_{p=1}^{n} \mathscr{D}\left(mC_n^{p}\right) h^i_M\left(\left(C_n^{-p} m^{-1}\mathbf{k}\right)\big|_M\right) \mathscr{D}\left(C_n^{-p} m^{-1}\right) \\
&= \mathscr{D}(m)\hat{h}^i_{\mathsf{c}(m)}\left(m^{-1}\mathbf{k}\right)\mathscr{D}(m)^{-1},
\end{aligned} \tag{B.14}$$

where in the second line we further used hat m acts trivially inside M (and therefore its addition to the argument of h^i_M does not alter the expression), and in the fourth line we substituted $p = n - l$. The final line above confirms that $\hat{h}^i_{\mathsf{c}(m)}(\mathbf{k})$ also respects Eq. (B.5b). Therefore, we have shown that $\hat{h}^i_{\mathsf{c}(m)}(\mathbf{k})$ is a term that appears in the 3D expansion $H^{(N)}(\mathbf{k})$ (even though it does not generally reduce to $h^i_M(\mathbf{k})$ in the mirror plane M).

Up to here, we have treated each of the two independent sets of symmetry-related mirror planes independently, reflected in the use of the generic mirror m. We now turn to step 2 of the above list. Looking up [80] representations under consideration (representations that stabilize TPs) for the two point groups $4mm$ and $6mm$, we observe that the following property is always satisfied:

$$\mathscr{D}(m_0') = \mathrm{e}^{\mathrm{i}\phi} U D(m_0) U^\dagger, \tag{B.15a}$$

$$\mathscr{D}((m_0')_\perp) = \mathrm{e}^{\mathrm{i}\phi_\perp} U D((m_0)_\perp) U^\dagger, \tag{B.15b}$$

for some $\phi, \phi_\perp \in \mathbb{R}$ and $U \in \mathsf{U}(3)$, with the particular values of ϕ, $\phi_\perp$ and U depending on the choice of irreducible corepresentations (ICRs) $\mathscr{D} = D^{2\mathrm{D}} \oplus D^{1\mathrm{D}}$ [225]. If we rotate the band basis by $U^\dagger$ (denoted by a tilde '~' over the representation symbol), then

$$\tilde{\mathscr{D}}(m_0') = \mathrm{e}^{\mathrm{i}\phi}\mathscr{D}(m_0), \tag{B.16a}$$

$$\tilde{\mathscr{D}}((m_0')_\perp) = \mathrm{e}^{\mathrm{i}\phi_\perp}\mathscr{D}((m_0)_\perp). \tag{B.16b}$$

Equation (B.16) imply that the constraints for the corresponding mirror plane M_0' in the rotated basis are identical to Eq. (B.6) (which captures

constraints for plane M_0 in the original basis). Thus, any term $\tilde{h}^i_{M_0'}(\mathbf{k})$ in the $\mathbf{k}\cdot\mathbf{p}$ model for M_0' in that basis is given by precisely the same matrix-valued polynomial function h_i (with the argument k_{M_0} replaced by $k_{M_0'}$) as the corresponding term $h^i_{M_0}(\mathbf{k})$ in $\mathbf{k}\cdot\mathbf{p}$ model for M_0 in the original basis:

$$\begin{aligned}\tilde{h}^i_{M_0'}(\mathbf{k}) &= U^\dagger h^i_{M_0'}(\mathbf{k})U \\ &= h_i(k_{M_0'}) = h^i_{M_0}(C_{2n}\mathbf{k}),\end{aligned} \tag{B.17}$$

where in indicating the momentum arguments we used that the (symmetry inequivalent) planes M_0 and M_0' (and the corresponding in-plane components k_{M_0} and $k_{M_0'}$) are related by a C_{2n} rotation (not an element of G). Note that in the resulting $\mathbf{k}\cdot\mathbf{p}$ Hamiltonian these terms appear with different coefficient functions $\mathbf{a}'$ compared to the ones that appear in the expansion for M_0:

$$\tilde{H}^{(N)}_{M_0'}[\mathbf{a}'] = \sum_i a_i'(k_z) h_i\left(k_{M_0'}\right). \tag{B.18}$$

Next, in step 3, we define the *reconstructed* $\mathbf{k}\cdot\mathbf{p}$ *model* as the family of Hamiltonians with symmetrized terms $\hat{h}^i_{\mathsf{c}(m_0)}(\mathbf{k})$ and $\hat{h}^i_{\mathsf{c}(m_0')}(\mathbf{k})$ parametrized by the k_z-dependent components of some vector $\mathbf{B}$. Since there are twice as many terms, $\mathbf{B}$ has twice as many components as $\mathbf{a}$ making it convenient to introduce vectors $\mathbf{b}$ and $\mathbf{b}'$, $\mathbf{B} = (\mathbf{b}, \mathbf{b}')$, such that the terms originating from $\mathsf{c}(m_0)$ and $\mathsf{c}(m_0')$ appear with components of $\mathbf{b}$ and $\mathbf{b}'$, respectively, as coefficients:

$$\hat{H}^{(N)}[\mathbf{B}](\mathbf{k}) = \sum_i \left(b_i(k_z)\hat{h}^i_{\mathsf{c}(m_0)}(\mathbf{k}) + b_i'(k_z)\hat{h}^i_{\mathsf{c}(m_0')}(\mathbf{k})\right). \tag{B.19}$$

Substituting Eq. (B.9), and comparing to Eq. (B.7) we can rewrite the terms as symmetrizations of $H^{(N)}_{M_0}[\mathbf{b}]$ and $H^{(N)}_{M_0'}[\mathbf{b}']$

$$\begin{aligned}\hat{H}^{(N)}[\mathbf{B}](\mathbf{k}) &= \sum_{l=0}^{n-1} \mathscr{D}(C_n)^l \left\{ H^{(N)}_{M_0}[\mathbf{b}]\left(\left(C_n^{-l}\mathbf{k}\right)\big|_{M_0}\right)\right. \\ &\qquad \left. + H^{(N)}_{M_0'}[\mathbf{b}']\left(\left(C_n^{-l}\mathbf{k}\right)\big|_{M_0'}\right)\right\}\mathscr{D}(C_n)^{-l} \\ &= \sum_{l=0}^{n-1} \mathscr{D}(C_n)^l \left\{ H^{(N)}_{M_0}[\mathbf{b}]\left(\left(C_n^{-l}\mathbf{k}\right)\big|_{M_0}\right)\right. \\ &\qquad \left. + UH^{(N)}_{M_0}[\mathbf{b}']\left(\left(C_{2n}C_n^{-l}\mathbf{k}\right)\big|_{M_0}\right)U^\dagger\right\}\mathscr{D}(C_n)^{-l},\end{aligned} \tag{B.20}$$

where for the last equality we applied Eq. (B.17) to the terms in $H^{(N)}_{M_0'}[\mathbf{b}']$.

The family of Hamiltonians $\hat{H}^{(N)}[\mathbf{B}]$ given by Eq. (B.20) is generally both incomplete (as a $\mathbf{k}\cdot\mathbf{p}$ in the full 3D momentum space), because potential terms that vanish in all mirror planes are missed out, and overparametrized, because some terms originating from $\mathsf{c}(m_0)$ and $\mathsf{c}(m_0')$ are linearly dependent (e.g., the constant terms). In step 4, we evaluate $\hat{H}^{(N)}[\mathbf{B}]$ in the mirror planes M_0 and M_0', where the incompleteness does not affect the result, and compare that result to $H^{(N)}_{M_0}[\mathbf{a}](\mathbf{k})$ and $H^{(N)}_{M_0'}[\mathbf{a}'](\mathbf{k})$, respectively. Let $\mathbf{k}^M = k\mathbf{e}_M + k_z\mathbf{e}_z \in M$ for $M \in \{M_0, M_0'\}$, then

$$\begin{aligned}\hat{H}^{(N)}[\mathbf{B}]\left(\mathbf{k}_{M_0}\right) &= H^{(N)}_{M_0}[\mathbf{a}]\left(\mathbf{k}_{M_0}\right)\\ &= \sum_i a_i(k_z)h_i(k),\end{aligned} \tag{B.21a}$$

$$\begin{aligned}U^\dagger\hat{H}^{(N)}[\mathbf{B}]\left(\mathbf{k}_{M_0'}\right)U &= \tilde{H}^{(N)}_{M_0'}[\mathbf{a}']\left(\mathbf{k}_{M_0'}\right)\\ &= \sum_i a_i'(k_z)h_i(k).\end{aligned} \tag{B.21b}$$

Recognizing the terms $h_i(k)$ on the both sides of the above two equations and comparing their respective coefficients, allows us to express $\mathbf{a}$ and $\mathbf{a}'$ in terms of $\mathbf{B}$. Subsequently, we can simply read off the relationship between $\mathbf{a}$ and $\mathbf{a}'$ (cf. Eqs. (4.17) to (4.19) in the main text) from their expressions in terms of $\mathbf{B}$. This comparison of coefficients automatically takes care of the overparametrization problem mentioned in the beginning of the present paragraph.

Performing this analysis for $4mm$ we find that the coefficients in Eq. (4.11) for $(k,0)$ and $k\left(\frac{1}{\sqrt{2}},\frac{1}{\sqrt{2}}\right)$ (dashed parameters) are related as follows: a and a' are independent, $b'=b$, $c'=c$ and $A'=\mp_p A$ [cf. Eq. (4.18)] with the sign defined in Eq. (4.4). For $6mm$ we compare the coefficients for the planes defined by $(k,0)$ and $k\left(\frac{\sqrt{3}}{2},\frac{1}{2}\right)$ (dashed parameters) and find, for type-A TPs that $a'=a$, $b'=b$, $c'=c$ and $A'=(\mp_p)(\pm_q)A$ [cf. Eq. (4.19)] with the signs again defined in Eq. (4.4). Note that for type-A TPs $\mp_t=\mp_q$. For type-B TPs on the other hand, we find that $a'=-a$, $b'=b$, $c'=c$ and $A'=-A$ [cf. Eq. (4.17)]. Detailed derivations of the above three results are provided in a supplementary MATHEMATICA notebook [225] accompanying the original publication [2].

C. Data on triple-point materials

In this appendix, we provide figures showing data for the various triple-point materials discussed in Part II. In Appendix C.1, we provide figures supporting the application of the triple-point classification to materials, while in Appendix C.2, we provide figures showing triple-point induced monopole charges in the materials listed in Table 5.1.

C.1. Triple-point classification

In this section, we provide figures Figs. C.1 to C.19 supporting the results in Table 4.6 that are not already included in Section 4.7. The presented data [225], published alongside the publication "Triple nodal points characterized by their nodal-line structure in all magnetic space groups" [2], clarify the types and values for n_a^{nexus} and μ listed in the table.

C.2. Triple-point induced Euler monopole charge

In Figs. C.20 to C.24 we show the data on material examples with triple-point induced Euler monopole charges summarized in Table 5.1. As discussed in Section 5.2.3, we demonstrate the relationship between the Zak-Berry phase and the Euler monopole charge in the presence of triple points or multiband nodal links. This data has been published [238] alongside the publication "Universal higher-order bulk-boundary correspondence of triple nodal points" [3].

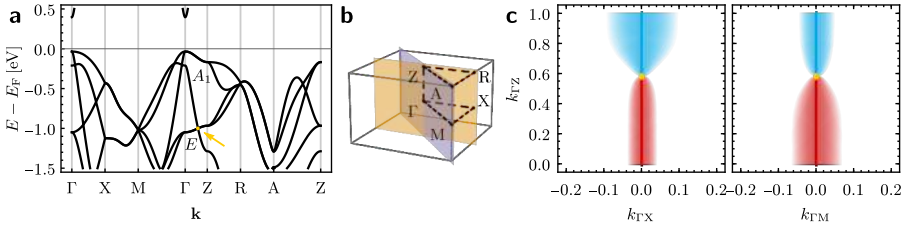

Figure C.1.: Triple point and nodal-line structure of Na_2LiN. The type-A triple point lies on the Λ line with little co-group $4/m'mm$. (**a**) Band structure along lines of symmetry. The triple point is indicated by a yellow dot and arrow and the bands forming the triple point are labelled by their irreducible corepresentations. (**b**) Brillouin zone (boundary in gray) with points and lines of symmetry (black dashed lines) and the two inequivalent mirror planes (orange and purple planes). (**c**) Size of the lower (red) and upper (blue) gap in the two mirror planes shown in panel (b) encoded by the intensity of the color (with a cutoff at a gap size of $0.01\,\mathrm{eV}$, i.e., gaps larger than that are shown in white). The triple point (yellow) and the central nodal line are emphasized by appropriately colored overlays.

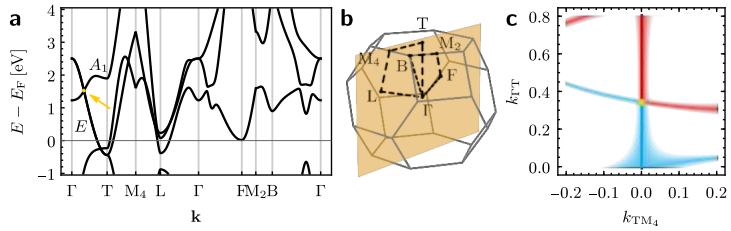

Figure C.2.: Triple point and nodal-line structure of P. The type-B_l triple point lies on the Λ line with little co-group $\bar{3}'m$. The organization of the panels is in one-to-one correspondence with Fig. C.1 with the difference that there is only one mirror plane. The cutoff on the gap size is $0.1\,\mathrm{eV}$. Due to the three-fold rotational symmetry, we conclude that $n_a^{\mathrm{nexus}} = 6$.

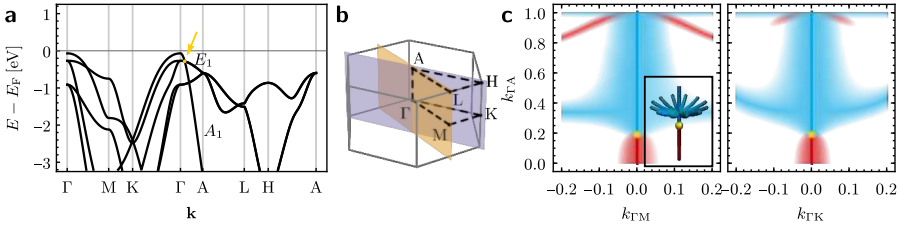

Figure C.3.: Type-A triple point and nodal-line structure of AlN. The type-A triple point lies on the Δ line with little co-group $6mm$ at $E_{\mathrm{TP}} = -0.28\,\mathrm{eV}$. The organization of the panels is in one-to-one correspondence with Fig. C.1 and the cutoff on the gap size is $0.05\,\mathrm{eV}$. Note the occurrence of the nearby nexus of $n_a^{\mathrm{nexus}} = 12$ (due to the six-fold rotational symmetry) blue nodal-line arcs with $\mu = 2$ in panel (c). The inset of panel (c) shows the nodal-line structure of the corresponding minimal $\mathbf{k}\cdot\mathbf{p}$ model, Eq. (4.50), with parameters tuned to qualitatively reproduce the situation in AlN. As expected, the $\mathbf{k}\cdot\mathbf{p}$ model does not reproduce the different curvature of the nodal-line arcs in the two inequivalent sets of mirror planes which is clearly visible in the data. As remarked upon in Section 4.3.2 this would be reflected in terms of higher order in k_x, k_y in the $\mathbf{k}\cdot\mathbf{p}$ expansion. Our theoretical arguments suggest that two parameters need be tuned to collide the nexus with the type-A TP.

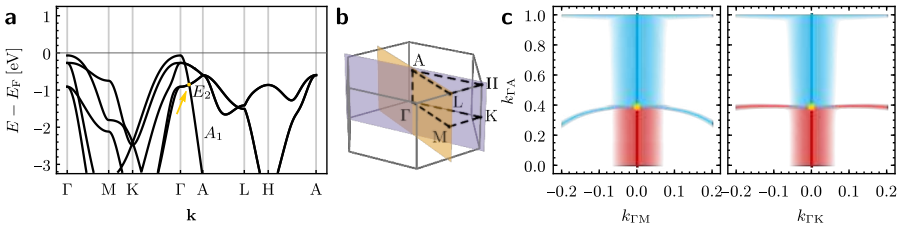

Figure C.4.: Type-B_q triple point and nodal-line structure of AlN. The type-B_q triple point lies on the Δ line with little co-group $6mm$ at $E_{\mathrm{TP}} = -0.85\,\mathrm{eV}$. The organization of the panels is in one-to-one correspondence with Fig. C.1 and the cutoff on the gap size is $0.05\,\mathrm{eV}$. Due to the six-fold rotational symmetry, we conclude that $n_a^{\mathrm{nexus}} = 12$.

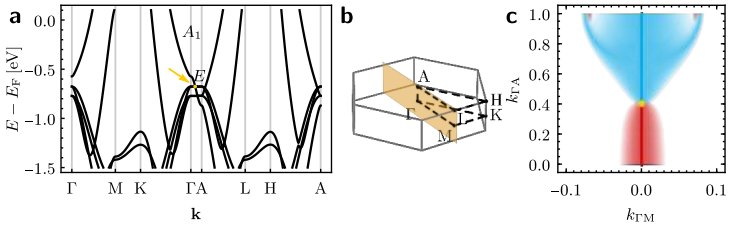

Figure C.5.: Triple point and nodal-line structure of Li_4N. The type-A triple point lies on the Δ line with little co-group $\bar{6}'m2'$. The organization of the panels is in one-to-one correspondence with Fig. C.1 with the difference that there is only one mirror plane. The cutoff on the gap size is $0.01\,\mathrm{eV}$. Note the occurrence of a nearby nexus of $n_a^{\mathrm{nexus}} = 6$ (due to the three-fold rotational symmetry) blue nodal-line arcs with $\mu = 2$ in panel (c). Our theoretical arguments suggest that only a single parameter needs be tuned to collide the nexus with the type-A TP.

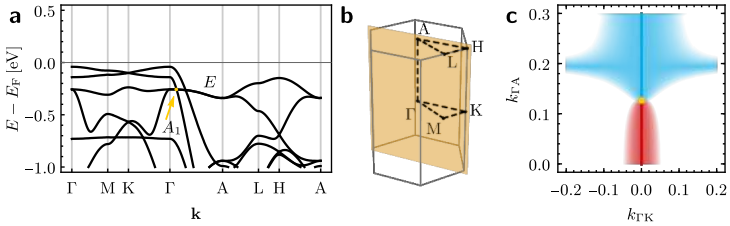

Figure C.6.: Triple point and nodal-line structure of Na_2O. The type-A triple point lies on the Δ line with little co-group $\bar{6}'m2'$. The organization of the panels is in one-to-one correspondence with Fig. C.1 with the difference that there is only one mirror plane. The cutoff on the gap size is $0.01\,\mathrm{eV}$. Note again the occurrence of a nearby nexus of $n_a^{\mathrm{nexus}} = 6$ (due to the three-fold rotational symmetry) blue nodal-line arcs with $\mu = 2$ in panel (c). Our theoretical arguments suggest that only a single parameter needs be tuned to collide the nexus with the type-A TP.

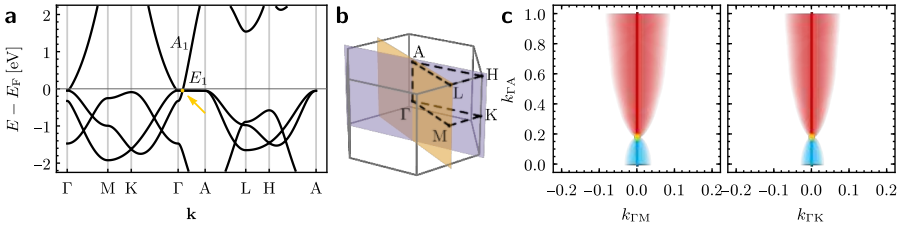

Figure C.7.: Triple point and nodal-line structure of Li_2NaN. The type-A triple point lies on the Δ line with little co-group $6/m'mm$. The organization of the panels is in one-to-one correspondence with Fig. C.1 and the cutoff on the gap size is $0.02\,\mathrm{eV}$. Our recent work [1] used this material to illustrate a relation between type-A TPs of spinless $\mathcal{PT}$-symmetric crystals to multiband nodal links.

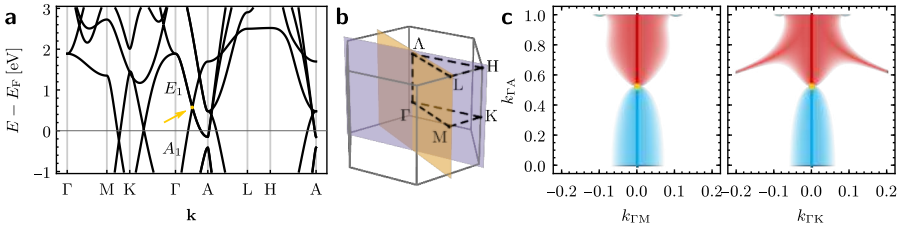

Figure C.8.: Type-A triple point and nodal-line structure of TiB_2. The type-A triple point lies on the Δ line with little co-group $6/m'mm$ at $E_{\mathrm{TP}} = 0.57\,\mathrm{eV}$. The organization of the panels is in one-to-one correspondence with Fig. C.1 and the cutoff on the gap size is $0.05\,\mathrm{eV}$. We do not identify a nexus point in this case; the nodal lines discernible in the right part of panel (c) seem to connect to the high-symmetry point K such that they cannot be considered to be near the triple point.

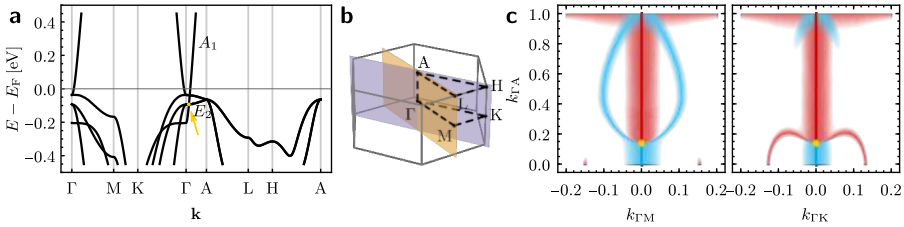

Figure C.9.: Type-B$_q$ triple point and nodal-line structure of Na$_3$N. The type-B$_q$ triple point lies on the Δ line with little co-group $6/m'mm$ at $E_{\mathrm{TP}} = -93\,\mathrm{meV}$. The organization of the panels is in one-to-one correspondence with Fig. C.1 and the cutoff on the gap size is $0.01\,\mathrm{eV}$. Due to the six-fold rotational symmetry, we conclude that $n_a^{\mathrm{nexus}} = 12$.

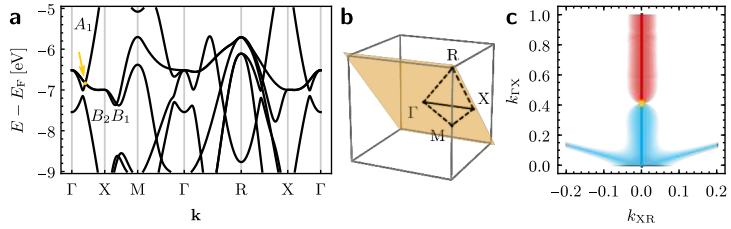

Figure C.10.: Triple point and nodal-line structure of C$_3$N$_4$ (SG 215). The type-A triple point lies on the Δ line with little co-group $\bar{4}'2'm$. The organization of the panels is in one-to-one correspondence with Fig. C.1 with the difference that there is only one mirror plane. The cutoff on the gap size is $0.02\,\mathrm{eV}$. We do not identify a nexus point in this case; the nodal lines discernible in panel (c) connect to the high-symmetry point Γ such that they cannot be considered to be near the triple point.

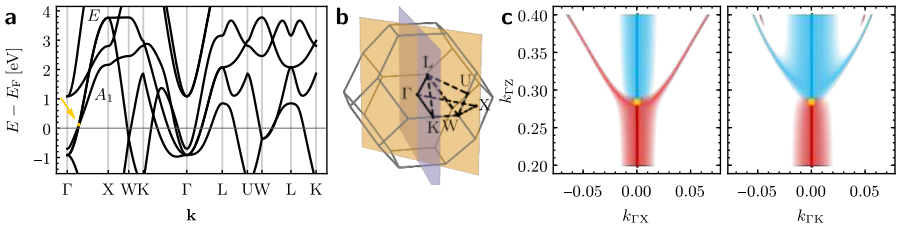

Figure C.11.: Second triple point and nodal-line structure of ZrO. The type-A triple point lies on the Δ line with little co-group $4/m'mm$ at $E_{\mathrm{TP}} = 0.12\,\mathrm{eV}$. The organization of the panels is in one-to-one correspondence with Fig. C.1 and the cutoff on the gap size is $0.02\,\mathrm{eV}$. Note the extremely close adjacency of the triple-point to two nexus points of $n_a^{\mathrm{nexus}} = 4$ (due to the four-fold rotational symmetry) nodal-line arcs each. According to our theoretical arguments, this is achieved by tuning a single model parameter. Furthermore, observe that the two nexus points are of *different* colors (in contrast to Fig. 4.14), suggesting $\mathrm{sign}(a_3 a_4) = -1$ in the $\mathbf{k} \cdot \mathbf{p}$ model in Eq. (4.49).

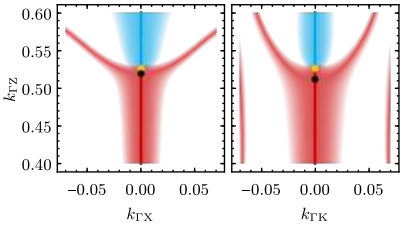

Figure C.12.: First triple point and nodal-line structure of ZrO with strain. Nodal line structure of ZrO with 5% uniaxial tensile strain in z-direction near the type-A triple point at $E_{\mathrm{TP}} = 2.0\,\mathrm{eV}$ on the Δ line with little co-group $4/m'mm$, cf. Fig. 4.14 for the same data in ZrO without strain. Size of the lower (red) and upper (blue) gap in the two mirror planes shown in Fig. 4.14b encoded by the intensity of the color (higher color saturation implies smaller energy gap between the corresponding pair of bands). The gap is only plotted up to a cutoff of $0.02\,\mathrm{eV}$ such that white color indicates a gap larger than that. The triple point (yellow) and the central nodal line are emphasized by appropriately colored overlays. In contrast to Fig. 4.14, we recognize two separate nexus points (indicated by black disks) not coinciding with the triple point. Thus, we conclude that the triple point is indeed type A and (due to the four-fold rotational symmetry) that $n_a^{\mathrm{nexus}} = 4$.

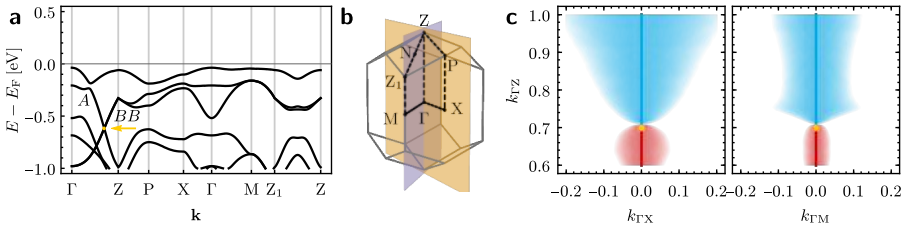

Figure C.13.: Triple point and nodal-line structure of SiO_2. The type-A triple point lies on the Λ line with little co-group $\bar{4}'$. The organization of the panels is in one-to-one correspondence with Fig. C.1 with the difference that the shown planes are *not* mirror planes. The cutoff on the gap size is $0.005\,\mathrm{eV}$. The little co-group $\bar{4}'$ contains neither a vertical mirror symmetry nor $\mathcal{PT}$ symmetry, such that nodal lines away from the rotation axis cannot be stabilized. We have performed DFT calculations in planes perpendicular to the central line and verified that.

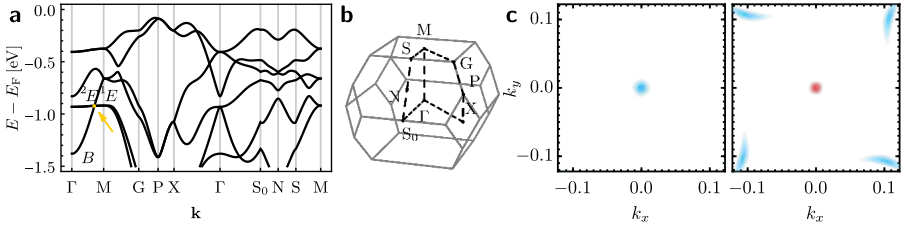

Figure C.14.: Triple point and nodal-line structure of Li_4HN. The type-A triple point lies on the Λ line with little co-group $4/m'$. (**a**) Band structure along lines of symmetry. The triple point is indicated by a yellow dot and arrow and the bands forming the triple point are labelled by their irreducible corepresentations. (**b**) Brillouin zone (boundary in gray) with points and lines of symmetry (black dashed lines). There are no mirror planes in this space group. (**c**) Size of the lower (red) and upper (blue) gap, encoded by the intensity of the color (with a cutoff in gap size at $0.02\,\mathrm{eV}$), in two horizontal planes (at fixed k_z) one slightly below (left) and one slightly above (right) the triple point. We find that no nodal-line arcs attach to the triple point, but we show the attachment of nodal-line arcs to a nexus point in Fig. C.15.

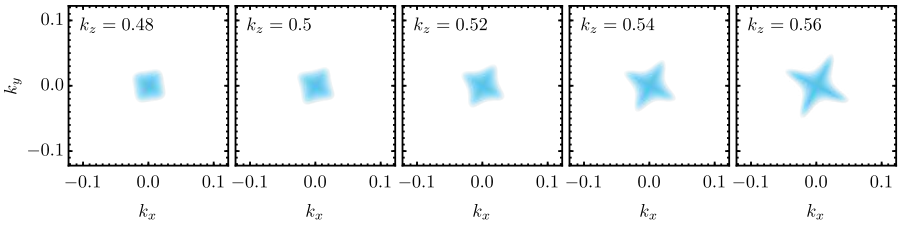

Figure C.15.: Nodal-line structure of Li_4HN near a nexus point. The nexus point lies on the Λ line with little co-group $4/m'$. Size of the lower (red) and upper (blue) gap, encoded by the intensity of the color (with a cutoff in gap size at $0.02\,\mathrm{eV}$), in horizontal planes at $k_z \in \{0.48, 0.5, 0.52, 0.54, 0.56\}$. We observe that four red nodal-line arcs attach to the nexus point lying on the red central nodal line, such that $n_a^{\mathrm{nexus}} = 4$. Furthermore, the nodal lines' symmetric arrangement indicates a quadratic attachment to the nexus point and therefore $\mu = 2$.

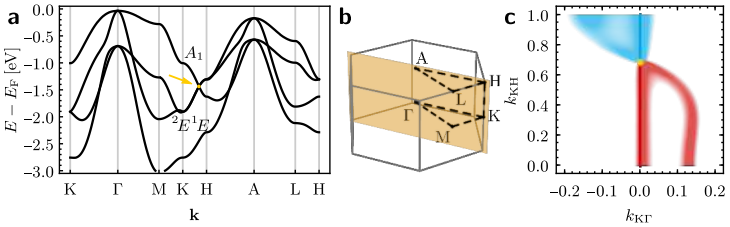

Figure C.16.: Triple point and nodal-line structure of MgH_2O_2. The type-B_l triple point lies on the P line with little co-group $\bar{3}'$. The organization of the panels is in one-to-one correspondence with Fig. C.1 with the difference that the shown plane is not a mirror plane. The cutoff on the gap size is $0.05\,\mathrm{eV}$. Instead we have performed DFT calculations in planes perpendicular to the central line and determined the approximate planes in which nodal lines attaching to the triple point appear. Here that plane is the $\Gamma\mathrm{KH}$-plane and its three mirror-symmetry-related copies, implying $n_a^{\mathrm{nexus}} = 6$.

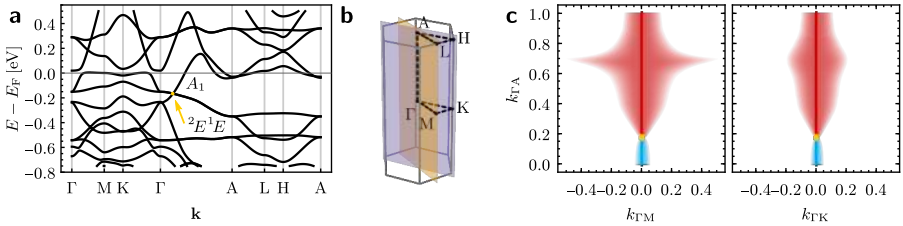

Figure C.17.: Triple point and nodal-line structure of $Li_2Co_{12}P_7$. The type-A triple point lies on the Δ line with little co-group $\bar{6}'$. The organization of the panels is in one-to-one correspondence with Fig. C.1 with the difference that the shown planes are *not* mirror planes. The cutoff on the gap size is $0.01\,\mathrm{eV}$. The little co-group $\bar{6}'$ contains neither a vertical mirror symmetry nor $\mathcal{PT}$ symmetry, such that nodal lines away from the rotation axis cannot be stabilized.

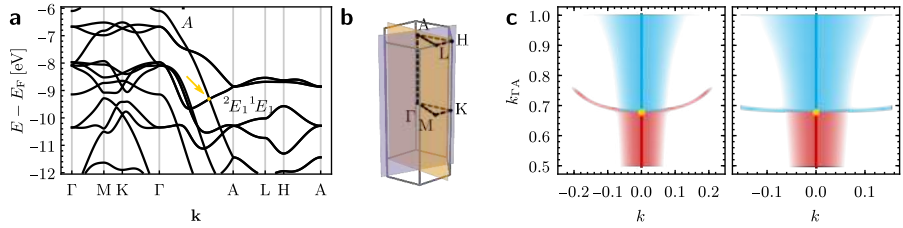

Figure C.18.: Type-B_q triple point and nodal-line structure of C_3N_4 (SG 176). The type-B_q triple point lies on the Δ line with little co-group $6/m'$ at $E_{\mathrm{TP}} = -9.3\,\mathrm{eV}$. The organization of the panels is in one-to-one correspondence with Fig. C.1 with the difference that the shown plane is not a mirror plane. The cutoff on the gap size is $0.05\,\mathrm{eV}$. Using additional DFT calculations in planes perpendicular to the central nodal line, we have determined that six nodal lines approximately lie in the planes indicated in panel (b) each, implying $n_a^{\mathrm{nexus}} = 12$. The green plane is spanned by $\mathbf{k}_{\Gamma\mathrm{A}}$ and $\mathbf{k} = 0.2\mathbf{k}_{\Gamma\mathrm{M}} + 0.11\mathbf{k}_{\Gamma\mathrm{M}'}$, where M' is the M-point rotated by $\frac{\pi}{3}$, and the red plane by $\mathbf{k}_{\Gamma\mathrm{A}}$ and $\mathbf{k} = 0.02\mathbf{k}_{\Gamma\mathrm{M}} + 0.2\mathbf{k}_{\Gamma\mathrm{M}'}$.

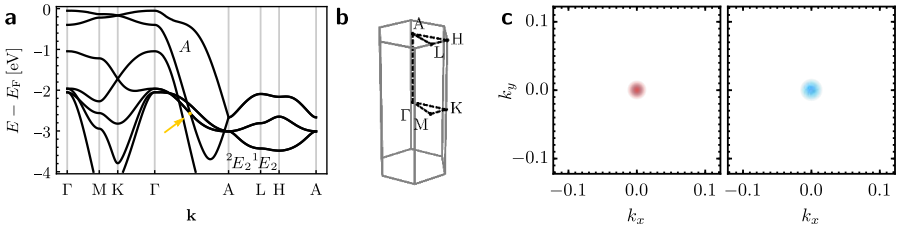

Figure C.19.: Type-A triple point and nodal-line structure of C_3N_4 (SG 176). The type-A triple point lies on the Δ line with little co-group $6/m'$ at $E_{\mathrm{TP}} = -2.6\,\mathrm{eV}$. The organization of the panels is in one-to-one correspondence with Fig. C.14 (but with a cutoff of $0.02\,\mathrm{eV}$) and again there are no nodal-line arcs connecting to the triple point.

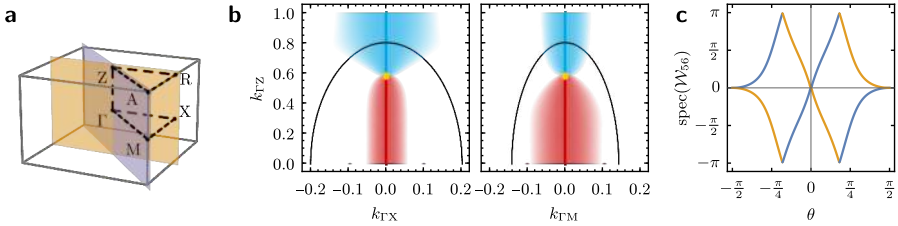

Figure C.20.: Euler monopole charge in Na_2LiN around Γ. (**a**) The Brillouin zone with high-symmetry points labeled and the relevant planes containing nodal lines indicated in color. (**b**) Size of the four relevant gaps (orange, red, blue, and purple, according to increasing energy; at the triple point the red and blue gaps are closed) in the two mirror planes shown in (a) encoded by the intensity of the color with a cutoff at a gap of $0.02\,\mathrm{eV}$. The triple point (yellow) and the central nodal line are emphasized by appropriately colored overlays. (**c**) Wilson loop spectrum computed for the specified bands on the ellipsoid indicated in (b). We observe that the Wilson loop spectrum winds twice, which implies $|\chi| = 2$.

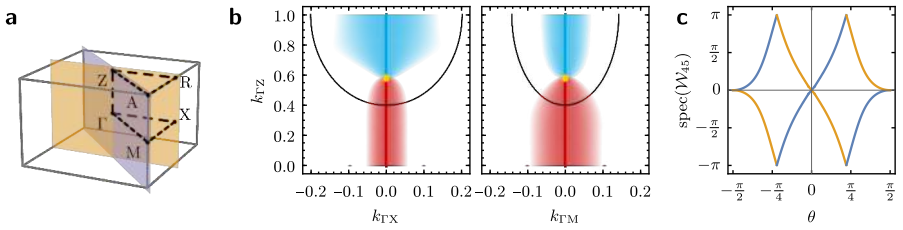

Figure C.21.: Euler monopole charge in Na_2LiN around Z. The organization of the panels is in one-to-one correspondence with Fig. C.20 (the same cutoff of $0.02\,\mathrm{eV}$ is used). In (c) we observe that the Wilson loop spectrum winds twice, which implies $|\chi| = 2$.

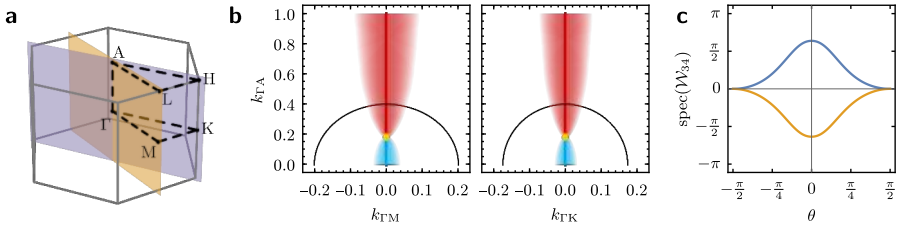

Figure C.22.: Euler monopole charge in Li_2NaN around Γ. The organization of the panels is in one-to-one correspondence with Fig. C.20 (cutoff $0.02\,\mathrm{eV}$). In panel (c) we observe that the Wilson loop spectrum winds twice, which implies $\chi = 0$.

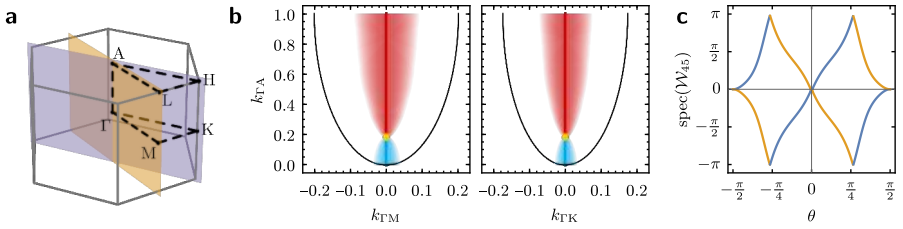

Figure C.23.: Euler monopole charge in Li_2NaN around A. The organization of the panels is in one-to-one correspondence with Fig. C.20 (cutoff $0.02\,\mathrm{eV}$). In panel (c) we observe that the Wilson loop spectrum winds twice, which implies $|\chi| = 2$.

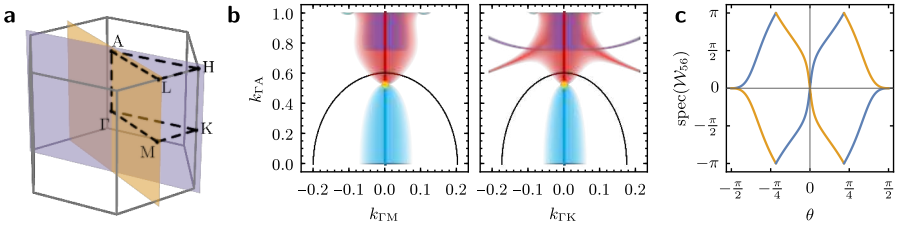

Figure C.24.: Euler monopole charge in TiB_2 around Γ. The organization of the panels is in one-to-one correspondence with Fig. C.20 (cutoff $0.05\,\mathrm{eV}$). In panel (c) we observe that the Wilson loop spectrum winds twice, which implies $|\chi| = 2$.

D. Quaternion charge across multiple Brillouin zones

This chapter is largely based on the supplement to the publication "Universal higher-order bulk-boundary correspondence of triple nodal points" [3]. Segments with significant text overlap with the published version may be subject to copyright by the American Physical Society.

In this appendix, we prove the following conjecture:

Conjecture 1. We assume an N-band system with $\mathcal{PT}$ symmetry squaring to $+1$, described in the orbital basis by a Hermitian Bloch Hamiltonian $H(\mathbf{k})$. Let $\gamma : t \in [0,1] \mapsto \gamma(t)$ be a closed contour without any band degeneracies on it that lies in the (first) BZ starting at the *base point* $P = \gamma(0) = \gamma(1)$, and let be $\mathbf{b}$ a reciprocal lattice vector. We define the following three paths:

(i) the shifted contour $\gamma'(t) = \gamma(t) + \mathbf{b}$,

(ii) the path $\gamma_{P,\mathbf{b}}$ along $\mathbf{b}$ connecting the base point P to $P' = \gamma'(0)$ (assuming once more that there are no band degeneracies along it), and

(iii) their concatenation (read from left to right)

$$\tilde{\gamma} = \gamma_{P,\mathbf{b}} \circ \gamma' \circ \gamma_{P,\mathbf{b}}^{-1}, \tag{D.1}$$

which is a closed contour with the same base point P as γ.

Then, the quaternion invariants on γ and $\tilde{\gamma}$ (computed with the same gauge choice for the real eigenstates at P, cf. Appendix D.4) are related by

$$\mathfrak{q}(\tilde{\gamma}) = \overline{F_{P,\mathbf{b}}}\,\mathfrak{q}(\gamma)\,\overline{F_{P,\mathbf{b}}}^{-1}, \tag{D.2}$$

where

$$\overline{F_{P,\mathbf{b}}} = \prod_{i\,:\,\mathrm{e}^{\mathrm{i}\varphi_i}=-1} \epsilon_i \tag{D.3}$$

with φ_i the Berry phase of band i along $\mathbf{b}$ and $\{\epsilon_i\}_{i=1}^N$ the generators ($\epsilon_i\epsilon_j + \epsilon_j\epsilon_i = -2\delta_{ij}$) of the Clifford algebra $\mathcal{C}\ell_{0,N}$ as used in the construction of

$\mathsf{Spin}(N)$ (cf. Appendix D.2.2). (Let us emphasize that this is *different* from the Clifford algebra $\mathcal{C}\ell_{0,N-1}$, the particular subset $\overline{P}_N$ of which corresponds to the generalized quaternion charge [65]; cf. Appendix D.2.3.) Note that the ordering of the factors in Eq. (D.3) does not affect Eq. (D.2) as long as the same ordering is used in both occurrences of $\overline{F_{P,\mathbf{b}}}$. Nevertheless, for concreteness, we fix the ordering such that factors with smaller subscript i appear to the right inside the product.

Before proving the above conjecture, let us briefly restate the corollary formulated and used in Section 5.2.2:

Corollary 1. Assume an N-band system with $\mathcal{PT}$ symmetry squaring to $+1$ described in the orbital basis by a Hermitian Bloch Hamiltonian $H(\mathbf{k})$. Let $\gamma : t \in [0,1] \mapsto \gamma(t)$ be a closed contour with no band degeneracies located inside the (first) BZ. The path starts at the *base point* $P = \gamma(0) = \gamma(1)$ and we decompose

$$\mathfrak{q}(\gamma) = s \prod_{j \in J} g_j \tag{D.4}$$

with $s \in \{\pm 1\}$, g_j the generators defined in Eq. (3.50) and $J \subseteq \{1, 2, \ldots, N-1\}$ a subset of the energy gaps of the N-band Hamiltonian (factors with smaller subscript j appearing to the right). Then, the quaternion charge on the corresponding contour $\tilde{\gamma}$ with the same base point and enclosing the same band inversions but in the BZ shifted by the reciprocal lattice vector $\mathbf{b}$ (cf. Fig. 5.3) is

$$\mathfrak{q}(\tilde{\gamma}) = (-1)^m \mathfrak{q}(\gamma), \tag{D.5}$$

where m is the number of elements of the set

$$\{ j \in J \,|\varphi_j \neq \varphi_{j+1} \} \tag{D.6}$$

with $\varphi_j \in \{0, \pi\}$ the Berry phase of the j^{th} band in the direction $\mathbf{b}$. [Note that in the conditioning in Eq. (D.6) the label $j+1$ may not be in the set J.]

Proof. Given Conjecture 1, the only thing to show is that Eq. (D.2) reduces to Eq. (D.5) given Eq. (D.4). The generators g_j of the generalized quaternion group can be defined in terms of the generators ϵ_i of $\mathcal{C}\ell_{0,N}$ [see Eq. (D.51)] as

$$g_1 = -\epsilon_1 \epsilon_2, \quad g_{j \geq 2} = \epsilon_j \epsilon_{j+1}. \tag{D.7}$$

The above two expressions can be jointly encoded as $g_j = (-1)^{\delta_{j1}} \epsilon_j \epsilon_{j+1}$. By combining Eqs. (D.2) and (D.4), we first find (through a repeated insertion of

the identity $\overline{F_{P,\mathbf{b}}}^{-1}\overline{F_{P,\mathbf{b}}} = 1$ into the product over $j \in J$) that

$$\begin{aligned}\mathfrak{q}(\tilde{\gamma}) &= s\left(\prod_{i\,:\,\mathrm{e}^{\mathrm{i}\varphi_i}=-1}\epsilon_i\right)\left(\prod_{j\in J} g_j\right)\left(\prod_{i\,:\,\mathrm{e}^{\mathrm{i}\varphi_i}=-1}\epsilon_i\right)^{-1} \\ &= s\prod_{j\in J}\left[\left(\prod_{i\,:\,\mathrm{e}^{\mathrm{i}\varphi_i}=-1}\epsilon_i\right)(-1)^{\delta_{j1}}\epsilon_j\epsilon_{j+1}\left(\prod_{i\,:\,\mathrm{e}^{\mathrm{i}\varphi_i}=-1}\epsilon_i\right)^{-1}\right]. \quad \text{(D.8)}\end{aligned}$$

Observe that for every $j \in J$, the conjugation with $\overline{F_{P,\mathbf{b}}} = \prod_{i\,:\,\mathrm{e}^{\mathrm{i}\varphi_i}=-1}\epsilon_i$ results in an overall minus sign if and only if exactly one of ϵ_j and ϵ_{j+1} is present in $\overline{F_{P,\mathbf{b}}}$; otherwise, the conjugation does not affect the factor $\epsilon_j\epsilon_{j+1}$. Therefore, the number of -1 factors picked up through the conjugation is equal to the number of $j \in J$ where $\mathrm{e}^{\mathrm{i}\varphi_j} \neq \mathrm{e}^{\mathrm{i}\varphi_{j+1}}$. This is equal to the order m of the set in Eq. (D.6), implying Eq. (D.5). □

In preparation for the proof of Conjecture 1, we prove several lemmas. For that we proceed as follows. In Appendix D.1 we discuss the form and the (non-)periodicity of a $\mathcal{PT}$-symmetric Bloch Hamiltonian in the extended momentum space (i.e., beyond the first Brillouin zone). In Appendices D.2 and D.3 we first revisit the construction of the double covers of $\mathsf{SO}(N)$ and of its subgroup P_N, and then show how to lift elements of $\mathsf{SO}(N)$ close to the identity after being conjugated by elements in $\mathsf{P}_{Nh} < \mathsf{O}(N)$. Armed with the derived lemmas, we continue by discussing (*i*) the quaternion charge on the various paths involved in the conjecture in Appendix D.4 and (*ii*) the Berry phases of the contour winding around the Brillouin zone torus in Appendix D.5. Finally, we use the derived lemmas and results to prove Conjecture 1 in Appendix D.6.

D.1. Bloch Hamiltonian

Before analyzing the quaternion charges, we review in the present section several properties of Bloch Hamiltonians in $\mathcal{PT}$-symmetric systems. Note that we adopt the Bloch convention which takes into account the positions of the orbitals within the unit cell when forming the Bloch basis, see Eq. (D.13). This is the convention in which the Berry curvature respects the symmetries of the lattice [88, 89] and the Zak phase of energy bands is in one-to-one correspondence with their electric polarization [126]. The prize to pay for this physical interpretability is that the resulting Bloch Hamiltonian may be non-periodic in reciprocal-lattice vectors.

Recall [66] that, due to $(\mathcal{PT})^2 = +1$, for each $\mathbf{k}$, there is a change of basis given by a unitary matrix $V_{\mathbf{k}}$ such that $\mathcal{PT}$ is represented by complex conjugation $\mathcal{K}$:

$$V_{\mathbf{k}} \overline{D}_{\mathbf{k}}(\mathcal{PT}) \mathcal{K} V_{\mathbf{k}}^{\dagger} = \mathcal{K} \tag{D.9}$$

(here the unitary matrix $\overline{D}_{\mathbf{k}}(\mathcal{PT})$ is the *corepresentation* $\mathcal{PT}$). It follows that

$$V_{\mathbf{k}} H(\mathbf{k}) V_{\mathbf{k}}^{\dagger} = H_{\mathrm{R}}(\mathbf{k}) \tag{D.10}$$

is a real symmetric matrix. Note that $V_{\mathbf{k}}$ is not unique, but any $W_{\mathbf{k}} V_{\mathbf{k}}$ for $W_{\mathbf{k}} \in \mathsf{O}(N)$ defines another such basis.

Given a real symmetric Hamiltonian $H_{\mathrm{R}}(\mathbf{k})$, it is natural to write its eigenstates in a real gauge; if we additionally order the eigenstates as columns from left to right according to increasing energy, we obtain the *eigenframe* $\mathsf{u} \in \mathsf{O}(N)$, and

$$H_{\mathrm{R}}(\mathbf{k}) = \mathsf{u}(\mathbf{k}) \mathcal{E}(\mathbf{k}) \mathsf{u}(\mathbf{k})^{\top}. \tag{D.11}$$

However, the orthogonal eigenframe is not unique, but exhibits a gauge degree of freedom, $\mathsf{u} \mapsto \mathsf{u}F$, where $F \in \mathsf{P}_{Nh} \cong \mathbb{Z}_2^N$ is a diagonal matrix of ± 1's. In particular, note that $F^2 = FF^{\top} = \mathbb{1}$.

It is important to note that while the eigenenergies are periodic in momentum space, the Bloch Hamiltonian $H(\mathbf{k})$ in general is only periodic up to a unitary transformation,

$$H(\mathbf{k} + \mathbf{b}) = U_{\mathbf{b}} H(\mathbf{k}) U_{\mathbf{b}}^{\dagger}, \tag{D.12}$$

where $\mathbf{b}$ is a reciprocal lattice vector, and the unitary matrix is defined up to an overall multiplication by a phase factor.

In the context of a tight-binding model with orbital α placed at position $\mathbf{r}_\alpha$ relative to the unit cell with origin at $\mathbf{R}$ and Hamiltonian $\hat{H}$, we define the Bloch basis

$$|\mathbf{k}, \alpha\rangle = \sum_{\mathbf{R}} \mathrm{e}^{\mathrm{i}\mathbf{k}\cdot(\mathbf{R}+\mathbf{r}_\alpha)} |\mathbf{R}, \alpha\rangle \,, \tag{D.13}$$

where $|\mathbf{R}, \alpha\rangle$ forms the tight-binding basis, and the sum is over Bravais lattice vectors $\mathbf{R}$. Then, the Bloch Hamiltonian $H(\mathbf{k})$ is the matrix with components $H^{\alpha\beta}(\mathbf{k})$ defined by

$$\langle \mathbf{k}, \alpha | \hat{H} | \mathbf{k}', \beta \rangle = H^{\alpha\beta}(\mathbf{k}) \delta_{\mathbf{k},\mathbf{k}'}. \tag{D.14}$$

and the unitary transformation in Eq. (D.12) is given by

$$U_{\mathbf{b}}^{\alpha\beta} = \mathrm{e}^{-\mathrm{i}\mathbf{b}\cdot\mathbf{r}_\alpha} \delta_{\alpha\beta} \tag{D.15}$$

in the orbital basis $|\mathbf{R}, \alpha\rangle$.

In the basis, where the Hamiltonian is real, we have the following lemma:

Lemma D.1.1. *In the context of an N-orbital tight-binding model with $\mathcal{PT}$ symmetry, $U_{\mathbf{b},\mathrm{R}} = V_{\mathbf{k}} U_{\mathbf{b}} V_{\mathbf{k}}^\dagger \in \mathsf{O}(N)$ and $U_{\mathbf{b},\mathrm{R}}$ is independent of $\mathbf{k}$.*

Proof. In real space $\mathcal{PT}$ acts like inversion, mapping a position vector $\mathbf{r}$ (relative to the center of the unit cell) to $-\mathbf{r}$. If $\mathcal{PT}$ is a symmetry of the system, then there are two options for each tight-binding orbital α: (1) it is mapped to itself (potentially to a Bravais-translation-related copy of itself in another unit cell) or (2) it is exchanged with another orbital. This implies that, in the orbital basis $|\mathbf{R}, \alpha\rangle$, the corepresentation matrix $\overline{D}_{\mathbf{k}}(\mathcal{PT})$ is block-diagonal with one- and 2D blocks. Below we consider both cases (1) and (2) to explicitly construct $V_{\mathbf{k}}$ such that

$$V_{\mathbf{k}}\, \overline{D}_{\mathbf{k}}(\mathcal{PT}) V_{\mathbf{k}}^\top = \mathbb{1}, \tag{D.16}$$

i.e., the unitary rotation from the orbital basis to the basis in which $\mathcal{PT}$ is represented by complex conjugation [cf. Eq. (D.9)].

Let us first consider option (1). For the orbital α to be mapped to itself under $\mathcal{PT}$, its position $\mathbf{r}_\alpha$ must be an inversion-symmetric point, i.e., $-\mathbf{r}_\alpha = \mathbf{r}_\alpha + \mathbf{R}_\alpha$ for some Bravais lattice vector $\mathbf{R}_\alpha$. Then, $\mathbf{r}_\alpha = -\frac{1}{2}\mathbf{R}_\alpha$, and the corresponding block of the corepresentation matrix must take the form

$$\overline{D}_{\mathbf{k}}(\mathcal{PT}) = \mathrm{e}^{-\mathrm{i}\mathbf{k}\cdot\mathbf{R}_\alpha + \mathrm{i}\phi_\alpha} \tag{D.17}$$

with some phase $\phi_\alpha \in \mathbb{R}$. One trivially verifies that $\overline{D}_{\mathbf{k}}(\mathcal{PT})\overline{D}_{\mathbf{k}}(\mathcal{PT})^* = \mathbb{1}$, as expected for spinless bands. We next observe that the corresponding block of $V_{\mathbf{k}}$ satisfying Eq. (D.16) is

$$V_{\mathbf{k}} = \mathrm{e}^{-\frac{1}{2}(-\mathrm{i}\mathbf{k}\cdot\mathbf{R}_\alpha + \mathrm{i}\phi_\alpha)}. \tag{D.18}$$

Therefore $U_{\mathbf{b}}$ defined in Eq. (D.15) is transformed to

$$U_{\mathbf{b},R} = V_{\mathbf{k}} \mathrm{e}^{-\mathrm{i}\mathbf{b}\cdot\mathbf{r}_\alpha} V_{\mathbf{k}}^\dagger = \mathrm{e}^{\mathrm{i}\frac{1}{2}\mathbf{b}\cdot\mathbf{R}}. \tag{D.19}$$

Note that $\mathbf{b}$ is a reciprocal lattice vector and $\mathbf{R}$ a Bravais lattice vector, such that $\frac{1}{2}\mathbf{b}\cdot\mathbf{R}$ is 0 or π (modulo 2π) and $U_{\mathbf{b},R} = \pm 1 \in \mathsf{O}(1)$ is independent of $\mathbf{k}$.

Next, we consider option (2). For concreteness let us assume that the orbitals α and β are mapped to each other, then the corresponding block of the (unitary) corepresentation matrix must be off-diagonal,

$$\overline{D}_{\mathbf{k}}(\mathcal{PT}) = \begin{pmatrix} 0 & \mathrm{e}^{\mathrm{i}\phi_{\alpha\beta}} \\ \mathrm{e}^{\mathrm{i}\phi_{\alpha\beta}} & 0 \end{pmatrix}, \tag{D.20}$$

where the phases of the off-diagonal matrix elements must be equal in order to satisfy $\overline{D}_{\mathbf{k}}(\mathcal{PT})\overline{D}_{\mathbf{k}}(\mathcal{PT})^* = \mathbb{1}$. Again we construct the corresponding block of

$V_{\mathbf{k}}$ satisfying Eq. (D.16):

$$V_{\mathbf{k}} = \frac{\mathrm{e}^{-\mathrm{i}\frac{1}{2}\phi_{\alpha\beta}}}{\sqrt{2}} \begin{pmatrix} 1 & 1 \\ \mathrm{i} & -\mathrm{i} \end{pmatrix}. \tag{D.21}$$

The fact that orbitals α and β are mapped to each other under $\mathcal{PT}$ implies that $-\mathbf{r}_\alpha = \mathbf{r}_\beta$ and thus

$$U_{\mathbf{b}} = \begin{pmatrix} \mathrm{e}^{-\mathrm{i}\mathbf{b}\cdot\mathbf{r}_\alpha} & 0 \\ 0 & \mathrm{e}^{\mathrm{i}\mathbf{b}\cdot\mathbf{r}_\alpha} \end{pmatrix}. \tag{D.22}$$

In the transformed basis, we therefore end up with

$$U_{\mathbf{b},R} = V_{\mathbf{k}} U_{\mathbf{b}} V_{\mathbf{k}}^\dagger = \begin{pmatrix} \cos(-\mathbf{b}\cdot\mathbf{r}_\alpha) & \sin(-\mathbf{b}\cdot\mathbf{r}_\alpha) \\ -\sin(-\mathbf{b}\cdot\mathbf{r}_\alpha) & \cos(-\mathbf{b}\cdot\mathbf{r}_\alpha) \end{pmatrix} \in \mathsf{O}(2), \tag{D.23}$$

which is independent of $\mathbf{k}$.

We have shown that the full $V_{\mathbf{k}}$ is block-diagonal and because $U_{\mathbf{b}}$ is diagonal [cf. Eq. (D.15)] this implies that $U_{\mathbf{b},R}$ is also block diagonal with $\mathbf{k}$-independent blocks either in $\mathsf{O}(1)$ or $\mathsf{O}(2)$. Therefore, $U_{\mathbf{b},R} \in \mathsf{O}(N)$ is $\mathbf{k}$-independent as well. □

D.2. Double covers of $\mathsf{SO}(N)$ and P_N

D.2.1. Lie algebra $\mathfrak{so}(N)$

We consider the special orthogonal group $\mathsf{SO}(N)$, whose Lie algebra is denoted $\mathfrak{so}(N)$. A basis for $\mathfrak{so}(N)$ is given by the $N \times N$ matrices

$$L_{ij} = -E_{ij} + E_{ji}, \quad i < j, \tag{D.24}$$

where $(E_{ij})_{ab} = \delta_{ai}\delta_{bj}$ is the matrix with a single non-zero element 1 at position (i, j). The matrices E_{ij} satisfy

$$E_{ij}E_{k\ell} = \delta_{jk}E_{i\ell}, \tag{D.25}$$

such that

$$[L_{ij}, L_{k\ell}] = -\delta_{i\ell}L_{kj} + \delta_{ik}L_{\ell j} - \delta_{j\ell}L_{ik} + \delta_{jk}L_{i\ell}, \tag{D.26}$$

which defines the Lie algebra.

D.2.2. Construction of $\mathsf{Spin}(N)$

The simply-connected double cover of $\mathsf{SO}(N)$, called $\mathsf{Spin}(N)$, can be constructed [348] via the Clifford algebra $\mathcal{C}\ell_{0,N}$ with generators ϵ_i satisfying

$$\epsilon_i\epsilon_j + \epsilon_j\epsilon_i = -2\delta_{ij}. \tag{D.27}$$

We note that the quadratic elements

$$t_{ij} = -\frac{1}{2}\epsilon_i\epsilon_j, \quad i < j, \tag{D.28}$$

satisfy the same commutation relation as Eq. (D.26):

$$[t_{ij}, t_{k\ell}] = -\delta_{i\ell}t_{kj} + \delta_{ik}t_{\ell j} - \delta_{j\ell}t_{ik} + \delta_{jk}t_{i\ell}, \tag{D.29}$$

such that we can construct the isomorphism

$$\begin{array}{rcl} \mathfrak{so}(N) & \to & \mathfrak{spin}(N) \\ L_{ij} & \mapsto & \overline{L_{ij}} = t_{ij} = -\frac{1}{2}\epsilon_i\epsilon_j \end{array}. \tag{D.30}$$

of the two Lie algebras.

Using the exponential map of elements in the Lie algebras, we obtain the corresponding Lie groups:

$$\mathrm{e}^{\sum_{i<j}\alpha_{ij}L_{ij}} \in \mathsf{SO}(N), \qquad \mathrm{e}^{\sum_{i<j}\theta_{ij}t_{ij}} \in \mathsf{Spin}(N). \tag{D.31}$$

The isomorphism of Lie algebras in Eq. (D.30) induces a homomorphism of the corresponding Lie groups. In particular, for elements of $\mathsf{SO}(N)$ close to the identity one can construct the *lift map*:

$$\bar{\cdot} : \mathrm{e}^{\sum_{i<j}\alpha_{ij}L_{ij}} \mapsto \mathrm{e}^{\sum_{i<j}\alpha_{ij}t_{ij}}. \tag{D.32}$$

For $A \in \mathsf{SO}(N)$ close to the identity, we denote the unique lift to $\mathsf{Spin}(N)$ close to the identity, as defined in Eq. (D.32), by $\overline{A}$.

We proceed to develop an elementary intuition about the lift map $\bar{\cdot} : \mathsf{SO}(N) \to \mathsf{Spin}(N)$ for elements close to the identity.

Because $\mathsf{Spin}(N)$ is the double cover of $\mathsf{SO}(N)$, we have the following short exact sequence of group homomorphisms:

$$1 \longrightarrow \mathbb{Z}_2 = \{\pm 1\} \xrightarrow{\varphi} \mathsf{Spin}(N) \xrightarrow{\sigma} \mathsf{SO}(N) \longrightarrow 1 \tag{D.33}$$

where $\varphi(\pm 1)$ is in the center of $\mathsf{Spin}(N)$, and σ is a two-to-one projection map. Let as clarify in some detail what the sequence in Eq. (D.33) entails. Since φ is a group homomorphism, we have

$$1 = \varphi(1) = \varphi((-1)(-1)) = \varphi(-1)\varphi(-1), \tag{D.34}$$

thus we identify $\varphi(-1) = -1 \in \mathsf{Spin}(N)$, i.e., as the nontrivial element of $\mathsf{Spin}(N)$ that commutes with all other elements of $\mathsf{Spin}(N)$. The exactness of the above sequence implies that

$$1 = (\sigma \circ \varphi)(\pm 1) = \sigma(\pm 1), \tag{D.35}$$

i.e., the center $\pm 1 \in \mathsf{Spin}(N)$ projects onto the identity element $1 \in \mathsf{SO}(N)$.

Now consider $M_1, M_2 \in \mathsf{Spin}(N)$ with $\sigma(M_1) = \sigma(M_2)$, then

$$\sigma(M_1 M_2^{-1}) = \sigma(M_1)\sigma(M_2)^{-1} = 1, \tag{D.36}$$

i.e., $M_1 M_2^{-1}$ is in the kernel of σ, which due to the exactness of the sequence is the image of φ; therefore

$$M_1 M_2^{-1} \in \{\pm 1\} \Rightarrow M_1 = \pm M_2. \tag{D.37}$$

We also have that

$$\sigma\left(\overline{A}\right) = A \tag{D.38}$$

(i.e., the lift map followed by the projection map is equivalent to the identity operation) for all elements $A \in \mathsf{SO}(N)$ close to identity.

One should bear in mind that we use the same symbol '$\overline{\ }$' for two different (but closely related) maps: (1) the isomorphism of the Lie algebras [Eq. (D.30)], and the lift map of Lie-group elements close to the identity [Eq. (D.32)]. These maps are canonically related, because the Lie algebra $\mathfrak{g}$ corresponds to the tangent space of the Lie group G at the identity.

Lemma D.2.1. *Let $A \in \mathsf{SO}(N)$ be close to the identity, A^{-1} its inverse (which is also close to the identity). Let us denote their (unique) lifts to $\mathsf{Spin}(N)$, according to Eq. (D.32), as $\overline{A}$ and $\overline{A^{-1}}$. Then:*

$$\overline{A}^{\,-1} = \overline{A^{-1}}. \tag{D.39}$$

Proof. Set $M_1 := \overline{A}^{\,-1}$, $M_2 := \overline{A^{-1}}$, then

$$\sigma(M_1) = \sigma\left(\overline{A}^{\,-1}\right) = \sigma\left(\overline{A}\right)^{-1} = A^{-1} = \sigma(M_2), \tag{D.40}$$

where we used that σ is a group homomorphism. It follows, according to Eq. (D.37), that

$$\overline{A} \cdot \overline{A^{-1}} = \pm 1. \tag{D.41}$$

However, because the left hand side is a product of elements close to the identity, the right hand side has to be close to the identity as well, such that it can only be 1 (and not -1). Thus, $\overline{A}^{-1} = \overline{A^{-1}}$, i.e., for elements $A \in \mathsf{SO}(N)$ close to the identity, the lift map commutes with the matrix inverse map. □

D.2.3. The group P_N and its double cover

We proceed to discuss the generalized quaternion charges, as introduced in the supplementary material of Ref. 65. Consider elements of the discrete subgroup,

$$\mathsf{P}_N = \left\langle \left\{ \mathrm{e}^{\pi L_{ij}} \right\}_{i<j} \right\rangle < \mathsf{SO}(N), \tag{D.42}$$

where the angular brackets denote the group generated by taking products of the elements of the set inside the brackets. Note that

$$L_{ij}^n = \begin{cases} \mathbb{1}, & n = 0 \\ (-1)^k L_{ij}, & n = 2k+1, k \in \mathbb{N}_0 \\ (-1)^k (E_{ii} + E_{jj}), & n = 2k, k \in \mathbb{N}_{>0} \end{cases}, \tag{D.43}$$

resulting in

$$\mathrm{e}^{\alpha L_{ij}} = \mathbb{1} + \sin(\alpha) L_{ij} + (\cos(\alpha) - 1)\,(E_{ii} + E_{jj}). \tag{D.44}$$

For the elements of P_N we thus have

$$\mathrm{e}^{\pi L_{ij}} = \mathbb{1} - 2(E_{ii} + E_{jj}), \tag{D.45}$$

i.e., diagonal matrices with $+1$ on the diagonal except for the i^{th} and j^{th} element, which are -1. Note that $\mathrm{e}^{-\pi L_{ij}} = \mathrm{e}^{\pi L_{ij}} = (\mathrm{e}^{-\pi L_{ij}})^{-1}$. (Let us also remark that throughout this supplemental material we do *not* use the Einstein summation convention, i.e., there is no implicit summation over repeated indices.)

The double cover of P_N, denoted $\overline{\mathsf{P}}_N < \mathsf{Spin}(N)$, can be constructed starting from the generators of P_N: $\mathrm{e}^{\alpha_{ij} L_{ij}}$ and applying the algebra isomorphism in the exponent, then

$$\overline{\mathsf{P}}_N = \left\langle \left\{ \mathrm{e}^{\pi t_{ij}} \right\}_{i<j} \right\rangle. \tag{D.46}$$

Since for $i \neq j$, $t_{ij}^2 = -\frac{1}{4}$, we find

$$\mathrm{e}^{\theta t_{ij}} = \cos\left(\frac{\theta}{2}\right) + 2t_{ij}\sin\left(\frac{\theta}{2}\right) \tag{D.47}$$

such that the generators of $\overline{\mathsf{P}}_N$ are $\mathrm{e}^{\pi t_{ij}} = 2t_{ij}$, and

$$\sigma\left(2t_{ij}\right) = \mathrm{e}^{\pi L_{ij}}. \tag{D.48}$$

The above results allow us to relate the generators $\{e_j\}_{j=1}^{N-1}$ of $\overline{\mathsf{P}}_N$ and of the Clifford algebra $\mathcal{C}\ell_{0,N-1}$ introduced in Ref. 65 to the generators $\{\epsilon_i\}_{i=1}^{N}$ of $\mathcal{C}\ell_{0,N}$ adopted in Appendix D.2.2, namely

$$e_j = 2t_{1,j+1} = -\epsilon_1\epsilon_{j+1}. \tag{D.49}$$

The same reference introduces an alternative, physically motivated set of generators

$$g_j = \begin{cases} e_1, & j = 1 \\ e_{j-1}e_j, & 2 \leq j \leq N-1 \end{cases}. \tag{D.50}$$

It follows from combining the preceding equations that

$$g_j = \begin{cases} -\epsilon_1\epsilon_2, & j = 1 \\ \epsilon_j\epsilon_{j+1}, & 2 \leq j \leq N-1 \end{cases}. \tag{D.51}$$

D.2.4. The group P_{Nh}

The group P_{Nh} of diagonal matrices with ± 1 on the diagonal is not a subgroup of $\mathsf{SO}(N)$, but a subgroup of $\mathsf{O}(N)$. It can be written as

$$\mathsf{P}_{Nh} = \mathsf{P}_N \cup (\mathbb{1} - 2E_{ii})\mathsf{P}_N \tag{D.52}$$

for any $1 \leq i \leq N$. In the following, we will consider conjugation of elements of $\mathsf{SO}(N)$ with elements of P_{Nh}. Since the determinant of a product equals the product of the determinants of its factors, conjugation of an element in $\mathsf{SO}(N)$ with an element of P_{Nh} does not leave $\mathsf{SO}(N)$.

Similarly, the double cover $\overline{\mathsf{P}}_{Nh}$ of P_{Nh} can be constructed as

$$\overline{\mathsf{P}}_{Nh} = \overline{\mathsf{P}}_N \cup \epsilon_i\overline{\mathsf{P}}_N \tag{D.53}$$

for any $1 \leq i \leq N$. Based on this and the construction of $\overline{\mathsf{P}}_N$, any $\mathfrak{p} \in \overline{\mathsf{P}}_{Nh}$ can, for example, be written as

$$\mathfrak{p} = \epsilon_1^{p_0}\prod_{i<j}(2t_{ij})^{p_{ij}} \tag{D.54}$$

for $p_0, p_{ij} \in \{0,1\}$. In this decomposition, p_0 distinguishes whether $\mathfrak{p}$ lies in the proper subgroup P_N ($p_0 = 0$) or not ($p_0 = 1$). Finally, we remark that

$$\sigma(\mathfrak{p}) = (\mathbb{1} - 2E_{ii})^{p_0} \mathrm{e}^{\pi \sum_{i<j} p_{ij} L_{ij}}. \tag{D.55}$$

for the projection of any element $\mathfrak{p} \in \overline{P}_{Nh}$.

D.3. Lift of conjugated elements

Lemma D.3.1. *We consider two basis elements of $\mathfrak{so}(N)$: L_{ij} $(i<j)$ and $L_{k\ell}$ $(k<\ell)$. Then $\mathrm{e}^{\pi L_{ij}} L_{k\ell} \mathrm{e}^{-\pi L_{ij}} \in \mathfrak{so}(N)$ and*

$$\overline{\mathrm{e}^{\pi L_{ij}} L_{k\ell} \mathrm{e}^{-\pi L_{ij}}} = \mathrm{e}^{\pi t_{ij}} t_{k\ell} \mathrm{e}^{-\pi t_{ij}} = (2t_{ij}) t_{k\ell} (2t_{ij})^{-1}, \tag{D.56}$$

which is an element of $\mathfrak{spin}(N)$.

Proof. Using Eqs. (D.24) and (D.45), and that

$$\forall i \neq j, k \neq \ell \quad : \quad E_{ii} L_{kl} E_{jj} = (-\delta_{ik}\delta_{j\ell} + \delta_{i\ell}\delta_{jk})\, E_{ij}, \tag{D.57a}$$

$$\forall k \neq \ell \quad : \quad E_{ii} L_{kl} E_{ii} = 0 \tag{D.57b}$$

we find after some algebra that

$$\begin{aligned} &\mathrm{e}^{\pi L_{ij}} L_{k\ell} \mathrm{e}^{-\pi L_{ij}} \\ &\quad = [\mathbb{1} - 2(E_{ii} + E_{jj})]\, L_{k\ell}\, [\mathbb{1} - 2(E_{ii} + E_{jj})] \\ &\quad = (1 - 2\,(\delta_{ik} + \delta_{i\ell} + \delta_{jk} + \delta_{j\ell}) + 4\,(\delta_{ik}\delta_{j\ell} + \delta_{i\ell}\delta_{jk}))\, L_{k\ell} \\ &\quad \overset{i\neq j}{=} (1 - 2\delta_{ik} - 2\delta_{i\ell})\,(1 - 2\delta_{jk} - 2\delta_{j\ell})\, L_{k\ell}. \end{aligned} \tag{D.58}$$

We observe that, since $i<j$ and $k<\ell$, the prefactors of $L_{\ell k}$ are ± 1, and thus $\mathrm{e}^{\pi L_{ij}} L_{k\ell} \mathrm{e}^{-\pi L_{ij}} = \pm L_{ij}$ is, up to a sign, one of the basis elements of $\mathfrak{so}(N)$. Applying the algebra isomorphism, this gives

$$\overline{\mathrm{e}^{\pi L_{ij}} L_{k\ell} \mathrm{e}^{-\pi L_{ij}}} = (1 - 2\delta_{ik} - 2\delta_{i\ell})\,(1 - 2\delta_{jk} - 2\delta_{j\ell})\, t_{k\ell}, \tag{D.59}$$

which is an element of $\mathfrak{spin}(N)$.

On the other hand, an explicit calculation [e.g., via a repeated application of Eqs. (D.27) and (D.28)] reveals that for $i<j$ and $k<\ell$

$$(2t_{ij}) t_{k\ell} (-2t_{ij}) = (1 - 2\delta_{ik} - 2\delta_{i\ell})\,(1 - 2\delta_{jk} - 2\delta_{j\ell})\, t_{k\ell}, \tag{D.60}$$

where $t_{k\ell} \in \mathfrak{spin}(N)$ and $\mathrm{e}^{\pi L_{ij}} = 2t_{ij} \in \overline{\mathsf{P}_N}$ Noting that $(2t_{ij})^{-1} = -2t_{ij}$, we observe that the right-hand sides of Eqs. (D.59) and (D.60) are equal, such the left-hand sides must be equal as well. □

Lemma D.3.2. *Let $A \in \mathsf{SO}(N)$ be close to the identity and $D \in \mathsf{P}_N$, then $DAD^{-1} \in \mathsf{SO}(N)$ is close to the identity as well, and*

$$\overline{DAD^{-1}} = \overline{D}\,\overline{A}\,\overline{D}^{\,-1}, \tag{D.61}$$

with $\overline{D}$ defined as follows: Any $D \in \mathsf{P}_N$ can be written as

$$D = \prod_{i<j} (\mathrm{e}^{\pi L_{ij}})^{d_{ij}} \tag{D.62}$$

for a (non-unique) set of $\{d_{ij}\}$, $d_{ij} \in \{0,1\}$, then

$$\overline{D} = \prod_{i<j} (2t_{ij})^{d_{ij}}, \tag{D.63}$$

where the ordering of the factors in Eq. (D.63) matches the one in Eq. (D.62).

Let us remark that while $\overline{A}$ is given by Eq. (D.32), $\overline{D}$ needs to be defined explicitly, since D is not an element close to the identity.

Proof. Obviously, any $D \in \mathsf{P}_N$ can be written as a (non-unique) product of generators:

$$D = \prod_{i<j} (\mathrm{e}^{\pi L_{ij}})^{d_{ij}}, \tag{D.64}$$

where $d_{ij} \in \{0,1\}$. First we consider $L_{k\ell} \in \mathfrak{so}(N)$, then

$$DL_{k\ell}D^{-1} = \mathrm{e}^{\pi L_{i'j'}} \cdots \mathrm{e}^{\pi L_{ij}} L_{k\ell} \mathrm{e}^{-\pi L_{ij}} \cdots \mathrm{e}^{-\pi L_{i'j'}}, \tag{D.65}$$

where only $\mathrm{e}^{\pi L_{ij}}$ with $i<j$ and $d_{ij}=1$ appear in the product. This is just consecutive conjugation by generators of P_N and, by Lemma D.3.1, the result of each conjugation is an element of $\mathfrak{so}(N)$ again, such that $DL_{k\ell}D^{-1} \in \mathfrak{so}(N)$ and

$$\overline{DL_{k\ell}D^{-1}} = \overline{D} t_{k\ell} \overline{D}^{\,-1}, \tag{D.66}$$

where

$$\overline{D} = \prod_{i<j} (\mathrm{e}^{\pi t_{ij}})^{d_{ij}} = \prod_{i<j} (2t_{ij})^{d_{ij}}. \tag{D.67}$$

Now, any $A \in \mathsf{SO}(N)$ close to the identity can be expanded in $\mathfrak{so}(N)$:

$$A \approx \mathbb{1} + \sum_{k<\ell} \alpha_{k\ell} L_{k\ell}. \tag{D.68}$$

Therefore,

$$DAD^{-1} = \mathbb{1} + \sum_{k<\ell} \alpha_{k\ell} DL_{k\ell}D^{-1} \tag{D.69}$$

is an element of $\mathsf{SO}(N)$ close to the identity and we can lift it to $\mathsf{Spin}(N)$ following Eq. (D.32), resulting in

$$\overline{DAD^{-1}} = 1 + \sum_{k<\ell} \alpha_{k\ell} \overline{D} t_{k\ell} \overline{D}^{-1} \tag{D.70}$$

$$= \overline{D} \left(1 + \sum_{k<\ell} \alpha_{k\ell} t_{k\ell} \right) \overline{D}^{-1} = \overline{D}\, \overline{A}\, \overline{D}^{-1}. \tag{D.71}$$

It remains to be shown that conjugation with $\overline{D}$ is independent of the choice of $\{d_{ij}\}$ (among the ones that give the same D) and their order. But this follows immediately, because the effect of conjugation with one factor in D amounts to just a single prefactor ± 1 [cf. the text following Eq. (D.58)] which is identical to the prefactor resulting from the conjugation with the corresponding factor in $\overline{D}$ [cf. Eq. (D.60)]. If two choices of $\{d_{ij}\}$ represent the same D, then in particular the overall prefactor is the same and thus the results of conjugating with the two versions of $\overline{D}$ match. □

Note that $\overline{D} \in \overline{\mathsf{P}}_N < \mathsf{Spin}(N)$ and it covers D, i.e.,

$$\sigma\left(\overline{D}\right) = D, \tag{D.72}$$

which follows directly from the definition of $\overline{D}$ and Eq. (D.48).

We now extend the above results to conjugation with an element of P_{Nh}.

Lemma D.3.3. *Let $L_{k\ell}$ $(k < \ell)$ be a basis element of $\mathfrak{so}(N)$, then $(\mathbb{1} - 2E_{ii})L_{k\ell}(\mathbb{1} - 2E_{ii}) \in \mathfrak{so}(N)$ and*

$$\overline{(\mathbb{1} - 2E_{ii})L_{k\ell}(\mathbb{1} - 2E_{ii})} = \epsilon_i t_{k\ell} \epsilon_i^{-1} \in \mathfrak{spin}(N), \tag{D.73}$$

where ϵ_i is the corresponding generator of $\mathcal{C}\ell_{0,N}$.

Proof. First observe that

$$(\mathbb{1} - 2E_{ii})L_{k\ell}(\mathbb{1} - 2E_{ii}) = \left[1 - 2\left(\delta_{ik} + \delta_{i\ell}\right)\right] L_{k\ell} \in \mathfrak{so}(N). \tag{D.74}$$

On the other hand, we find that

$$\epsilon_i t_{k\ell}(-\epsilon_i) = \left[1 - 2\left(\delta_{ik} + \delta_{i\ell}\right)\right] t_{k\ell}, \tag{D.75}$$

which implies that

$$\overline{(\mathbb{1} - 2E_{ii})L_{k\ell}(\mathbb{1} - 2E_{ii})} = \epsilon_i t_{k\ell}(-\epsilon_i) \in \mathfrak{spin}(N). \tag{D.76}$$

Note that $\epsilon_i^{-1} = -\epsilon_i$, because $\epsilon_i^2 = -1$. □

Lemma D.3.4. *Let $A \in \mathsf{SO}(N)$ be close to the identity and $P \in \mathsf{P}_{Nh}$, then $PAP^{-1} \in \mathsf{SO}(N)$ is close to the identity as well, and*

$$\overline{PAP^{-1}} = \overline{P}\,\overline{A}\,\overline{P}^{-1}, \tag{D.77}$$

where $\overline{P}$ is defined as

$$\overline{P} = \epsilon_1^{(1-\det(P))/2}\overline{D} \tag{D.78}$$

for $D = (\mathbb{1} - 2E_{11})^{(1-\det(P))/2}P \in \mathsf{P}_N$ and $\overline{D}$ defined according to Eq. (D.63).

Note that $\overline{P}$ must be explicitly defined because P is not close to the identity, implying that $\overline{P}$ has a sign ambiguity. This ambiguity is irrelevant for Eq. (D.77), because the $\pm$ sign appears twice and therefore cancels. Nevertheless, for concreteness we opt to work with the particular choice of sign fixed by Eq. (D.78).

Proof. Obviously, for any $P \in \mathsf{P}_{Nh}$,

$$D = (\mathbb{1} - 2E_{11})^{(1-\det(P))/2}P \in \mathsf{P}_N, \tag{D.79}$$

because

$$\det(D) = (-1)^{(1-\det(P))/2}\det(P) = \det(P)^2 = +1. \tag{D.80}$$

If $\det(P) = +1$, then $D = P$ and the statement of Lemma D.3.4 reduces to the already proved Lemma D.3.2. On the other hand, if $\det(P) = -1$, we have $D = (\mathbb{1} - 2E_{11})P$ and

$$PAP^{-1} = (\mathbb{1} - 2E_{11})DAD^{-1}(\mathbb{1} - 2E_{11}). \tag{D.81}$$

Lemma D.3.2 implies that $B = DAD^{-1} \in \mathsf{SO}(N)$ is close to the identity and $\overline{B} = \overline{D}\,\overline{A}\,\overline{D}^{-1}$, such that we only need to prove that for any $B \in \mathsf{SO}(N)$ close to the identity $(\mathbb{1} - 2E_{11})B(\mathbb{1} - 2E_{11}) \in \mathsf{SO}(N)$ is close to the identity and

$$\overline{(\mathbb{1} - 2E_{11})B(\mathbb{1} - 2E_{11})} = \epsilon_1\overline{B}\epsilon_1^{-1}. \tag{D.82}$$

But this follows from Lemma D.3.3 with analogous arguments as those used in the proof of Lemma D.3.2 □

Note that given some $P \in \mathsf{P}_{Nh}$ as a matrix

$$P = \operatorname{diag}(p_1, p_2, \ldots, p_N) = \prod_{i\,:\,p_i=-1}(\mathbb{1} - 2E_{ii}) \tag{D.83}$$

with $p_i \in \{\pm 1\}$ we can use Lemma D.3.3 to conclude that the $\overline{P}$ defined above has the canonical parametrization

$$\overline{P} = \prod_{i\,:\,p_i=-1} \epsilon_i, \tag{D.84}$$

which is obtained by replacing each factor of $(\mathbb{1} - 2E_{ii})$ with ϵ_i. The choice of sign mentioned above now corresponds to fixing the ordering of the factors in Eq. (D.84). Here we choose the convention that in Eqs. (D.83) and (D.84) factors with smaller indices appear to the right.

Finally, we consider the conjugation of an element of $\overline{\mathsf{P}}_N$ with an element of $\overline{\mathsf{P}}_{Nh}$.

Lemma D.3.5. *Let* $\mathfrak{d} \in \overline{\mathsf{P}}_N$ *and* $\mathfrak{p} \in \overline{\mathsf{P}}_{Nh}$*, then*

$$\mathfrak{p}\mathfrak{d}\mathfrak{p}^{-1} = s(\mathfrak{d},\mathfrak{p})\mathfrak{d} \tag{D.85}$$

with $s(\mathfrak{d},\mathfrak{p}) \in \{-1,+1\}$.

Proof. First we recall from Appendix D.2 that any $\mathfrak{d} \in \overline{\mathsf{P}}_N$ can be written as

$$\mathfrak{d} = \prod_{k<\ell} (-\epsilon_k\epsilon_\ell)^{d_{k\ell}} \tag{D.86}$$

for some (non-unique) $d_{k\ell} \in \{0,1\}$ and any $\mathfrak{p} \in \overline{\mathsf{P}}_{Nh}$ can be written as

$$\mathfrak{p} = \epsilon_1^{p_0} \prod_{i<j} (-\epsilon_i\epsilon_j)^{p_{ij}} \tag{D.87}$$

for $p_0 \in \{0,1\}$ and some (non-unique) $p_{ij} \in \{0,1\}$, where $\{\epsilon_i\}_{i=1}^N$ are the generators of $\mathcal{C}\ell_{0,N}$.

Equations (D.28) and (D.75) imply that for $k < \ell$

$$\epsilon_i\epsilon_k\epsilon_\ell\epsilon_i^{-1} = \left[1 - 2\left(\delta_{ik} + \delta_{i\ell}\right)\right]\epsilon_k\epsilon_\ell, \tag{D.88}$$

such that

$$\epsilon_i\mathfrak{d}\epsilon_i^{-1} = \underbrace{\left(\prod_{k<\ell}\left[1 - 2\left(\delta_{ik} + \delta_{i\ell}\right)\right]^{d_{k\ell}}\right)}_{=:s(\mathfrak{d},\epsilon_i)\in\{-1,+1\}}\mathfrak{d}. \tag{D.89}$$

Therefore,

$$\begin{aligned}\mathfrak{p}\mathfrak{d}\mathfrak{p}^{-1} &= \epsilon_1^{p_0}\left(\prod_{i<j}\epsilon_i^{p_{ij}}\epsilon_j^{p_{ij}}\right)\mathfrak{d}\left(\prod_{i<j}{}'\epsilon_j^{-p_{ij}}\epsilon_i^{-p_{ij}}\right)\epsilon_1^{-p_0} \\ &= \underbrace{\left(s(\mathfrak{d},\epsilon_1)^{p_0}\prod_{i<j}\left(s(\mathfrak{d},\epsilon_i)s(\mathfrak{d},\epsilon_j)\right)^{p_{ij}}\right)}_{=:s(\mathfrak{d},\mathfrak{p})}\mathfrak{d},\end{aligned} \tag{D.90}$$

where the dashed product indicates reversed order of the terms. The prefactor $s(\mathfrak{d},\mathfrak{p})$ is obviously just a sign, because all the factors $s(\mathfrak{d},\epsilon_i)$ are just signs. The independence of this conclusion and in particular of the prefactor $s(\mathfrak{d},\mathfrak{p}) \in \{\pm 1\}$ from the parametrization of $\mathfrak{d}$ and of $\mathfrak{p}$ follows trivially, because the left hand side of the above equation is obviously independent of those parametrizations, and the same is true for the remainder $\mathfrak{d}$ on the right-hand side of the equation. □

D.4. Quaternion invariant

Recall the definition [65, 66] of the quaternion invariant on a closed path γ (here assumed to be completely contained in the first Brillouin zone) based at point P, which we introduced in Section 3.4.2. We will in the following label the same point as $(0,0)$ (the numbers do not correspond to the $\mathbf{k}$-space coordinates). It is assumed that there is no band degeneracy of the N-band real-symmetric Hamiltonian $H_{\mathrm{R}}(\mathbf{k})$ along γ. We partition the path into infinitesimally spaced points, which we label $(0,1),(0,2),\ldots,(0,n-1)$. The next point in the sequence is $(0,n) = P$, i.e., the initial point again. (The motivation for the additional 0's in the label for each listed point will become clear in later paragraphs.)

At each point $\mathbf{k}$ on γ we can find the eigenframe [Eq. (D.11)] $\mathsf{u}(\mathbf{k})$. However, as discussed above, it is not unique and has the gauge freedom $\mathsf{u} \mapsto \mathsf{u}F$, where $F \in \mathsf{P}_{Nh}$. Starting with an initial right-handed eigenframe $\mathsf{u}_{0,0} \in \mathsf{SO}(N)$ of $H_{\mathrm{R}}(P)$, we define the eigenframes $\mathsf{u}_{0,j}$ of H_{R} at the subsequent points such that the rotation $\mathsf{u}_{0,j}^{\top}\mathsf{u}_{0,j+1}$ is close to identity $\mathbb{1} \in \mathsf{SO}(N)$. We will refer to this continuous choice of frame either as a *parallel transport* or *monodromy* of $\mathsf{u}_{0,0}$. In the last step of the closed path γ, we define $\underline{\mathsf{u}}_{0,0}$ such that $u_{0,n-1}^{\top}\underline{u}_{0,0}$ is close to identity; the underline indicates that the final $\underline{\mathsf{u}}_{0,0}$ is in general different from the initial $\mathsf{u}_{0,0}$ due to the possible presence of Berry phases on γ. We denote the gauge transformation that relates the two eigenframes as $F_\gamma \in \mathsf{P}_N$, i.e.

$$\underline{\mathsf{u}}_{0,0} = \mathsf{u}_{0,0}F_\gamma. \tag{D.91}$$

The quanternion charge is then defined as

$$\mathfrak{q}(\gamma) = \overline{\mathsf{u}_{0,0}^\top \mathsf{u}_{0,1}} \cdot \overline{\mathsf{u}_{0,1}^\top \mathsf{u}_{0,2}} \cdot \ldots \cdot \overline{\mathsf{u}_{0,n-1}^\top \underline{\mathsf{u}}_{0,0}}, \tag{D.92}$$

where $\overline{\mathsf{u}_{0,j}^\top \mathsf{u}_{0,j+1}}$ is defined according to Eq. (D.32), since $\mathsf{u}_{0,j}^\top \mathsf{u}_{0,j+1} \in \mathsf{SO}(N)$ is close to the identity by construction. Note that $\mathfrak{q}(\gamma)$ implicitly depends on both the base point P of the closed path γ as well as on the choice of gauge of the initial eigenframe $\mathsf{u}_{0,0}$.

Let us also establish the notation for the other two paths that we defined in Conjecture 1. We partition $\gamma_{P,\mathbf{b}}$ that connects $P = (0,0)$ to $P + \mathbf{b} = P' = (m,0)$ into infinitesimally spaced points labelled sequentially as $(0,0),(1,0),(2,0),\ldots,(m-1,0),(m,0)$. Note that this path is not closed, $P' \neq P$; in particular, the Hamiltonians $H(P)$ and $H(P')$ may differ by the unitary transformation in Eq. (D.12).

Furthermore, we partition the shifted (closed) contour γ' based at P' into the points $(m,j) = (0,j) + \mathbf{b}$ for $1 \leq j \leq n$. Note that the energy spectra on γ and γ' are identical, i.e., by our previous assumption there is no band degeneracy on γ'.

Analogously to the case of γ, we define the eigenframes $\mathsf{u}_{i,0}$, $1 \leq i \leq m$, on $\gamma_{P,\mathbf{b}}$ such that the rotation $\mathsf{u}_{i,0}^\top \mathsf{u}_{i+1,0}$ is close to identity $\mathbb{1} \in \mathsf{SO}(N)$ (i.e., through parallel transport), and similarly for $\mathsf{u}_{m,j}$, $1 \leq j \leq n$.

The final frame on γ', i.e., at P' *after* traversing γ', is related to the initial frame on γ' via a gauge transformation $F_{\gamma'} \in \mathsf{P}_N$ [cf. Eq. (D.91)]

$$\underline{\mathsf{u}}_{m,0} = \mathsf{u}_{m,0} F_{\gamma'}. \tag{D.93}$$

Therefore, the eigenframes on $\gamma_{P,\mathbf{b}}^{-1}$ are not $\mathsf{u}_{i,0}$ and we instead define new eigenframes $\underline{\mathsf{u}}_{i,0}$, $1 \leq i \leq m$, through parallel transport, i.e., such that $\underline{\mathsf{u}}_{i,0}^\top \underline{\mathsf{u}}_{i-1,0}$ is close to identity $\mathbb{1} \in \mathsf{SO}(N)$ (note the reversed order in the subscript i because the path $\gamma_{P,\mathbf{b}}$ is traversed in reverse). The final frame on $\gamma_{P,\mathbf{b}}^{-1}$, defined via parallel transport as well, is instead denoted by $\underline{\mathsf{u}}_{0,0}$ to avoid confusion with the already defined $\underline{\mathsf{u}}_{0,0}$ [however, we will later show that $\underline{\mathsf{u}}_{0,0} = \underline{\mathsf{u}}_{0,0}$, cf. Eq. (D.112)]. All the frames on $\gamma_{P,\mathbf{b}}^{-1}$ are related to the corresponding frames on $\gamma_{P,\mathbf{b}}$ by some gauge transformation $F_{(i,0)} \in \mathsf{P}_N$: for $1 \leq i \leq m$

$$\underline{\mathsf{u}}_{i,0} = \mathsf{u}_{i,0} F_{(i,0)}, \tag{D.94a}$$

where $F_{(m,0)} = F_{\gamma'}$; for the last point on $\gamma_{P,\mathbf{b}}^{-1}$ we have

$$\underline{\mathsf{u}}_{0,0} = \mathsf{u}_{0,0} F_{(0,0)}. \tag{D.94b}$$

Lemma D.4.1. *Under the assumptions of Conjecture 1, $F_{(i,0)}$ defined in Eq. (D.94) and $F_{\gamma'}$ defined in Eq. (D.93) are equal,*

$$\forall 0 \leq i \leq m : F_{(i,0)} = F_{\gamma'}. \tag{D.95}$$

Proof. The statement follows from Eq. (D.93) due to the monodromy (flatness) of the parallel transport. We construct an explicit proof via recursion starting from $i = m$ [cf. Eq. (D.93)]. Assuming $F_{(i+1,0)} = F_\gamma$ for some $0 \leq i < m$, the frame $\underline{\mathsf{u}}_{i,0}$ is defined via parallel transport such that

$$\underline{\mathsf{u}}_{i+1,0}^\top \underline{\mathsf{u}}_{i,0} = F_{\gamma'}^\top \mathsf{u}_{i+1,0}^\top \mathsf{u}_{i,0} F_{(i,0)} \tag{D.96}$$

is close to the identity. On the other hand the frames $\mathsf{u}_{i,0}$, $0 \leq i \leq m$, are defined such that $\mathsf{u}_{i,0}^\top \mathsf{u}_{i+1,0}$ is close to the identity, which is equivalent to the condition that $\mathsf{u}_{i+1,0}^\top \mathsf{u}_{i,0}$ is close to the identity. Thus, $F_{(i,0)}$ and $F_{\gamma'}$ have to be close, but because the gauge transformations $F_{\gamma'}$ and $F_{(i,0)}$ are diagonal with ± 1's on the diagonal, it follows that $F_{(i,0)} = F_{\gamma'}$. □

Lemma D.4.2. *Under the assumptions of Conjecture 1, the two gauge transformations F_γ, defined in Eq. (D.91), and $F_{\gamma'}$, defined in Eq. (D.93), are equal*

$$F_{\gamma'} = F_\gamma. \tag{D.97}$$

The physical interpretation of this result is that the Berry phases of the individual bands on closed paths γ and γ' match.

Proof. The gauge transformations F_γ and $F_{\gamma'}$ are defined as gauge transformations at P and P', respectively. We can obtain an eigenframe of $H(P + \mathbf{b})$ from the initial eigenframe $\mathsf{u}_{0,0}$ of $H(P)$ in two distinct but canonical ways. On the one hand, through parallel transport we have defined an eigenframe $\mathsf{u}_{m,0}$ at P'. On the other hand, the unitary relation through $U_{\mathbf{b},\mathrm{R}}$ defines the eigenframe $U_{\mathbf{b},\mathrm{R}}\mathsf{u}_{0,0}$ at P'. These two eigenframes in general differ by a gauge transformation $F_{P,\mathbf{b}} \in \mathsf{P}_{Nh}$, so we write

$$U_{\mathbf{b},\mathrm{R}}\mathsf{u}_{0,0} = \mathsf{u}_{m,0} F_{P,\mathbf{b}}. \tag{D.98}$$

Thus, we have

$$F_{P,\mathbf{b}} = \mathsf{u}_{m,0}^\top U_{\mathbf{b},\mathrm{R}} \mathsf{u}_{0,0}. \tag{D.99}$$

We emphasize that it is possible for $F_{P,\mathbf{b}}$ to have a negative determinant. This happens when an odd number of bands carry nontrivial Berry phase π in the $\mathbf{b}$ direction.

It also follows from the monodromy (flatness) of the parallel transport that

$$U_{\mathbf{b},\mathrm{R}}\mathsf{u}_{0,j} = \mathsf{u}_{m,j}F_{P,\mathbf{b}} \tag{D.100}$$

for all j, such that we can rewrite $\mathsf{u}_{m,j}$ in terms of $\mathsf{u}_{0,j}$:

$$\mathsf{u}_{m,j} = U_{\mathbf{b},\mathrm{R}}\mathsf{u}_{0,j}{F_{P,\mathbf{b}}}^{\top}. \tag{D.101}$$

For the same reason, i.e., monodromy, an analogous equation holds for $\underline{\mathsf{u}}_{m,0}$ and $\underline{\mathsf{u}}_{0,0}$, which are defined via parallel transport from $\mathsf{u}_{m,n-1}$ and $\mathsf{u}_{0,n-1}$, respectively:

$$\underline{\mathsf{u}}_{m,0} = U_{\mathbf{b},\mathrm{R}}\underline{\mathsf{u}}_{0,0}F_{P,\mathbf{b}}^{\top} \tag{D.102}$$

Together with Eqs. (D.91) and (D.101), this gives

$$\begin{aligned}\underline{\mathsf{u}}_{m,0} &= U_{\mathbf{b},\mathrm{R}}\mathsf{u}_{0,0}F_{\gamma}F_{P,\mathbf{b}}^{\top}\\ &= \mathsf{u}_{m,0}F_{P,\mathbf{b}}F_{\gamma}F_{P,\mathbf{b}}^{\top}.\end{aligned} \tag{D.103}$$

By comparing Eq. (D.103) to Eq. (D.93), we see that $F_{\gamma'} = F_{P,\mathbf{b}}F_{\gamma}F_{P,\mathbf{b}}^{\top}$. However, since F_{γ}, $F_{\gamma'}$ and $F_{P,\mathbf{b}}$ are all elements of P_{Nh} (i.e., diagonal matrices with ± 1 on the diagonal) and therefore commute with each other, we immediately find $F_{\gamma'} = F_{\gamma}$. □

Besides the quaternion charge $\mathfrak{q}(\gamma')$ defined analogously to Eq. (D.92), we now define the total eigenframe rotations along $\gamma_{P,\mathbf{b}}$ and $\gamma_{P,\mathbf{b}}^{-1}$

$$\mathfrak{b}\left(\gamma_{P,\mathbf{b}}\right) = \overline{\mathsf{u}_{0,0}^{\top}\mathsf{u}_{1,0}}\cdot\overline{\mathsf{u}_{1,0}^{\top}\mathsf{u}_{2,0}}\cdot\ldots\cdot\overline{\mathsf{u}_{m-1,0}^{\top}\mathsf{u}_{m,0}}, \tag{D.104}$$

$$\mathfrak{b}\left(\gamma_{P,\mathbf{b}}^{-1}\right) = \overline{\underline{\mathsf{u}}_{m,0}^{\top}\underline{\mathsf{u}}_{m-1,0}}\cdot\ldots\cdot\overline{\underline{\mathsf{u}}_{2,0}^{\top}\underline{\mathsf{u}}_{1,0}}\cdot\overline{\underline{\mathsf{u}}_{1,0}^{\top}\underline{\mathsf{u}}_{0,0}}. \tag{D.105}$$

With these definitions, we can proceed to prove several relations between the introduced elements in $\mathsf{Spin}(N)$. One should bear in mind that $\mathfrak{b}\left(\gamma_{P,\mathbf{b}}\right)$ depends not only on the base point P but also implicitly on the initial frame $\mathsf{u}_{0,0}$; the quaternion charge $\mathfrak{q}(\gamma')$ depends implicitly on P, $\mathsf{u}_{0,0}$ and the path $\gamma_{P,\mathbf{b}}$, while $\mathfrak{b}\left(\gamma_{P,\mathbf{b}}^{-1}\right)$ additionally depends on the whole path γ. Therefore, the following statement only make sense in the context of Conjecture 1, i.e., when we consider a path $\tilde{\gamma} = \gamma_{P,\mathbf{b}}\circ\gamma'\circ\gamma_{P,\mathbf{b}}^{-1}$ with base point P, fixed initial frame $\mathsf{u}_{0,0}$.

Lemma D.4.3. *Under the assumptions of Conjecture 1, we have*

$$\mathfrak{q}(\gamma') = \overline{F_{P,\mathbf{b}}}\mathfrak{q}(\gamma)\overline{F_{P,\mathbf{b}}}^{-1}, \tag{D.106}$$

where

$$F_{P,\mathbf{b}} = \mathsf{u}_{m,0}^{\top} U_{\mathbf{b},\mathrm{R}} \mathsf{u}_{0,0} \in \mathsf{P}_{Nh} \tag{D.107}$$

and given the above $F_{P,\mathbf{b}}$, $\overline{F_{P,\mathbf{b}}}$ *is defined according to Eq.* (D.78).

Proof. Equation (D.101) allows us to rewrite the factors in the definition of $\mathfrak{q}(\gamma')$ [Eq. (D.92)]: for $1 \leq j < n-1$

$$\begin{aligned}\overline{\mathsf{u}_{m,j}^{\top}\mathsf{u}_{m,j+1}} &= \overline{F_{P,\mathbf{b}}\mathsf{u}_{0,j}^{\top}\left(U_{\mathbf{b},\mathrm{R}}\right)^{\top} U_{\mathbf{b},\mathrm{R}}\mathsf{u}_{0,j+1}F_{P,\mathbf{b}}^{\top}} \\ &= \overline{F_{P,\mathbf{b}}\mathsf{u}_{0,j}^{\top}\mathsf{u}_{0,j+1}F_{P,\mathbf{b}}^{-1}} \\ &= \overline{F_{P,\mathbf{b}}} \cdot \overline{\mathsf{u}_{0,j}^{\top}\mathsf{u}_{0,j+1}} \cdot \overline{F_{P,\mathbf{b}}}^{-1},\end{aligned} \tag{D.108}$$

where we used that $U_{\mathbf{b},\mathrm{R}}$ and $F_{P,\mathbf{b}}$ are orthogonal and applied Lemma D.3.4 with $\overline{F_{P,\mathbf{b}}}$ as defined therein. Thus, in $\mathfrak{q}(\gamma')$ all the $\overline{F_{P,\mathbf{b}}}$ between the factors cancel and we are left with

$$\begin{aligned}\mathfrak{q}(\gamma') &= \overline{\mathsf{u}_{m,0}^{\top}\mathsf{u}_{m,1}} \cdot \overline{\mathsf{u}_{m,1}^{\top}\mathsf{u}_{m,2}} \cdot \ldots \cdot \overline{\mathsf{u}_{m,n-1}^{\top}\underline{\mathsf{u}}_{m,0}} \\ &= \overline{F_{P,\mathbf{b}}}\mathfrak{q}(\gamma)\overline{F_{P,\mathbf{b}}}^{-1},\end{aligned} \tag{D.109}$$

as desired. □

Lemma D.4.4. *Under the assumptions of Conjecture 1, we have*

$$\mathfrak{b}\left(\gamma_{P,\mathbf{b}}^{-1}\right) = \mathfrak{q}(\gamma)^{-1}\mathfrak{b}\left(\gamma_{P,\mathbf{b}}\right)^{-1}\mathfrak{q}(\gamma). \tag{D.110}$$

Proof. Applying Lemmas D.4.1 and D.4.2 to Eq. (D.94) gives for all $1 \leq i \leq m$ that

$$\underline{\mathsf{u}}_{i,0} = \mathsf{u}_{i,0}F_{\gamma} \tag{D.111}$$

and

$$\underline{\mathsf{u}}_{0,0} = \mathsf{u}_{0,0}F_{\gamma} = \underline{\mathsf{u}}_{0,0}. \tag{D.112}$$

Substituting Eqs. (D.111) and (D.112) into the expression for $\mathfrak{b}\left(\gamma_{P,\mathbf{b}}^{-1}\right)$ in Eq. (D.105), and applying Lemma D.3.2, we find for $0 \leq i \leq m$

$$\begin{aligned}\overline{\underline{\mathsf{u}}_{i,0}^{\top}\mathsf{u}_{i-1,0}} &= \overline{F_{\gamma}^{-1}\mathsf{u}_{i,0}^{\top}\mathsf{u}_{i-1,0}F_{\gamma}} \\ &= \overline{F_{\gamma}}^{-1} \cdot \overline{\mathsf{u}_{i,0}^{\top}\mathsf{u}_{i-1,0}} \cdot \overline{F_{\gamma}},\end{aligned} \tag{D.113}$$

such that

$$\mathfrak{b}\left(\gamma_{P,\mathbf{b}}^{-1}\right) = \overline{F_{\gamma}}^{-1} \cdot \overline{\mathsf{u}_{m,0}^{\top}\mathsf{u}_{m-1,0}} \cdot \ldots \cdot \overline{\mathsf{u}_{1,0}^{\top}\mathsf{u}_{0,0}} \cdot \overline{F_{\gamma}}. \tag{D.114}$$

Since $\mathsf{u}_{i-1,0}^\top \mathsf{u}_{i,0} \in \mathsf{SO}(N)$ is close to the identity, we can apply Lemma D.2.1 and find

$$\overline{\mathsf{u}_{i-1,0}^\top \mathsf{u}_{i,0}}^{-1} = \overline{\left(\mathsf{u}_{i-1,0}^\top \mathsf{u}_{i,0}\right)^\top} = \overline{\mathsf{u}_{i,0}^\top \mathsf{u}_{i-1,0}}. \tag{D.115}$$

On the other hand, by inverting Eq. (D.104) we obtain

$$\begin{aligned} \mathfrak{b}\left(\gamma_{P,\mathbf{b}}\right)^{-1} &= \overline{\mathsf{u}_{m-1,0}^\top \mathsf{u}_{m,0}}^{-1} \cdot \ldots \cdot \overline{\mathsf{u}_{1,0}^\top \mathsf{u}_{2,0}}^{-1} \cdot \overline{\mathsf{u}_{0,0}^\top \mathsf{u}_{1,0}}^{-1} \\ &\overset{\text{Eq. (D.115)}}{=} \overline{\mathsf{u}_{m,0}^\top \mathsf{u}_{m-1,0}} \cdot \ldots \cdot \overline{\mathsf{u}_{2,0}^\top \mathsf{u}_{1,0}} \cdot \overline{\mathsf{u}_{1,0}^\top \mathsf{u}_{0,0}} \end{aligned} \tag{D.116}$$

and by comparing to Eq. (D.114) find that

$$\mathfrak{b}\left(\gamma_{P,\mathbf{b}}^{-1}\right) = \overline{F_\gamma}^{-1} \mathfrak{b}\left(\gamma_{P,\mathbf{b}}\right)^{-1} \overline{F_\gamma}. \tag{D.117}$$

Additionally, recall that $\overline{F_\gamma}$ satisfies

$$\sigma\left(\overline{F_\gamma}\right) = F_\gamma \tag{D.118}$$

and by the definition of the quaternion invariant in Eq. (D.92),

$$\sigma(\mathfrak{q}(\gamma)) = \mathsf{u}_{0,0}^\top \mathsf{u}_{0,1} \mathsf{u}_{0,1}^\top \mathsf{u}_{0,2} \ldots \mathsf{u}_{0,n-1}^\top \underline{\mathsf{u}}_{0,0} = \mathsf{u}_{0,0}^\top \underline{\mathsf{u}}_{0,0} = F_\gamma, \tag{D.119}$$

such that, according to Eq. (D.37),

$$\mathfrak{q}(\gamma) = \pm \overline{F_\gamma}. \tag{D.120}$$

Thus,

$$\mathfrak{b}\left(\gamma_{P,\mathbf{b}}^{-1}\right) = \mathfrak{q}(\gamma)^{-1} \mathfrak{b} \gamma_{P,\mathbf{b}}^{-1} \mathfrak{q}(\gamma), \tag{D.121}$$

because the inverse $\mathfrak{q}(\gamma)^{-1}$ comes with the same sign as $\mathfrak{q}(\gamma)$ and consequently the overall sign ambiguity cancels. □

D.5. Berry Phases

Lemma D.5.1. *The gauge transformation relating the eigenframes at P and $P + \mathbf{b}$ with the reciprocal lattice vector $\mathbf{b}$,*

$$F_{P,\mathbf{b}} = \mathsf{u}_{m,0}^\top U_{\mathbf{b},\mathrm{R}} \mathsf{u}_{0,0} \in \mathsf{P}_{Nh}, \tag{D.122}$$

is given by the Berry phases φ_i of the bands $1 \leq i \leq N$ in the direction $\mathbf{b}$:

$$F_{P,\mathbf{b}} = \mathrm{diag}\left(\mathrm{e}^{\mathrm{i}\varphi_1}, \mathrm{e}^{\mathrm{i}\varphi_2}, \ldots, \mathrm{e}^{\mathrm{i}\varphi_N}\right). \tag{D.123}$$

Proof. Recall the construction of the eigenframes following the path $\gamma_{P,\mathbf{b}}$. At each of the infinitesimally spaced points $(0,0),(1,0),\ldots,(m,0)$, we find a right-handed eigenframe $\hat{\mathsf{u}}_{i+1,0} \in \mathsf{SO}(N)$. At P we fix an arbitrary gauge

$$\mathsf{u}_{0,0} := \hat{\mathsf{u}}_{0,0} \in \mathsf{SO}(N) \tag{D.124}$$

and then recursively choose the right gauge as follows: given $\mathsf{u}_{i-1,0}$ the next eigenframe (in the right gauge) is

$$\mathsf{u}_{i,0} = \hat{\mathsf{u}}_{i,0} F_i \tag{D.125}$$

with $F_i \in \mathsf{P}_N$ such that

$$\mathsf{u}_{i-1,0}^\top \mathsf{u}_{i,0} = \mathsf{u}_{i-1,0}^\top \hat{\mathsf{u}}_{i,0} F_i \tag{D.126}$$

is close to the identity. The latter is equivalent to

$$\operatorname{sign}\operatorname{diag}\left(\mathsf{u}_{i-1,0}^\top \hat{\mathsf{u}}_{i,0} F_i\right) = \mathbb{1}, \tag{D.127}$$

where, given a matrix M, $\operatorname{sign}\operatorname{diag}(M)$ is the matrix with entries

$$\left(\operatorname{sign}\operatorname{diag}(M)\right)_{ij} = \operatorname{sign}(M_{ii})\delta_{ij}. \tag{D.128}$$

Obviously, for any matrix $D \in \mathsf{P}_{Nh}$,

$$[\operatorname{sign}\operatorname{diag}(M)]D = \operatorname{sign}\operatorname{diag}(MD), \tag{D.129a}$$
$$D[\operatorname{sign}\operatorname{diag}(M)] = \operatorname{sign}\operatorname{diag}(DM), \tag{D.129b}$$

such that from Eqs. (D.127) and (D.129a) we get

$$F_i^\top = \operatorname{sign}\operatorname{diag}\left(\mathsf{u}_{i-1,0}^\top \hat{\mathsf{u}}_{i,0}\right). \tag{D.130}$$

Expressing $\mathsf{u}_{i,0}^\top$ from Eq. (D.125) and using Eq. (D.129b), we further obtain

$$F_i^\top = F_{i-1}^\top \operatorname{sign}\operatorname{diag}\left(\hat{\mathsf{u}}_{i-1,0}^\top \hat{\mathsf{u}}_{i,0}\right), \tag{D.131}$$

which constitutes a recursion relation for the gauge transformations F_i.

With $F_0 = \mathbb{1}$ [cf.Eq. (D.124)], the above recursion relation has solution

$$F_j = \prod_{i=1}^{j} \operatorname{sign}\operatorname{diag}\left(\hat{\mathsf{u}}_{i,0}^\top \hat{\mathsf{u}}_{i-1,0}\right), \tag{D.132}$$

where factors with smaller i appear to the *right* (note also the reversed ordering of the $\hat{\mathsf{u}}_{i,0}$ in each factor due to the transposition). Then, according to Eq. (D.125)),

$$\mathsf{u}_{m,0} = \hat{\mathsf{u}}_{m,0} \left(\prod_{i=1}^{m} \operatorname{sign} \operatorname{diag} \left(\hat{\mathsf{u}}_{i,0}^{\top} \hat{\mathsf{u}}_{i-1,0} \right) \right), \tag{D.133}$$

such that

$$F_{P,\mathbf{b}} = \left(\prod_{i=1}^{m} \operatorname{sign} \operatorname{diag} \left(\hat{\mathsf{u}}_{i-1,0}^{\top} \hat{\mathsf{u}}_{i,0} \right) \right) \hat{\mathsf{u}}_{m,0}^{\top} U_{\mathbf{b},\mathrm{R}} \hat{\mathsf{u}}_{0,0}. \tag{D.134}$$

where factors with smaller i appear to the *left*. Note that $F_{P,\mathbf{b}} \in \mathsf{P}_{Nh}$, such that we can apply Eq. (D.129a) with $M = \hat{\mathsf{u}}_{m-1,0}^{\top} \hat{\mathsf{u}}_{m,0}$ and $D = F_{P,\mathbf{b}}$ and obtain

$$\begin{aligned} F_{P,\mathbf{b}} = \left(\prod_{i=1}^{m-1} \operatorname{sign} \operatorname{diag} \left(\hat{\mathsf{u}}_{i-1,0}^{\top} \hat{\mathsf{u}}_{i,0} \right) \right) \times \\ \times \operatorname{sign} \operatorname{diag} \left(\hat{\mathsf{u}}_{m-1,0}^{\top} \hat{\mathsf{u}}_{m,0} \hat{\mathsf{u}}_{m,0}^{\top} U_{\mathbf{b},\mathrm{R}} \hat{\mathsf{u}}_{0,0} \right). \end{aligned} \tag{D.135}$$

Orthogonality of $\hat{\mathsf{u}}_{m,0}$ finally gives

$$F_{P,\mathbf{b}} = \left(\prod_{i=1}^{m-1} \operatorname{sign} \operatorname{diag} \left(\hat{\mathsf{u}}_{i-1,0}^{\top} \hat{\mathsf{u}}_{i,0} \right) \right) \operatorname{sign} \operatorname{diag} \left(\hat{\mathsf{u}}_{m-1,0}^{\top} U_{\mathbf{b},\mathrm{R}} \hat{\mathsf{u}}_{0,0} \right), \tag{D.136}$$

where again factors with smaller i appear to the *left*.

Next, we consider the Berry phase φ_j of the j^{th} band along $\gamma_{P,\mathbf{b}}$. As we have seen in Section 3.1.1, it can be defined in terms of the corresponding Wilson operator $\mathcal{W}_j(\gamma_{P,\mathbf{b}})$. Rewriting Eq. (3.6) in terms of frames we find the following expression. Let $\mathbf{u}_j^{(i)}$ be the j^{th} column of the eigenframe $\hat{\mathsf{u}}_{i,0}$, i.e., the j^{th} eigenvector of the real Bloch Hamiltonian at the point $(i, 0)$ (in an arbitrary gauge), then

$$\mathcal{W}_j \left(\gamma_{P,\mathbf{b}} \right) = \frac{\left(U_{\mathbf{b},\mathrm{R}} \mathbf{u}_j^{(0)} \right)^{\top}}{\left| \left(U_{\mathbf{b},\mathrm{R}} \mathbf{u}_j^{(0)} \right)^{\top} \mathbf{u}_j^{(m-1)} \right|} \left(\prod_{i=1}^{m-1} \frac{\mathbf{u}_j^{(i)} \left(\mathbf{u}_j^{(i)} \right)^{\top}}{\left| \left(\mathbf{u}_j^{(i)} \right)^{\top} \mathbf{u}_j^{(i-1)} \right|} \right) \mathbf{u}_j^{(0)} \tag{D.137}$$

where factors with smaller i appear to the right, and we continue to assume the limit of a partitioning into infinitesimal steps. Rearranging the terms, we

arrive at (factors with smaller i still appear to the right)

$$\mathcal{W}_j\left(\gamma_{P,\mathbf{b}}\right) = \frac{\left(U_{\mathbf{b},\mathrm{R}}\mathbf{u}_j^{(0)}\right)^\top \mathbf{u}_j^{(m-1)}}{\left|\left(U_{\mathbf{b},\mathrm{R}}\mathbf{u}_j^{(0)}\right)^\top \mathbf{u}_j^{(m-1)}\right|}\left(\prod_{i=1}^{m-1}\frac{\left(\mathbf{u}_j^{(i)}\right)^\top \mathbf{u}_j^{(i-1)}}{\left|\left(\mathbf{u}_j^{(i)}\right)^\top \mathbf{u}_j^{(i-1)}\right|}\right). \tag{D.138}$$

Since $\mathcal{W}$ is a number, it is its own transpose and we find

$$\mathcal{W}_j\left(\gamma_{P,\mathbf{b}}\right) = \left(\prod_{i=1}^{m-1}\frac{\left(\mathbf{u}_j^{(i-1)}\right)^\top \mathbf{u}_j^{(i)}}{\left|\left(\mathbf{u}_j^{(i-1)}\right)^\top \mathbf{u}_j^{(i)}\right|}\right)\frac{\left(\mathbf{u}_j^{(m-1)}\right)^\top U_{\mathbf{b},\mathrm{R}}\mathbf{u}_j^{(0)}}{\left|\left(\mathbf{u}_j^{(m-1)}\right)^\top U_{\mathbf{b},\mathrm{R}}\mathbf{u}_j^{(0)}\right|}, \tag{D.139}$$

where factors with smaller i now appear to the *left* because of the transposition. Each factor is just a phase, and because the eigenvectors are real (by assumption) this implies that it is a just a sign. Assuming that the points along the path are sufficiently close, the denominators are all close to 1 and we can rewrite the Wilson operator as

$$\mathcal{W}_j\left(\gamma_{P,\mathbf{b}}\right) = \left(\prod_{i=1}^{m-1}\operatorname{sign}\left(\left(\mathbf{u}_j^{(i-1)}\right)^\top \mathbf{u}_j^{(i)}\right)\right)\operatorname{sign}\left(\left(\mathbf{u}_j^{(m-1)}\right)^\top U_{\mathbf{b},\mathrm{R}}\mathbf{u}_j^{(0)}\right). \tag{D.140}$$

We observe that

$$\left(\hat{\mathbf{u}}_{i-1,0}^\top \hat{\mathbf{u}}_{i,0}\right)_{jj} = \left(\mathbf{u}_j^{(i-1)}\right)^\top \mathbf{u}_j^{(i)}, \tag{D.141}$$

such that

$$\left(F_{P,\mathbf{b}}\right)_{ij} = \mathcal{W}_i(\gamma_{P,\mathbf{b}})\delta_{ij}. \tag{D.142}$$

With the definition of the Berry phase, $\mathcal{W}_i(\gamma_{P,\mathbf{b}}) = \mathrm{e}^{\mathrm{i}\varphi_i}$, the desired Eq. (D.123) follows. □

D.6. Proof of Conjecture 1

We can finally prove Conjecture 1.

Proof. By definition, the quaternion charge of $\tilde{\gamma}$ is

$$\mathfrak{q}(\tilde{\gamma}) = \mathfrak{b}\left(\gamma_{P,\mathbf{b}}\right)\mathfrak{q}(\gamma')\mathfrak{b}\left(\gamma_{P,\mathbf{b}}^{-1}\right) \tag{D.143}$$

and using Lemmas D.3.5, D.4.3 and D.4.4, this gives

$$\begin{aligned}
\mathfrak{q}(\tilde{\gamma}) &= \mathfrak{b}\left(\gamma_{P,\mathbf{b}}\right) \underbrace{\overline{F_{P,\mathbf{b}}}\mathfrak{q}(\gamma)\overline{F_{P,\mathbf{b}}}^{-1}}_{=s\left(\mathfrak{q}(\gamma),\overline{F_{P,\mathbf{b}}}\right)\mathfrak{q}(\gamma)} \mathfrak{q}(\gamma)^{-1}\mathfrak{b}(\gamma_{P,\mathbf{b}})^{-1}\mathfrak{q}(\gamma) \\
&= \mathfrak{b}\left(\gamma_{P,\mathbf{b}}\right) s\left(\mathfrak{q}(\gamma), \overline{F_{P,\mathbf{b}}}\right) \underbrace{\mathfrak{q}(\gamma)\mathfrak{q}(\gamma)^{-1}}_{=1} \mathfrak{b}(\gamma_{P,\mathbf{b}})^{-1}\mathfrak{q}(\gamma) \\
&= \underbrace{\mathfrak{b}\left(\gamma_{P,\mathbf{b}}\right)\mathfrak{b}(\gamma_{P,\mathbf{b}})^{-1}}\underbrace{s\left(\mathfrak{q}(\gamma), \overline{F_{P,\mathbf{b}}}\right)\mathfrak{q}(\gamma)}_{=\overline{F_{P,\mathbf{b}}}\mathfrak{q}(\gamma)\overline{F_{P,\mathbf{b}}}^{-1}} \\
&= \overline{F_{P,\mathbf{b}}}\mathfrak{q}(\gamma)\overline{F_{P,\mathbf{b}}}^{-1}
\end{aligned} \tag{D.144}$$

with $\overline{F_{P,\mathbf{b}}}$ defined according to Eq. (D.78), given

$$F_{P,\mathbf{b}} = \mathsf{u}_{m,0}^{\top} U_{\mathbf{b},\mathrm{R}} \mathsf{u}_{0,0} \in \mathsf{P}_{Nh}. \tag{D.145}$$

But according to Lemma D.5.1

$$F_{P,\mathbf{b}} = \mathrm{diag}\left(\mathrm{e}^{\mathrm{i}\varphi_1}, \mathrm{e}^{\mathrm{i}\varphi_2}, \ldots, \mathrm{e}^{\mathrm{i}\varphi_N}\right). \tag{D.146}$$

where $\varphi_i \in \{0, \pi\}$ is the Berry phase of the i^{th} band in the direction $\mathbf{b}$ and, according to Eq. (D.84),

$$\overline{F_{P,\mathbf{b}}} = \overline{\prod_{i\,:\,\mathrm{e}^{\mathrm{i}\varphi_i}=-1} (\mathbb{1} - 2E_{ii})} = \prod_{i\,:\,\mathrm{e}^{\mathrm{i}\varphi_i}=-1} \epsilon_i, \tag{D.147}$$

as desired. The ordering of the product in Eq. (D.147) is fixed by the convention in Lemma D.5.1 such that ϵ_i with smaller i appear to the right. Without fixing the ordering in the product, there would be a sign ambiguity in $\overline{F_{P,\mathbf{b}}}$, because $F_{P,\mathbf{b}}$ is not close to the identity. However, note that in Eq. (D.144) $\overline{F_{P,\mathbf{b}}}$ appears twice, such that result holds for both choices of the sign. □

E. Symmetry indicator for Euler monopole charge

This chapter is largely based on Appendix B to the publication "Universal higher-order bulk-boundary correspondence of triple nodal points" [3]. Segments with significant text overlap with the published version may be subject to copyright by the American Physical Society.

In this Appendix, we derive two results discussed in Sections 6.1.2 and 6.2: (1) a symmetry indicator for the Euler monopole charge in the presence of rotational symmetry, and (2) conditions on the combinations of ICRs that necessarily lead to a gapless bulk on at least one side of the triple-point pair. While we first derive both results assuming presence of $\mathcal{PT}$ symmetry, in Appendix E.4, we generalize (2) to the case where $\mathcal{PT}$ is absent.

The presented arguments are based on analyzing the spectrum of Wilson loop operators on certain appropriately chosen paths. As discussed in Section 3.1.1, Wilson loop operators are defined in terms of projectors onto occupied eigenstates $|u_i(\mathbf{k})\rangle$ of the Bloch Hamiltonian $H(\mathbf{k})$. We organize the occupied eigenstates into an $N \times N_{\text{occ}}$ matrix

$$\mathsf{u}(\mathbf{k}) = \big(|u_1(\mathbf{k})\rangle \quad |u_2(\mathbf{k})\rangle \quad \cdots \quad |u_{N_{\text{occ}}}(\mathbf{k})\rangle\big), \tag{E.1}$$

where N is the total number of bands and N_{occ} is the number of occupied bands. In the presence of $\mathcal{PT}$ symmetry satisfying $(\mathcal{PT})^2 = +1$, we always adopt a basis of the Hilbert space in which $\mathcal{PT}$ is represented by complex conjugation $\mathcal{K}$. Then, the Bloch Hamiltonian is a real-symmetric matrix, and the eigenstates (as well as the matrix $\mathsf{u}(\mathbf{k})$) can be gauged to be real. To determine the advertised properties of triple-point pairs, we need to study how the spectrum of the Wilson-operator on certain appropriately chosen paths is constrained by $\mathcal{PT}$, m_v, and C_n symmetries.

The discussion in this appendix is structured as follows. In Appendix E.1 we study how C_n rotational symmetry constrains the Wilson loop operator on an appropriately chosen path, composed of two C_n-related segments. Next, in Appendix E.2, we use the previous result to relate the Berry phase of the occupied bands on a particular choice of path to the C_n eigenvalues of the occupied bands at the high-symmetry line, and in Appendix E.3 we derive

a symmetry-indicator formula for the Euler monopole charge. Finally, in Appendix E.4 we extend the discussion of inadmissible triple-point pairs to systems without $\mathcal{PT}$ symmetry.

E.1. Symmetry-constraint on Wilson loop operator

We define the following family of closed contours

$$\Gamma(\phi) = \gamma(\phi)^{-1} \circ \gamma(0) \tag{E.2}$$

consisting of half circles given by $\gamma(\phi) : \theta \in [0, \pi] \mapsto \gamma(\theta, \phi)$ with

$$\gamma(\theta, \phi) = R \begin{pmatrix} \sin(\theta)\cos(\phi) \\ \sin(\theta)\sin(\phi) \\ -\cos(\theta) \end{pmatrix}. \tag{E.3}$$

One example of such a contour is illustrated in Fig. 6.4 in green color. We abbreviate $\mathsf{u}(\theta, \phi) = \mathsf{u}(\gamma(\theta, \phi))$, $\mathsf{u}_0 = \mathsf{u}(0, \phi)$ and $\mathsf{u}_1 = \mathsf{u}(\pi, \phi)$ for any $\phi \in [0, 2\pi)$.

Recall from Eq. (3.6), that given any closed path $\Gamma(t)$ defined on $t \in [0, 1]$, the Wilson loop operator is defined by

$$\mathcal{W}(\Gamma)_{mn} = \lim_{\delta t \to 0} \langle u_m(\Gamma(1))| \prod_{t}^{1 \leftarrow 0} \mathbb{P}(\Gamma(t))|u_n(\Gamma(0))\rangle\,, \tag{E.4}$$

where δt is the discretization of t in the product, the arrow over the product symbol indicates the ordering of the factors from small to large values of t (i.e., in this case factors with smaller t are to the right), and

$$\mathbb{P}(\mathbf{k}) = \sum_{j=1}^{N_{\text{occ}}} |u_j(\mathbf{k})\rangle\langle u_j(\mathbf{k})| \tag{E.5}$$

is the projector onto the occupied subspace. Observing that

$$\mathsf{u}(\mathbf{k})\mathsf{u}(\mathbf{k})^\dagger = \sum_{j=1}^{N_{\text{occ}}} |u_j(\mathbf{k})\rangle\langle u_j(\mathbf{k})| = \mathbb{P}(\mathbf{k}), \tag{E.6}$$

we can rewrite the expression for the Wilson loop operator in matrix form ($\mathcal{W}$ is an $N_{\text{occ}} \times N_{\text{occ}}$ matrix)

$$\mathcal{W}(\Gamma) = \lim_{\delta t \to 0} \mathsf{u}(\Gamma(1))^\dagger \prod_{t}^{1 \leftarrow 0} \mathsf{u}(\Gamma(t))\mathsf{u}(\Gamma(t))^\dagger \mathsf{u}(\Gamma(0)). \tag{E.7}$$

The Wilson loop operator for one of the closed contours $\Gamma(\phi)$ defined above is then found to be

$$\begin{aligned}\mathcal{W}(\phi) &= \mathcal{W}(\Gamma(\phi)) \\ &= \lim_{\delta\theta\to 0} \mathsf{u}_0^\dagger \left[\prod_\theta^{0\to\pi} \mathsf{u}(\theta,\phi)\mathsf{u}(\theta,\phi)^\dagger\right]\left[\prod_\theta^{\pi\leftarrow 0} \mathsf{u}(\theta,0)\mathsf{u}(\theta,0)^\dagger\right]\mathsf{u}_0. \end{aligned} \tag{E.8}$$

Reordering the terms in the products, this becomes

$$\begin{aligned}&= \lim_{\delta\theta\to 0} \mathsf{u}_0^\dagger\mathsf{u}_0 \left[\prod_\theta^{0\to\pi-\delta\theta} \mathsf{u}(\theta,\phi)^\dagger\mathsf{u}(\theta+\delta\theta,\phi)\right]\mathsf{u}_1^\dagger\times \\ &\quad\times \mathsf{u}_1\left[\prod_\theta^{\pi-\delta\theta\leftarrow 0} \mathsf{u}(\theta+\delta\theta,0)^\dagger\mathsf{u}(\theta,0)\right]\mathsf{u}_0 \\ &= \lim_{\delta\theta\to 0}\left[\prod_\theta^{0\to\pi-\delta\theta} V(\theta,\phi)^\dagger\right]\left[\prod_\theta^{\pi-\delta\theta\leftarrow 0} V(\theta,0)\right]\mathsf{u}_0 \end{aligned} \tag{E.9}$$

with

$$V(\theta,\phi) = \mathsf{u}(\theta+\delta\theta,\phi)^\dagger\mathsf{u}(\theta,\phi). \tag{E.10}$$

If we choose the real gauge along $\Gamma(\phi)$ by monodromy, $V(\theta,\phi)\in\mathsf{SO}(N_{\text{occ}})$.

The C_n rotational symmetry relates eigenstates at points in momentum space related by that symmetry:

$$\mathsf{u}(C_n\mathbf{k}) = D(C_n)\mathsf{u}(\mathbf{k})\mathcal{B}(\mathbf{k}), \tag{E.11}$$

where $D(C_n)$ is the corepresentation matrix of C_n in the chosen basis, i.e., where $D(\mathcal{PT}) = \mathbb{1}$, and $\mathcal{B}(\mathbf{k})\in\mathsf{O}(N_{\text{occ}})$ is a sewing matrix [142]. Thus, for any θ,ϕ

$$\mathsf{u}\left(\theta,\phi+\frac{2\pi}{n}\right) = D(C_n)\mathsf{u}(\theta,\phi)\mathcal{B}(\theta,\phi). \tag{E.12}$$

Substituting this into the expression for the Wilson loop operator, we find

$$\begin{aligned}\mathcal{W}\left(\phi+\frac{2\pi}{n}\right) = \lim_{\delta\theta\to 0}\mathsf{u}_0^\dagger\left[\prod_\theta^{0\to\pi} D(C_n)\mathsf{u}(\theta,\phi)\mathsf{u}(\theta,\phi)^\dagger D(C_n)^\dagger\right]\times \\ \times\left[\prod_\theta^{\pi\leftarrow 0}\mathsf{u}(\theta,0)\mathsf{u}(\theta,0)^\dagger\right]\mathsf{u}_0, \end{aligned} \tag{E.13}$$

where the sewing matrices canceled out. Reordering the terms again,

$$= \lim_{\delta\theta\to 0} \mathsf{u}_0^\dagger D(C_n)\mathsf{u}_0 \left[\prod_\theta^{0\to\pi-\delta\theta} \mathsf{u}(\theta,\phi)^\dagger \mathsf{u}(\theta+\delta\theta,\phi)\right] \times$$
$$\times\, \mathsf{u}_1^\dagger D(C_n)^\dagger \mathsf{u}_1 \left[\prod_\theta^{\pi-\delta\theta\leftarrow 0} \mathsf{u}(\theta+\delta\theta,0)^\dagger \mathsf{u}(\theta,0)\right] \mathsf{u}_0. \tag{E.14}$$

Note that

$$\begin{aligned} \mathsf{u}_0^\dagger D(C_n)\mathsf{u}_0 &= D_0(C_n), \\ \mathsf{u}_1^\dagger D(C_n)\mathsf{u}_1 &= D_1(C_n) \end{aligned} \tag{E.15}$$

gives the corepresentation matrices $D_{0,1}(C_n)$ of only the occupied bands at $\Gamma(0)$ and $\Gamma(1/2)$ (i.e., at the south and north pole), respectively. Thus,

$$\mathcal{W}\left(\phi+\frac{2\pi}{n}\right) = \lim_{\delta\theta\to 0} D_0(C_n)\left[\prod_\theta^{0\to\pi-\delta\theta} V(\theta,\phi)^\dagger\right] \times$$
$$\times\, D_1(C_n)^\dagger \left[\prod_\theta^{\pi-\delta\theta\leftarrow 0} V(\theta,0)\right] \mathsf{u}_0. \tag{E.16}$$

Defining

$$P(\phi) = \left[\prod_\theta^{\pi-\delta\theta\leftarrow 0} V(\theta,\phi)\right] \in \mathsf{SO}(N_{\mathrm{occ}}), \tag{E.17}$$

we arrive at Eq. (6.2) of Section 6.1.2,

$$\mathcal{W}\left(\phi+\frac{2\pi}{n}\right) = D_0(C_n)P(\phi)^\dagger D_1(C_n)^\dagger P(\phi)\mathcal{W}(\phi). \tag{E.18}$$

E.2. Berry phase on a symmetric path

The constraint on the Wilson loop operator derived above has implications for the Berry phase of the occupied bands computed on the contours $\Gamma(\phi)$. It follows from Eq. (3.11) that the Berry phase is given by $\varphi = \arg\det\mathcal{W}$, such that

$$\varphi\left(\phi+\frac{2\pi}{n}\right) = \arg\det\left[D_0(C_n)P(\phi)^\dagger D_1(C_n)^\dagger P(\phi)\mathcal{W}(\phi)\right].$$

Using that inside the determinant all matrices commute,

$$\begin{aligned} &= \arg\det\mathcal{W}(\phi) + \arg\det\left[D_0(C_n)D_1(C_n)^\dagger\right] \\ &= \varphi(\phi) + \arg\det\left[D_0(C_n)D_1(C_n)^\dagger\right] \mod 2\pi, \end{aligned} \tag{E.19}$$

which is exactly Eq. (6.3). The difference in Berry phase on the two contours is found to be

$$\Delta\varphi = \arg\det\left[D_0(C_n)D_1(C_n)^\dagger\right]. \tag{E.20}$$

Recall that in the presence of $\mathcal{PT}$ symmetry, the Berry phase on any closed loop is (as well as their differences) quantized to 0 versus π, and that the Berry curvature vanishes identically away from the nodal lines [173]. It therefore follows that the trivial value, $\Delta\varphi = 0$, indicates that there is an *even* number of nodal lines enclosed by the contour $\gamma(\phi + 2\pi/n)^{-1} \circ \gamma(\phi)$, while a nontrivial value, $\Delta\varphi = \pi$, indicates an *odd* number. This implies that each $\frac{2\pi}{n}$ sector of the spherical surface is penetrated by an even (odd) number of nodal lines in the principal gap and thus, if $\Delta\varphi = \pi$, that the surface *must* contain gapless points.

E.3. Symmetry indicators for Euler monopole charge

We now specialize to the case where $N_{\text{occ}} = 2$ and assume that $D_{0,1}(C_n) \in \mathsf{SO}(2)$. Since the n^{th} power of $D_{0,1}(C_n)$ gives the identity, it follows that for $i \in \{0, 1\}$:

$$D_i(C_n) = \mathrm{e}^{-\frac{2\pi\mathrm{i}}{n} r_i^{(n)} s_y} \quad \text{with} \quad r_i^{(n)} \in \mathbb{Z} \tag{E.21}$$

and Pauli matrices s_i acting on the space of the two valence bands. Because $\mathsf{SO}(2)$ is an Abelian group, we find that

$$\begin{aligned}\mathcal{W}\left(\phi + \frac{2\pi}{n}\right) &= D_0(C_n)D_1(C_n)^\dagger \lim_{\delta\theta\to 0}\left[\prod_\theta^{0\to\pi-\delta\theta} V(\theta,\phi)^\dagger\right]\left[\prod_\theta^{\pi-\delta\theta\leftarrow 0} V(\theta,0)\right]\mathsf{u}_0 \\ &= D_0(C_n)D_1(C_n)^\dagger \mathcal{W}(\phi).\end{aligned} \tag{E.22}$$

From the family of Wilson loop operators $\mathcal{W}(\phi)$ for $\phi \in [0, 2\pi)$, the Euler class can be obtained [66]. Since $\mathcal{W}(\phi) \in \mathsf{SO}(2)$, there is a $\zeta(\phi) \in [0, 2\pi)$ such that

$$\mathcal{W}(\phi) = \mathrm{e}^{\mathrm{i}\zeta(\phi)s_y} \tag{E.23}$$

given by the Pfaffian of the logarithm

$$\zeta(\phi) = \mathrm{Pf}\left[\log \mathcal{W}(\phi)\right] \mod 2\pi. \tag{E.24}$$

The phase $\zeta(\phi)$ changes continuously in ϕ as long as the two-band subspace is separated from the other bands by energy gaps, and its winding number

determines the Euler class as

$$\chi = \frac{1}{2\pi}\int_0^{2\pi} \frac{\mathrm{d}\zeta(\phi)}{\mathrm{d}\phi} = \frac{1}{2\pi}\left[\zeta(2\pi) - \zeta(0)\right]. \tag{E.25}$$

We remark that the above expression should be read with caution. Namely, a gauge transformation $\mathsf{u}_0 \mapsto \mathsf{u}_0 U$ with $U \in \mathsf{O}(2)$ at the base point of the closed path Γ transforms the Wilson loop operator as follows

$$\mathcal{W}(\phi) \mapsto U^\top \mathcal{W}(\phi) U, \tag{E.26}$$

such that $\zeta(\phi) \mapsto \zeta'(\phi)$ with

$$\begin{aligned}\zeta'(\phi) &= \mathrm{Pf}\left\{\log\left[U^\top \mathcal{W}(\phi) U\right]\right\} \mod 2\pi \\ &= \mathrm{Pf}\left\{U^\top \log\left[\mathcal{W}(\phi)\right] U\right\} \mod 2\pi.\end{aligned}$$

Using that $\mathrm{Pf}(BAB^\top) = \det(B)\mathrm{Pf}(A)$, we obtain

$$= \det(U)\zeta(\phi) \mod 2. \tag{E.27}$$

Since $\det(U) = \pm 1$, the sign of $\zeta(\phi)$ and therefore χ is gauge-dependent [66]. Therefore, the well-defined topological invariant that we can extract is the *absolute value* $|\chi|$ of the Euler monopole charge.

Equation (E.22) implies that

$$\begin{aligned}\zeta\left(\phi + \frac{2\pi}{n}\right) &= \mathrm{Pf}\left[\log \mathrm{e}^{\frac{2\pi\mathrm{i}}{n}\left(r_1^{(n)} - r_0^{(n)}\right)s_y + \mathrm{i}\zeta(\phi)s_y}\right] \\ &= \frac{2\pi}{n}\left(r_1^{(n)} - r_0^{(n)}\right) + \zeta(\phi) \mod 2\pi\end{aligned} \tag{E.28}$$

and applying that identity n times gives

$$\zeta\left(\phi + 2\pi\right) = 2\pi\left(r_1^{(n)} - r_0^{(n)}\right) + \zeta(\phi) \mod 2\pi. \tag{E.29}$$

Therefore, the Euler class is

$$\chi = r_1^{(n)} - r_0^{(n)} \mod n. \tag{E.30}$$

Recall that the parity of χ is the second Stiefel-Whitney class

$$w_2 = \chi \mod 2. \tag{E.31}$$

Observe that for odd n, Eq. (E.30) leaves the parity of χ undetermined. It follows that for C_3, w_2 is not constrained by symmetry, which is consistent with what we demonstrated in Section 6.3.4.

E.4. Gaplessness in absence of $\mathcal{PT}$ symmetry

Here, we discuss the implications of Eq. (E.19) (the derivation of which only assumes the C_n rotational symmetry) in the *absence* of $\mathcal{PT}$ symmetry. By adjusting a few steps leading to Eq. (E.20), one should recognize that the Berry phase on any closed loop of the form $\Lambda(n,\phi) = \gamma(\phi + 2\pi/n)^{-1} \circ \gamma(\phi)$ (and assuming the trajectory does not encounter nodes in the principal gap) is given by

$$\varphi_n = \arg\det\left[D_0(C_n)D_1(C_n)^\dagger\right], \tag{E.32}$$

independent of ϕ. In the presence of $\mathcal{PT}$, we have argued that the Berry phase on any closed path [including the phase φ_n on $\Lambda(n,\phi)$] is quantized to 0 versus π, and that $\varphi_n = \pi$ implies an odd number of nodal lines to pass through the loop. If $\mathcal{PT}$ is absent but vertical mirror symmetries (m_v) are present, then an analogous quantization of Berry phase can be established for loops that are symmetric under mirror reflection [100, 145, 349], and nodal lines can only be stabilized inside mirror planes. In this case, a π Berry phase implies that the mirror-symmetric loop encloses an odd number of nodal lines inside the mirror-invariant plane. (The cases with neither $\mathcal{PT}$ nor m_v are dealt with trivially towards the end of this section).

In the relevant magnetic point groups with rotational symmetry C_n, with vertical mirror symmetry, but without $\mathcal{PT}$ symmetry (cf. Table 4.1), we can therefore choose ϕ such that $\gamma(\phi)$ lies within one of the mirror planes m_1, $\gamma(\phi + 2\pi/n)$ in its copy m_1' related by C_n symmetry, and the two parts of the contour are mapped onto each other by the mirror symmetry with mirror plane m_2 lying between m_1 and m_1'. However, we need to be more careful, because ϕ is now fixed to a mirror plane and therefore $\gamma(\phi)$ might contain band nodes in the principal gap.

If $\gamma(\phi)$ does not contain any band nodes, then $\varphi_n = \pi$ implies that m_2 contains an odd number of nodal lines as illustrated in Fig. 6.4(b) for $\Lambda(4,0) = \Gamma(2\pi/4)$. On the other hand, if $\gamma(\phi)$ does contain M_1 band nodes, we exclude them by modifying γ to γ_ϵ such that the band nodes are circumvented (but enclosed by the loop) with infinitesimal half circles, see Fig. E.1a. Now $\Lambda_\epsilon(n,\phi) = \gamma_\epsilon(\phi + 2\pi/n)^{-1} \circ \gamma_\epsilon(\phi)$ is not mirror symmetric anymore, but it is still composed of two segments related by rotational symmetry; therefore, the Berry phase on $\Lambda_\epsilon(n,\phi)$ is still φ_n. We next compose $\Lambda_\epsilon(n,\phi)$ with an infinitesimal circular contour $\eta_\epsilon^{(i)}(\phi)$ around each excluded band node on $\gamma_\epsilon(\phi)$ such that the resulting loop $\Lambda_\epsilon'(n,\phi)$ does *not* include the band nodes anymore. Observe that this new path is mirror symmetric with respect to m_2, and its Berry phase is therefore quantized to $\{0,\pi\}$, cf. Fig. E.1b. Additionally, the Berry phase on $\eta_\epsilon^{(i)}(\phi)$ is quantized as well and is indeed π, because it

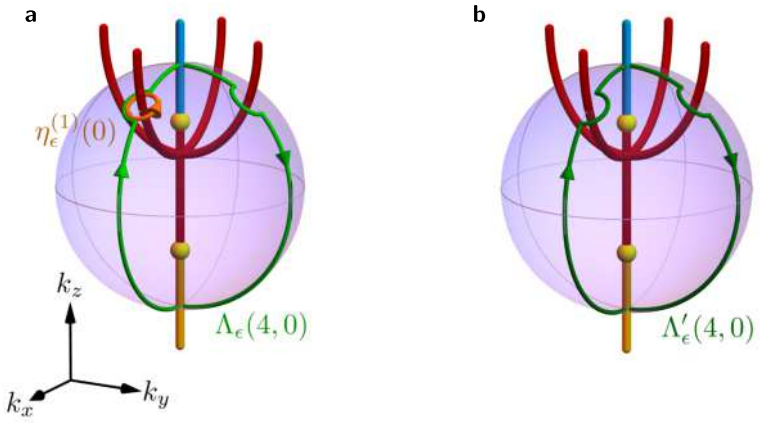

Figure E.1.: Derivation of the gaplessness in the presence of triple-point pairs. Illustration of the closed loops considered in Appendix E.4 for the particular case $n = 4$. (**a**) The contour $\Lambda_\epsilon(n,\phi)$ (green) consists of two rotation-related semi-circular arcs inside rotation-related mirror planes (here m_x and m_y). If mirror-protected nodal lines occur along the contour, we avoid them with infinitesimal half circles perpendicular to the mirror plane containing the avoided nodal lines. The infinitesimal circular contour $\eta_\epsilon^{(1)}(\phi)$ enclosing the nodal line is illustrated as a dark orange ring; it is symmetric under m_y. (**b**) Composition of $\Lambda_\epsilon(n,\phi)$ with $\eta_\epsilon^{(1)}(\phi)$ results in the new contour $\Lambda'_\epsilon(n,\phi)$, which is symmetric under the diagonal mirror symmetry $m_{\bar{x}y}$.

is itself mirror-symmetric (albeit with respect to m_1 rather than m_2) and by assumption it encloses exactly one band node. Thus, the Berry phase on $\Lambda'_\epsilon(n,\phi)$ satisfies

$$\varphi'_n = \varphi_n + M_1\pi \mod 2\pi \tag{E.33}$$

and it determines the parity of the number M_2 of nodal lines in the mirror plane m_2, i.e.,

$$\varphi'_n = M_2\pi \mod 2\pi. \tag{E.34}$$

By combining the previous two equations, we obtain

$$\varphi_n = (M_1 + M_2)\pi \mod 2\pi, \tag{E.35}$$

meaning that $\varphi_n \in \{0,\pi\}$ determines the parity of the number of nodal lines in mirror planes m_1 and m_2 together, i.e., exactly the ones passing through a $\frac{2\pi}{n}$ sector of the enclosing sphere, just as in the presence of $\mathcal{PT}$.

Let us finally remark that for triple points stabilized by $C_n\mathcal{PT}$ with $n = 4, 6$, we only need to consider the case *with* mirror symmetry, because if no mirror

symmetry is present, then nodal lines cannot be stabilized away from the rotation axis (see also the discussion in Section 6.2.4). Therefore, there are no stable band nodes bound to the enclosing sphere. But the case of $C_n\mathcal{PT}$ and mirror symmetry, reduces to the case $C_{n'}$ with $n' = n/2 \in \{2, 3\}$ and mirror symmetry that we have discussed in the previous two paragraphs.

In conclusion, we have shown that even in the absence of $\mathcal{PT}$ symmetry,

$$\det D^{2\mathrm{D}}(C_n) \neq D_a^{1\mathrm{D}}(C_n) D_b^{1\mathrm{D}}(C_n) \tag{E.36}$$

implies that the bulk in the orange or blue k_z-ranges is necessarily gapless. It remains to check this condition for all possible combinations of ICRs. To that end, recall from Section 6.2.4 that in the presence of vertical mirror symmetry, addition of $\mathcal{PT}$ does not change the ICRs and Table 6.1 still applies, giving the same result as in the presence of $\mathcal{PT}$. The only remaining cases are the magnetic point groups $\bar{4}'2'm$ and $\bar{6}'m2'$. For the former we find $\det D^{2\mathrm{D}}(C_2) = 1$, $D_{a,b}^{1\mathrm{D}}(C_2) = 1$ and for the latter $\det D^{2\mathrm{D}}(C_3) = 1$, $D_{a,b}^{1\mathrm{D}}(C_3) = 1$, such that in both cases none of the combinations of ICRs are necessarily gapless.

F. Computation of the corner charges

This chapter is largely based on Appendix D to the publication "Universal higher-order bulk-boundary correspondence of triple nodal points" [3]. Segments with significant text overlap with the published version may be subject to copyright by the American Physical Society.

In this appendix we provide technical details on some of the methods used in the extraction of the corner charges from the charge distribution obtained from exact diagonalization of the tight-binding models discussed in Sections 6.3 and 6.4. First, note that if the electronic or ionic charge distribution leads to finite charge on different Wyckoff positions in the unit cell, we are left with an ionic crystal [257]. Therefore, a coarse-graining or smoothing via a moving average is necessary to properly define edge and surface charge. In Appendix F.1 we present a discrete method that performs this task. While this coarse-graining easily removes strong oscillations of the charge distribution on sub-unit-cell length scales, oscillations due to trivial edge-localized states can remain [150] and obscure the corner charge. To deal with that, Appendix F.2 introduces a method that we developed to remove the signal due to such edge states. The method applies to the case when the *total* edge charge per unit cell (of the ribbon, i.e., the collection of sites periodically repeated in the ribbon geometry) is vanishing, but the presence of edge-localized states induces a nontrivial profile of the charge density as a function of the distance to the boundary, as has been observed for Sc_3AlC.

F.1. Coarse-graining of charge distribution

To coarse-grain the electric charge distribution defined on the *original lattice*, we first need to choose the *target lattice*. The choice of target lattice defines the coarse-graining length scale. To coarse-grain over a single unit cell with multiple sites, it is convenient to consider a single Wyckoff position of maximal symmetry to define the target lattice. Some examples are shown in Fig. F.1. Note that it is also possible to coarse-grain over larger lengths scales, i.e., multiple unit cells. Such a situation is depicted in Fig. F.1c where coarse-graining is performed

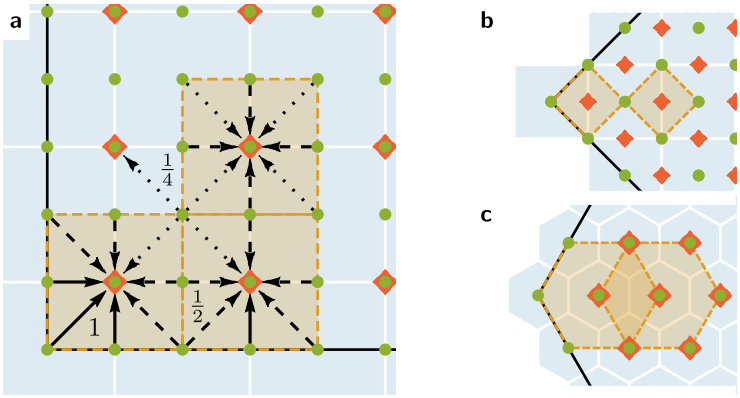

Figure F.1.: Discrete coarse-graining method. (**a**) The charge on the original lattice (defined by the unit cells shaded in blue and sublattice sites shown as green disks) is redistributed to the target lattice (defined by the red diamond sites). Here the lattice corresponding to the projection of Sc_3AlC (see Section 6.4) is shown. Each site in the target lattice is assigned a coarse-graining cell (unit cell of that lattice; shaded in orange). The charge on each green site is then redistributed (black arrows) with equal weights (weight 1 shown by solid, $\frac{1}{2}$ by dashed, and $\frac{1}{4}$ by dotted lines) to all those red sites whose coarse-graining cell is adjacent to the green site. Only a few arrows are shown to maintain clarity of the illustration. (**b,c**) Definitions of the original (green) and target (red) lattice and the coarse-graining cell (orange) for the C_4- and C_6-symmetric models discussed in Section 6.3, respectively. Note that in (c) the coarse-graining cells overlap; as a consequence, the original and the target lattice coincide except for a missing layer on the boundary.

over seven original hexagonal unit cells. However, note that due to overlapping of the coarse-graining cells, the Wigner-Seitz tessellation formed around the coarse-graining centers (not illustrated) coincides with the original honeycomb lattice.

The coarse-graining is performed by redistributing the charge from the original to the target lattice. If a site on the original lattice belongs to m coarse-graining cells, then a fraction $\frac{1}{m}$ of the total charge on the original site is distributed to each of the corresponding target sites. Consequently, charge on corner sites is generally transferred to a single target site. In Fig. F.1a, where we illustrate the coarse-graining as applied to Sc_3AlC, redistribution weights of magnitude 1, $\frac{1}{2}$ and $\frac{1}{4}$ are illustrated with solid, dashed and dotted arrows, respectively.

We have applied the coarse-graining method to achieve a charge redistribution

in all the discussed models. In particular, Fig. 6.14 shows a comparison of the charge distribution before and after coarse-graining for the C_4-symmetric model of Section 6.3.1. The definitions of the original and target lattice as well as the coarse-graining unit cell are shown in Fig. F.1b. Figures F.1a and F.1c give the same information for the model of Sc_3AlC (cf. Section 6.4) and the C_6-symmetric models (cf. Sections 6.3.2 and 6.3.3), respectively.

F.2. Removal of edge signal from charge distribution

Even after coarse-graining (as described above), charge oscillations caused by trivial edge-localized states can remain. Note that in contrast to the oscillations on sub-unit-cell scale, these remaining oscillations are generally perpendicular to the edges, and vanish in the bulk. Since, the total corner and edge charges are defined via integration over regions with boundaries perpendicular to the edges of the sample [150], the remaining oscillations do not prevent us from computing these total charges, see Fig. 6.27 for such a calculation on the *original* coarse-grained data. However, such oscillations can visually obscure the localization properties of the charge. Here, we discuss a method to subtract such edge-localized oscillations for the cases where the total edge charge per unit cell (of the ribbon geometry) vanishes. The method applies to C_n-symmetric systems with $n \geq 3$, where the bulk as well as the finite-size sample satisfy the symmetry requirement. For concreteness we choose $n = 4$ for the following discussion. In particular, the described setup directly applies to the case of Sc_3AlC as presented in Section 6.4.

Two separate calculations need to be performed: one on a ribbon with $2N-1$ layers of unit cells, illustrated in Fig. F.2a, and one on a flake with N *shells*of unit cells, illustrated in Fig. F.2b, such that there is a direct correspondence between the layers and the shells. Due to the rotational symmetry, the four sides of each shell are equivalent and only a single orientation of the ribbon needs to be computationally modelled. Note that compatible fillings (in particular, the same choice of chemical potential) need to be considered for the two systems. The charge distributions obtained for both geometries first need to be coarse-grained to the level of unit-cells, such that the coarse-grained lattice has a single site per unit cell. Figure F.2 shows that coarse-grained lattice, which corresponds to the underlying Bravais lattice.

From the calculation on the ribbon, the total charge q_i per unit cell in the i^{th} layer can easily be extracted. On the flake, we then redistribute the charge as indicated in Fig. F.2b with arrows: from a site in the j^{th} shell (but not on one

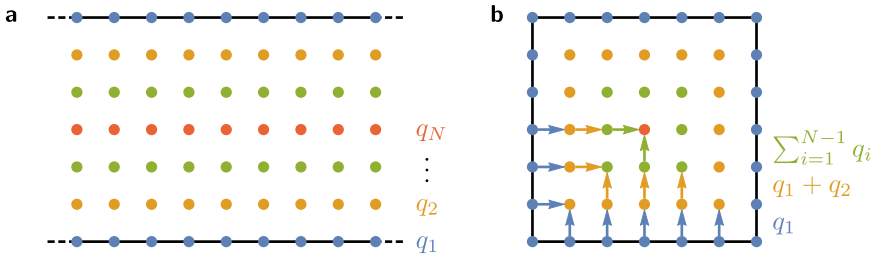

Figure F.2.: Removal of edge signal from charge distribution. Illustration for a C_4-symmetric system with vanishing total edge charge per unit cell (of the ribbon geometry). The solid black lines in both panels represent the boundary of the lattice. (**a**) Ribbon geometry extended in the horizontal direction with $2N - 1 = 7$ unit cells (dots colored according to their distance to the boundary) in the vertical direction (corresponding to $N = 4$ inequivalent layers). We denote by q_i the charge per unit cell on the i^{th} layer (which is constant within the layer). (**b**) Flake geometry for the same system. Here, *shells* of unit cell sites (dots) correspond to the layers from the ribbon geometry (indicated by the corresponding color). The charge on the whole flake is redistributed according to the arrows indicated in the bottom-left part of the system. The amount of charge that is transferred from a site that belongs to the j^{th} shell to the next one is given by $\sum_{i=1}^{j} q_j$, where q_i are the charges determined in the ribbon geometry. Note that the charge redistribution flows perpendicular to the boundary; therefore, no charge is transferred between the corners.

of the diagonals) the charge $\sum_{i=1}^{j} q_i$ is transferred to the $(j+1)^{\text{th}}$ shell. There is no charge transfer *away* from sites that lie on one of the diagonals. Therefore, this procedure seemingly leads to a charge accumulation on the diagonals and in the center. However, recall that, by assumption, the total edge charge vanishes, such that in the limit of large N, $\sum_{i=1}^{N} q_i = 0$. Consequently, the accumulated charge compensates oscillations on the diagonals and converges to zero at the center of the flake. Furthermore, note that the charge redistribution flows strictly *perpendicular* to the flake boundaries; therefore, no charge is transferred between the corners of the flake, keeping its value invariant (up to corrections that are exponentially small in the system size).

The effect of the method can be seen in Fig. 6.27, where the original (coarse-grained) distribution is shown in panels (a,b), and the charge distribution after removing the edge signal is displayed in panels (c,d). We remark that the data in panels (c,d) have undergone one additional coarse-graining step *after* the removal of the edge charge. Compared to panels (a), the localization of the corner charge in panel (b) is visually much more manifest.

Bibliography

[1] P. M. Lenggenhager, X. Liu, S. S. Tsirkin, T. Neupert, and T. Bzdušek, "From triple-point materials to multiband nodal links", Phys. Rev. B **103**, L121101 (2021).

[2] P. M. Lenggenhager, X. Liu, T. Neupert, and T. Bzdušek, "Triple nodal points characterized by their nodal-line structure in all magnetic space groups", Phys. Rev. B **106**, 085128 (2022).

[3] P. M. Lenggenhager, X. Liu, T. Neupert, and T. Bzdušek, "Universal higher-order bulk-boundary correspondence of triple nodal points", Phys. Rev. B **106**, 085129 (2022).

[4] P. M. Lenggenhager, A. Stegmaier, L. K. Upreti, T. Hofmann, T. Helbig, A. Vollhardt, M. Greiter, C. H. Lee, S. Imhof, H. Brand, T. Kießling, I. Boettcher, T. Neupert, R. Thomale, and T. Bzdušek, "Simulating hyperbolic space on a circuit board", Nat. Commun. **13**, 4373 (2022).

[5] P. M. Lenggenhager, J. Maciejko, and T. Bzdušek, "Non-Abelian hyperbolic band theory from supercells", Phys. Rev. Lett. **131**, 226401 (2023).

[6] D. M. Urwyler, P. M. Lenggenhager, I. Boettcher, R. Thomale, T. Neupert, and T. Bzdušek, "Hyperbolic topological band insulators", Phys. Rev. Lett. **129**, 246402 (2022).

[7] A. Chen, Y. Guan, P. M. Lenggenhager, J. Maciejko, I. Boettcher, and T. Bzdušek, "Symmetry and topology of hyperbolic Haldane models", Phys. Rev. B **108**, 085114 (2023).

[8] T. Tummuru, A. Chen, P. M. Lenggenhager, T. Neupert, J. Maciejko, and T. Bzdušek, "Hyperbolic non-Abelian semimetal", preprint, arXiv:2307.09876 (2023).

[9] E. Noether, "Invariante Variationsprobleme", Nachr. d. König. Gessellsch. d. Wiss. zu Göttingen, Math.-phys. Klasse, 235 (1918).

[10] F. Bloch, "Über die Quantenmechanik der Elektronen in Kristallgittern", Z. Phys. **52**, 555 (1929).

[11] E. Schrödinger, "An undulatory theory of the mechanics of atoms and molecules", Phys. Rev. **28**, 1049 (1926).

[12] L. D. Landau, "On the theory of phase transitions. I.", Phys. Z. Sowjet. **11**, 26 (1937).

[13] L. D. Landau, "On the theory of phase transitions. II.", Phys. Z. Sowjet. **11**, 545 (1937).

[14] K. von Klitzing, G. Dorda, and M. Pepper, "New method for high-accuracy determination of the fine-structure constant based on quantized Hall resistance", Phys. Rev. Lett. **45**, 494 (1980).

[15] R. B. Laughlin, "Quantized Hall conductivity in two dimensions", Phys. Rev. B **23**, 5632(R) (1981).

[16] D. J. Thouless, M. Kohmoto, M. P. Nightingale, and M. den Nijs, "Quantized Hall conductance in a two-dimensional periodic potential", Phys. Rev. Lett. **49**, 405 (1982).

[17] C. L. Kane and E. J. Mele, "Z_2 Topological order and the quantum spin hall effect", Phys. Rev. Lett. **95**, 146802 (2005).

[18] C. L. Kane and E. J. Mele, "Quantum spin Hall effect in graphene", Phys. Rev. Lett. **95**, 226801 (2005).

[19] M. König, S. Wiedmann, C. Brüne, A. Roth, H. Buhmann, L. W. Molenkamp, X.-L. Qi, and S.-C. Zhang, "Quantum spin Hall insulator state in HgTe quantum wells", Science **318**, 766 (2007).

[20] D. Hsieh, D. Qian, L. Wray, Y. Xia, Y. S. Hor, R. J. Cava, and M. Z. Hasan, "A topological Dirac insulator in a quantum spin Hall phase", Nature **452**, 045302 (2008).

[21] S. Pancharatnam, "Generalized theory of interference, and its applications", Proc. Natl. Acad. Sci. India A **44**, 247 (1956).

[22] H. C. Longuet-Higgins, U. Öpik, M. H. L. Pryce, and R. A. Sack, "Studies of the Jahn-Teller effect .II. The dynamical problem", Proc. R. Soc. A **244**, 1 (1958).

[23] M. V. Berry, "Quantal phase factors accompanying adiabatic changes", Proc. R. Soc. London, Se. A **392**, 45 (1984).

[24] M. Z. Hasan and C. L. Kane, "Colloquium: topological insulators", Reviews of Modern Physics **82**, 3045 (2010).

[25] M. Zahid Hasan, S.-Y. Xu, and M. Neupane, "Topological insulators, topological dirac semimetals, topological crystalline insulators, and topological kondo insulators", in *Topological insulators* (John Wiley and Sons, Ltd, 2015) Chap. 4, pp. 55–100.

[26] C. Herring, "Accidental degeneracy in the energy bands of crystals", Phys. Rev. **52**, 365 (1937).

[27] X. Wan, A. M. Turner, A. Vishwanath, and S. Y. Savrasov, "Topological semimetal and Fermi-arc surface states in the electronic structure of pyrochlore iridates", Phys. Rev. B **83**, 205101 (2011).

[28] H. Weyl, "Gravitation and the electron", Proc. Natl. Acad. Sci. U.S.A. **15**, 323 (1929).

[29] H. Weyl, "Elektron und Gravitation. I", Z. Phys. **56**, 330 (1929).

[30] C. Shekhar, A. K. Nayak, Y. Sun, M. Schmidt, M. Nicklas, I. Leermakers, U. Zeitler, Y. Skourski, J. Wosnitza, Z. Liu, Y. Chen, W. Schnelle, H. Borrmann, Y. Grin, C. Felser, and B. Yan, "Extremely large magnetoresistance and ultrahigh mobility in the topological Weyl semimetal candidate NbP", Nat. Phys. **11**, 645 (2015).

[31] M. Samanta, H. Tan, S. Laha, H. A. Vignolo-González, L. Grunenberg, S. Bette, V. Duppel, P. Schützendübe, A. Gouder, B. Yan, and B. V. Lotsch, "The Weyl semimetals MIrTe4 (M = Nb, Ta) as efficient catalysts for dye-sensitized hydrogen evolution", Adv. Energy Mater. **13**, 2300503 (2023).

[32] G. B. Osterhoudt, L. K. Diebel, M. J. Gray, X. Yang, J. Stanco, X. Huang, B. Shen, N. Ni, P. J. W. Moll, Y. Ran, and K. S. Burch, "Colossal mid-infrared bulk photovoltaic effect in a type-I Weyl semimetal", Nature Materials **18**, 471 (2019).

[33] Z.-M. Yu, Z. Zhang, G.-B. Liu, W. Wu, X.-P. Li, R.-W. Zhang, S. A. Yang, and Y. Yao, "Encyclopedia of emergent particles in three-dimensional crystals", Sci. Bull. **67**, 375 (2022).

[34] G.-B. Liu, Z. Zhang, Z.-M. Yu, S. A. Yang, and Y. Yao, "Systematic investigation of emergent particles in type-iii magnetic space groups", Phys. Rev. B **105**, 085117 (2022).

[35] Z. Zhang, G.-B. Liu, Z.-M. Yu, S. A. Yang, and Y. Yao, "Encyclopedia of emergent particles in type-IV magnetic space groups", Phys. Rev. B **105**, 104426 (2022).

[36] A. B. Khanikaev, S. H. Mousavi, W.-K. Tse, M. Kargarian, A. H. MacDonald, and G. Shvets, "Photonic topological insulators", Nat. Mater. **12**, 233 (2013).

[37] Y. Tokura, K. Yasuda, and A. Tsukazaki, "Magnetic topological insulators", Nat. Rev. Phys. **1**, 126 (2019).

[38] L. M. Nash, D. Kleckner, A. Read, V. Vitelli, A. M. Turner, and W. T. M. Irvine, "Topological mechanics of gyroscopic metamaterials", Proc. Natl. Acad. Sci. U.S.A **112**, 14495 (2015).

[39] R. Süsstrunk and S. D. Huber, "Observation of phononic helical edge states in a mechanical topological insulator", Science **349**, 47 (2015).

[40] C. He, X. Ni, H. Ge, X.-C. Sun, Y.-B. Chen, M.-H. Lu, X.-P. Liu, and Y.-F. Chen, "Acoustic topological insulator and robust one-way sound transport", Nat. Phys. **12**, 1124 (2016).

[41] C. H. Lee, S. Imhof, C. Berger, F. Bayer, J. Brehm, L. W. Molenkamp, T. Kiessling, and R. Thomale, "Topolectrical circuits", Commun. Phys. **1**, 39 (2018).

[42] S. Imhof, C. Berger, F. Bayer, J. Brehm, L. W. Molenkamp, T. Kiessling, F. Schindler, C. H. Lee, M. Greiter, T. Neupert, and R. Thomale, "Topolectrical-circuit realization of topological corner modes", Nat. Phys. **14**, 925 (2018).

[43] T. Hofmann, T. Helbig, F. Schindler, N. Salgo, M. Brzezińska, M. Greiter, T. Kiessling, D. Wolf, A. Vollhardt, A. Kabaši, C. H. Lee, A. Bilušić, R. Thomale, and T. Neupert, "Reciprocal skin effect and its realization in a topolectrical circuit", Phys. Rev. Res. **2**, 023265 (2020).

[44] A. A. Houck, H. E. Türeci, and J. Koch, "On-chip quantum simulation with superconducting circuits", Nat. Phys. **8**, 292 (2012).

[45] B. M. Anderson, R. Ma, C. Owens, D. I. Schuster, and J. Simon, "Engineering topological many-body materials in microwave cavity arrays", Phys. Rev. X **6**, 041043 (2016).

[46] M. Fitzpatrick, N. M. Sundaresan, A. C. Y. Li, J. Koch, and A. A. Houck, "Observation of a dissipative phase transition in a one-dimensional circuit QED lattice", Phys. Rev. X **7**, 011016 (2017).

[47] S. Schmidt and J. Koch, "Circuit QED lattices: Towards quantum simulation with superconducting circuits", Ann. Phys. (Berl.) **525**, 395 (2013).

[48] D. L. Underwood, W. E. Shanks, J. Koch, and A. A. Houck, "Low-disorder microwave cavity lattices for quantum simulation with photons", Phys. Rev. A **86**, 023837 (2012).

[49] J. Maldacena, "The large-N limit of superconformal field theories and supergravity", Int. J. Theor. Phys. **38**, 1113 (1999).

[50] E. Witten, "Anti-de Sitter space and holography", Adv. Theor. Math. Phys. **2**, 253 (1998).

[51] S. A. Hartnoll, A. Lucas, and S. Sachdev, *Holographic quantum matter* (The MIT Press, Mar. 2018).

[52] S. Ryu and T. Takayanagi, "Holographic derivation of entanglement entropy from the anti-de Sitter space/conformal field theory correspondence", Phys. Rev. Lett. **96**, 181602 (2006).

[53] G. Vidal, "Entanglement renormalization", Phys. Rev. Lett. **99**, 1 (2007).

[54] D. T. Son, "Toward an AdS/cold atoms correspondence: A geometric realization of the Schrödinger symmetry", Phys. Rev. D **78**, 046003 (2008).

[55] G. Vidal, "Class of quantum many-body states that can be efficiently simulated", Phys. Rev. Lett. **101**, 110501 (2008).

[56] H. Matsueda, M. Ishihara, and Y. Hashizume, "Tensor network and a black hole", Phys. Rev. D **87**, 066002 (2013).

[57] B. Swingle, "Entanglement renormalization and holography", Phys. Rev. D **86**, 065007 (2012).

[58] J. Haegeman, T. J. Osborne, H. Verschelde, and F. Verstraete, "Entanglement renormalization for quantum fields in real space", Phys. Rev. Lett. **110**, 100402 (2013).

[59] L. Boyle, M. Dickens, and F. Flicker, "Conformal quasicrystals and holography", Phys. Rev. X **10**, 011009 (2020).

[60] H. S. M. Coxeter, "Regular honeycombs in hyperbolic space", in Proc. icm, Vol. 3 (Citeseer, 1954), pp. 155–169.

[61] H. S. M. Coxeter, "Crystal symmetry and its generalizations", Proceed. trans. R. Soc. Can. **51**, 1 (1957).

[62] J. Maciejko and S. Rayan, "Hyperbolic band theory", Sci. Adv. **7**, eabe9170 (2021).

[63] I. Boettcher, A. V. Gorshkov, A. J. Kollár, J. Maciejko, S. Rayan, and R. Thomale, "Crystallography of hyperbolic lattices", Phys. Rev. B **105**, 125118 (2022).

[64] J. Maciejko and S. Rayan, "Automorphic Bloch theorems for hyperbolic lattices", Proc. Natl. Acad. Sci. U.S.A. **119**, e2116869119 (2022).

[65] Q. Wu, A. A. Soluyanov, and T. Bzdušek, "Non-Abelian band topology in noninteracting metals", Science **365**, 1273 (2019).

[66] A. Bouhon, Q. Wu, R.-J. Slager, H. Weng, O. V. Yazyev, and T. Bzdušek, "Non-Abelian reciprocal braiding of Weyl nodes and its manifestation in ZrTe", Nat. Phys. **16**, 1137 (2020).

[67] H. S. M. Coxeter, "The non-Euclidean symmetry of Escher's picture 'Circle Limit III'", Leonardo **12**, 19 (1979).

[68] A. J. Kollár, M. Fitzpatrick, and A. A. Houck, "Hyperbolic lattices in circuit quantum electrodynamics", Nature **571**, 45 (2019).

[69] I. Boettcher, P. Bienias, R. Belyansky, A. J. Kollár, and A. V. Gorshkov, "Quantum simulation of hyperbolic space with circuit quantum electrodynamics: from graphs to geometry", Phys. Rev. A **102**, 032208 (2020).

[70] K. Ikeda, S. Aoki, and Y. Matsuki, "Hyperbolic band theory under magnetic field and Dirac cones on a higher genus surface", J. Phys.: Condens. Matter **33**, 485602 (2021).

[71] K. Ikeda, Y. Matsuki, and S. Aoki, "Algebra of hyperbolic band theory under magnetic field", Can. J. Phys., 10.1139/cjp-2022-0145 (2023).

[72] E. Kienzle and S. Rayan, "Hyperbolic band theory through Higgs bundles", Adv. Math. **409**, 108664 (2022).

[73] Á. Nagy and S. Rayan, "On the hyperbolic Bloch transform", Ann. Henri Poincaré, 10.1007/s00023-023-01336-8 (2023).

[74] A. Attar and I. Boettcher, "Selberg trace formula in hyperbolic band theory", Phys. Rev. E **106**, 034114 (2022).

[75] F. R. Lux and E. Prodan, "Spectral and combinatorial aspects of Cayley-crystals", Ann. Henri Poincaré, 10.1007/s00023-023-01373-3 (2023).

[76] R. Mosseri and J. Vidal, "Density of states of tight-binding models in the hyperbolic plane", Phys. Rev. B **108**, 035154 (2023).

[77] C. J. Bradley and A. P. Cracknell, *The mathematical theory of symmetry in solids: representation theory for point groups and space groups* (Clarendon Press, Oxford, 1972).

[78] E. P. Wigner, *Gruppentheorie und ihre Anwendung auf die Quantenmechanik der Atomspektren* (Friedrich Vieweg und Sohn, 1931).

[79] E. P. Wigner, *Group theory and its application to the quantum mechanics of atomic spectra*, translated from German by J. J. Griffin (Academic Press, 1931).

[80] *Bilbao Crystallographic server*, https://www.cryst.ehu.es.

[81] R. S. Mulliken, "Electronic structures of polyatomic molecules and valence. IV. Electronic states, quantum theory of the double bond", Phys. Rev. **43**, 279 (1933).

[82] G. Koster, *Properties of the thirty-two point groups*, M.I.T. Press research monographs (M.I.T. Press, 1963).

[83] L. Elcoro, B. Bradlyn, Z. Wang, M. G. Vergniory, J. Cano, C. Felser, B. Andrei Bernevig, D. Orobengoa, G. De La Flor, and M. I. Aroyo, "Double crystallographic groups and their representations on the Bilbao Crystallographic Server", J. Appl. Crystallogr. **50**, 1457 (2017).

[84] Y. Xu, L. Elcoro, Z. D. Song, B. J. Wieder, M. G. Vergniory, N. Regnault, Y. Chen, C. Felser, and B. A. Bernevig, "High-throughput calculations of magnetic topological materials", Nature **586**, 702 (2020).

[85] L. Elcoro, B. J. Wieder, Z. Song, Y. Xu, B. Bradlyn, and B. A. Bernevig, "Magnetic topological quantum chemistry", Nat. Commun. **12**, 5965 (2021).

[86] J. O. Dimmock, "Representation theory for nonunitary groups", J. Math. Phys. **4**, 1307 (1963).

[87] T. Janssen, "On projective unitary-antiunitary representations of finite groups", J. Math. Phys. **13**, 342 (1972).

[88] E. Dobardžić, M. Dimitrijević, and M. V. Milovanović, Phys. Rev. B **91**, 125424 (2015).

[89] M. Fruchart, D. Carpentier, and K. Gawedzki, "Parallel transport and band theory in crystals", EPL **106**, 60002 (2014).

[90] L. Fu, C. L. Kane, and E. J. Mele, "Topological insulators in three dimensions", Phys. Rev. Lett. **98**, 106803 (2007).

[91] J. E. Moore and L. Balents, "Topological invariants of time-reversal-invariant band structures", Phys. Rev. B **75**, 121306 (2007).

[92] D. Hsieh, Y. Xia, L. Wray, D. Qian, A. Pal, J. H. Dil, J. Osterwalder, F. Meier, G. Bihlmayer, C. L. Kane, Y. S. Hor, R. J. Cava, and M. Z. Hasan, "Observation of unconventional quantum spin textures in topological insulators", Science **323**, 919 (2009).

[93] R. Roy, "Topological phases and the quantum spin hall effect in three dimensions", Phys. Rev. B **79**, 195322 (2009).

[94] L. Fu and C. L. Kane, "Topological insulators with inversion symmetry", Phys. Rev. B **76**, 045302 (2007).

[95] Y. L. Chen, J. G. Analytis, J.-H. Chu, Z. K. Liu, S.-K. Mo, X. L. Qi, H. J. Zhang, D. H. Lu, X. Dai, Z. Fang, S. C. Zhang, I. R. Fisher, Z. Hussain, and Z.-X. Shen, "Experimental realization of a three-dimensional topological insulator, Bi_2Te_3", Science **325**, 178 (2009).

[96] F. D. M. Haldane, "Model for a quantum Hall effect without Landau levels: condensed-matter realization of the "parity anomaly"", Phys. Rev. Lett. **61**, 2015 (1988).

[97] F. Wilczek and A. Zee, "Appearance of gauge structure in simple dynamical systems", Phys. Rev. Lett. **52**, 2111 (1984).

[98] J. Zak, "Berry's geometrical phase for noncyclic hamiltonians", EPL **9**, 615 (1989).

[99] A. Alexandradinata, X. Dai, and B. A. Bernevig, "Wilson-loop characterization of inversion-symmetric topological insulators", Phys. Rev. B **89**, 155114 (2014).

[100] J. Zak, "Berry's phase for energy bands in solids", Phys. Rev. Lett. **62**, 2747 (1989).

[101] R. D. King-Smith and D. Vanderbilt, "Theory of polarization of crystalline solids", Phys. Rev. B **47**, 1651(R) (1993).

[102] D. Vanderbilt and R. D. King-Smith, "Electric polarization as a bulk quantity and its relation to surface charge", Phys. Rev. B **48**, 4442 (1993).

[103] R. Resta, "Macroscopic polarization in crystalline dielectrics: the geometric phase approach", Rev. Mod. Phys. **66**, 899 (1994).

[104] A. W. Ludwig, "Topological phases: classification of topological insulators and superconductors of non-interacting fermions, and beyond", in Phys. scr. Vol. 2016, T168 (Oct. 2015).

[105] A. Altland and M. R. Zirnbauer, "Nonstandard symmetry classes in mesoscopic normal-superconducting hybrid structures", Phys. Rev. B **55**, 1142 (1997).

[106] S. Ryu, A. P. Schnyder, A. Furusaki, and A. W. W. Ludwig, "Topological insulators and superconductors: tenfold way and dimensional hierarchy", New J. Phys. **12**, 065010 (2010).

[107] A. Kitaev, "Periodic table for topological insulators and superconductors", AIP Conf. Proc. **1134**, 22 (2009).

[108] A. P. Schnyder, S. Ryu, A. Furusaki, and A. W. W. Ludwig, "Classification of topological insulators and superconductors", AIP Conf. Proc. **1134**, 10 (2009).

[109] T. Damhus, "Double groups as symmetry groups for spin-orbit coupling Hamiltonians", Match **16**, 21 (1984).

[110] L. Fu, "Topological crystalline insulators", Phys. Rev. Lett. **106**, 106802 (2011).

[111] T. H. Hsieh, H. Lin, J. Liu, W. Duan, A. Bansil, and L. Fu, "Topological crystalline insulators in the snte material class", Nat. Commun. **3**, 982 (2012).

[112] P. Dziawa, B. J. Kowalski, K. Dybko, R. Buczko, A. Szczerbakow, M. Szot, E. Łusakowska, T. Balasubramanian, B. M. Wojek, M. H. Berntsen, O. Tjernberg, and T. Story, "Topological crystalline insulator states in $Pb_{1-x}Sn_xSe$", Nat. Mat. **11**, 1023 (2012).

[113] R. S. K. Mong, A. M. Essin, and J. E. Moore, "Antiferromagnetic topological insulators", Phys. Rev. B **81**, 245209 (2010).

[114] Y. Tanaka, Z. Ren, T. Sato, K. Nakayama, S. Souma, T. Takahashi, K. Segawa, and Y. Ando, "Experimental realization of a topological crystalline insulator in SnTe", Nat. Phys. **8**, 800 (2012).

[115] S.-Y. Xu, C. Liu, N. Alidoust, M. Neupane, D. Qian, I. Belopolski, J. D. Denlinger, Y. J. Wang, H. Lin, L. A. Wray, G. Landolt, B. Slomski, J. H. Dil, A. Marcinkova, E. Morosan, Q. Gibson, R. Sankar, F. C. Chou, R. J. Cava, A. Bansil, and M. Z. Hasan, "Observation of a topological crystalline insulator phase and topological phase transition in $Pb_{1-x}Sn_xSe$", Nat. Commun. **3**, 1192 (2012).

[116] B. Bradlyn, L. Elcoro, J. Cano, M. G. Vergniory, Z. Wang, C. Felser, M. I. Aroyo, and B. A. Bernevig, "Topological quantum chemistry", Nature **547**, 298 (2017).

[117] G. H. Wannier, "The structure of electronic excitation levels in insulating crystals", Phys. Rev. **52**, 191 (1937).

[118] G. H. Wannier, "Dynamics of band electrons in electric and magnetic fields", Rev. Mod. Phys. **34**, 645 (1962).

[119] W. Kohn, "Analytic properties of bloch waves and wannier functions", Phys. Rev. **115**, 809 (1959).

[120] W. Kohn, "Theory of the insulating state", Phys. Rev. **133**, A171 (1964).

[121] J. D. Cloizeaux, "Analytical properties of n-dimensional energy bands and wannier functions", Phys. Rev. **135**, A698 (1964).

[122] N. Marzari and D. Vanderbilt, "Maximally localized generalized Wannier functions for composite energy bands", Phys. Rev. B **56**, 12847 (1997).

[123] N. Marzari, A. A. Mostofi, J. R. Yates, I. Souza, and D. Vanderbilt, "Maximally localized wannier functions: theory and applications", Rev. Mod. Phys. **84**, 1419 (2012).

[124] C. Brouder, G. Panati, M. Calandra, C. Mourougane, and N. Marzari, "Exponential localization of wannier functions in insulators", Phys. Rev. Lett. **98**, 046402 (2007).

[125] A. Nelson, T. Neupert, T. Bzdušek, and A. Alexandradinata, "Multicellularity of Delicate Topological Insulators", Phys. Rev. Lett. **126**, 216404 (2021).

[126] A. Nelson, T. Neupert, A. Alexandradinata, and T. Bzdušek, "Delicate topology protected by rotation symmetry: crystalline Hopf insulators and beyond", Phys. Rev. B **106**, 075124 (2022).

[127] J. Zak, "Band representations of space groups", Phys. Rev. B **26**, 3010 (1982).

[128] L. Michel and J. Zak, "Connectivity of energy bands in crystals", Phys. Rev. B **59**, 5998 (1999).

[129] L. Michel and J. Zak, "Elementary energy bands in crystalline solids", EPL **50**, 519 (2000).

[130] J. Cano, B. Bradlyn, Z. Wang, L. Elcoro, M. G. Vergniory, C. Felser, M. I. Aroyo, and B. A. Bernevig, "Building blocks of topological quantum chemistry: elementary band representations", Phys. Rev. B **97**, 035139 (2018).

[131] M. G. Vergniory, L. Elcoro, Z. Wang, J. Cano, C. Felser, M. I. Aroyo, B. A. Bernevig, and B. Bradlyn, "Graph theory data for topological quantum chemistry", Phys. Rev. E **96**, 023310 (2017).

[132] B. Bradlyn, L. Elcoro, M. G. Vergniory, J. Cano, Z. Wang, C. Felser, M. I. Aroyo, and B. A. Bernevig, "Band connectivity for topological quantum chemistry: band structures as a graph theory problem", Phys. Rev. B **97**, 035138 (2018).

[133] H. C. Po, A. Vishwanath, and H. Watanabe, "Symmetry-based indicators of band topology in the 230 space groups", Nat. Commun. **8**, 50 (2017).

[134] Z. Song, T. Zhang, Z. Fang, and C. Fang, "Quantitative mappings between symmetry and topology in solids", Nat. Commun. **9**, 3530 (2018).

[135] E. Khalaf, "Higher-order topological insulators and superconductors protected by inversion symmetry", Phys. Rev. B **97**, 205136 (2018).

[136] J. Kruthoff, J. de Boer, J. van Wezel, C. L. Kane, and R.-J. Slager, "Topological Classification of Crystalline Insulators through Band Structure Combinatorics", Phys. Rev. X **7**, 041069 (2017).

[137] M. G. Vergniory, L. Elcoro, C. Felser, N. Regnault, B. A. Bernevig, and Z. Wang, "A complete catalogue of high-quality topological materials", Nature **566**, 480 (2019).

[138] X. Zhang, H. X. Wang, Z. K. Lin, Y. Tian, B. Xie, M. H. Lu, Y. F. Chen, and J. H. Jiang, "Second-order topology and multidimensional topological transitions in sonic crystals", Nat. Phys. **15**, 582 (2019).

[139] F. Tang, H. C. Po, A. Vishwanath, and X. Wan, "Comprehensive search for topological materials using symmetry indicators", Nature **566**, 486 (2019).

[140] F. Tang, H. C. Po, A. Vishwanath, and X. Wan, "Efficient topological materials discovery using symmetry indicators", Nat. Phys. **15**, 470 (2019).

[141] F. Tang, H. C. Po, A. Vishwanath, and X. Wan, "Topological materials discovery by large-order symmetry indicators", Sci. Adv. **5**, eaau8725 (2019).

[142] C. Fang, M. J. Gilbert, and B. A. Bernevig, "Bulk topological invariants in noninteracting point group symmetric insulators", Phys. Rev. B **86**, 115112 (2012).

[143] L. Fu and C. L. Kane, "Topological insulators with inversion symmetry", Phys. Rev. B **76**, 045302 (2007).

[144] L. Fu and C. L. Kane, "Time reversal polarization and a Z_2 adiabatic spin pump", Phys. Rev. B **74**, 195312 (2006).

[145] T. L. Hughes, E. Prodan, and B. A. Bernevig, "Inversion-symmetric topological insulators", Phys. Rev. B **83**, 245132 (2011).

[146] W. P. Su, J. R. Schrieffer, and A. J. Heeger, "Solitons in polyacetylene", Phys. Rev. Lett. **42**, 1698 (1979).

[147] W. A. Benalcazar, T. Li, and T. L. Hughes, "Quantization of fractional corner charge in C_n-symmetric higher-order topological crystalline insulators", Phys. Rev. B **99**, 245151 (2019).

[148] W. A. Benalcazar, B. A. Bernevig, and T. L. Hughes, "Quantized electric multipole insulators", Science **357**, 61 (2017).

[149] F. Schindler, M. Brzezi ńska, W. A. Benalcazar, M. Iraola, A. Bouhon, S. S. Tsirkin, M. G. Vergniory, and T. Neupert, "Fractional corner charges in spin-orbit coupled crystals", Phys. Rev. Res. **1**, 033074 (2019).

[150] H. Watanabe and S. Ono, "Corner charge and bulk multipole moment in periodic systems", Phys. Rev. B **102**, 165120 (2020).

[151] R. Takahashi, T. Zhang, and S. Murakami, "General corner charge formula in two-dimensional C_n-symmetric higher-order topological insulators", Phys. Rev. B **103**, 205123 (2021).

[152] Y. Fang and J. Cano, "Filling anomaly for general two- and three-dimensional C_4 symmetric lattices", Phys. Rev. B **103**, 165109 (2021).

[153] D. T. Son and B. Z. Spivak, "Chiral anomaly and classical negative magnetoresistance of Weyl metals", Phys. Rev. B **88**, 104412 (2013).

[154] X. Huang, L. Zhao, Y. Long, P. Wang, D. Chen, Z. Yang, H. Liang, M. Xue, H. Weng, Z. Fang, X. Dai, and G. Chen, "Observation of the chiral-anomaly-induced negative magnetoresistance in 3D Weyl semimetal TaAs", Phys. Rev. X **5**, 031023 (2015).

[155] S.-Y. Xu, I. Belopolski, N. Alidoust, M. Neupane, G. Bian, C. Zhang, R. Sankar, G. Chang, Z. Yuan, C.-C. Lee, S.-M. Huang, H. Zheng, J. Ma, D. S. Sanchez, B. Wang, A. Bansil, F. Chou, P. P. Shibayev, H. Lin, S. Jia, and M. Z. Hasan, "Discovery of a Weyl fermion semimetal and topological Fermi arcs", Science **349**, 613 (2015).

[156] B. Q. Lv, H. M. Weng, B. B. Fu, X. P. Wang, H. Miao, J. Ma, P. Richard, X. C. Huang, L. X. Zhao, G. F. Chen, Z. Fang, X. Dai, T. Qian, and H. Ding, "Experimental discovery of Weyl semimetal TaAs", Phys. Rev. X **5**, 031013 (2015).

[157] A. A. Soluyanov, D. Gresch, Z. Wang, Q.-S. Wu, M. Troyer, X. Dai, and B. A. Bernevig, "Type-II Weyl semimetals", Nature **527**, 495 (2015).

[158] S. M. Young, S. Zaheer, J. C. Y. Teo, C. L. Kane, E. J. Mele, and A. M. Rappe, "Dirac semimetal in three dimensions", Phys. Rev. Lett. **108**, 140405 (2012).

[159] B.-J. Yang and N. Nagaosa, "Classification of stable three-dimensional Dirac semimetals with nontrivial topology", Nat. Commun. **5**, 4898 (2014).

[160] Z. K. Liu, B. Zhou, Y. Zhang, Z. J. Wang, H. M. Weng, D. Prabhakaran, S.-K. Mo, Z. X. Shen, Z. Fang, X. Dai, Z. Hussain, and Y. L. Chen, "Discovery of a three-dimensional topological Dirac semimetal Na_3Bi", Science **343**, 864 (2014).

[161] A. A. Burkov, M. D. Hook, and L. Balents, "Topological nodal semimetals", Phys. Rev. B **84**, 235126 (2011).

[162] C. Fang, H. Weng, X. Dai, and Z. Fang, "Topological nodal line semimetals", Chin. Phys. B **25**, 117106 (2016).

[163] R. Yu, Z. Fang, X. Dai, and H. Weng, "Topological nodal line semimetals predicted from first-principles calculations", Front. Phys. **12**, 127202 (2017).

[164] Y. Kim, B. J. Wieder, C. L. Kane, and A. M. Rappe, "Dirac Line Nodes in Inversion-Symmetric Crystals", Phys. Rev. Lett. **115**, 036806 (2015).

[165] Y.-H. Chan, C.-K. Chiu, M. Y. Chou, and A. P. Schnyder, "Ca_3P_2 And other topological semimetals with line nodes and drumhead surface states", Phys. Rev. B **93**, 205132 (2016).

[166] T. Bzdušek, Q.-S. Wu, A. Rüegg, M. Sigrist, and A. A. Soluyanov, "Nodal-chain metals", Nature **538**, 75 (2016).

[167] Z. Yan, R. Bi, H. Shen, L. Lu, S.-C. Zhang, and Z. Wang, "Nodal-link semimetals", Phys. Rev. B **96**, 041103(R) (2017).

[168] R. Bi, Z. Yan, L. Lu, and Z. Wang, "Nodal-knot semimetals", Phys. Rev. B **96**, 201305(R) (2017).

[169] M. Ezawa, "Topological semimetals carrying arbitrary Hopf numbers: Fermi surface topologies of a Hopf link, Solomon's knot, trefoil knot, and other linked nodal varieties", Phys. Rev. B **96**, 041202(R) (2017).

[170] H. Park, W. Gao, X. Zhang, and S. S. Oh, "Nodal lines in momentum space: topological invariants and recent realizations in photonic and other systems", Nanophotonics **11**, 2779 (2022).

[171] Q.-F. Liang, J. Zhou, R. Yu, Z. Wang, and H. Weng, "Node-surface and node-line fermions from nonsymmorphic lattice symmetries", Phys. Rev. B **93**, 085427 (2016).

[172] D. F. Agterberg, P. M. R. Brydon, and C. Timm, "Bogoliubov Fermi surfaces in superconductors with broken time-reversal symmetry", Phys. Rev. Lett. **118**, 127001 (2017).

[173] T. Bzdušek and M. Sigrist, "Robust doubly charged nodal lines and nodal surfaces in centrosymmetric systems", Phys. Rev. B **96**, 155105 (2017).

[174] W. Wu, Y. Liu, S. Li, C. Zhong, Z.-M. Yu, X.-L. Sheng, Y. X. Zhao, and S. A. Yang, "Nodal surface semimetals: theory and material realization", Phys. Rev. B **97**, 115125 (2018).

[175] Z.-M. Yu, W. Wu, Y. X. Zhao, and S. A. Yang, "Circumventing the no-go theorem: A single Weyl point without surface Fermi arcs", Phys. Rev. B **100**, 041118(R) (2019).

[176] B. Bradlyn, J. Cano, Z. Wang, M. G. Vergniory, C. Felser, R. J. Cava, and B. A. Bernevig, "Beyond Dirac and Weyl fermions: Unconventional quasiparticles in conventional crystals", Science **353**, aaf5037 (2016).

[177] B. J. Wieder, Y. Kim, A. M. Rappe, and C. L. Kane, "Double dirac semimetals in three dimensions", Phys. Rev. Lett. **116**, 186402 (2016).

[178] N. B. M. Schröter, S. Stolz, K. Manna, F. de Juan, M. G. Vergniory, J. A. Krieger, D. Pei, T. Schmitt, P. Dudin, T. K. Kim, C. Cacho, B. Bradlyn, H. Borrmann, M. Schmidt, R. Widmer, V. N. Strocov, and C. Felser, "Observation and control of maximal chern numbers in a chiral topological semimetal", Science **369**, 179 (2020).

[179] M. Yao, K. Manna, Q. Yang, A. Fedorov, V. Voroshnin, B. Valentin Schwarze, J. Hornung, S. Chattopadhyay, Z. Sun, S. N. Guin, J. Wosnitza, H. Borrmann, C. Shekhar, N. Kumar, J. Fink, Y. Sun, and C. Felser, "Observation of giant spin-split fermi-arc with maximal chern number in the chiral topological semimetal ptga", Nat. Commun. **11**, 2033 (2020).

[180] Z. Zhu, G. W. Winkler, Q. S. Wu, J. Li, and A. A. Soluyanov, "Triple point topological metals", Phys. Rev. X **6**, 031003 (2016).

[181] J. Kim, H.-S. Kim, and D. Vanderbilt, "Nearly triple nodal point topological phase in half-metallic GdN", Phys. Rev. B **98**, 155122 (2018).

[182] Y. Chen, Y. Xie, Y. Gao, P.-Y. Chang, S. Zhang, and D. Vanderbilt, "Nexus networks in carbon honeycombs", Phys. Rev. Materials **2**, 044205 (2018).

[183] A. Das and S. Pujari, "Topological character of three-dimensional nexus triple point degeneracies", Phys. Rev. B **102**, 235148 (2020).

[184] T. T. Heikkilä and G. E. Volovik, "Nexus and Dirac lines in topological materials", New J. Phys. **17**, 093019 (2015).

[185] T. Hyart and T. T. Heikkilä, "Momentum-space structure of surface states in a topological semimetal with a nexus point of Dirac lines", Phys. Rev. B **93**, 235147 (2016).

[186] H. Weng, C. Fang, Z. Fang, and X. Dai, "Topological semimetals with triply degenerate nodal points in θ-phase tantalum nitride", Phys. Rev. B **93**, 241202(R) (2016).

[187] B. Q. Lv, Z. L. Feng, Q. N. Xu, X. Gao, J. Z. Ma, L. Y. Kong, P. Richard, Y. B. Huang, V. N. Strocov, C. Fang, H. M. Weng, Y. G. Shi, T. Qian, and H. Ding, "Observation of three-component fermions in the topological semimetal molybdenum phosphide", Nature **546**, 627 (2017).

[188] J. Wang, X. Sui, W. Shi, J. Pan, S. Zhang, F. Liu, S.-H. Wei, Q. Yan, and B. Huang, "Prediction of Ideal Topological Semimetals with Triply Degenerate Points in the $NaCu_3Te_2$ Family", Phys. Rev. Lett. **119**, 256402 (2017).

[189] G. Chang, S. Y. Xu, S. M. Huang, D. S. Sanchez, C. H. Hsu, G. Bian, Z. M. Yu, I. Belopolski, N. Alidoust, H. Zheng, T. R. Chang, H. T. Jeng, S. A. Yang, T. Neupert, H. Lin, and M. Z. Hasan, "Nexus fermions in topological symmorphic crystalline metals", Sci. Rep. **7**, 1 (2017).

[190] X. Zhang, Z.-M. Yu, X.-L. Sheng, H. Y. Yang, and S. A. Yang, "Coexistence of four-band nodal rings and triply degenerate nodal points in centrosymmetric metal diborides", Phys. Rev. B **95**, 235116 (2017).

[191] J.-Z. Ma, J.-B. He, Y.-F. Xu, B. Q. Lv, D. Chen, W.-L. Zhu, S. Zhang, L.-Y. Kong, X. Gao, L.-Y. Rong, Y.-B. Huang, P. Richard, C.-Y. Xi, E. S. Choi, Y. Shao, Y.-L. Wang, H.-J. Gao, X. D. Dai, C. Fang, H.-M. Weng, G.-F. Chen, T. Qian, and H. Ding, "Three-component fermions with surface Fermi arcs in tungsten carbide", Nat. Phys. **14**, 349 (2018).

[192] K. Wang, J.-X. Dai, L. B. Shao, S. A. Yang, and Y. X. Zhao, "Boundary criticality of $\mathcal{PT}$-invariant topology and second-order nodal-line semimetals", Phys. Rev. Lett. **125**, 126403 (2020).

[193] C. Fang, Y. Chen, H.-Y. Kee, and L. Fu, "Topological nodal line semimetals with and without spin-orbital coupling", Phys. Rev. B **92**, 081201(R) (2015).

[194] J. Ahn, S. Park, D. Kim, Y. Kim, and B.-J. Yang, "Stiefel-Whitney classes and topological phases in band theory", Chin. Phys. B **28**, 117101 (2019).

[195] E. Lee, R. Kim, J. Ahn, and B.-J. Yang, "Two-dimensional higher-order topology in monolayer graphdiyne", npj Quantum Mater. **5**, 1 (2020).

[196] J. Ahn, S. Park, and B.-J. Yang, "Failure of nielsen-ninomiya theorem and fragile topology in two-dimensional systems with space-time inversion symmetry: application to twisted bilayer graphene at magic angle", Phys. Rev. X **9**, 021013 (2019).

[197] E. Yang, B. Yang, O. You, H.-C. Chan, P. Mao, Q. Guo, S. Ma, L. Xia, D. Fan, Y. Xiang, and S. Zhang, "Observation of non-Abelian nodal links in photonics", Phys. Rev. Lett. **125**, 033901 (2020).

[198] J. Kang and O. Vafek, "Non-Abelian Dirac node braiding and near-degeneracy of correlated phases at odd integer filling in magic-angle twisted bilayer graphene", Phys. Rev. B **102**, 035161 (2020).

[199] J. Ahn, D. Kim, Y. Kim, and B.-J. Yang, "Band topology and linking structure of nodal line semimetals with $\mathbb{Z}_2$ monopole charges", Phys. Rev. Lett. **121**, 106403 (2018).

[200] A. Tiwari and T. Bzdušek, "Non-Abelian topology of nodal-line rings in $\mathcal{PT}$-symmetric systems", Phys. Rev. B **101**, 195130 (2020).

[201] N. D. Mermin, "The topological theory of defects in ordered media", Rev. Mod. Phys. **51**, 591 (1979).

[202] A. Bouhon, T. Bzdušek, and R.-J. Slager, "Geometric approach to fragile topology beyond symmetry indicators", Phys. Rev. B **102**, 115135 (2020).

[203] F. N. Ünal, A. Bouhon, and R.-J. Slager, "Topological Euler class as a dynamical observable in optical lattices", Phys. Rev. Lett. **125**, 053601 (2020).

[204] Z. Wang, B. J. Wieder, J. Li, B. Yan, and B. A. Bernevig, "Higher-order topology, monopole nodal lines, and the origin of large Fermi arcs in transition metal dichalcogenides XTe_2 (X = Mo, W)", Phys. Rev. Lett. **123**, 186401 (2019).

[205] Z. Yang, C.-K. Chiu, C. Fang, and J. Hu, "Jones polynomial and knot transitions in Hermitian and non-Hermitian topological semimetals", Phys. Rev. Lett. **124**, 186402 (2020).

[206] M. Nakahara, *Geometry, topology and physics*, Graduate student series in physics (Hilger, Bristol, 1990).

[207] Y. X. Zhao and Y. Lu, "$\mathcal{PT}$-symmetric real Dirac fermions and semimetals", Phys. Rev. Lett. **118**, 056401 (2017).

[208] S. Park, Y. Hwang, H. C. Choi, and B.-J. Yang, "Topological acoustic triple point", Nat. Commun. **12**, 6781 (2021).

[209] X. Feng, W. Wu, Y. Huang, Z.-M. Yu, and S. A. Yang, "Triply degenerate point in three-dimensional spinless systems", Phys. Rev. B **104**, 115116 (2021).

[210] L. Tian, Y. Liu, W.-W. Yu, X. Zhang, and G. Liu, "Triple degenerate point in three dimensions: theory and realization", Phys. Rev. B **104**, 045137 (2021).

[211] H. Miao, T. T. Zhang, L. Wang, D. Meyers, A. H. Said, Y. L. Wang, Y. G. Shi, H. M. Weng, Z. Fang, and M. P. M. Dean, "Observation of double Weyl phonons in parity-breaking FeSi", Phys. Rev. Lett. **121**, 035302 (2018).

[212] D. Takane, Z. Wang, S. Souma, K. Nakayama, T. Nakamura, H. Oinuma, Y. Nakata, H. Iwasawa, C. Cacho, T. Kim, K. Horiba, H. Kumigashira, T. Takahashi, Y. Ando, and T. Sato, "Observation of chiral fermions with a large topological charge and associated fermi-arc surface states in CoSi", Phys. Rev. Lett. **122**, 076402 (2019).

[213] Z. Rao, H. Li, T. Zhang, S. Tian, C. Li, B. Fu, C. Tang, L. Wang, Z. Li, W. Fan, J. Li, Y. Huang, Z. Liu, Y. Long, C. Fang, H. Weng, Y. Shi, H. Lei, Y. Sun, T. Qian, and H. Ding, "Observation of unconventional chiral fermions with long fermi arcs in CoSi", **567**, 496 (2019).

[214] D. S. Sanchez, I. Belopolski, T. A. Cochran, X. Xu, J.-X. Yin, G. Chang, W. Xie, K. Manna, V. Süß, C.-Y. Huang, N. Alidoust, D. Multer, S. S. Zhang, N. Shumiya, X. Wang, G.-Q. Wang, T.-R. Chang, C. Felser, S.-Y. Xu, S. Jia, H. Lin, and M. Z. Hasan, "Topological chiral crystals with helicoid-arc quantum states", Nature **567**, 500 (2019).

[215] N. B. M. Schröter, D. Pei, M. G. Vergniory, Y. Sun, K. Manna, F. de Juan, J. A. Krieger, V. Süss, M. Schmidt, P. Dudin, B. Bradlyn, T. K. Kim, T. Schmitt, C. Cacho, C. Felser, V. N. Strocov, and Y. Chen, "Chiral topological semimetal with multifold band crossings and long fermi arcs", Nature Physics **15**, 759 (2019).

[216] J. Krempaský, L. Nicolai, M. Gmitra, H. Chen, M. Fanciulli, E. B. Guedes, M. Caputo, M. Radović, V. V. Volobuev, O. Caha, G. Springholz, J. Minár, and J. H. Dil, "Triple-point fermions in ferroelectric gete", Phys. Rev. Lett. **126**, 206403 (2021).

[217] G. P. Mikitik and Y. V. Sharlai, "Band-contact lines in the electron energy spectrum of graphite", Phys. Rev. B **73**, 235112 (2006).

[218] T.-T. Zhang, Z.-M. Yu, W. G. Guo, D. Shi, G. Zhang, and Y. Yao, "From type-II triply degenerate nodal points and three-band nodal rings to type-II Dirac points in centrosymmetric Zirconium Oxide", J. Phys. Chem. Lett. **8**, 5792 (2017).

[219] Y. Xie, J. Cai, J. Kim, P.-Y. Chang, and Y. Chen, "Hopf-chain networks evolved from triple points", Phys. Rev. B **99**, 165147 (2019).

[220] L. Jin, X. Zhang, X. Dai, H. Liu, G. Chen, and G. Liu, "Centrosymmetric Li_2NaN: A superior topological electronic material with critical-type triply degenerate nodal points", J. Mater. Chem. C **7**, 1316 (2019).

[221] L. Jin, X. Zhang, T. He, W. Meng, X. Dai, and G. Liu, "Electronic structure, doping effect and topological signature in realistic intermetallics $Li_{3-x}Na_xM$ ($x = 3, 2, 1, 0$; $M = N, P, As, Sb, Bi$)", Phys. Chem. Chem. Phys. **22**, 5847 (2020).

[222] M. I. Aroyo, J. M. Perez-Mato, D. Orobengoa, E. Tasci, G. De La Flor, and A. Kirov, "Crystallography online: Bilbao Crystallographic server", Bulg. Chem. Commun. **43**, 183 (2011).

[223] M. I. Aroyo, J. M. Perez-Mato, C. Capillas, E. Kroumova, S. Ivantchev, G. Madariaga, A. Kirov, and H. Wondratschek, "Bilbao Crystallographic Server: I. Databases and crystallographic computing programs", Z. Kristallogr. Cryst. Mater. **221**, 15 (2006).

[224] M. I. Aroyo, A. Kirov, C. Capillas, J. M. Perez-Mato, and H. Wondratschek, "Bilbao Crystallographic Server. II. Representations of crystallographic point groups and space groups", Acta Crystallogr. A **62**, 115 (2006).

[225] P. M. Lenggenhager, X. Liu, T. Neupert, and T. Bzdušek, *Data and code for: Triple nodal points characterized by their nodal-line structure in all magnetic space groups*, DOI: 10.3929/ethz-b-000500759, 2022.

[226] D. Gresch, "Identifying topological semimetals", PhD thesis (ETH Zürich, 2017).

[227] E. L. Rees, "Graphical discussion of the roots of a quartic equation", Am. Math. Mon. **29**, 51 (1922).

[228] *Topological materials database*, `https://www.topologicalquantumchemistry.com`.

[229] M. G. Vergniory, B. J. Wieder, L. Elcoro, S. S. P. Parkin, C. Felser, B. A. Bernevig, and N. Regnault, "All topological bands of all stoichiometric materials", Science **376**, eabg9094 (2022).

[230] G. Kresse and J. Furthmüller, "Efficient iterative schemes for ab initio total-energy calculations using a plane-wave basis set", Phys. Rev. B **54**, 11169 (1996).

[231] G. Kresse and D. Joubert, "From ultrasoft pseudopotentials to the projector augmented-wave method", Phys. Rev. B **59**, 1758 (1999).

[232] J. P. Perdew, K. Burke, and M. Ernzerhof, "Generalized gradient approximation made simple", Phys. Rev. Lett. **77**, 3865 (1996).

[233] M. Iraola, J. L. Mañes, B. Bradlyn, M. K. Horton, T. Neupert, M. G. Vergniory, and S. S. Tsirkin, "Irrep: symmetry eigenvalues and irreducible representations of ab initio band structures", Comput. Phys. Commun **272**, 108226 (2022).

[234] D. Vanderbilt, *Berry Phases in Electronic Structure Theory: Electric Polarization, Orbital Magnetization and Topological Insulators* (Cambridge University Press, 2018).

[235] G. Pizzi, V. Vitale, R. Arita, S. Blügel, F. Freimuth, G. Géranton, M. Gibertini, D. Gresch, C. Johnson, T. Koretsune, et al., "Wannier90 as a community code: new features and applications", J. Phys. Condens. Matter **32**, 165902 (2020).

[236] A. A. Soluyanov and D. Vanderbilt, "Computing topological invariants without inversion symmetry", Phys. Rev. B **83**, 235401 (2011).

[237] D. Gresch, G. Autès, O. V. Yazyev, M. Troyer, D. Vanderbilt, B. A. Bernevig, and A. A. Soluyanov, "Z2Pack: Numerical implementation of hybrid wannier centers for identifying topological materials", Phys. Rev. B **95**, 075146 (2017).

[238] P. M. Lenggenhager, X. Liu, T. Neupert, and T. Bzdušek, *Data and code for: Universal higher-order bulk-boundary correspondence of triple nodal points*, DOI: 10.3929/ethz-b-000490611, 2021.

[239] J. Gao, Q. Wu, C. Persson, and Z. Wang, "Irvsp: To obtain irreducible representations of electronic states in the VASP", Comput. Phys. Commun. **261**, 107760 (2021).

[240] D. Varjas, T. Rosdahl, and A. R. Akhmerov, "Qsymm: Algorithmic symmetry finding and symmetric hamiltonian generation", New J. Phys. **20**, 093026 (2018).

[241] Q. Wu, S. Zhang, H.-F. Song, M. Troyer, and A. A. Soluyanov, "WannierTools: An open-source software package for novel topological materials", Comput. Phys. Commun. **224**, 405 (2018).

[242] S. S. Tsirkin, "High performance Wannier interpolation of Berry curvature and related quantities with WannierBerri code", npj Quantum Mater. **7**, 33 (2021).

[243] R. Kubo, "Statistical-mechanical theory of irreversible processes. I. General theory and simple applications to magnetic and conduction problems", J. Phys. Soc. Japan **12**, 570 (1957).

[244] D. A. Greenwood, "The Boltzmann equation in the theory of electrical conduction in metals", Proc. Phys. Soc. **71**, 585 (1958).

[245] S. Barati and S. H. Abedinpour, "Optical conductivity of three and two dimensional topological nodal-line semimetals", Phys. Rev. B **96**, 155150 (2017).

[246] A. Bouhon, A. M. Black-Schaffer, and R.-J. Slager, "Wilson loop approach to fragile topology of split elementary band representations and topological crystalline insulators with time-reversal symmetry", Phys. Rev. B **100**, 195135 (2019).

[247] A. Alexandradinata, J. Höller, C. Wang, H. Cheng, and L. Lu, "Crystallographic splitting theorem for band representations and fragile topological photonic crystals", Phys. Rev. B **102**, 115117 (2020).

[248] J. Noh, W. A. Benalcazar, S. Huang, M. J. Collins, K. P. Chen, T. L. Hughes, and M. C. Rechtsman, "Topological protection of photonic mid-gap defect modes", Nat. Photonics **12**, 408 (2018).

[249] X.-Q. Sun, S.-C. Zhang, and T. Bzdušek, "Conversion rules for Weyl points and nodal lines in topological media", Phys. Rev. Lett. **121**, 106402 (2018).

[250] H.-X. Wang, Z.-K. Lin, B. Jiang, G.-Y. Guo, and J.-H. Jiang, "Higher-Order Weyl Semimetals", Phys. Rev. Lett. **125**, 146401 (2020).

[251] S. A. A. Ghorashi, T. Li, and T. L. Hughes, "Higher-Order Weyl Semimetals", Phys. Rev. Lett. **125**, 266804 (2020).

[252] Q. Wei, X. Zhang, W. Deng, J. Lu, X. Huang, M. Yan, G. Chen, Z. Liu, and S. Jia, "Higher-order topological semimetal in acoustic crystals", Nat. Mater. **20**, 812 (2021).

[253] M. Lin and T. L. Hughes, "Topological quadrupolar semimetals", Phys. Rev. B **98**, 241103(R) (2018).

[254] D. Călugăru, V. Juričić, and B. Roy, "Higher-order topological phases: a general principle of construction", Phys. Rev. B **99**, 1 (2019).

[255] B. J. Wieder, Z. Wang, J. Cano, X. Dai, L. M. Schoop, B. Bradlyn, and B. A. Bernevig, "Strong and fragile topological Dirac semimetals with higher-order Fermi arcs", Nat. Commun. **11**, 627 (2020).

[256] H. Qiu, M. Xiao, F. Zhang, and C. Qiu, "Higher-order dirac sonic crystals", Phys. Rev. Lett. **127**, 146601 (2021).

[257] H. Watanabe and H. C. Po, "Fractional corner charge of sodium chloride", Phys. Rev. X **11**, 041064 (2021).

[258] S. Ren, I. Souza, and D. Vanderbilt, "Quadrupole moments, edge polarizations, and corner charges in the Wannier representation", Phys. Rev. B **103**, 035147 (2021).

[259] K. Persson, *Materials data on Sc_3AlC (SG:221) by Materials Project*, DOI: 10.17188/1207828, Feb. 2016.

[260] A. Jain, S. P. Ong, G. Hautier, W. Chen, W. D. Richards, S. Dacek, S. Cholia, D. Gunter, D. Skinner, G. Ceder, and K. a. Persson, "The materials project: a materials genome approach to accelerating materials innovation", APL Mater. **1**, 011002 (2013).

[261] X. Liu and S. S. Tsirkin, in preparation (2021).

[262] X. Liu, *Code for symmetrizing a wannier90_hr file*, `https://github.com/Liu-Xiaoxiong/symmetrize_wann_matrix`, 2021.

[263] Y.-H. Chan, B. Kilic, M. M. Hirschmann, C.-K. Chiu, L. M. Schoop, D. G. Joshi, and A. P. Schnyder, "Symmetry-enforced band crossings in trigonal materials: accordion states and weyl nodal lines", Phys. Rev. Materials **3**, 124204 (2019).

[264] M. M. Hirschmann, A. Leonhardt, B. Kilic, D. H. Fabini, and A. P. Schnyder, "Symmetry-enforced band crossings in tetragonal materials: Dirac and Weyl degeneracies on points, lines, and planes", Phys. Rev. Materials **5**, 054202 (2021).

[265] A. Leonhardt, M. M. Hirschmann, N. Heinsdorf, X. Wu, D. H. Fabini, and A. P. Schnyder, "Symmetry-enforced topological band crossings in orthorhombic crystals: Classification and materials discovery", Phys. Rev. Materials **5**, 124202 (2021).

[266] J. Yang, C. Fang, and Z.-X. Liu, "Symmetry-protected nodal points and nodal lines in magnetic materials", Phys. Rev. B **103**, 245141 (2021).

[267] B. Jiang, A. Bouhon, Z.-K. Lin, X. Zhou, B. Hou, F. Li, R.-J. Slager, and J.-H. Jiang, "Experimental observation of non-Abelian topological acoustic semimetals and their phase transitions", Nat. Phys. **17**, 1239 (2021).

[268] B. Peng, A. Bouhon, B. Monserrat, and R.-J. Slager, "Phonons as a platform for non-Abelian braiding and its manifestation in layered silicates", Nat. Commun. **13**, 423 (2022).

[269] D. Wang, Y. Wu, Z. Q. Zhang, and C. T. Chan, "Non-Abelian frame charge flow in photonic media", Phys. Rev. X **13**, 021024 (2023).

[270] M. Takeichi, R. Furuta, and S. Murakami, "Morse theory study on the evolution of nodal lines in $\mathcal{PT}$-symmetric nodal-line semimetals", Phys. Rev. B **107**, 085139 (2023).

[271] J. Yu, Y.-A. Chen, and S. Das Sarma, "Euler-obstructed Cooper pairing: Nodal superconductivity and hinge Majorana zero modes", Phys. Rev. B **105**, 104515 (2022).

[272] R. Takahashi and T. Ozawa, "Bulk-edge correspondence of Stiefel-Whitney and euler insulators through the entanglement spectrum and cutting procedure", Phys. Rev. B **108**, 075129 (2023).

[273] G. W. Winkler, S. Singh, and A. A. Soluyanov, "Topology of triple-point metals", Chin. Phys. B **28**, 077303 (2019).

[274] S.-S. Wang, Y. Liu, Z.-M. Y. Yu, X.-L. Sheng, and S. A. Yang, "Hourglass Dirac chain metal in rhenium dioxide", Nat. Commun. **8**, 1844 (2017).

[275] R. Yu, H. Weng, Z. Fang, X. Dai, and X. Hu, "Topological nodal-line semimetal and Dirac semimetal state in antiperovskite Cu_3PdN", Phys. Rev. Lett. **115**, 036807 (2015).

[276] H. Weng, Y. Liang, Q. Xu, R. Yu, Z. Fang, X. Dai, and Y. Kawazoe, "Topological node-line semimetal in three-dimensional graphene networks", Phys. Rev. B **92**, 045108 (2015).

[277] C. Chen, Z. Su, X. Zhang, Z. Chen, and X.-L. Sheng, "From Multiple Nodal Chain to Dirac/Weyl Semimetal and Topological Insulator in Ternary Hexagonal Materials", J. Phys. Chem. C **121**, 28587 (2017).

[278] A. Das, E. Cornfeld, and S. Pujari, "Punctured-Chern topological invariants for semimetallic band structures", Phys. Rev. Lett. **130**, 186202 (2023).

[279] D. Wang, B. Yang, Q. Guo, R.-Y. Zhang, L. Xia, X. Su, W.-J. Chen, J. Han, S. Zhang, and C. T. Chan, "Intrinsic in-plane nodal chain and generalized quaternion charge protected nodal link in photonics", Light Sci. Appl. **10**, 83 (2021).

[280] H. Park, S. Wong, X. Zhang, and S. S. Oh, "Non-abelian charged nodal links in a dielectric photonic crystal", ACS Photonics **8**, 2746 (2021).

[281] D. Wang, B. Yang, M. Wang, R.-Y. Zhang, X. Li, Z. Q. Zhang, S. Zhang, and C. T. Chan, "Observation of non-Abelian charged nodes linking nonadjacent gaps", Phys. Rev. Lett. **129**, 263604 (2022).

[282] Y. Liu, N. Zou, S. Zhao, X. Chen, Y. Xu, and W. Duan, "Ubiquitous topological states of phonons in solids: silicon as a model material", Nano Lett. **22**, 2120 (2022).

[283] M. Wang, S. Liu, Q. Ma, R.-Y. Zhang, D. Wang, Q. Guo, B. Yang, M. Ke, Z. Liu, and C. T. Chan, "Experimental observation of non-Abelian earring nodal links in phononic crystals", Phys. Rev. Lett. **128**, 246601 (2022).

[284] L. Šmejkal, J. Sinova, and T. Jungwirth, "Beyond conventional ferromagnetism and antiferromagnetism: a phase with nonrelativistic spin and crystal rotation symmetry", Phys. Rev. X **12**, 031042 (2022).

[285] L. Šmejkal, A. H. MacDonald, J. Sinova, S. Nakatsuji, and T. Jungwirth, "Anomalous Hall antiferromagnets", Nature Reviews Materials **7**, 482 (2022).

[286] C. He, X. Ni, H. Ge, X.-C. Sun, Y.-B. Chen, M.-H. Lu, X.-P. Liu, and Y.-F. Chen, "Acoustic topological insulator and robust one-way sound transport", Nat. Phys. **12**, 1124 (2016).

[287] R. Süsstrunk and S. D. Huber, "Classification of topological phonons in linear mechanical metamaterials", Proc. Natl. Acad. Sci. U.S.A **113**, E4767 (2016).

[288] D. B. Litvin and W. Opechowski, "Spin groups", Physica **76**, 538 (1974).

[289] D. B. Litvin, "Spin point groups", Acta Crystallogr. A **33**, 279 (1977).

[290] J. Yang, Z.-X. Liu, and C. Fang, "Symmetry invariants of spin space groups in magnetic materials", preprint, arXiv:2105.12738 (2021).

[291] V. A. Toponogov, *Differential Geometry of Curves and Surfaces: A Concise Guide*, edited by V. Y. Rovenski, 1st ed., See Eq. (2.131) on p. 132 (Birkhäuser Boston, MA, 2006).

[292] N. Balazs and A. Voros, "Chaos on the pseudosphere", Phys. Rep. **143**, 109 (1986).

[293] J. W. Cannon, W. J. Floyd, R. Kenyon, and W. R. Parry, in *Flavors of geometry*, Vol. 31, edited by S. Levy (Cambrdige University Press, Cambridge, 1997), pp. 59–159.

[294] U. Leonhardt and T. G. Philbin, "General relativity in electrical engineering", New J. Phys. **8**, 247 (2006).

[295] J. Cserti, "Application of the lattice Green's function for calculating the resistance of an infinite network of resistors", Am. J. Phys. **68**, 896 (2000).

[296] J. Cserti, G. Széchenyi, and G. Dávid, "Uniform tiling with electrical resistors", J. Phys. A Math. Theor. **44**, 215201 (2011).

[297] J. Ningyuan, C. Owens, A. Sommer, D. Schuster, and J. Simon, "Time- and site-resolved dynamics in a topological circuit", Phys. Rev. X **5**, 021031 (2015).

[298] V. V. Albert, L. I. Glazman, and L. Jiang, "Topological properties of linear circuit lattices", Phys. Rev. Lett. **114**, 173902 (2015).

[299] T. Helbig, T. Hofmann, C. H. Lee, R. Thomale, S. Imhof, L. W. Molenkamp, and T. Kiessling, "Band structure engineering and reconstruction in electric circuit networks", Phys. Rev. B **99**, 161114 (2019).

[300] P. M. Lenggenhager, A. Stegmaier, L. K. Upreti, T. Hofmann, T. Helbig, A. Vollhardt, M. Greiter, C. H. Lee, S. Imhof, H. Brand, T. Kießling, I. Boettcher, T. Neupert, R. Thomale, and T. Bzdušek, *Supplementary Movie to Simulating hyperbolic space on a circuit board*, `https://www.nature.com/articles/s41467-022-32042-4#Sec15`, 2022.

[301] M. Conder, *Quotients of triangle groups acting on surfaces of genus 2 to 101*, `https://www.math.auckland.ac.nz/~conder/TriangleGroupQuotients101.txt`, 2007.

[302] F. R. Lux and E. Prodan, "Converging periodic boundary conditions and detection of topological gaps on regular hyperbolic tessellations", Phys. Rev. Lett. **131**, 176603 (2023).

[303] A. Jahn, Z. Zimborás, and J. Eisert, "Central charges of aperiodic holographic tensor-network models", Phys. Rev. A **102**, 042407 (2020).

[304] Z.-R. Liu, C.-B. Hua, T. Peng, and B. Zhou, "Chern insulator in a hyperbolic lattice", Phys. Rev. B **105**, 245301 (2022).

[305] Y.-L. Tao and Y. Xu, "Higher-order topological hyperbolic lattices", Phys. Rev. B **107**, 184201 (2023).

[306] Z.-R. Liu, C.-B. Hua, T. Peng, R. Chen, and B. Zhou, "Higher-order topological insulators in hyperbolic lattices", Phys. Rev. B **107**, 125302 (2023).

[307] D. M. Urwyler, "Hyperbolic topological insulator", 10.13140/RG.2.2.34715.34081, MA thesis (University of Zürich, Switzerland, 2021).

[308] R. Haydock, V. Heine, and M. J. Kelly, "Electronic structure based on the local atomic environment for tight-binding bands", J. Phys. C **5**, 2845 (1972).

[309] J. P. Gaspard and F. Cyrot-Lackmann, "Density of states from moments. application to the impurity band", J. Phys. C **6**, 3077 (1973).

[310] R. Haydock, V. Heine, and M. J. Kelly, "Electronic structure based on the local atomic environment for tight-binding bands. II", J. Phys. C **8**, 2591 (1975).

[311] F. Sausset and G. Tarjus, "Periodic boundary conditions on the pseudosphere", J. Phys. A: Math. Theor. **40**, 12873 (2007).

[312] W. Abikoff, "The uniformization theorem", Am. Math. Mon. **88**, 574 (1981).

[313] C. C. Sims, *Computation with finitely presented groups*, Encyclopedia of Mathematics and its Applications (Cambridge University Press, 1994).

[314] M. Conder and P. Dobcsányi, "Applications and adaptations of the low index subgroups procedure", Math. Comput., 485 (2005).

[315] D. Firth, "An algorithm to find normal subgroups of a finitely presented group, up to a given finite index", PhD thesis (University of Warwick, Coventry, United Kingdom, 2004).

[316] F. Rober, *The GAP package LINS*, `https://github.com/FriedrichRober/LINS`, 2020.

[317] J. Cano and B. Bradlyn, "Band representations and topological quantum chemistry", Annu. Rev. Condens. Matter Phys. **12**, 225 (2020).

[318] P. M. Lenggenhager, J. Maciejko, and T. Bzdušek, *HyperCells: A GAP package for constructing primitive cells and supercells of hyperbolic lattices*, `https://github.com/patrick-lenggenhager/HyperCells`, 2023.

[319] T. Bzdušek and J. Maciejko, "Flat bands and band-touching from real-space topology in hyperbolic lattices", Phys. Rev. B **106**, 155146 (2022).

[320] N. Cheng, F. Serafin, J. McInerney, Z. Rocklin, K. Sun, and X. Mao, "Band theory and boundary modes of high-dimensional representations of infinite hyperbolic lattices", Phys. Rev. Lett. **129**, 088002 (2022).

[321] W. Zhang, H. Yuan, N. Sun, H. Sun, and X. Zhang, "Observation of novel topological states in hyperbolic lattices", Nat. Commun. **13**, 2937 (2022).

[322] W. Zhang, F. Di, X. Zheng, H. Sun, and X. Zhang, "Hyperbolic band topology with non-trivial second chern numbers", Nat. Commun. **14**, 1083 (2023).

[323] Q. Pei, H. Yuan, W. Zhang, and X. Zhang, "Engineering boundary-dominated topological states in defective hyperbolic lattices", Phys. Rev. B **107**, 165145 (2023).

[324] A. Chen, H. Brand, T. Helbig, T. Hofmann, S. Imhof, A. Fritzsche, T. Kießling, A. Stegmaier, L. K. Upreti, T. Neupert, T. Bzdušek, M. Greiter, R. Thomale, and I. Boettcher, "Hyperbolic matter in electrical circuits with tunable complex phases", Nat. Commun. **14**, 622 (2023).

[325] A. Stegmaier, L. K. Upreti, R. Thomale, and I. Boettcher, "Universality of Hofstadter butterflies on hyperbolic lattices", Phys. Rev. B **128**, 166402 (2022).

[326] R. Jackiw and C. Rebbi, "Solitons with fermion number 1/2", Physical Review D **13**, 3398 (1976).

[327] B. A. Bernevig, T. L. Hughes, and S.-C. Zhang, "Quantum spin hall effect and topological phase transition in hgte quantum wells", Science **314**, 1757 (2006).

[328] A. Kitaev, "Anyons in an exactly solved model and beyond", Ann. Phys. **321**, 2 (2006).

[329] S.-C. Zhang and J. Hu, "A four-dimensional generalization of the quantum Hall effect", Science **294**, 823 (2001).

[330] X.-L. Qi, T. L. Hughes, and S.-C. Zhang, "Topological field theory of time-reversal invariant insulators", Phys. Rev. B **78**, 195424 (2008).

[331] R. Miranda, *Algebraic curves and Riemann surfaces* (American Mathematical Society, Providence, 1995).

[332] W. Lück, "Approximating L^2-invariants by their finite-dimensional analogues", Geom. Funct. Anal. **4**, 455 (1994).

[333] *GAP – Groups, Algorithms, and Programming, Version 4.11.1* (2021).

[334] W. Fulton and J. Harris, *Representation theory* (Springer, New York, 1991).

[335] D. J. S. Robinson, *A course in the theory of groups*, 2nd ed. (Springer, New York, 1996).

[336] P. M. Lenggenhager, J. Maciejko, and T. Bzdušek, *HyperBloch: A Mathematica package for hyperbolic tight-binding models and the supercell method*, `https://github.com/patrick-lenggenhager/HyperBloch`, 2023.

[337] O. Derzhko, J. Richter, and M. Maksymenko, "Strongly correlated flat-band systems: the route from Heisenberg spins to Hubbard electrons", Int. J. Mod. Phys. B **29**, 1530007 (2015).

[338] A. E. Brouwer and W. H. Haemers, *Spectra of graphs* (Springer, 2012).

[339] M. Asaduzzaman, S. Catterall, J. Hubisz, R. Nelson, and J. Unmuth-Yockey, "Holography on tessellations of hyperbolic space", Phys. Rev. D **102**, 034511 (2020).

[340] R. C. Brower, C. V. Cogburn, A. L. Fitzpatrick, D. Howarth, and C.-I. Tan, "Lattice setup for quantum field theory in AdS_2", Phys. Rev. D **103**, 094507 (2021).

[341] P. Basteiro, G. D. Giulio, J. Erdmenger, J. Karl, R. Meyer, and Z.-Y. Xian, "Towards explicit discrete holography: Aperiodic spin chains from hyperbolic tilings", SciPost Phys. **13**, 103 (2022).

[342] P. Basteiro, R. N. Das, G. D. Giulio, and J. Erdmenger, "Aperiodic spin chains at the boundary of hyperbolic tilings", preprint, arXiv:2212.11292 (2022).

[343] J. Chen, F. Chen, Y. Yang, L. Yang, Z. Chen, Y. Meng, B. Yan, X. Xi, Z. Zhu, G.-G. Liu, P. P. Shum, H. Chen, R.-G. Cai, R.-Q. Yang, Y. Yang, and Z. Gao, "AdS/CFT correspondence in hyperbolic lattices", preprint, arXiv:2305.04862 (2023).

[344] S. Yu, X. Piao, and N. Park, "Topological hyperbolic lattices", Phys. Rev. Lett. **125**, 053901 (2020).

[345] R. Mosseri, R. Vogeler, and J. Vidal, "Aharonov-Bohm cages, flat bands, and gap labeling in hyperbolic tilings", Phys. Rev. B **106**, 155120 (2022).

[346] G. Harari, M. A. Bandres, Y. Lumer, M. C. Rechtsman, Y. D. Chong, M. Khajavikhan, D. N. Christodoulides, and M. Segev, "Topological insulator laser: Theory", Science **359**, eaar4003 (2018).

[347] M. A. Bandres, S. Wittek, G. Harari, M. Parto, J. Ren, M. Segev, D. N. Christodoulides, and M. Khajavikhan, "Topological insulator laser: Experiments", Science **359**, eaar4005 (2018).

[348] P. Woit, *Lecture notes on Clifford algebras and Spin groups*, `http://www.math.columbia.edu/%7Ewoit/LieGroups-2012/cliffalgsandspingroups.pdf`, accessed on 2022/02/15, 2012.

[349] T. Bzdušek, "Symmetry and topology of nodal semimetals", 10.3929/ethz-b-000216959, PhD thesis (ETH Zürich, 2017).

[350] P. M. Lenggenhager, D. E. Gökmen, Z. Ringel, S. D. Huber, and M. Koch-Janusz, "Optimal renormalization group transformation from information theory", Phys. Rev. X **10**, 011037 (2020).

List of publications and preprints

9. T. Tummuru, A. Chen, **P. M. Lenggenhager**, T. Neupert, J. Maciejko, and T. Bzdušek, "Hyperbolic non-Abelian semimetal", preprint, arXiv:2307.09876 (2023)

8. **P. M. Lenggenhager**, J. Maciejko, and T. Bzdušek, "Non-Abelian hyperbolic band theory from supercells", Phys. Rev. Lett. **131**, 226401 (2023)

7. A. Chen, Y. Guan, **P. M. Lenggenhager**, J. Maciejko, I. Boettcher, and T. Bzdušek, "Symmetry and topology of hyperbolic Haldane models", Phys. Rev. B **108**, 085114 (2023)

6. D. M. Urwyler, **P. M. Lenggenhager**, I. Boettcher, R. Thomale, T. Neupert, and T. Bzdušek, "Hyperbolic topological band insulators", Phys. Rev. Lett. **129**, 246402 (2022)

5. **P. M. Lenggenhager**, X. Liu, T. Neupert, and T. Bzdušek, "Universal higher-order bulk-boundary correspondence of triple nodal points", Phys. Rev. B **106**, 085129 (2022)

4. **P. M. Lenggenhager**, X. Liu, T. Neupert, and T. Bzdušek, "Triple nodal points characterized by their nodal-line structure in all magnetic space groups", Phys. Rev. B **106**, 085128 (2022)

3. **P. M. Lenggenhager**, A. Stegmaier, L. K. Upreti, T. Hofmann, T. Helbig, A. Vollhardt, M. Greiter, C. H. Lee, S. Imhof, H. Brand, T. Kießling, I. Boettcher, T. Neupert, R. Thomale, and T. Bzdušek, "Simulating hyperbolic space on a circuit board", Nat. Commun. **13**, 4373 (2022)

2. **P. M. Lenggenhager**, X. Liu, S. S. Tsirkin, T. Neupert, and T. Bzdušek, "From triple-point materials to multiband nodal links", Phys. Rev. B **103**, L121101 (2021)

1. **P. M. Lenggenhager**, D. E. Gökmen, Z. Ringel, S. D. Huber, and M. Koch-Janusz, "Optimal renormalization group transformation from information theory", Phys. Rev. X **10**, 011037 (2020)

Curriculum vitae

Education

2019 – 2023 **Doctoral Studies in Physics**
Paul Scherrer Institut and ETH Zürich, Switzerland
Associated PhD student at University of Zurich, Switzerland
Advisors: Prof. Dr. Tomáš Bzdušek, Prof. Dr. Manfred Sigrist

2018 – 2019 **Caltech Visiting Student**
Caltech, USA
ETH Master's thesis with Prof. Dr. Gil Refael (see below)

2016 – 2019 **Master of Science ETH in Physics** (with distinction)
ETH Zürich, Switzerland
Thesis: "*Quantum control of dynamically induced topology*"
Advisors: Prof. Dr. Gil Refael, Prof. Dr. Gianni Blatter

2012 – 2015 **Bachelor of Science ETH in Physics**
ETH Zürich, Switzerland
Thesis: "*Low-frequency resonators on superconducting chips*"
Advisors: Dr. Anton Potočnik, Prof. Dr. Andreas Wallraff

Selected Scholarships and Awards

2012 – 2021 Supported by the Swiss Study Foundation

2016 Gold medal at International Young Physicist's Tournament as a team leader of the Swiss team; Ekaterinburg, Russia

2012 Best Matura and best Matura Project
MNG Rämibühl, Zürich, Switzerland

2011 – 2012 Winner of the Swiss Young Physicist's Tournament 2011/12

Outreach

2013 – 2023 Swiss/International Young Physicist's Tournament
Board member of Pro IYPT-CH, coach, and juror

One of the cornerstones of condensed matter physics, the description of wave functions on periodic lattices in terms of energy bands of Bloch states, serves as the unifying thread in this thesis. This description is often referred to as *band theory*. Within its context, topological states of matter and metamaterials have taken shape as key frontiers in recent years. Related to those frontiers, this thesis delves into seemingly distinct areas: multigap topology and lattices in negatively curved space, known as *hyperbolic lattices*. While these two themes may appear disconnected at first, they are intrinsically tied together by concepts such as symmetry, topology, metamaterials, and the ubiquitous role of band theory.